

0830-M-10
0312

NAS 1.55:3096

NASA Conference Publication 3096

16th Space Simulation Conference

*Confirming Spaceworthiness
Into the Next Millennium*

*Proceedings of a conference held at
the Marriott Hotel
Albuquerque, New Mexico
November 5-8, 1990*

NASA

kw

2

16th Space Simulation Conference

*Confirming Spaceworthiness
Into the Next Millennium*

Joseph L. Stecher III, *Editor*
NASA Goddard Space Flight Center
Greenbelt, Maryland

Proceedings of a conference sponsored by the
National Aeronautics and Space Administration, the
Institute of Environmental Sciences, the American
Institute for Aeronautics and Astronautics, and the
American Society for Testing and Materials and held at
the Marriott Hotel
Albuquerque, New Mexico
November 5-8, 1990



National Aeronautics and
Space Administration
Office of Management
Scientific and Technical
Information Division

1991

1

PREFACE

The Sixteenth Space Simulation Conference was held at the Marriott Hotel, Albuquerque, New Mexico, November 5 to 8, 1990. This conference is hosted by the Institute of Environmental Sciences (IES) and supported by the American Institute of Aeronautics and Astronautics (AIAA) and the American Society for Testing and Materials (ASTM). National Aeronautics and Space Administration (NASA) supports the conference by publication of these proceedings.

Confirming Spaceworthiness into the Next Millennium, the theme for this year's conference addressed subjects of continuing interest such as spacecraft testing, dynamic testing, materials, and thermal testing.

Dr. Al Narath, President Sandia National Laboratories, was the guest speaker for the luncheon. There was an informative tour of the Sandia Laboratories which included points of interest such as the National Atomic Museum.

I wish to thank the committee members that made these proceedings possible. My thanks go to Dr. Raymond D. Rempt, Technical Chairman, and the people on his technical committee, Joseph L. Stecher III, Publication Chairman—NASA Goddard Space Flight center, John D. Campbell, IES Meeting Manager, and last but not least, thanks to Janet A. Ehmann, IFS Program Coordinator and her staff for handling all of the details which produced this successful conference.

Richard Hartenbaum
General Chairman

COMMITTEES FOR
16TH SPACE SIMULATION CONFERENCE

MEETING MANAGEMENT COMMITTEE

General Chairman:	Richard Hartenbaum, GE Astro Space Division
Technical Program:	Raymond D. Rempt, Boeing Aerospace Company
IES Meeting Manager:	John D. Campbell, Consultant
Publication Chairman:	Joseph L. Stecher III, NASA Goddard Space Flight Center
Publication Cochairman:	Alda Simpson, NASA Goddard Flight Center
IES Executive Director:	Janet A. Elmann, Institute of Environmental Sciences
IES Program Coordinator:	Vinette N. Kopetz, Institute of Environmental Sciences

TECHNICAL PROGRAM COMMITTEE

Greg Proulx, Hughes Aircraft Company
Paul Forney, Lockheed Palo Alto Research Laboratories
J.D. Glover, Rockwell International Corporation
John W. Harrell, Jet Propulsion Laboratory
Albert R. Lunde, Boeing Aerospace
Rolf Mamen, Canadian Space Agency
Robert P. Parrish, Jr., Martin Marietta Corporation
George F. Wright, Jr., Sandia National Laboratories

JOINT POLICY COMMITTEE

IES

John D. Campbell, Consultant
Joseph L. Stecher, NASA/Goddard Space Flight Center

ASTM

Eugene N. Borson, The Aerospace Corporation
George F. Wright, Jr., Sandia National Laboratories

AIAA

George Mikk, Perkin-Elmer Corporation
Doug McKenney, Boeing Aerospace Company

CONTENTS

SESSION I: SPACECRAFT TESTING

Chairman: John W. Harrell, Jet Propulsion Laboratory

Co-Chairman: Alda Simpson, NASA Goddard Space Flight Center

SOLAR THERMAL VACUUM TESTS OF MAGELLAN SPACECRAFT	1
James C. Neuman, Martin Marietta Astronautics Group	
THE TEST FACILITY REQUIREMENTS FOR THE THERMAL VACUUM THERMAL BALANCE TEST OF THE COSMIC BACKGROUND EXPLORER OBSERVATORY	21
Laura J. Milam, Goddard Space Flight Center	
SCD 02 THERMAL DESIGN	35
Humberto P. Cardoso, Instituto de Pesquisas Espaciais (INPE), Brazil	
SCD1 THERMAL DESIGN AND TEST RESULT ANALYSIS	36
Humberto P. Cardoso, Issamu Muraoka, Marcia B.H. Mantelli, and Rosangela M.G. Leite, Instituto de Pesquisas Espaciais, Brazil	
THERMAL BALANCE TESTING OF THE ANIK-E SPACECRAFT	52
Alex Golob, Cristian Ruel and Marc Donato, SPAR	

SESSION II: PRESSURE EXCHANGE

Chairman: A.R. Lunde, Boeing Aerospace Company

Co-Chairman: J.R. Castle, Spectrolab

AN OUTGASSING MODEL OF NON-METALLIC MATERIALS FOR THE ASCENT OF A TITAN IV LAUNCH VEHICLE	55
R.D. Barrows and S.L. VanLoon, Martin Marietta Astronautics	
THE PERFORMANCE OF MULTILAYER INSULATION IN A RAPIDLY DEPRESSURIZING ENVIRONMENT	56
Ronald A. Efromson, M.I.T., Lincoln Laboratory	
HIGH VACUUM FACILITY FOR HYDRAZINE THRUSTER TESTING	73
Patrick F. Neary, TRW	
FLOW FIELDS OF LOW PRESSURE VENT EXHAUSTS	75
John J. Scialdone, NASA/Goddard Space Flight Center	
MULTIPURPOSE HARDENED SPACECRAFT INSULATION	84
Carlos H. Steimer, TRW	

SESSION III: INFRARED TEST FACILITIES: PART I

Chairman: Paul Forney, Lockheed Palo Alto Research Laboratory

OPTICAL TESTING CRYOGENIC THERMAL VACUUM FACILITY	113
Patrick W. Dohogne and Warren A. Carpenter, CBI Technical Services Co.	
BOEING INFRARED SENSOR (BIRS) CALIBRATION FACILITY	133
John D. Hazen, Boeing Aerospace & Electronics and L.V. Scorsone, Pitt-Des Moines, Inc.	
INFRARED SENSOR TEST METHODOLOGY AND FACILITIES	157
Jere J. Matty, AF/DOTF, and Ronald Dawbarn, Calspan, AEDC	

SESSION IV: INFRARED SENSOR TEST FACILITIES: PART II

Chairman: P. Brinkman, ESA/ESTEC

THERMAL CONTROL FOR THE GROUND SIMULATION OF A SPACE IR SENSOR SYSTEM	179
E. Lee and A. Warren, Grumman Space Systems Division, and G. Gasser and M. Tierney, Itek Optical Systems	
SPECIAL REQUIREMENTS IN THE DESIGN OF A SENSOR TEST AND INTEGRATION LABORATORY	180
S. Bellanca and E. Lee, Grumman Space Systems Division	
IAL SPACE: A TEST LABORATORY FOR THE ISO CRYOGENIC PAYLOAD	181
A. Cucchiaro, M. Henrist, J.P. Macau, N. Ninane, and R. Blanpain, IAL Space	

SESSION V: DYNAMIC TESTING

Chairman: G. Proulx, Hughes Aircraft Company

NON-LINEAR GENERATION OF ACOUSTIC NOISE IN THE I.A.R. SPACECRAFT CHAMBER BY MANUAL OR AUTOMATIC CONTROL	195
R. Westley, K. Nguyen, and M.S. Westley, Institute for Aerospace Research, National Research Council, Canada	
DETAILED MODAL TESTING OF A SOLID ROCKET MOTOR USING A PORTABLE TEST SYSTEM	211
Vladimir Glozman, California State Polytechnic University, and Ralph D. Brillhart, SDRC	
INNOVATIONS IN DYNAMIC TEST RESTRAINT SYSTEMS	227
Christopher J. Fuld, McDonnell Douglas Space Systems Company	

SESSION VI: MATERIAL DEGRADATION IN ORBIT

Chairman: R. Mamen, David Florida Laboratory

Co-Chairman: J.S. Hansen, University of Toronto

ATOMIC OXYGEN EFFECTS ON BORON NITRIDE AND SILICON NITRIDE: A COMPARISON OF GROUND BASED AND SPACE FLIGHT DATA	249
J.B. Cross, Los Alamos National Laboratory, E.H. Lan and C.A. Smith, McDonnell Douglas Space Systems Company, and W.J. Whatley, Sparta, Inc.	
ADVANCES IN ATOMIC OXYGEN SIMULATION	259
J.F. Froechtenigt and Lyle E. Bareiss, Martin Marietta Corporation	
SPACE ENVIRONMENTAL EFFECTS ON SPACECRAFT THERMAL CONTROL COATINGS	266
L.G. Bartosik and H.W. Babel, McDonnell Douglas Space Systems Company	
SPACE SIMULATION TEST FOR THERMAL CONTROL MATERIALS	267
W.R. Hardgrove, TRW	

SESSION VII: FACILITIES

Chairman: J.D. Glover, Rockwell International Corporation

Co-Chairman: C.P. Wright, TRW

SPACE SIMULATION FACILITIES: PROVIDING A STABLE THERMAL VACUUM FACILITY	289
Martin L. Tellalian, CBI	
THE SPACE SIMULATION FACILITIES AT IAL SPACE	314
M. Henrist, A. Cucchiaro, I. Domken, and J.P. Macau, IAL Space	
CONTAMINATION CONTROL PROGRAM FOR THE COSMIC BACKGROUND EXPLORER: AN OVERVIEW	323
Richard Barney, NASA/Goddard Space Flight Center	

SESSION VIII: NEW APPROACHES

Chairman: G.F. Wright, Jr., Sandia National Laboratories

Co-Chairman: R.E. Sheldahl, Sandia National Laboratories

A UNIQUE APPROACH TO SPACE THERMAL SIMULATION	343
D.Q. Durant, McDonnell Douglas Space Systems Company	
THERMAL/VACUUM VS. THERMAL ATMOSPHERIC TESTING OF SPACE FLIGHT ELECTRONIC ASSEMBLIES	344
Mark Gibbel, The Gibbel Corporation	

PROPOSAL FOR A CONCEPTUALLY NEW COMPACT COLLECTING OPTICS FOR POWERFUL LIGHT SOURCES	357
G. Saenger, ESA/ESTEC	

SESSION IX: UNIQUE TESTS AND REQUIREMENTS

Chairman: R.P. Parrish, Jr., Martin Marietta Corporation
Co-Chairman: R.G.D. Chambers, Martin Marietta Corporation

AEOLIAN REMOVAL OF DUST TYPES FROM PHOTOVOLTAIC SURFACES ON MARS	379
James R. Gaier and Marla E. Perez-Davis, NASA/Lewis Research Center, and Mark Marabito, Cleveland State University	
EXPERIMENTAL DETERMINATION OF SATELLITE BOLTED JOINTS THERMAL RESISTANCE	397
Marcia Barbosa Henriques Mantelli and Jose Edson Basto, Brazilian Institute for Space Research	
MAGNETIC CLEANLINESS VERIFICATION APPROACH ON TETHERED SATELLITE	415
Piero Messidoro, Massimo Braghin, and Maurizio Grande, Aeritalia Space Systems Group	
A FLIGHT EXPERIMENT TO DETERMINE GPS PHOTOCHEMICAL CONTAMINATION ACCUMULATION RATES	435
A.C. Tribble and J.W. Haffner, Rockwell International	
SIMULATION OF MARTIAN DUST ACCUMULATION ON SURFACES	447
Marla E. Perez-Davis and James R. Gaier, NASA/Lewis Research Center; Robert Kress, University of Akron; and Justus Grimalda, M.I.T.	
TRANSFER ORBIT STAGE MECHANISMS THERMAL VACUUM TEST	457
Scott T. O'Leary, Martin Marietta Astronautics Group	

SESSION X: PANEL DISCUSSION

Moderator: E.H. Borson, The Aerospace Corporation

SESSION I

SPACECRAFT TESTING

SOLAR THERMAL VACUUM TESTS OF MAGELLAN SPACECRAFT*

**James C. Neuman
Martin Marietta Astronautics Group**

ABSTRACT

The Magellan solar/thermal/vacuum test involved a number of unique requirements and approaches. Because of the need to operate in orbit around Venus, the solar intensity requirement ranged up to 2.3 "suns" or Earth-equivalent solar constants. Extensive modifications to the solar simulator portion of the test facility were required to achieve this solar intensity. Venus albedo and infrared emission were simulated using temperature-controlled movable louver panels to allow the spacecraft to a view either a selectable-temperature black heat source with closed louvers, or the chamber coldwall behind open louvers. The spacecraft was mounted on an insulated hydraulically-actuated turntable/tilt-beam gimbal fixture to accommodate several positions relative to the solar beam and albedo simulator. Innovative methods were used to tilt both the gimbal fixture and the solar simulator mirror to maximize spacecraft illumination coverage in the solar beam.

The test conditions included widely varying solar intensities, multiple sun angles to the spacecraft, alternate (redundant) hardware configurations, steady-state and transient cases, and cruise and orbital power profiles. "Margin" testing was also performed, wherein supplemental heaters were mounted to internal thermal blankets to verify spacecraft performance at higher-than-expected temperatures. The test was highly successful, uncovering some spacecraft anomalies and verifying the thermal design. The test support equipment experienced some anomalous behavior and a significant failure during the test. Analytical temperature predictions compared favorably with test results with a few notable exceptions.

INTRODUCTION

The Magellan spacecraft is a three axis stabilized, fine pointing, fully redundant radar carrier using stellar inertial references and reaction wheel torquing. The overall dimensions of the spacecraft are 6.3m by 9.1m. The spacecraft was provided by Martin Marietta under contract to the Jet Propulsion Laboratory.

* This report was prepared for the Jet Propulsion Laboratory, California Institute of Technology, sponsored by the National Aeronautics and Space Administration.

The 3.7-meter diameter parabolic high gain antenna (HGA) dominates the forward end of the spacecraft, used for radar data taking at S-Band and for playback to Earth at X-band. Medium gain and low gain links are also provided.

The radar electronics, telecommunications equipment, batteries and attitude control system are housed in the forward equipment module adjacent to the antenna. The command and data system, power system and attitude control electronics are located in the decagonal Voyager bus structure.

The power system is a direct energy transfer type which provides 28 Vdc and 2.4 kHz inverted power using 2 each 3 by 3 meter solar panels and two NiCad batteries. The solar panels (not used in STV test) are partially populated with optical solar reflectors to reduce panel temperatures. The command and data system is a multi-processor design which is a modification to the Galileo spare unit. The propulsion system includes a solid rocket motor for Venus orbit insertion (not used in STV test) and a mono-propellant system (dry for STV test) for midcourse corrections, thrust vector control and reaction wheel desaturation. The spacecraft test configuration is shown in Figure 1.

The Magellan mission launched a single spacecraft to Venus in May 1989. The mission design includes the use of a Type IV Earth-Venus transfer trajectory. This results in the spacecraft traversing a heliocentric angle of slightly greater than 540° during cruise. This particular trajectory was selected because of the timing of its availability, its relatively low Earth escape energy requirement and its moderate approach velocity at Venus, which made the mission possible with the Space Shuttle Atlantis and the Inertial Upper Stage (IUS).

Magellan will be placed in a near polar elliptical orbit with a periapsis altitude of 250 km. The spacecraft will map 25 km swaths from the North Pole to 74° South latitude. The orbit period of 3.15 hours will result in an East West displacement of each successive swath, due to Venus rotation, of about 18 km, thus assuring continuity of the coverage. Coverage of the planet above 74° South latitude is achieved in one Venus rotation of 243 Earth days.

Mapping begins over the North Pole, continues through periapsis, and lasts for 37.2 minutes. During mapping and data recording, the spacecraft points the HGA to the left, looking in the direction of orbital motion. The look-angle (the angle between the local vertical and the HGA boresight direction) is varied with altitude in the elliptical orbit, to optimize the radar performance. After each mapping pass, the spacecraft turns and points the HGA at Earth for playback of the recorded mapping data.

The playback is accomplished in two intervals separated by a star calibration (STARCALS) near apoapsis. During the STARCAL, the spacecraft gyros are recalibrated with reference to the star scanner to assure that the HGA pointing during the next mapping swath will meet the radar pointing requirements.¹

Several of these mission scenarios were simulated in the STV test. This paper contains a description of the test objectives, the facility and configuration (including the modifications required to accommodate the spacecraft), the timeline, the test execution and the test results, concluding with some lessons learned.

TEST OBJECTIVES

The objectives of the Magellan Solar Thermal Vacuum (STV) Test were as follows:

1. a. Provide data for the validation of the Magellan thermal math models.
b. Verify thermal subsystem performance.
2. Demonstrate integrated system performance at cold and hot ("margin") temperature levels.

In addition to the formal objectives, the following special requirements were to be implemented:

1. Provide an appropriate thermal environment for characterization of spacecraft systems such as radar performance testing, articulation mechanism functional testing, and radio performance testing.
2. Provide for shunted power adjustments to validate shunt radiator thermal design and workmanship and provide testing to satisfy protoflight testing criteria.

No system-level thermal cycling tests were explicitly required. However, the cycling which occurred as a result of varying test conditions, margin testing and mapping orbital simulations provided system-level workmanship confidence to supplement component- and subsystem-level thermal cycling tests.

TEST FACILITY 2, 3, 4

The test facility was located in the Space Simulation Laboratory, Martin Marietta Astronautics Group, near Denver, Colorado. The Magellan test used the 8.8m dia X 19.8m high (29'X65') chamber configuration, the solar simulator modified to produce 2.3 suns intensity, and portions of the thermal environment simulator to form the albedo simulator.

TEST CONFIGURATION

The Magellan (MGN) spacecraft is a protoflight vehicle and therefore actual flight hardware was used in the test configuration, with the following exceptions:

1. No solar array panels. Simulated by temperature-controlled aluminum structure supporting the sun sensor units.
2. The hydrazine tank was dry with pad pressure to maximize response rates.
3. Test batteries installed (identical to flight batteries).

Magellan's size and the requirement to illuminate both its long axis and its transverse axis with the solar beam introduced the need to tilt both the gimbal and the solar mirror. The gimbal tilt was constant throughout the test and was accomplished by constructing an adapter with the required tilt. The adapter picked up three of the four mounting hardpoints in the chamber floor and accommodated the gimbal's four mounting legs. Stress and dynamic analysis verified the capability of the tilted gimbal structure to withstand the off-nominal loading. The gimbal tilt and spacecraft position envelopes are shown in Figure 2.

The solar mirror tilt was accomplished by installing longer suspension turnbuckles in the secondary support structure. Since the mirror was supported primarily by a single-axis beam which could be rotated, turnbuckle adjustments could be used to tilt the mirror. The solar mirror tilt was not constant during the test, requiring a -2° mechanical tilt (-4° solar incidence angle) for cases 1 and 2 where sun directly along the MGN +Z axis was required, and $+2^\circ$ (mechanical) for the remaining cases when sun perpendicular to the +Z axis was required. The mirror could not be repositioned while under vacuum, thereby necessitating a return to ambient conditions between cases 2 and 3. Figure 3 shows the unusual resulting geometries for the various test cases. The net result of the gimbal and mirror tilts was a nearly complete illumination of the entire spacecraft, with only a small crescent-

shaped portion of the HGA plus two Rocket Engine Modules (REM) and a sun sensor outside the beam in cases 1 and 2, and only the extreme tip of the HGA outside the beam in cases 4-13.

Venus albedo (reflected sunlight) is as high as 78%. When combined with a 2-"sun" solar intensity, over 1.5 "suns" of additional sunlight can be expected in the Magellan mission. This energy could not be applied to the test configuration in the solar spectrum since only one sun source was available. An albedo simulator was therefore constructed to provide additional energy to the spacecraft. The albedo simulator used 18 existing temperature-controlled 1.8m X 1.8m louver panels, each with eight louver blades, mounted in a new frame to provide a known infrared (IR) heat source. The louvers could be opened to allow the spacecraft to view liquid-nitrogen-cooled shrouds, or closed and heated to simulate Venus albedo and planetary IR emissions. The location was chosen as representative since Venus albedo can be incident from virtually any angle in the actual mission. The albedo simulator was also available for emergency safing (warming of the chamber environment) in case of a long-term solar simulator failure. The albedo simulator is depicted in Figure 4.

Redundant guard heaters were used to null heat loss to the gimbal and cable bundle. Heaters were also used to simulate the presence of the solar panels, which were omitted due to their prohibitive size, for sun sensor and solar array drive motor conductive environments. Cabling was routed through the insulated aft end of the spacecraft, and was insulated and guard-heated. Guard heaters totalled 630 Watts in seven zones (1260 Watts for both redundant sets).

An additional set of test heaters was installed within the spacecraft to provide artificial heating for higher-than-expected temperature testing of the complete spacecraft. This testing was referred to as "margin" testing since its purpose was to evaluate system performance at elevated temperatures, thereby demonstrating "margin" above expected levels. The non-redundant margin heaters were attached to large interior insulation blankets such that blanket emittance was not compromised, and were controlled with dedicated thermocouples including an autonomous overtemperature kill capability. A total of 5500 Watts were provided in eight zones.

Test instrumentation consisted of 372 type E thermocouples placed to provide information for component temperature requirements compliance, thermostat function, external heat flux level, and thermal math model correlation. Each thermocouple was bonded to its substrate material. Additionally, 84 flight temperature sensors (platinum resistors) were available for comparison to and supplementation of the test thermocouples. A further 26 flight sensors became available when the spacecraft's radar was active. The data were displayed, printed, and plotted realtime and were stored on magnetic tape for post-test processing.

TIMELINE

The test timeline was established after consideration of a number of factors, primarily driven by the desire to maximize the variety of conditions and to envelope the extreme conditions. Since the spacecraft is designed to operate under continuous motion while mapping Venus, consideration was given to duplicating this motion on the gimbal structure while operating the radar in synchronization. However, because of constraints due to physical envelope in the chamber, and in an attempt to minimize unnecessary test complexity, a series of fixed attitudes was chosen instead. The criteria used to select the test cases were as follows:

1. Include at least one situation where two successive cases are identical with the exception of a substantial change in solar intensity (used to determine sensitivity to solar absorptivity).
2. Provide several "pure" transients to correlate thermal capacitance of the spacecraft; "pure" transients are those where a minimum of step changes are made to the environment or the spacecraft power state (preferably only one).
3. Provide six days vacuum before radar power-up as requested by Hughes Aircraft (HAC), the radar contractor.
4. Include at least one transient eclipse case.
5. Place the sun on the spacecraft faces containing the most thermally sensitive equipment.
6. Provide for integrated system performance testing at hot and cold conditions.
7. Provide for special component performance testing of tape recorders, radios, star scanner, and shunt radiators.

Thirteen planned test cases resulted from these criteria and the test objectives. Figure 3 depicts the various spacecraft attitudes for each of the 13 test cases. Each case is described in the following paragraphs:

- Case 1 The intent of this case was to simulate the cold thermal design point for the majority of the spacecraft heaters and thermostats. Since the HGA effectively shadows most of the spacecraft, a near-Earth (1.0 solar constant) HGA-to-sun attitude presents the coldest possible cruise conditions for most components and therefore, the cold thermal design

case. In order to establish the acceptability of heater sizes and thermostat setpoints, it was important to achieve thermal stabilization under these cold conditions.

During this case the albedo simulator was in its cold configuration, with louvers open and heaters inactive. The chamber solar mirror position for this case was at -2° tilt to provide a true HGA-to-sun attitude due to the off-center positioning of the gimbal. Initially, all thermal components were enabled such that heater activity occurred on the primary string. After stabilization, the primary string was disabled such that heater activity occurred on the secondary string. Since the secondary string of heaters operates at a lower temperature setpoint than the primary string, the disabling of the primary string, combined with a duty cycle evaluation, could be used to infer heater design margin. A maximum duty cycle of 80% on the secondary string was required. The power state of the spacecraft during the stabilization was the nominal cruise state on "A" side components.

Since this case represented the cold case for many components, it also provided appropriate conditions for verification of integrated system performance at minimum expected temperatures. During cases 1 and 2, identification of any required thermal design changes was a high priority. This was necessary so that any changes could be implemented during chamber return to ambient after case 2.

- Case 2 The intent of this case was to provide a steady state hot case for the HGA area. This case verified that solar focusing by the parabolic HGA onto the subreflector was thermally acceptable. In attitude, in albedo simulator configuration, and in power state, case 2 was identical to the stabilization portion of case 1. Primary heaters were enabled to minimize warmup time in anticipation of return to ambient conditions. The solar intensity, however, was increased to 2.3 suns to provide maximum heating to the HGA. Due to relatively low mass/area ratios in the HGA componentry, stabilization would be reached sooner than in the remainder of the spacecraft, so this case was a transient case (meaning lack of stabilization at equilibrium for the majority of the components).

At this point, the chamber was returned to ambient conditions, the lid removed and solar mirror recon-

figured to +2° mechanical tilt for the remainder of the test. Inspection of the spacecraft was performed. The spacecraft was also repositioned as discussed in case 3. The lid was replaced and the chamber returned to vacuum conditions. This time-point started the 6-day clock while the radar was to remain powered off. All thermal components were enabled for the remainder of the solar thermal vacuum testing.

- Case 3 The intent of this case was to simulate worst-case solar exposure to the bay 3 and 4 area. This condition is prevalent during the playback portion of some mapping orbits. The reason for the 20° off-point from true +Y-to-sun was to avoid pointing the star scanner boresight directly at the sun. Full near-Venus solar intensity of 2.3 suns (1.94 suns expected plus 20% margin) was selected. The albedo simulator was in its hot configuration with louvers closed and heaters active (temperature controlled to -59°C) to simulate Venus albedo (239 mW/cm², 199 expected +20% margin) considering appropriate wavelength conversions.

The vehicle power state was: radar turned completely off, radios in playback mode as if radar data were being transmitted and tape recorders in standby mode. Case 3 was a steady state case, where stabilization was required for math model correlation purposes. Time was allocated after stabilization for system performance evaluation, during which time the battery reconditioning circuits were tested.

At this point, the spacecraft was repositioned to point the +X face towards the sun. The repositioning was performed under vacuum conditions and involved a 20° pitch-down rotation and a 90° roll. During the repositioning, the sun was dowsed to prevent the possibility of excessive solar loading on the low gain antenna as it passed through the concentrated beam above the solar snout. The albedo simulator remained active (louvers closed, -59°C).

- Case 4 The intent of this case was to begin a series of solar exposures to the radar area for math model correlation purposes. The solar intensity was set at 1.0 equivalent sun, the albedo simulator was active with its louvers closed and its temperature set to -59°C. This was a stabilization case for correlation purposes and to establish a known initial condition

for later transient exposure. System performance evaluation time was not allocated here as it would invalidate the equilibrium condition established.

- Case 5 This case was intended to provide a "pure" transient condition for math model correlation purposes. The case was identical to case 4 except for a step increase of solar intensity from 1.0 to 1.6 suns. This case established thermal control subsystem response to infer sensitivity to surface solar absorptivity.
- Case 6 The intent of case 6 was to establish a known equilibrium condition with the radar powered in standby mode, in order to reach approximate mapping temperatures prior to the first mapping sequence in case 7. The radar could now be powered up because six days had elapsed since pump down. Therefore, this case was essentially a continuation of case 5, except for radar power up.
- Case 7 This case represented a hot mapping transient orbit at Venus. An orbital component power profile was simulated with the radar cycling from map to standby to map, tape recorders cycling from record to playback to record, and radios cycling on and off in mapping mode. Repetitive orbital simulations of 3.15 hours each, back-to-back, were conducted until a pseudo-steady state condition was established. The vehicle attitude did not change; the sun was constantly positioned normal to the +X side of the spacecraft. The solar intensity remained at 1.6 suns and the albedo simulator remained active (louvers closed, heated to -59°C).
- Case 8 This case was intended to drive +X side components above flight allowable levels by activating supplemental test heaters. The case was identical to case 7, except the power to the internal supplemental margin heaters was increased until the first component in each of eight zones reached approximately its previous test level less 5°C at the hottest point in the orbital cycle. At this point, system performance was evaluated at elevated temperatures. The goal was that a minimum of four simulated orbits (12.6 hours) be spent at elevated temperatures.
- Case 9 This case simulated an eclipse event. It was intended primarily for math model correlation purposes as the duration exceeded flight requirements. The environment was modified by dowsing the

solar simulator and powering the albedo simulator off (louvers open) at the cold point in the cyclic orbital simulation. The power state was maintained in playback mode for a constant dissipation over the length of the eclipse. Spacecraft power was supplied by the on-board batteries. In order to maximize information for math model correlation, the length of the eclipse was not preset. The eclipse was terminated when the battery depth-of-discharge (DOD) reached 80%.

At this point, the spacecraft was repositioned to point the -X face towards the sun. The repositioning was performed under vacuum conditions and involved a 180° roll. During the repositioning, the albedo simulator was active (louvers closed, -59°C) and the sun was dowsed.

- Case 10 This case was equivalent to case 6 in that it was a preparatory equilibrium case for the mapping case to follow. The environment was identical to case 6 except for the attitude change to -X-to-sun and a solar intensity reduction to 1.0 sun. The power state was identical except that "B" side components were powered rather than "A" side for case 6. Finally, the radar was powered to standby. Spacecraft batteries experienced recharging early in this case as a result of the case 9 discharging.
- Case 11 This case was functionally similar to case 7, with repetitive 3.15 hour back-to-back orbital simulations. The attitude (-X-to-sun), sun intensity (1.0) and powered components ("B" side) were the operative differences between cases 11 and 7, all other aspects being identical. Again, as in case 7, repetitive orbital simulations were planned until pseudo-steady state conditions were achieved.
- Case 12 This case was similar to case 8, representing another margin test, this time to force the -X components beyond flight allowable levels. The same margin heaters were used, with the same philosophy as case 8, to achieve elevated temperatures. Environmentally and electrically, it was to be a continuation of case 11, except the margin heaters were activated. System performance was again evaluated as elevated temperatures were achieved. The goal was that a minimum of four simulated orbits (12.6 hours) be spent at elevated temperatures.
- Case 13 The last case was functionally similar to case 9 in simulating another eclipse. The environment was

modified as in case 9 (dowse sun, albedo simulator off), a constant playback mode was selected, batteries supplied spacecraft power, and duration was determined by battery DOD.

Following case 13, the chamber was returned to ambient conditions and the spacecraft was inspected and found to be in excellent condition.

TEST EXECUTION

The test was executed nearly according to plan. Pumpdown was initiated at 1900 GMT, 8 July 1988. Case 1 began at 08:35 GMT, 9 July 1988. Stabilization was reached at 12:30 GMT, 11 July at which time primary heaters were deactivated, allowing secondary heaters to control. Primary heaters were reactivated at 01:50, 12 July. At 05:51, 12 July, all solar illumination was lost when a lamp exploded, damaging a second lamp in the process and shutting down the solar simulator. The albedo simulator was immediately closed and warmed to save the spacecraft while repairs were undertaken. Solar was restored at 10:35, 12 July, and testing resumed with no detrimental effects on the spacecraft. At 02:12, 13 July, case 2 began with a step increase in solar intensity to 2.3 suns. Case 2 completed with HGA stabilization at 06:45, 13 July. Repressurization was complete at 00:52, 14 July.

Spacecraft inspection revealed several areas where closeout tape had become debonded. These areas were reworked. The sun sensors were removed since their extreme thermal environments had been experienced. A loose thermocouple wire was discovered to be interfering with louver operation (detected in test data in case 1) and was rebonded. The mirror tilt was adjusted and the spacecraft was repositioned for case 3.

The second pumpdown began 09:00 GMT, 15 July. Case 3 began 01:26, 16 July, and was completed without anomaly at 18:18, 17 July. The spacecraft was repositioned under vacuum and case 4 began at 20:00, 17 July. At 13:50, 18 July, the gimbal tilt was detected to be 4.3° too large and was corrected, while efforts began to understand the cause of the error. During this case the sunside spacecraft/gimbal adapter guard heaters ceased to operate as solar illumination warmed the normally heated spacecraft-gimbal interface. Temperatures did not rise substantially over the control setpoints, so near zero heat transfer was nearly maintained. Case 4 was completed and case 5 initiated at 20:14, 19 July, with a step change of solar intensity from 1.0 to 1.6 suns.

During case 5, the adapter temperature increased with the higher illumination, and the spacecraft began receiving conducted heat from this source. Although not desirable, the additional heat

could be accounted for in post-test analysis and correlation. Also during this case, the sunlit rocket engine modules (REM) unexpectedly reached flight allowable temperatures. Case 5 ended at 13:10, 21 July, and case 6 immediately began with radar power-on. Case 6 stabilization was reached at 22:52, 22 July.

Case 7 began repetitive mapping orbits for the first time in prelaunch testing. A minor water leak in the solar dowsers cooling was detected and the water circuit was shut off (unnecessary unless dowsers are closed). The gimbal tilt beam slipped again, this time 11°, at 13:51, 23 July, and the hydraulic fluid level was observed to be low. Replenishment of fluid cured the mysterious gimbal movements. During case 7, unexpected noise in radar data was detected. Case 7 was completed at 15:43, 24 July, after 13 consecutive successful orbits.

At 15:59, case 8 began with the turnon of the margin heaters while mapping continued. The heaters were adjusted over the next seven orbits to maximize the number of components reaching their previous (component or subsystem) test temperatures less 5°C. The first of four stabilized orbits was begun with orbit number 21 at 15:44, 25 July. The 24th orbit and case 8 were completed at 04:24, 26 July.

Case 9, the first intentional eclipse case, began at 04:34 with solar system shutdown. Eighty percent (80%) DOD on batteries was reached at 07:22 signaling the end of case 9. Spacecraft repositioning for the remaining cases was then accomplished.

At this point a significant deviation from the pretest plan was made: since the spacecraft was still at elevated temperatures from case 8 margin testing, it was decided to perform the case 12 margin testing out of sequence for schedule considerations. Case 12 began at 07:44, 26 July. Case 12 was completed nominally at 09:45, 27 July, and about 13 hours of radio subsystem characterization testing was accomplished before the start of case 10 at 22:55, 27 July. Case 10 was completed without anomaly at 18:30, 29 July, and case 11 began immediately. During case 11, the radar noise was correlated to propulsion line heater activity. Stabilization was reached at 17:51, 30 July, after six mapping orbits and the second eclipse (case 13) was initiated with termination at 80% DOD at 20:25, 30 July. Upon completion of the 13 thermal cases essentially on schedule, star scanner, radar and radio characterization testing was undertaken. Repressurization was begun at 18:04, 31 July, and ambient conditions were reached at 00:18, 1 August 1988.

RESULTS

The test met all thermal objectives and requirements. The spacecraft overall thermal balance was as expected, falling within about 5°C of predictions in all cases, with several local exceptions:

1. The HGA temperatures were 10° to 20°C low compared to predictions, discounting the area of the HGA which was not fully illuminated. This error was attributed to the need to instrument large curved areas with thermocouples which can only measure local temperatures. Since math models predict average temperatures over the large area, substantial errors can be expected without detailed local modeling of the actual thermocouple position. No action was taken since temperatures remained within allowable limits.
2. A portion of the radio experienced colder-than-expected temperatures (about 9°C low). This was attributed to an undersized heater and a faulty thermostat placement controlling the heater; a heater size increase and thermostat relocation later corrected the problem.
3. The heater for one of the tape recorders was slightly undersized. No action was taken as test conditions were deemed significantly colder than expected flight conditions. Flight temperatures have remained nominal.
4. The radar baseplate temperature gradients were larger than expected, requiring that the heater setpoints be adjusted up 6°C to ensure all parts of the radar remain within allowable temperature limits.
5. A sun sensor thermostat appeared to "dither" or cycle rapidly with a small deadband. Later analysis proved this indication to be faulty, caused by relative locations of heater, thermostats, and thermocouple on a low-conductivity thin plate.
6. The propulsion lines were about 15°C warmer than expected. This discrepancy was later traced to a difference in temperature sensor location between preliminary design and as-built position, plus an area error in math modeling.
7. The Rocket Engine Modules exceeded expected values by as much as 20°C. Later analysis identified the probable cause as solar entrapment in the engine catalyst bed thermal standoff. A hardware modification was made to

shield the area from sunlight, but no retest was performed due to lack of available test hardware. Flight experience has shown that the anomaly was not corrected by the modification, and the REMs continue to operate above expected temperatures.

8. The electronics bus temperature gradients were about 4°C larger than expected. The math model was corrected.
9. The white paint on four solar array holddown structures did not adhere. They were cleaned and repainted after STV test.
10. An S-Band transmitter failed immediately after STV test; chip capacitors were diagnosed as having been overstressed during earlier component testing and were replaced.
11. The radar noise/heater cycling anomaly was later determined to be a propulsion line heater damaged in installation and shorted to structure. It was replaced post-test.

Figure 5 shows representative test data compared with math model results. In this figure the electronics bus is "unrolled" and bay numbers are indicated on the abscissa.

CONCLUSIONS

The Magellan STV test was an unqualified success, demonstrating thermal subsystem performance, evaluating system integrated performance at extreme temperatures, and providing necessary data for math model validation. It was also successful in uncovering several workmanship, analytical and design errors whose effects would have ranged from minor to substantial in flight. It was not successful in identifying one major design flaw (REM), primarily because the test was designed to evaluate the integrated system, not necessarily previously tested subsystems. The REMs had been tested as a subsystem, but not under solar simulation.

The STV test also employed innovative solutions to minimize costs under stringent physical constraints in the test facility.

Among the lessons learned from the Magellan test include:

1. System-level thermal balance testing should be required for new hardware designs. Solar simulation should also be a requirement whenever feasible.

2. Careful attention should be paid to conductive and radiative interfaces with facilities to minimize effects which could compromise test results.
3. Thermal design modifications should be verified by test to ensure successful problem resolution.

REFERENCES

1. Brown, Charles D. and Parker, Gary L.: The 1989 Magellan Mission to Venus, International Astronautical Federation Paper IAF-87-444, October 6, 1987.
2. Parrish, Robert P.: Performance and Operating Characteristics of a 4.88-M Diameter Solar Simulator for Viking Space Simulation Tests, NASA SP-379, 1975, pp. 409-418.
3. Parrish, Robert, P.: P78-2 (SCATHA) Satellite Thermal Balance Test - A Laboratory Test, Proceedings of the 11th Space Simulation Conference, NASA Conference Publication 2150, 1980, pp. 298-304.
5. Storrs, Hal B.: Development of a Thermal Environment Simulator for Large Test Articles in a Vacuum, Proceedings of the 13th Space Simulation Conference, NASA Conference Publication 2340, 1984, pp. 1-7.

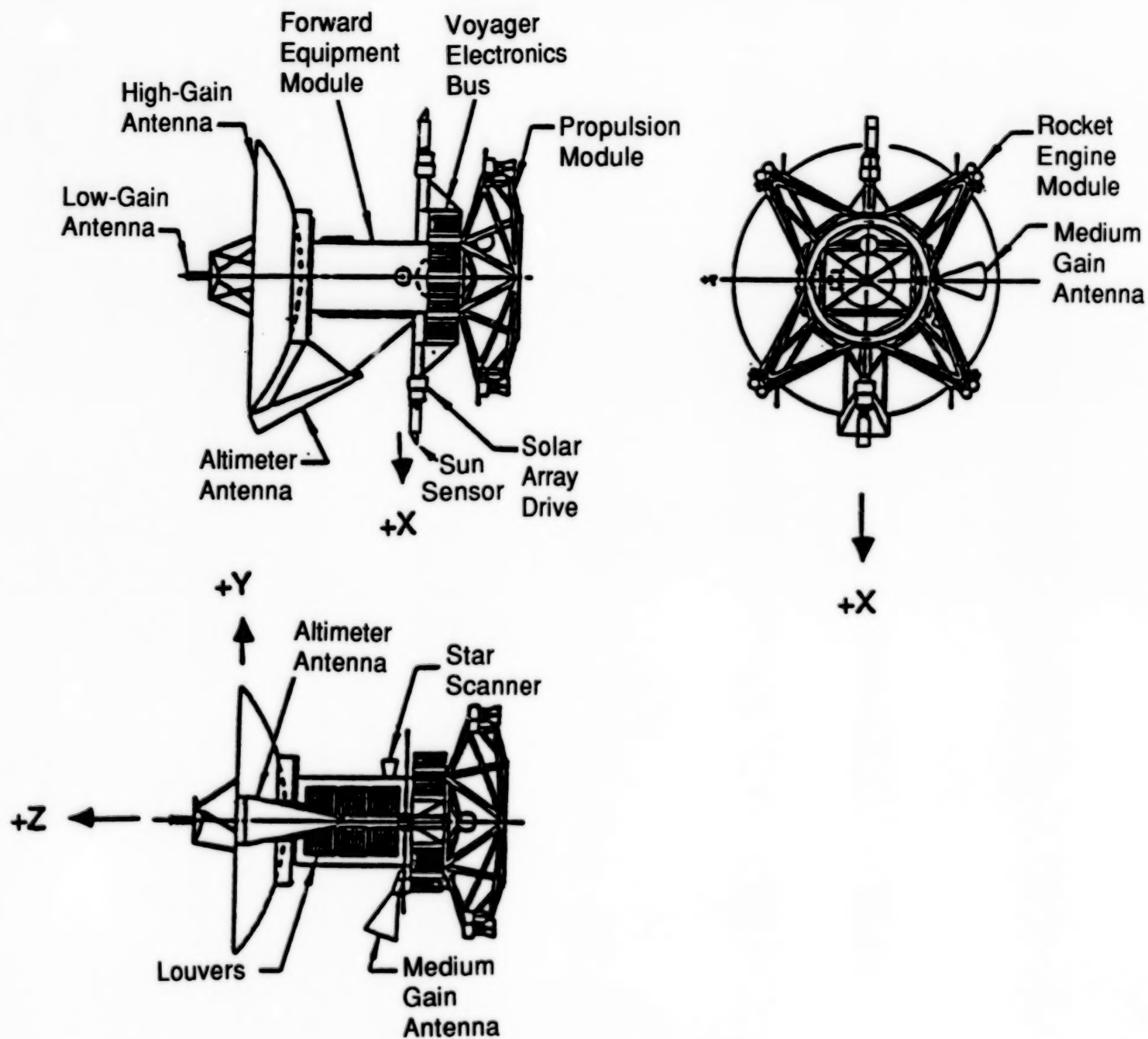


Figure 1. Magellan Test Configuration

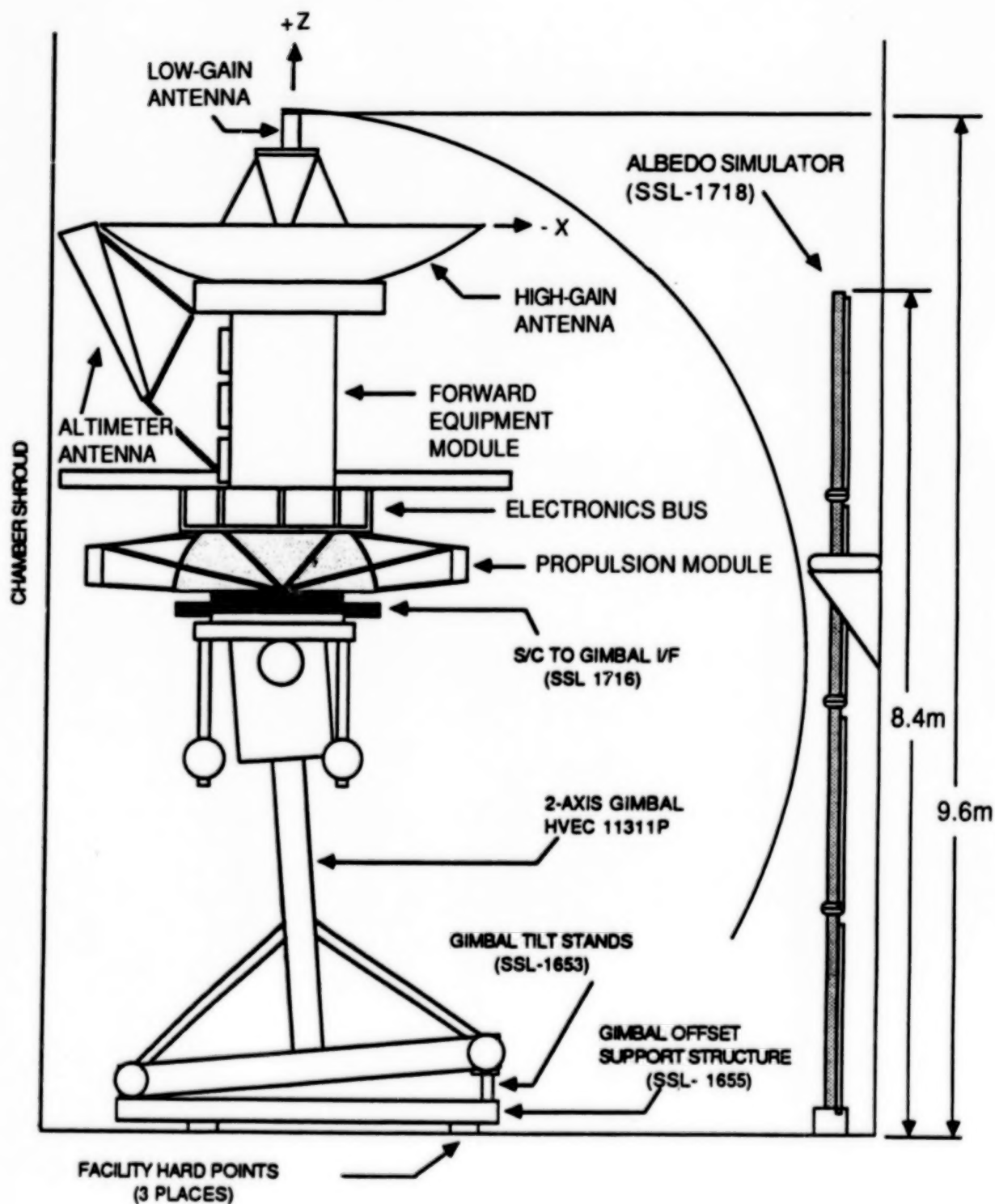


Figure 2. Magellan Installed on Gimbal Fixture

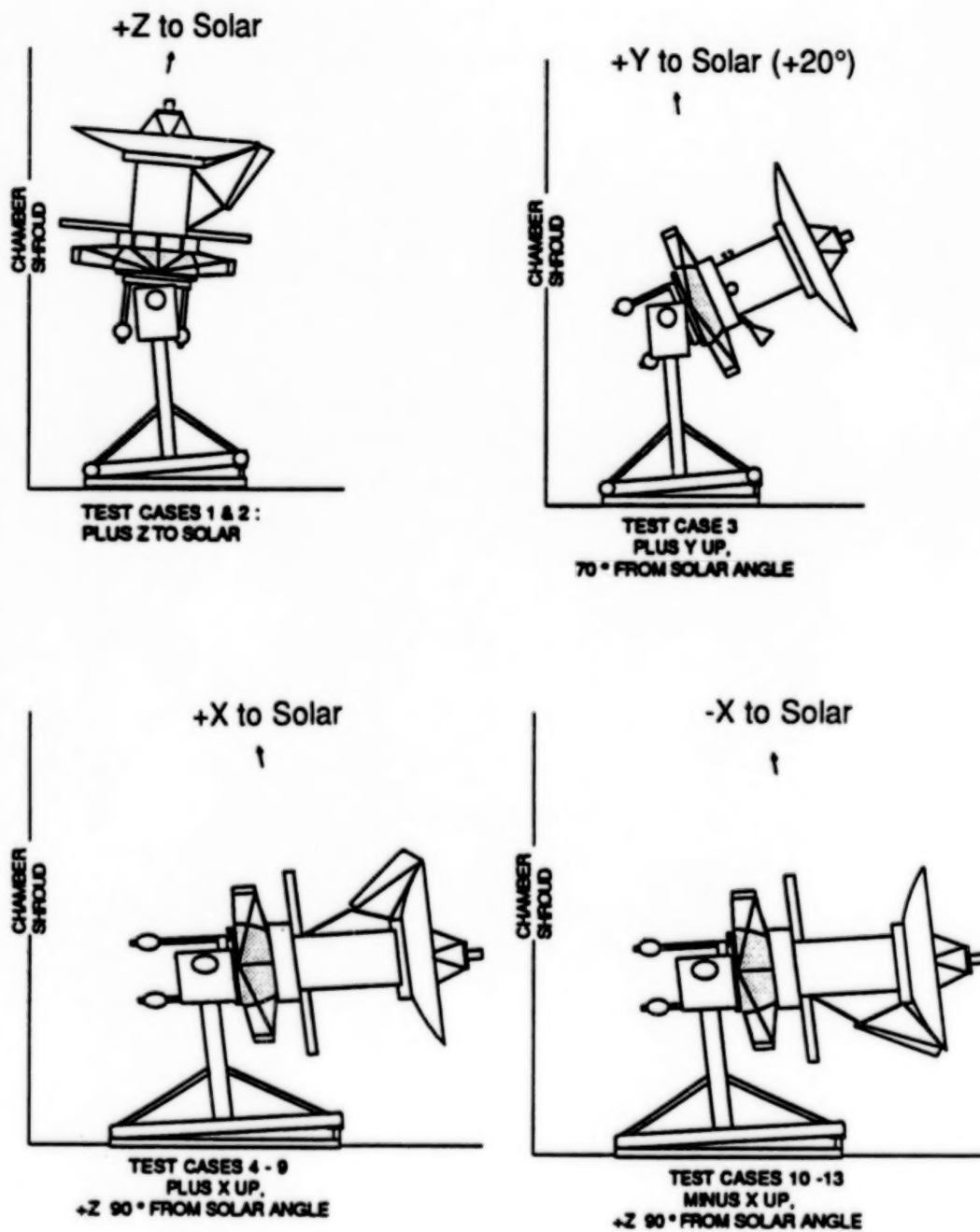


Figure 3. Spacecraft Test Attitudes

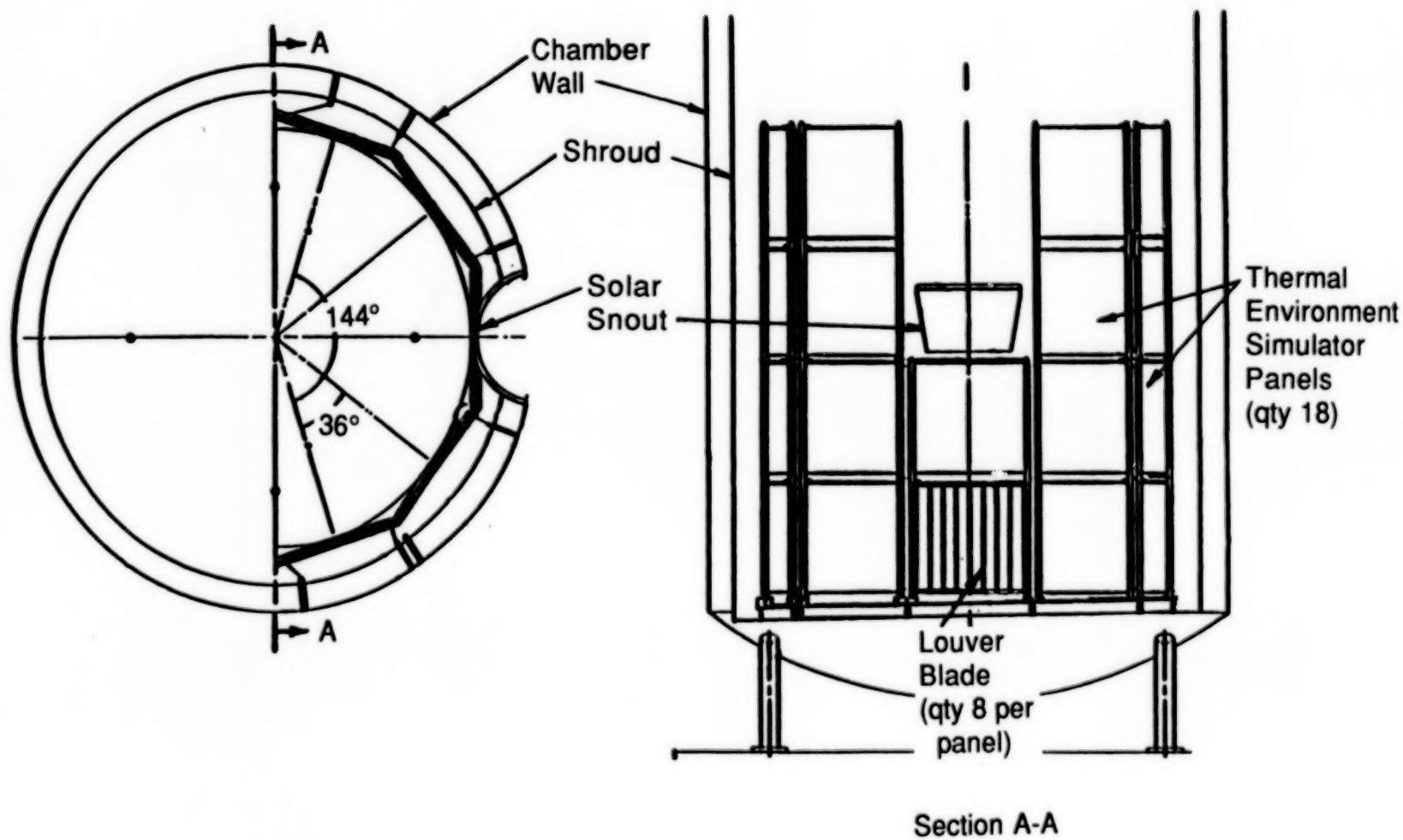


Figure 4. Albedo Simulator

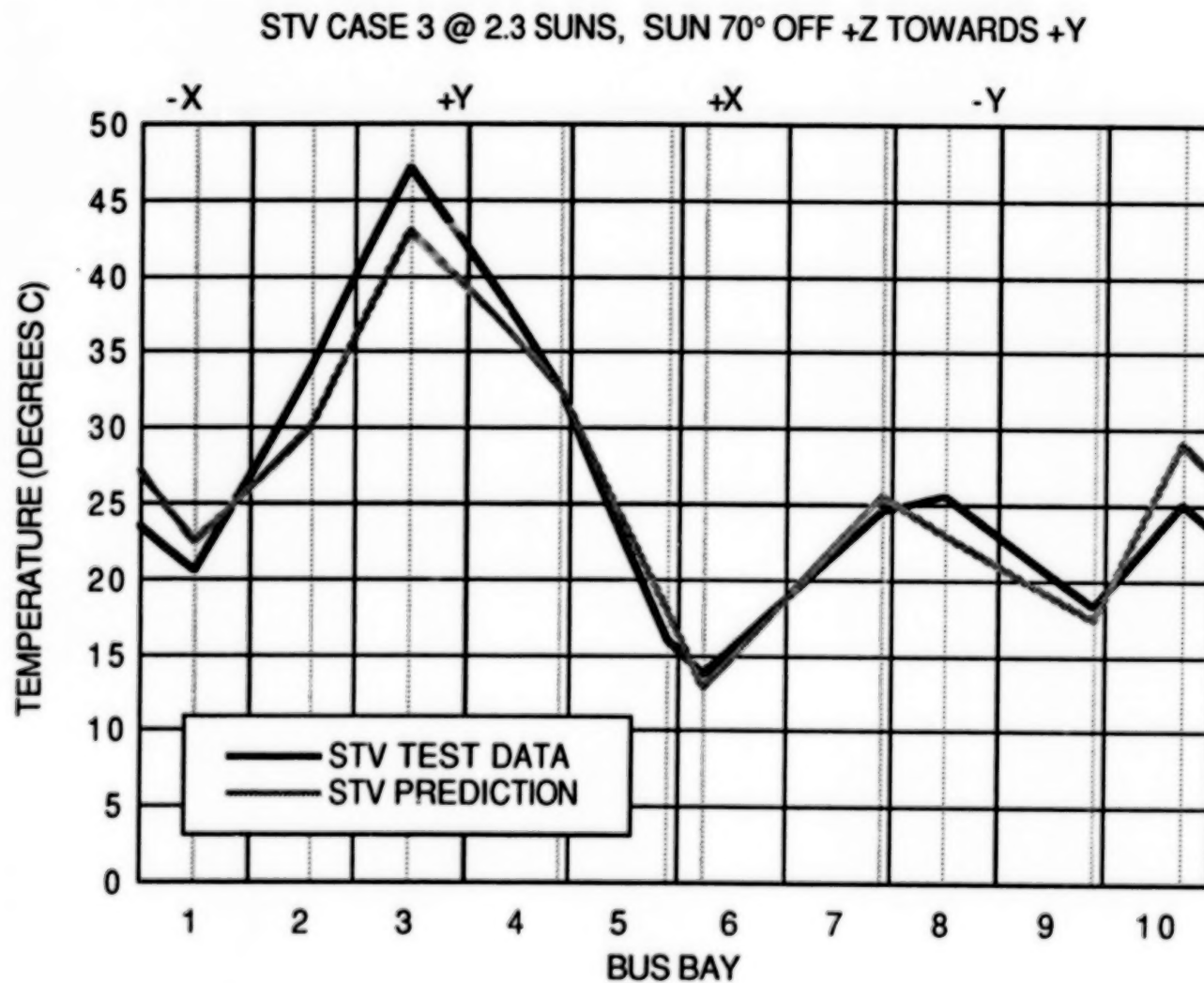


Figure 5. Electronics Bus Test Temperatures vs Math Model Predictions

**The Test Facility Requirements For The Thermal Vacuum
Thermal Balance Test of the Cosmic Background
Explorer Observatory**

By

Laura J. Milam

**Environmental Test and Integration Branch
Engineering Services Division
Goddard Space Flight Center
Greenbelt, Maryland**

ABSTRACT

The Cosmic Background Explorer Observatory (COBE) underwent a thermal vacuum/thermal balance test in the Space Environment Simulator (SES) at the Space Simulation Test Laboratory, Goddard Space Flight Center. This was the largest and most complex test ever accomplished at this facility. The 4 meter X 4 meter (13 feet X 13 feet) spacecraft weighed approximately 2223 kilograms (4900 pounds) for the test. The test set-up included simulator panels for the inboard solar array panels, simulator panels for the flight cowlings, Sun and Earth Sensor stimuli, Thermal/Radio Frequency Shield heater stimuli and a cryopanel for thermal control in the Attitude Control System/Shunt Dissipator area. The fixturing also included a unique 4.3 meter (14 feet) diameter Gaseous Helium Cryopanel which provided a 20 Kelvin environment for the calibration of one of the spacecraft's instruments, the Differential Microwave Radiometer. This cryogenic panel caused extra contamination concerns and a special method was developed and written into the test procedure to prevent the high buildup of condensibles on the panel which could have led to backstreaming of the thermal vacuum chamber. The test was completed successfully with a high quality simulated space environment provided to the spacecraft. This paper describes the test requirements, test set-up, special fixturing requirements, the related contamination concerns and a general discussion of the test and test results.

INTRODUCTION

The Cosmic Background Explorer (COBE) Observatory, (Figure 1) launched in November 1989 aboard a Delta launch vehicle into a sun synchronous polar orbit, was built and tested at the NASA/Goddard Space Flight Center, Greenbelt, MD. The mission objective of the Observatory was built to explore and study the 3 Kelvin Cosmic Background Radiation measuring light in wavelengths from 1 micrometer to 1 centimeter. The Observatory carries three instruments. The Differential Microwave Radiometer and the two cryogenically cooled instruments, the Far Infrared Absolute Spectrophotometer (FIRAS) and the Diffuse Infrared Background Experiment (DIRBE)

The COBE Observatory underwent a combined thermal vacuum, thermal balance and mission simulation test. The 24 day test was completed in June, 1989. The test took place in the

8.5 meter x 12.2 (28 feet X 40 feet) Space Environment Simulator (SES) in the NASA Goddard Space Flight Center Space Simulation Test Engineering Environmental Test Laboratory.

SPACECRAFT TEST CONFIGURATION

The COBE Observatory is approximately 4 meters (13 feet) tall and approximately 4 meters (13 feet) wide at its widest diameter (Figure 2). The spacecraft weighed approximately 2223 kilograms (4900 pounds) for the test. The major changes to the flight configuration which affected the test set-up (ref. 1) were as follows:

- o The Wallops Flight Facility (WFF) and the Tracking Data Relay Satellite (TDRS) Omni Antenna and the support boom was not installed.
- o The flight Solar Arrays and Cowlings were not installed.
- o The DMR horns had temperature controlled targets inside them and the flight contamination covers were removed.
- o Two spacecraft power cables were routed through an external diode box.
- o Helium was not flowed through the flight dewar aperture cover.
- o The flight dewar ejectable cover remained in place. The DIRBE and FIRAS instruments were not exposed to the chamber environment.
- o A test multilayer insulation thermal blanket was used instead of the flight Thermal/Radio Frequency Shield thermal blanket.
- o Plumbing lines were used to vent the flight dewar.
- o Test-only temperature controlled survival heaters were installed on the Thermal/RF Shield panels.

TEST REQUIREMENTS

As in any thermal vacuum test, this highly complex test set-up was designed to meet the test objectives of the COBE Observatory and to provide the Observatory with the best possible space simulation. The following are the major test objectives of the COBE Observatory and some of the specific test objectives which influenced the test set-up (ref. 1) are also listed.

- o Provide the assurance that specified mission objectives will be met.
- o Verify the functional operation of the flight components at elevated and lower than expected flight temperatures thereby proving that there is design margin at the system level.
- o Provide confidence that the Observatory will survive the thermal environments imposed upon COBE during launch and mission sequence.
- o Determine operating and performance characteristics of COBE during a simulated orbital environment.
- o To obtain a pumpdown curve and contamination measurements that will allow for a formulation of an estimate of the potential of COBE to self-contaminate its instruments.

- o Verify the flight worthiness of COBE.
- o Validate the data flow paths for nominal and contingency mission operating procedures between the COBE spacecraft systems and the Payload Operating Control Center (POCC) under simulated mission conditions.
- o Perform tests to demonstrate compatibility with Ground and Space Networks.

Specific Thermal Objectives

- o Verify that the thermal mathematical model used to thermally design COBE and which will be used to support the mission, sufficiently represents COBE.
- o Verify the thermal performance of the thermal/RF shield.
- o Thermally cycle the COBE electronics at least four times between their qualification temperatures

Specific DMR Objectives

- o To simulate early mission conditions, in which the instruments rely on survival heaters to prevent extremely cold temperatures.
- o Establish thermal balance temperatures for the DMR heads with a variety of heater combinations.
- o Measure offset while viewing equal temperature cold targets with all radiometers at operational temperatures.
- o Measure stability of instruments at operational temperatures, while viewing cold targets.
- o Attempt calibration by differentially warming targets with heaters.

Specific Power Objectives

- o Demonstrate the ability of the shunts to dissipate the maximum load imposed upon them under hot conditions.

Specific Attitude Control Objectives

- o Stimulate the Coarse Sun Sensors to demonstrate that they operate properly.

TEST SET-UP

The same test set-up was used for all three phases of the test, thermal vacuum, thermal balance and mission simulation (Figure 3).

Fixturing

The Observatory was mounted to a aluminum Payload Attach Fitting (PAF) which is the interface to the Delta rocket. The PAF was mounted onto a cylindrical aluminum support structure which was bolted to the chamber's 2.7 meters (9 foot) payload table. Mounted inside the support structure was a temperature controlled Diode Box through which one of the

Observatory's power cables were installed (Figure 5). Inside of the PAF, a cryopanel was mounted which was used for the Attitude Control/Shunt Dissipator. A Zero-Q interface provided temperature equilibrium between the PAF and the Observatory. The flight cowlings were replaced by 6 flux temperature controlled heaters panels. Three flux temperature controlled panels were mounted to simulate the in-board flight solar array panels. A large aluminum structure was built and hung in the chamber which provided radiant heat to approximately 25 percent of the Thermal/RF Shield. Six heater plates mounted on poles which resembled STOP signs, were mounted in the appropriate places to provide radiant heat to the Observatory's sun and earth sensors (Figure 6). Lights mounted in special fixtures were used as stimuli for the sensor. A 453.6 Kilograms (1000 pound) 4.3 meter (14 foot) gaseous Helium cryopanel was mounted in a support frame and hung over the Observatory to provide a 20 Kelvin environment for the DMR heads. A multilayer insulation blanket was mounted around the periphery of the cryopanel so that the entire area within the thermal shield would not be influenced by the chamber walls. A copper strap was clamped to the cryopanel and mounted on the 31 gigahertz (GHz) radiometer head to provide a conductive heat sink. Vent lines for the flight LHe Dewar was brought out through chamber penetrations.

Contamination Control Measuring Devices

Also a major part of the test requirements and which added complexity to the test set-up, were the contamination measuring devices. Three temperature controlled 10 megahertz (MHz) Quartz Crystal Microbalances were used to measure the real time quantitative outgassing of contaminants from the Observatory. The QCMs were spaced radially from the DMR heads. Each device was placed .6 meters (2 feet) from the Observatory at heights of 74, 142 and 224 cm (29, 56 and 88 inches) measured from the spacecraft support structure. The QCM's were operated at -40°C and -60°C. A Residual Gas Analyzer was used to provide a real time analysis of gases and chemical elements in the chamber. A Coldfinger, which is a cylindrical device was used to provide a quantitative and qualitative idea of the amount of outgassing occurring when the device is activated at LN2 temperature during the last eight hours of the test. A Scavenger Plate, with the same purpose as the Coldfinger was also used, but this device is activated for the entire test. Six COBE project provided Witness Mirrors were installed in strategic locations on the Observatory and were used to detect molecular and particulate contamination.

Test Instrumentation

A large and diverse amount of test instrumentation was used on the Observatory and the fixturing. A significant amount of ground support equipment was required for operating the test instrumentation as well as the flight instrumentation. For thermal temperature measurements, 160 copper-constantan thermocouples were mounted on the Observatory. Approximately 200 copper-constantan thermocouples were mounted on the various fixtures. Twelve silicon diodes were mounted on the 20K cryopanel. Twenty Eight heaters circuits were mounted on the Observatory in various places including the Thermal/RF Shield. Seventy heater circuits controlled the fixturing. Also, there were 13 strain gauges and 3 accelerometers mounted on the flight dewar.

DISCUSSION

Major Test Preparations

The most difficult preparation task in terms of dollars and hours was the refurbishment of the SES Helium Skid. The original purpose of the Helium Skid was to operate the chamber 20K Helium Cryopanel. In the test, the Helium Skid was used to cool the 20 K Helium Cryopanel which was mounted over the spacecraft. After the Helium Skid was refurbished, the plumbing had to be rerouted to accommodate the lines to the test Helium Cryopanel. All total the task took two

years to complete. The 28 year old Helium Skid was a major concern because its reliability was in question up to the week before the test and it was critical to the success of the test. The Helium Skid performed flawlessly throughout the duration of the test. Several chamber shroud and gimbal leaks developed prior to the test, all were repaired except for a gimbal leak which only occurred during LN2 operations.

The 453.6 kilograms (1000 pound) 4.3 meters (14 foot) 20K GHe cryopanel was made in two pieces and required a massive support structure which was mounted onto the chamber gimbal. The cryopanel was mounted 6 meters (20 feet) above the payload table and a minimum of 15 centimeters (6 inches) above the Observatory with one end of the panel raised higher than the other to prevent contamination from dripping onto the spacecraft.

The Thermal/RF Shield stimulus panel which backed 25 percent of the Thermal/RF Shield was also hung from the chamber gimbal and was difficult to install because of its height above the chamber floor and its ten separate panels.

Caution was used for handling and mounting the cowling panels and the solar array simulators because they mounted directly to the flight spacecraft.

A bakeout and test verification run was completed prior to the flight test to bakeout the chamber and fixturing and to verify the proper operation of the Helium Skid and the 20K cryopanel, the ACS/Shunt dissipator cryopanel, 5 temperature conditioning units, all test heater circuits and thermocouples, to thermally map the SES chamber for test thermal analysis purposes and to determine the temperature gradients across a test cowling. Stainless Steel wire was strung across the chamber to provide strain relief for the test cabling.

This test was the first test to be completed using the new Space Simulation Laboratory data acquisition system. Another unusual aspect of the test set-up was the use of an air conditioning system which cooled the spacecraft during ambient testing. The air conditioner was kept outside the chamber and lines made of cleanroom bagging material was routed through special holes in the test cowlings. Another first was in using the new data system to control the 70 flux controlled heater circuits, which greatly simplified the task.

Certainly not the least challenging part of the test set-up was installing the spacecraft around the fixturing, removing the protective cleanroom bagging (and then reinstalling the bag post test), building enough scaffolding to sufficient height to allow access to critical portions of the Observatory, hooking up the cryogenic lines, the instrumentation, and properly positioning the fixturing.

All of the pretest and post test chamber activities were accomplished under Class 110,000 cleanroom conditions with all personnel wearing full cleanroom garments.

Test Description

THE COBE Observatory underwent a 4-cycle thermal vacuum test and a hot and cold case thermal balance test with a mission simulation test simulating several orbits of the spacecraft (ref. 2) (Figure 4).

The chamber shrouds remained at LN2 temperature, -191°C , for the duration of the test. The 133 flight and test heater circuits provided the necessary heated environment for the spacecraft. The test started with a long hot soak, during which time the experimenters hoped that most of the outgassing of the Observatory would occur. The Mission Simulation tests were run during the hot and cold thermal balance phases so a kind of cyclic stabilization was established (ref 3.). The test duration was 24 days.

Special Concerns

The major concern of the test was the buildup of gas condensibles on the 20K GHe cryopanel which averaged between 18K and 20K during the test. Prior verification testing of the panel had shown that if enough gas condensed on the panel and the panel warmed up, the chamber pressure would rise rapidly above 3×10^{-3} Torr which would cause backstreaming of the diffusion pumps (the pumps do not have main valves) which would be a catastrophic event. To prevent this problem, the test procedure was written to warm up the cryopanel to 40K, a sufficient temperature to release the gas condensibles, every 2 or 3 days. This procedure was accomplished during temperature transition periods to not interfere with the hardware testing.

Another concern was the "cold leak" in the chamber gimbal. The gimbal was not flooded with LN2 except for critical Attitude Control testing and only when the 20K cryopanel was warm.

Safety was always a concern. A test run and a critical lift procedure was written for the raising and lowering of the 20K cryopanel. This massive panel was hinged on one side and was raised in a nearly 90 degree vertical position for the installation of the spacecraft and was then lowered via an electric winch to its supports for the test configuration.

The COBE LHe Dewar was brought into the chamber at superfluid conditions (less than 2.8K) and the dewar had to be properly vented throughout the test. Also the dewar Aperture Cover Bandclamp was heated during the test to prevent possible release of the cover which would have exposed the 2K FIRAS and DIRBE instruments to a much warmer environment resulting in a catastrophic ice build-up. The Observatory pyrotechnic devices were safed to prevent accidental firing.

Stringent cleanroom rules were strictly enforced to prevent molecular or particulate contamination.

Test Results

The detailed test results are beyond the scope of this paper, however, an overview of the results and some test problems which affected the facility will be discussed. The first problem which occurred caused the thermal system and the diffusion pumps to be secured. An o-ring froze causing the dewar vent line to leak helium. The vent line was pumped on with the chamber at 3×10^{-3} Torr and the test was able to continue (ref. 2). Later on in the test, the same leak caused the chamber shrouds to be secured again. The chamber pressure remained on the 10^{-8} Torr range for the majority of the test. For the last two days of the test, the pressure rose to the 10^{-7} Torr range and stayed there. Leakchecks were performed as a precaution but no explanation was found. One of the 17 chamber diffusion pumps failed, but the test was not affected.

The procedure for warming the 20K panel was very successful. The chamber pressure rose no more than one decade. Due to the cold leak, the gimbal was not flooded with LN2 for the majority of the test. This caused the Earth Sensors to be "noisy" and only two of the three sensors were operated for most of the test (ref. 3). The gimbal was flooded several times with LN2, with the 20K cryopanel warm, to allow all three of the Earth Sensors to be operated.

Chamber vibration and RF interference did not interfere with FIRAS functional testing as had been expected. While there were a few anomalies which occurred with the DMR

instrument, the test was very successful because the 20K cryopanel provided the necessary environment for the radiometer heads to be tested at their operating temperatures.

All contamination criteria was successfully passed. Overall the COBE Observatory test objectives were met.

SUMMARY

This was by far the largest most complex test ever accomplished at the Goddard Space Simulation Test Laboratory. The many different unique fixtures and multitude of instrumentation caused the test preparations to be spanned over a period of several years. All of the man-hours and dollars spent for hardware culminated into an overall successful test in which the COBE Observatory test objectives were met. The Observatory is now making astronomical history as it orbits the Earth making a Skymap which scientists will use to attempt to find the origins of our great Universe.

ACKNOWLEDGEMENTS

The author wishes to acknowledge and thank her colleague, Mr. Lyle Knight, for taking over the task of lead test engineer during the COBE Observatory test and writing the test report while she was on maternity leave. The author also wishes to thank all of the members of the Space Simulation Test Engineering Section and NSI Technology Services, Inc. without whose support this test would not have been possible.

REFERENCES

1. "Procedure For the Thermal Vacuum/Thermal Balance (TV/TB) And Mission Simulation Test of the Cosmic Background Explorer Observatory," COBE-PR-754-1113--3200-01D, Space Simulation Test Engineering Section Procedure #7544-4-89, April 1989.
2. "Goddard Space Flight Center Environmental Test Report," Space Simulation Test Engineering Section Procedure 37544-4-89R, August 1989.
3. "Test Report for the Thermal Balance/Thermal Vacuum/Mission Simulation Test of the Cosmic Background Explorer (COBE)," COBE-TR-750-1113-3200-01D, November 1989.

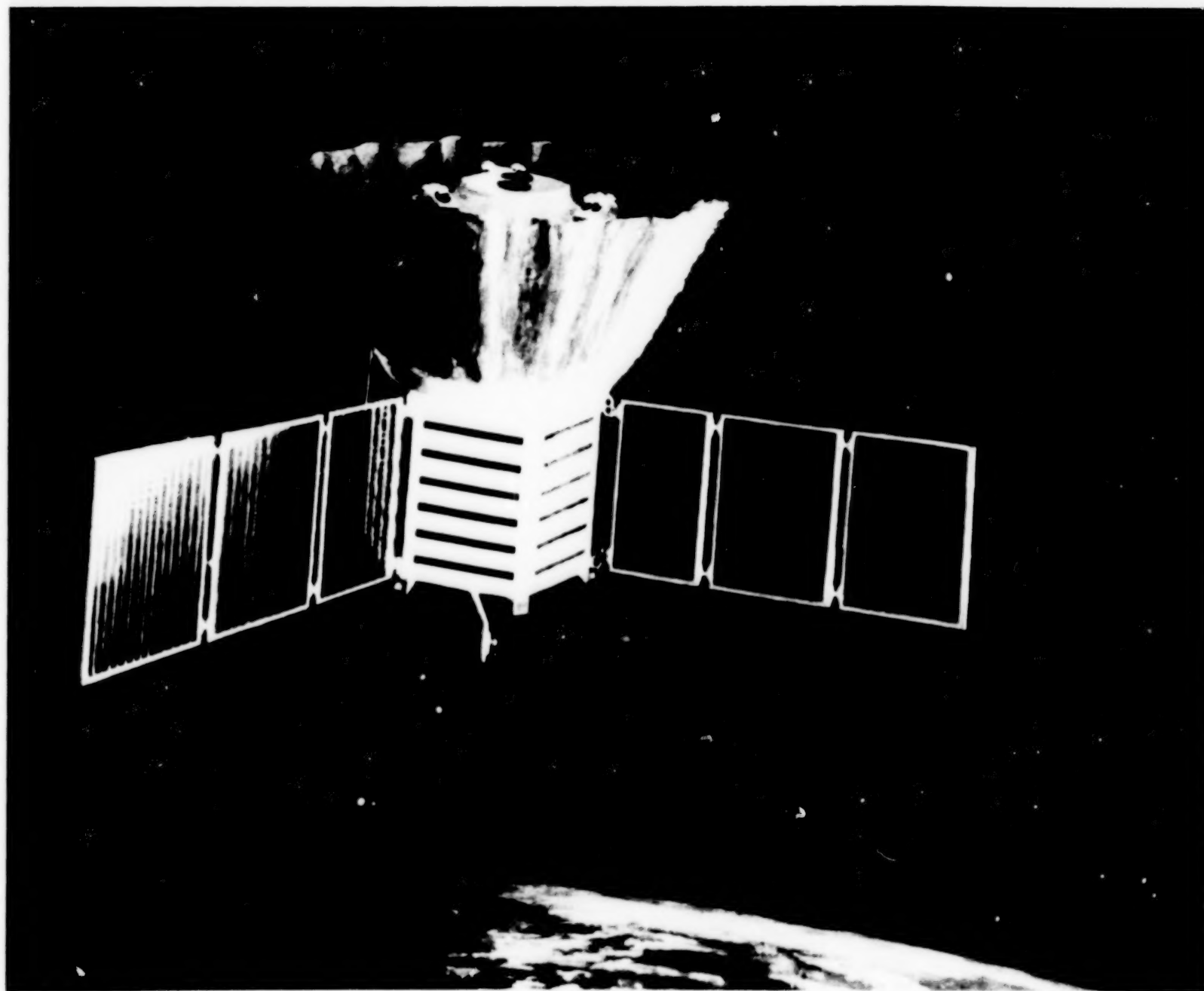


Figure 1. The Cosmic Background Explorer Observatory

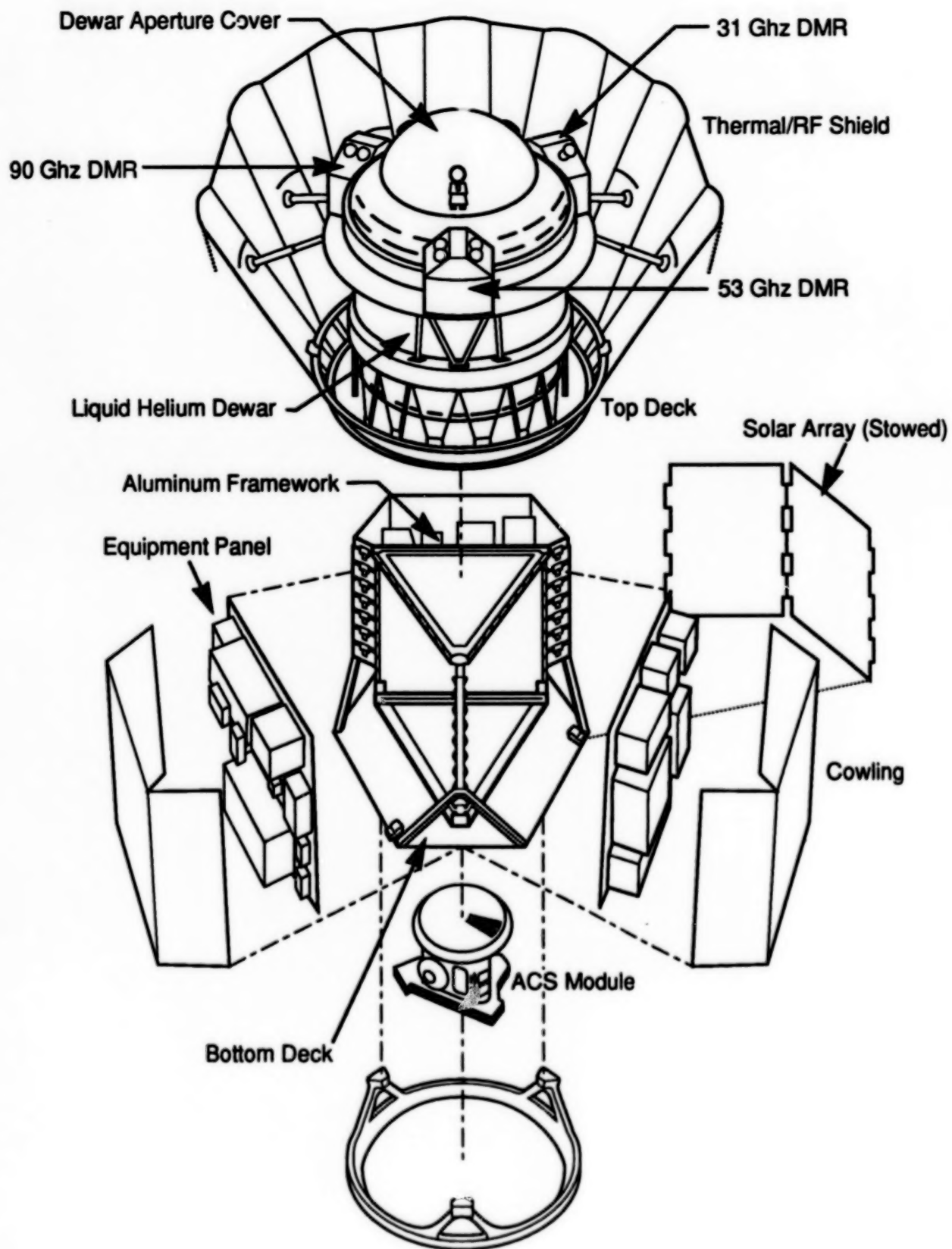


Figure 2. COBE Observatory (Exploded View)

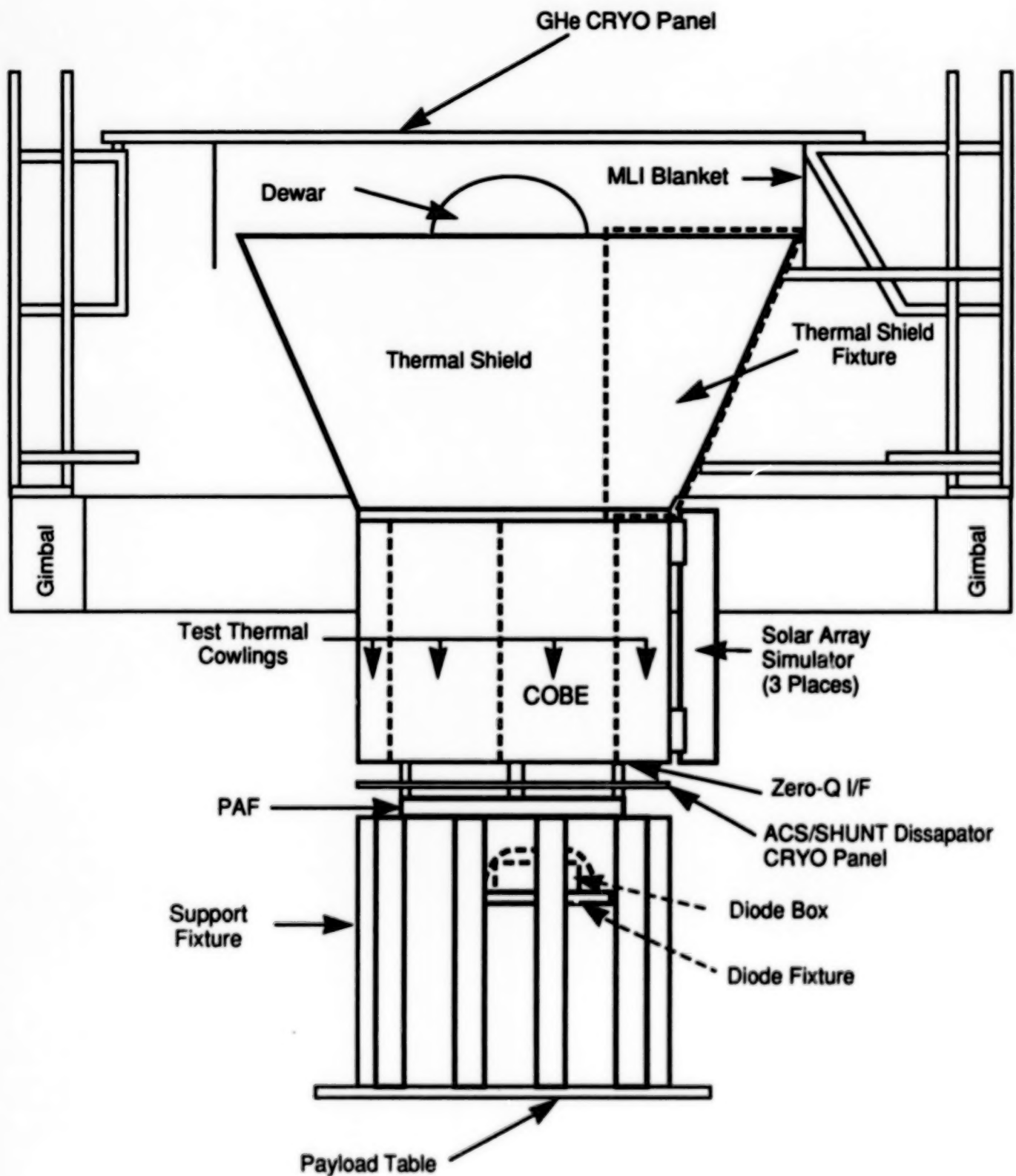


Figure 3. COBE SES Test Setup

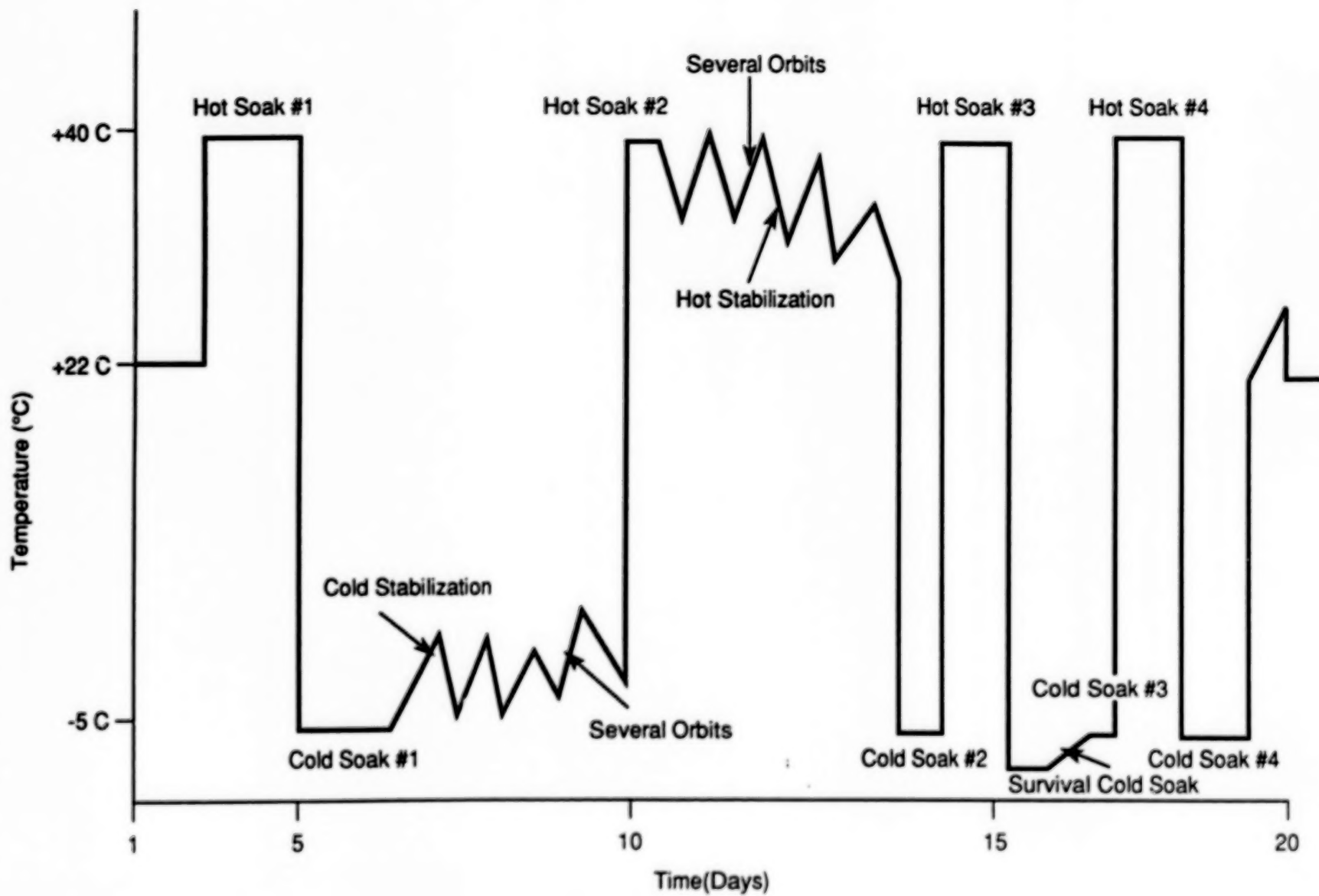


Figure 4. COBE TV/TB Mission Simulation Test Profile

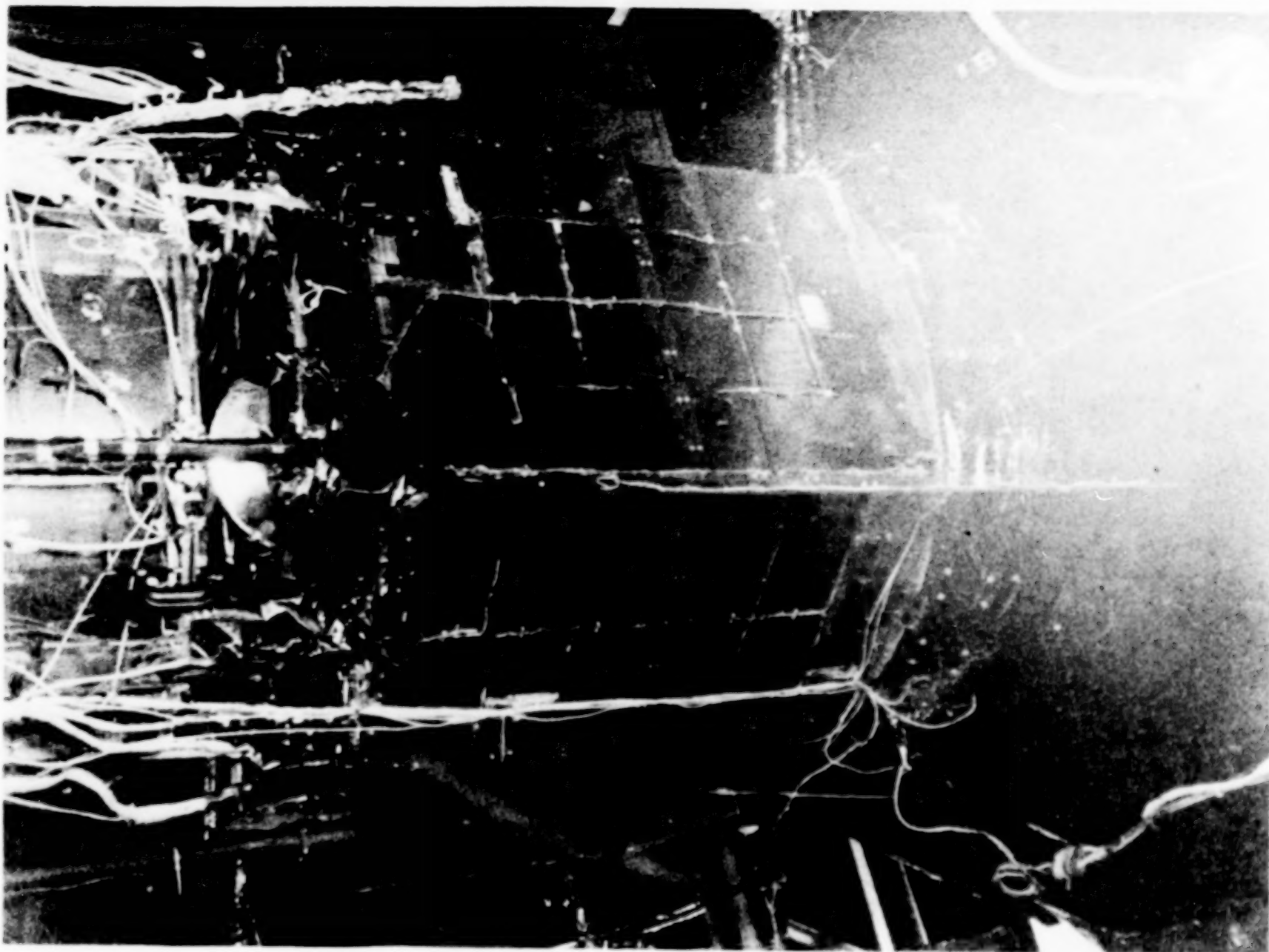


Figure 6. COBE In SES

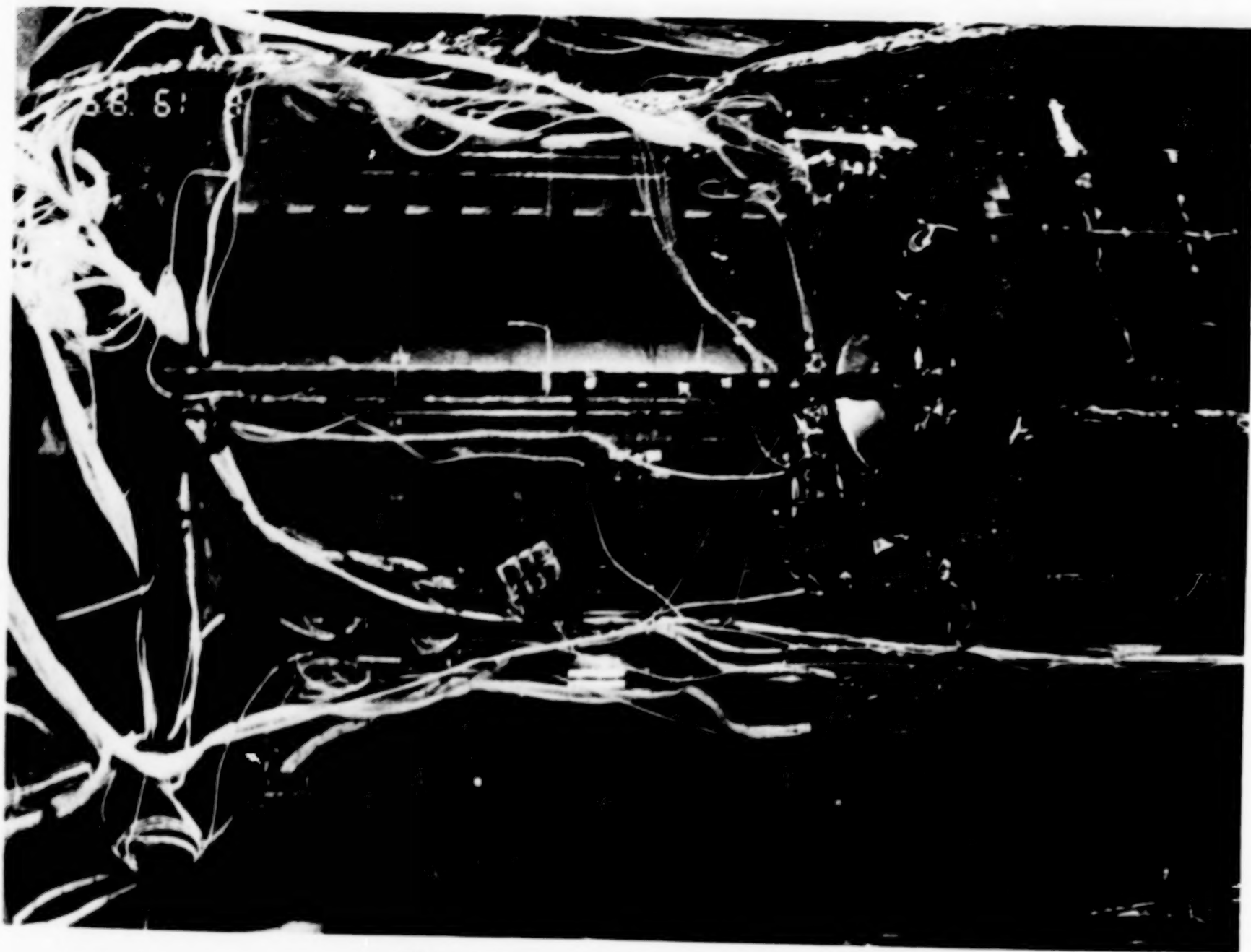


Figure 5. Instrumentation and Test Harnesses

SCD 02 THERMAL DESIGN

by

**Humberto Pontes Cardoso
Instituto de Pesquisas Espaciais-INPE
12201 Sao Jose dos Campos - SP - Brazil**

ABSTRACT

The SCD 02 Data Collecting Satellite has the following characteristics: 115 kg weight, octagonal prism shape, 1 m diameter, and 0.67 m height.

Its specified orbit is a near-circular one, 700 km altitude, is inclined 25 deg with respect to the equator line, and has 100 min period.

The electric power is supplied by eight solar panels installed on the lateral sides of the satellite. The equipment is located on the central (both faces) and lower (internal face) panels.

The satellite is spin stabilized and its attitude control is such that during its lifetime, the solar aspect angle will vary between 80 and 100 deg with respect to its spin axis.

Two critical cases were selected for thermal control design purposes:

Hot case: maximum solar constant, solar aspect angle equal to 100 deg, minimum eclipse time and maximum internal heat dissipation.

A passive thermal design concept was achieved and the maximum and minimum equipment operating temperatures were obtained through a 109 node finite difference mathematical model.

SCD1 THERMAL DESIGN AND TEST RESULT ANALYSIS

HUMBERTO P. CARDOSO

ISSAMU MURAOKA, MARCIA B. H. MANTELLI, ROSANGELA M. G. LEITE

INSTITUTO DE PESQUISAS ESPACIAIS, BRAZIL

ABSTRACT

The SCD1 (Satelite de Coleta de Dados 1) is a spin stabilized low-Earth orbit satellite dedicated to the collection and distribution of environmental data. It was completely developed at the Brazilian Institute for Space Research (INPE) and is scheduled to be launched in 1992.

The SCD1 passive thermal control design configuration is presented and the thermal analysis results are compared with the temperatures obtained from a Thermal Balance Test. The correlation between the analytical and experimental results is considered very good.

Numerical flight simulations show that the thermal control design can keep all the subsystem temperatures within their specified temperature range.

INTRODUCTION

The Data Collecting Satellite 1 (SCD1), is the first satellite completely designed and built in Brazil. It is part of an ambitious program that intends to enable Brazilian scientists and industry to develop and fabricate launchers, and more suitable satellites for Brazilian needs. SCD1 is an experimental satellite and its mission is to collect meteorological data sent from automatic ground stations, and relay them to a central ground station. As of now the satellite is being assembled, and it is scheduled to be launched in 1992.

The SCD1 is a small satellite weighing 115 kg, its shape is a right octagonal prism, whose base fits in a 1 m diameter circle and is 67 cm high.

Its specified orbit is circular at 750 km altitude, inclined 25 degrees with respect to the equator.

The electric power (around 80w) is supplied by nine solar panels installed on the eight lateral panels and on the upper octagonal one. The equipment are located on the lower (internal face) central (both faces) and upper (internal face) panels.

The satellite is spin stabilized and its attitude control is such that during its life time (1 year) the sun rays will never strike the lower panel.

Three critical cases were selected for thermal control design purposes: two cold cases and one hot case.

A passive thermal design concept was developed and the equipment operating temperature ranges were obtained through a mathematical model and validated by a Thermal Balance Test (TBT).

SATELLITE DESCRIPTION

The SCD1 primary structure consists of a central tube, two octagonal panels, and four stiffening bars. Eight rectangular solar panels and one octagonal top, close the two enclosures where the equipment are installed. Figure 1 shows an exploded view of the spacecraft with all the electronic subsystems.

The electronic boxes are installed on the internal face of lower panel, both faces of central panel and inner face of upper panel. On the lower panel there are four electronic boxes (Battery, PCU, Magnetometer Electronics, and Magnetometer Sensor), and two circular holes where the two Shunt Dissipators are fixed. On the lower face of the central panel, seven electronic boxes are settled (Decoder, PDU, DC/DC Converter, Sun Sensor f 1 and f 2, DCP Transponder, and UPC). The last six boxes (TMTC Transponders f 1 and f 2, Encoder, Diplex f 1 and f 2, and UPD/C) are installed on the central panel upper face. A Nutation Damper and a Torque Coil are fixed on the inner face of the upper panel.

DESIGN CONSTRAINTS AND REQUIREMENTS

The complete mission is divided in six phases: Count-Down; Launch; Acquisition; Acceptance; Routine; Attitude Change.

The Count-Down phase is scheduled to last 5 days and consists of the final system test before launch. During this time the spacecraft will be powered via umbilical connector.

The Launch phase lasts 11 minutes corresponding to the time period between lift-off and separation. At 100 seconds from lift-off the aerodynamic fairing will be jettisoned and the satellite exposed to solar radiation and aerodynamic heating.

The acquisition phase involves the orbit and attitude determination. The orbit determination lasts 11h and 40 min (7 complete orbits) while the attitude determination lasts 38 hours more.

The acceptance phase starts just after the attitude acquisition phase and lasts one month. During this period in-orbit tests are effected and the collected data quality verified.

The routine phase, in which the SCD1 will fulfill its data collecting mission, lasts 11 months.

The attitude change phase occurs whenever the satellite attitude is out of specification. Attitude manoeuvres are accomplished by telecommand activation of an on board magnetic torque coil.

The combination of the orbit and attitude parameters during SCD1 lifetime, creates some severe thermal constraints to its operation.

Its relatively low altitude (750 km), makes the Earth and Albedo radiation effects significant when compared to the direct Sun radiation. The orbit inclination (25 deg) imposes an angle variation between sun vector and orbit plane from 1.5 to 48.5 degrees. This variation causes an eclipse period variation from 35 to 29 minutes for an orbit period of 100 minutes.

The attitude control obtained by spin stabilization and nutation damper action, and manoeuvres done by the torque coil imposes a solar aspect angle variation from 0 to 90 deg which means an absorbed heat load variation of about 37% during one year.

In general, the electronic equipment present low dissipation values, and the total power dissipated by the spacecraft (not including the Shunt Dissipators) varies from 22.9 W to 37.6 W according to the mission phase. Table 1 shows the equipment average dissipation values for minimum and maximum total heat dissipation operating modes, and the ones for normal operating mode. Shunt Dissipators are the most dissipative subsystem, which average power can vary from 2.2 W to 11.7 W with a peak of 47 W.

The operating temperature range specified for each equipment is shown in Table 2. Two equipment are considered critical: the Battery that has the narrower temperature range (-5 to 25 °C) and the DCP Transponder, whose lower temperature limit is the highest (0 °C).

The thermal control design shall keep all the subsystem temperatures within the specified range for all the satellite operating modes during the routine phase, and it shall warrant the subsystem integrities during non operating modes and other mission phases.

The thermal control subsystem shall be based only on passive techniques.

THERMAL CONTROL DESIGN

Due to the satellite orbit and attitude, one can select three critical cases for the thermal control design. The first one, so called AGEOMIN, corresponds to the situation in which the angle between the sun vector and the orbit plane, and the angle between the sun vector and the spin axis, are simultaneously zero. The second one, so called LATMIN, corresponds to the case where the angle between the sun vector and the orbit plane is zero, and the angle between the sun the vector and the spin axis is equal 90 degrees. The third one, so called AGEOMAX, corresponds to the case where the angle between the sun vector and the orbit plane is maximum (48.5 deg), and the angle between the sun vector and the spin axis is zero.

In the AGEOMIN case, the sun rays strike perpendicularly the upper panel, and the eclipse period is maximum. It causes simultaneously the minimum temperature on the lower panel, and the maximum temperature on the upper panel. Therefore, the largest temperature gradient through the satellite structure occurs in this case.

In the LATMIN case the sun vector is perpendicular to the spin axis, and the eclipse period is maximum. This case corresponds to the minimum spacecraft heat load, and the minimum temperature of the central panel.

In the AGEOMAX case the maximum heat load occurs, bringing all the electronic equipment of central and lower panels to their maximum flight temperatures.

These conditions impose three different main heat path throughout the satellite structure. The first one occurs in the AGEOMIN case when the heat flux comes from the upper panel, mainly by radiation. Part of the heat is reradiated by the lateral panels and the rest reaches the lower panel. The second one occurs in the LATMIN case, when the heat flux coming from the lateral panels heats nearly uniformly all the equipment, and is reradiated by all the satellite external surfaces. In the AGEOMAX case, which presents an intermediate situation, the heat flux comes from the lateral and the upper panels.

Based on this observations, the thermal control strategy was defined. The three main points of this strategy are:

- since in the AGEOMIN case, the lower panel temperature tends to be low, it is necessary to minimize the heat losses through the lateral and lower panels,

- in the LATMIN case the central panel equipment temperatures tend to be low. It is necessary to warrant that enough heat flux from the lateral panels reaches this panel, keeping it above the minimum specified temperature levels,

- in the AGEOMAX case the whole satellite temperature becomes high. It is necessary to minimize the absorbed heat loads to decrease the temperature level.

It can be seen that some points of the thermal control strategy are in conflict with each other, thus suggesting that a compromise solution is necessary.

To accomplish the strategy described above, the following measures are adopted:

- the lower panel external surface is covered with a low emissivity and low solar absorptivity coating;

- the available areas for thermal control on the upper panel are covered with high emissivity and low solar absorptivity coating;

- the available areas for thermal control on the lateral panels are covered by low emissivity and low solar absorptivity coating;

- the inner surfaces of the lateral panels, in the region between the lower and central panels, are also covered with low emissivity coating;

- the lateral panels are insulated from the octagonal panels by fiberglass washers;

- the Battery is completely covered by a low emissivity coating, its base is bonded to the lower panel, and the external satellite surface underneath the battery is covered with a mosaic to adjust its temperature level;

- the DCP Transponder is completely covered with a low emissivity coating, and it is conductively insulated from the central panel by means of fiberglass washers;

- PCU, DC/DC Converter, and TMTC Transponders f1 and f2, are thermally bonded to their panels;

- the upper face of the Encoder box is covered with low emissivity coating;
- the upper face TMTC Transponder f1 and f2, and their lateral faces that see the lateral panels are covered with low emissivity coating;
- the Shunt Dissipator is insulated from the lower panel by stainless steel washers, and its external surface is covered with high emissivity and low solar absorptivity coating;
- the rest of the satellite inner surface is covered with high emissivity coating.

THERMAL ANALYSIS

To define the thermo-optical properties and to verify the performance of the thermal control design, a 111 node finite differences model was developed. Figures 2 to 5 show the nodal breakdown. This model was generated and solved by a computer program developed at INPE, based on the TMG and SINDA programs.

To perform the thermal analysis the minimum internal heat dissipation mode was associated with the two cold cases (AGEOMIN and LATMIN), and the maximum internal heat dissipation was associated with the hot case (AGEOMAX). After some iterations a suitable thermal control design was achieved. Figure 6 shows the resulting thermal control configuration.

THERMAL BALANCE TEST

In order to validate the mathematical thermal model and to qualify the thermal control design concept, a full scale Thermal Model (TM) was built and underwent to a Thermal Balance Test (TBT).

The TBT was performed in a 3m x 3m Thermal-Vacuum Chamber. The space environment was simulated by a black shroud cooled by LN₂. The heat loads were simulated by skin heaters fixed on all the TM external surfaces and inside the electronic box mock-ups. The vacuum level was below 1E-5 Torr.

The complete TBT was divided in five phases: two static and four dynamic. It started with the STATIC AGEOMAX case, followed by DYNAMIC AGEOMAX, DYNAMIC LATMIN, DYNAMIC AGEOMIN, and finally STATIC AGEOMIN. It lasts nearly 62 hours and was accomplished successfully.

By comparison of experimental and the predicted temperatures, it was identified discrepancies caused by either out of specification conditions in the TBT, or by problems in the mathematical model. The most important discrepancies were:

- the actual heat loads were 5 to 10% lower than the specified ones,
- the emissivity of the central tube extension was above its normal condition due to the application of unspecified tape over it, to hold heater wiring,
- the heat capacitance of the lateral and upper panels were underestimated,

- joint conductances were underestimated,

After eliminating these discrepancies, the mathematical thermal model was adjusted, and a new temperature distribution was calculated. Table 3 shows the average differences between the predicted and the measured temperatures, and the standard deviation before and after the model adjustment. Figures 7 to 11 show the equipment temperature difference histograms for the adjusted model.

FLIGHT PREDICTIONS

After the mathematical thermal model adjustment, all the critical flight conditions were simulated to verify the thermal control subsystem performance. Figure 12 shows the predicted in flight normal operating equipment temperature ranges versus the specified ones.

CONCLUSION

TBT results showed a good correlation with the analytical predictions. The flight simulations showed that the equipment temperatures for the normal satellite operating mode will be kept in their specified range. For the other mission phases and operating modes it was verified that the equipment temperatures never exceed their acceptance limits.

TABLE 1.- AVERAGE EQUIPMENT HEAT DISSIPATION

EQUIPMENT	Qmin (W)	Qmax (W)	Qnormal (W)
BATTERY	1.1	2.2	1.4
MAGNET. ELECTRONICS	0	.4	.10
PCU	4.9	8.0	5.9
DC/DC CONVERTER	3.9	6.9	4.3
SOLAR SENSOR	0	.2	.10
DCP TRANSPONDER	0	.42	.42
TC DECODER	5.5	5.5	5.5
UPC	0	2.5	2.5
UPD/C	0	3.5	0
TM ENCODER	0	0	.28
TR/TX 2	3.75	3.75	3.8
TR/TX 1	3.75	4.26	4.3
TORQUE COIL	0	0	0

TABLE 2.- OPERATING TEMPERATURE RANGE

EQUIPMENT	Tmin (C)	Tmax (C)	START UP (C)
TOP SOLAR CELLS	-60	80	-80
LATERAL SOLAR CELLS	-60	45	-80
BATTERY	-5	25	-15
MAGNET. SENSOR	-20	60	-30
MAGNET. ELECTRONICS	-20	60	-30
PCU	-10	50	-20
SHUNT DISSIPATOR	-10	60	-20
DC/DC CONVERTER	-10	50	-20
SOLAR SENSOR	-30	60	-40
SOLAR SENSOR ELETR.	-20	60	-30
DCP TRANSPONDER	0	40	-10
TC DECODER	-10	40	-20
UPC	-10	40	-20
UPD/C	-10	40	-20
TM ENCODER	-10	40	-20
TR/TX	-10	40	-20
DIPLEXER	-10	40	-20
HYBRID	-40	100	-40
PDU	-10	50	-20
NUTATION DAMPER	-50	75	-60
TORQUE COIL	-60	75	-70
DIODE PLATE	-40	60	-50

TABLE 3.- AVERAGE TEMPERATURE DIFFERENCES BEFORE AND AFTER MODEL ADJUSTMENT

PHASE	BEFORE ADJUSTMENT		AFTER ADJUSTMENT	
	T _{meas} -T _{pred} (C)	(C)	T _{meas} -T _{pred} (C)	(C)
STATIC AGEOMAX	-4.0	2.5	-.30	1.6
DYNAMIC AGEOMAX	-4.3	2.5	-.90	1.9
DYNAMIC LATMIN	-3.8	4.8	-.10	2.4
DYNAMIC AGEOMIN	-4.1	3.7	-1.3	2.7
STATIC AGEOMIN	-2.8	3.4	.50	2.2

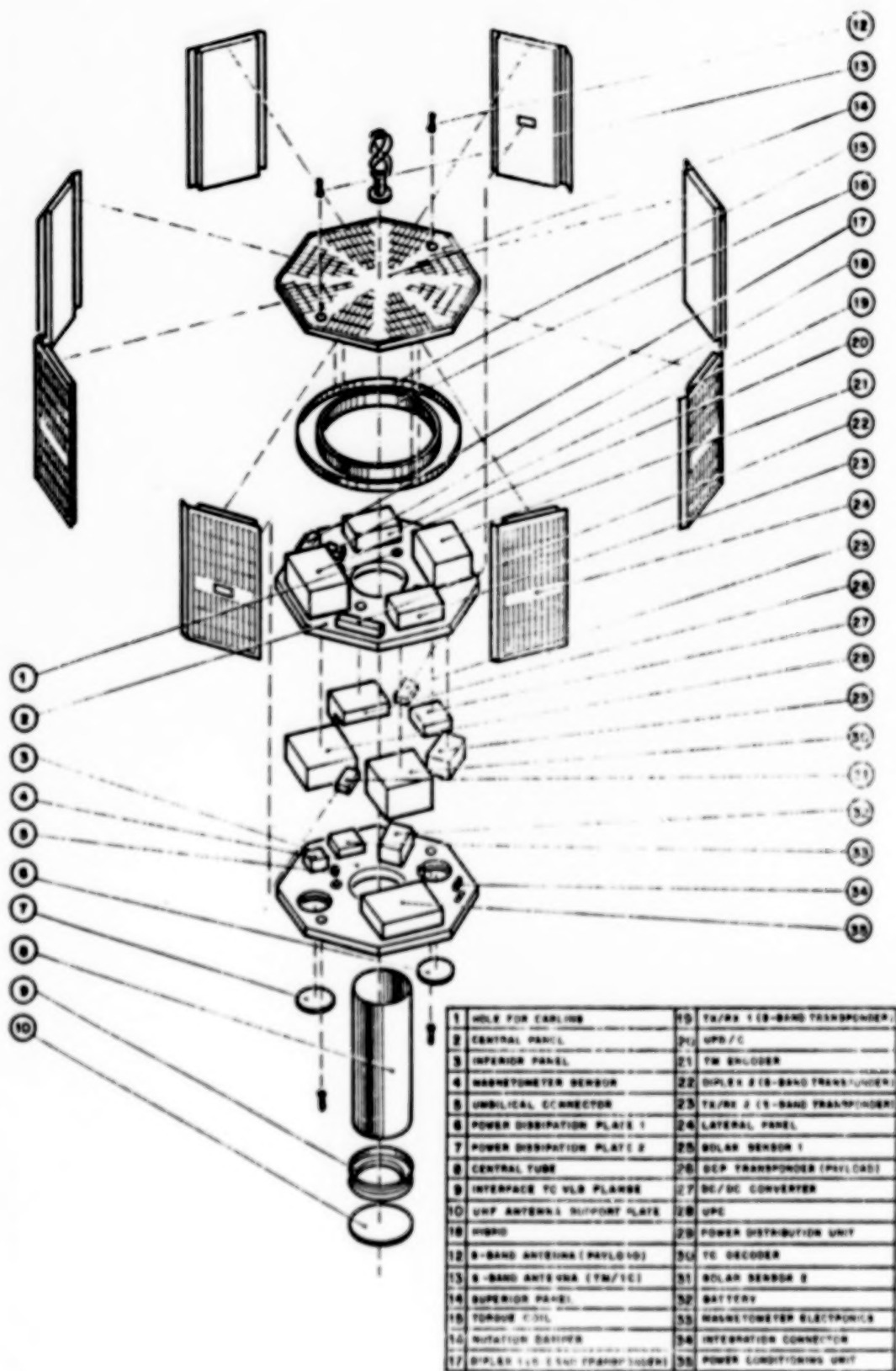


FIGURE 1.- SCD1 EXPLODED VIEW

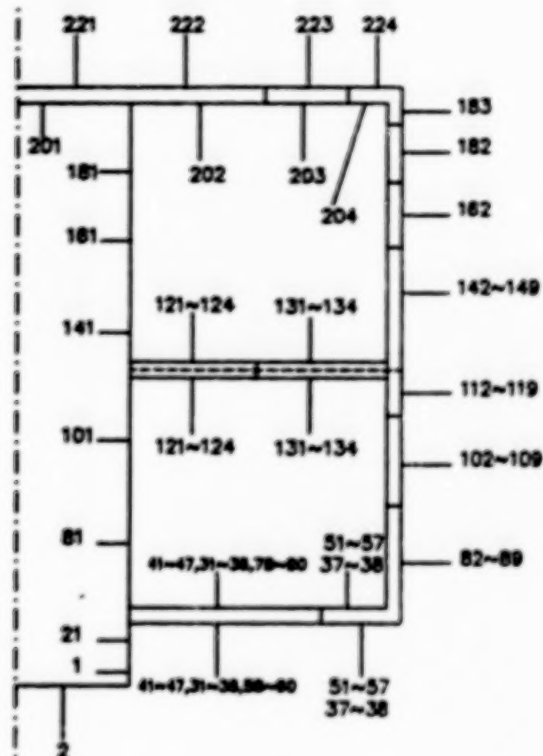


FIGURE 2.- SCD1 NODAL BREAK DOWN : CROSS SECTION

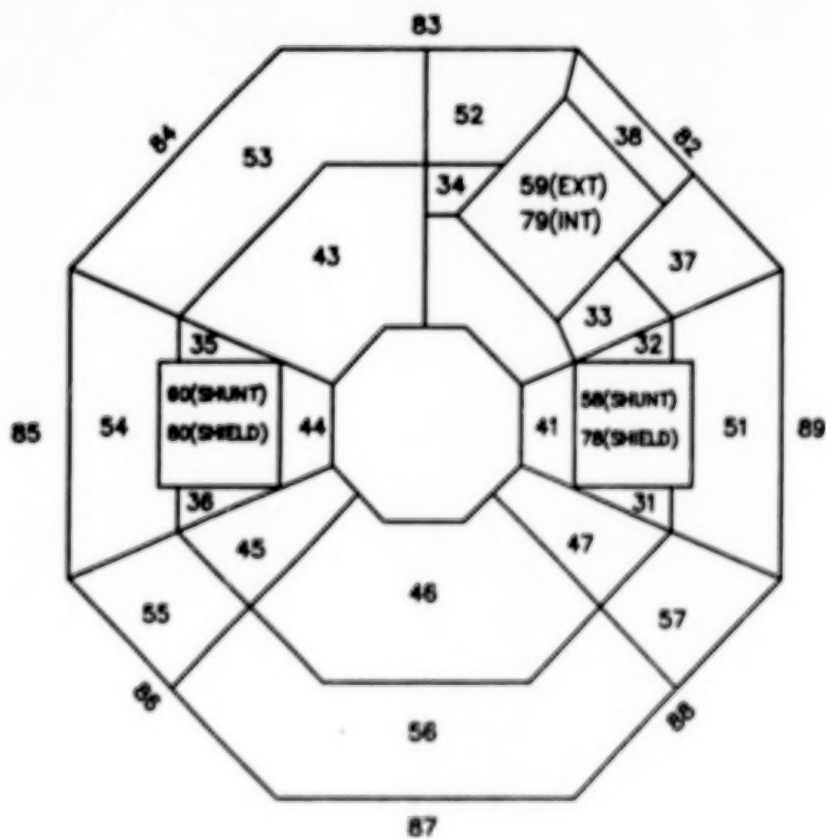


FIGURE 3.- SCD1 NODAL BREAK DOWN : LOWER PANEL

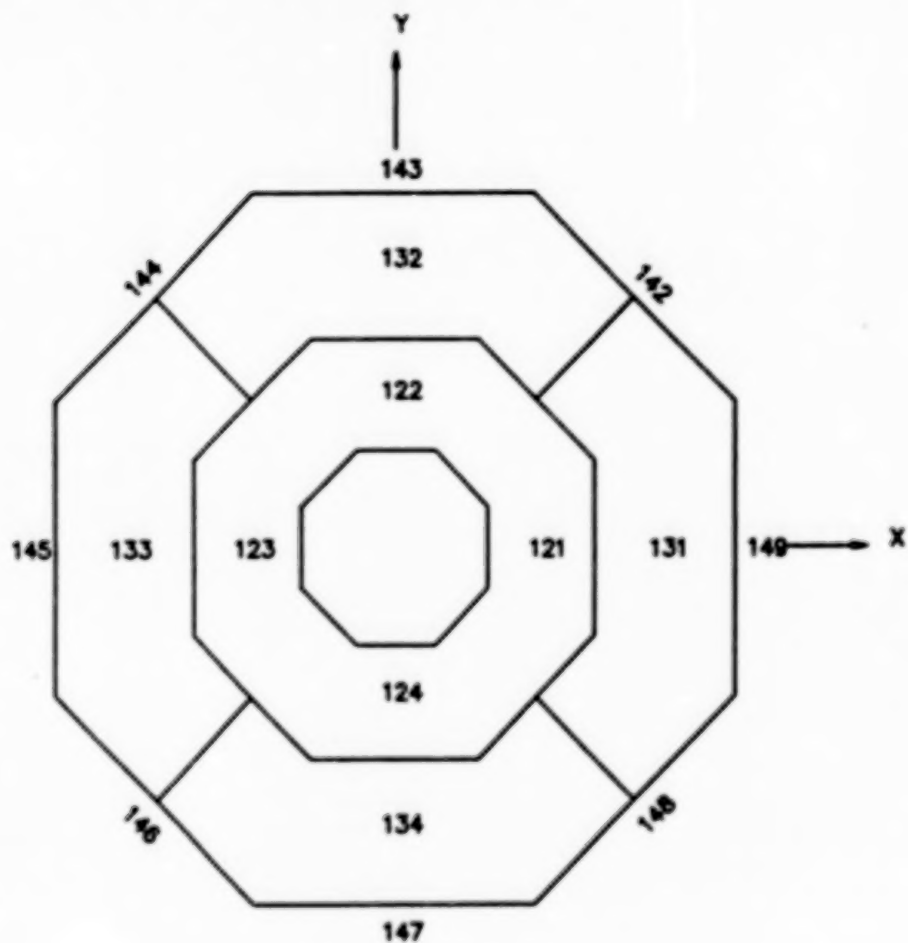


FIGURE 4.- SCD1 NODAL BREAK DOWN : CENTRAL PANEL

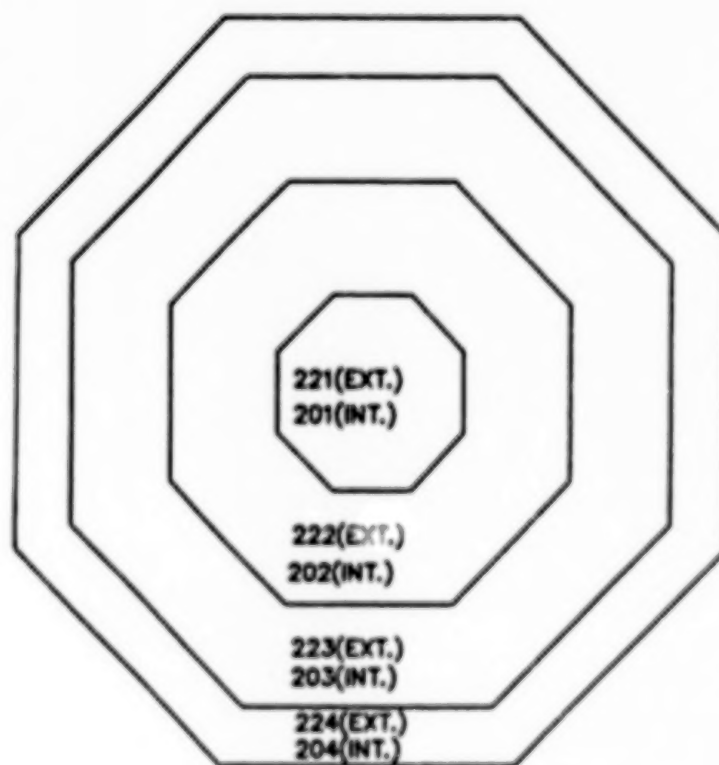


FIGURE 5.- SCD1 NODAL BREAK DOWN : UPPER PANEL

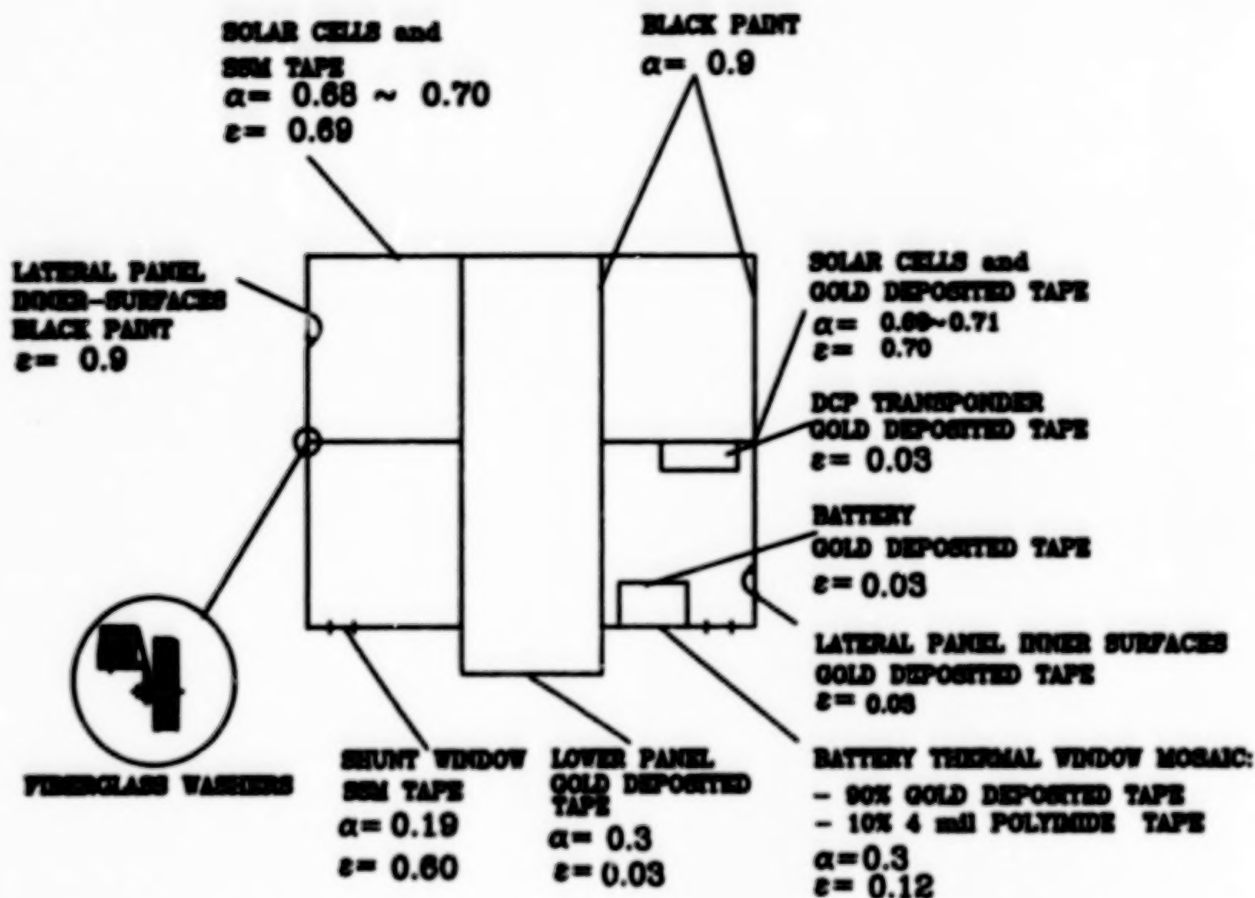


FIGURE 6.- SCD1 THERMAL CONTROL SUBSYSTEM DESCRIPTION

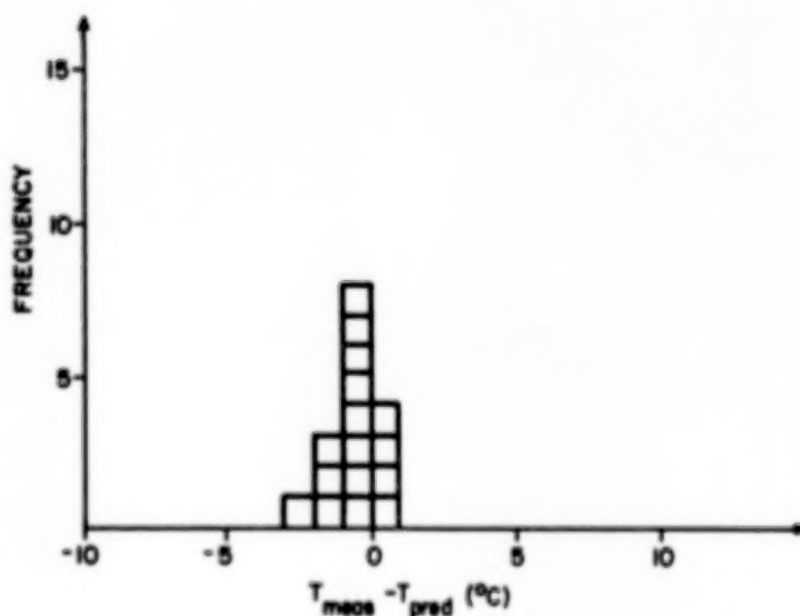


FIGURE 7.- MEASURED-PREDICTED TEMPERATURES (STA. AGEOMAX)

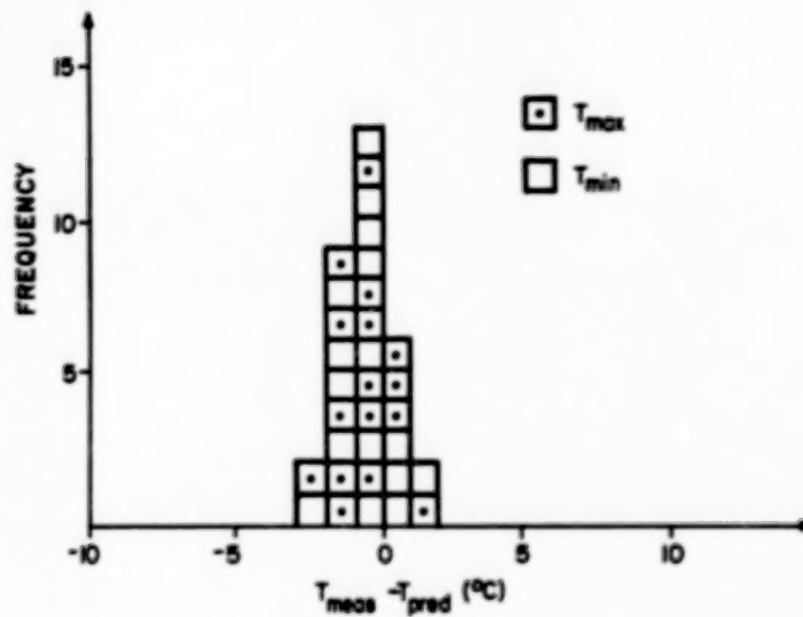


FIGURE 8.- MEASURED-PREDICTED TEMPERATURES (DYN. AGEOMAX)

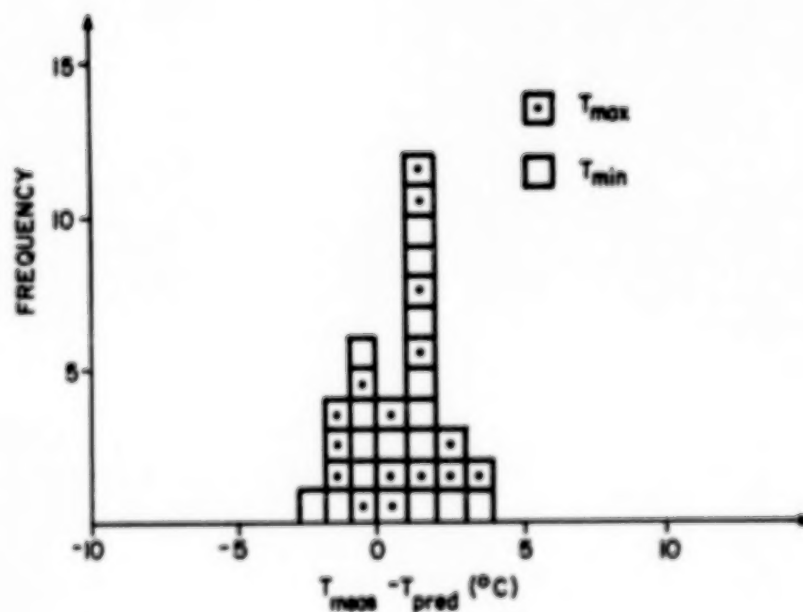


FIGURE 9.- MEASURED-PREDICTED TEMPERATURES (DYN. LATMIN)

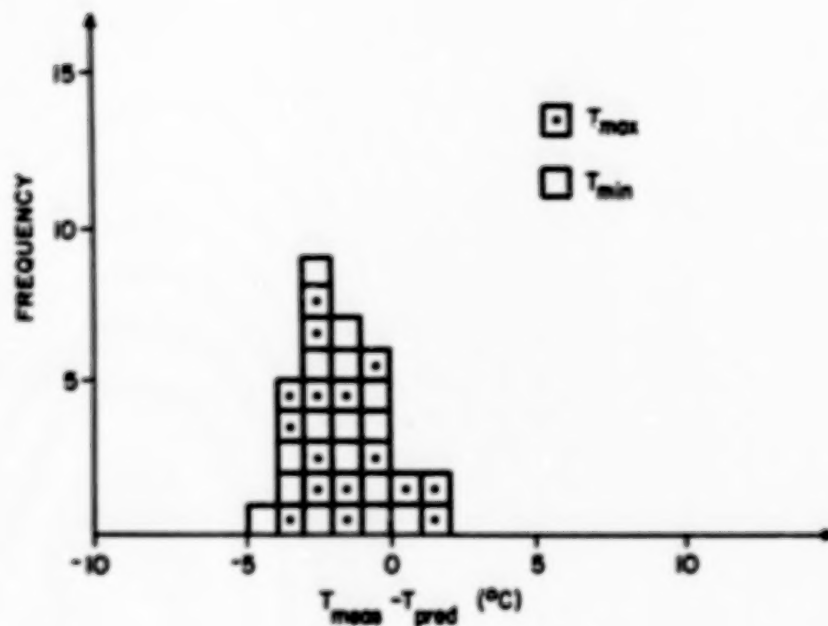


FIGURE 10.- MEASURED-PREDICTED TEMPERATURES (DYN. AGEOMIN)

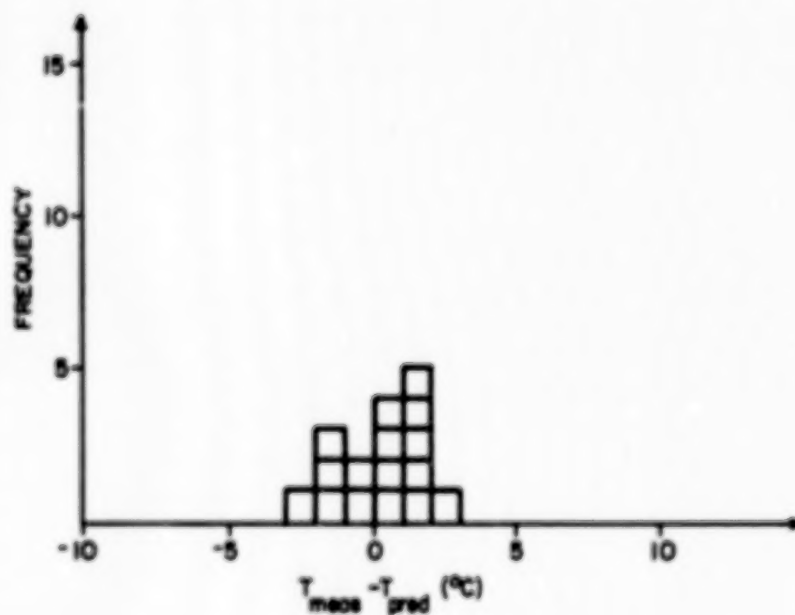


FIGURE 11.- MEASURED-PREDICTED TEMPERATURES (STA. AGEOMIN)

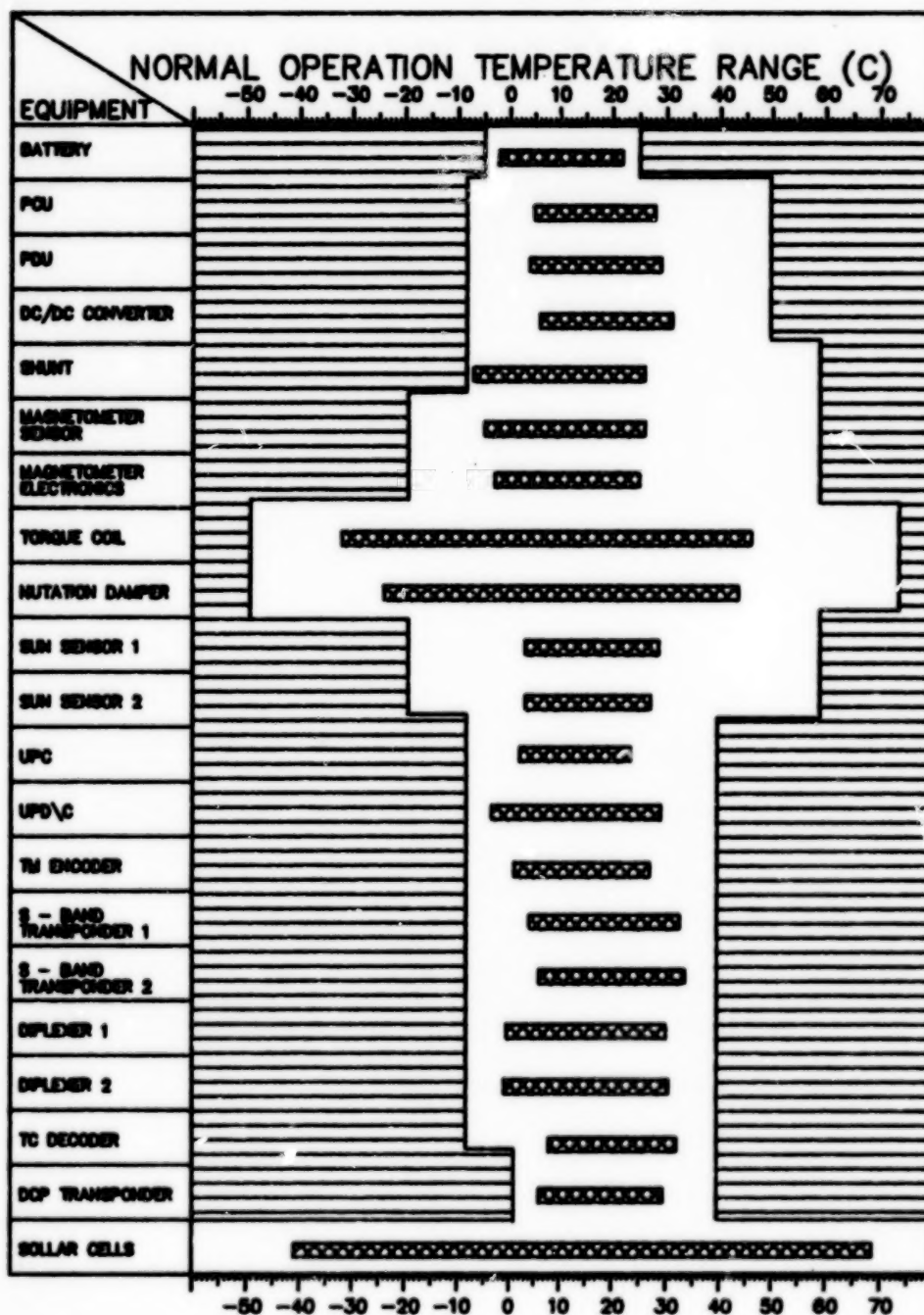


FIGURE 12.- FLIGHT PREDICTION VERSUS SPECIFIED TEMPERATURE RANGE

THERMAL BALANCE TESTING OF THE ANIK-E SPACECRAFT

by

**Alex Golob, Cristian Ruel and Marc Donato
Spar/DFL, Ottawa
and
Spar, Ste-Anne-de-Bellevue**

ABSTRACT

Spar Aerospace, Ltd. of Canada has recently successfully completed the first of two infrared thermal balance/thermal vacuum tests on Canada's next generation of telecommunications satellites: Anik-E, scheduled for a first launch in early 1991. Anik-E is a two-spacecraft program using a three-axis stabilized General Electric 5000 series bus as the vehicle for its payload. The test was performed in the David Florida Laboratory, Ottawa, in February/March of 1990 and lasted approximately 35 days. Results show that it progressed normally as predicted with few anomalies.

The infrared test setup consists of the mechanical hardware required to support the spacecraft within the thermal vacuum chamber and the infrared rig which surrounds the spacecraft. The rig consists of a frame which supports highly specular aluminum baffles and Research Inc. quartz-lined infrared heat lamps.

Spar developed a software package which calculated the lamp positions to provide the necessary uniform heat flux, based on the required heat inputs on the various isothermal zones of the spacecraft for the different phases of the test. Infrared heat sensors, called radiometers, were installed on the spacecraft surfaces. These were connected to the facility data processing system and continually monitored the flux absorbed by the various spacecraft surfaces throughout the test.

The test setup had distinct advantages. It enabled testing to progress directly from the thermal balance to thermal vacuum. Waveguide runs were installed for the communications portion of the testing prior to pumpdown. This precluded the requirement to return to ambient to reconfigure the setup and saved one week of schedule.

The test on the second spacecraft is scheduled for June 1990, and will be performed with no major changes. The test configuration was based on previous experience from other programs and required innovative design, planning and setup. This paper describes the test design philosophy, facilities, the hardware and software used in the thermal testing of Anik-E and the results of the predictions and tests.

• **SESSION II**
PRESSURE EXCHANGE

AN OUTGASSING MODEL OF NON-METALLIC MATERIALS FOR THE ASCENT OF A TITAN IV LAUNCH VEHICLE

**R.D. Barrows and S.L. VanLoon
Martin Marietta Astronautics
M.S. L5744
P.O. Box 179
Denver, Colorado 80201**

ABSTRACT

Outgassing of non-metallic materials and components inside of Titan IV's 2A compartment during ascent may present a problem to the payload community in relation to molecular deposition and degradation of sensitive payload surfaces. The procedure currently being developed to model the amounts, transport, and deposition of outgassed molecular contaminants onto a payload's sensitive surface consists of three phases. The first phase involves the development of a thermogravimetric method that recreates the increasing temperature and decreasing pressure profiles expected in the 2A compartment of the TIV launch vehicle during ascent. The second phase involves the determination of deposition rates of outgassed materials onto a payload surface, and the subsequent evaporation rate as a function of temperature of deposited material. The third phase takes the temperature and pressure profiles from phase one, the deposition and evaporation rates and kinetic coefficients determined in phase two, and incorporates them into the SPACE II computer program to determine which payload surfaces are most susceptible to molecular deposition from TIV's outgassing sources, and the level of permanent deposition expected on those surfaces.

THE PERFORMANCE OF MULTILAYER INSULATION IN A RAPIDLY DEPRESSURIZING ENVIRONMENT*

Ronald A. Efromson
Lincoln Laboratory, Massachusetts Institute of Technology
Lexington, Massachusetts 02173-9108

ABSTRACT

The performance of multilayer insulation in a rapidly depressurizing environment is determined by the variation of heat transfer with internal pressure and the pressure history of the interstitial gas. Measurements of thermal performance were made on three multilayer insulation configurations at room temperature and steady-state pressures from 10^{-6} to 10^{-1} torr. The heat transfer due to gas conduction alone correlated with the kinetic theory of gases in the molecular flow regime. Pressure histories were measured in a unique apparatus which simulated the depressurization rate of a boost vehicle. The pressure histories on both sides of two of the configurations were measured to bound the actual interstitial pressure. The results of the two types of measurements agreed with earlier work and were combined to make performance predictions using an actual ascent pressure history.

INTRODUCTION

The performance of multilayer insulation (MLI) in a rapidly depressurizing environment is of interest in some ballistic missile applications. This performance is determined by the variation of heat transfer with internal pressure and the pressure history of the interstitial gas. If both of these relationships are known, the insulation performance can be predicted for all times. The objectives of this study were to quantify the pressure dependence and determine pressure histories of some typical MLI configurations.

Thermal conductivity and effective emissivity are measures of the rate of heat transfer through a material. At low internal pressures, heat is transferred through MLI by a combination of radiation between adjacent layers and conduction through material contact points. At higher internal pressures, heat is also conducted by molecular collisions with the layers. To determine the contribution due to gas conduction alone, the heat transfer rates through three multilayer configurations were measured at room temperature, at a series of steady-state pressures between 10^{-6} and 10^{-1} torr. A ten layer, a four layer, and a two layer configuration were investigated.

To determine the pressure history of the interstitial gas in broadside venting MLI, the ascent pressure history of a boost vehicle was simulated. The pressures on both sides of the MLI were measured during the rapid depressurization of one side. The actual interstitial pressure was thus bounded by the two measured pressures. The ten layer and four layer blankets were investigated, and pressures between atmospheric and 10^{-6} torr were recorded.

After a brief comparison of the measures of thermal performance, the kinetic theory of gas conduction in the molecular flow regime will be presented. The two types of measurements performed will then be described. Finally, some predictions of MLI performance will be made using an actual ascent pressure history.

*This work was sponsored by the Strategic Defense Initiative Organization.

HEAT TRANSFER THEORY

THERMAL PERFORMANCE

The performance of MLI can be expressed in three ways, each of which has advantages and disadvantages. If the sample configuration and boundary conditions are known, each can be calculated from the other.

The effective thermal conductivity (k_{eff}) between parallel plates is defined in terms of the total heat flux (Q/A), whose units are power per unit area, as

$$k_{eff} = (Q/A) t / (T_H - T_C)$$

where t is the thickness of the sample and T_H and T_C are the hot and cold boundary temperatures respectively. Effective thermal conductivity has the same units as, and therefore is comparable to, the thermal conductivity of other insulations and materials. However, the thickness of the sample must be known accurately and the thickness of MLI is usually variable. This parameter is useful for comparing materials whose properties vary linearly with thickness but it does not take into account the fourth-power dependence on temperature of radiation heat transfer. Effective thermal conductivity was used originally by the cryogenic industry in the comparison of MLI with similar boundary temperatures.

The effective heat transfer coefficient (h_{eff}) is simply the effective thermal conductivity per unit thickness.

$$h_{eff} = (Q/A) / (T_H - T_C)$$

This parameter has the units of a heat transfer coefficient and has the advantage of not depending explicitly on material thickness. It should be used for comparing materials of equal thickness or, in the case of MLI, equal numbers of layers.

Since the number of applications for MLI at different boundary temperatures has increased, effective emissivity (ϵ_{eff}) has been used for performance comparison¹. It is defined as

$$\epsilon_{eff} = (Q/A) / \sigma (T_H^4 - T_C^4)$$

where σ is the Stefan-Boltzmann constant. Effective emissivity includes the temperature variation of radiant heat transfer and should be used to compare configurations with dissimilar boundary temperatures and the same thickness or number of layers. It should be noted that at higher internal pressures, effective emissivity can be greater than one, and its use is therefore more appropriate at lower pressures. In keeping with the current trend, and to avoid explicit use of material thickness, effective emissivity will be used here.

PRESSURE DEPENDENCE

The pressure dependence of MLI thermal performance is determined by the variation with pressure of the total heat transfer through the insulation. Under high vacuum, below 10^{-6} torr, heat is transferred by a combination of solid conduction ($(Q/A)_{sc}$) and radiation ($(Q/A)_{rad}$). At higher internal pressures, heat is also conducted by molecular collisions ($(Q/A)_{gc}$) with the layers. The total heat transferred is the sum of the heat transferred by each of these three modes.

$$Q/A = (Q/A)_{sc} + (Q/A)_{rad} + (Q/A)_{gc}$$

For given boundary temperatures, the amount of heat conducted through material contact points has been assumed to be constant, independent of the pressure of the interstitial gas. The amount of heat radiated between adjacent layers was also assumed to be constant for given boundary temperatures. This assumption is valid because the change in radiative heat flux resulting from a change in the layer temperature profile would be much smaller than the heat flux causing the change in the temperature profile. The pressure dependence of the thermal performance is therefore entirely due to the variation of gas conduction.

When the mean free path of the gas molecules is greater than the characteristic dimensions of the configuration, the gas is characterized by molecular flow. In a ten layer blanket 2.5 mm thick, the distance between radiation shields is about .25 mm. The mean free path of an air molecule is greater than this dimension for any pressure less than .2 torr. For a two layer configuration of the same thickness, the onset of the transition to continuum flow occurs at .02 torr. Therefore, the flow was assumed to be in the molecular regime for the pressures investigated here.

GAS CONDUCTION

In the molecular flow regime, the heat transferred between two surfaces is expressed by Knudsen's theory of free molecular conduction².

$$(Q/A)_m = \frac{1}{2} \frac{\alpha}{2-\alpha} \frac{\gamma+1}{\gamma-1} \left(\frac{R}{2\pi M T_c} \right)^{\frac{1}{2}} P \Delta T$$

where α is the accommodation coefficient of the surfaces

γ is the ratio of specific heats at constant pressure and volume

R is the universal gas constant

M is the molecular weight of the air

P is the pressure of the interstitial gas

and ΔT is the temperature difference between the two surfaces. The accommodation coefficient was taken to be an average value of .9^{2,3,4}.

The temperature difference used to calculate this heat flux is the temperature difference between two adjacent surfaces. It is related to the total temperature difference between the hot and cold boundary surfaces by the number of surface pairs (n), or spaces, between the boundary surfaces. Simply dividing the total temperature difference by the number of spaces in between,

$$\Delta T = (T_H - T_C) / n$$

assumes a linear temperature profile, which is sufficiently accurate to first order. This illustrates the effect of layers as barriers to molecular flow.

For the ten layer blanket tested, the number of spaces was taken to be 9 plus 1 additional space on top, between the blanket and a temperature controlled surface. Similarly, n was taken to be 4 for the four layer blanket. For the two layer configuration tested, the total temperature difference was used because each of the two layers was in contact with one of the temperature controlled surfaces.

A measurement of the heat flux under high vacuum represented a measure of radiation and solid conduction without a contribution from gas conduction. By measuring the heat flux at higher pressures, the theoretical pressure dependence of thermal conductivity could be verified.

EFFECTIVE EMISSIVITY MEASUREMENTS

PROCEDURE

The heat flux through samples of MLI was measured in a guarded hot-plate calorimeter mounted in a bell-jar vacuum system. The test setup is shown schematically in Figure 1. The main heater was held at about 40 C and the liquid cooled heat sinks at about 0 C so that the sample average was near room temperature. The temperature controlled surfaces were separated by small fiberglass spacers at three locations around the guard heater circumference.

The temperature of the guard heater was maintained within 2 C of the main heater temperature to minimize the heat leak in the radial direction. No extra guard heater was required around the test samples because the radiation leak to the room temperature surroundings was small. Two samples, of each configuration tested, and two heat sinks were used so that all power into the main heater flowed out axially through sample material. Hence, the area of the main heater and only half of the measured power to it were used in the calculation of effective emissivity. The samples tested were 20 cm in diameter, and the main heater was 10 cm in diameter.

To control the pressure, a provision for nitrogen gas to be introduced into the bell jar through a needle valve was included. By adjusting the gate valve to the vacuum pump and the needle valve controlling the nitrogen flow rate, any pressure above 7×10^{-6} torr could be maintained. An ionization vacuum gauge measured pressures below 4×10^{-2} torr.

Three MLI configurations were measured. The first was a ten layer blanket with mesh spacers. The layers were 8 micron thick Kapton* film, aluminized on both sides, perforated with 1.3 mm diameter holes which accounted for 2.2% of the area. The mesh consisted of pairs of 25 micron diameter Dacron* fibers in a 3 mm grid pattern. The blanket was approximately 2.5 mm thick so the temperature controlled surfaces were separated by 2.9 mm thick spacers.

The second configuration tested was a four layer blanket made of the same materials. It was approximately .9 mm thick, and 1.5 mm thick fiberglass spacers were used.

The third configuration consisted of two layers of 130 micron thick Kapton film, aluminized on one side, separated by the 2.9 mm spacers. The first layer was laid on the lower temperature controlled surface, aluminum side up, and the fiberglass spacers were placed around the edge. The second layer was then held in place by the upper temperature controlled surface, aluminum side down. The layer separation varied across the sample, but the aluminized surfaces did not touch at any point. Two samples of each configuration were assembled.

Each measurement required from 3 to 5 days to equilibrate in both pressure and temperature. This was due to the large outgassing surface area, low pumping speed, low powers, relatively large thermal masses, and low conductivities involved. Equilibrium was reached when the average boundary temperatures had not changed more than .1 C in four hours and the pressure had not changed more than 1/100 of the current decade. Measurements were made at a low pressure, increasingly higher pressures, intermediate pressures to check reproducibility, and finally the lowest pressure.

*Kapton polyimide film and Dacron polyester fibers, manufactured by E. I. du Pont de Nemours & Co., Inc.

RESULTS

The effective emissivities at various pressures are shown in Figure 2 for the three configurations tested. The squares, triangles and circles represent measurements of the two, four and ten layer configurations respectively. Effective emissivities were calculated from measured heat fluxes and boundary temperatures. The curves were calculated by adding the heat flux given by the theory of free molecular gas conduction to the lowest measured heat flux, in each case, and then converting to effective emissivity. Thus, the theoretical curves are forced to fit the experimental data at their lowest points and the theory describes only the increase in heat transfer due to gas conduction.

DISCUSSION

The variation in performance with pressure of any multilayer configuration can be predicted given a value of effective emissivity at high vacuum. The effective emissivity in the absence of gas molecules is a measure of the heat transfer by radiation and solid conduction alone. The kinetic theory of gas conduction describes well the increase in heat transfer with increasing pressure.

This relationship is shown graphically in Figure 3 for the case of ten layer blankets. The effective emissivity as a function of pressure of the blanket tested, both experiment and theory, is shown along with the theoretical predictions for two hypothetical higher performance blankets. A configuration with higher performance has lower radiation and solid conduction heat transfer and a lower high-vacuum effective emissivity. The straight line is the effective emissivity resulting from gas conduction alone. The theoretical curves are simply the sum of this straight line and the various high-vacuum effective emissivities. As the interstitial gas pressure increases, gas conduction dominates radiation and solid conduction, and the performance of all ten layer blankets converge.

A comparison of these results with those found originally in reference 5, is shown in Figure 4. The circles are the present measurements of a ten layer blanket. The curves are equivalent emissivity calculated for a .25 cm thickness of two types of MLI from reference 5. The kinetic theory of gas conduction, the solid line, fits the present data better (for pressures above 2×10^{-3} torr where gas conduction dominates) than that of the earlier work.

A pressure of 10^{-4} torr or less is sufficient to ensure the minimum effective emissivity for any particular ten layer blanket. This is true for any practical configuration of ten layers. But, for the configuration tested, a pressure of about 10^{-3} torr is sufficient. This pressure is probably applicable to any easily attainable configuration of ten layers.

PRESSURE HISTORY MEASUREMENTS

PROCEDURE

The four and ten layer blankets described above were tested to determine the interstitial pressure as a function of time during broadside venting. A single sample was mounted in the stainless steel chamber shown schematically in Figure 5. The volume of this chamber, 8 liters, was minimized to make the vacuum pumping rate as fast as possible.

The blanket sample was mounted so as to divide the chamber into two volumes. The sample was clamped around the circumference with an aluminum ring as shown in Figure 5. The volume on one side, the pumped region, was evacuated in three stages: a carbon vane mechanical pump, a liquid nitrogen sorption pump, and the opening of an 18 cm diameter gate valve. The gate

valve opened to a 40,000 liter vacuum chamber and its liquid helium cryogenic pump. The pressure in this large chamber was less than 2×10^{-6} torr at the start of each test run. The actual volume on the other side of the sample, the enclosed region, was 4 liters.

The pressures on both sides of the test sample were measured using thermocouple gauges and ionization vacuum gauges with 2.5 cm diameter inlet ports. These gauges were located as close as possible to the sample as shown in Figure 5. The pressures measured by the sets of gauges in each region tracked closely when the chamber was evacuated without any sample in place.

No clean-room procedures were followed when handling the sample materials. They were handled without gloves, in a normally humid environment, just prior to mounting in the test chamber. The test samples represented materials that may have been in storage for some time and that were handled without any particular precautions.

RESULTS AND DISCUSSION

Representative measured pressure histories are shown in Figure 6. The lower curves show the pressures measured in the pumped region outside the four or ten layer test blanket. The other curves are the corresponding pressures measured in the region enclosed by the sample blanket. The pressures measured on either side of the blanket bounded the actual interstitial pressure within the blanket, which would have had a gradient from layer to layer. The pressure measured in the enclosed region was thus higher than any pressure within the blanket. The tests were repeatable. The results shown in Figure 6 are similar to many other runs performed under similar conditions.

The pressure in the enclosed region was always higher than the pressure in the pumped region due to the presence of the blanket. Any delay in pressure change during the initial rapid depressurization was due to resistance to the flow of gas passing through the blanket from the enclosed region. Delays are evident in both of the cases shown in Figure 6. Delay times from 0 to 15 seconds were observed. The delay time is related to the conductance of the blanket.

In each test, the rate of depressurization slowed after about one minute. The pressure and the rate of pressure change in the enclosed region at this time, depended on the number of layers in the sample being tested. These are the effects of material outgassing and its dependence on surface area. In general, water vapor is the major contributor to outgassing⁶ followed by contamination. These results agree with those of reference 7 in which pressures leveled out around 10^{-3} torr and material outgassing was indicated.

The results of three consecutive tests of the ten layer blanket are shown in Figure 7. The chamber was blackfilled with dry nitrogen between runs. The pressures shown were measured in the enclosed region. When repeated in succession, some residual water vapor and contaminants were removed and each test resulted in lower pressures. The apparent continuation of the same pressure profile, after initial rapid depressurization, indicates that outgassing limited the interstitial pressure.

When pumped overnight, the pressure in the region enclosed by the ten layer blanket dropped to the 10^{-5} torr range but was still one decade higher than that on the pumped side. This residual pressure could still be the effect of outgassing.

PERFORMANCE PREDICTIONS

The results of the two types of measurements were combined to predict the performance of a multilayer configuration in a rapidly depressurizing environment. It was assumed that the blanket

performance measured at steady-state pressure would result at each time during a pressure transient. Also, the pressure history measured in the region enclosed by the test blanket was assumed to be a conservative estimate of the actual interstitial pressure. These two assumptions allow the blanket performance to be estimated as a function of time.

As an example, Figure 8 shows the actual ascent pressure history of a boost vehicle and the estimated interstitial pressure within a ten layer blanket during the first five minutes of flight. The maximum measured delay time of 15 seconds was applied down to 5×10^{-3} torr after which the pressure history of Figure 6 measured in the enclosed region was assumed.

Values of effective emissivity from the theoretical curve of Figure 2 were inserted for each pressure. The resulting predicted performance of the ten layer blanket is shown in Figure 9. The ultimate performance of the blanket is also indicated for comparison.

Once the pressure within the ten layer blanket reaches 10^{-3} torr, the effective emissivity will be within 15% of its ultimate value. This will occur in about five minutes. In the same time, the pressure inside the four layer blanket would have reached 2×10^{-4} torr and its performance would be within 5% of its ultimate.

CONCLUSIONS

The effective emissivity of a ten layer insulation blanket was found to be nearly constant up to 10^{-3} torr, a pressure higher than has been reported previously. The effective emissivity of a similar four layer blanket was nearly constant up to 10^{-4} torr. As pressure increases from high vacuum, insulation layers act not only as radiation shields but also as shields to molecular flow. The increase in heat transfer with increasing pressure correlated with the kinetic theory of gas conduction in the molecular flow regime. Therefore, the performance of a multilayer configuration at any pressure can be determined from the effective emissivity of the particular configuration under high vacuum.

The interstitial gas pressure inside each test configuration was bounded by measuring the pressures on both sides during the rapid depressurization of one side. The pressure inside the ten layer blanket was at most 10^{-3} torr after three minutes. The pressure inside the four layer blanket was less than 2×10^{-4} torr in the same time. The measurements indicated that outgassing, rather than restriction to flow, limits the performance of multilayer insulation. These results were combined with the measurements of effective emissivity to provide performance predictions. For example, on an actual boost vehicle, either of the multilayer blankets tested could attain within 15% of their ultimate performance in about five minutes.

REFERENCES

1. The Infrared Handbook, Wolfe and Zissis ed., 1985.
2. M. Knudsen, The Kinetic Theory of Gases, Methuen , London, 1934.
3. G. N. Patterson, Molecular Flow of Gases, Wiley, New York, 1956.
4. A. Roth, Vacuum Technology, North-Holland, Amsterdam, 1976.
5. M. P. Hnilicka, Engineering Aspects of Heat Transfer in Multilayer Reflective Insulation and Performance of NRC Insulation, Advances in Cryogenic Engineering 5, 1959.
6. A. P. M. Glassford, Outgassing Behavior of Multilayer Insulation Materials, Journal of Spacecraft and Rockets 7, 12, December 1970.
7. J. W. Price, Measuring the Gas Pressure Within a High-Performance Insulation Blanket, Advances in Cryogenic Engineering 13, 1967.

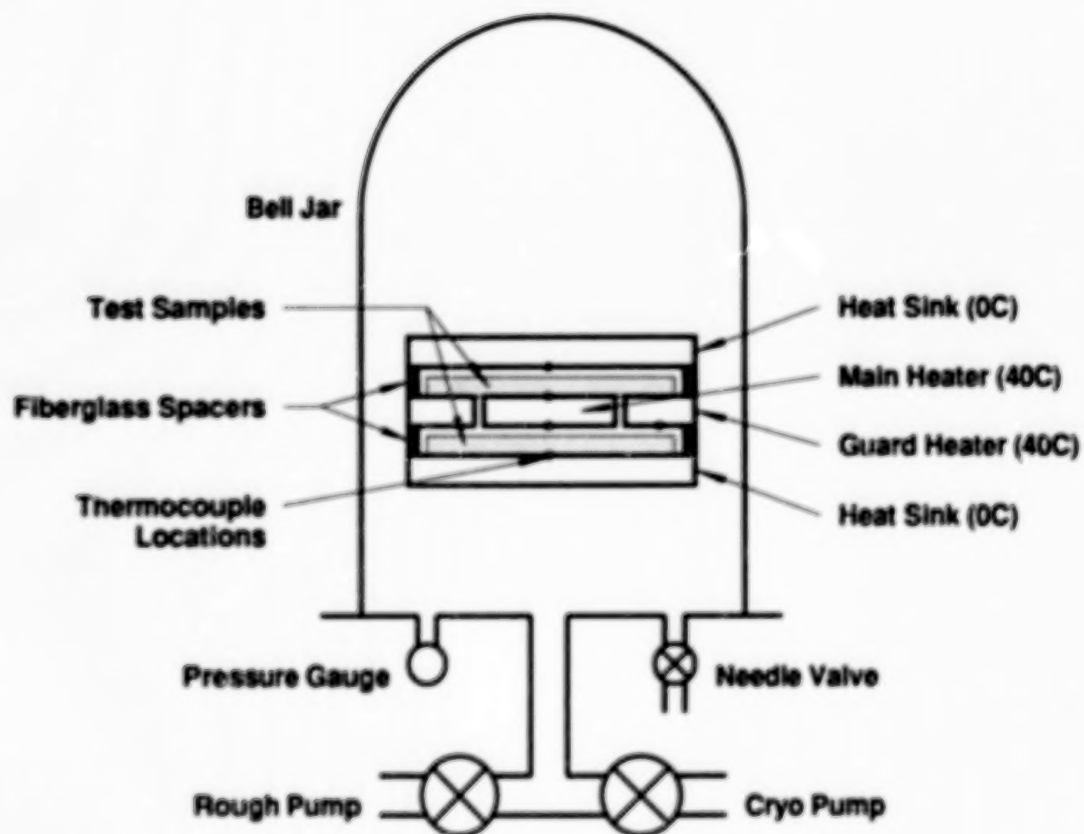


Figure 1. Guarded Hot Plate Calorimeter in Vacuum System

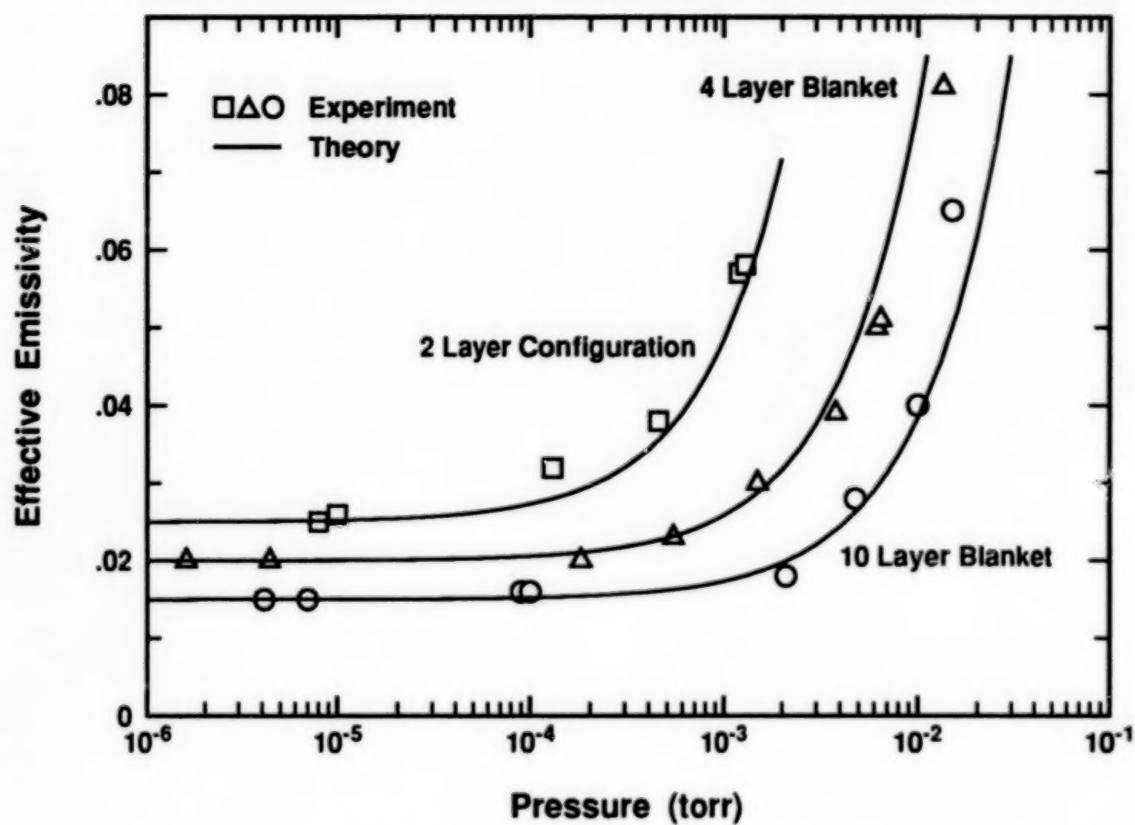


Figure 2. The Variation of Effective Emissivity with Pressure

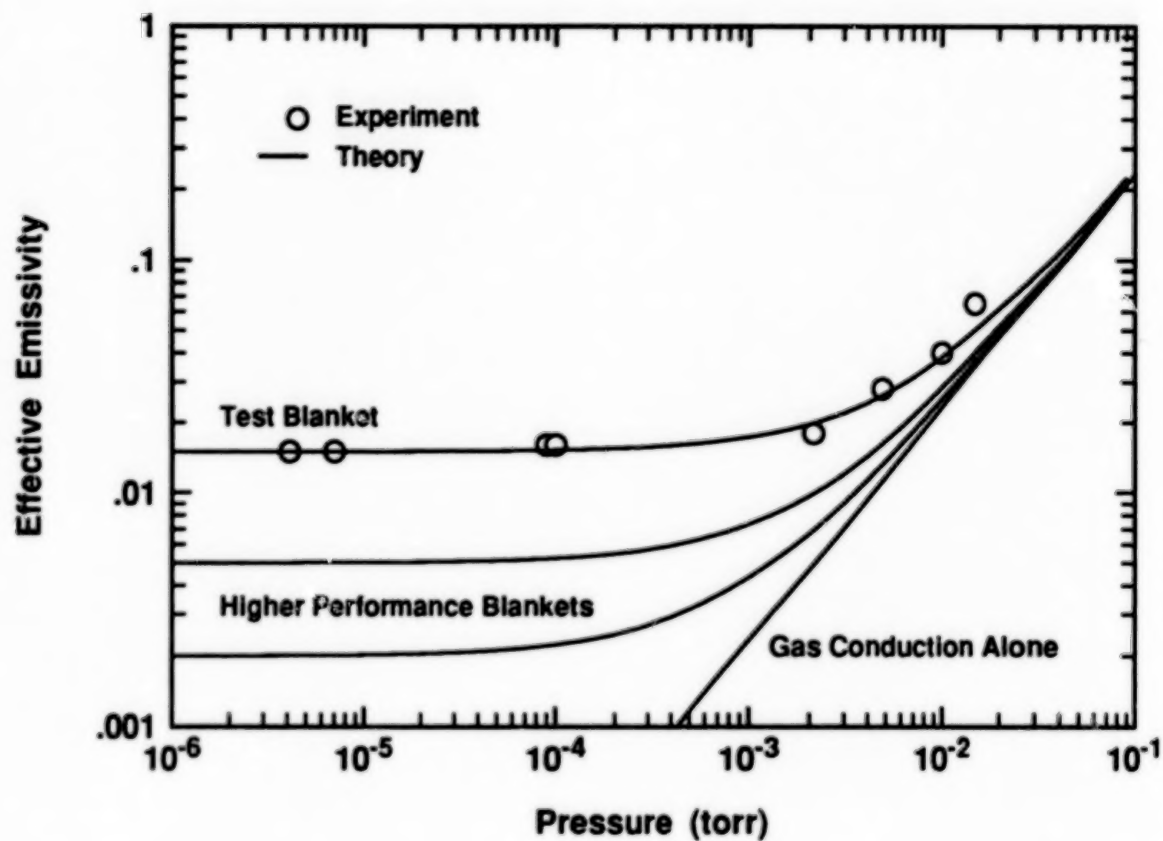


Figure 3. Ten Layer Blanket Performance With Gas Conduction

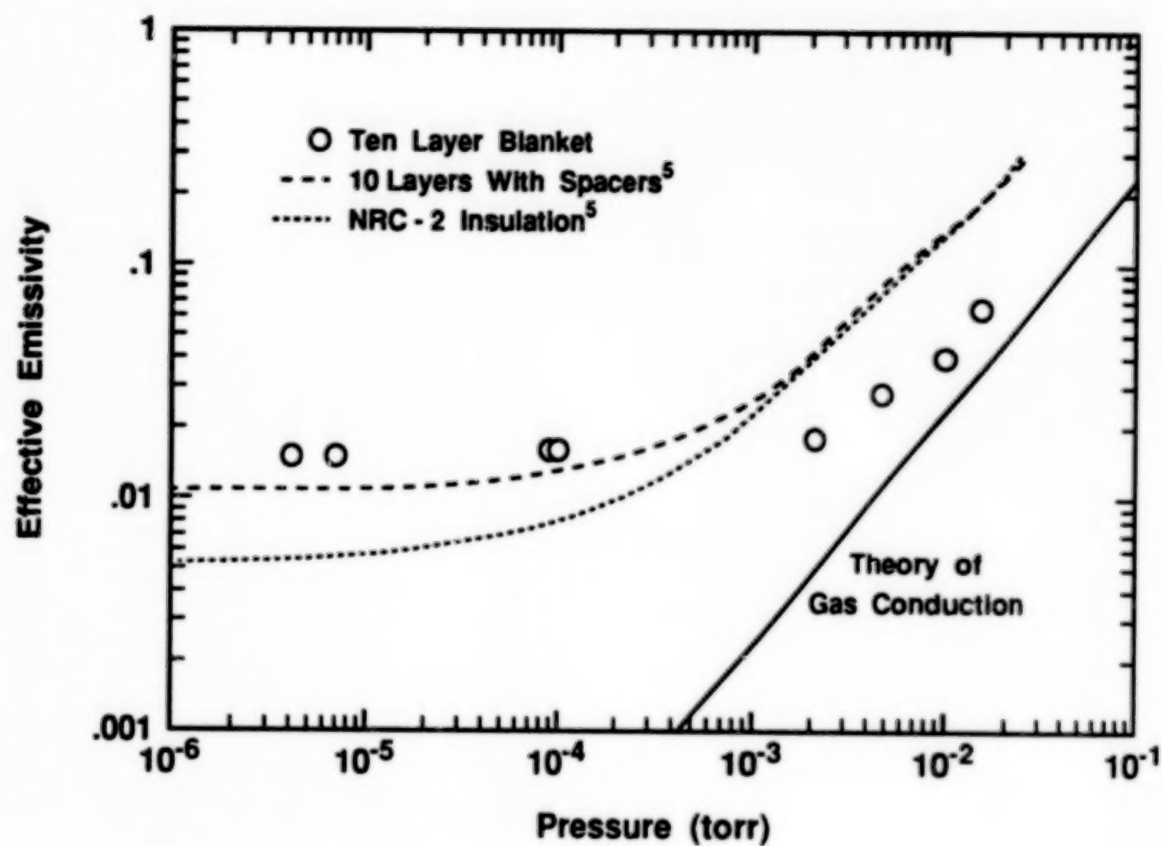


Figure 4. A Comparison of Blanket Performance.

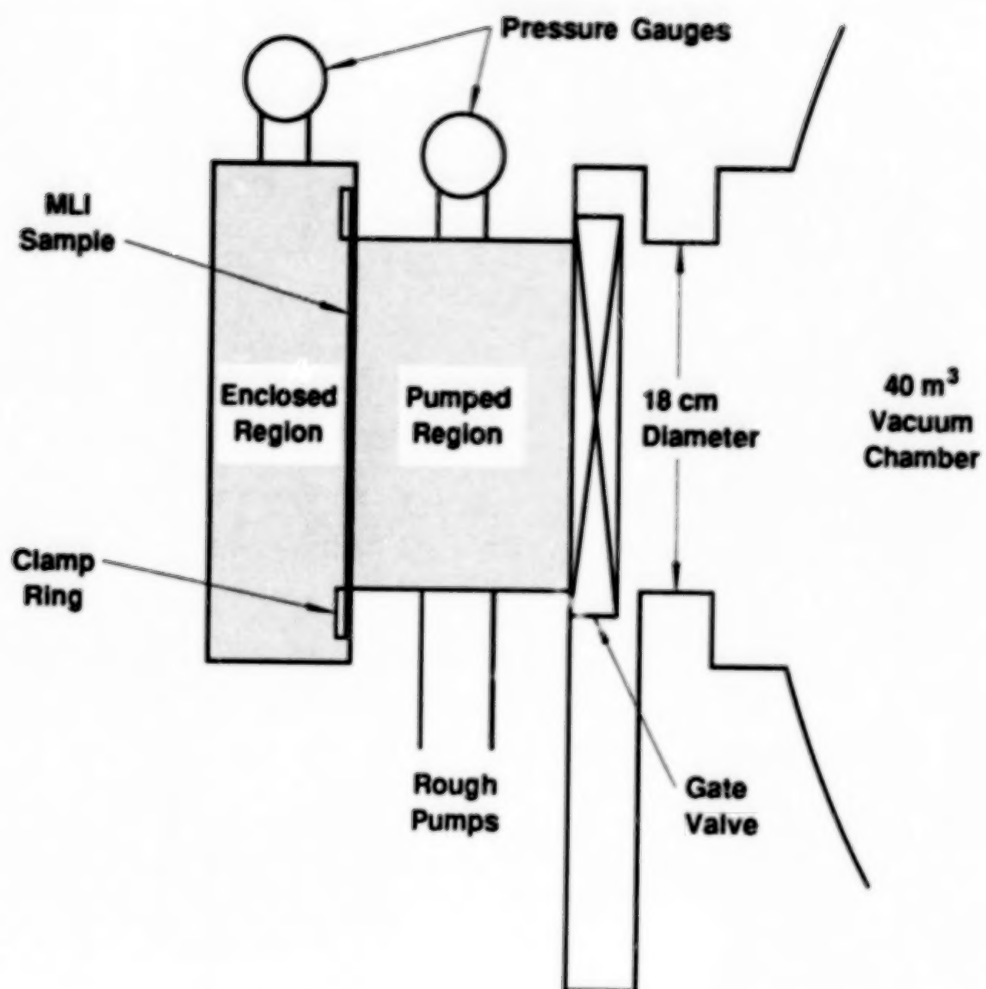


Figure 5. Pressure History Measurement Chamber

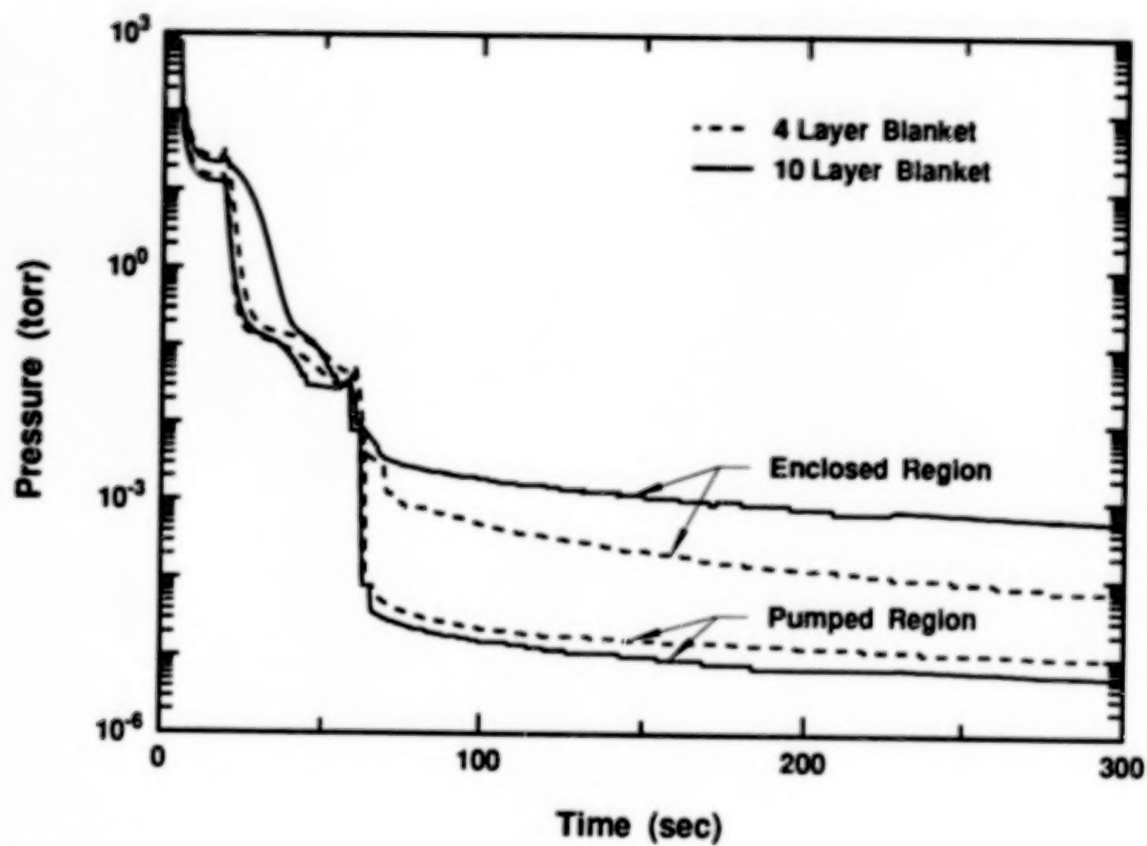


Figure 6. Measured Pressure Response During Rapid Depressurization

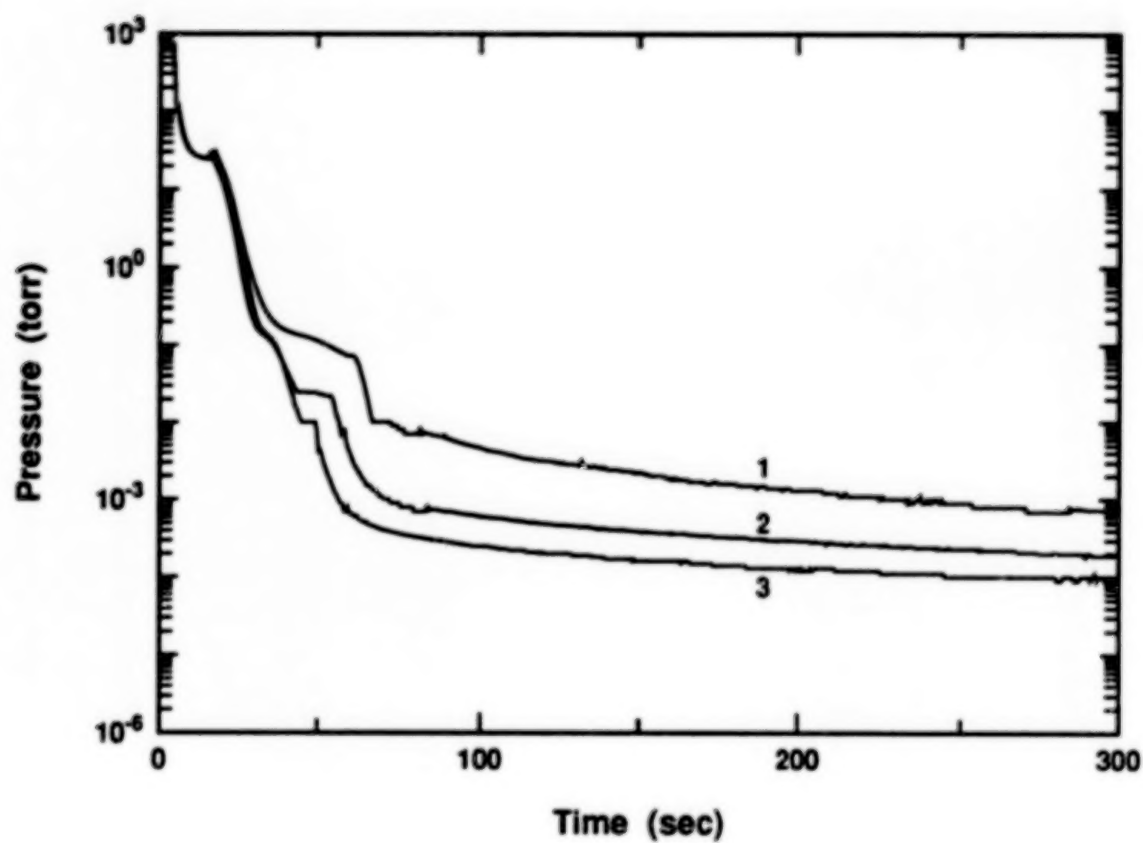


Figure 7. Consecutive Depressurizations of a Ten Layer Blanket

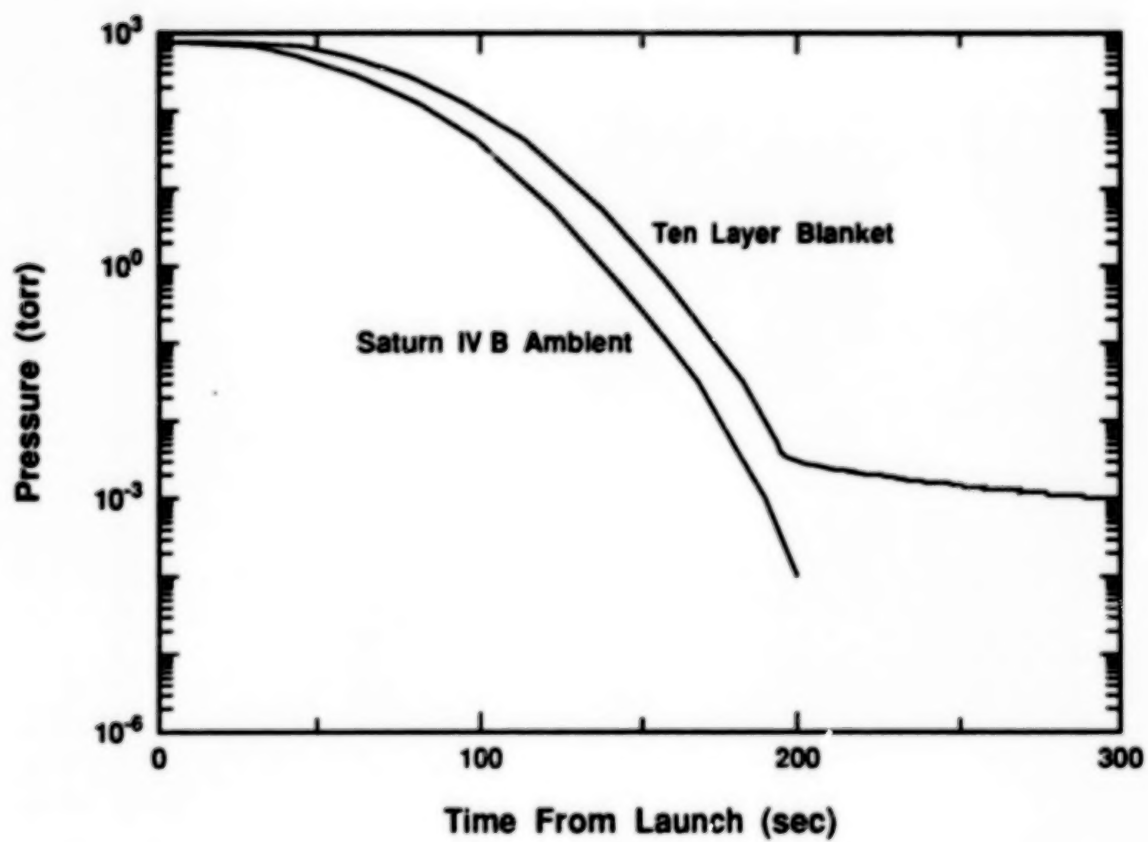


Figure 8. Actual Ascent Pressure History and Estimated MLI Response

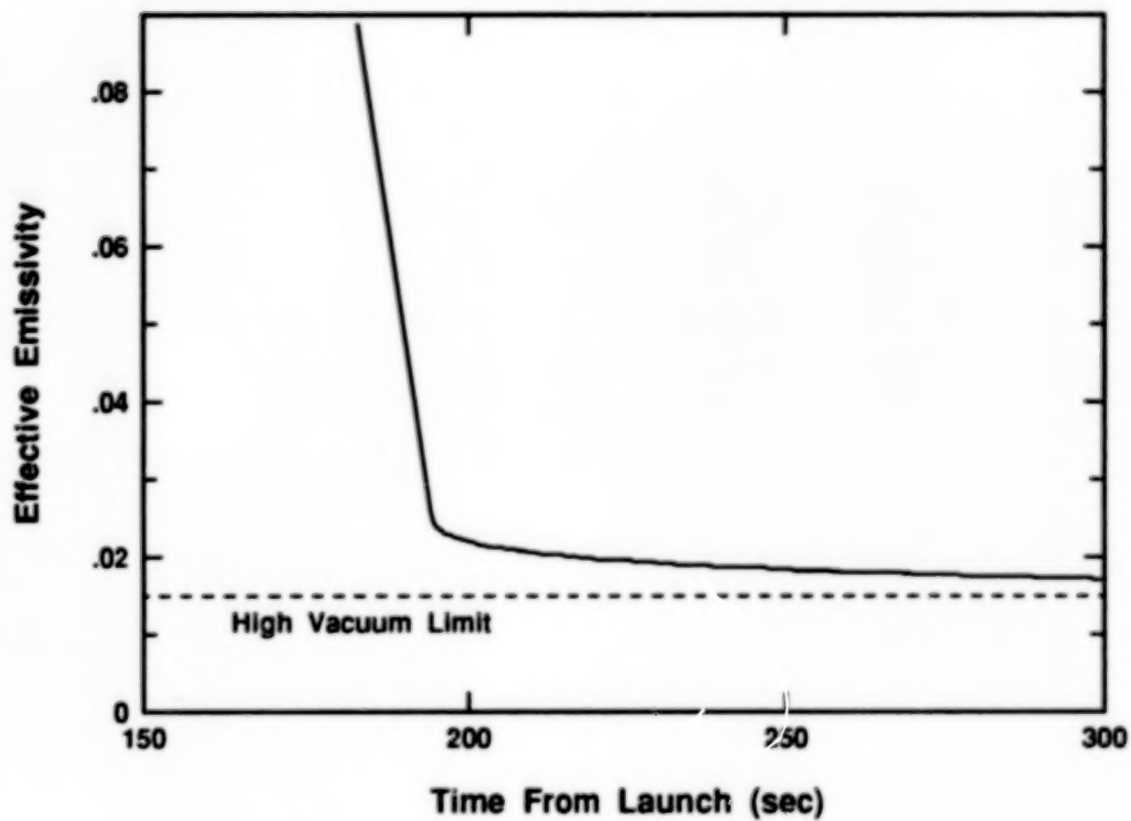


Figure 9. Predicted Ten Layer Blanket Performance

HIGH VACUUM FACILITY FOR HYDRAZINE THRUSTER TESTING

Patrick F. Neary
TRW
One Space Park
Redondo Beach, CA 90278
MI/1275

ABSTRACT

This paper describes an ongoing modification of a large (30-foot sphere) vacuum chamber to accommodate the ignition of an arcjet hydrazine thruster while maintaining a vacuum level of 1.0×10^{-5} torr or less. The vacuum facility consists of a 20-foot stainless steel vacuum tank with an internal LN_2 shroud, four 35-inch cryopumps and an 8-inch turbopump. To maintain a vacuum level of 1.0×10^{-5} torr or less, 900 sq. ft. of liquid helium (LHe) shroud surface has been installed to maintain the vacuum level and pumping requirements in Table I.

A vacuum level of 1.0×10^{-5} torr or less will allow the hydrazine thrust to exit the thruster nozzle and radiate into a space type environment so that plume flow field can be analyzed and compared to the analytical model density distribution profile. Some of the other arcjet thruster characteristics that will be measured are the electromagnetic interference (EMI) and exhaust contamination. This data will be used to evaluate if the arcjet thruster with its high specific impulse (450 sec, average) in comparison to current chemical propulsion thruster can be used for the next generation of communication satellites.

The LHe system is gravity-feed, with external LHe dewars that supply an internal 5001 LHe dewar with a phase separator which in turn supplies the LHe shrouds. The LHe shroud panel temperature must be maintained at 4.8°K or less to retain the hydrogen in a solid state on the LHe shroud panels. The hydrogen is a by-product of the hydrazine from the exhaust plume. The LHe shroud system consists of five 6-foot-wide by 15-foot-long shroud panels which are located inside the vacuum chamber. Each LHe shroud panel is positioned inside the chamber so the thruster plume will not radiate directly on the LHe shrouds.

The test is scheduled to start on May 1, 1990 and the data will be available on June 1, 1990.

Table I. Facility Pumping Capability and Arcjet Thruster Specifications

<u>Facility Pumping Capability</u>	
4 - 35" Cryopumps	
1 - 8" Turbopump	
30-foot-diameter 80°K Shroud	
900 square feet of LHe Shroud with the following pumping capability:	
N ₂	24.4 torr l/sec
H ₂	48.3 torr l/sec
<u>Arcjet Thruster Operational Specifications</u>	
Hydrazine Flow Rate	1.0×10^{-4} lbm/sec
Ignition Duration	16 hours
Vacuum Level Required	1.0×10^{-5} torr or less
Thrust	0.038 - 0.045 lbf

FLOW FIELDS OF LOW PRESSURE VENT EXHAUSTS

John J. Scialdone

NASA Goddard Space Flight Center, Greenbelt, MD 20771

ABSTRACT

The flow fields produced by low pressure gas vents have been described based on experimental data obtained from tests in a large vacuum chamber. The gas density, pressure, and flux at any location in the flow field are calculated based on the vent plume description and the knowledge of the flow rate and velocity of the venting gas. The same parameters and the column densities along a specified line of sight traversing the plume are also obtained and shown by a computer-generated graphical representation. The fields obtained with a radially scanning Pitot probe within the exhausting gas are described by a power of the cosine function, the mass rate and the distance from the exit port. The field measurements were made for gas at pressures ranging from 2 to 50 torr venting from pipe fittings with diameters of 3/16 inch to 1-1/2 inch I.D. (4.76 mm to 38.1 mm). The N_2 mass flow rates ranged from $2E-4$ to $3.7E-1$ g/s.

Introduction

Many spacecraft and the space station in particular, require venting of gases. The venting may be used to dispose of waste gases, to produce low-pressure drag makeup propulsion, or simply to provide low-level propulsion for attitude control or transfer. Contrary to these benefits, gas ventings in orbit have objectionable effects. The vented gases modify the environment and interfere with scientific and technical activities. They degrade the thermo-optical properties of surfaces where they may deposit or induce objectionable torque disturbances to the spacecraft. The environment modification may result in gaseous obscuration and molecular scattering in the field of view of an observatory instrument or of an observer. The vented gas deposited on critical surfaces can result in the complete degradation of an instrument or a system. The disturbance torque from a vent may result in a considerable expenditure of spacecraft propulsive power to correct for the unwanted disturbances.

This paper provides experimental data on the flow field produced by the gas vented in a large vacuum chamber from a pipe having inside diameters ranging from 3/16 to 1-1/2 in. The pressure of N_2 in the pipe ranged from 2 to 50 torr and the mass rates from (2×10^{-4}) to (3.7×10^{-1}) g/s. The flow fields were obtained by measuring the dynamic pressures (ρV^2) radially about the exhaust using a simple Pitot probe. The $\theta_{1/2}$ angle corresponding to 50 percent of the maximum Pitot pressures at the vent centerline was used with other parameters to provide an analytical description of the plume.

The characterization of the plumes and a knowledge of the vent gas terminal velocity allows, as shown, an estimate of the flux, the density, and the pressure at various locations in the plume flow field including surfaces where contamination may occur as a result of plume impingement. It provides for the evaluation of the column density along a line of sight traversing the plume, and for estimation of the return flux from the self scattering of the gas within the plume and with the ambient residual atmosphere. Also, the flow field description provides the definition of the gas propulsive thrust vector.

The paper indicates the techniques employed for the plume description, the measurements made, the parameters affecting the plume, and the analysis for the implementation of the results in a form which can be used for other plume conditions. A computer program has been written to plot in a normalized format the plume flux contours which also represent the density and pressure contours. The inclusion of these plots of a line describing an observation line of sight crossing the plume provides gaseous parameters of interest along that line and the evaluation of the column density.

The experimental investigation described here was carried out several years ago as the basis for a space experiment. The experiment described in Reference (1) measured the return flux scattered by the ambient atmosphere of a source of gas (neon) ejected on command from the spacecraft. The data reported here were needed to obtain an analytical description of the emitted neon plume. The investigation sought to produce a plume having a Lambertian distribution, which would offer a sufficient ambient scattering cross section for the return flux and, at the same time, provide a very low thrust and a low exhaust mass rate.

Experimental Procedures

The radial distribution of the gas flow vented from pipes of various diameters and for various mass flows was measured in a large vacuum chamber (3.65 m diameter, 4.57 m high) using the arrangement shown in Figure 1. A variable-size gas fitting was fitted to a 92-cm long, 4.76-mm I.D. Teflon tube. A Baratron^(R) capacitance pressure manometer, which when properly calibrated and temperature-controlled, can measure pressures down to 10^{-5} torr, was connected to the other end of the Teflon tube. The reference pressure of the Baratron was the chamber pressure. A sintered flow restrictor was located approximately 12 cm upstream of the pressure-measuring Baratron. The restrictor provided a neon flow of 4333 std cm^3/min at 525 psig supply pressure and conductance of about $1.96 cm^3$, as determined from previous

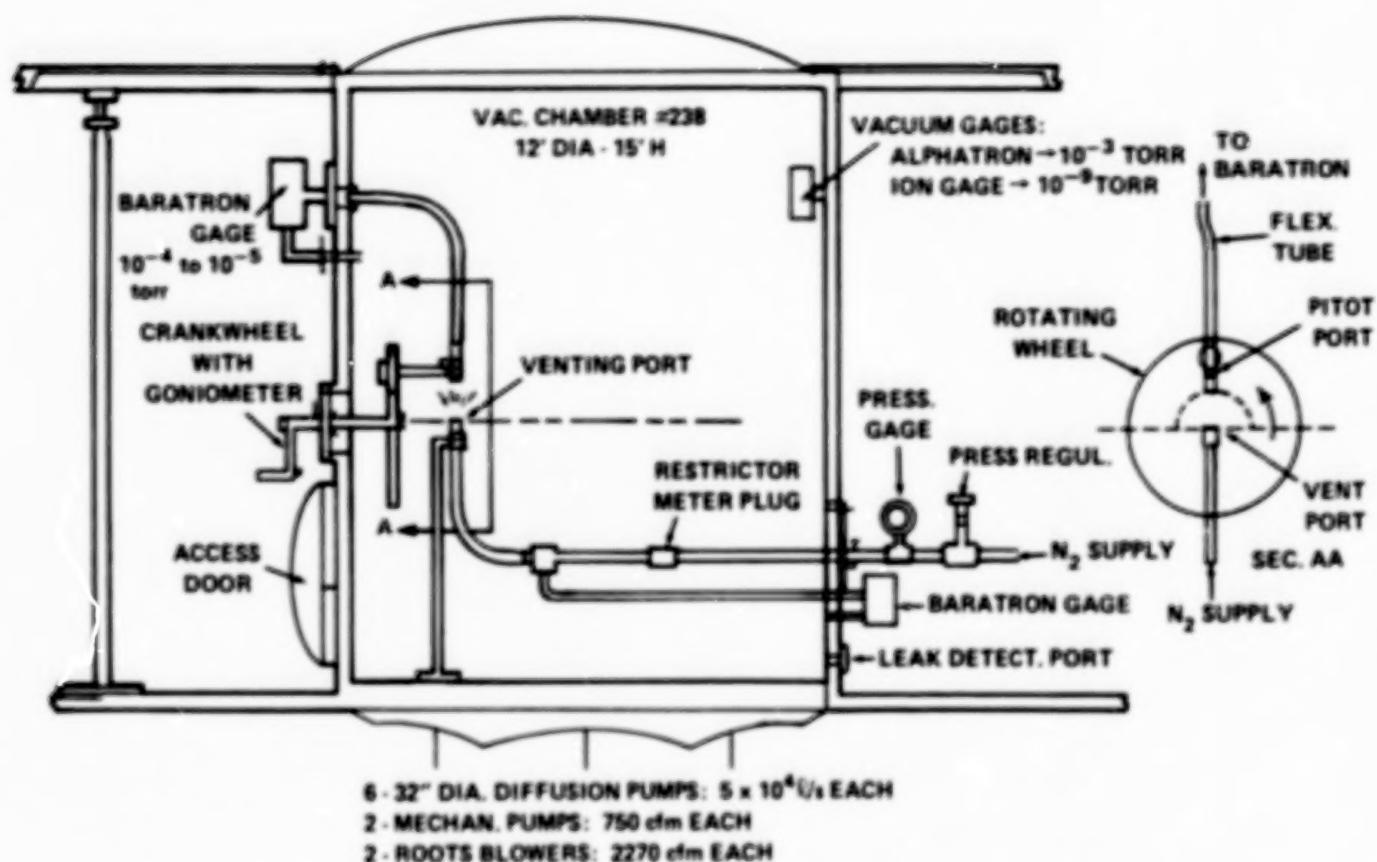


Figure 1. Vacuum system and test arrangement for vent plume flow field description.

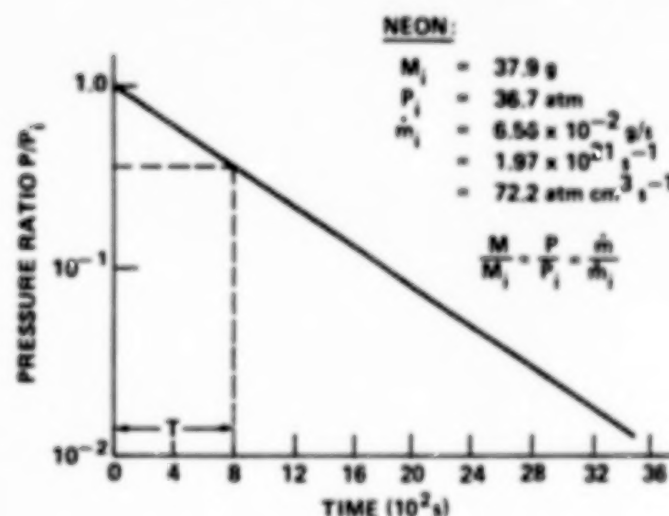


Figure 2. Neon pressure, mass, and flow rate versus time.

independent tests. The same restrictor, as will be shown, provided a nitrogen flow of 79 percent that of the neon, or 3440 $\text{stl cm}^3/\text{min}$.

A pressure gage, a pressure regulator, and the supply of N_2 were located upstream of the restrictor outside the vacuum chamber. The rate of gas exhausted from the pipe was known from other tests as a function of the supply pressure upstream of the porous plug restrictor and as a

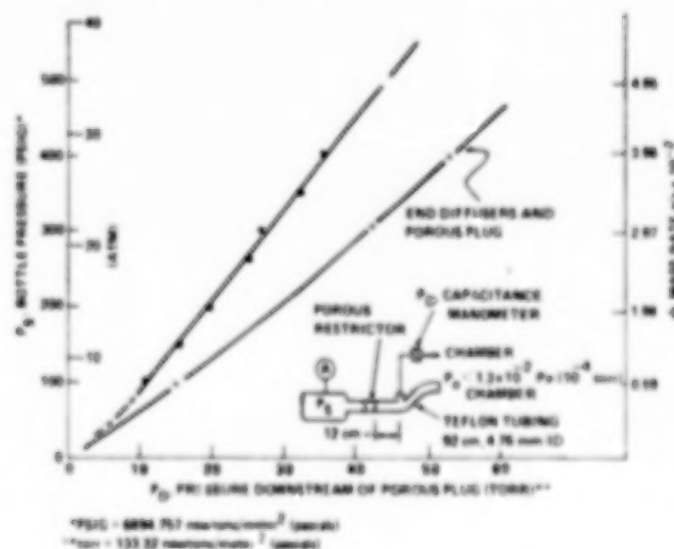


Figure 3. N_2 Downstream pressures and mass rates versus reservoir pressures.

function of the supply pressure depletion time as shown in Figure 2. Also, the pressure (P_2), downstream of the plug, was recorded as a function of the supply pressure (P_1) with and without a flow diffuser at the end of the Teflon tube (Figure 3). The diffuser, with a conductance greater than 5 l/s was to provide a spread out of the flow at the exit. The exit venting port at the end of the Tetco tubing, as shown in Figure 1, was firmly held at the centerline, same as measured

distance away, of a wheel which could be rotated from the outside of the vacuum chamber. The wheel had a slot for the mounting of a bracket holding a fitting attached at the extremity of a flexible tube connected to one of the sides of a Baratron capacitance manometer mounted outside the chamber. The other side of the Baratron was connected to the chamber pressure.

The slot in the rotatable wheel provided for changing the distance between the flow exhaust port and the fitting. The fitting, as a Pitot tube entrance, recorded the dynamic pressure in the gas stream (ρV^2) (dyne/cm²). The Pitot tube fitting was precisely aligned with the centerline of the exhaust vent fitting. The wheel angular motion, and hence, the angular position of the Pitot detector with respect to the centerline of the flow, was measured by a goniometric scale attached to the wheel crank, outside the chamber. Any angular positions could be held indefinitely for measurements under steady flow conditions. The 12-foot (3.65-m) diameter by 15-foot (4.57-m) high vacuum chamber was provided with 6 32-inch diameter diffusion pumps, each having 5×10^4 l/s pumping speed, 2 mechanical pumps, and 2 roots blowers. The pumping system was capable of maintaining chamber pressures lower than 10^{-7} torr. The chamber pressure was measured with an Alphatron gage down to a pressure of 10^{-3} and below this pressure with an ion gage. During the test, with the N₂ being vented in the chamber, the pressure was, in general, in the 10^{-4} torr range; i.e., about 5 to 6 orders of magnitude lower than the pressure (2 to 50 torr) downstream of the restrictor, and upstream of the gas exit.

The pressure data were collected manually for rotation steps of 5° and 10°, turning the Pitot detector both clockwise and counterclockwise starting with the 0° angle corresponding to the aligned detector and venting gas outlet. Measurements were not carried out, in general, beyond 90° from the centerline. At that time, and for the purpose of the test investigation, there was no interest in the backflow (> 90°) measurements. Backflow measurements would have provided flow directed toward the rear of the exhaust vent and would have included measurements beyond the Prandtl-Mayer angles. However, there were occasions when some measurements were made beyond 90°. On those occasions, and in some of those instances, negative pressures (chamber pressures higher than the flow pressure) were noted. This may have been indicative of gas flow creating a venturi effect at the detector entrance.

Several tests were carried out with the detector at various distances from the exit vent. But the majority and most conclusive tests were carried out with the detector 5.1 cm away from the vent exit. The detector tubing was also varied using either a 3/8-inch or a 1/8-inch internal diameter (9.52 mm or 3.17 mm).

Test Parameters

Flow Rate—The nitrogen flow rate was obtained from the appropriate modification of the flow rate found experimentally for the neon. The N₂ rate as dictated by the porous restrictor plug was measured to be $Q = 4333 \text{ atm cm}^3/\text{min}$ ($72.21 \text{ cm}^3/\text{s}$) (54.88 torr l/s) when the pressure upstream of the restriction was 525 psig (36.73 atm). The corresponding conductance was $1.96 \text{ cm}^3/\text{s}$. The mass flow rate at standard condition was $\dot{m} = 6.44 \times 10^{-2} \text{ g/s}$ and the molecular flow rate was $n = 1.94\text{E}21 \text{ molec/s}$. The flow at the restrictor was sonic or choked since the downstream pressures were always $P_D \ll P_S$.

The equivalent N₂-choked flow accounting for the difference in molecular masses and specific heat ratio can be evaluated from Reference 2,

$$\frac{Q_N}{Q_{N_2}} = \left(\frac{M_{N_2}}{M_N} \right)^{1/2} \frac{\left[\gamma \left(\frac{2}{\gamma+1} \right)^{\frac{\gamma+1}{\gamma-1}} \right]_N}{\left[\gamma \left(\frac{2}{\gamma+1} \right)^{\frac{\gamma+1}{\gamma-1}} \right]_{N_2}} = 0.84 \left(\frac{0.6839}{0.725} \right) = 0.794 \quad (1)$$

where $M_{N_2} = 20 \text{ g/mole}$, $M_N = 28 \text{ g/mole}$, $\gamma_{N_2} = 1.66$, $\gamma_N = 1.4$.

The N₂ flow rate is then $57.33 \text{ atm cm}^3/\text{s}$ (5.2 E-2 g/s ; 1.56 E-21 s^{-1}) for a supply pressure of 525 psi and the restrictor conductance is $1.55 \text{ cm}^3/\text{s}$.

Pressure Downstream of the Restrictor, Upstream of the Exit—The pressure downstream of the restrictor as a function of the restrictor upstream pressure was measured in a vacuum chamber and is reported in Figure 3. The measurements were made with a capacitance manometer using the vacuum chamber pressure as a reference pressure. The pressure was measured at about 12 cm downstream of the restrictor and about 80 cm from the end of the Teflon tubing. The long length of tubing was made necessary by installation requirements for the neon supply reservoir location aboard the spacecraft.

The N₂ mass flow rate is shown on the same plot in terms of the supply pressure. The plot also included the downstream pressure when a diffuser was added at the end of the tubing. That diffuser had a conductance much greater than that of the restrictor plug. It was employed to spread out the flow at the exit of the tubing. It did not, however, provide the intended function.

Exit Flow Velocities—A choking critical velocity exists at the tubing exit when the downstream to the exit pressure for N₂ is $P_e < .53 P_D$. The pressure P_D , as shown, varied from about 50 torr down to 1 or 2 torr, while the chamber pressure (P_c) was always several orders of magnitude lower than that. The

critical velocity for the N_2 at $T = 290$ K can be calculated as:

$$V_c = \left(\frac{2\gamma}{\gamma+1} \frac{RT}{M} \right)^{1/2} = 316 \text{ m/s} \quad (2)$$

where $\gamma = 1.4$, $M = 28$, and $R = 8.31 \times 10^7$ erg/mole K is the gas constant. The terminal velocity reached downstream of the exit port, for an adiabatic isentropic expansion, is

$$V_T = \left(\frac{2\gamma}{\gamma-1} \frac{RT}{M} \right)^{1/2} = 725 \text{ m/s.} \quad (3)$$

The Mach number based on the critical velocity is $M = (V_T)/(V_c) = 2.44$ at the terminal velocity. The temperature at this Mach number is

$$T = T_o \left(1 + \frac{\gamma-1}{2} M^2 \right)^{-1} = 132 \text{ K.} \quad (4)$$

The distance Z downstream of the exit port of diameter D where the maximum adiabatic terminal velocity has been established, can be estimated based on an approximate relationship valid for $Z/D \gg 1$ and $\rho/\rho_s \ll 1$, Refs. 3, 4, 5, 6.

$$M = \left(\frac{\gamma+1}{\gamma-1} \right)^{1/4} \left(\frac{Z/D}{4} \right)^{\gamma-1} \quad (5)$$

which for the value of $M = 2.44$ indicates that $Z \sim 0.63D$. This indicates that at the distance of 5.1 cm (or 6.8 cm) used in the present tests for the location of the Pitot tube, the flow would have reached maximum velocity.

Exhaust Exit Ports--The exhaust port provided by pipe fittings, varied from 3/16 inch (0.476 cm) to 1-1/2 inches (3.18 cm) internal diameter. The diffuser had a centered exit area corresponding to 7/8 inch (2.23 cm) in diameter. For all tests, with the exception of one, the length of the pipe fittings to their internal diameters (L/D) were much greater than one.

Test Data

The experimental flow fields measured for various vent sizes and vent pressures are shown in Figures 4 through 10. The vent upstream pressures varied from about 2 to 50 torr and the downstream chamber pressures ranged down to 10^{-4} torr during the measurements. The mass flow rates were from 3.7×10^{-1} to 2×10^{-4} g/s. For some initial measurements carried out in a small vacuum chamber and reported here for completeness, the chamber pressures ranged from 10^{-3} to 10^{-1} torr. The various parameters for the test conditions are indicated on the plots. The plots also indicate the value of angle $\theta_{1/2}$. This is the angle corresponding to the Pitot measurement pressure value of 1/2 the maximum pressure measured at the centerline of the flow. The magnitude of that angle is a measure of the plume spread. For the present test parameters, the $\theta_{1/2}$ angle varied from an aver-

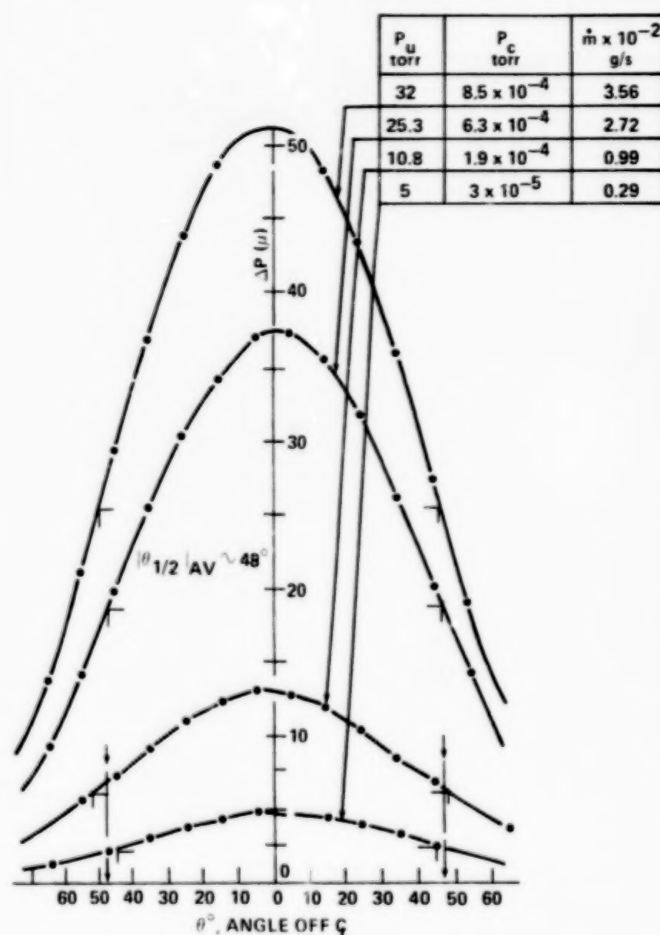


Figure 4. Pitot pressures as a function of angles off ζ . Pitot opening dia., $d = 3/8$ in; radial distance of Pitot, $r = 5.1$ cm; pipe exit I.D. = 3/16 in. (4.76 mm).

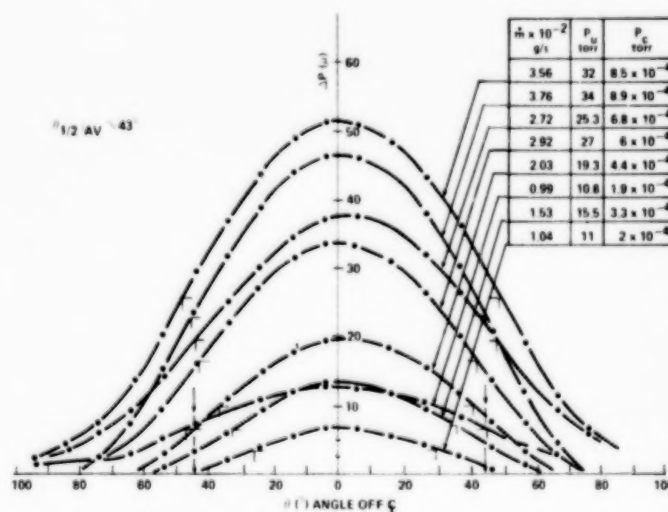


Figure 5. Pitot pressures as a function of angles off ζ of pipe flow. Pitot opening dia., $d = 1/8$ in.; radial distance of Pitot, $r = 5.1$ cm; pipe exit I.D. = 3/16 in. (4.76 mm).

age value of 48 degrees when the pressures in the chamber were in the 10^{-4} torr range and average values of 18 to 20 degrees when those pressures were in the 10^{-1} torr range. Flow field results with the high chamber background pressures using 1/4-, 3/8-, and 3/4-inch (6.25, 9.52 and 19.05 mm) diameter exhaust pipe openings and for a 0.196-in. (0.498-mm) diameter, 0.029-inch (0.736-mm) thickness orifice, are also being reported. These results were obtained when the downstream chamber pressures were in the 10^{-3} torr range or higher. The lowest upstream pressure was 2 torr which resulted in a 3- to 4-order-of-magnitude-difference between upstream and downstream pressures.

Data Reduction and Application

The normalized Pitot pressures versus angles obtained from the tests, when superimposed on a graph (Figure 11) showing the function of $\cos^n \theta$ for values of n from 1 to 5, show that the pressures can be represented for a considerable range of angles (from 0° to $75-80^\circ$) quite well by a cosine power function. The data obtained for the 3/16-inch (4.76-mm) diameter pipe, $P_u = 25.3$ torr, $P_c = 6.3 \times 10^{-4}$ torr, $\theta_{1/2} = 48$, and for those of the 1-1/2-inch (38.1-mm) diameter pipe, $P_u = 37$, $P_c = 9.3 \times 10^{-4}$, $\theta_{1/2} = 40^\circ$, have been superimposed on the cosine plots. The divergence occurs beyond $75-80^\circ$ where the data obtained from the measurements is not available, or careful measurements were not taken, at those angles. The Pitot pressures for those large angles were less than 5 percent of the maximum ΔP pressure at the centerline.

The fraction of gas included at those angles is about 2 percent of the total, and in those regions, the plumes may be represented by an exponential function. This was not done because of the limited data available.

The value of the exponent of the cosine function appropriate for each distribution can be obtained as shown in Figure 12 by plotting on log paper $\cos^n \theta$ versus the normalized Pitot pressure, $\Delta P / \Delta P_{\max}$. The slope of the curve provides the value of n . The straight lines were drawn attempting a best fit. It is apparent that the experimental data fit the straight line reasonably well with the divergence occurring at the large angles. The $\theta_{1/2}$ angle from these plots is seen to become smaller as the size of the vent grows from 3/16 inch to 1-1/2 inch (4.76 mm to 38.1 mm). The exponent of the cosine grows from about $n = 1.74$ to $n = 2.51$. It is, therefore, reasonable to use a cosine function to represent the plumes investigated here. However, one should be aware that at large angles, an error is being introduced.

The flux of gas ϕ ($\text{g cm}^{-2} \text{ s}^{-1}$; $\text{cm}^{-2} \text{ s}^{-1}$) exhausting from one of the above openings can be represented, based on the above discussion, by $\phi = k \cos^n \theta$ where k is a constant to be determined. The elemental mass of gas $d\dot{m}$ in traversing an element area of dA of an axisymmetrical plume will be ϕdA and the total mass rate will be

$$\dot{m} = \int_A \phi dA.$$

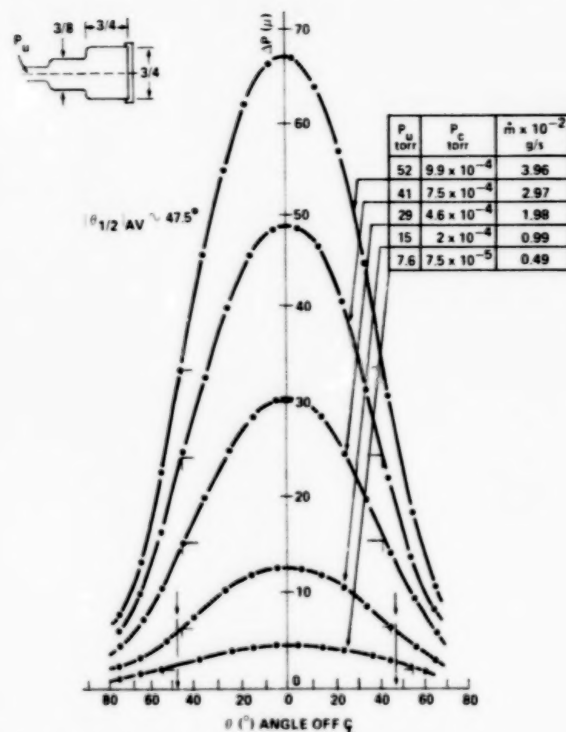


Figure 6. Pitot pressures as a function of angles off ζ of pipe flow. Pitot opening dia., $d = 1/8$ in.; radial distance of Pitot, $r = 5.1$ cm; pipe exit I.D. = $3/4$ in. (1.90 cm).

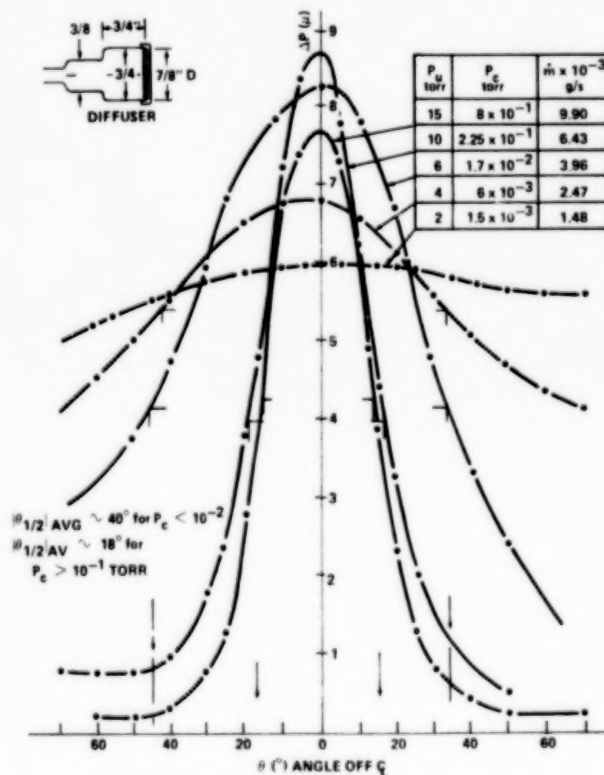


Figure 7. Pitot pressures as a function of angles off ζ of pipe flow. Pitot opening dia., $d = 1/8$ in.; radial distance of Pitot, $r = 5.1$ cm; diffuser $7/8$ in. dia (2.22 cm).

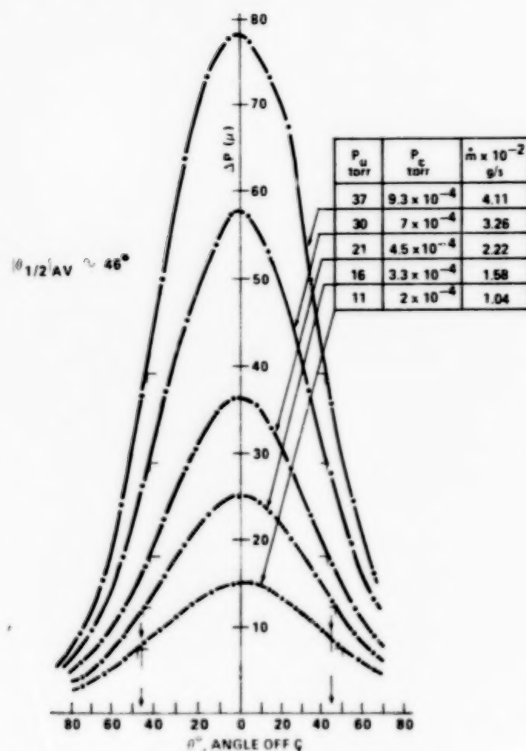


Figure 8. Pitot pressure as a function of angles off \bar{Q} of pipe flow. Pitot opening dia., $d = 3/8$ in.; radial distance of Pitot, $r = 5.1$ cm; pipe exit I.D. = 1 in. (2.54 cm).

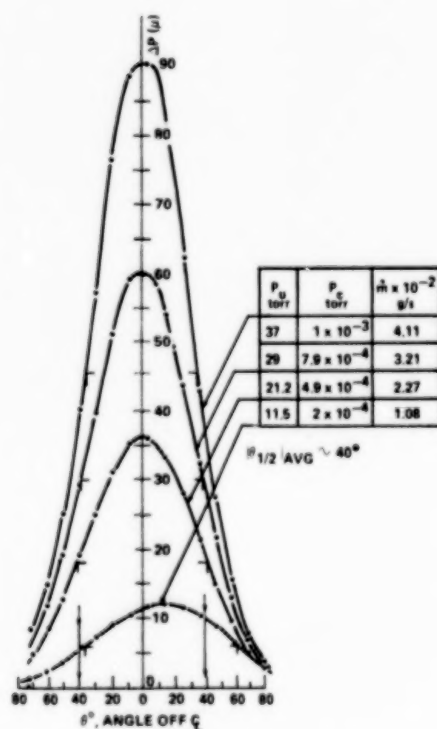


Figure 9. Pitot pressure as a function of angles off \bar{Q} of pipe flow. Pitot opening dia., $d = 1/8$ in.; radial distance, $r = 5.1$ cm.; pipe exit I.D. = 1.5 in. (3.81 cm).

The element of area using polar coordinates is

$$dA = r d\theta (r \sin\theta d\varphi) = r^2 \sin\theta d\theta d\varphi$$

where $0 < \theta < \pi/2$ is the angle of the centerline of the plume to the element of area, $0 < \varphi < 2\pi$ is the angle of symmetry, and r is the distance from the center of the source at the exit to the element of area.

The integration giving the total flow rate is then

$$\begin{aligned} \dot{m} &= \int_A \phi dA = k \int \cos^n \theta (r^2 \sin\theta d\theta d\varphi) = \\ &= k \int_0^{2\pi} r^2 d\varphi \int_0^{\pi/2} \cos^n \theta \sin\theta d\theta = \\ &= k \left[2\pi r^2 \left(-\frac{\cos^{n+1} \theta}{n+1} \right)^{\pi/2} \right] = \frac{2\pi r^2}{n+1} k \end{aligned}$$

$$\text{and the constant is } k = \dot{m} \left(\frac{n+1}{2\pi r^2} \right). \quad (6)$$

The flux at a distance r and angle θ from the centerline is given in terms of the total mass rate being exhausted

$$\phi = \frac{n+1}{2\pi r^2} \dot{m} \cos^n \theta \quad (\text{g cm}^{-2} \text{s}^{-1}; \text{cm}^{-2} \text{s}^{-1}; \text{moles s}^{-1} \text{cm}^{-2}) \quad (7)$$

where the units of the flux depend on the units of \dot{m} and r .

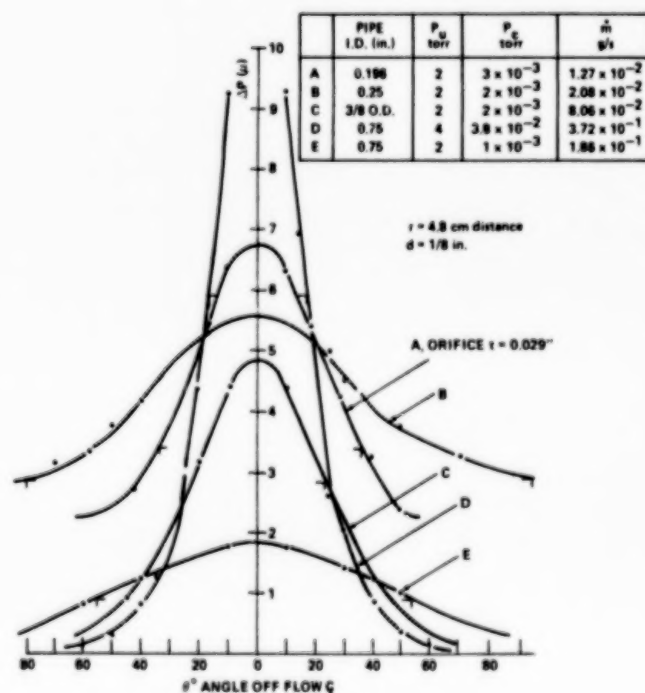
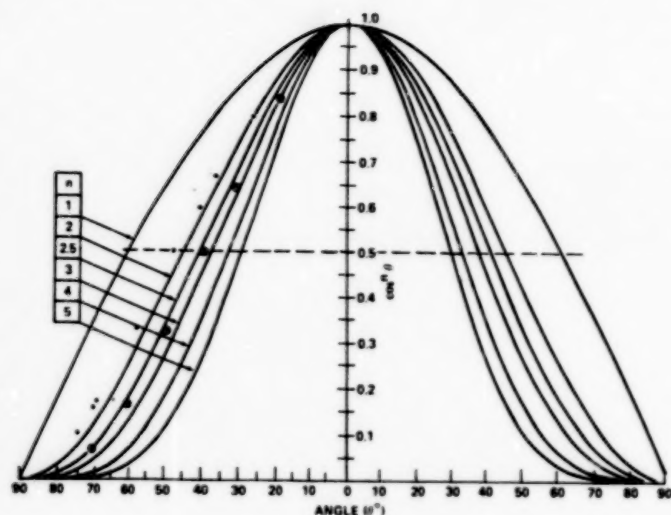


Figure 10. Pitot pressures as a function of angles off \bar{Q} of pipe flow.



• I.D. 3/16 in. (4.76 mm), $P_s = 275$ psig, $P_u = 25.3$ torr, $P_c = 6.3 \times 10^{-4}$, $d = 1/8$ in @ 5.1 cm
 • I.D. 1-1/2 (38.1 mm), $P_s = 415$ psig, $P_u = 37$ torr, $P_c = 9.3 \times 10^{-4}$ torr, $d = 1/8$ in @ 5.1 cm

Figure 11. $\cos^n \theta$ versus θ .

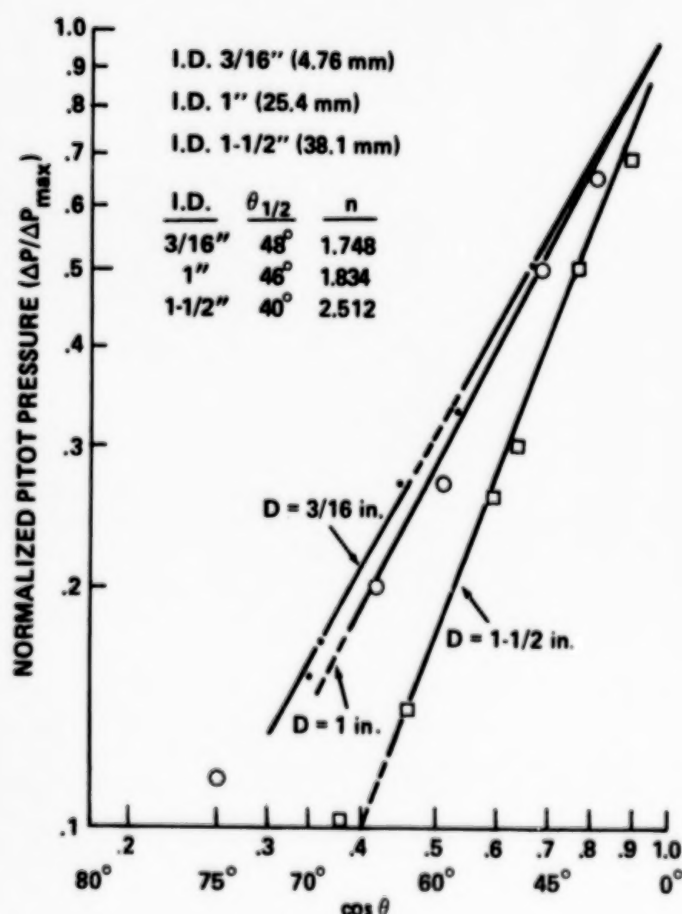


Figure 12. Normalized pressure vs. $\cos \theta$.

Application

The expression for the flux also indicates the density at any distance r and angle θ , if the velocity of the flux is known. This density, since $\rho = \phi/V$, is

$$\rho = \left(\frac{n+1}{2\pi r^2} \right) \frac{\dot{m}}{V} \cos^n \theta \quad (\text{g cm}^{-3}; \text{cm}^{-3}) \quad (8)$$

The pressure, $P = \rho KT = \rho (RT)/(M)$ for a temperature $T(K)$, molecular mass M (gr/mole), and $R = 62.36 \times 10^3$ torr $\text{cm}^3/\text{mole K}$ the gas constant is,

$$P = \left(\frac{n+1}{2\pi r^2} \right) \frac{\dot{m}}{V} \frac{RT}{M} \cos^n \theta \quad (\text{torr}) \quad (9)$$

Given then the experimental data on the flow field or simply the angle $\theta_{1/2}$, the mass flow rate \dot{m} , the temperature and the terminal velocity one can estimate pressure, density, and flux at any location within the hemisphere of the gas discharge. These parameters are important for the assessment of contamination hazards to systems exposed to the vented gases, and for an estimate of either the mass or the number column density along a line of sight. The column density is obtained by performing the integration

$$N = \int_0^x \rho dx = \int_0^x \frac{n+1}{2\pi x^2} \frac{\dot{m}}{V} \cos^n \theta dx \quad (10)$$

where x is the distance along the line of sight. By an appropriate description of the line of sight, e.g., by a line $y = ax + b$ described by its angle and origin with respect to the gas source, one can obtain the parameters of interest as the line of sight intersects the plume.

Two computer programs have been written to provide graphically and numerically, those parameters. One needs to input ϕ/\dot{m} values and n for the plume description; the parameters a and b for the equation describing the line of sight; m (meters), the distance along the line of sight; and the increment of dm (meters) sought for the integration and evaluation of the column density. An example of the plots provided by these programs is shown in Figure 13. For generality, the fluxes as a function of the distances are reported in terms of ϕ/\dot{m} (cm^{-2}) as is the sum of the flux contributions,

$$\sum_0^d \frac{\phi}{\dot{m}} d \quad (\text{cm}^{-2} \text{m})$$

along the LOS. With the exhaust rate \dot{m} , and V the exhaust velocity, one can obtain the flux and the column density, N

$$N = \sum_0^d \frac{\phi}{\dot{m}} \frac{\dot{m}}{V} d \quad (\text{g/cm}^2, \text{cm}^{-2}) \quad (11)$$

Similarly, the pressure can be obtained in the same manner using the appropriate expressions.

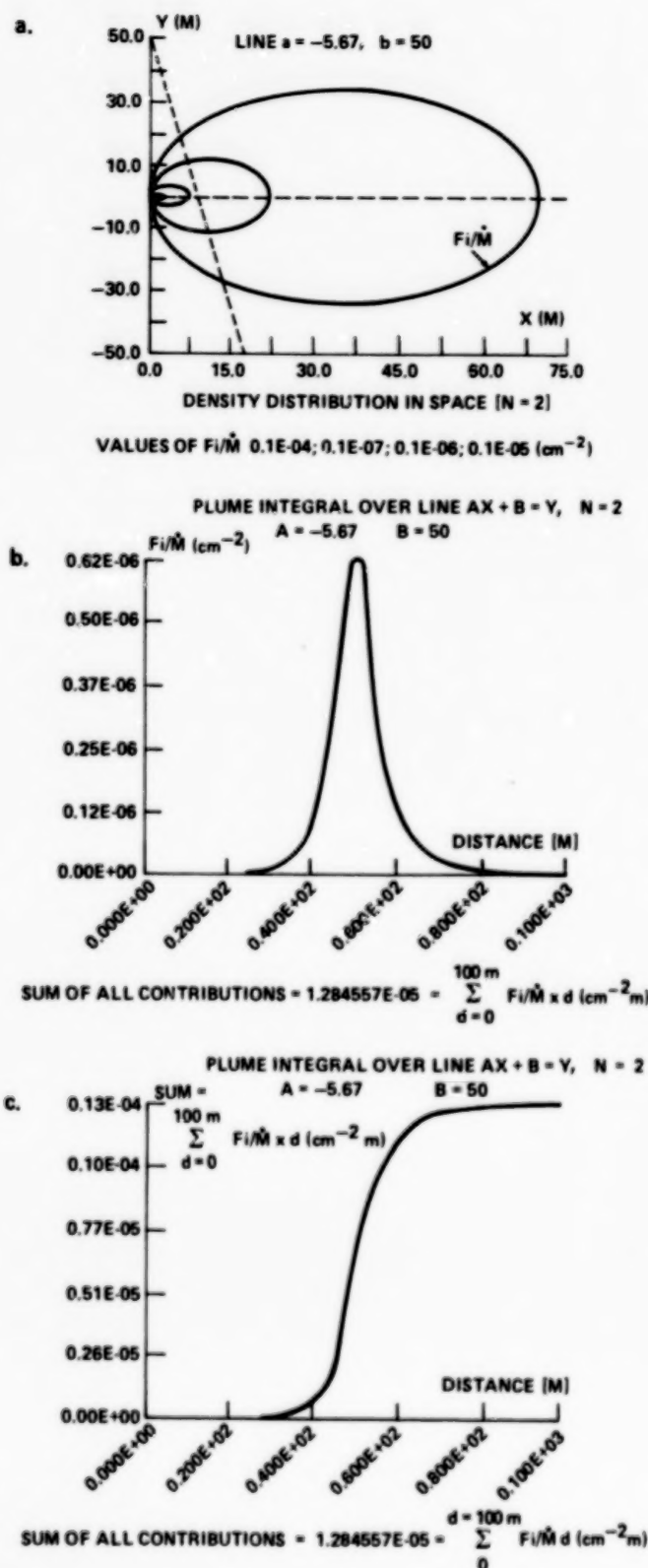


Figure 13. Flux density contours, flux density along a line of sight, and sum of flux density along the line for an $N = 2$ plume.

Conclusions

The radial and angular distribution of the gas flow from openings with large L/D , and diameters ranging from 3/16 inch to 1-1/2 inches (4.76 mm to 38.1 mm) were measured in a large chamber where the pressure was maintained in the 10^{-4} torr range, or lower. The N_2 flow ranged from 2×10^{-4} gr/s to 3.7×10^{-1} gr/s and the pressures upstream of the exhaust vent ranged from 2 torr to 52 torr. Some preliminary tests were carried out in a small chamber. In those tests, the chamber pressures varied from 10^{-1} torr to 10^{-3} torr. A Pitot probe was used to measure the flow rate momentum at various angles from the centerline of the exhaust flow.

The diameter of the Pitot tube opening and its distance from the exhaust aperture were also changed in two instances to evaluate their effects.

The measurements indicated that for the range of upstream pressures and mass flows employed in these tests, the chamber downstream pressure must be about 5 orders of magnitude lower than the pressures at the exhaust. Under those conditions one obtains full lateral expansion of the plume.

The angle, $\theta_{1/2}$, corresponding to 50 percent of the maximum pressure in the flow field at centerline, varies from 40° to 48° when the pressure upstream of the exhaust varies from 2 torr to 50 torr and the chamber pressure is about 4×10^{-4} torr, or lower.

The half angle increases as the pipe opening diameter decreases.

The effect of the downstream pressure severely restricts the spreading of the plume.

The diameter of the Pitot detector was varied from 1/8 inch to 3/8 inch (3.17 mm to 9.52 mm). The change did not affect the measurements. The measurements at each angle from the plume centerline were made by holding the angular positions for a sufficient length of time to insure steady pressure flow conditions at those locations.

The distance of the Pitot detector (5.1 cm or 6.8 cm) did not affect the flow distribution. This indicates that the flow was frozen at those distances. The magnitude of the pressure readings decreased with the square of the distance.

Most of the flow patterns were obtained with the detector located 5.1 cm from the exit port. This corresponded to a downstream distance of about 10 diameters for 0.476-cm diameter pipe and 1.33 diameters for the 3.81-cm diameter pipe.

Measurements beyond 80° were not available because of the limitation in the pressure readings and the lack of interest at those large angles at the time the measurements were made. However, more than 95 percent of the plume mass is contained within the half angles of 75° and about 75 percent of the same mass is within the half angle of 40° .

The flux at the distance r and angle θ from the centerline can be described by a power of the cosine function up to a half angle of about 75° . The flux beyond those angles may be described by an exponential function. This, however, was

not attempted. If one chooses to describe the plume with a cosine function up to 90° half angle, the error is then less than 10 percent.

The coefficient in the expression of the cosine function for the plume description includes the mass rate from the vent, the distance at which the flux is being measured, and a factor which includes the power of the cosine function; i.e.,

$$\phi = \frac{n+1}{2\pi r^2} \dot{m} \cos^n \theta.$$

The power of the cosine function can be obtained by plotting on log coordinates the normalized Pitot pressures versus the cosine of the angle. The power can also be ob-

tained by establishing the angle from the centerline where the Pitot pressure is 50 percent of the maximum pressure corresponding to the 0° angle. That value reported on a graph of the cosine to various powers of cosine, can provide the power of n by comparison.

The plume description with the appropriate equation can provide the densities, pressures, and fluxes at any distance and angle from the exhaust aperture within the hemisphere in which the gas is exhausted. Also, one can obtain the same parameters along a line of sight traversing the plume at any angle and originating at a plane parallel to the aperture. The data provide simultaneously the column density which is an important parameter in scientific measurements.

References

1. Scialdone, J.J., "Correlation of Self-Contamination Experiments in Orbit and Scattering Return Flux Calculation," NASA TN-D-8438, March 1977.
2. Santeler, D.J. et al., "Vacuum Technology and Space Simulation," NASA SP-105, 1966, page 92.
3. Fite, W.L., "Expansion of Gases from Molecular Beam Sources," Research Note #1, January 1971, Extranuclear Laboratory, Inc., Pittsburgh, PA.
4. Ashkenas, H., and F.S. Sherman, "The Structure and Utilization of Supersonic Free Jets in Low Density Wind Tunnels," in *Rarefied Gas Dynamics*, 4th International Symposium, Vol. II, Edited by J.H. deLeeuw, 1966, page 84.
5. Anderson, J.B. et al., "Studies of Low Density Supersonic Jet," in *Rarefied Gas Dynamics*, 4th International Symposium, Vol. II, edited by J.H. deLeeuw, 1966, page 106.
6. French, J.B., "Molecular Beams for Rarefied Gas Dynamics Research," NATO Advisory Group for Aerospace Research and Development, Agardograph 112.

MULTIPURPOSE HARDENED SPACECRAFT INSULATION

Carlos H. Steimer
TRW Inc., Space & Defense Sector
Space & Technology Group

ABSTRACT

TRW has successfully developed and implemented a Multipurpose Hardened Spacecraft Multilayer Insulation (MLI) system which meets diverse survivability and performance requirements.

Within the definition and confines of a MLI assembly (blanket), the design:

- a. Provides environmental protection from natural and induced nuclear, thermal, and electromagnetic radiation
- b. Provides adequate electrostatic discharge protection for a geosynchronous satellite
- c. Provides adequate shielding to meet radiated emissions requirements
- d. Will survive ascent differential pressure loads between enclosed volume and space.

This paper describes the MLI design which meets these requirements and discusses design evolution and verification.

The application is for MLI blankets which closeout the area between the laser crosslink subsystem (LCS) equipment and the DSP spacecraft compartment. Ancillary requirements were implemented to ease installation at launch facility and to survive ascent acoustic and vibration loads. Directional venting accommodations were also incorporated to avoid contamination of LCS telescope, spacecraft sensors, and second surface mirrors (SSMs).

As the MLI design matured, requirements were changed or better defined, resulting in a long and tedious conceptualization and testing phase. The challenges to the insulation personnel to accommodate these diverse and dynamic requirements were significant, if not at times painful.

SCOPE

The process undertaken by TRW to develop, verify, and test a MLI configuration that met all requirements was a long and tedious one taking over four years to complete. Several design iterations were required to incorporate ancillary requirements.

The narrative form was used to capture the evolution of the design. The intent of this paper is two-fold:

1. To describe the new MLI configuration that meets diverse performance requirements by documenting its construction and assembly/fabrication methodology

2. To reinforce the need for concurrent engineering (CE) as a major part in any hardware development phase. Lessons learned during this process do well in bolstering this argument.

The appendix presents design criteria as edicted toward the end of the hardware development phase. As sometimes happens in research and development, the actual "requirements definition" package was written after the start of the design phase. An example of the 'tiger team' instead of 'concurrent engineering' mentality.

BACKGROUND

A decision was made at the inception of the program to provide radiation protection to sensitive LCS equipment using hardened MLI closeouts for the open (to space) areas between the DSP spacecraft bay and the LCS radiators. The LCS design, by a separate contractor, was too mature and the weight penalty too large to harden the electronics boxes themselves.

The author believes (hindsight, of course) that this decision might have been different if it was tempered by emphasis on CE activity rather than cost trade-offs.

SUBSYSTEM DESCRIPTION

Figure 1 describes LCS hardware configuration, DSP spacecraft structure (bay), and MLI closeouts. Electronic equipment (mounted to the equipment frame) and the telescope comprise the LCS subsystem. All LCS equipment, with the exception of the gimbaled telescope, is supported by the frame which is mounted vertically in the spacecraft bay. The equipment frame and the telescope are independently supported at the same three points in the bay by essentially separate truss systems.

Second surface mirror radiators are mounted on the front (spacecraft +X) of the electronic equipment to radiate heat outward. These radiators are beryllium and are fairly stiff and light. Detectors and lasers support the two lower radiators and are in turn supported by the optics assembly which is attached by a three point mount to the lower part of the equipment frame. The radiators are attached at their edges to the DSP bay by the LCS MLI closeouts.

REQUIREMENTS DEFINITION AND IMPLEMENTATION

PHASE 1. THERMAL INSULATION BLANKETS HARDENED FOR RADIATION PROTECTION

Initial requirements established the utilization of a tantalum metal foil (0.001 in. thick) within the MLI construction to provide the hardening. This 1 mil thick tantalum foil would provide the radiation hardening equivalent of 0.090 in. thick aluminum. The thin foil was malleable and could be readily formed into the polyimide and polyester MLI shapes. At this point, cognizant engineering groups decided that this would be the optimum and most cost effective method of implementing the hardening requirement. Figure 2A shows the typical construction (Phase I) of the MLI closeouts. The tantalum foil is encapsulated by 1 mil polyimide tape to provide protection from abrasion during forming and assembly into the MLI.

Due to the hardening requirement, the design of the closeouts was predicated on 100% line-of-sight protection from any potential natural or induced nuclear

radiation source in space. Insulation development personnel attacked the problem by assuming that the closeouts, which closed out the spaces between LCS electronic radiators and spacecraft structure, had to "hold water." This analogy served well to implement the "line-of-sight" design requirements.

The three-dimensional shape of the thermal MLI closeout designs required forming of the tantalum to duplicate the thermal MLI shape. This required a significant amount of new fabrication and assembly methodology development. Stress relief holes at corners, normally required in sheet metal or MLI fabrication, could not be incorporated. In this case, any aperture, no matter how small, negated the radiation protection. Workarounds for thin foil forming methods were developed to alleviate this problem.

During the configuration development phase, tantalum barriers were necessary at certain interfaces to support the "line-of-sight" protection requirement. This is shown typically in figure 2B.

A closeup of a typical blanket is shown in figure 3. The blankets shown in the figure are flight-like with the exception of the use of nonperforated plastic films.

After completion of the development and subsequent preliminary blanket drawings, the MLI closeouts were incorporated into a CAD mechanical ICD drawing of the LCS hardware and the spacecraft structure. Line-of-sight analyses were then conducted to determine if the closeout configuration met the radiation protection criteria.

OTHER DESIGN REQUIREMENTS ESTABLISHED DURING PHASE 1

Nylon velcro (hook and pile) interfaces were established as the interface between the LCS hardware and the DSP spacecraft bay. This was driven by (1) LCS contractor hardware was to be integrated into the DSP spacecraft at the launch site facility, and (2) TRW closeouts were to be integrated for several qualification and acceptance tests at both the LCS contractor facility and at TRW. Interface requirements were established as a part of the applicable mechanical ICD.

At this time, standard geosynchronous electrostatic discharge grounding accommodations were incorporated. These included, at that time, outer (space facing) and inner layer VDA grounding with redundant ground tabs.

At the end of this phase, TRW personnel supported thermal-vacuum testing of the LCS at the contractor facility. The LCS thermal-vacuum support fixture somewhat duplicated the configuration of the DSP spacecraft bay into which the LCS was to be integrated for flight. This provided TRW personnel with an excellent opportunity to verify the form and fit of the closeouts and their installability. Various design (shape) changes were incorporated into the closeout design as a result of these "fit-checks" and subsequently incorporated to the ICD.

During this activity, a strawman procedure was cowritten by the LCS contractor and TRW to define mechanical activities and schedule requirements for the activity at the launch site. Integration of the LCS occurs late in the launch preparation sequence, with complex parallel and serial mechanical activities required.

PHASE 2. MLI CONFIGURATION DESIGN MODIFIED DUE TO RADIATED EMISSIONS SHIELDING REQUIREMENTS (EMC ENHANCEMENTS)

Later in the program, requirements were formalized to the insulation group based on the electromagnetic shielding effectiveness characteristics of the closeouts. Electromagnetic compatibility (EMC) became an issue after the LCS electrical interface requirements were well defined.

Tailored requirements were established for the closeouts after samples of the current closeout design were tested for EMC effectiveness. The closeouts would provide the LCS equipment with a degree of shielding effectiveness equivalent to at least 20 dB of attenuation between 14 kHz and 18 kHz with the following exceptions:

- a. Between 10 MHz and 20 MHz, the closeouts shall provide at least 10 dB of attenuation
- b. Between 1 GHz and 2.4 GHz, the closeouts shall provide at least 35 dB of attenuation.

These criteria significantly impacted the closeout configuration design insofar as their assembly. Enhancements to the design included primarily:

- a. A change to conductive stainless steel velcro interfaces (MLI to spacecraft and MLI to LCS radiators)
- b. The use of conductive epoxy (Ecco-Bond 57C) for all metal-to-metal interfaces (i.e., metalized velcro to tantalum).

The MLI construction incorporating these requirements is shown in figure 4. Solutions were more complex than just changing to metalized velcro. All metal-to-metal surfaces and interfaces had to be contiguous. Implementation necessitated some structural changes to the DSP spacecraft bay. Adding secondary support brackets, to simplify the complicated geometry of the spacecraft at the velcro faying surfaces, was required. The locations in question are shown in figure 5. The "as-is" interfaces were altered to facilitate velcro installation and bonding. The modifications incorporated into the spacecraft bay design are depicted in figure 6.

Figure 7 shows a typical grounding tab implemented into the MLI to meet EMC requirements. Ground-to-structure is through the metalized velcro interface.

At this point, project management decided that the thermal insulation closeouts were now taking on significantly more performance characteristics and were multi-purpose in their function. It became necessary to capture all requirements with a "specification" identifying all design criteria. Germane excerpts from this specification are included in the appendix. Paragraph 3.3.2 of the appendix delineates, in detail, the design criteria incorporated for the closeouts as a result of the EMC effectiveness testing.

Writing this specification required that all players (engineering disciplines) gathered together to identify interdependencies and impacts. Concurrent engineering activity at last.

PHASE 3. MLI CONFIGURATION DESIGN MODIFIED DUE TO CONTAMINATION REQUIREMENTS/CONCERNS

A concern that surfaced during the writing of this specification, was the effects of contamination on the LCS telescope. Contamination of the LCS SSM radiators and another TRW sensor installed on the +Z surface of the spacecraft were secondary concerns.

The MLI closeout design included stainless steel velcro interfaces around the periphery of the individual closeouts to attach them to the TRW spacecraft structure and to the LCS radiators. The concern was that during ascent, particulate contamination entrapped in the bay would vent through the velcro interfaces and deposit on telescope, sensors, and SSMs. Contamination analysis validated these concerns resulting in a requirement to seal the velcro interface by overtaping with polyimide tape. Overtaping negated the purpose of the velcro interfaces since now the closeouts would not be easily removed and reinstalled. Calmer heads prevailed as schedule time for this activity was included as part of the final integration activities at the launch facility.

This change also forced a change in base aluminized plastic materials comprising the multilayer construction of the blankets. In the original design, blanket venting itself occurred through the edges of the assembly. With edges now sealed, a change to perforated aluminized plastic filler and outer layer materials was made. Analysis of the particulate contamination available within the MLI itself was also made. Results were acceptable and the change approved.

The contamination issue resulted in a major design change to incorporate a vent in one of the closeouts. Vent design and size was driven by differential pressure requirements during ascent (0.1 psid). Its location and direction of discharge was critical as was EMC shielding requirements. The vent design is described in figure 8. Vent EMC design criteria is described in the appendix, paragraph 3.3.2.2.

ACOUSTIC DEVELOPMENT TEST

The MLI closeout designs were frozen. A flight-like set of the closeouts was fabricated and were installed into a structural test configuration (see figure 9) of the LCS and the DSP spacecraft. Open areas between LCS SDM radiators and spacecraft bay are shown in figures 10A and 10B. These same areas with MLI closeouts installed are shown in figures 11A and 11B. A closeup of the insulated assembly is shown in figure 12. The purpose of the test was to verify their capability to withstand the predicted acoustic environment to be imposed during ascent. Test requirements for this acoustic test are presented in the appendix, paragraph 4.1.2.1.

The test was successful and TRW breathed a sigh of "its over and we made it." A closeout design that meet all (it was believed) requirements was finally on paper.

PHASE 4. MLI CONFIGURATION DESIGN MODIFIED DUE TO LAUNCH ACOUSTIC/VIBRATION ENVIRONMENTS (RADIATOR DEFLECTIONS)

As it turned out it was not true. Data was published reporting the results of static analysis using an analytical model of the LCS and spacecraft. The impact of this data on the closeout design needed to be understood.

Relative movements between the radiator edges and DSP will result from both the high frequency acoustic and structure-borne vibration and from the low frequency flight loads vibrations. At any point in flight there will be vibrations from both frequency ranges. Test or analysis cannot normally treat both effects simultaneously, so they are commonly treated separately as was done for the MLI closeouts.

The closeout performance during high frequency acoustic and structure-borne vibration was verified during the aforementioned acoustic test.

To understand the impact of the closeouts on the radiators during flight load events in the low frequency region, the only type of analysis available at this time was static analysis using peak accelerations. Load factors for this analysis were determined from "final design load cycle" results for the Titan and the shuttle. Since redesign of the closeouts was in process, waiting for more comprehensive deflection data, from coupled loads or base shake analysis efforts planned in the future, was not an option.

From the structural dynamics point of view, equipment (mounted to the equipment frame) and the telescope are primary mass components. Detectors, lasers, lower radiators, and optics assembly account for about 116 lb of the approximately 300 lb subsystem.

The radiators, which are attached to the spacecraft bay by the closeouts, must be able to accommodate any relative movement between radiators and structure since the only load path intended is through the three point mount.

Static analysis data indicated that worst-case relative displacements across the LCS/DSP interface were:

MAXIMUM RELATIVE DISPLACEMENT IN EACH DIRECTION (in.)*

dX	dY	dZ	Z Level
0.112	0.067	0.031	LR lower edge
0.099	0.067	0.031	LR upper edge
0.077	0.067	0.028	DR upper edge
0.063	0.051	0.023	ER lower edge
0.063	0.053	0.023	ER upper edge

* TRW document, IOC L122.2.90-103, "LCS/DSP Closeout Compliance Requirements," from E. A. Verner and A. J. Dunn, dated 11 May 1990.

These values include 10 mil (30) for the acoustic response in the X direction normal to the radiators (see figure 13) to account for the acoustic (high frequency) vibrations. A factor of 1.4 was recommended to show adequate margin for qualification, considering the inconsistencies in installation.

The impact on the current design had to be evaluated. Could compliance of the closeouts accommodate the expected relative displacements as defined by the data presented above?

COMPLIANCE TEST

Compliance testing was in order. A simplified test was designed to verify whether the current design could withstand expected deflections. Fabrication of a test article that duplicated the worst case configuration as defined by the data was needed.

The test article was approximately a 1 ft² assembly duplicating the two lower edge (+Z) laser radiator corners (at + and -Y). Full size representations of the 211-1, -2, and the -209 closeouts were fabricated. Since the test article was approximately 1/3 as wide (Y axis) as the flight article, a proportionally sized vent box was incorporated to duplicate its effect on the compliance of the MLI corner assembly (test article is shown in figure 14).

Upon initial installation of the test article in the fixture, a nominal (flight integrated) separation between laser radiator edge and spacecraft structure was established. The test encompassed: first compressing (-dX) the test fixture attachment plate (laser radiator simulator) by 50% of the maximum (dX = 0.157; worst-case = LR, lower edge + margin) required per the data in the above table; and then tensioning (+dX) the same distance.

The first test (one cycle) resulted in failure of the bond line at the corners, between velcro and simulated radiator. After two weeks of "intensive" brainstorming (the tiger-team mentality), involving design reviews of alternate concepts to make the MLI corner assembly more compliant, a candidate was selected. A test article incorporating this "flexible" design was fabricated. Basically this design incorporated a joint/corner (between the -209 and -211 closeouts) with a built-in convex curvature. This curvature would act like a "spring". Setting it at nominal distance (dX) upon installation would essentially precompress this "spring," allowing it to be further compressed when loaded in the -dX direction and expand when tensioned in the +dX direction.

Another test was performed using the same setup as before, but subjecting the assembly to 100 cycles. The result, failure at the velcro hook and pile interfaces themselves. Failure meant that separation of the hook from the pile exceeded the maximum allowed gap of 0.050 in.

LET US "DO IT RIGHT" APPROACH

Never has the saying "...back to the drawing board" been more appropriate. At this time a total redesign of the MLI closeout laser radiator joint/corner configuration was undertaken. Supporting the MLI design group were members of the stress, structures, and material engineering groups ("It is never too late for CE"). The knowledge base acquired to date served well in identifying and eliminating design concepts that would adversely affect the EMC enhancements, the radiation protection criteria, and the installability concerns. Acceptance of the design was also predicated on proving that the closeouts would survive acoustic and vibration loads during ascent without any loss in performance. By this time, the "closeout design problem" had manifested itself as a 'show stopper' to project, company, and customer. Extreme interest in "solutions" was the byline from all interested persons.

Previous compliance testing, as described above, only subjected the closeouts to deflections in one axis (X). In flight, loads would be applied simultaneously in all three axes causing deflections in all three directions.

It was obvious that a test program to simultaneously load a full size test article (radiator) in all three axes was not practical or cost effective.

FULL SIZE MOCKUP

The next best thing was to design and fabricate a full scale, high fidelity and dynamic mockup of the LCS/spacecraft bay assembly. The design will incorporate a worm gear assembly attached to the simulated radiators. This assembly will allow the radiators to traverse in the X and Y axes (Z axis deflections negligible) from any point within the envelope created by the required deflections (+ margin).

A flight-like set of the closeouts will be installed on the mockup for demonstration purposes. Actuation through all axes will be possible. Interim visual inspections and photographic documentation will reveal any failures at the velcro interfaces or at the Ecco-Bond lines.

SUCCESS (IS IMMINENT)

The design is "not on paper" as of this writing. Assembly of the mockup and integration of the closeouts will occur in September 1990. We fully expect to demonstrate acceptable compliance using the dynamic mockup. It is five years since the design and verification process started. We did our "real" concurrent engineering work in the fourth year.

CONCLUSION

Sometimes implementing requirements into the hardware design goes well, sometimes it does not. This narrative provides a good example of when it does not. When I first wrote this paper, it was not as a narrative but was written in the classical "technical paper" form. The latter form, I thought, did not lend itself in meeting my two objectives.

"Cost and schedule" is what we all live by in this industry. Hindsight shows that implementing radiation protection within the MLI was probably the wrong decision when incurred costs are used as the measuring tool. Five years ago, hardening the LCS equipment electronic boxes would probably have cost less even with the weight penalty. Five years ago, understanding the importance of concurrent engineering would probably have facilitated the design and verification process of hardening through the use of MLI. Performance requirements/criteria could have been implemented as shown in figure 15. That is the significance of the lessons learned during this process.

Technically, we at TRW gained a lot of valuable experience.

a. The technology of hardening spacecraft structure and/or hardware through the multilayer insulation is valuable and will certainly be used again.

b. The assembly and fabrication methods to enhance the EMC shielding effectiveness of MLI will also be beneficial to other applications.

Insofar as schedule, "luck" played a big part in schedule considerations. The need date for the hardened MLI flight hardware somehow kept slipping due to other reasons not associated with the MLI design problem. Five sets of very expensive closeouts are not required until late next year.

APPENDIX

HARDENED MLI CLOSEOUT SPECIFICATION

Today's design for the MLI closeouts encompass a diverse and complex set of requirements which have successfully been implemented for flight application.

Germane excerpts from the governing specification are presented here.
(Extracted from TRW Document IOC L125.2.90-005, "EQ Spec for LCS Closeouts Revised per 1-4-90 Meeting," from J. Lloyd Petty, dated 22 Jan 1990.)

3. CHARACTERISTICS

3.1 Functional Description. The closeouts function as follows:

- a. Complete the thermal enclosure of the sensor components when mounted to the spacecraft body.
- b. Provide line-of-sight protection of sensor electronic equipment (boxes) from prompt radiation through the use of a tantalum layer in the MLI blanket.
- c. Provide easy access to sensor equipment by being removable using velcro fastener systems.
- d. Provide vent of ambient pressure from the sensor compartment during launch. Vent will not allow a line-of-sight path to contamination-sensitive surfaces.

3.1.1 Functional. The closeouts help to maintain thermal balance while protecting the sensor equipment from natural and induced radiation. The closeouts will be electromagnetically compatible with other spacecraft subsystems and will be grounded for protection against electrostatic discharges.

3.1.2 Pressure/Altitude, Venting. The vent design shall ensure that the maximum delta pressure from inside to outside the sensor compartment is less than 0.1 psi.

The ambient pressure characteristics during STS ascent/descent are defined in EV1-48, and for Titan IV ascent in figure A-1.

3.1.2.1 Natural and Induced Radiation. The sensor shall be protected from the natural and induced radiation environment as defined in (applicable TRW document). There shall be no line-of-sight radiation permitted to strike the sensor electronic components (boxes).

3.1.2.2 Weight. The weight of a set of closeouts shall not exceed 4 lb.

3.2 Environmental Conditions. The closeouts shall be designed to withstand or shall be protected against the worst probable combination of environments as specified below, and shall operate as specified herein without performance degradation.

3.2.1 Operating Environments

3.2.1.2 Pressure/Altitude. The closeouts will be capable of operating at atmospheric pressure between sea level and $10E-10$ torr (verifiable to $5 \times 10E-5$ torr).

3.2.1.3 Acoustic Field. The closeouts shall be designed to withstand the acoustic environment imposed by the launch vehicle during launch and ascent as defined in 3.3.6 of EV1-48.

3.3 Design and Construction. The closeouts design shall be in accordance with the requirements herein.

3.3.1 Parts, Materials, and Processes

3.3.1.1 Materials and Processes. Only materials and processes conforming to all requirements (applicable TRW document) shall be considered standard and shall be used. The approved materials and processes shall be as specified in (applicable TRW document).

3.3.1.2 Dissimilar Metals. Protection of dissimilar metal combinations shall be in accordance with MIL-STD-889. The worst-case environment, including storage, shall be considered.

3.3.1.3 Magnetic Materials. Magnetic materials shall be used only if necessary for equipment operation. Those magnetic materials used shall cause minimum permanent, induced, and transient external magnetic fields.

3.3.1.4 Fungus-inert Materials. Materials that are nutrients for fungus shall not be used when their use can be avoided. Materials shall be treated in accordance with MIL-T-152 if not hermetically sealed. If materials are used in a hermetically sealed enclosure, fungicidal treatment will not be necessary.

3.3.1.5 Finish. All surface finishes shall meet the environmental, bonding, and thermal property requirements as specified in DOD-E-8983.

3.3.1.6 Outgassing. Low outgassing polymeric materials shall be used where sensitive thermal control and other surfaces are in direct line-of-sight and where temperature differences can exist between such surfaces. Materials shall be selected for low outgassing per (applicable TRW document).

3.3.1.7 Insulating and Dielectric Materials. Not applicable.

3.3.1.8 Thermophysical Properties. The thermophysical properties of the thermal materials used in the closeout design are the same as summarized in (applicable TRW document).

3.3.1.9 Contamination Control

3.3.1.9.1 Contamination Path. The vent design shall allow no contaminants a line-of-sight path to the optical sensor, radiator mirrors, or surfaces of sensors and detectors.

3.3.1.9.2 Closeout Surface Cleanliness. At scheduled general cleanings and prior to final closeout installation, the exterior and interior surfaces of the closeouts shall be free from such visible contamination as scale, particles, corrosion, dirt, grease, oil, or other foreign materials when examined under white light (to 150 fc) from a distance of 1 to 2 ft as specified in (applicable TRW document).

3.3.1.9.3 Allowable Molecular Levels. Prior to final closeout installation the allowable molecular deposition levels on the internal and external surfaces shall be $<0.001 \text{ g/ft}^2$ as specified in (applicable TRW document).

3.3.2 Electromagnetic Compatibility. The sensor closeout will provide the sensor equipment compartment with a degree of shielding effectiveness. The closeouts shall provide at least 20 dB of attenuation between 14 kHz and 18 MHz with the following exceptions:

a. Between 10 MHz and 20 MHz, the closeouts shall provide at least 10 dB of attenuation.

b. Between 1 GHz and 2.4 GHz, the closeouts shall provide at least 35 dB of attenuation for the sensor not to interfere with or be interfered by (applicable satellite) communication links.

3.3.2.2 Vent Openings Shielding. All vent openings shall be designed to provide shielding effectiveness which is not less than 35 dB of attenuation between 1 GHz and 2.4 GHz.

3.3.2.3 Mating Joints. Conductive hook and pile fastener tape (velcro or equivalent) shall be used on all closeout/spacecraft, closeout/radiator, closeout/radiator cover, and closeout/closeout mating joints. The fastener tape shall be replaced after 11 cycles of attachment/detachment.

3.3.2.4 Fastener Tape Attachment. The fastener tape shall be bonded to the closeout tantalum layer with ECCO-Bond 57C. The fastener tape shall be continuous along the circumference of the individual closeouts and the sensor's spacecraft equipment bay except at corners where the fastener tape is cut and butt joined. The maximum gap between pieces of tape at the corners and butt joints shall be 0.05 in.

3.3.2.5 Fastener Tape Resistance. The dc electrical resistance, measured through the thickness of the fastener tape prior to bonding, shall be 2 ohms maximum.

3.3.2.6 Sealing of Fastener Tape With RTV. The primary around the edge of the fastener tape shall be filled with a bead of RTV, to entrap the ECCO-Bond within the bonding area of the fastener tape.

3.3.2.7 Sealing of Fastener Tape Interfaces. Clear kapton tape shall be applied, continuous or overlapped, to cover edges of mated hook to pile fastener tape.

3.3.2.8 Apertures

3.3.2.8.1 Fastener Tape Mating Surfaces. Using magnification, there shall be no clear aperture with a linear dimension greater than 0.05 in along any of the fastener tape mating surfaces.

3.3.2.8.2 Tantalum Layer. Using magnification, there shall be no clear aperture with a linear dimension greater than 0.05 in. in the tantalum layer.

3.3.2.9 Staples for Added Strength. Corrosion resistant steel staples, which may be used to provide additional strength to the bond of fastener tape to the MLI closeouts, shall not be removed from the blanket once installed.

3.3.2.10 Tantalum Sheet Lap Joints. All bonding of the closeouts tantalum sheet lap joints shall be done with ECCO-Bond 57C, and shall extend along the entire length of the bond joint.

3.3.3 Grounding of Closeouts

3.3.3.1 Ground Design. The closeouts shall be grounded to the spacecraft structure by means of conductive fastener tape. The ground shall include the outer layer of MLI, the tantalum foil layer used for radiation shield, and the inner layer of MLI.

3.3.3.2 Grounding Levels. The dc electrical resistance measured from any point on the closeout surface through the fastener tape to the adjacent spacecraft structure shall be 35 ohms maximum for EMC for electrostatic discharge (ESD).

3.3.4 Mechanical Compliance

3.3.4.1 Induced Loads. The induced load levels shall result in a positive margin of safety in the sensor.

3.3.5 Interchangeability. Each closeout shall be directly interchangeable in form, fit, and function with other closeouts of the same part number.

3.3.6 Safety. The closeouts shall be designed to meet the requirements of NHB 1700.7, paragraph 209-3 (flammable material).

3.3.7 Human Performance/Human Engineering. TRW will follow the applicable human engineering standards established in MIL-STD-1472.

4. QUALITY ASSURANCE PROVISIONS

4.1 General. Quality assurance controls for fabrication, inspection, and testing of the closeouts shall be in accordance with (applicable TRW document).

4.1.1 Failure Criteria. The closeouts shall exhibit no failure, malfunction, or out-of-tolerance performance or degradation as a result of examinations and tests specified herein. Any such failure, malfunction, out-of-tolerance performance, or degradation shall be cause for Material Review Board action. Retest requirements shall be in accordance with MIL-STD-1540.

4.1.1.2 Government Inspection. The procuring agency, or its designated representative, shall have the option to witness all formal tests, all environmental exposures, pre- and post-exposure examinations of tested items, and to verify all test equipment and calibration data.

4.1.2 Development Tests

4.1.2.1 Acoustic Test. An acoustic test shall be performed on a test of representative flight-like closeouts when installed between the structural development model of test sensor and the spacecraft test model. The test shall verify their capability to withstand the predicted acoustic environment to be imposed on the closeouts in flight.

Test Requirements

a. The closeout test articles shall be subjected to a broadband random incidence sound field with an overall pressure level of 145.2 dB (re: 0.0002 dyne/cm²).

b. The octave band sound pressure levels shall be as specified in Table II, column 3 of EV1-48A.

c. The acoustic environment shall be applied to the test article for a period of three minutes.

4.1.2.2 Shielding Effectiveness Test. The closeouts' shielding effectiveness shall be demonstrated by conducting a laboratory test using an EMC engineering approved test sample.

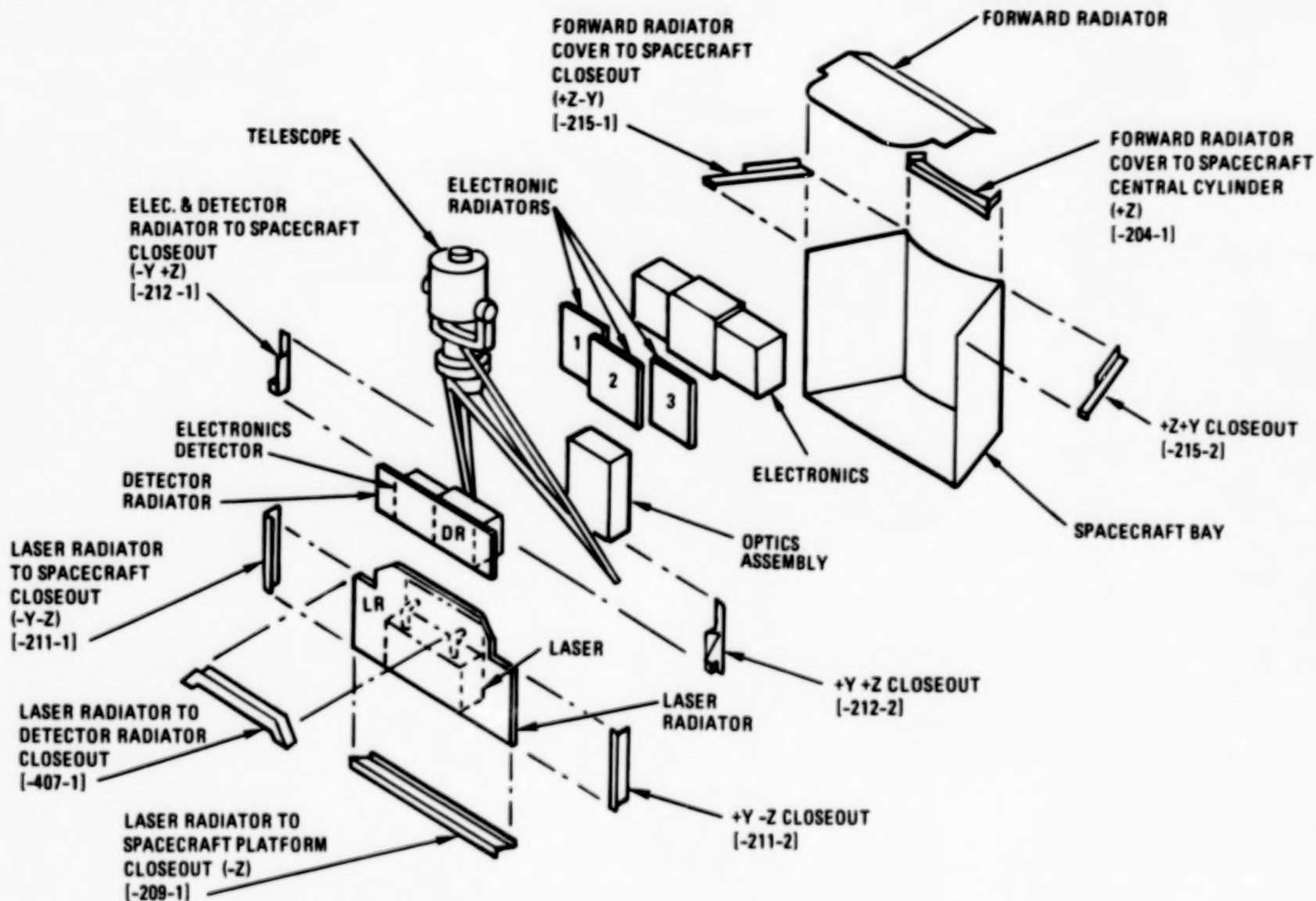
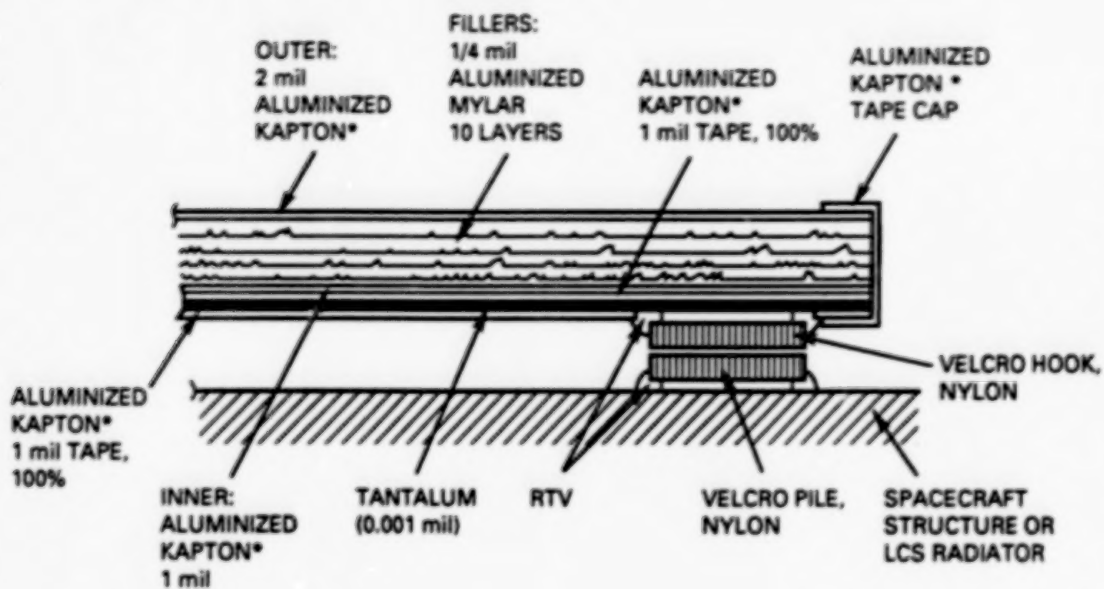


Figure 1. Laser Crosslink Subsystem (LCS) Closeouts - Overview



* Ⓢ KAPTON IS A REGISTERED TRADEMARK OF THE DUPONT CORPORATION

Figure 2A. MLI Closeout Cross-Section, Typical Construction (with tantalum)

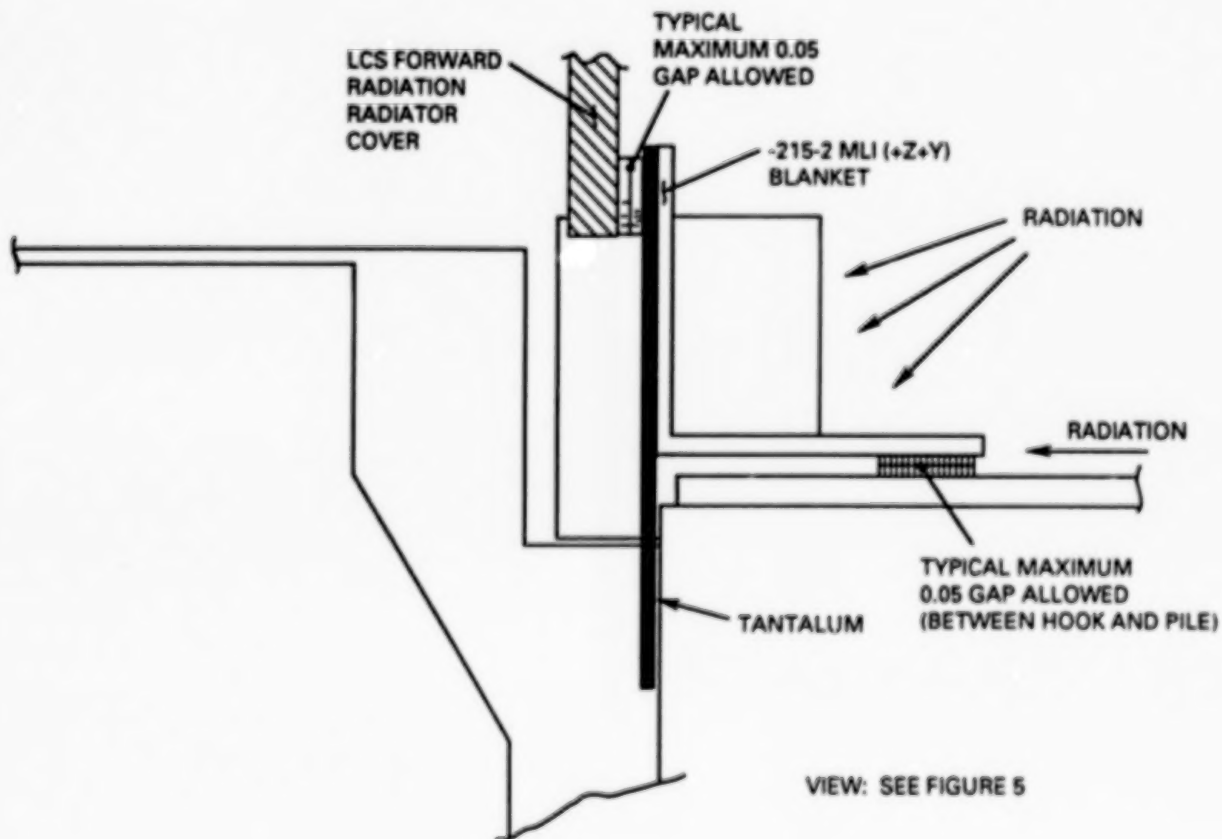


Figure 2B. Typical Tantalum Barrier Closeout Design Radiation Protection Method; Typical for 100% Line-of-Sight



Figure 3A. LCS MLI Closeout (-212)

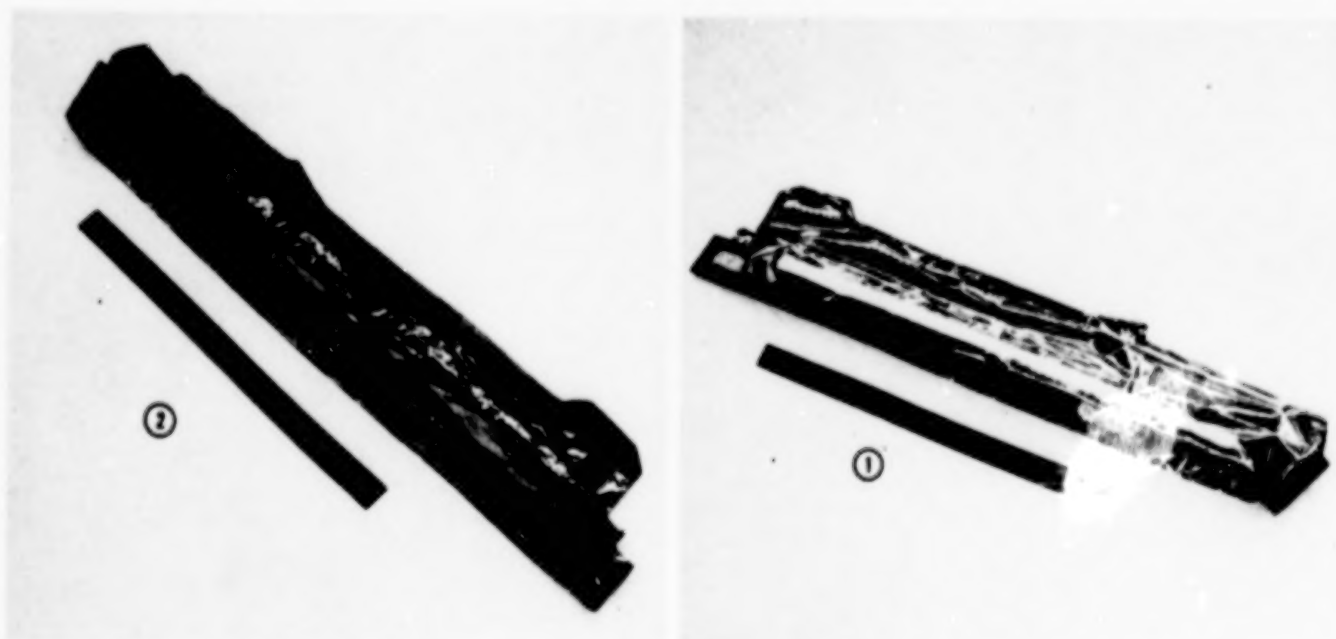
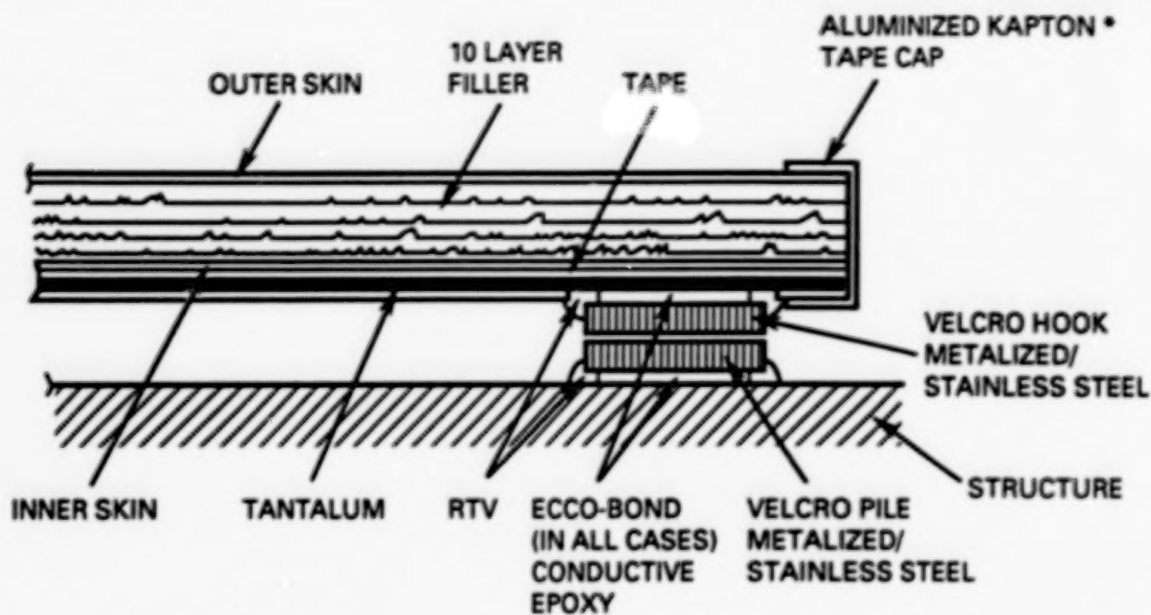


Figure 3B. LCS MLI Closeout
[(1) -215 space side; (2) -215 structure side]



* KAPTON IS A REGISTERED TRADEMARK OF THE DUPONT CORPORATION

Figure 4. Typical MLI Closeout Construction with EMC Enhancements

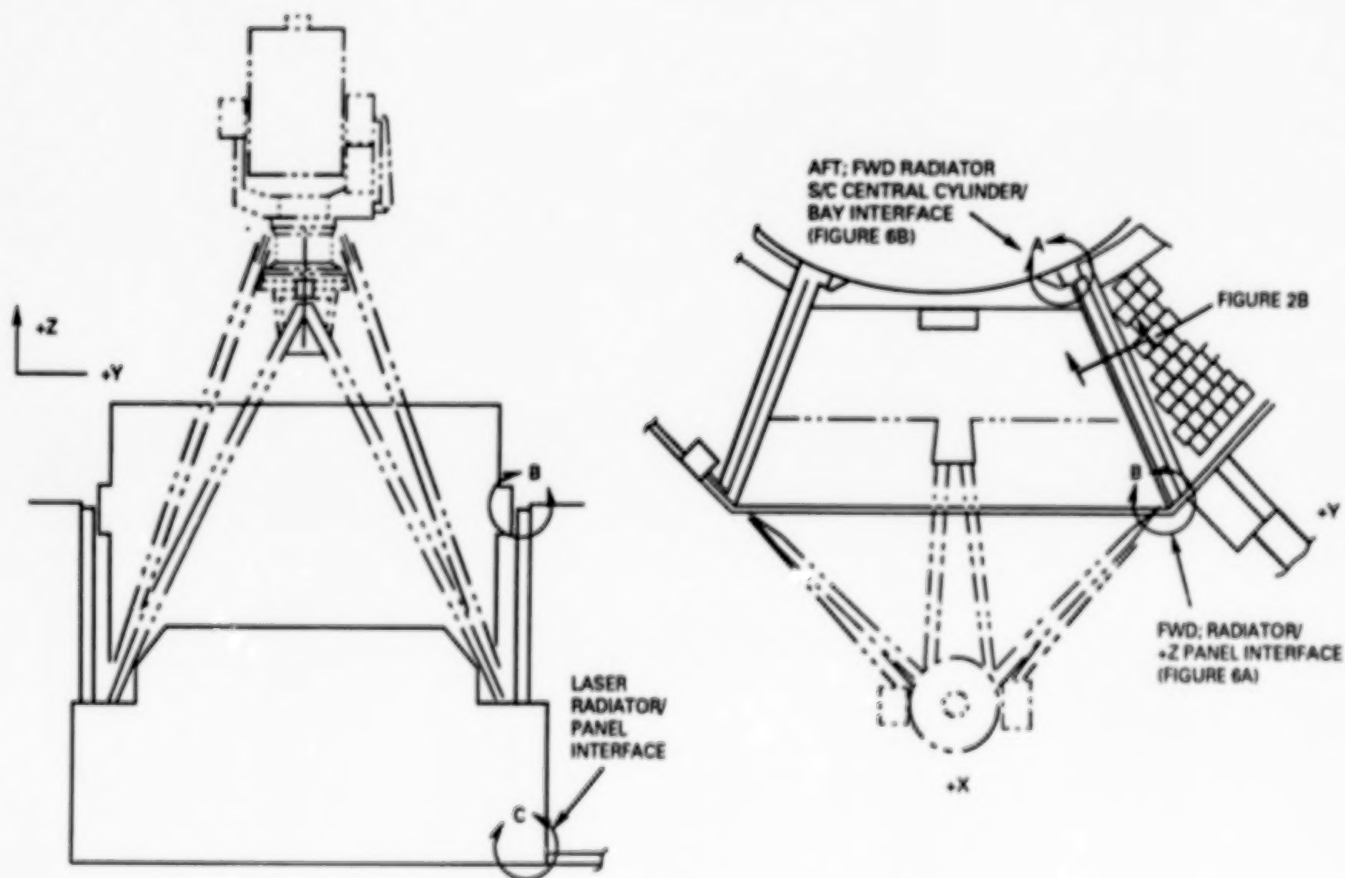


Figure 5. LCS/Spacecraft Bay Assembly - Overview

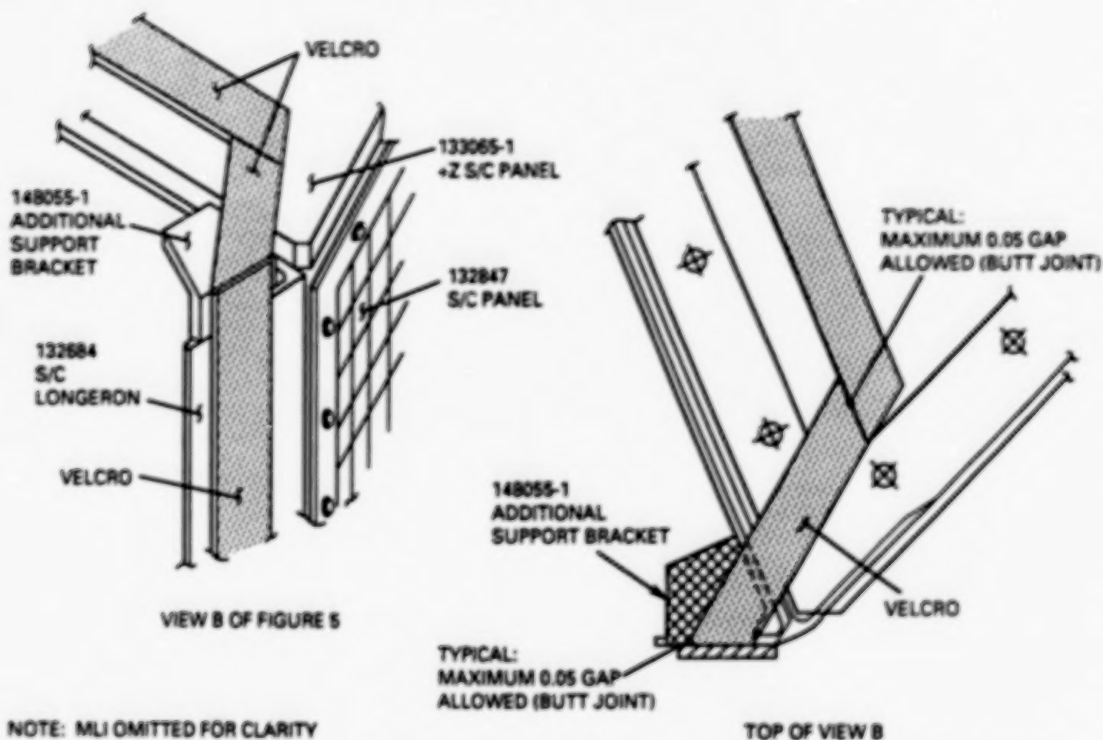


Figure 6A. +Z FWD Spacecraft Bay Interface; Continuous Stainless Steel Velcro/Bond Method; Modifications for EMC Enhancements Implementation

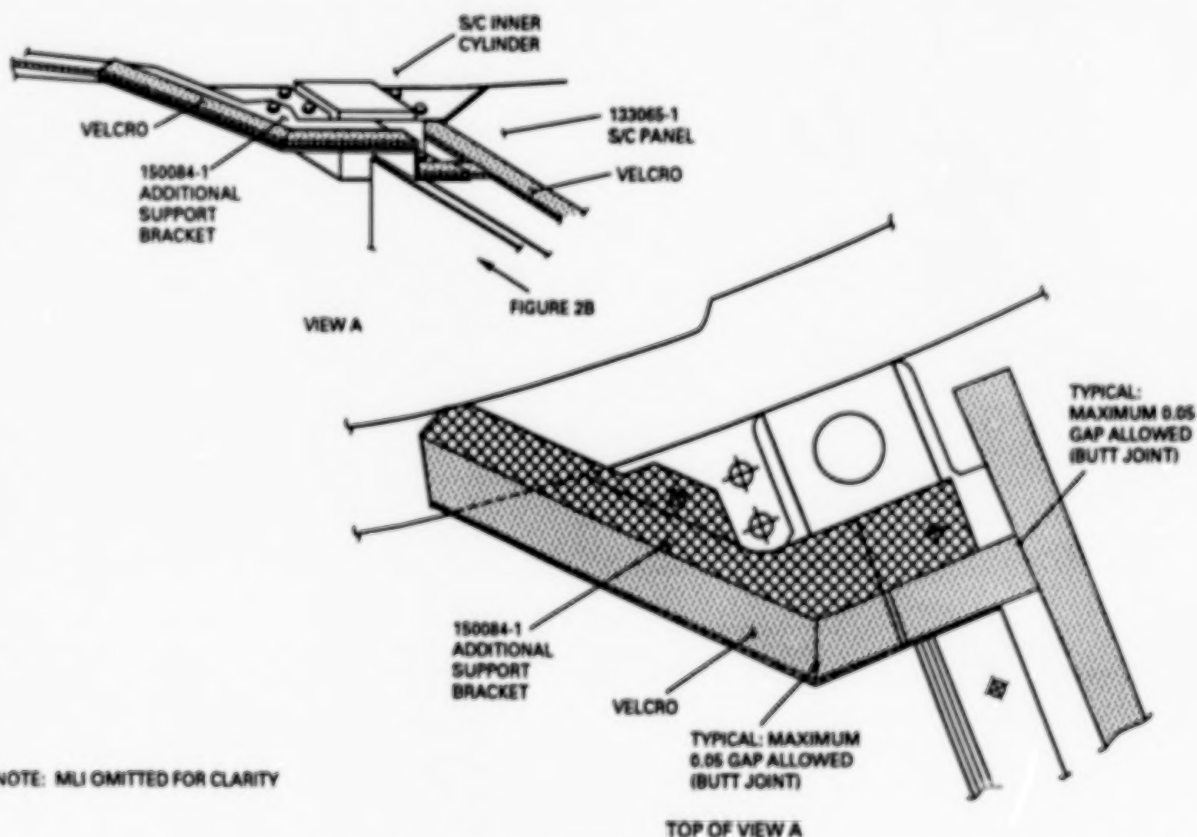
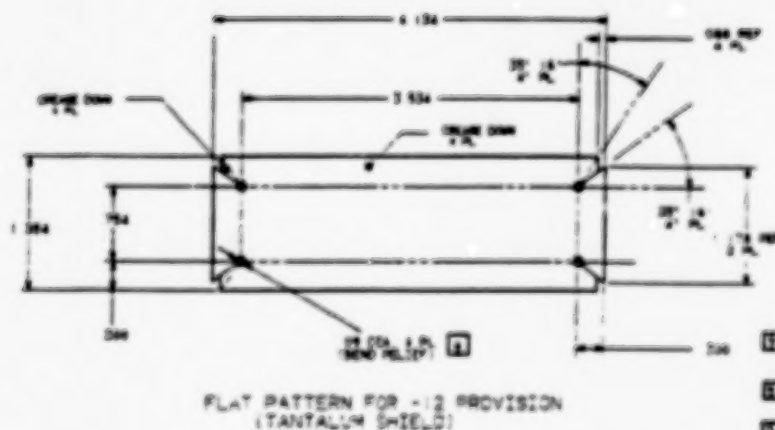
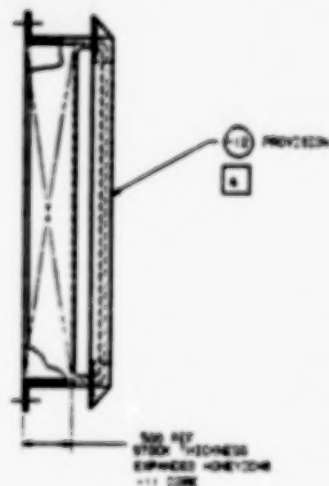
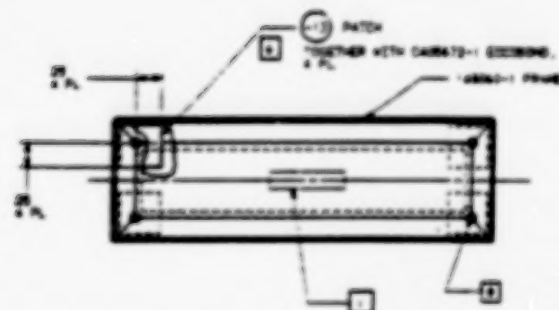
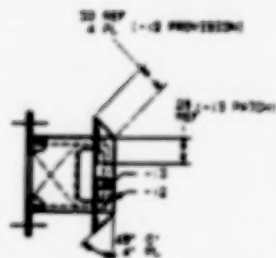
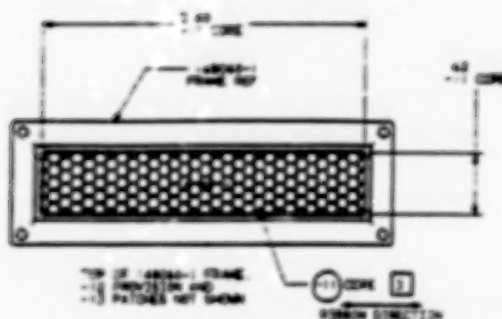


Figure 6B. +Z Aft Spacecraft Bay Interface; Continuous Velcro/Bond Method; Modifications for EMC Enhancements Implementation

-13 DETAIL
PAGE 4/4



NOTES: UNLESS OTHERWISE SPECIFIED

- 1 PART IDENTIFICATION PER PW-3-4-0103
LOCATE ADDRESS AS SHOWN
- 2 FABRICATE PER PW-20700
- 3 BOND -11 COME TO 148660 FRAME PER PW-23-02
ACCEPTABLE TO THEN ADHESIVE WITH TOLUENE
- 4 FILLET R .03 MAX.
- 5 MATERIAL SHALL MEET THE CHEMISTRY AND QUALITY REQUIREMENTS
PER AND THEN FURNISH MATERIAL IN AS ROLLED CONDITION
THICKNESS TOLERANCE + .001 / - .000
- 6 CLEAN -12 PROVISION AND -13 PATCH PER PW-4-3-1 PRIOR TO
APPLYING CAPW-11 SECONDARY
ATTACH -13 PATCH TO -12 PROVISION LEAD CAPW-11 SECONDARY
- 7 BOND -12 PROVISION / -13 PATCH ASST TO 148660 FRAME PER PW-23-02
ACCEPTABLE TO THEN ADHESIVE WITH TOLUENE
- 8 VERIFY THAT ALL DR DIA BOND REINFT HOLES IN -12 PROVISION
ARE COMPLETELY COVERED AND REINFORCED WITH -13 PATCHES
- 9 VENDOR ITEM SEE SPEC CONTROL DRAWING

[illegible]

Figure 8. Vent Box Assembly - LCS Compartment

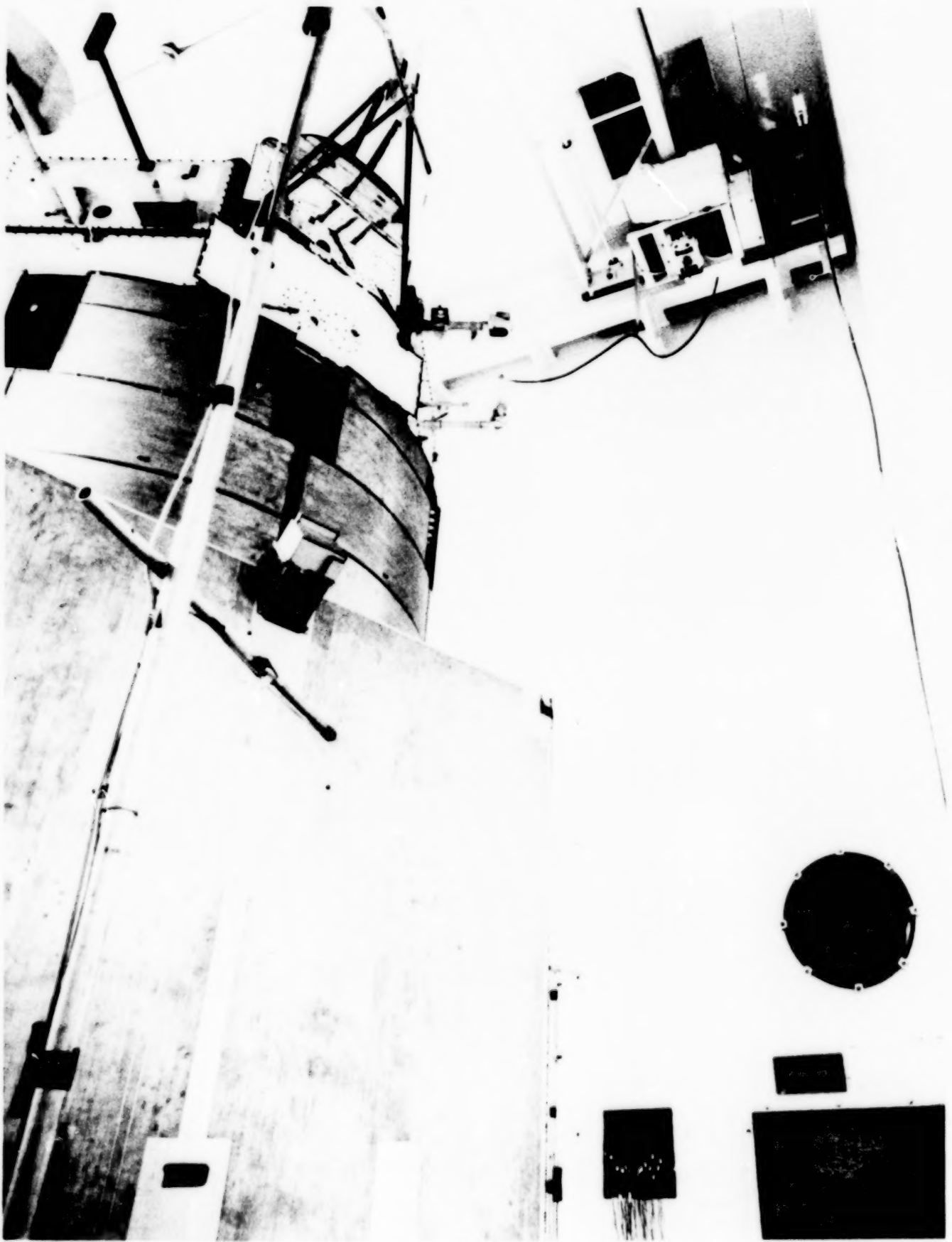


Figure 9. LCS Structural Development Model and DSP Structural Test Model
(preparation for acoustic test)



Figure 10A. LCS SDM/STM Acoustic Test Article (-Y View)

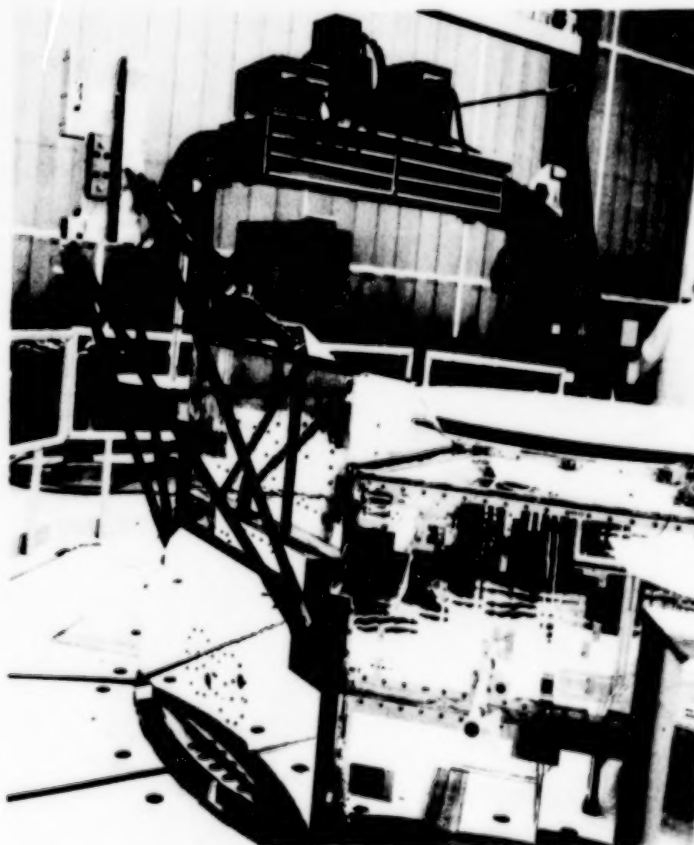


Figure 10B. LCS SDM/STM Acoustic Test Article (+Y View)

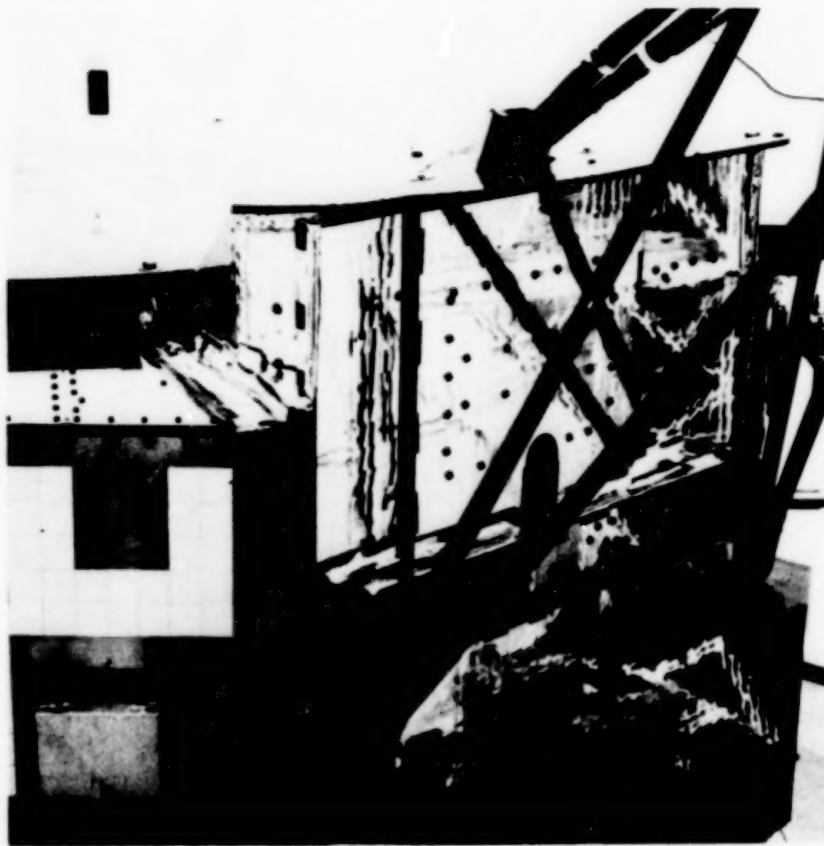


Figure 11A. LCS SDM/STM Acoustic Test Article With MLI Closeouts (-Y View)

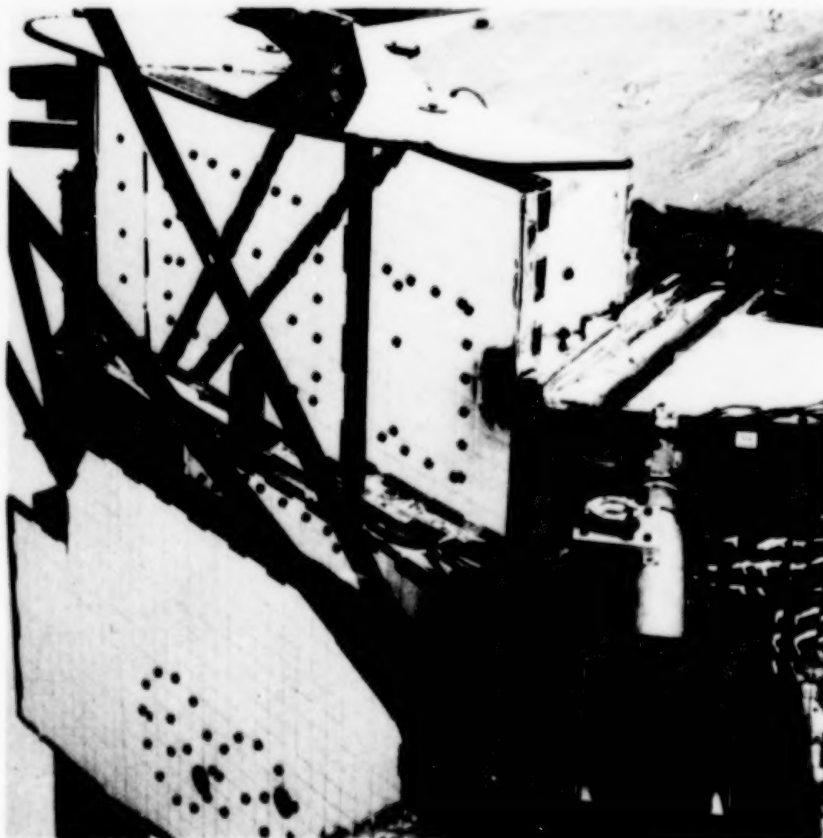


Figure 11B. LCS SDM/STM Acoustic Test Article With MLI Closeouts (+Y View)

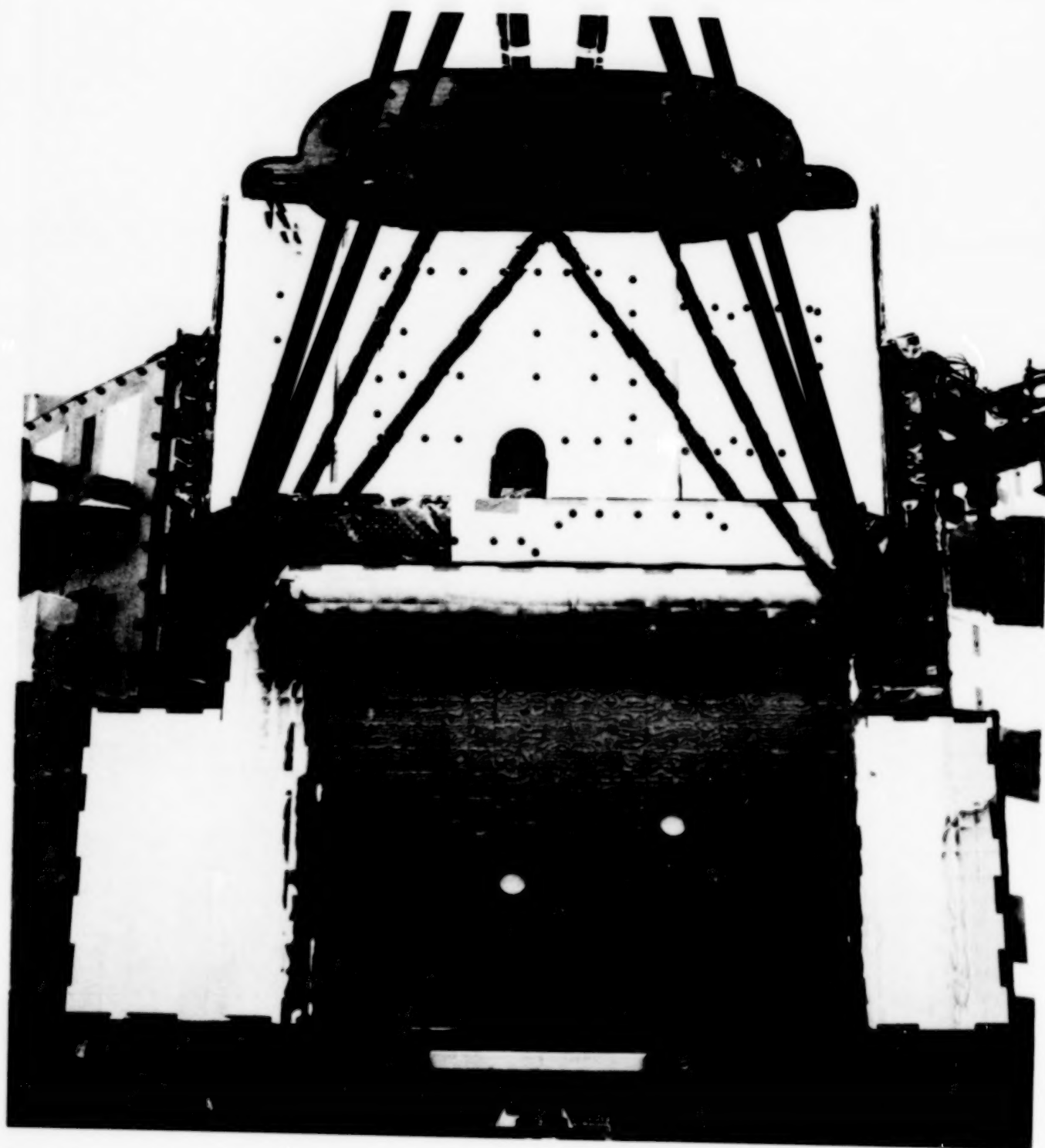


Figure 12. LCS SDM/STM Acoustic Test Article (Front View)

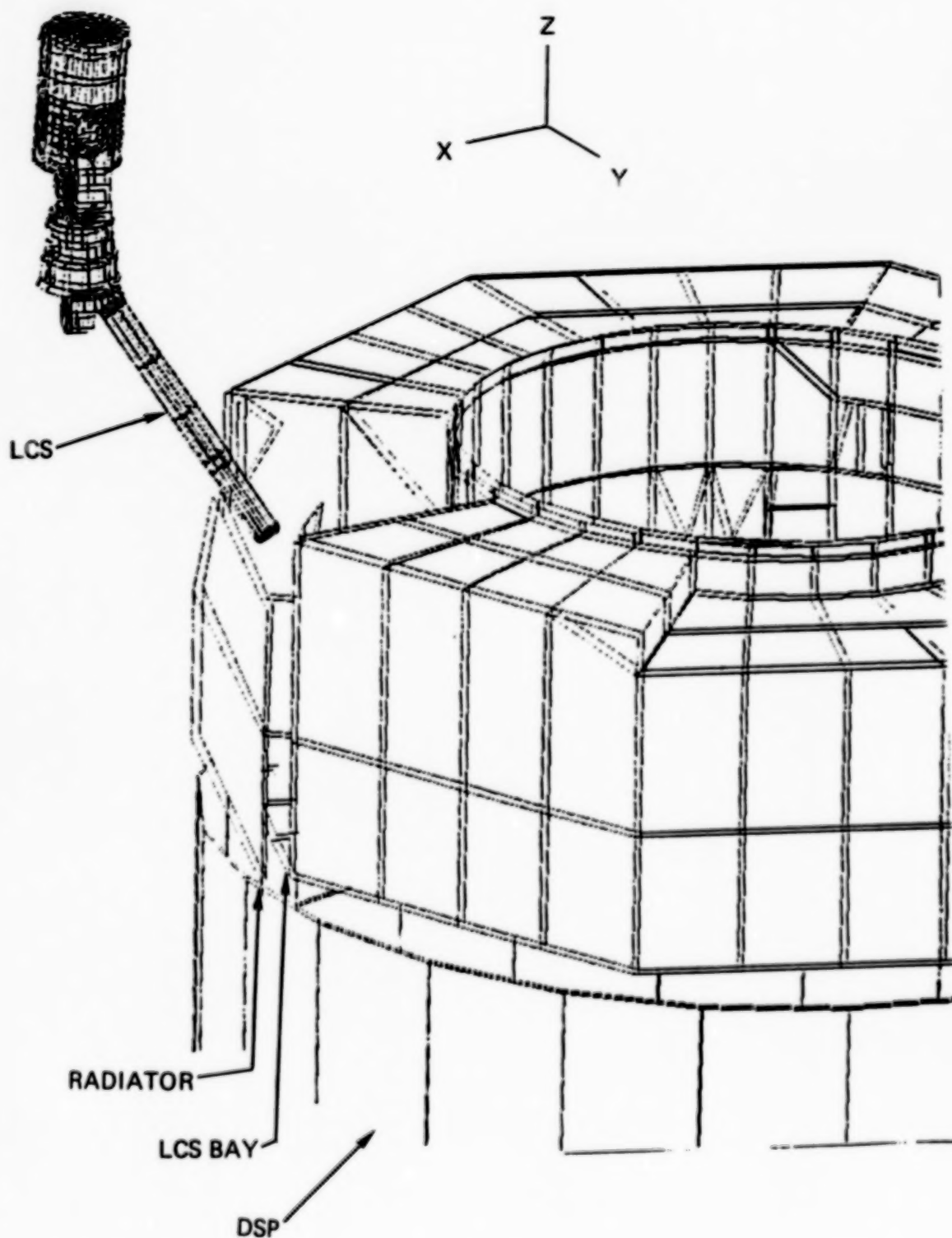


Figure 13. Static Displacement Plot of DSP/LCS Coupled Model
(one load case)

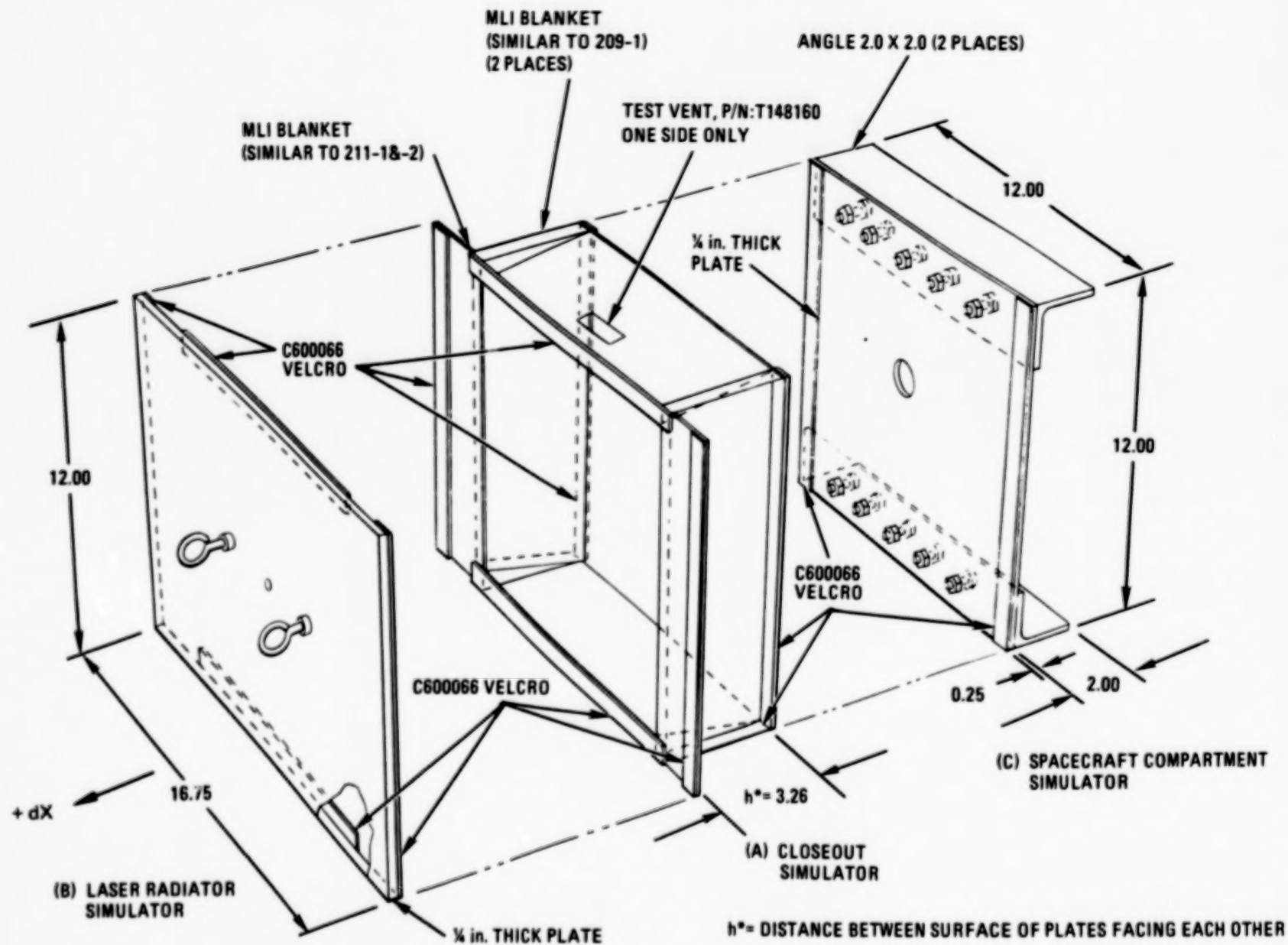
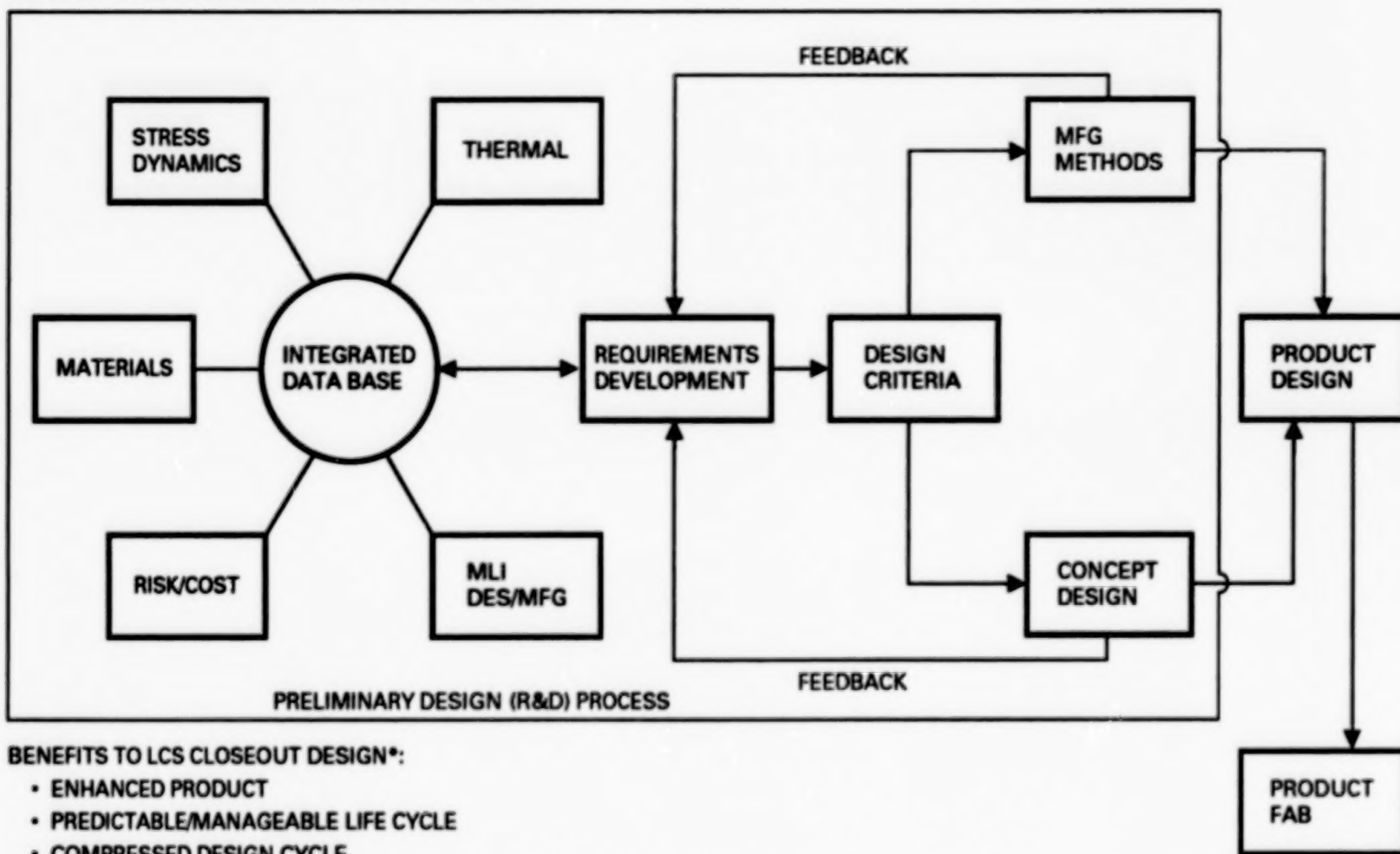


Figure 14. MLI Closeout Compliance Test Article/Test Setup

IF I KNEW (THEN) ABOUT CONCURRENT ENGINEERING



BENEFITS TO LCS CLOSEOUT DESIGN*:

- ENHANCED PRODUCT
- PREDICTABLE/MANAGEABLE LIFE CYCLE
- COMPRESSED DESIGN CYCLE
- REDUCED COSTS (EOs, SCRAP, REWORK, NONVALUED ADDED TASKS)
- SHORTER MANUFACTURING CYCLE
- TO ANY PRODUCT DESIGN

Figure 15. Concurrent Engineering Applied

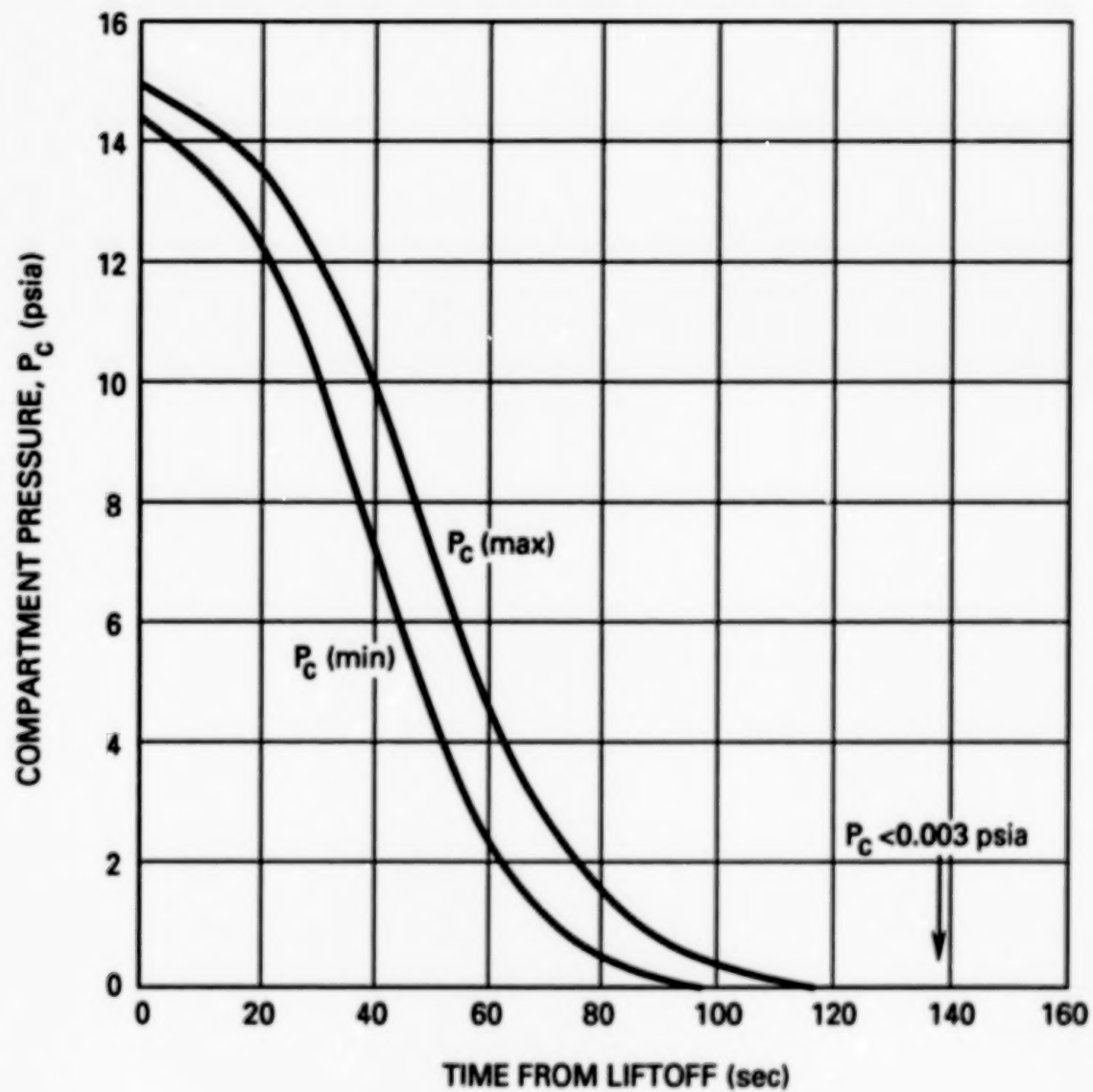


Figure A-1. Titan IV Pressure History During Ascent

110

SESSION III

INFRARED SENSOR TEST FACILITIES: PART I

OPTICAL TESTING CRYOGENIC THERMAL VACUUM FACILITY ¹

Patrick W. Dohogne and Warren A. Carpenter
CBI Technical Services Co.

ABSTRACT

The construction of a turnkey cryogenic vacuum test facility was recently completed by CBI at Griffiss AFB's Rome Air Development Center (RADC). The facility will be used to measure and record the surface profile of large (up to 2 m (6.5 ft) diameter and 540 kg (1200 lb)) optics under simulated space conditions.

The vacuum test chamber is a vertical stainless steel cylinder with a 3.5 m (11.5 ft) diameter and a 7 m (23 ft) tangent length. The cylinder is comprised of two flanged spool sections to accommodate different test configurations. Laser interferometers are mounted on optical benches located on the top chamber head. The surface profile of the test specimen is measured by the interferometer viewed through a 46 cm (18 in) diameter optical port. The chamber interior is accessed by pneumatically lowering the bottom chamber head into a pit with four pneumatic cylinders.

The chamber was designed to maximize optical testing quality by minimizing the vibrations between the laser interferometer and the test specimen. This was accomplished by designing the chamber for a high natural frequency and vibration isolating the chamber.

An optical test specimen is mounted on a movable presentation stage. The presentation stage provides coarse elevation adjustment to ± 0.158 cm (1/16 in) accuracy of the specimen from 0 to 90 cm (0 to 36 in). During thermal vacuum testing, the specimen may be positioned to ± 0.00025 cm (0.0001 in) accuracy with a fine adjustment mechanism.

The chamber is evacuated by a close coupled Roots-type blower and rotary vane pump package and two cryopumps. The vacuum system is designed to evacuate the chamber to 1.1×10^{-3} Pa (8.0×10^{-6} torr) in less than five hours with the thermal shrouds at ambient temperature. A chamber pressure of 2.7×10^{-6} Pa (2.0×10^{-8} torr) was measured with a nude ionization gauge during performance testing with cold thermal shrouds.

¹ Constructed under contract to Rome Air Development Center, Griffiss Air Force Base, NY

The chamber is equipped with an optically dense gaseous nitrogen cooled thermal shroud. Remote controlled shutters on top of the shroud are opened after specimen temperature stabilization to allow interferometry measurements.

The thermal shroud is used to cool or warm the optical test specimen at a controlled rate. To minimize test specimen thermal stresses, a differential temperature control system is utilized. The control system automatically controls the thermal shroud temperature to maintain the test specimen temperature gradient within safe tolerance.

A control system is provided to automatically evacuate the chamber and cooldown the test specimen to the selected control temperature. After initial control inputs, the control system automatically functions without operator input.

INTRODUCTION

CBI has constructed a state-of-the-art turnkey thermal vacuum facility for testing optics under simulated space conditions at Griffiss AFB's Rome Air Development Center (see Figure 1). The facility will use two RADC-supplied laser interferometers to measure and record the surface profile of large optics which are exposed to cryogenic and vacuum environments. An optic which has been tested by RADC and a comparison of the optic's room temperature and cryogenic surface profiles are shown in Figures 2 and 3. The project was a competitively bid, fixed price contract to provide a complete test facility including a building addition to house the new facility. The contract was awarded in May 1987 and the facility was completed in June 1989.

The test chamber is a vibration isolated vertical cylinder with a 3.5 m (11.5 ft) diameter and a 7 m (23 ft) tangent length (see Figure 4). The chamber is equipped with an optically dense shroud and thermal system capable of maintaining any temperature in a range from 100 K to 300 K. The thermal control system is designed to control test specimen temperatures to very stringent tolerances. A unique presentation stage and fine elevation adjustment system were designed and constructed to allow precise remote positioning of the test specimens while the chamber is under vacuum. Provisions have been made for the future addition of a 20 K helium supply system and thermal shroud.

Some of the key facility features required by RADC included:

- A minimum overall natural frequency of 30 hertz for the entire chamber assembly including the presentation stage.
- A presentation stage capable of coarse specimen elevation

adjustment from 0 to 90 cm (0 to 36 inches).

- . A three point specimen elevation fine adjustment system with a 2.5 cm (1 inch) travel range and 0.0025 cm (0.001 inch) resolution.
- . A five hour pumpdown from atmospheric pressure to 1.1×10^{-3} Pa (8.0×10^{-6} torr).
- . A thermal system capable of maintaining a constant test specimen temperature within the temperature range of 100 K to 300 K.
- . A test specimen temperature control system capable of maintaining the differential temperature across the specimen to less than 15 K.
- . A data acquisition system capable of monitoring and recording shroud and test specimen temperatures and chamber pressure.
- . A facility control system equipped with an automatic pumpdown sequence.

During facility performance testing, all RADC specifications were met or improved upon.

TEST FACILITY BUILDING AND SYSTEMS

The building addition provided by CBI is designed to meet all of RADC's testing needs. The building is a four story structure which houses the vacuum chamber, a mechanical equipment room for the pumping and thermal system skids, a mezzanine area for storage and office space, a ground floor delivery/storage/cleaning area for test specimens, and additional office and laboratory areas. The building is designed to allow the installation of additional equipment for future expansion of the facility. The building was completed first and the vacuum chamber and subsystems were added at a later date. A removable roof hatch was used to facilitate installation of the vacuum chamber with a crane.

The building is equipped with a 3 ton, two axis crane for transporting test specimens, moving the top chamber head and upper spool piece, and for performing maintenance tasks on the shroud and other chamber-mounted equipment. The chamber test area is also equipped with a temperature and humidity controlled Class 100,000 clean room air conditioning system.

VACUUM CHAMBER

PHYSICAL CHARACTERISTICS

The vacuum chamber is a vertical cylinder with a 3.5 m (11.5 ft) outer diameter and a 7 m (23 ft) tangent length. The cylinder is comprised of two flanged spool sections to accommodate different test configurations. The upper spool piece is 2.13 m (7 ft) in length and may be removed from the main chamber spool piece with an overhead crane. A stiffened support ring located at the top of the main chamber spool piece is used to support the vessel on vibration isolators. Two external ring stiffeners are welded to the vessel shell to provide additional stiffness and strength.

The top chamber head is a 3.5 m (11.5 ft) diameter ASME flanged and dished (F and D) head. The top head may also be removed from the vessel with the overhead crane. The head is equipped with a 46 cm (18 in) diameter viewport and two optical benches (see Figure 5). The viewport is fabricated from BK-7 glass and has a special coating applied to its surfaces to reduce reflectivity to 0.4% throughout the wavelength range of the two interferometers.

The bottom chamber head is also a 3.5 m (11.5 ft) diameter ASME F and D head. The chamber interior is accessed by lowering the head into a pit with four pneumatic cylinders (see Figure 6). The bottom head handling system is designed to keep the head level while it is travelling and to consistently locate the head in the proper presentation stage loading and chamber closing positions. External stiffeners welded to the head provide the required stiffness and strength to support the presentation stage and test specimen.

The vessel is equipped with 49 nozzles. The nozzles are used for shroud inlet and outlet connections, vacuum and repressurization system connections, electrical feedthru ports, the fine adjustment system, and multi-purpose use ports for use by RADC. Twenty-three hardpoints are provided on the top head and cylindrical shell for mounting RADC-supplied equipment.

The vessel shell, heads, nozzles, and all internal fixtures are fabricated from Type 304 stainless steel polished to a No. 4 finish. All external stiffeners, pad plates, and attachments are fabricated from A36 carbon steel.

CHAMBER VIBRATION ISOLATION

The vacuum chamber and ancillary equipment are designed to minimize vibration transmission to the optical test specimen and laser interferometers. The entire chamber assembly including the presentation stage was required to have an overall natural frequency of at least 30 hertz. The following features are incorporated into the chamber design to ensure that the chamber vibration criteria are

met:

- Four pneumatic vibration isolators with 1.5 hertz vertical natural frequencies and 9070 kg (20,000 lb) load capacities are used to vibration isolate the chamber. The isolators are located beneath the stiffened support ring located at the top of the main chamber spool piece.
- Several in-house finite element analyses were performed to determine the optimum chamber and presentation stage stiffening arrangement to meet the 30 hertz natural frequency requirement. Analyses results indicated that a combination of external chamber stiffeners on the vessel shell and bottom head, an internal presentation stage rail support structure, and adjustable length presentation stage stiffening members would be required to meet this criteria.
- All piping and wiring directly connected to the chamber are vibration isolated by using stainless steel bellows and flexible conduit.
- Rotating equipment (such as mechanical vacuum pumps) are mounted on elastomeric isolator pads to minimize vibration transmission to the vacuum chamber. If necessary, rotating equipment is shut off during interferometer testing.

The natural frequency of the entire chamber assembly was calculated to be 31 hertz.

OPTICS HANDLING SYSTEM

PRESENTATION STAGE

Optical test specimens as large as 2 m (6.5 ft) in diameter and weighing up to 540 kg (1200 lb) may be mounted on a moveable presentation stage (see Figure 7). The presentation stage is used to load optical specimens into the vacuum chamber and to provide coarse elevation adjustment of the specimen from 0 to 90 cm (0 to 36 in). A scissors-type lift is used to provide coarse elevation adjustment of the presentation stage and is accurate to ± 0.158 cm (1/16 in).

The presentation stage is manually rolled into the chamber on floor-mounted rails. Removable rail pieces are used to temporarily bridge the gap between the building floor and the rail support structure inside the vessel.

The scissors lift is powered by a frequency controlled electric motor and a gear reducer which are mounted on a separate, mobile cart. The presentation stage and power cart are temporarily connected by a universal-jointed drive shaft. Coarse elevation adjustment may be made inside or outside of the chamber. However,

the power cart is not vacuum compatible and must be removed from the chamber prior to testing.

After the optical specimen has been raised to the proper elevation, the presentation stage is bolted to the rail support structure. Adjustable length stiffening members are then bolted between the presentation stage and the rail support structure to increase the overall natural frequency of the structure.

The rail structure is attached to the bottom head with eight Invar restraint rods which provide horizontal stiffness to the rail structure and presentation stage. The rail structure, presentation stage and optical test specimen are supported by the three point fine adjustment drive system.

The presentation stage and rail support structure were fabricated primarily from Type 304 stainless steel. Bolts and other threaded connections were fabricated from bronze to prevent galling. Sliding or moving parts which require lubrication were coated with Teflon (manufactured by E. I. du Pont de Nemours & Co.) or a vacuum-compatible dry lubricant such as tungsten disulfide.

FINE ADJUSTMENT DRIVE SYSTEM

A remote-controlled, three point elevation adjustment system is provided to allow precise positioning of the optical test specimen while the chamber is at both cryogenic and vacuum conditions. The system is comprised of three equally spaced fine adjustment drive mechanisms (see Figure 8). Each drive mechanism has a vertical post which is used to support the rail structure, presentation stage and optical test specimen. The posts penetrate the bottom head through bellows-sealed nozzles. The bellows are used to maintain chamber vacuum integrity while the posts move in the vertical direction. The posts are supported by beams which are attached to the bottom head with hinge mechanisms. Each post has a roller to allow movement between the beam and the post. The posts are located very close to the hinged end of the beams to provide motion reduction from the jack screw drive system. The opposite ends of the beams are connected to ball-type jack screws with a 0.025 cm (0.01 in) pitch. Each jack screw drive is equipped with a stepping motor and a fail-safe magnetic brake.

The stepping motors are used to drive the ball screws. The motion of the ball screws in the vertical direction causes the free end of the beam and the vertical support posts to travel up and down. The lever action of the beam reduces the support post travel by a factor of 15. This, in combination with the slow stepping motor speeds and the fine pitch of the ball screws enable the fine adjustment mechanisms to position the optical test specimen to ± 0.00025 cm (0.0001 in) resolution over a total travel range of ± 1.27 cm (0.5 in) from the initial presentation stage loading position. This design provided RADC with an adjustment system that

has a resolution ten times better than specified.

Limit switches are installed on each drive mechanism to prevent them from exceeding travel limits. The limit switches are also used to indicate when the mechanisms are in the initial presentation stage loading position.

The fine adjustment mechanisms are operated from a portable control panel located near the optical benches. A stepping motor programming/control panel is provided to control the motion of the stepping motors. One stepping motor may be operated at a time from the control panel. Stepping motor rotational direction, speed, and travel distance are manually controlled by the operator or programmed into the stepping motor indexers for automatic operation. Indicator lights operated by the drive mechanism limit switches are also provided to show position status.

VACUUM PUMPING SYSTEM

The vacuum pumping system is capable of evacuating the 76.5 m³ (2700 ft³) chamber from atmospheric pressure to 1.1×10^{-3} Pa (8.0×10^{-6} torr) in less than five hours with the shrouds at room temperature. The vacuum pumping system is comprised of a two stage mechanical pumping package and two cryopumps.

The Leybold, Inc. close coupled mechanical pump package is designed to evacuate the chamber from atmospheric pressure to 2.7 Pa (0.02 torr) in less than two hours. The pumps are also used to evacuate and regenerate the cryopumps. A mechanically refrigerated, optically dense cold trap is installed in the chamber roughing line as protection against oil backstreaming into the chamber.

Two Leybold, Inc. cryopumps are used to evacuate the chamber from a pressure of 2.7 Pa (0.02 torr) to a pressure of 1.1×10^{-3} Pa (8.0×10^{-6} torr) in less than 3 hours. The pumps have a gross nitrogen pumping speed of 10,000 l/s. The pumps are equipped with remote start/stop capability and a GN₂ regeneration system.

During performance testing, the vacuum pumping systems evacuated the chamber to a pressure of 1.1×10^{-3} Pa (8.0×10^{-6} torr) within the timespan specified by RADC. A chamber pressure of 2.7×10^{-6} Pa (2.0×10^{-8} torr) was measured by a nude ionization gauge while the thermal shrouds were at a temperature of 100 K.

The chamber repressurization system is equipped with a throttling valve to allow variable chamber repressurization rates. The system is capable of repressurizing the chamber in less than 30 minutes. The air used to repressurize the chamber is filtered through a high efficiency particulate (HEPA) filter to minimize chamber contamination.

The chamber roughing line, the cryopumps, and the chamber repressurization system are isolated from the chamber with electro-pneumatically operated high vacuum gate valves. The valves were directly mounted on the chamber nozzles.

THERMAL SYSTEM

THERMAL SHROUDS

The thermal shroud is designed to provide a 3.2 m (10.5 ft) diameter by 3.05 m (10.0 ft) high optically dense working volume for cryogenic testing of optical test specimens. The thermal shroud is comprised of 7 flow-adjustable control zones. Four 3.05 m (10 ft) high shroud zones are used to form the cylindrical working volume around the rail assembly, presentation stage, and test specimen. The ends of the cylinders are covered by cone-shaped shroud sections. A rectangular-shaped cold plate is installed on the presentation stage to cryogenically shield the bottom of the test specimen from the "warm" presentation stage.

To maximize radiation heat transfer between the thermal shroud and the test specimen, the shroud interior surfaces have been painted with a high emissivity black paint. To minimize radiation heat transfer between the thermal shroud and the chamber shell, the exterior shroud surfaces have been electropolished.

Individual inlets and outlets are provided for each shroud section. Removeable vacuum jacketed flex hoses are used to minimize vibration transmission to the vessel and to allow the shrouds to be easily removed from the chamber. Each shroud outlet is equipped with a remote-controlled valve to allow balanced gas flow through each section, thus minimizing the temperature gradient throughout the entire shroud system.

The top shroud cone has a 1.8 m (6 ft) hole to permit interferometer measurements to be made. To maintain optical density and to ensure uniform specimen cooldown, the hole is covered with two conductively cooled, semi-circular covers. The interior surface of the covers are painted black and the exterior surface is covered with multi-layer insulation (MLI) to minimize heat transfer from the vessel shell. Braided copper straps are bolted to the covers and to the top cone to provide conductive cooling. The covers are remotely opened and closed during interferometer testing by cable and pulley systems which are driven by two externally mounted, pneumatically powered rack and pinion gear mechanisms. The pulley drive shafts penetrate the chamber through an O-ring sealed rotary feedthrus.

Penetrations are provided in the shroud to allow access from the chamber interior to the multi-purpose ports. The penetrations are normally covered with conductively cooled aluminum port covers. Provisions have also been made for the future addition of a 20 K

helium shroud to be installed inside the existing working volume.

THERMAL SYSTEM EQUIPMENT

The thermal system is a closed-loop GN_2 system designed to maintain the thermal shrouds at any temperature in a range from 100 K to 300 K. The equipment used to circulate the GN_2 through the shrouds to maintain the desired temperature includes a cryogenic blower, liquid nitrogen heat exchanger, electric heater, and all associated piping and valving between the individual components and the thermal shrouds.

The thermal system blower is a water-cooled, stainless steel centrifugal blower which is designed to provide a mass flow rate of 2040 kg/hr (4500 lb/hr) at a boost of 69 kPa (10 psi). The blower is equipped with a close-coupled encapsulated motor to eliminate the maintenance requirements associated with cryogenic blowers equipped with mechanical seals. The blower is equipped with heaters, thermocouples, and temperature controllers to automatically maintain proper bearing temperatures when the thermal system is operating at cryogenic temperatures.

Cryogenic cooling is provided by a stainless steel heat exchanger. LN_2 flows into one side of the exchanger and is vaporized by the GN_2 circulating through the other side of the exchanger. The flow of LN_2 into the exchanger is regulated by a modulating control valve.

A cryogenic-compatible electric heater is used for warming the shroud and test specimen. The heater output is regulated by an SCR controller.

DATA ACQUISITION AND CONTROL SYSTEM

DATA ACQUISITION SYSTEM

The data acquisition system consists of a Hewlett Packard HP 9000 computer and a HP 3852 data acquisition/control unit. The system is programmed to monitor 14 shroud temperatures (inlet and outlet temperature of each shroud zone), 20 test specimen temperatures, and the chamber pressure. Type T thermocouples are used to measure temperature and a combination of Convector (manufactured by Granville-Phillips Co.) and ionization gauges are used to measure chamber pressure. The system is configured to store the data on computer disks for future analysis. A user-friendly, menu-driven control program was written to allow facility operators to easily run the system. The control program allows the operator to change data sampling rates during long duration tests.

THERMAL SYSTEM CONTROLLER

The data acquisition system is also used in conjunction with a PID controller to maintain the shroud and test specimen temperatures within operator specified tolerances. A menu-driven control program is used to specify the following operating parameters:

- . Final test specimen temperature. This parameter may have any value in the temperature range of 100 K to 300 K.
- . Maximum allowable temperature difference between any two points on the test specimen. Some test specimens are sensitive to thermal stresses/distortion and therefore cannot tolerate a large differential temperature. The minimum value for this parameter is 3 K.
- . Maximum allowable temperature difference between the average shroud and average test specimen temperatures. A large value for this parameter increases the heat transfer rate between the test specimen and the thermal shroud. This in turn decreases the time required to warm or cool the specimen to the desired temperature. However, those test specimens which are sensitive to thermal stresses must be cooled or warmed at a slow, uniform rate. The minimum value for this parameter is 6 K.

These parameters may be changed at any time during testing from a menu displayed on the computer monitor.

The data acquisition system is programmed to measure the shroud and test specimen temperatures every 15 seconds. Based on the test specimen and shroud temperatures and the given operator parameters, the program calculates and transmits a temperature setpoint to the controller. The controller regulates the operation of the heat exchanger LN₂ control valve and the electric heater SCR to maintain the test specimen and shroud temperatures within operating limits. Local displays on the data acquisition controller and the temperature controller are used to alert the operator if a thermocouple fails, a fault exists in the data acquisition system, or if one of the operator specified parameters is exceeded. The control system is also equipped with a manual override capability to allow the operator to change the shroud temperature setpoint or to change the operational status of the LN₂ control valve or the electric heater.

Since the primary objective of the thermal system is to uniformly cool or warm test specimens, RADDC specifications did not require a specific shroud temperature ramp rate. To ensure that a specimen is cooled uniformly, the shroud temperature ramp rate is limited to 0.4 K/min (0.7° F/min) by the thermal system controller.

FACILITY CONTROL SYSTEM

Most of the facility equipment is operated from a main control console located next to the chamber bottom head. The vacuum systems, the repressurization system, the thermal system, the GN₂ utility system, and the data acquisition system are operated from this central station. The controls and indicators for these systems are part of a graphic schematic of the vacuum and test facility systems. A programmable logic controller (PLC) is used to control equipment sequencing and interlocking.

The control system is equipped with an automatic pumpdown sequence. Once initiated, the control system will automatically evacuate the chamber, start the thermal system, and cool the test specimen to the desired temperature. System operation may also be manually controlled by facility operators from the main control console.

A locally mounted control panel is provided to control the operation of the bottom head handling system. As previously discussed, a portable fine adjustment drive control panel is located near the optical benches at the top of the chamber. The top cone shroud cover movement systems are also controlled from this panel.

UTILITY SUPPLY SYSTEMS

The facility is equipped with a 22,700 liter (6000 gallon) LN₂ storage dewar. An electric LN₂ vaporizer is used to provide GN₂ to all pneumatic users. These users include the bottom head handling system, the cryopump regeneration system, the top cone shroud cover movement system, and all air operated valves.

SUMMARY

Several innovative design approaches were utilized by CBI to meet RADC's needs for testing large optics under vacuum and cryogenic conditions. The key areas which were identified as critical to the successful design of the facility included:

- . Overall chamber natural frequency and vibration isolation system
- . Presentation stage and fine adjustment system
- . Thermal control system

CBI utilized finite element analysis techniques during the design stages of this project to ensure that the overall natural frequency of the chamber, presentation stage, and optical benches was at least 30 hertz. The integration of this design with the pneumatic

vibration isolation system allowed CBI to meet RADC's need for a stable testing platform.

CBI's innovative design of the presentation stage and fine adjustment system provided RADC a versatile system for transporting and positioning optics in the vacuum chamber. The design concept used for the fine adjustment system provided RADC ten times better resolution than required.

The thermal control system utilizes a CBI developed software package to precisely regulate the optic temperature, thermal gradient across the optic, and the shroud temperature to minimize thermal stresses and distortion in the optic. The software package is a user friendly, menu driven program which is also capable of storing large quantities of thermal test data.

During facility performance testing, it was demonstrated the facility met or improved upon all RADC requirements. The facility has been successfully used by RADC to test optics under cryogenic and vacuum conditions.

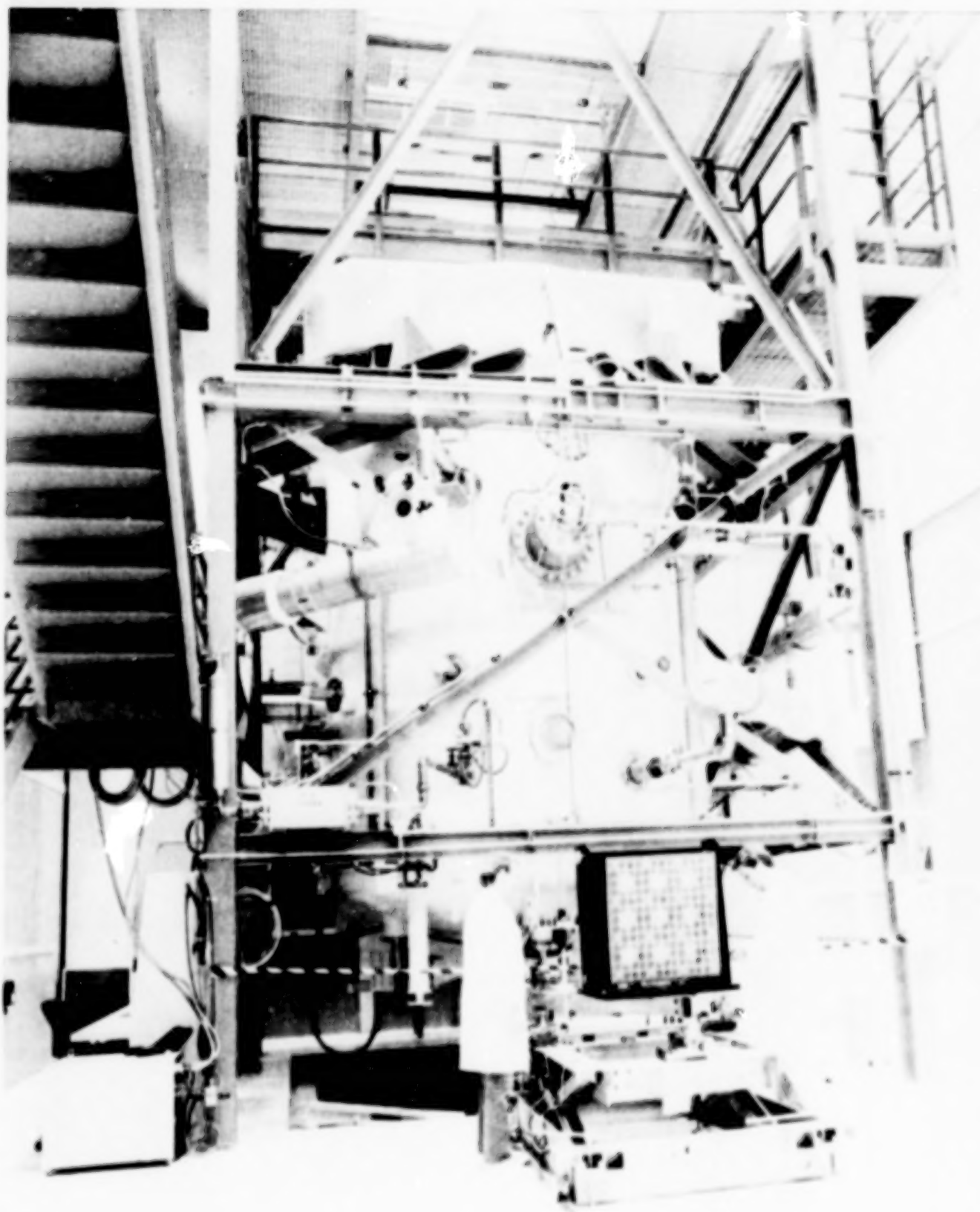


FIGURE 1: RADC THERMAL VACUUM TEST FACILITY

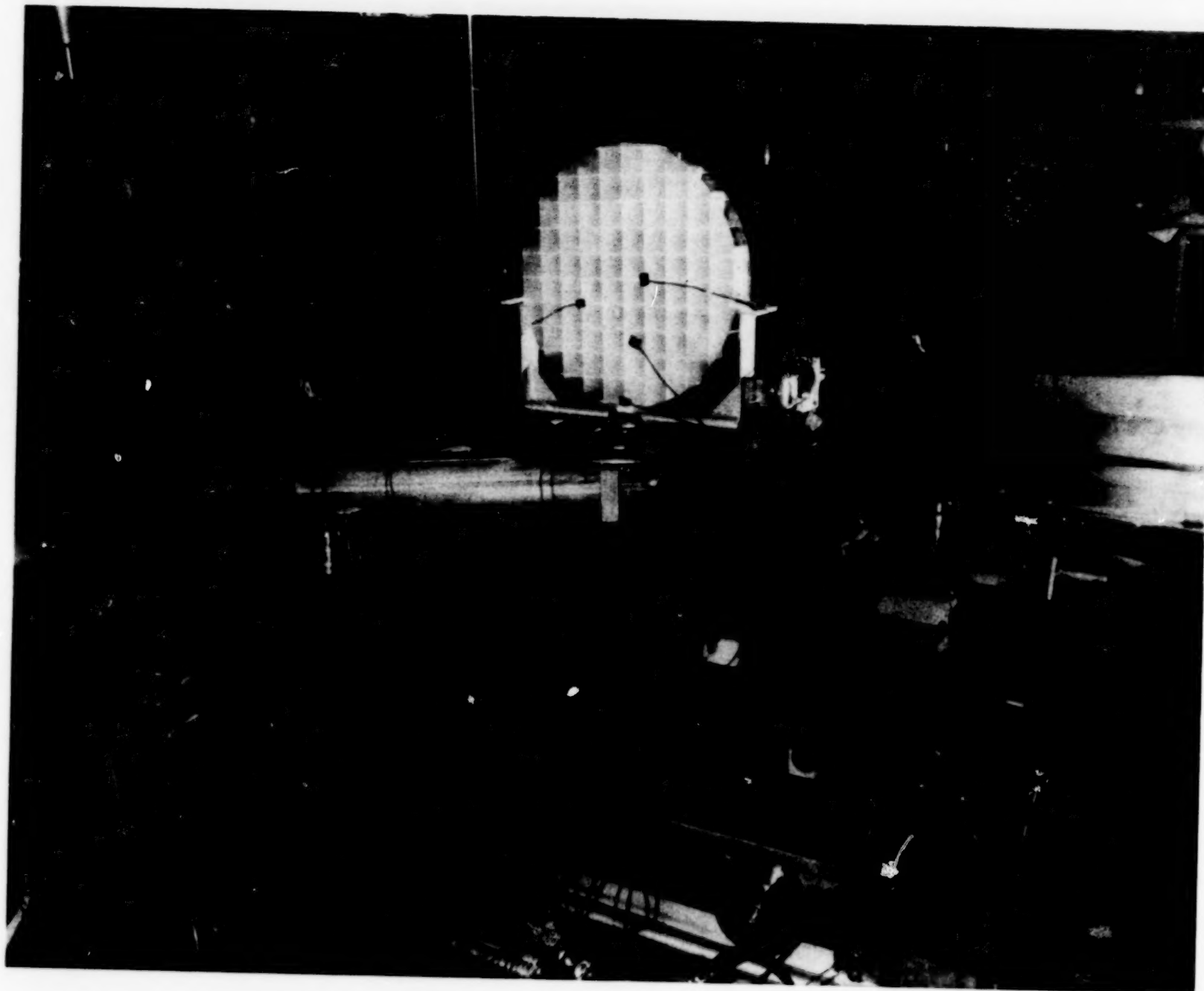


FIGURE 2: TEST OPTIC MOUNTED ON PRESENTATION STAGE

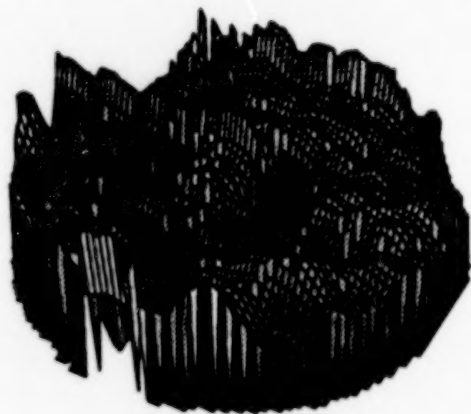
0.5 Meter Frit-bonded Mirror Phase Maps



Baseline



123° Kelvin



123° Difference



Baseline Difference

FIGURE 3: SURFACE PROFILES OF TEST OPTIC

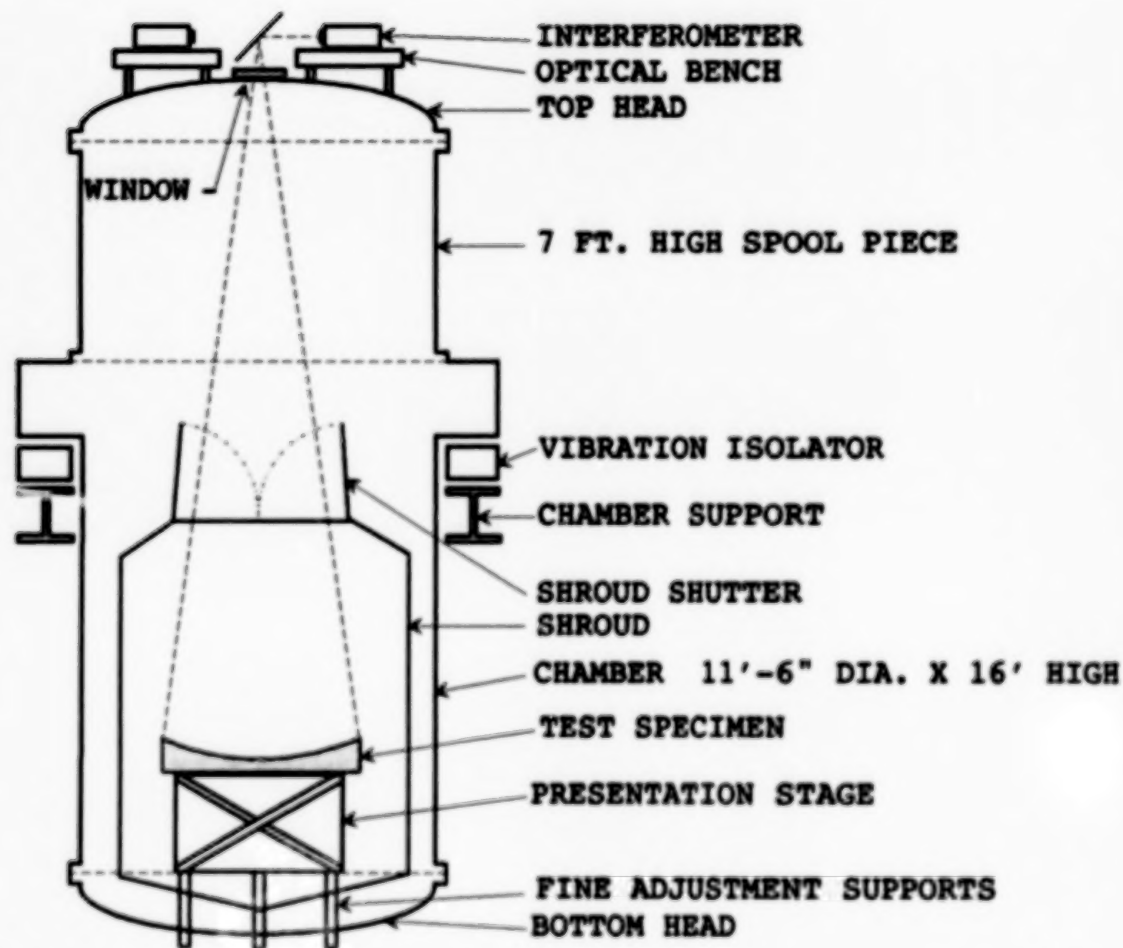


FIGURE 4: CROSS SECTIONAL VIEW OF VACUUM CHAMBER

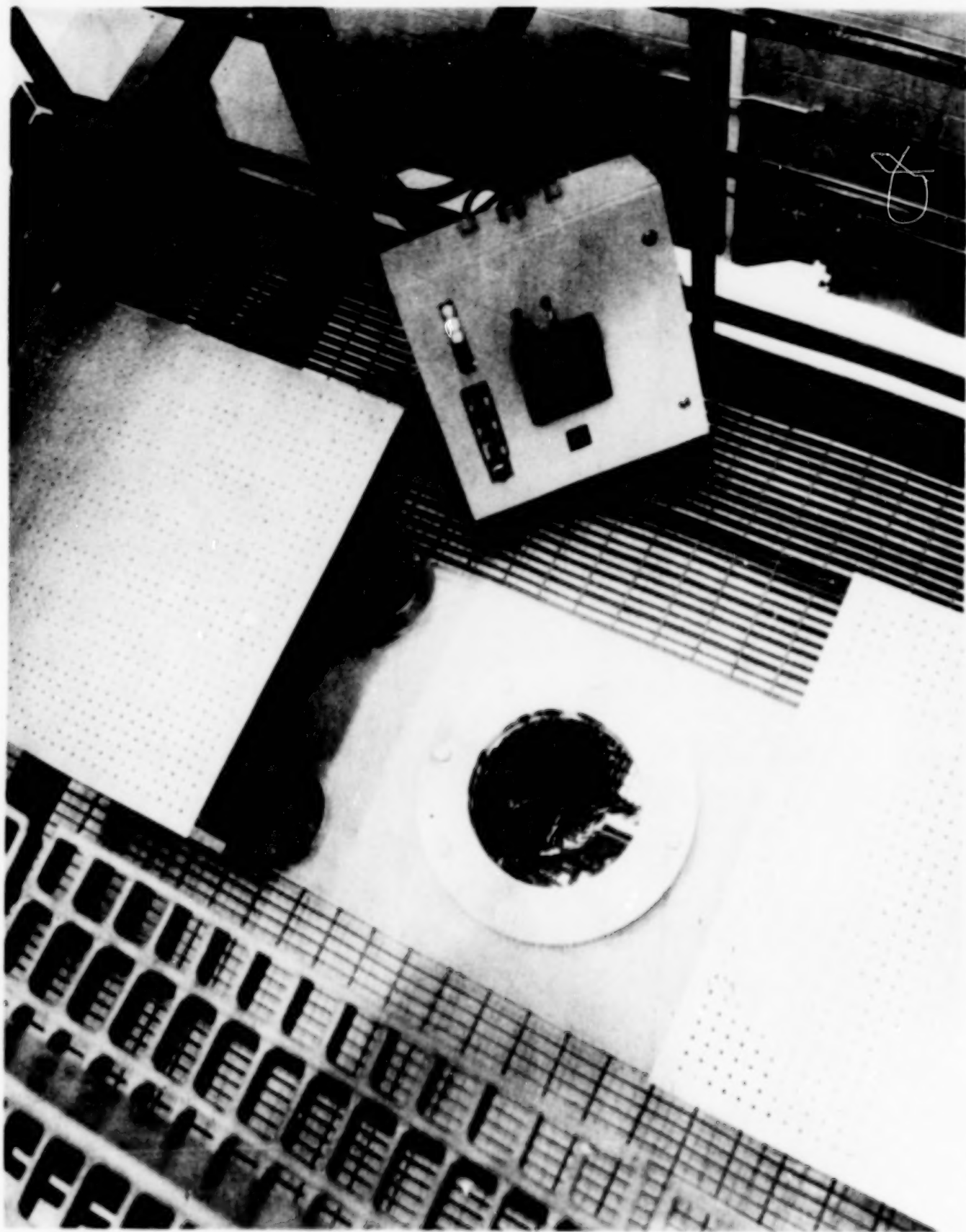


FIGURE 5: VIEWPORT AND OPTICAL BENCHES

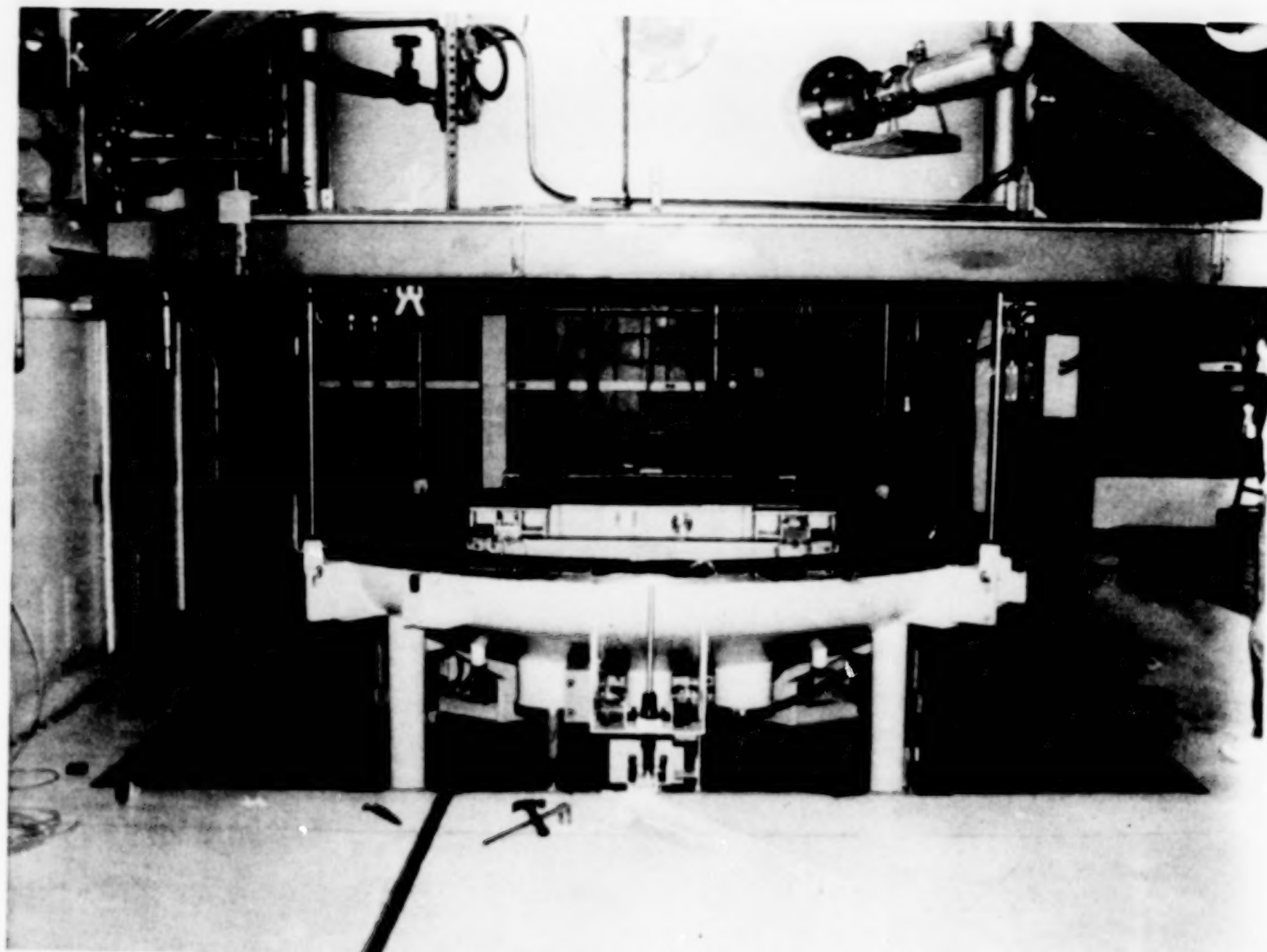


FIGURE 6: LOWERING BOTTOM HEAD INTO PIT

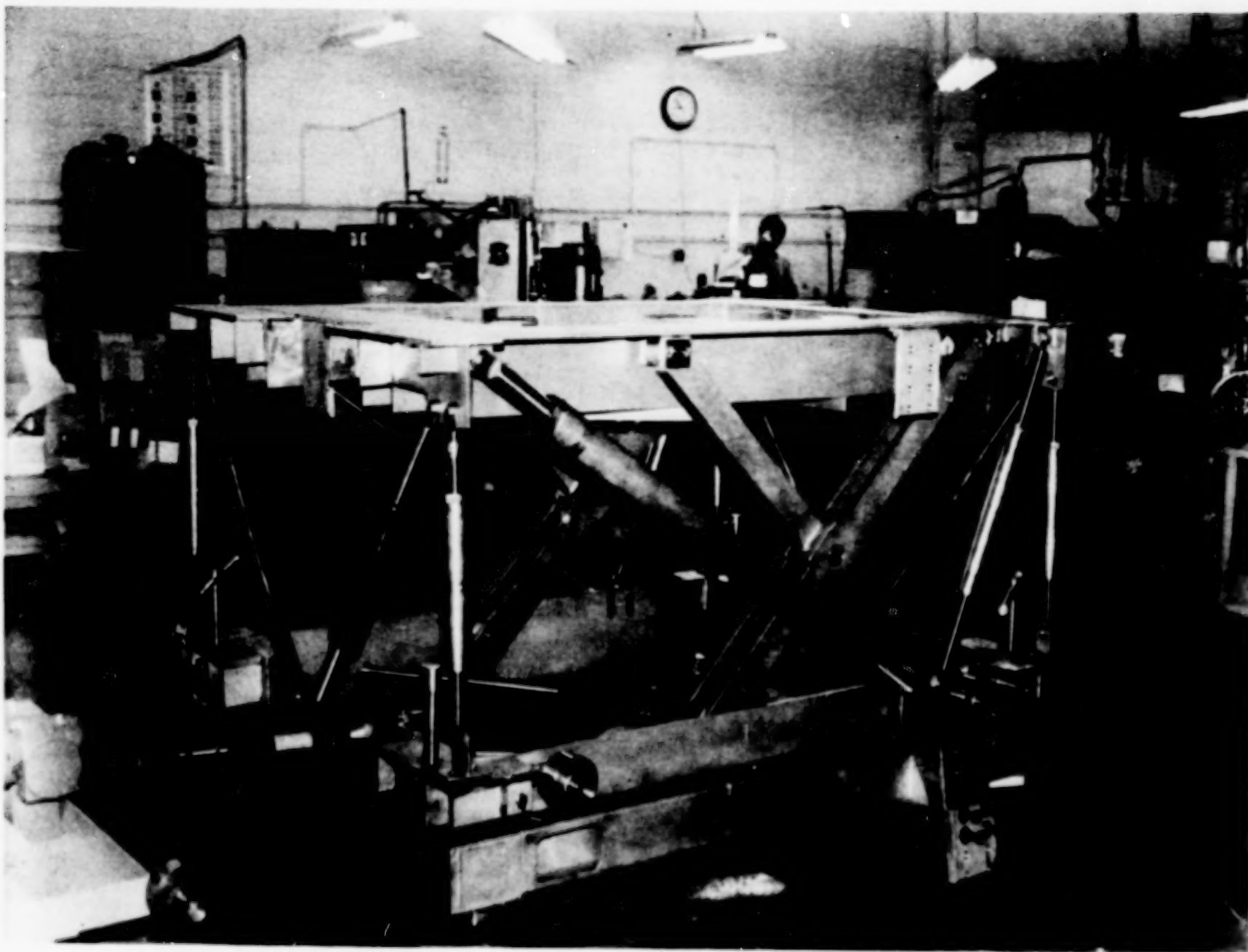


FIGURE 7: PRESENTATION STAGE

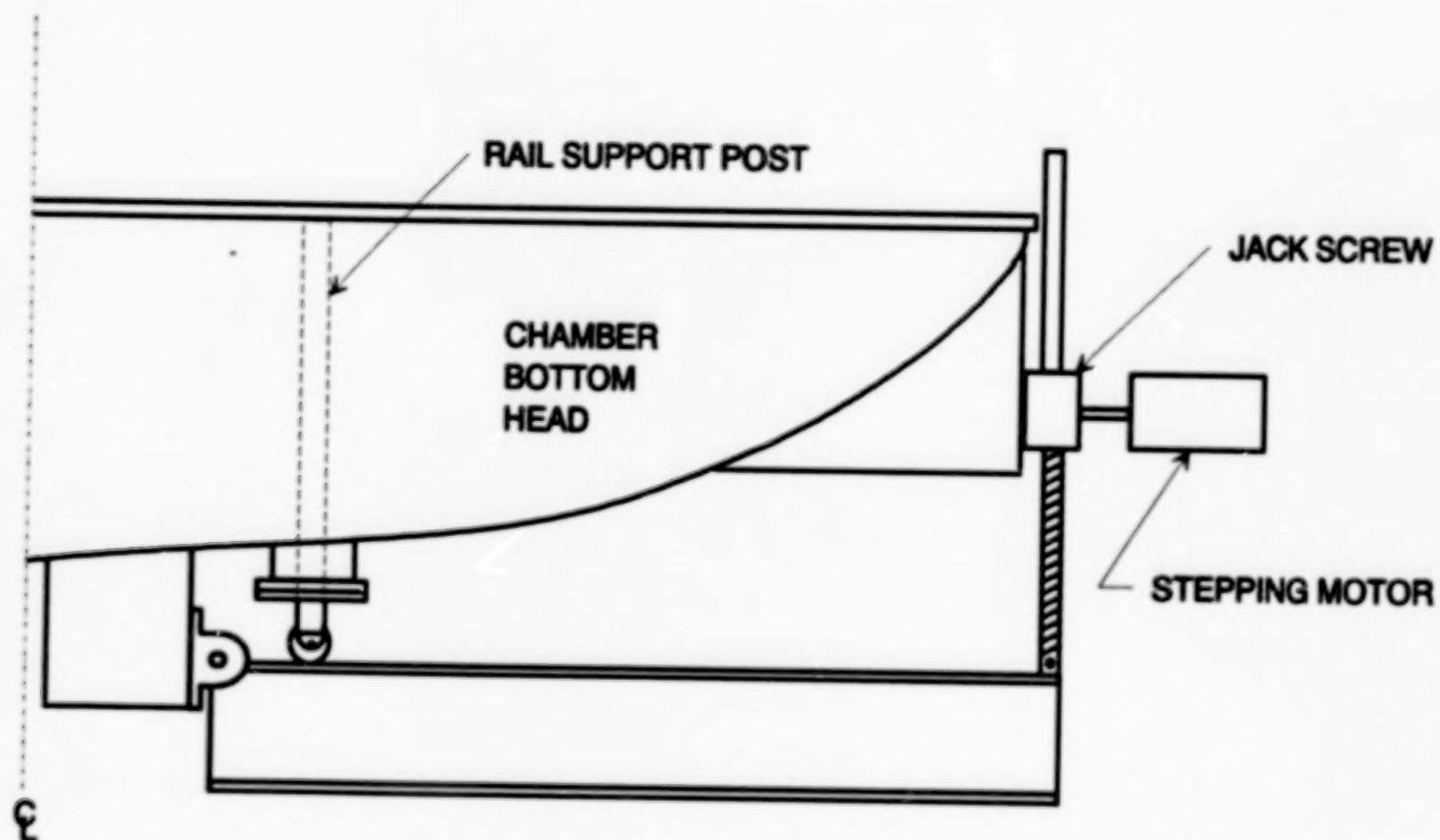


FIGURE 8: FINE ELEVATION ADJUSTMENT MECHANISM

BOEING INFRARED SENSOR (BIRS) CALIBRATION FACILITY

John D. Hazen
Boeing Aerospace & Electronics, Seattle, WA, USA
and
L. V. Scorsone
Pitt-Des Moines, Inc. (PDM), Pittsburgh, PA, USA

ABSTRACT

The Boeing Infrared Sensor (BIRS) Calibration Facility represents a major capital investment by The Boeing Company in optical and infrared technology. The facility was designed and built for the calibration and testing of the new generation large aperture long wave infrared (LWIR) sensors, seekers and related technologies. Capability exists to perform both radiometric and goniometric calibrations of large infrared sensors under simulated environmental operating conditions. The system is presently configured for endoatmospheric calibrations with a uniform background field which can be set to simulate the expected mission background levels. During calibration, the sensor under test is also exposed to expected mission temperatures and pressures within the test chamber. Capability exists to convert the facility for exoatmospheric testing.

The first major test runs in the facility were completed during 1989 with very satisfactory results. This paper will describe the configuration of the system and hardware elements and address modifications made to date.

Pitt-Des Moines, Inc. (PDM) of Pittsburgh, PA was the contractor for the turnkey design and construction of the test chambers and thermal vacuum systems. Hughes Danbury Optical Systems (formerly Perkin Elemer Optical Systems) was the hardware supplier for the optical hardware. The Boeing Company performed all optical assembly, integration, testing and alignment on site.

INTRODUCTION & SYSTEM DESCRIPTION

The system consists of two major vacuum chambers, a small window subchamber, a mounting slab, an infrared source generator, beam expansion optics and a sensor support mount designed to support the sensor in a simulated operating environment. The system is shown schematically in Figure 1.

The BIRS vacuum chamber consists of two main chambers called the optics chamber (OC) and the sensor chamber (SC). The optics chamber is maintained at a pressure of 1.0×10^{-7} torr or lower and the equipment within the chamber operated at near liquid nitrogen temperature. This equipment includes the Beam Expansion (BX) optics and the Scan Mirror Assembly (SMA). The sensor chamber is held at a nominal pressure of 90 torr and a temperature of 220°K to 240°K.

INTRODUCTION & SYSTEM DESCRIPTION (Continued)

The Window Subchamber (WSC) is a third small chamber located between the optics and the sensor chamber and provides for isolation of the WSC optical elements during sensor installation by means of a 1.5m (60 inch) gate valve located on the sensor chamber side of the WSC. This allows the optical system to remain at high vacuum and low temperature conditions, maintaining its optical stability and eliminating the time required to warm up and cool down the optical system. This chamber is physically located within the optics chamber at the interface between the optics and sensor chamber.

The pressure boundary between the high vacuum optics chamber and the altitude sensor chamber during test is provided by an Output Window Assembly (OWA) located within the WSC. This large zinc selenide infrared transmitting window passes the calibration beam from the optics chamber to the sensor chamber and also serves to reflect a uniform radiation background generated by the Background Signal Generator (BGSG) which is a high emissivity plate that radiates to the sensor pupil via reflection off a Background Signal Generator mirror and the OWA.

Figure 2 is a schematic elevation view of the optical system.

Infrared beam expansion is accomplished using the Beam Expander (BX) equipment which is located in the optics chamber. The BX is a three mirror afocal telescope which takes a collimated input beam from the Modified Portable Optics Sensor Tester (MPOST) (GFE) and expands it to a 0.8 meter (32 inch) collimated output beam. The BX mirrors and structure are normally cooled to near 80°K.

A Scan Mirror Assembly (SMA) is provided which reflects the input beam from MPOST into the BX optics. The SMA can be used to accurately position the stationary beam during the goniometric calibration mode and is used to scan the beam across the sensor during the radiometric calibration mode.

The input calibration beam is inserted into the optics chamber from MPOST via the Input Window Assembly (IWA). The IWA forms the contamination seal with the optics chamber incorporating an 11 inch diameter ZnSe window. This window in conjunction with the output window assembly also serves to remove polarization effects. It is capable of being cooled to 104°K with 80°K subcooled LN₂ when MPOST is attached to the chamber. Also included in this assembly is the input coldwell which is a series of optically dense baffles cooled to 80°K.

SYSTEM COMPONENTS

Optics Chamber

The optics chamber is a rectangular stiffened vacuum chamber having inside dimensions of 3.35m wide x 3.35m high x 5.5m long (11' wide x 11' high x 18' long). The material is 304 stainless steel with carbon steel stiffeners designed for the full vacuum load. The stainless steel interior surfaces are polished to a simulated No. 4 finish. The optics chamber rests upon the seismic slab which also supports the optical test equipment inside the chamber. Figure 3 is a schematic elevation of the optics chamber.

A full opening door is provided on one end of the chamber for optics system installation, alignment and maintenance. A rectangular configuration was chosen for this vessel and the sensor chamber. This decision was based on a trade study which indicated circular vessels would provide excess volume and would be difficult to connect to the seismic slab. Further, it was determined that a rectangular chamber better accommodates installation and removal of a thermal shroud around the beam expander and scan mirror structure. Optics Systems penetrations provided for the support legs of the beam expander and scan mirror are unique in that a flexible seal assembly was provided which decoupled the chamber shell from the leg so that no detrimental vibratory inputs were transmitted into the optics system. The optics chamber is fully lined with an optically dense LN₂ cooled shroud. External valved cryopumps provide high vacuum pumping.

Sensor Chamber

The sensor chamber is also a rectangular stiffened vacuum chamber having inside dimensions of 4.9m wide x 4.6m high x 7m long (16' wide x 15' high x 23' long). Chamber materials are Type 304 stainless steel. Carbon steel stiffeners are provided to resist full vacuum load. The sensor chamber is hard mounted to the seismic slab which also provides independent support for the sensor assembly by a series of legs penetrating the shell. These legs are decoupled from the chamber shell identically to the optical elements described previously.

The sensor chamber is provided with two full cross sectional opening doors, providing full access to the interior for loading and unloading the sensor. In addition, a personnel door is provided in one of the full opening doors to allow entry to the sensor chamber without removal of the full door. Figure 4 is a schematic elevation of the sensor chamber looking toward the sensor chamber.

In addition to the penetrations for the sensor mount system legs, the chamber is provided with a 1.5 meter (60 inch) diameter penetration for a remotely operated gate valve which isolates the window subchamber from the sensor chamber. The design and operation of the gate valve will be described later.

Sensor Chamber (Continued)

The sensor chamber is fully lined with a unique, passive thermal shield (insulation system) which isolates the chamber shell from the nominal 13,715m (45,000 feet) altitude environment, i.e. 90 torr and -45°C. This insulation system consists of a rigid polystyrene foam with a stainless steel skin which is evacuated to a low micron level. This provides an effective insulation for the external chamber shell from the high altitude environment of the sensor chamber.

Vacuum Systems

Optics Chamber

The vacuum systems for the optics chamber consists of:

1. A mechanical pump/blower combination with LN₂ cold trap capable of rough pumping to less than 50 microns.
2. Three 500mm (20 inch) diameter externally mounted cryopumps provide high vacuum pumping to 1×10^{-8} torr. Each is equipped with a large diameter isolation valve.
3. A 150mm (6 inch) turbomolecular pump is provided with a manifold allowing it to pump either the optics or sensor chamber. This pump is primarily used during the leak checking phases.

Sensor Chamber

The vacuum system for the sensor chamber consists of a 3-stage blower system capable of roughing the sensor chamber from 760 to 90 torr with a simultaneous 0.23 kg/sec (0.5 lb/sec) GN₂ inbleed. The roughing system is also capable of pumping 0.16 kg/sec (0.35 lb/sec) GN₂ inbleed while maintaining the pressure between 90 to 60 torr.

LN₂ Thermal System

The LN₂ thermal system is comprised of a recirculating LN₂ system operating in a subcooled mode with the heat gain being rejected into a bath of boiling LN₂ at atmospheric pressure. This system is shown schematically in Figure 5.

The heat loads on the system are as follows:

- Optics Chamber Shroud Zones
- Beam Expander & Scan Mirror Zones
- Scan Mirror & Input Window Assemblies
- MPOST Zones
- Sensor Chamber Zones (future)

LN₂ Thermal System (Continued)

These systems are supplied liquid nitrogen at approximately 80°K and return liquid to the cooling coil in the dewar at approximately 95°K or less, depending on the heat load in each respective system.

In addition to recirculating loads described above, the LN₂ subcooler furnishes LN₂ for two GN₂ thermal units. These units are consumers of LN₂ on a continuous basis requiring make up of LN₂ into the recirculating LN₂ stream. LN₂ make up is accomplished by reducing the pressure on the suction side of the LN₂ pumps and injecting make up LN₂ in the low pressure zone from an external storage tank operating at about 48.3 kPa (7 psig). Pressure reduction is accomplished by a throttle valve located before the connection to the external LN₂ tank.

The subcooler has the capability of absorbing 85,900 kcal/hr (100 kw) of heat from the system while maintaining all operating heat loads (zones) at a nominal temperature of 80°K. Uniformity of the supply temperature is critical to the stability of the optical elements. During baseline operation, temperature stability is maintained within ± 1 K.

The optics chamber shroud construction consists of extruded aluminum panels having integral tube passages. The emissivity of the shroud on the inside surface is 0.9 with the side facing the chamber 0.1. The design of the shroud is unique in that all penetrations and closures prevent any surface outside of the shroud with a temperature of 95°K or greater from being observed with less than 2 reflections off optically dense baffling with a surface emittance of greater than 0.9. The shrouds are also removable from the chamber for cleaning. Conflat flange LN₂ connections are provided for each shroud section. These connections are interior to vacuum chamber and underwent extensive leak checking during the acceptance test program to ensure leak tight performance.

GN₂ Thermal Systems

Two GN₂ thermal units are provided. The sensor chamber thermal unit has the primary function of providing a cold inbleed gas source to maintain the sensor chamber at ambient temperatures consistent with altitude operation at 60 torr to 90 torr while being actively pumped by the sensor chamber roughing system. This inbleed in effect subjects the sensor unit under test to environmental conditions as though it were "flying" at altitude. GN₂ is supplied to the sensor chamber thermal unit by an LN₂ vaporizer operating from a conventional LN₂ storage tank. A stream of LN₂ from the subcooler is mixed to the GN₂ stream in an LN₂/GN₂ mixer to provide a varying output stream temperature between 140°K - 300°K with a maximum throughput of 0.32 kg/sec (0.7 lb/sec). The unit is also provided with a warmup heater for use in warming optics' chamber shrouds and optics zones. This unit is shown schematically in Figure 6.

GN₂ Thermal Systems (Continued)

The other GN₂ thermal unit has the function of providing temperature controlled GN₂ to a group of zones in the window subchamber and sensor chamber. It circulates GN₂ on a closed loop basis. This is accomplished by using a conventional reciprocating compressor in series with an aftercooler, heat exchangers, heaters, LN₂/GN₂ mixer, preheaters and trim heaters. This system is shown schematically in Figure 7. GN₂ is supplied to this system from the same high pressure storage vaporizer system that supplies the sensor chamber thermal unit. A pressure regulator in this supply line reduces the pressure to 172.4 kPa (25 psig) and subsequently through downstream heat exchangers, etc. to ultimately serve as a thermal conditioning fluid for end users in the window subchamber and gate valve. Two output streams are provided which can be set at different temperatures. From these use points the gas is recirculated back to compressor suction. This system has the capacity of circulating 365 kg/hr (800 lb/hr) in a temperature range of 140°K to 300°K at a maximum pressure of 414 kPa (60 psig). A key requirement of this unit is providing the GN₂ which cools the titanium adapter for the OWA. Accurate temperature stability is required so as not to induce thermal strains in the OWA bezel structure.

Control System

The BIRS facility is controlled from a central control console that is functionally divided into three sections:

- Thermal-Vacuum Control
- Optical Control
- Data Acquisition System

The thermal-vacuum control console section receives data from facility instrumentation which displays on an integrated graphics panel which has associated symbolic and written legends defining system control functions. All remote facility operations are manually controlled from this panel with the status of all major functions displayed. Alarms and interlocking of all functions are accomplished at this panel. Control logic and interlocks were provided by means of a PLC (Programmable Logic Controller). An effort was made to limit the amount of interlocks to as few as possible to allow for maximum operator flexibility and test configurations. Redundant PLC's were not provided; however, all equipment and valves have been designed to go to a failsafe mode in the event of a system failure. The PLC provides automatic operation of the system in the event of designated emergencies, such as loss of prime power or overpressure of the OWA. The optical control system allows for monitoring and setting of temperatures of all optical elements and provides control capability of the Sensor Mount Subsystem (SMS) and Scan Mirror Assembly (SMA). The data acquisition system gathers and records all facility data and provides real time plots of data showing trends, etc.

Key Optical Elements

Beam Expander

The Beam Expander (BX) enlarges the incoming source beam to approximately 3 times its initial diameter. It is an afocal system with a Cassegrain telescope consisting of parabolic input or tertiary mirror coupled to a hyperbolic secondary and parabolic primary mirror. The BX is off-axis in both field and aperture and thereby provides an unobscured collimated output beam of approximately 0.8 meters (32 inch) in the present configuration. The primary mirror is a nominal 1 meter (41 inch) diameter solid piece of zerodur weighing over 409 kg (900 lbs). The tertiary mirror also of solid zerodur is nominally 0.76 meters (30 inches) diameter and weighs 136 kg (300 lbs). The secondary mirror is much smaller and is fabricated of fused silica. All mirrors have gold coating and protective overcoats. The LN₂ cooled BX optical bench is fabricated from Invar 36 for minimum dimensional variations from ambient to cryogenic conditions. Figure 8 shows a representation of the beam expander and mirrors.

Scan Mirror Assembly (SMA)

The SMA consists of a servo driven cryogenically cooled fused silica mirror assembly which allows the accurate positioning of the output beam when used in the stare mode. In the scanning mode, the SMA allows the output beam to be scanned across the test sensor at various rates. Azimuth and elevation servo electronics are controlled by computer.

Output Window Assembly (OWA)

The Output Window is one of the most important single components in the facility. The ZnSe blank was generated by a continuous and uninterrupted chemical vapor deposition oven run of over 900 hours. The finished window is 0.79m (31-inches) in diameter and 33mm (1.3 inches) thick and represents the largest ZnSe window of its type in the world. As with the Input Window, the Output Window is mounted in a titanium bezel for CTE matching. It is held in place by a thin bead of Crest 7450 adhesive around the perimeter which also forms the vacuum seal. Special heaters precisely control the edge temperature of the window. Because of the small thickness to diameter ratio, the window is not capable of supporting a full atmospheric pressure load. For safety, it is limited to differential pressure loads of the order of 120 torr. The purpose of the Window sub-chamber with the 1.5m (60 inch) Gate Valve to the Sensor chamber is to maintain the controlled Output Window pressure load while allowing free access to the Sensor Chamber.

Special Features

The stringent requirements of providing an optimum environment for the optics system and sensor required that the vacuum chambers and supporting subsystems accommodate many unique operating criteria. The following items are herein described to identify some of these components and system requirements.

Seismic Slab

A seismic slab was provided to minimize the optical system components response to vibrations from the environment and the experiment itself. A schematic of this system is shown in Figure 9. A ground vibration survey was conducted at the facility site as well as identification of other disturbances such as vehicular traffic, cranes, local handling equipment, pumps, etc.

Criteria for structural and dynamic requirements for the seismic slab are as follows:

- a) Optical beam drift due to seismic slab deformations to be less than 0.5 microradian over a 1-30 minute time period.
- b) Long term drift (deformation) were to be minimized by design, material choice and fabrication control. Included in this requirement is the prevention of cracking of the seismic slab.
- c) Provision for a procedure to determine when a recalibration of the slab is required due to change in shape of the seismic slab as a result of curving due to temperature gradients.

In order to satisfy these requirements, an 1800 metric ton concrete slab disconnected from the building floor slab was selected to be supported on piling driven to a load bearing stratum. A dynamic vibration analysis was carried out to determine that the short term beam jitter could be accommodated.

Horizontal and vertical vibration data were collected for the BIRS site. This data was put into the form of a site specific response spectra which provided a range of frequency dependent accelerations resulting from the ground vibrations. A computer model of the chamber, seismic slab, and optical mounts connected to the seismic slab was prepared. The response of this model to the accelerations determined by the ground vibration study was calculated and compared to the allowable response "budget" for the optical system.

To limit vibrations into the chamber from rotating mechanical equipment and piping, all vacuum pumping skids, LN₂ pumping systems and GN₂ thermal units were mounted on vibration isolation mounts. Flexible metal hoses were used throughout the piping system to reduce vibrations into the chamber.

In order to meet the long term drift requirement, the services of a concrete design specialist was obtained to provide a design of a concrete mix and reinforcing which would minimize long term creep and cracking. Crack control reinforcing steel and low heat of hydration concrete was used in the seismic slab to ensure slab performance. The pouring sequence of the slab was carefully controlled and monitored as well. The slab is provided with an inspection gallery around its perimeter for visual inspection of the slab for cracking and signs of distress across its full thickness. For the recalibration requirement, a series of thermocouples were embedded in the concrete to measure temperatures. This data was used to determine any differentials that might exist (vertically and horizontally) that would cause geometric movement of the top surface of the slab.

Sensor Chamber Gate Valve

A large 1.5 meter (60 inch) diameter remotely controlled gate valve was provided to isolate the sensor chamber environment from the output window. Also, it serves to isolate the window subchamber during the period of window temperature conditioning.

Some of the specific design requirements for the valve were as follows:

- . Valve to be remotely operable to cover and seal the window subchamber at one atmosphere differential pressure.
- . Valve closure repeatability to be ± 1.7 mm (± 0.065 inch) (a calibration mirror is located on the inside of the gate valve).
- . The seal of the gate valve (O-ring) was required to be warm to permit operation and sealing at all chamber conditions.

To achieve the remotely operable requirement, the valve assembly was suspended from an upper rail system which laterally translated the valve cover to allow a full diameter opening. Translation was achieved by using a roller chain drive system which was powered by a motorized worm gear reducer operating through a fluidic coupling. Use of the roller chain system also allowed for accurate position indication and adaptation of suitable interlocks with other systems. Once the valve gate seal plate is positioned over the mating flange, initial contact pressure for the seal is accomplished with four pneumatic cylinders which reach between the carriage frame and the valve plate. In order to maintain the seal at a warm condition, both the flanges and the O-ring seal were provided with a series of strip heaters mounted on each flange, clamped into contact and energized as required to maintain the metal temperatures above freezing for all operating conditions. Heaters are shielded from the view of the test sensor. Connected to the gate valve are shroud components which move into position when the gate valve is moved away from the window subchamber, thereby allowing the optical beam to pass onto the sensor. The shroud components operate nominally between 220°K and 250°K using GN₂ as a cooling medium. Supply to these shroud components required a festooning system for GN₂ supply hoses and instrumentation wiring.

Sensor Chamber Insulation

The specification required that the sensor chamber be designed with a passive thermal shroud which would isolate the chamber shell from the 90 torr, low temperature environment. The objective of this isolation was to prevent condensation on the external surfaces of the chamber. The internal insulation was to have a metallic surface to facilitate cleaning. Details of the system are shown on Figure 10.

Sensor Chamber Insulation (Continued)

Consideration of an externally applied insulation was not practical considering vessel sealing, stiffeners and appurtenances such as penetrations let alone the room cleanliness considerations (Class 10,000). The design that resulted to satisfy the above criteria was to apply a load bearing insulation material to the interior face of the chamber wall, cover the insulation with a metallic skin, and evacuate the space between the skin and the chamber wall to minimize the internal pressure load on the thin skin. The insulation material chosen was a load bearing styrofoam applied in two layers with staggered seams. The rigid insulation was held in place by use of thermally non-conducting studs as shown in the figure. Once the insulation had been applied, embedments were attached to the inside face of the insulation that served as retainer points which maintained the stainless steel skin in intimate contact with the insulation. These retainers allowed the skin to thermally move yet maintain proper support. All joints in the metallic skin were seal welded and leak checked to verify leak tightness.

Valve Box

As was discussed previously for the LN_2 and GN_2 thermal control systems, the facility utilized a considerable number of flow control (zone) valves. The normal method of insulation for such valves is to either mechanically insulate the valve with conventional insulation, or to provide a vacuum around the portion of the valve subject to low temperature with appropriate bonnet lengths to provide a thermal distance piece. This project required approximately 36 small diameter zone control valves. The insulation and arrangement concept employed was to utilize an arrangement called a "valve-box". It consists of collecting the valves into as small a region as possible and providing a common vacuum enclosure which provides the insulation required. Schematically, this arrangement is shown in Figure 11. Each valve is arranged such that the bonnet and operator extend through the face of the valve box for normal actuator connections. To enable the maximum number of valves to be placed in the valve box, the electronic to pneumatic converters used for control valve positioning were mounted on a separate rack adjacent to the valve box. This saved considerable space on the valve box since only pneumatic tubing was required to be run to the valves. Piping connections to the valves are made inside the box and pass through an isolation plate prior to entering the independent vacuum space of the respective chamber. Pumping of the valve box is accomplished with a small cryopump or turbo pump. Vacuum is maintained in the valve box in the same manner as would be accomplished in a vacuum jacketed dewar of large size. All internal lines are insulated with MLI to minimize radiation heat loads.

Modifications

For a facility with the complexity and size of BIRS, it is inevitable that various problems will surface that were not anticipated. The challenge of the facility team is to find solutions to the problems without affecting the performance and functionality of other parts of the system. Several problems of this type were found in BIRS as a result of our first sensor tests. Those noteworthy of mention include the compliances of the Sensor Mount Subsystem (SMS) and the overheating of the SMA azimuth motor.

Sensor Mount Subsystem (SMS)

The SMS is a three point kinematic mount system with 6 degree of freedom adjustability for fine positioning of a test sensor in front of the BIRS beam. This system can be operated remotely with the chamber under test conditions of temperature and pressure. During an initial sensor warm functional checkout, it was discovered that a significant motion of the sensor support platform was occurring in the longitudinal (parallel to SC axis) axis. Compliances in the system elements and the nature of the design to provide longitudinal positioning were determined to be the causes of this motion which was unacceptable both from a chamber integrity standpoint and for sensor stability. An ingenious system of high pressure locking struts was developed and tested in the laboratory. See Figure 12. The telescoping struts with high tolerance end bearings would allow positioning of the test article within the SMS range of motion. Once positioning was completed, the locking collars were pressurized with GN_2 to 20,685 kPa (3,000 psig) effectively locking the strut into a rigid unit. One end of the strut was connected directly to the sensor leg mounting block and the other to the main chamber leg support structure. This in essence provided a direct link from the sensor platform to the seismic slab embedded pedestal bypassing the total SMS mechanism and compliances. Resulting stiffness increases were on the order of a factor of 500 to 1. Observed motions dropped from the 1.27 cm (0.5 inch) range to the 0.05 mm (0.002 inch) range.

SMA Azimuth Motor Overheating

During initial testing, it was determined that the existing azimuth motor would overheat during periods of sustained scanning or staring at points near the edge of the angular range. A careful study and subsequent testing of a surrogate winding indicated that the problem was insufficient heat transfer from the windings to the cryogenically cooled core/case assembly. To rework this motor would require the removal of the SMA from the chamber and subsequent total disassembly. All alignment work of the optics would have to be redone. Since these were not desirable alternatives, both cost and schedule wise, a design was developed to retrofit the SMA in place using an externally mounted cryogenically cooled linear motor assembly. This linear motor actuates the mirror along the edge of the horizontal axis creating a moment arm rather than acting directly on the azimuth axis of rotation.

The motor is designed to meet all the existing SMA performance parameters and will use the existing servo control system. Presently, this modification is in the process of final installation.

SUMMARY & FUTURE OBJECTIVES

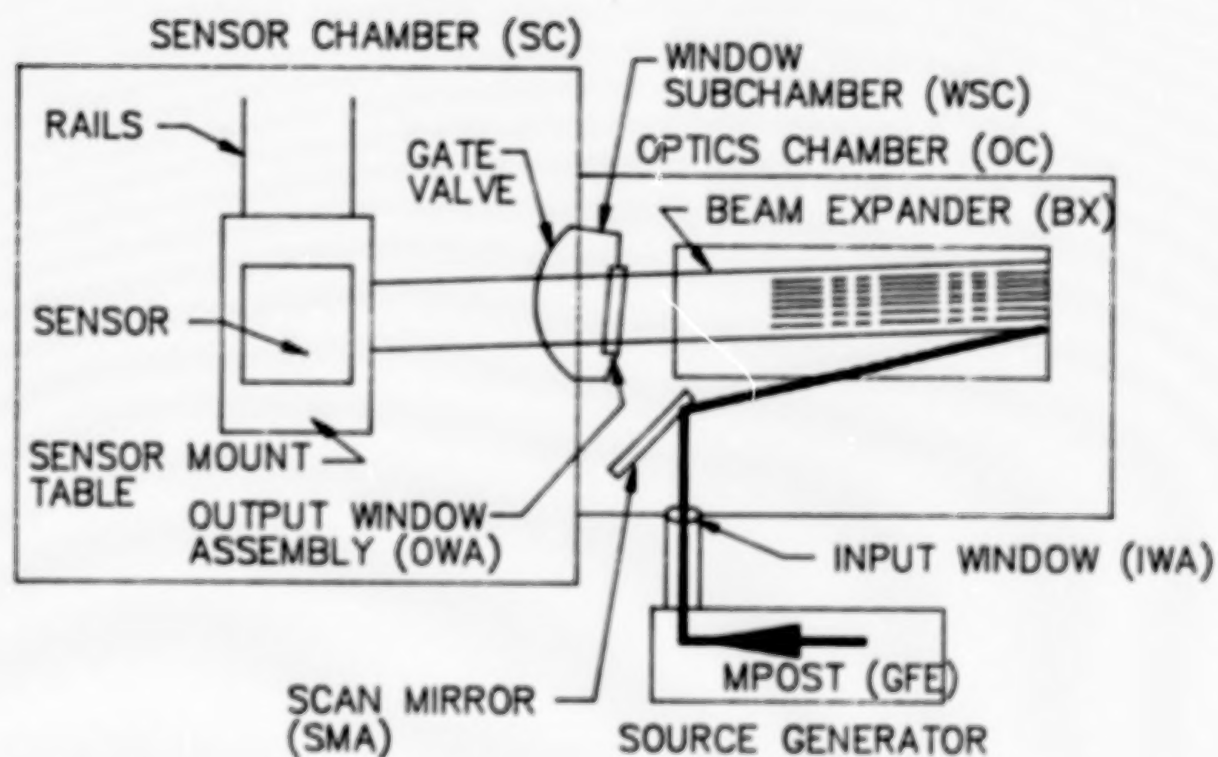
This paper has presented a summary of the key features and configuration of the BIRS system. Insight has been provided on several interesting problems that were encountered and their solutions. As is the case in most facilities of this type, new challenges arise as each test progresses.

SUMMARY & FUTURE OBJECTIVES (Continued)

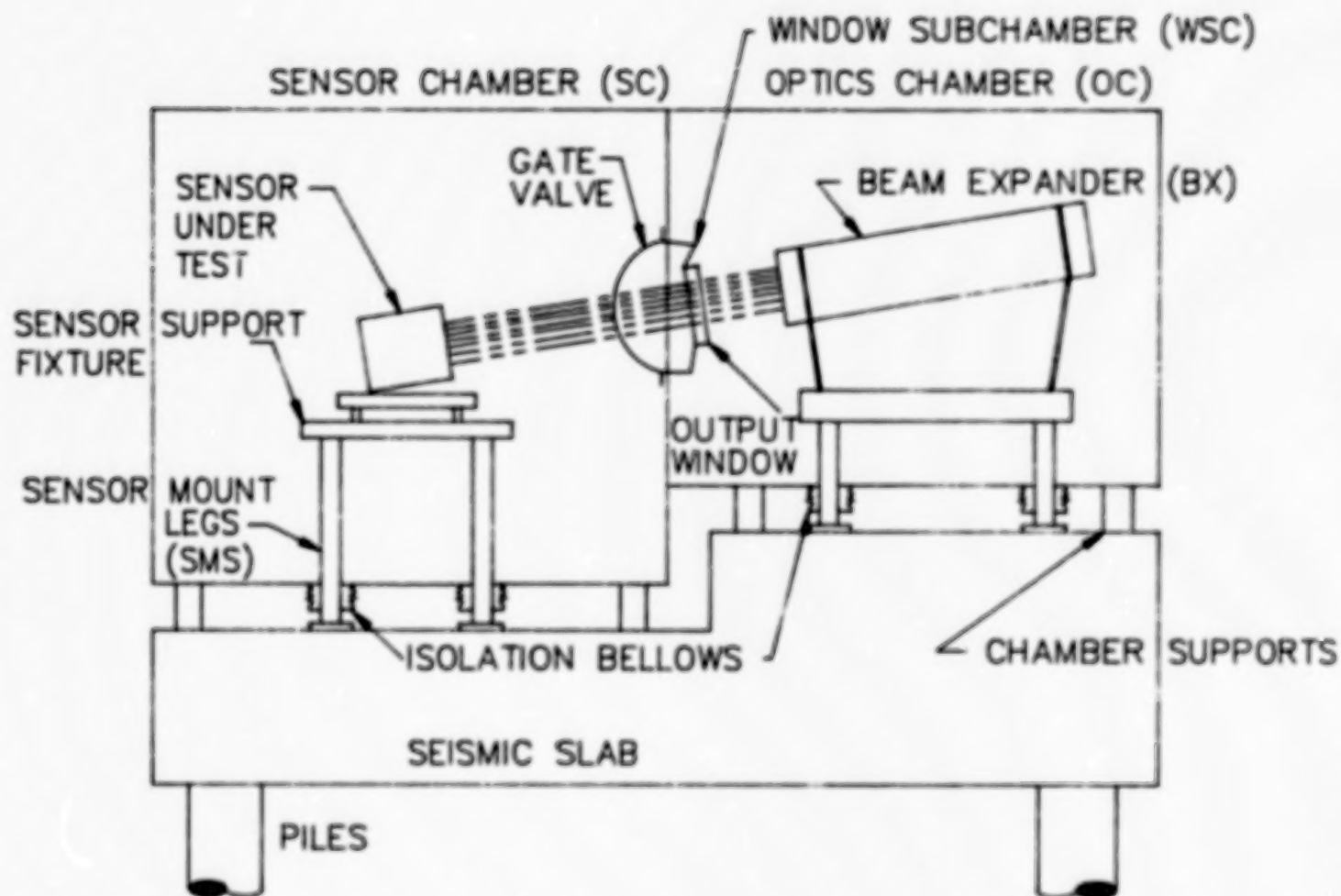
While the present configuration of the facility is geared toward a specific testing requirement, the BIRS facility was designed to accommodate growth and adaptation to other capabilities. While it is not possible to build a facility capable of meeting all test requirements for projects in the future, it was possible to provide a sound baseline facility which can be used as a starting point for future test programs. Initial planning has been performed to support growth in the following areas:

- Add capability to calibrate exoatmospheric sensors
- Add capability to test and calibrate space optical systems
- Develop hardware-in-the-loop capability

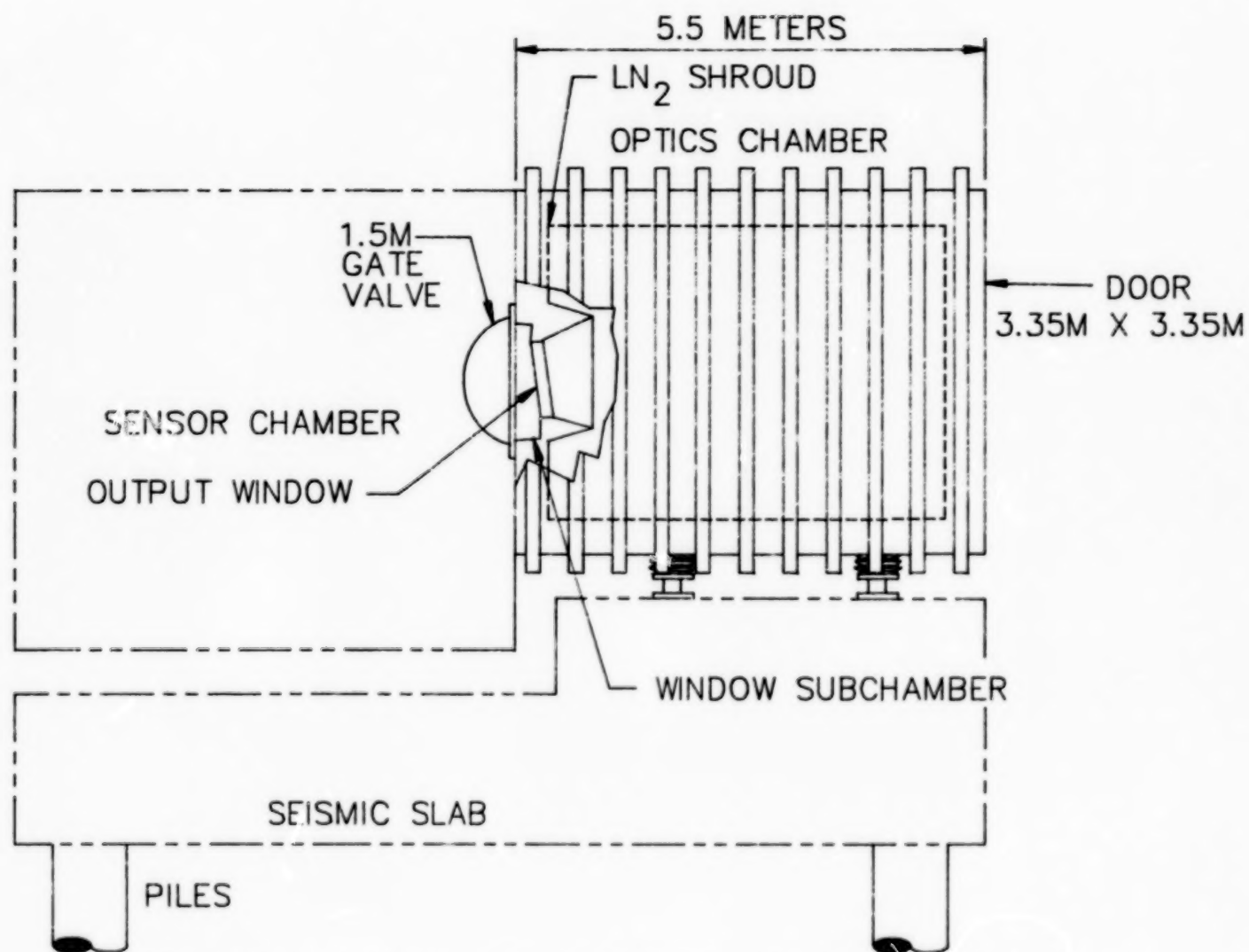
The facility represents a significant capability for infrared testing and calibration and will be available to all members of the U.S. infrared community. It is anticipated that this will include both support to government programs and other aerospace companies.



SCHEMATIC PLAN VIEW OF BIRS FACILITY
FIGURE 1



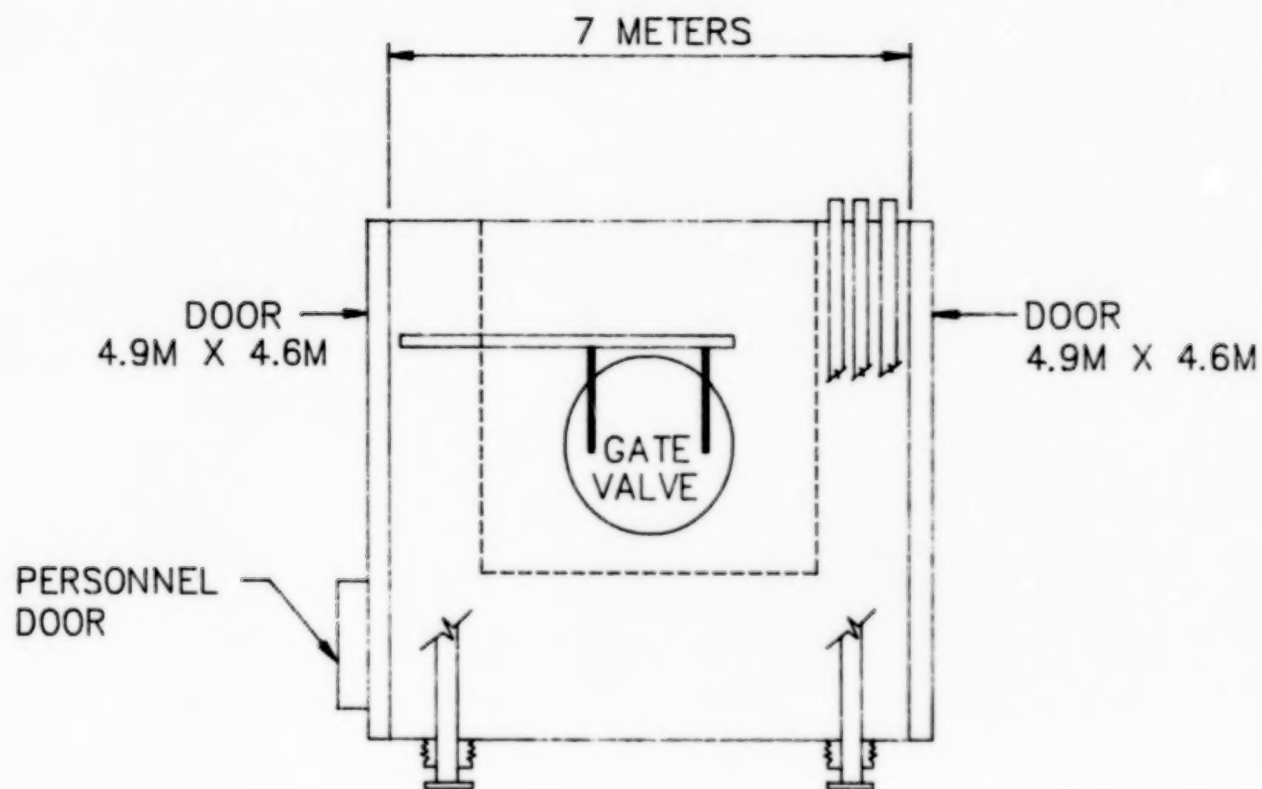
SCHEMATIC ELEVATION VIEW OF BIRS FACILITY
FIGURE 2



ELEVATION VIEW OF OPTICS CHAMBER

FIGURE 3

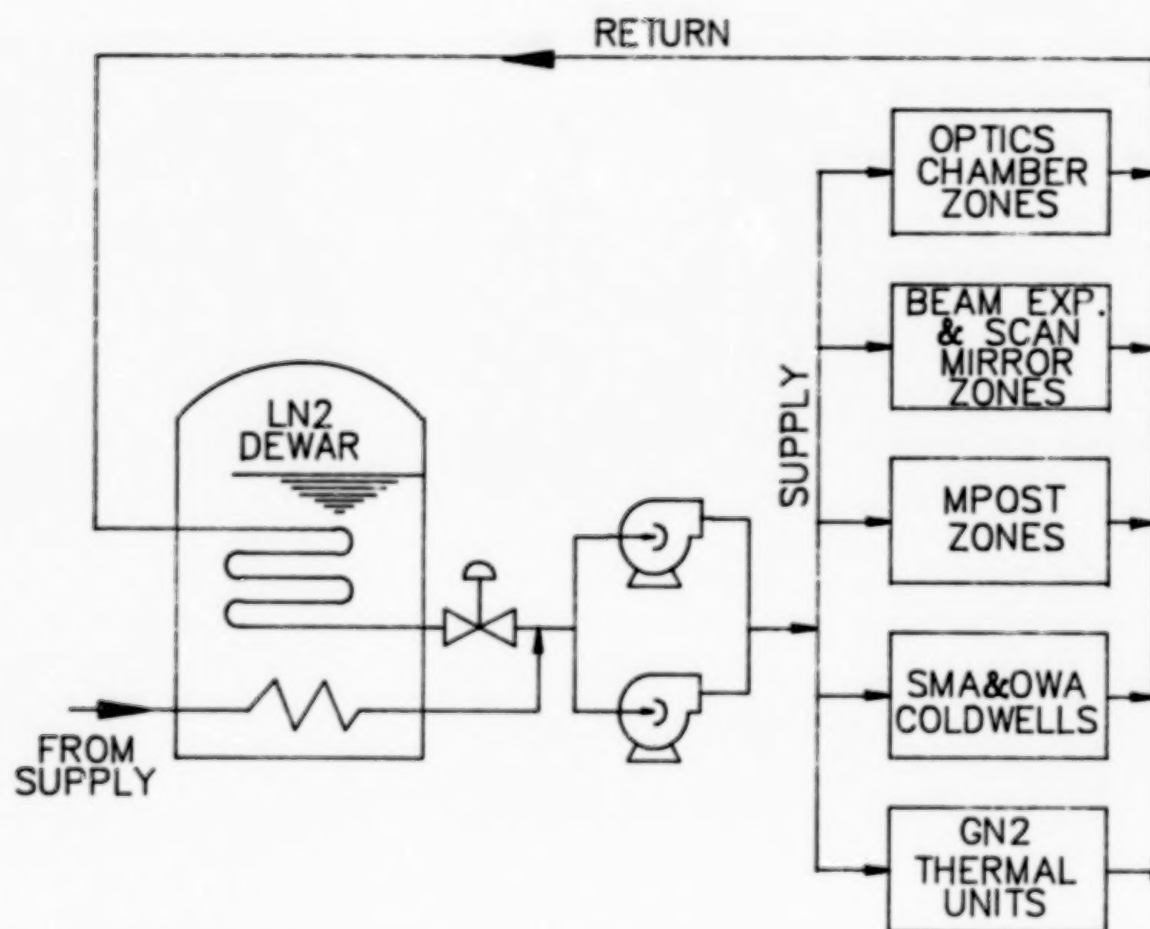
(4)



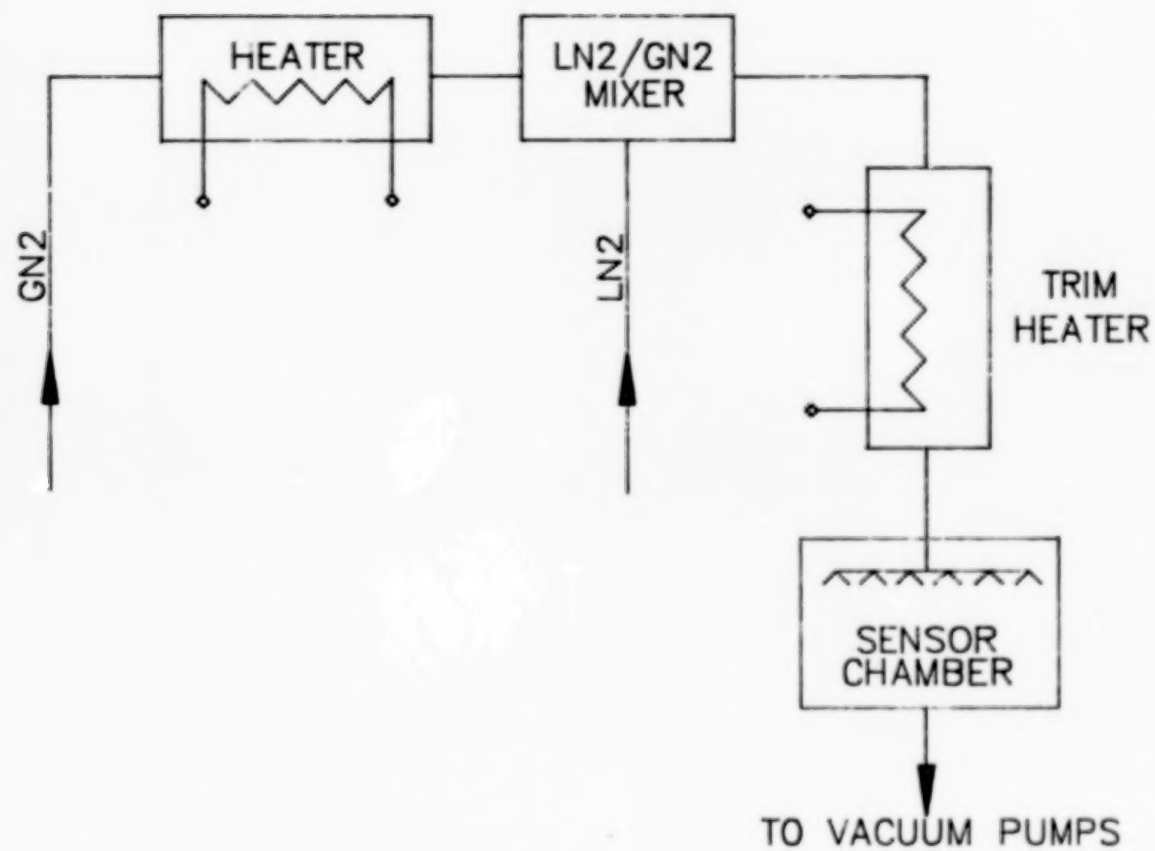
ELEVATION VIEW OF SENSOR CHAMBER
LOOKING TOWARDS OPTICS CHAMBER

FIGURE 4

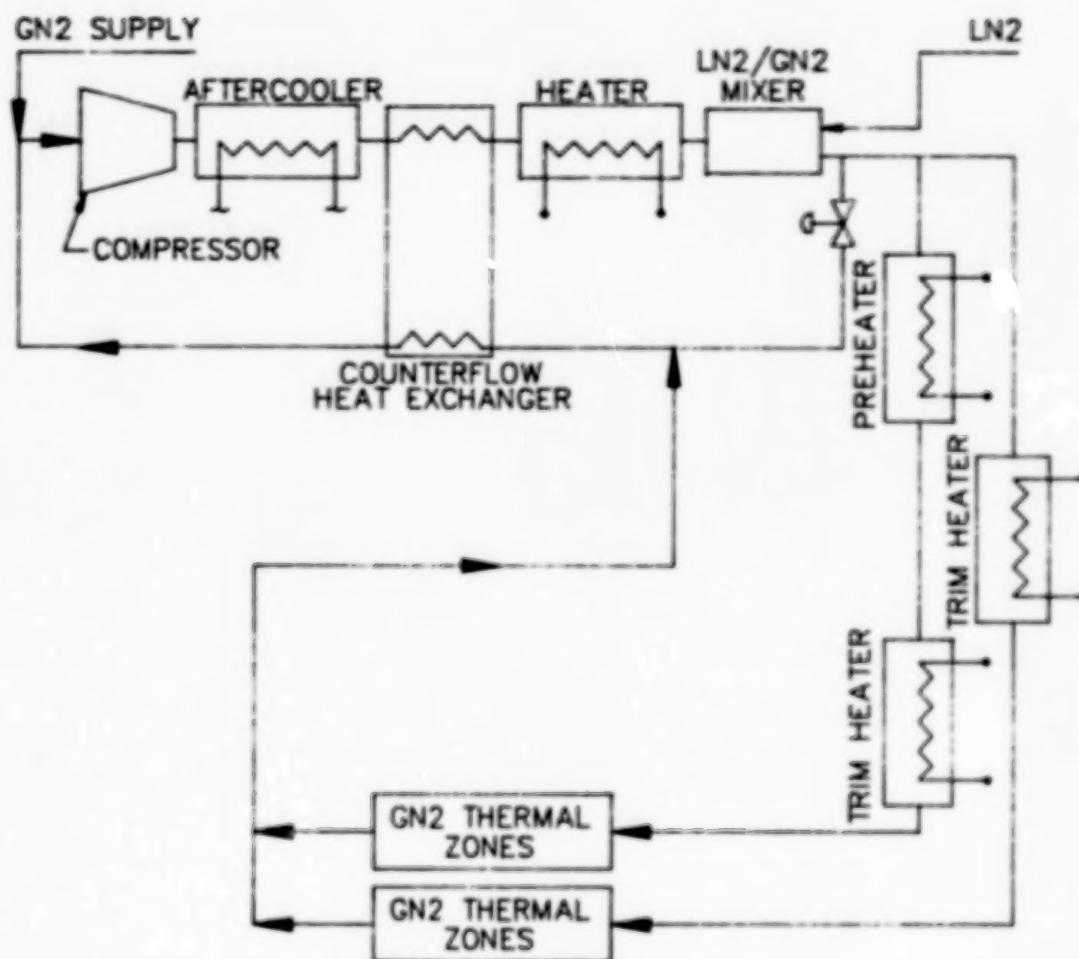
145



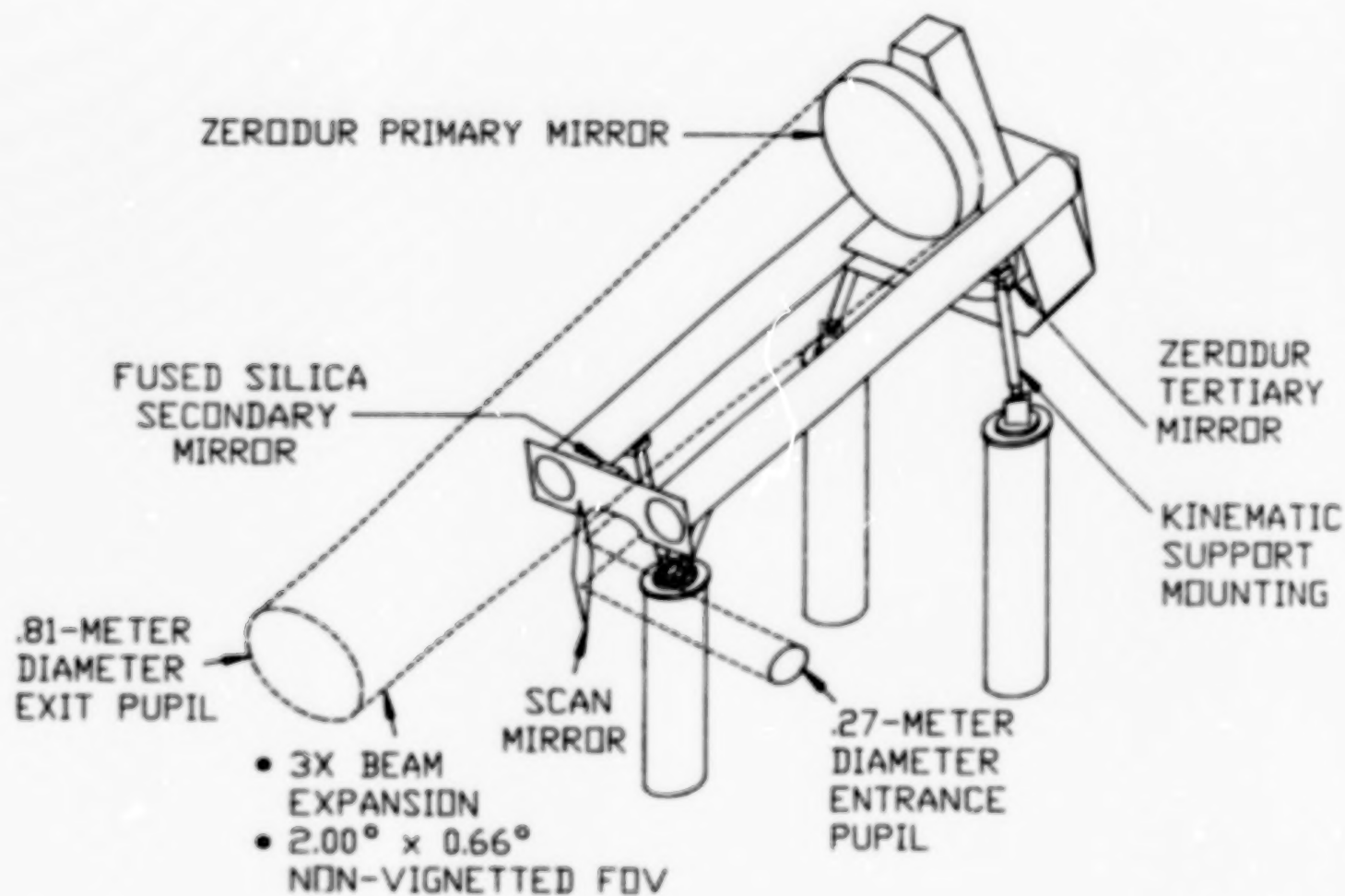
LIQUID NITROGEN THERMAL SYSTEM
FIGURE 5



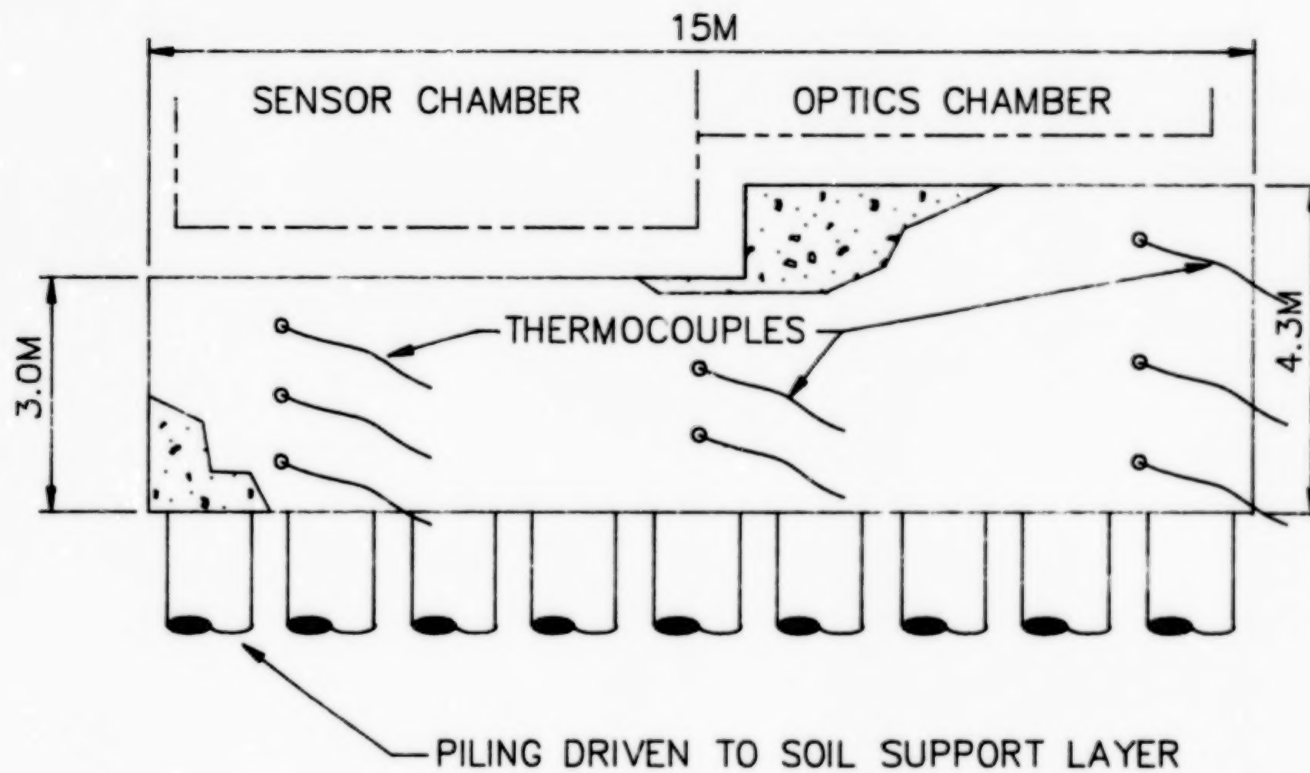
SENSOR CHAMBER GN2 THERMAL UNIT
FIGURE 6



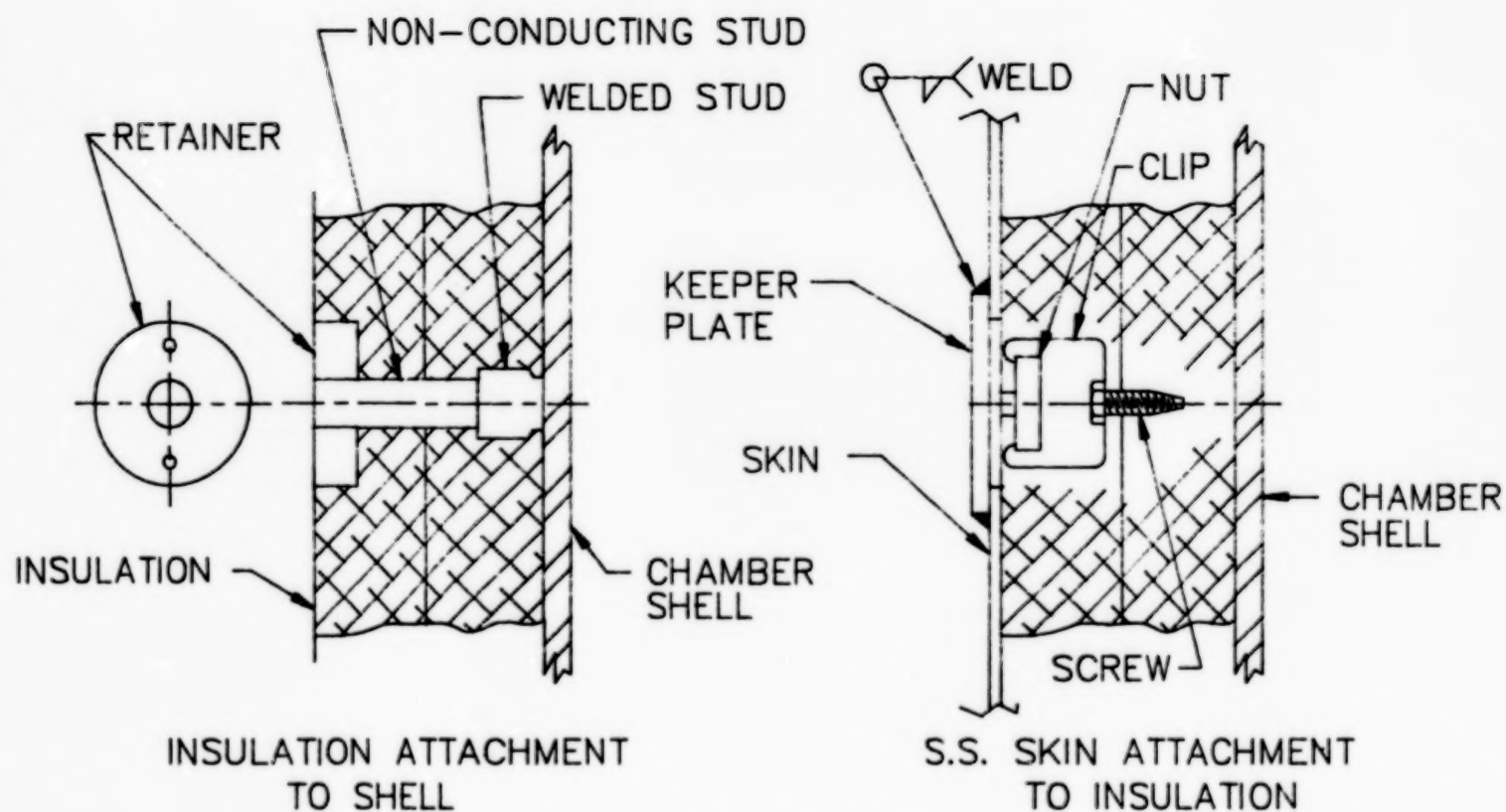
RECIRCULATING GN2 THERMAL UNIT
FIGURE 7



BIRS BEAM EXPANDER
FIGURE 8

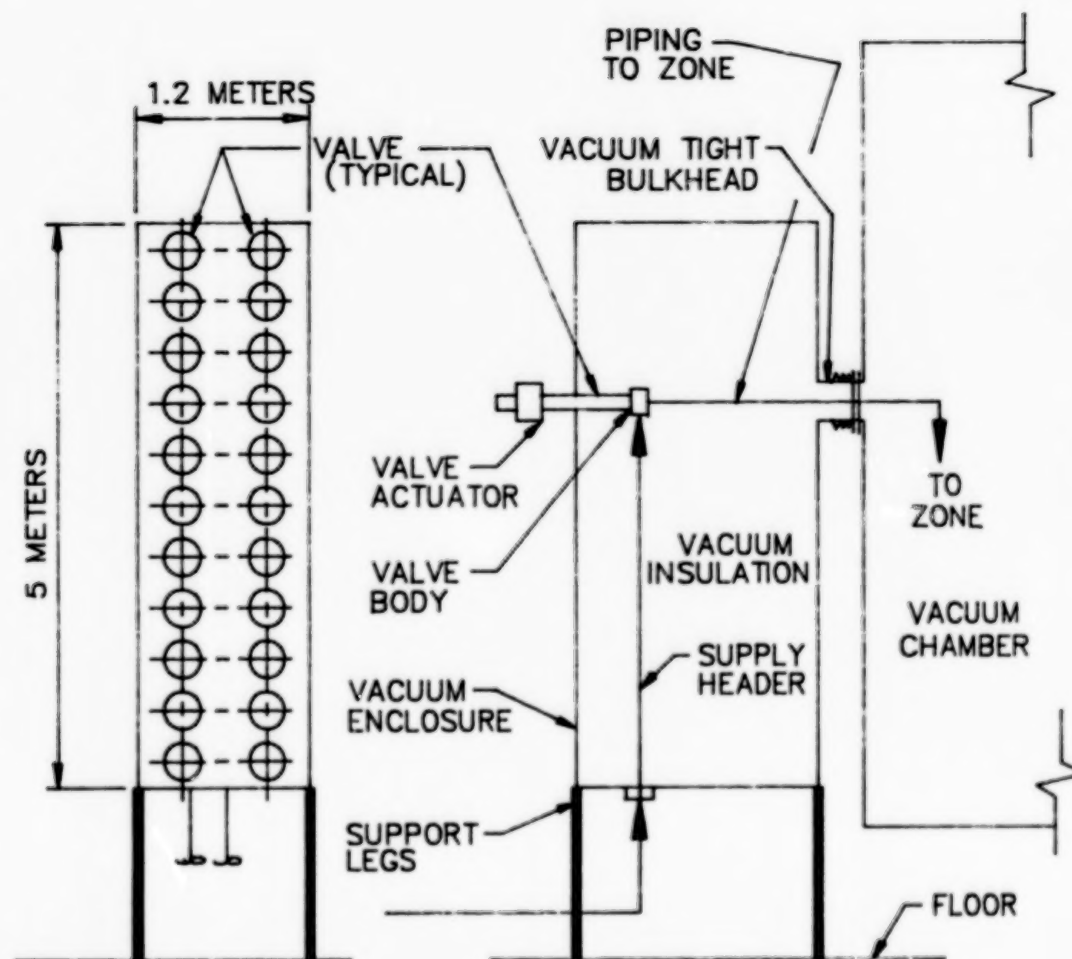


1815 TONNE SEISMIC SLAB
FIGURE 9



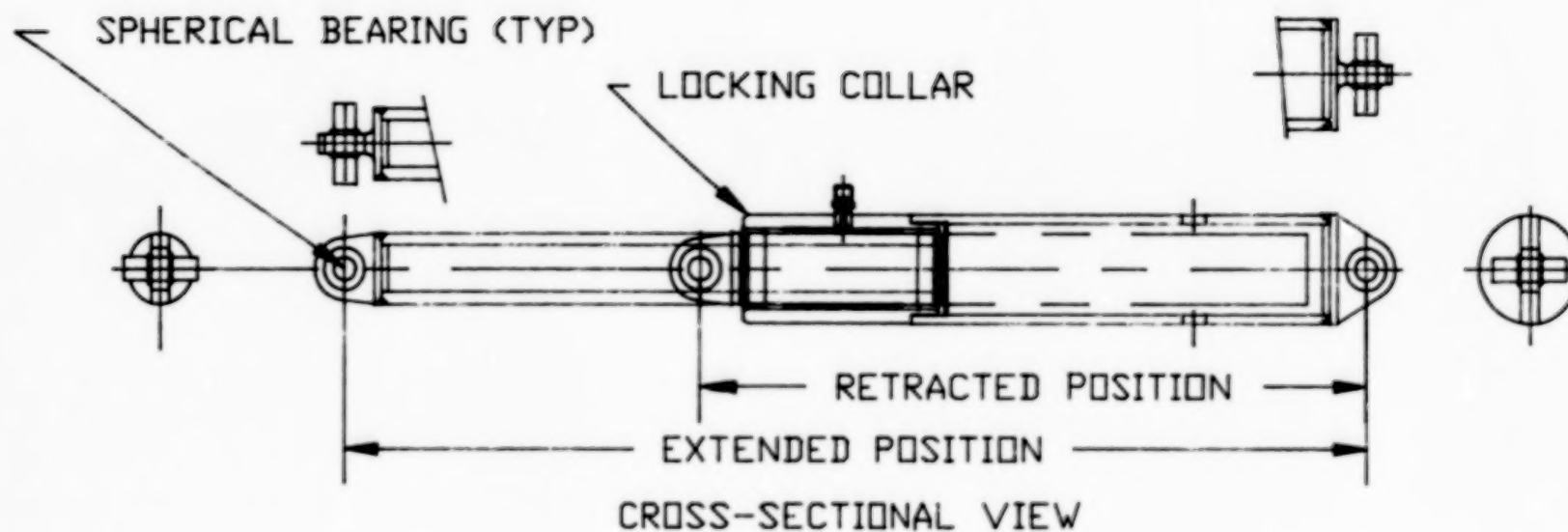
SENSOR CHAMBER INSULATION
FIGURE 10

153



VALVE BOX SCHEMATIC
FIGURE 11

155-



SENSOR MOUNT SUBSYSTEM LOCKING STRUT
FIGURE 12

INFRARED SENSOR TEST METHODOLOGY AND FACILITIES*

Jere J. Matty
AF/DOTF

and

Ronald Dawbarn
Calspan Corporation, AEDC Operations
Arnold Engineering Development Center
Arnold Air Force Base, Tennessee 37389

ABSTRACT

As the Air Force Systems Command-designated Center of Expertise for Space Simulation Testing, AEDC has defined a test methodology for the ground testing of infrared sensor systems. This test methodology and the test facilities envisioned to implement it were the topic of a paper entitled "Surveillance Systems Test and Evaluation Facilities", by Mr Ronald Dawbarn and me presented at the 14th Space Simulation Conference in 1986. This paper is a progress report on the implementation of that test methodology and describes the status of the test facilities presently existing or under construction to implement it.

INTRODUCTION

In May of 1984 the Air Force Systems Command designated AEDC as the Center of Expertise for space environment and simulation testing. In this capacity, the Center is to provide test and evaluation expertise in several assigned functional areas, including space sensors. AEDC has extensive experience in the test and evaluation of space systems and infrared (IR) sensors in particular. Figure 1 presents a summary of the testing record in the area of infrared sensor systems. The period from 1982 to 1983 was spent in a major modification of the primary test chamber, 7V. The test and evaluation of such systems is particularly challenging when one considers that they must be able to operate in hostile natural and man-made environments against extremely large numbers of targets (see Fig. 2).

Performance Testing Levels

Obviously, the duplication of the entire sensor environment in a ground test facility is impractical and unnecessary. AEDC has undertaken the task of defining a test methodology for IR space sensors as a way to break their evaluation into reasonable segments. Through studies conducted by AEDC support contractors and contractors outside of AEDC, a common set of sensor test issues were identified (see Fig. 3). These issues can be addressed through a family of ground test facilities as indicated in Fig. 4. Of particular interest on this chart is the Focal Plane Array Test Chamber (FPATC) and the Large Sensor Test Chamber (LSTC) testing levels, which together address approximately 85 percent of the common sensor issues. The development and status of these various

*The research reported herein was performed by the Arnold Engineering Development Center (AEDC), Air Force Systems Command. Work and analysis for this research were done by personnel of the Air Force and personnel of Calspan Corporation/AEDC Operations, operating contractor for the AEDC flight dynamics facilities. Further reproduction is authorized to satisfy needs of the U. S. Government.

This paper is cleared for public release.

test facilities at AEDC will be the focus of this present work and are depicted in simplified fashion in Fig. 5.

Focal Plane Array (FPA) Level Testing

The goal of testing at this level is the functional validation and characterization of the FPA with point and extended sources. The FPA is the common element in all IR sensor systems, whether a surveillance sensor or a seeker, starrer or a scanner. The AEDC Component Checkout Chamber was modified in 1988 to conduct testing at this level and renamed the Focal Plane Characterization Chamber (FPCC). This is a multipurpose chamber with point and extended blackbody sources traceable to National Institute for Science and Technology (NIST) standards. In addition, the chamber is equipped with spectral calibration capability. The FPA chips are mounted in individual test dewars which permit immediate check-out of wiring connections and provides chip cool-down to operating temperatures. These dewars are quickly interchanged on the test chamber, permitting high volume testing. Real-time graphical data display capability is also provided with this facility (see Fig. 6). The facility is capable of producing 75-m spot sizes and target temperatures from 77 to 1,000°K. The basic capabilities of the facility are outlined in Fig. 7, and Fig. 8 summarizes the FPA performance parameters available. A wide range of data presentation formats are possible, as depicted in Fig. 9. In summary, the AEDC FPCC is a state-of-the-art IR test capability designed to support high-throughput FPA characterization testing. Test capabilities include radiometric flood, spot, and spectral response. Future capability enhancements include module testing and radiation testing.

FPA/Signal/Data Processor Level Testing

The goal of testing at this level is to provide mission scenarios to the sensor focal plane/signal/data processors. The scenes can involve many dynamic objects moving against complex backgrounds (see Fig. 10). The concept chosen for the prototype AEDC FPATC employs a laser-based, direct write scene generator. Testing at this level is economical from a facility standpoint as the sensor telescope is not involved; therefore, the large optics normally required to fill the entrance aperture are unnecessary. This facility was identified as meeting approximately 65 percent of the sensor ground test issues depicted in Fig. 4 and is presently under construction at AEDC. The facility makes use of IR lasers and beam steering devices to "paint" a scene over the sensor's FPA. An early concept for the facility is depicted in Fig. 11. This facility is scheduled to begin operation in FY93.

FPA/Signal/Data Processor/Telescope Level Testing

Testing at this level involves both off-axis rejection (OAR) and integrated sensor functionality testing, i.e., radiometric and goniometric calibration.

OAR testing can be accomplished in a chamber or optics laboratory designed for this purpose. This type of testing is usually accomplished with a surrogate focal plane for the detector and a high-powered CO₂ laser as the source. The AEDC Mark I is ideal for this type of testing because of its size, and it has been used in the past for this purpose.

Integrated sensor functionality testing at this level requires the sensor entrance aperture to be filled. The entrance aperture will size the facility optics which, in turn, size the entire facility along with the choice of scene generation technology. Two facilities are under development at AEDC to meet IR sensor testing needs at this level: the LWIR Environmental Threat Simulator (LETS) and the Large Sensor Test Chamber (LSTC).

The LETS facility is an extensive modification to the existing AEDC 7V facility. The facility is designed to conduct calibration and mission scenario testing of exo-atmospheric IR seekers in the 15-cm entrance aperture diameter range. Real time environment and target simulation is planned for this very versatile facility to reduce the risk and the number of flight tests which might be needed in a development program (see Fig. 12). Figure 13 depicts the LETS layout and the high-level capability planned for the facility. Significant progress has been made on this facility, as shown in Fig. 14. Initial operation is scheduled for FY92.

The LSTC facility will be designed to conduct calibration and mission scenario testing of space surveillance sensors. LSTC will be somewhat similar to the LETS facility, but will be sized for sensors with entrance apertures roughly twice as large. Requirements for the facility have been well documented by the Strategic Defense Initiative Organization (SDIO), the Army's Strategic Defense Command (SDC), and the Air Force's Space Systems Division (SSD). The concept definition contract will be conducted in FY90, with one of the options being a modification to the existing AEDC 10V facility depicted in Fig. 15. Because of the wider wavelength requirement for the LSTC, the scene generation technology will be somewhat different from that employed in the LETS facility, but will be able to provide the complexity required for scenario testing at the sensor level. The facility is scheduled to begin operation in late FY93.

Survivability Testing Level

Figure 4 also mentions survivability testing being conducted in the Radiation Effects Test Facility (RETF). Several studies have been conducted on test facilities at this level. The result of this work is a facility named DECADE to be constructed by the Defense Nuclear Agency at AEDC. An early concept for this facility, is shown in Fig. 16. This facility will provide the ability to test relatively large segments (1 m²) of space system electronics in a simulated nuclear environment to ensure system hardness in operational scenarios. The facility is scheduled to begin operation in FY95.

CONCLUSIONS

AEDC, as the AFSC designated center of expertise for space system testing, has developed a test methodology for sensor systems and planned the associated facilities. This paper has presented a broad overview of the status of that effort. Many of the sensor systems currently in development are adopting this method of ground testing to minimize their risks as they move into the flight test portion of their program.

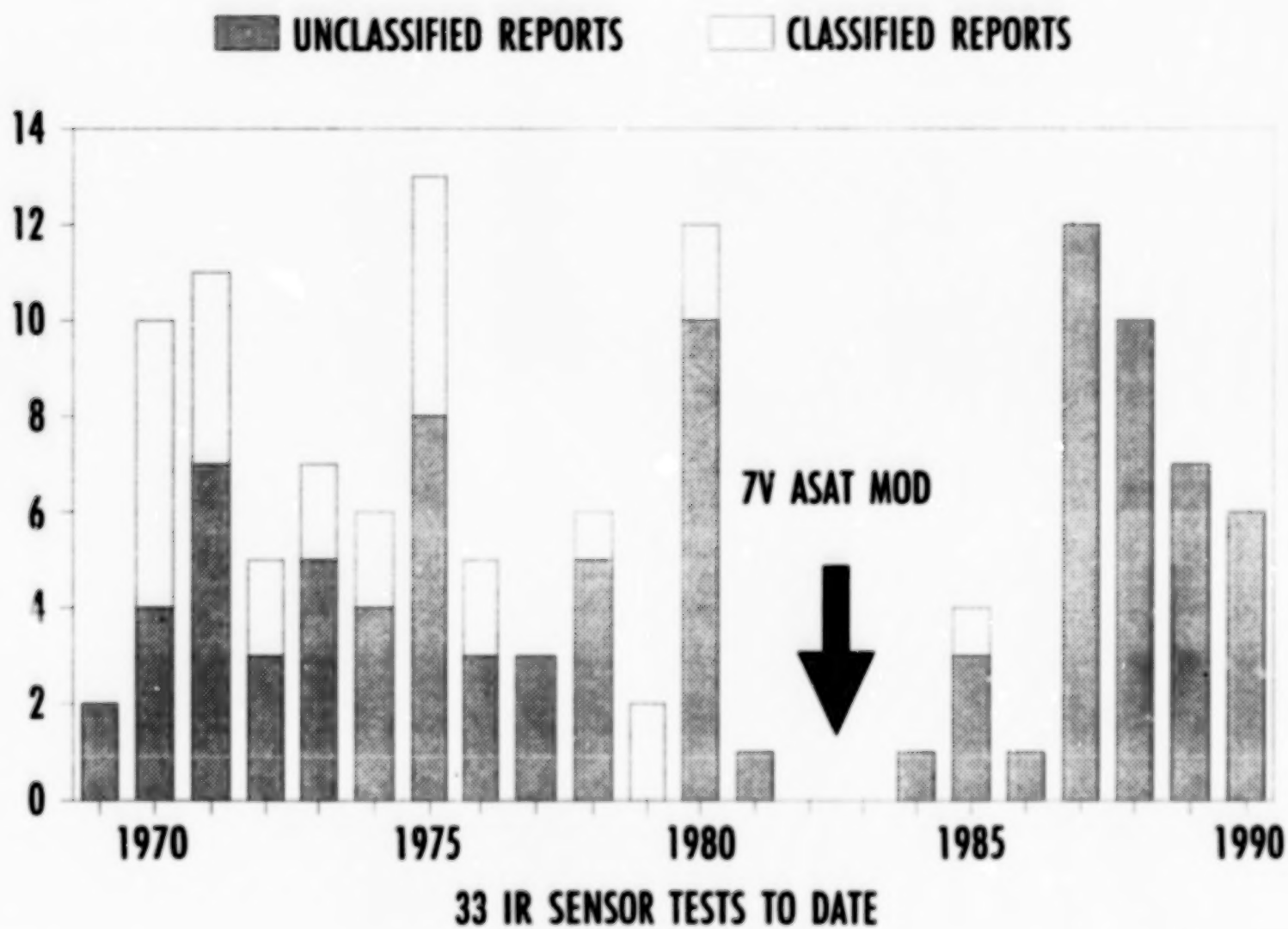


Fig. 1. AEDC infrared experience.

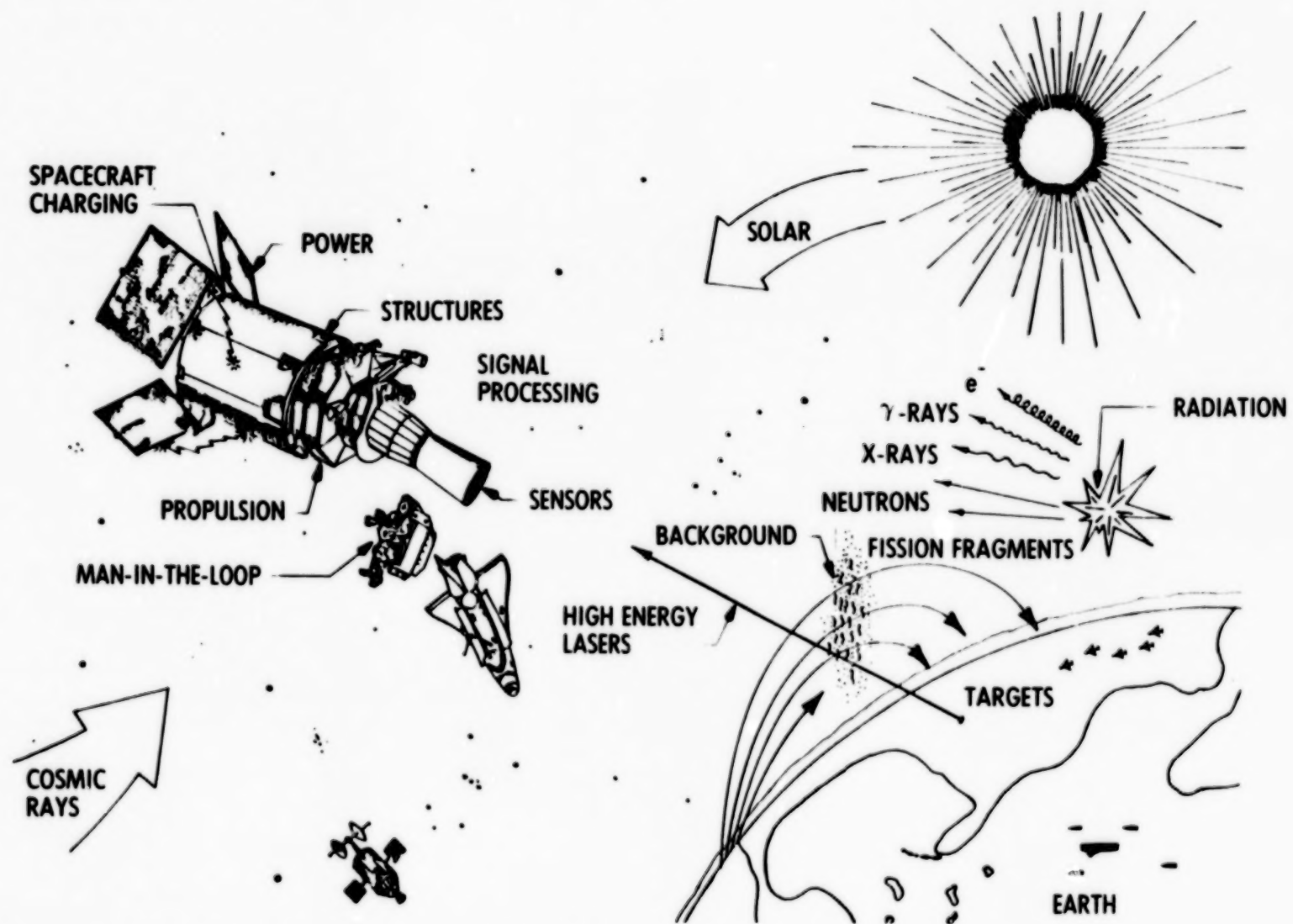


Fig. 2. Surveillance sensor operational environment.

SENSOR ISSUE	SSTS	BSTS	GSTS	BP/SBI	ERIS
PRODUCIBILITY	X	X	X		
SENSITIVITY/RANGE PERFORMANCE	X	X	X	X	X
CSO RESOLUTION	X	\	X		X
ANGULAR MEASUREMENT PRECISION	X	X	X	X	X
RADIOMETRIC MEASUREMENT PRECISION	X		X		\
STRUCTURED BACKGROUND REJECTION	X	X	X	X	X
CLUSTER PROCESSING	X		X		
EXTENDED TARGET TRACKING		\		X	X
THROUGHPUT	X	X	X		
PERFORMANCE IN NUCLEAR ENVIRONMENT	X	X	X	X	X
CONTAMINATION*	X	X	X	X	X

* ISSUE NOT NOTALLY RESOLVED BY THESE FACILITIES

Fig. 3. Sensor issue/sensor system correlation matrix.

SENSOR ISSUE	OPTICAL TEST FACILITY	COMPONENT CHECKOUT CHAMBER	FOCAL PLANE ARRAY TEST CHAMBER	RADIATION EFFECTS TEST FACILITY	LARGE SENSOR TEST CHAMBER	TOTAL ISSUE RESOLUTION
PRODUCIBILITY	30	17	37		16	100
SENSITIVITY/RANGE PERFORMANCE	18	18	57		7	100
CSO RESOLUTION	4		77	2	17	100
ANGULAR MEASUREMENT PRECISION	3	10	68	1	18	100
RADIOMETRIC MEASUREMENT PRECISION	1	9	68	2	20	100
STRUCTURED BACKGROUND REJECTION	1		84	1	14	100
CLUSTER PROCESSING	1		85	1	13	100
EXTENDED TARGET TRACKING	1	5	74		20	100
THROUGHPUT			93**		7	100
PERFORMANCE IN NUCLEAR ENVIRONMENT			57	32	11	100
CONTAMINATION*	24	2	23		51	100
TOTAL	83(7)	61(5)	723(65)	39(4)	194(19)	1100(100)

* ISSUE NOT TOTALLY RESOLVED BY THESE FACILITIES

** USES EMULATOR AND ANALOG SIMULATIONS

XX(YY)

XX IS THE PERCENTAGE OF THIS TEST ISSUE WHICH HAS BEEN RESOLVED BY THIS TEST

YY IS THE PERCENTAGE OF TOTAL

Fig. 4. Sensor issue/test facility correlation matrix.

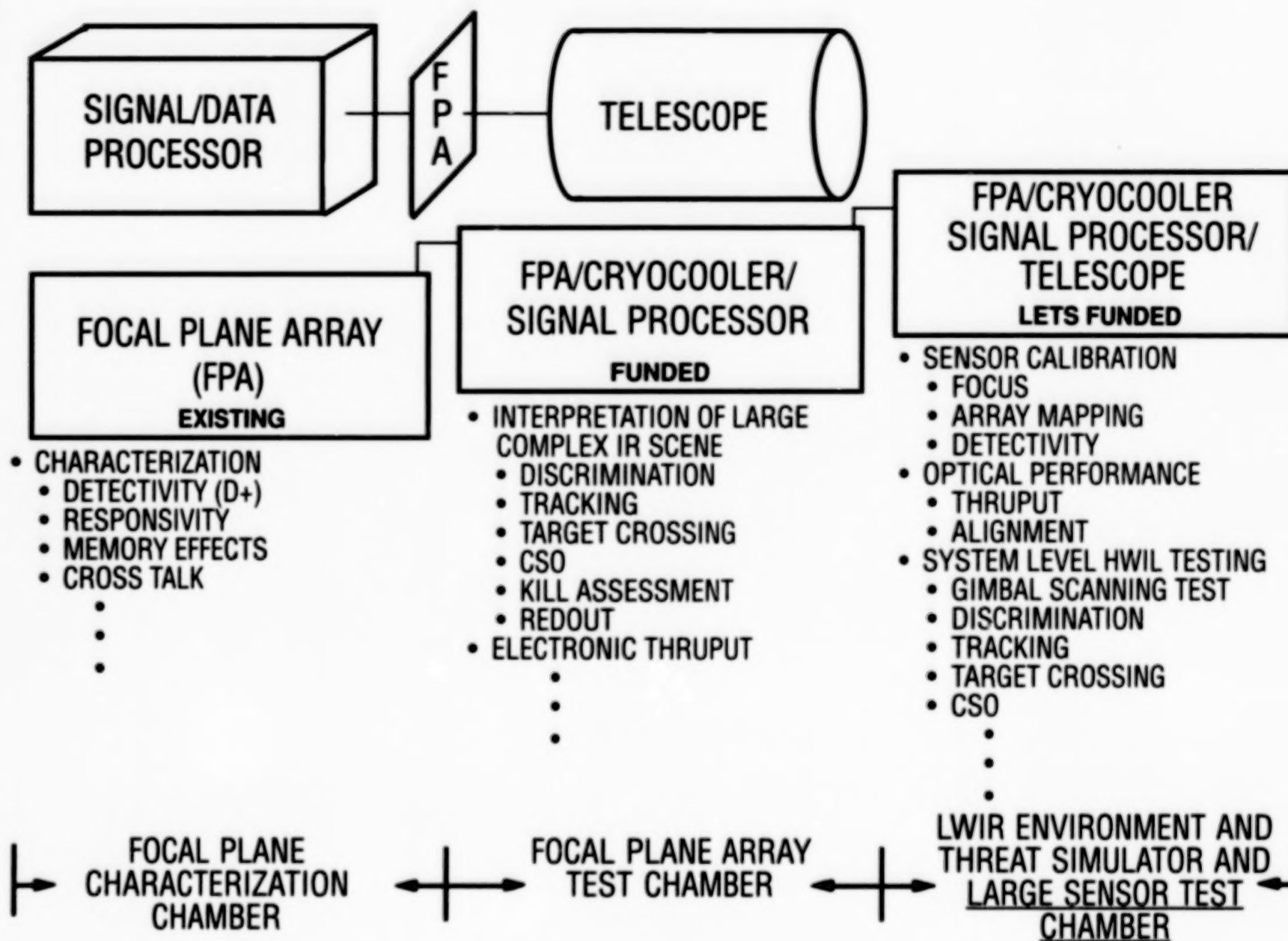


Fig. 5. IR sensor performance testing levels.



- RADIOMETRIC CHARACTERIZATIONS
- MULTIPURPOSE TEST CHAMBER
- WIDE RANGE OF TEST PARAMETERS
- HIGH-SPEED DATA ACQUISITION AND CONTROL SYSTEM
- REAL TIME GRAPHICAL DATA DISPLAYS

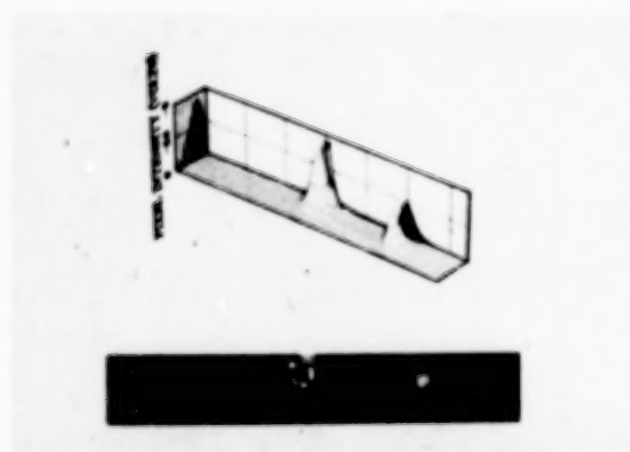
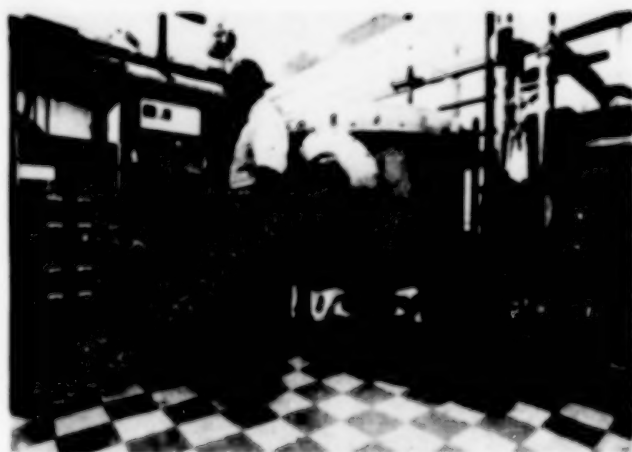
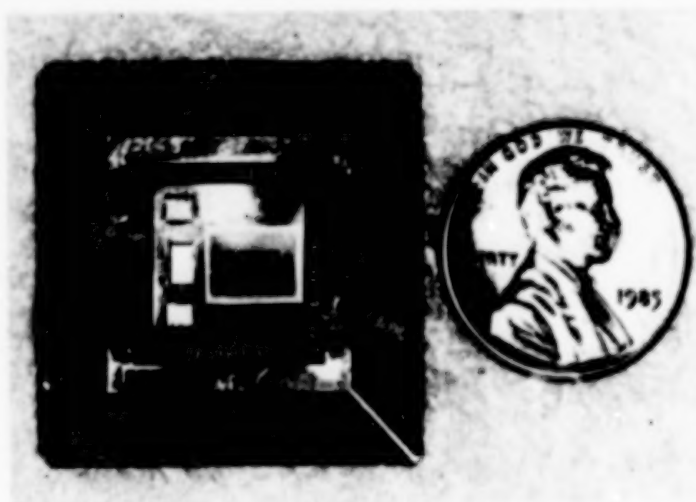
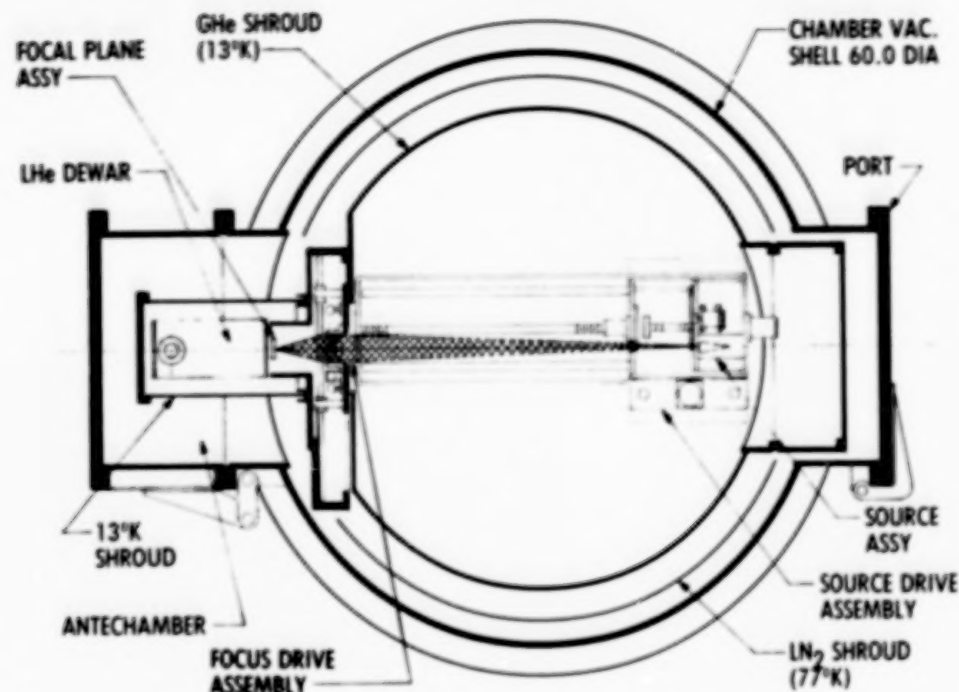


Fig. 6. Focal plane characterization testing.

REQUIREMENT

- SDI SUPPORT
- RADIOMETRIC FPA TESTING
- VERIFICATION/CHARACTERIZATION
- EVALUATE TECHNOLOGY ADVANCES
- SELECT FLIGHT COMPONENTS



CAPABILITIES

- TEMPERATURE RANGE 2 TO 300°K (-465 TO 80°F)
- BACKGROUND 10^7 TO 10^{13} PHOTONS/SEC·CM²·SR
- NOISE LEVEL < 100 NE ELECTRONS
- SPOT SIZE 75μm (3 MILS)
- TARGET TEMPERATURES 77 TO 1000°K (-321 TO 1341°F)

Fig. 7. Focal plane array (FPA) support.

SPECTRAL BAND(S)
MAX OPERATING TEMPERATURE
OPERABLE TEMPERATURE RANGE
OPERABLE LIFE
BACKGROUND IRRADIANCE
INTEGRATION TIME
ARRAY CONFIGURATION
PIXEL SIZE, CENTER-TO-CENTER
PIXEL SHAPE
PIXEL SPACING
NOISE EQUIVALENT INPUT

DYNAMIC RANGE
LINEARITY
RESPONSE UNIFORMITY
RADIOMETRIC STABILITY
CROSSTALK
RECOVERY TIME
POWER CONSUMPTION
DEGRADED CHANNELS
D*
QUANTUM EFFICIENCY

Fig. 8. FPA performance parameters menu.

- TABULAR DATA
 - ENGINEERING UNITS
 - STANDARD DEVIATIONS
- 2/3-DIM GRAPHICS
- TREND PLOTS
- HISTOGRAMS
- MAGNETIC DISKS/TAPE
- AEDC TEST SUMMARY REPORTS

FLOOD SOURCE									
Run Number: 120 (Tare: 110)					Temperature: 10.10 Deg Kelvin				
Focal Plane ID: XXX-XXX #XXX					Bias: -0.500 Volts				
Array Dimensions: 10 x 40					Gain: 10.0				
Signal Power Flux: 0.455E-07 W/cm ²					Integration Time: 1.000 msec				
Signal Average: -0.128E+01 Volts					Capacitance: 0.204 pF				
No. Pixels in Avg: 1774					Current: -0.262E-10 Amps				
Signal STD Deviation: 0.528E-01 Volts					Responsivity: -0.576E+01 Amp Watt				
ROW	2	4	6	8	10	1 2 SD	Volts	#	
1	-2	-1	-1	0	-1	-2	-1	0	
2	-1	0	0	0	1	-1	-1	0	
3	1	-3	-1	-1	0	0	2	0	0
4	-1	-1	-1	-1	0	0	0	0	0
5	-1	-1	-1	-1	0	0	0	0	1
6	-1	-1	-1	-1	0	0	0	1	0
7	-1	-1	-1	-1	0	0	1	0	0
8	-2	-1	-1	-1	-1	2	-1	0	
9	-1	-1	-1	-2	-1	-1	-1	0	
10	-2	-2	-2	-2	-1	-1	-1	-1	
11	-2	-2	-2	-2	-1	-2	-1	-2	
12	-2	-2	-1	-1	-1	-1	-1	-1	
13	-2	3	1	2	-1	-1	-1	-1	0
14	-1	-1	-1	-1	-1	-1	-1	0	
15	-1	-1	-1	-1	-1	0	0	4	0
16	-1	-1	-1	-1	-1	0	0	1	0
17	-1	-1	-1	-1	-1	-1	0	1	0
18	-1	-1	-1	-1	-1	0	1	5	0
19	-2	-1	-1	-1	-1	-1	-1	-1	
20	-2	-1	-1	-2	-1	-1	-1	-1	
21	-2	-1	-1	-1	-1	-1	-1	0	
22	-2	-1	-1	-1	-1	-1	2	-1	
23	-1	-2	-1	-2	-1	-1	-1	-1	
24	-2	-2	-1	-2	-1	-1	-1	-1	
25	-2	-2	-2	-2	-1	-1	-1	-1	
26	-2	-2	-2	-2	-1	-1	-1	-1	
27	-2	-2	-2	-2	-1	-1	-1	-1	
28	-2	-1	-2	-2	-2	-1	-2	-1	
29	-2	-2	-1	-1	-2	-2	-1	-1	
30	-2	-2	-2	-2	-1	-2	-1	-1	
31	-2	-2	-2	-2	-2	-2	-2	-2	
32	-3	-2	-2	-2	-1	-2	-2	-1	
33	0	-2	-2	-2	-1	-2	-2	-2	
34	-2	-2	-1	-2	-2	-2	-1	-2	
35	-2	-2	-1	-3	-2	-2	-2	-2	
36	-2	-2	-2	-2	-2	-2	-2	-2	
37	-2	-2	-2	-2	-2	-2	-2	-2	
38	-2	-2	-1	-2	-2	-2	-2	-2	
39	-2	-2	-1	-2	-2	-2	-1	-2	
40	-1	-1	-2	-1	0	2	-2	1	0

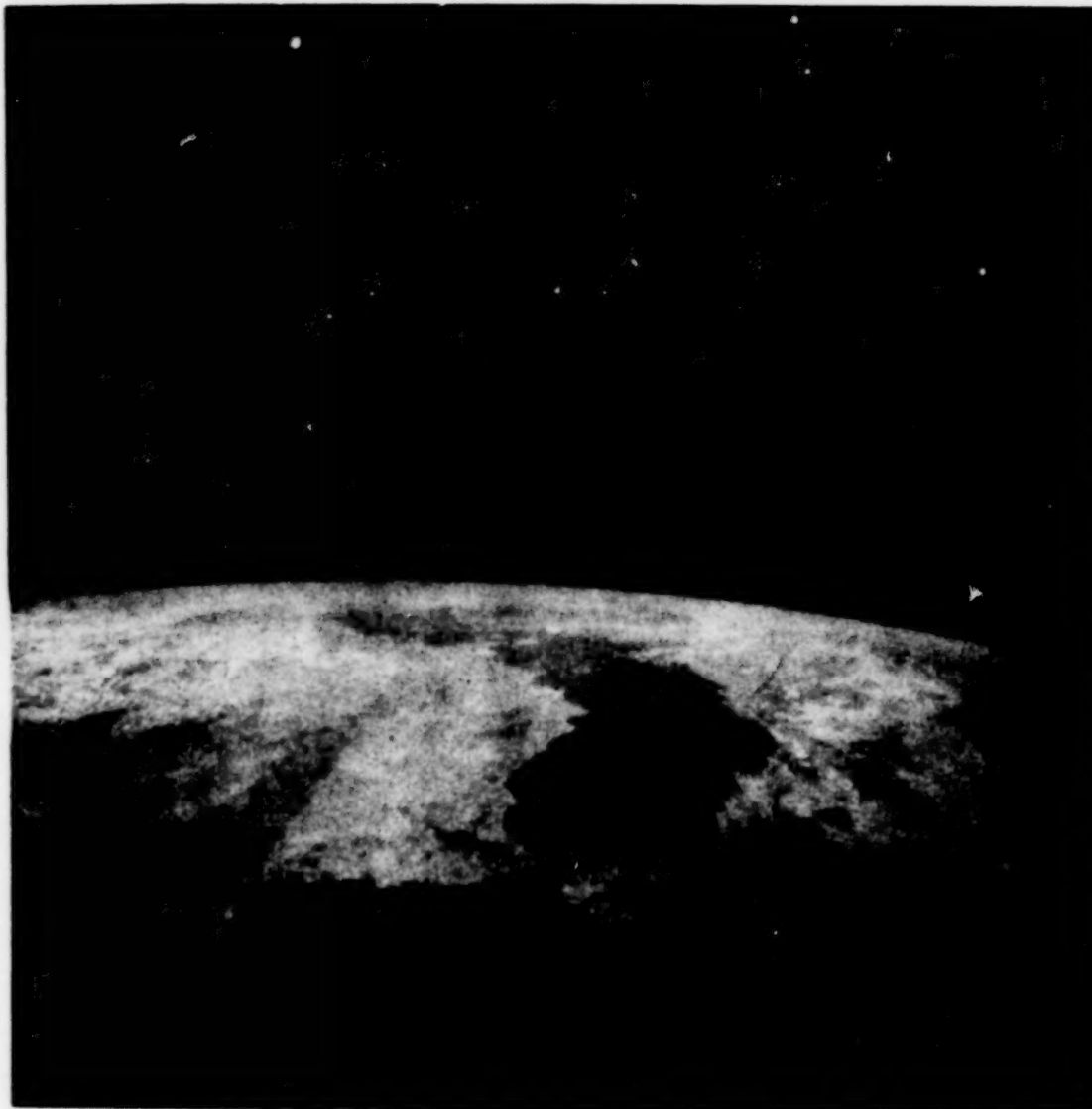
Fig. 9. FPA data presentation formats.

168

TARGETS:
SATELLITES
ASAT

RV
PBV

AIR VEHICLE
SHIPS
CRUISE MISSILE



ABOVE
THE
HORIZON
(ATH)
SCENE

- 10K BACKGROUND
- 10^5 STARS/DEG²
- 500 TARGETS/DEG²

EARTH
LIAB

BELOW
THE
HORIZON
(BTH)

- 270K BACKGROUND
 - CLOUD CLUTTER
 - SOLAR GLINT
-

Fig. 10. Illustration of ATH/BTH scene from space platform.

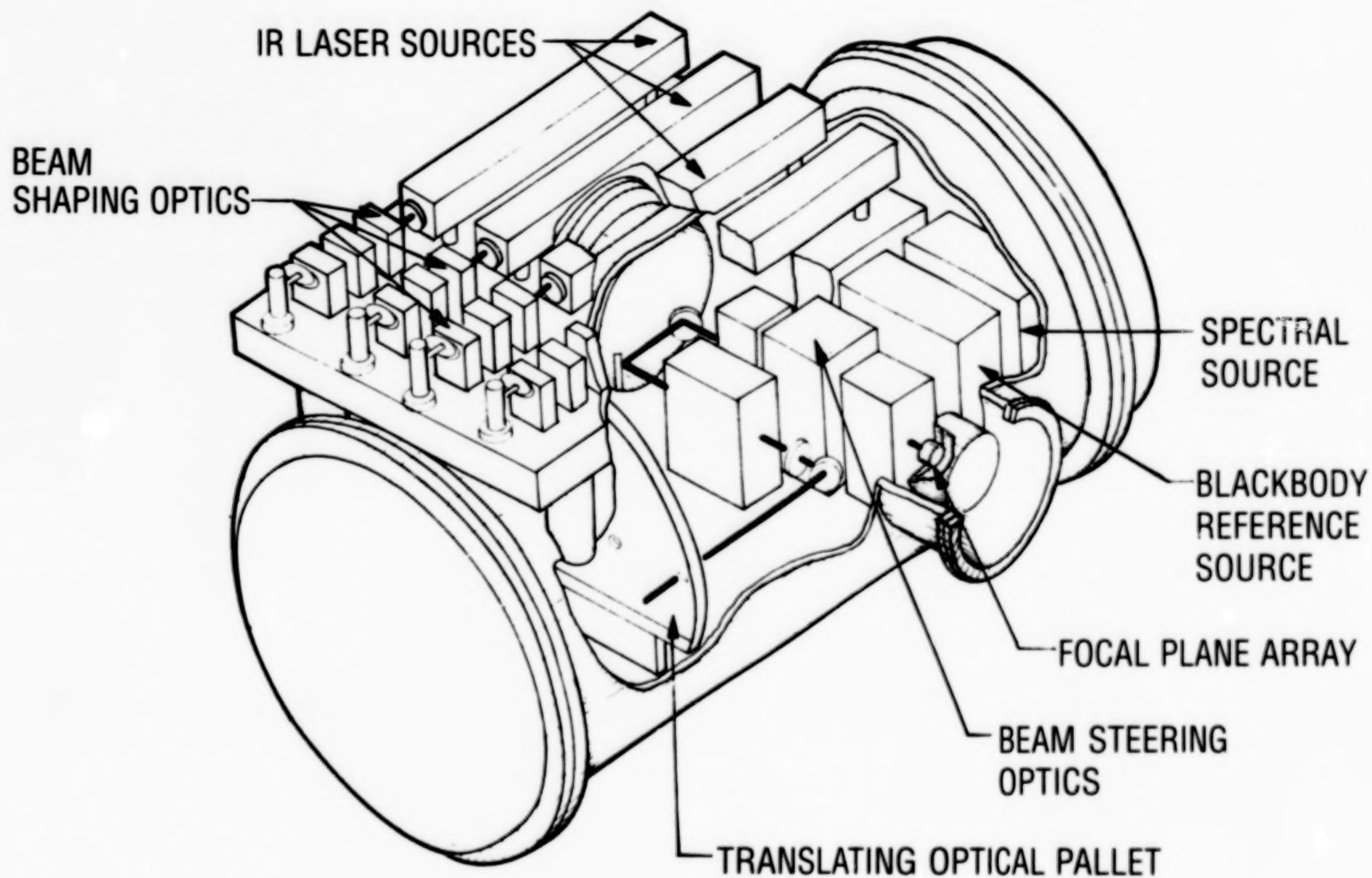
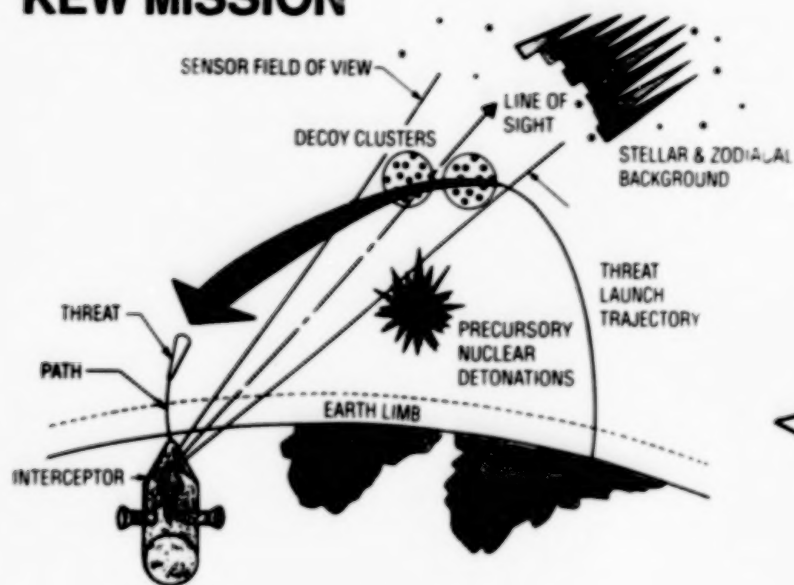


Fig. 11. Proposed FPATC configuration.

KEW MISSION



171

SDI BENEFITS

- REAL-TIME/ENVIRONMENT SIMULATION
- H/W & S/W RELIABILITY EVALUATION
- INDEPENDENT GOV'T EVALUATION
- MULTI-USE, UPGRADEABLE CAPABILITY
- FLIGHT TEST COST/RISK REDUCTION

OBJECTIVES

DEVELOP GROUND VERIFICATION
FACILITY TO EVALUATE ADVANCED
EXO-SEEKER TECHNOLOGIES OF GBI

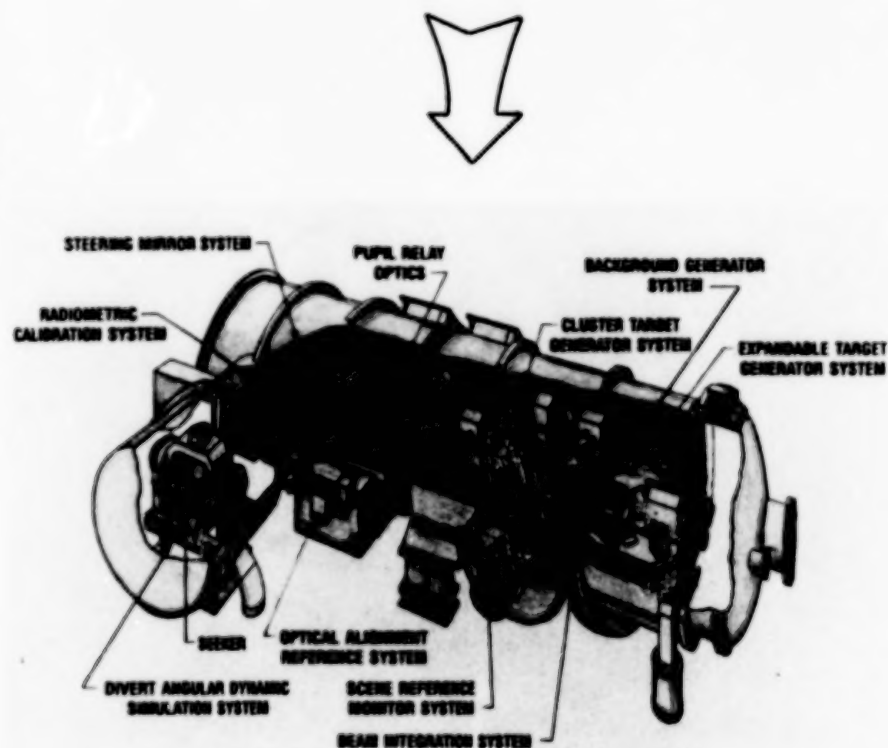
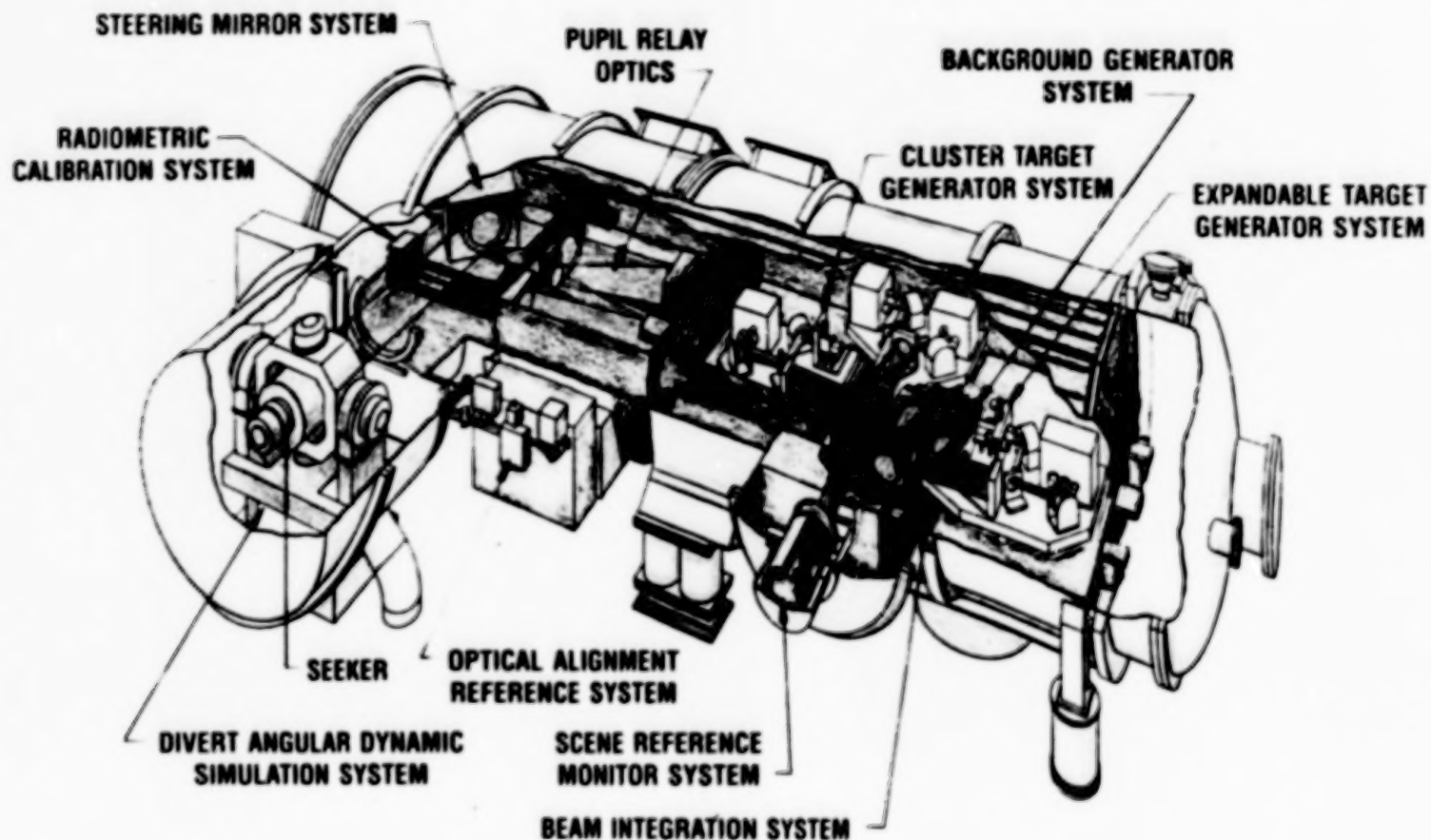


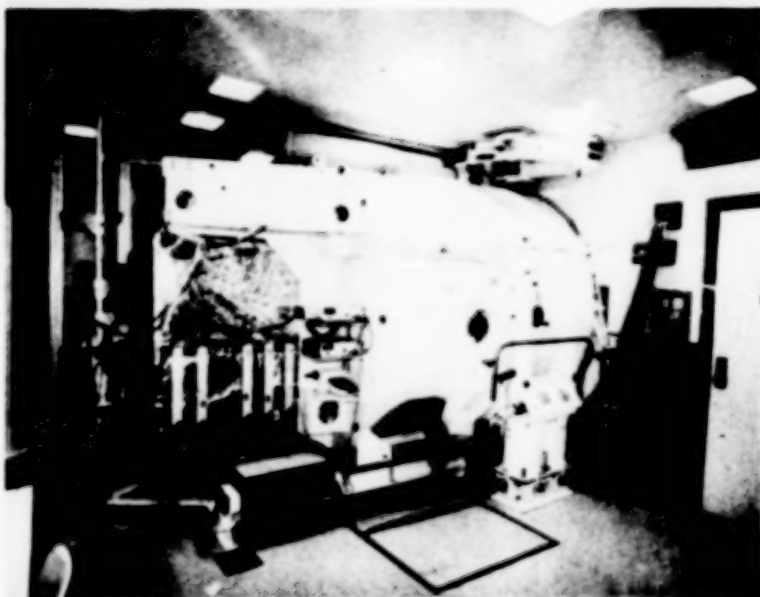
Fig. 12. LETS facility development.



FEATURES:

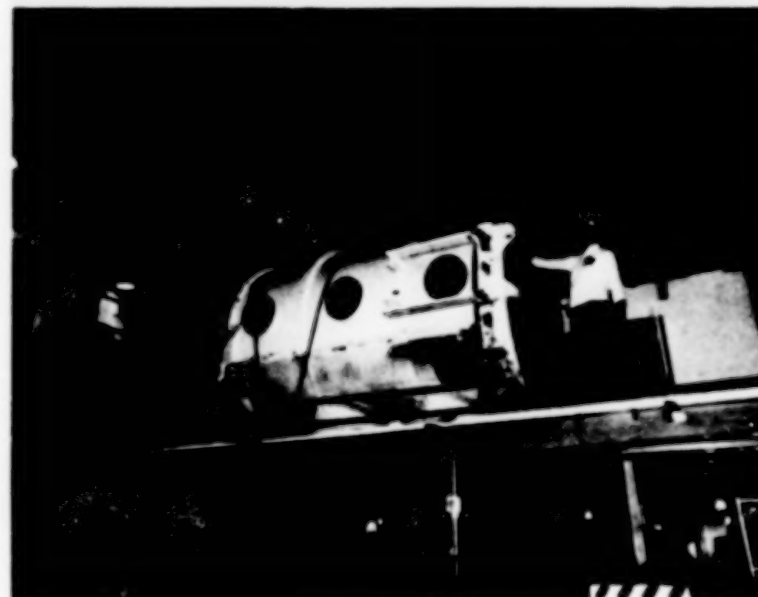
- CRYO-VACUUM ENVIRONMENT 20 K, $<10^{-6}$ TORR
- SEISMIC ISOLATION $\leq 10 \mu\text{rad}$
- DYNAMIC MULTIPLE TARGET SCENE
- STRIATED, DISTRIBUTED, FLASH BACKGROUNDS
- DADS $\pm 1.5 \text{ deg}$, $<100 \text{ deg/sec}^2$ (PITCH, YAW, ROLL)

Fig. 13. LETS chamber.



CHAMBER MODS

- DEMOLITION COMPLETED - OCT 89
- REWORK STARTED - DEC 89
- COMPLETION TARGET - MAY 90



CLEAN ROOM MODS

- DEMOLITION STARTED - SEP 89
- START CONSTR - JAN 90
- COMPLETION TARGET - SEP 90

Fig. 14. LETS facility status.

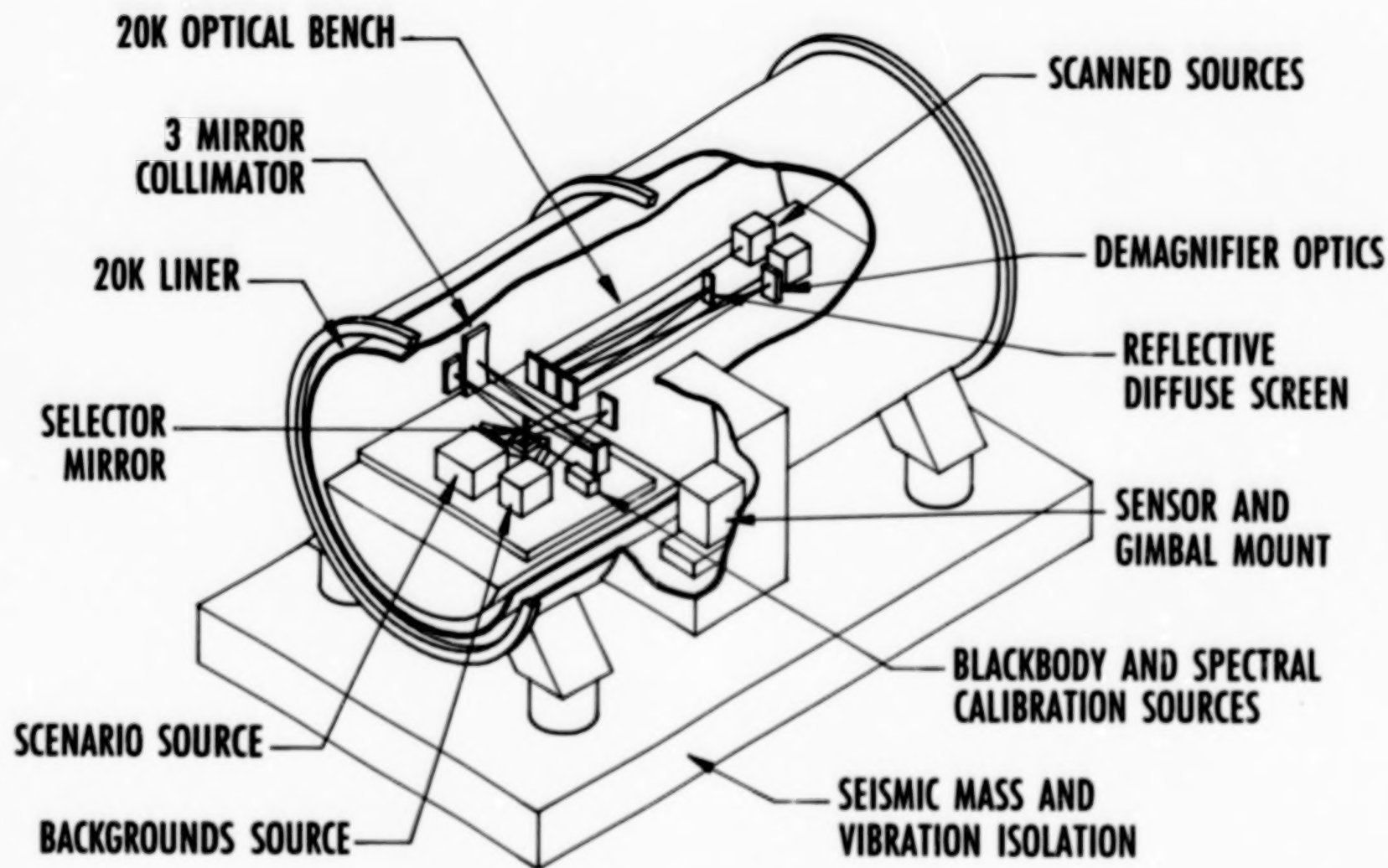


Fig. 15. LSTC conceptual design.

174

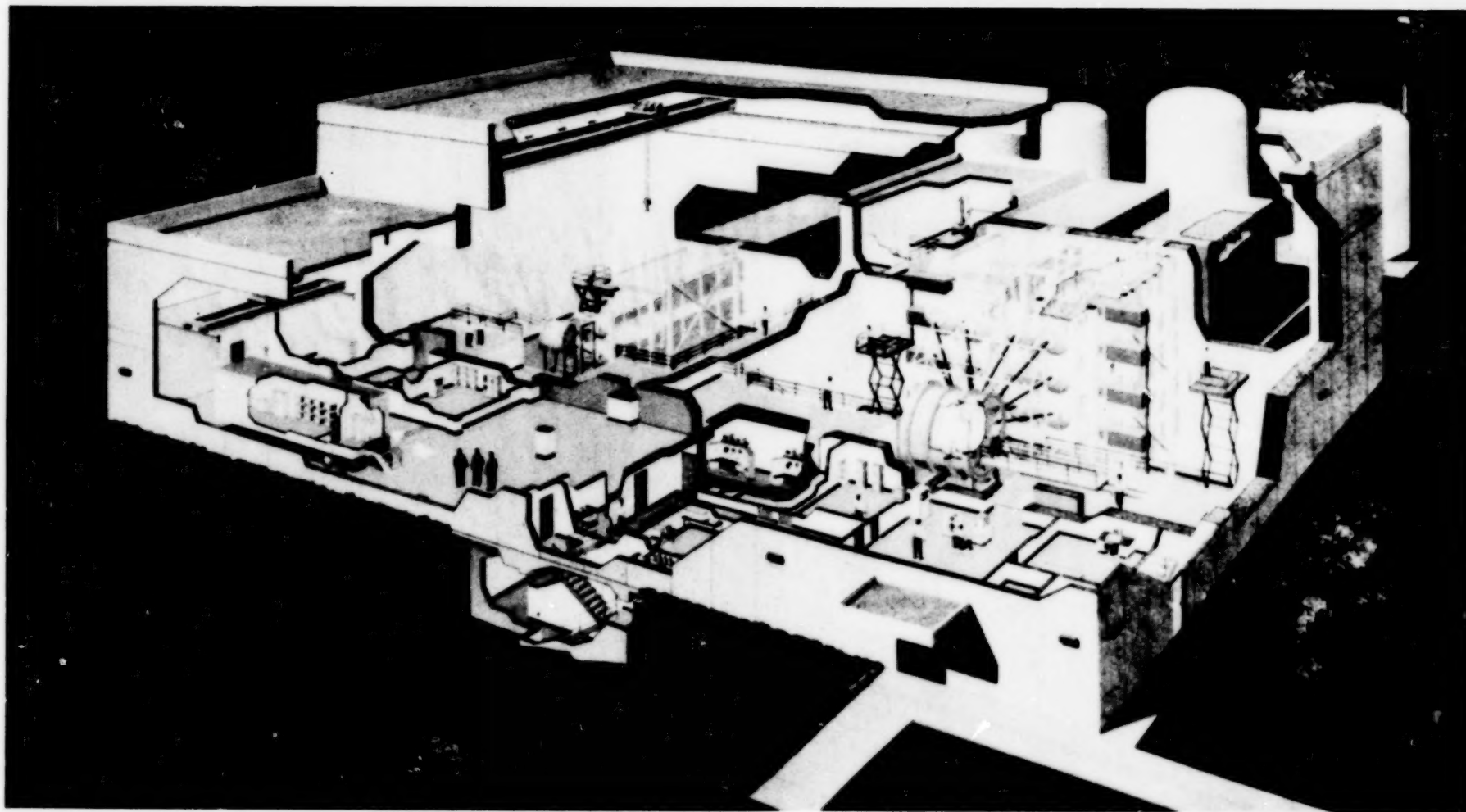


Fig. 16. DECADE Radiation Effects Test Facility.

SESSION IV

INFRARED SENSOR TEST FACILITIES: PART II

THERMAL CONTROL FOR THE GROUND SIMULATION OF A SPACE IR SENSOR SYSTEM

**E. Lee and A. Warren
Grumman Space Systems Division
An Operating Division of Grumman Corporation**

**G. Gasser and M. Tierney
Itek Optical Systems
A Division of Litton Industries**

ABSTRACT

Active and passive thermal controls for simulations of a space IR sensor system operating in cryogenic temperatures were designed, built, and tested from a component level to a system level. The test results from component tests and integrated system tests have compared very well with theoretical predictions, and thus verify component and integrated thermal math models. These verified models can be modified for use to predict flight systems thermal performance.

Thermal vacuum simulations and demonstration of a space IR system consisted of a target and background scene generator, telescope mirrors supported by a graphite-epoxy metering structure, and an IR sensor. These components are required to operate at cryogenic temperature levels. Each component has its unique thermal control requirement. The electro-optical devices operated in the scene generator are required to be maintained at room temperature, while the other areas are operating at 220K. Target and scene blackbodies are operating at temperatures varying from 300K to 1100K. In order to minimize the heat transfer from these blackbodies to the surrounding structure, an active thermal control system using vaporized LN₂ is used. The structure environment is maintained at 220K by electrical heating elements in an enclosed shroud. Mirrors in the telescope area are maintained at 120K by using shroud enclosed electrical heaters. Additional individual mirror heaters are used during warmup cycles to minimize mirror surface contaminations. To prevent and minimize temperature gradients in large mirrors during warmup phase, the chamber shroud temperature is controlled to a required temperature rise rate. The IR sensor is maintained at 120K during demonstration tests using heater and cold straps connected to the chamber shroud.

This paper contains descriptions of thermal control systems for the test article from component design level to integrated system level, discussions of component and integrated demonstration tests, and correlation of test data with thermal finite difference models.

SPECIAL REQUIREMENTS IN THE DESIGN OF A SENSOR TEST AND INTEGRATION LABORATORY

S. Bellanca and E. Lee
An Operating Division of Grumman Corporation
Grumman Space Systems Division

J. Campbell
Consultant

ABSTRACT

Special requirements are imposed on the design and operation of a sensor test and integration laboratory. Cryogenic temperature, vibration isolation for electro-optical equipment, contaminant control, thermal control to reduce or minimize thermally induced stresses on mirrors and supporting metering structure, thermal vacuum chamber shroud temperature uniformity and varying temperature control capability to bring optical equipment from cryogenic temperature to ambient environment, and real-time data processing are some of the stringent requirements that must be addressed before a facility can be accepted to perform sensor test and integration. Most of the sensor tests are performed at cryogenic temperature, and thermal isolation of the test article from the ambient temperature is a strong consideration for the thermal vacuum chamber design. Additionally, equipment heat and parasitic heat sources must be able to remove from the chamber without exceeding the chamber shroud temperature gradients.

This paper will describe how these requirements were met in the design, build, and acceptance test of the Grumman Sensor Test and Integration Laboratory (STIL). Thermal vacuum chamber characteristics and its supporting data acquisition and display system, real-time data processing, test control, and some of the chamber acceptance test results are also presented. A brief description of a sensor test that is currently being conducted at the STIL facility, and the corresponding test results are also included.

IAL SPACE : A TEST LABORATORY FOR THE ISO CRYOGENIC PAYLOAD.

A. CUCCHIARO, M. HENRIST, J-P. MACAU, N. NINANE and
R. BLANPAIN.

Centre de Recherches IAL SPACE - Université de Liège
ANGLEUR - LIEGE (Belgium)

1) INTRODUCTION

The ESA Infrared Space Observatory (ISO) satellite is a 3 axes pointed platform designed to make accurate pointed observations of astronomical objects and sources in the wavelength range between 2.5 and 200 microns.

ISO is composed of a service module and a payload module which is a large cylindrical vacuum vessel. The vessel is in fact a cryostat (capacity of 2250 l of liquid He II) which contains the telescope and the four focal scientific instruments. The latter being cooled up to a temperature less than 4K.

The qualification of the payload requires to measure respectively :

- the image quality of the telescope through WFE (wave front error) measurements,
- the optical alignment of the scientific instruments with respect to the telescope axis and the telescope focus, and this under cryogenic conditions (typically 5K).

Consequently, since 1988, the FOCAL 5 IAL Space facility (see the paper of M. HENRIST et al. in the same proceedings) has been upgraded in order to perform the cryogenic optical tests of the ISO optical subsystem.

2) EXPERIMENTAL CONSTRAINTS

Optical testing under cryogenic conditions represents a certain number of constraints, the main ones being :

- the cool down and the warm-up phases of the experimental set up components (optics, thermal shrouds, thermal baffles, telescope assembly...) must be achieved in a way which avoids excessive stresses in the different

materials,

- the alignment between the different optical elements (telescope, OGSE, baffles,...) must be kept inside severe margins between 300K and 5K,
- the WFE measurements for image quality evaluation are achieved through interferometric methods which need high mechanical stability even in cryogenic conditions,
- the thermal control, the monitoring and the thermal measurements require to acquire, store and analyse in real time (high frequency scanning) data of about 150 sensors with a high accuracy,
- the thermal losses must be minimized in order to avoid thermal overgradients between the different components of the tested device and to reduce the consumption of cryogenic fluid.

Consequently, a dedicated experimental set-up has been designed, manufactured and installed in FOCAL 5 in order to fulfil the test objectives taking into account this above-mentioned constraints.

3) CRYOGENIC EXPERIMENTAL SET-UP

3.1. Cryogenic box.

The experimental set-up which has been developed allows to perform the cryogenic optical tests for the single optical components as well as for the overall telescope assembly of the ISO payload. The configuration for the complete telescope assembly is shown on figure 1.

The basis was to create a cryogenic environment to cool and warm up the experimental components as fast as possible without introducing excessive stresses in/or between the different materials. One way was to use only the radiative transfer by enclosing the specimens within cold boxes, but the cooling time has been estimated of about 6 months which was unacceptable in terms of time schedule. Another way was to fill the cold enclosure with a conductive gas (e.g. gaseous helium). This solution led also to an excessive cooling time (2 weeks).

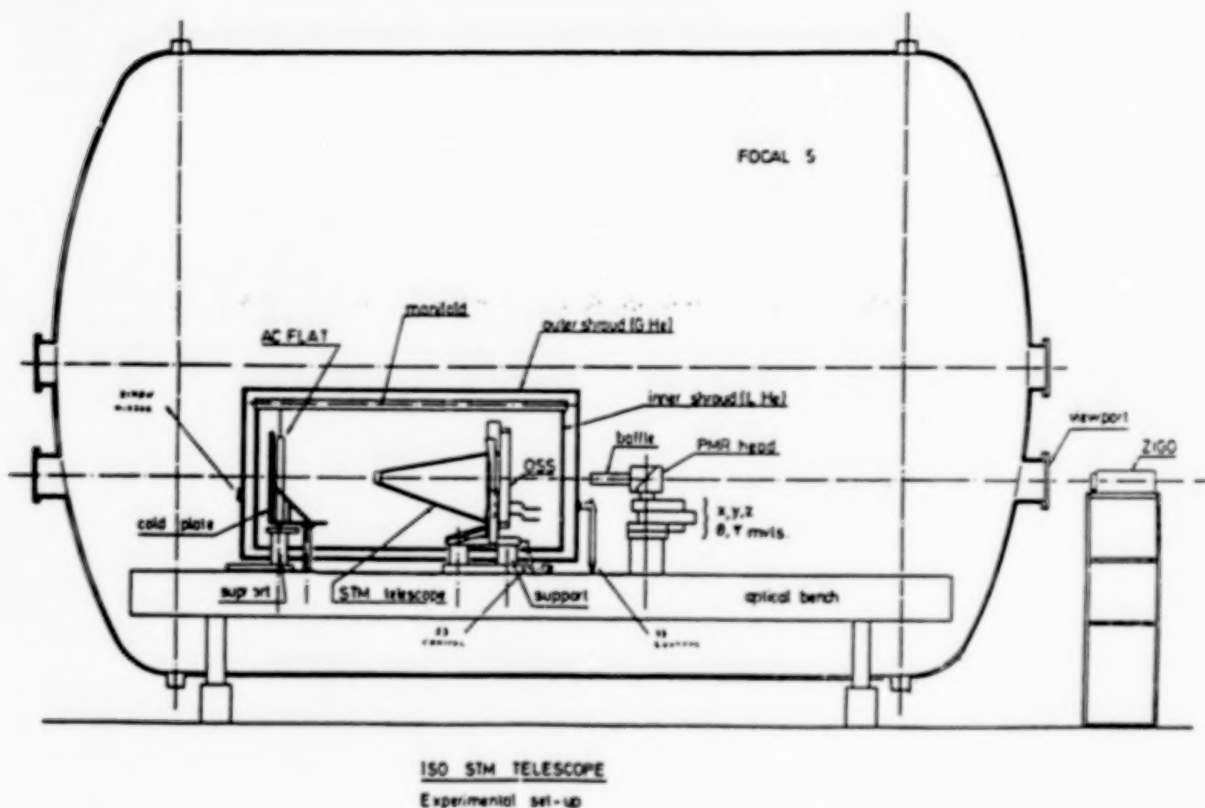


Figure 1 : Experimental set-up configuration.

The solution chosen combines the radiative transfer effect which reduces the thermal gradients and consequently the stresses, with a conductive coupling through straps. This allows to reduce the thermal cycle (cool down and warm up) to about 6 days.

As shown on fig 1, the cold enclosure is a double wall cryobox fed by liquid helium (at 4.6K). The guard wall is fed by liquid nitrogen (77K). Inside, the specimens and their supports are cooled in conductive mode through flexible copper straps (see fig 2) attached to cold plates where circulates refrigerated gaseous helium. As the optics of the specimens are mechanically coupled to the cold plates, it has been found that the induced vibrations were lower using gaseous helium rather than liquid. By this way, the warming sequence and the subsequent baking is also easier using hot gaseous helium.

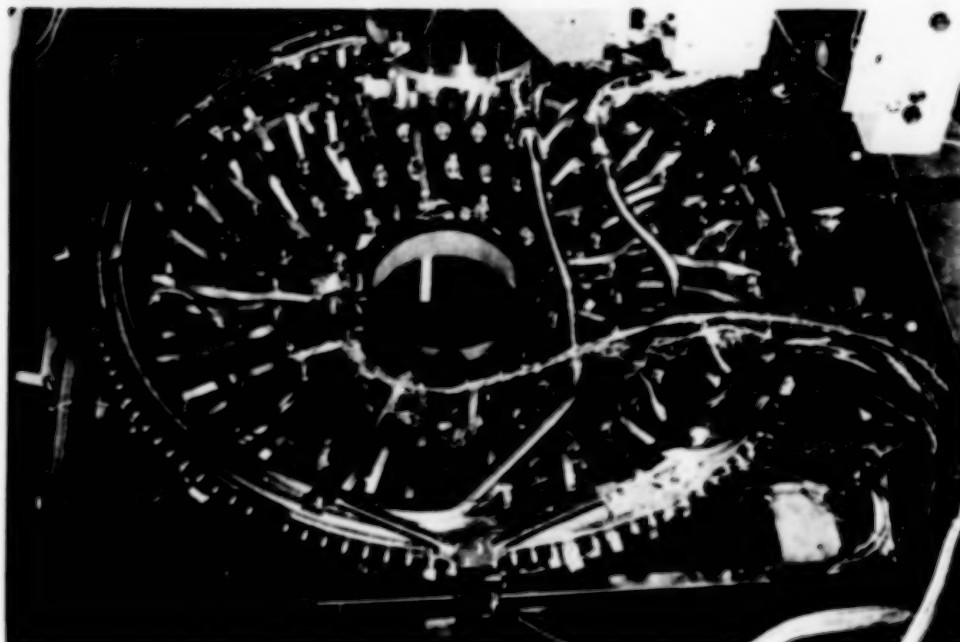


Figure 2 : Strapping of calibration minor.

3.2. Optical supports.

A critical problem encountered concerns the supports of the optical devices. Indeed :

a) the optics and the different mechanical structures must be cooled up to 5K whereas the optical bench which supports the overall system must stay at 300K.

b) for WFE measurements, the optical alignment must be kept during the cool down and warm up phases and this without induced low frequency vibrations.

The solution adopted to face these problems is represented on fig 3.

- The bottom part of the support, the one comprising the different movements (tilt, rotation) allowing initial alignment and which is interfaced with the optical bench is manufactured in invar for thermal expansion reasons.

- The central part is composed by two quartz tubes and an intermediate invar plate. The quartz tubes present the advantages that the material have :

- a thermal expansion coefficient close to zero
- a very low thermal conductivity
- a good strength under heavy loads.

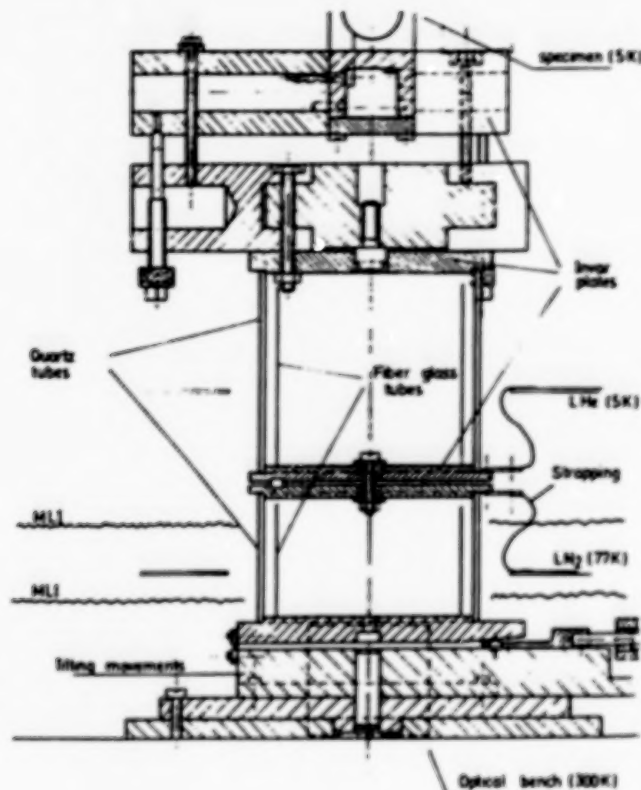


Figure 3 : Typical cryogenic support.

The intermediate invar plate is connected by copper straps to the double wall cryo-box and constitute a thermal barrier for the heat flux coming from the bench.

- The upper part has also been realized in invar.

The risks of quartz breakage are warranted by a fiber glass tube inside the quartz one and does contribute neither to the thermal conductivity nor to the mechanical properties of the support.

The overall structure of the support is completely decoupled from the rest of the cryo-box in order to keep the required vibrational stability.

3.3. Liquefier.

As previously mentioned, the cryogenic box as well as the cold plates are respectively fed with liquid and refrigerated helium. In fact, to perform the cryo-test, there were two solutions :

- to use helium dewars
- to produce cold helium with a liquefier.

The liquefier option has been chosen because :

- a) it allows to use at the same time liquid and gaseous helium which is very important at the level of the cold plates vibration problem.
- b) the number and the duration of the cryo test justify the investment.

c) the driving of the thermal cycles is more flexible and the liquefier allows continuous operation. The model installed in the IAL Space facilities is the KPS model 1630 which provides liquid helium at 4.6K and gaseous refrigerated helium at a minimum of 4.6K with a total capacity of 40 l/h or equivalent in refrigerated gas.

3.4. Instrumentation of the experimental set-up.

The thermal control of the overall experimental set-up requires to manage in real time, high accuracy data in the temperature range from 4K to 50K. The number of sensors is close to 150 and have been homemade and calibrated. They are diodes fed by DC at 10 microamps. The temperature is given by the electrical resistance of the diode.

The sensors are calibrated in a cryostat by comparison with a standard sensor delivered by Lake Shore (California). The junctions are encapsulated in small copper cylinders. The wires are thermalized by many loops around the diode inside the copper cylinder which is screwed on the surface to be measured.

The accuracy obtained is $\pm 0.1K$ between 4K and 50K.

3.5. Control and monitoring system.

The control of the overall experimental set-up is achieved through thermal data acquired by a 3497 data logger and managed by a HP 9000, serie 370, working station.

A dedicated software (home made), working under Unix, X windows and NFS, allows multitasking programs. The users can define easily in real time :

- sensors groups
- gradient groups
- scanning speed
- drawings
- temperature curves
- histograms
- synopses
- alarms and warmings.

Examples of such displays can be found on fig 4, 5 and 6. These synopses shows the performances of the cryogenic box as well as the ones of the control and monitoring system.

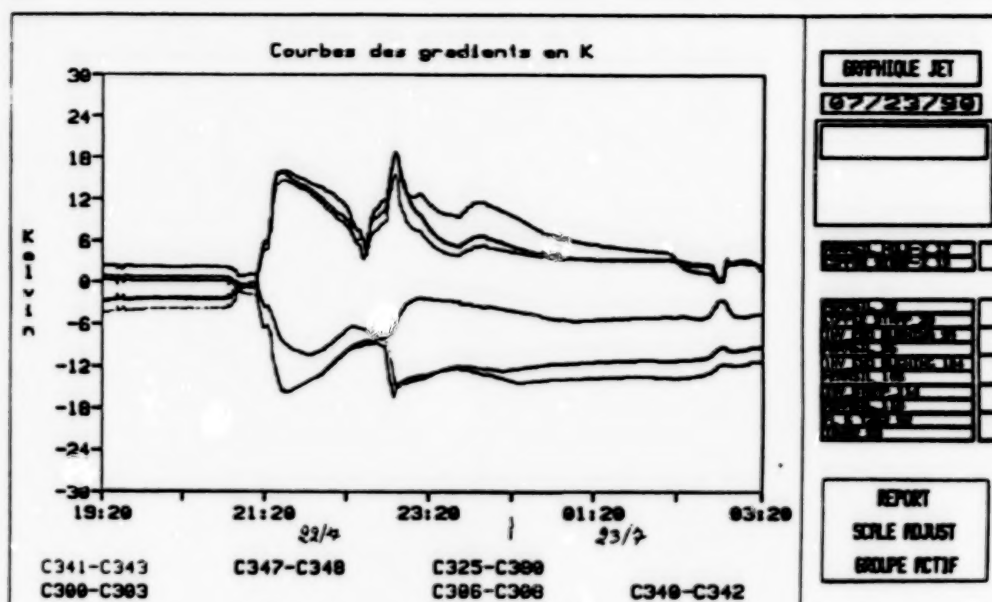


Figure 6

4) PERFORMANCES AND RESULTS

Up to now, the cryogenic tests performed in IAL Space facility concern the structural and thermal model of the ISO optical subsystem. The concerned items tested have been :

- the primary mirror
- the Calibration autocollimation flat mirror
- the telescope (see fig 7)

After a cool down sequence of about 80 hours, a thermal equilibrium between the different parts of each specimen has been reached. The temperatures were comprised everywhere between 4.6K and 10K. This being good enough to allow a close estimation of the thermomechanical behaviour of each specimen tested. The warm-up sequence has needed a equivalent time duration (3.5 days).

The optical quality of the individual mirrors or of the overall telescope was performed through interferograms taken from an interferometer Zygo MARK IV working in phase mode.

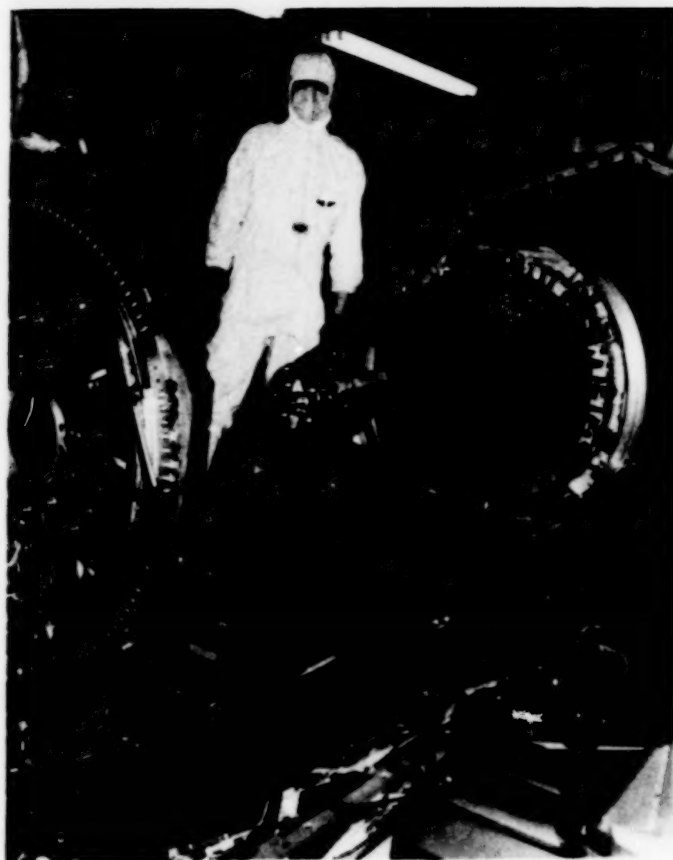


Figure 7 : ISO STM TELESCOPE

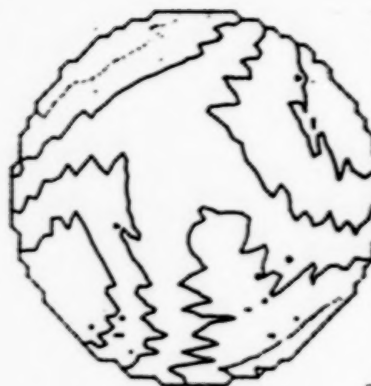
This method implies a very good position stability of the optics to be measured with regards to the reference optical cavity which is situated outside the cryogenic box (see fig 1). A typical example of interferogram taken at cryotemperature of about 5K can be found on fig 8. It concerns the overall STM Telescope.

*** WAVEFRONT ***

02-APR-1990/13:55:10

KIKAR AT
12 K.

Part ID :
Serial # : \\
Analysis : phase
F/NO : plano
Fast : off
Averages : 1
Trim : 0
Calibrate : ON
AGC : ON
Scale : 0.50
Wave Out : 0.6328
Reference : none
Remove : TLT PWR



0.247
0.187
0.148
0.099
0.049
no
data

PV : 0.296 PTS : 33029
RMS : 0.049

	MAGNITUDE	ANGLE
POWER	-1.4899	N/A

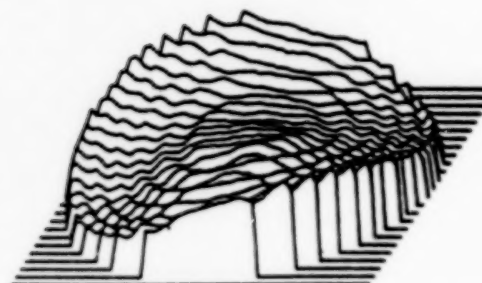
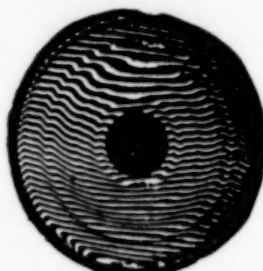


Figure 8

The future tests will be dedicated to the Flight models of all the items which have been mentioned. For these, in addition, to the constraints already described, the particular contamination will constitute a major problem one will be faced with. Indeed a specification of 1.5 ppm/per day is hard to reach with the experimental conditions hereabove presented.

BIBLIOGRAPHY.

- (1) A.M. DAVIDSON ESA BULLETIN 57 p 53 February 1989.

SESSION V
DYNAMIC TESTING

NON-LINEAR GENERATION OF ACOUSTIC NOISE IN THE I.A.R. SPACECRAFT
CHAMBER BY MANUAL OR AUTOMATIC CONTROL*

R. Westley, K. Nguyen and M.S. Westley
Institute for Aerospace Research,
National Research Council, Canada.

ABSTRACT

The requirement to produce high level acoustic noise fields with increasing accuracy in environmental test facilities dictates that a more precise understanding is required of the factors controlling non-linear noise generation.

This paper gives details of various non-linear effects found in acoustic performance data taken from the I.A.R. Spacecraft Acoustic Chamber. This type of data has enabled the I.A.R. to test large spacecraft to relatively tight acoustic tolerances over a wide frequency range using manually set controls.

An analog random-noise automatic control system was available and modified to provide automatic selection of the chamber's spectral sound pressure levels. The automatic control system when used to complete a typical qualification test appeared to equal the accuracy of the manual system and had the added advantage that parallel spectra could be easily achieved during preset tests.

INTRODUCTION

The Institute for Aerospace Research (I.A.R.) of the National Research Council, Canada, operates a spacecraft acoustic test chamber for aerospace research and development at the Aeroacoustic Facility (ref. 1) of the Structures and Materials Laboratory.

The spacecraft chamber has been required to generate high level acoustic noise fields with increasing spectral accuracy to simulate rocket and aeroengine noise for qualification testing of aerospace structures and equipment. In the future it is likely that this trend will continue and therefore: acoustic test sound level spectra may need to be controlled to accuracies of ± 1 dB; the spectra may be defined in finer bands than the 1/3 or 1/1 octave bands at present in use; sound level tolerances at low and high frequencies may be tightened to match those at mid frequencies; exploratory tests at progressively higher levels may be restricted to one relatively low level test, e.g. -10 dB, for expensive spacecraft.

Complications to the production of accurate acoustic levels for spacecraft tests are that the generation process is highly non-linear and not easily predicted, and that the acoustic absorption and insertion effects of a large spacecraft are not accurately known in advance of the spacecraft being placed and tested in the chamber. The short duration of a spacecraft acoustic test will usually preclude any manual readjustments of the generators' controls being made during the test. Although spectral level test requirements cover the range of frequencies from 20 Hz to 10 kHz, it should be noted that presently available commercial electro-pneumatic noise generators may only have direct control in the nominal frequency ranges of up to 500 Hz for 30 kW generators, and up to 1,250 Hz for 10 kW generators.

*Investigation supported by the Institute for Aerospace Research, N.R.C.C., under Intense Noise Project #23310.

The remainder of the spectral levels in the higher frequency ranges have to be filled by non-linear harmonics from lower frequency inputs and by auxiliary aerodynamic (ref 2) or loudspeaker noise sources (ref 3).

It is therefore essential for accurate manual control and for the design of automatic control systems that quantitative data be assembled of the effects of the main control parameters (electrical current and gas pressure) on the non-linear acoustic performances. The main purpose of this paper is to illustrate some of these non-linear effects by presenting performance data from a 30 kW type generator that was connected to the I.A.R. Spacecraft Chamber by a 32 Hz horn and which was being used to produce qualification test spectrum at overall levels of 146.6 dB for Ariane or Space Shuttle type launches.

The I.A.R. Spacecraft Chamber has floor dimensions of 9.75 m (32.0 ft) x 6.9 m (22.6 ft) and a height of 8.0 m (26.2 ft) giving a total internal volume of about 540 m³ (19,000 ft³). A side view of the chamber with its complement of three 30 Kw, one 10 kW and four N.A.E. aerodynamic generators connected to 25, 32, 100 and 200 Hz horns is shown in figure 1.

SYMBOLS

I	r.m.s. of electrical current supplied to generator	(amp)
IdB	$20 \log_{10}(I)$, electrical current level	(ref 1 amp)
P	air pressure supplied to generator	(p.s.i.g.)
dB	1/3 octave sound pressure level	(ref 20 μ Pa)
O.A.S.P.L.	overall sound pressure level (25 Hz - 10 kHz)	(ref 20 μ Pa)

ACOUSTIC PERFORMANCE TESTS (MANUAL CONTROL)

Manual Control System

The noise generator's control system is illustrated in figure 2. The manual control system consisted of an electrical random noise generator which supplied spectrally shaped drive current to the armature of the electro-pneumatic generator. The drive current spectrum was shaped over the frequency range of 25 to 630 Hz by fifteen adjustable 1/3 octave filters located in the equaliser unit. The overall current, (I), was adjusted to the required level by the gain on the audio power amplifier. Compressed air was supplied at selectable pressures, (P), to the generator and in most of the tests described here was held constant at 30 or 10 p.s.i.g. The acoustic sound pressure level spectrum in the chamber was measured by an array of six 1/2-in. diameter pressure response condenser microphones and the averaged spectrum was displayed and recorded on a 1/3 octave real time analyser.

Preliminary Set-up

In a preliminary experiment, to meet the representative spacecraft qualification tolerances over the 25-500 Hz range, the air supply pressure was set to 30 p.s.i.g. and the gains of the power amplifier and the fifteen equaliser filters were adjusted until the sound level spectrum in the chamber was as close as practicable to the mean spectrum between the two tolerance lines for the frequency range of 25 to 500 Hz. The drive current which best met this mean spectrum occurred at 18.5 IdB,

although it will be noted in figure 3 that the spectrum and the overall level tolerances can be met over a wider range of frequencies when the current is increased to 20 and 21 IdB. The 18.5 IdB setting was used as a reference in the following tests.

Variation of Sound Spectra Levels with Drive Current (30 p.s.i.g.)

The air supply was selected at a fixed value of 30 p.s.i.g. and sound level spectra were recorded for a series of drive current levels. Figure 4 shows selected spectra over the drive current range of 0 to 21 IdB with the corresponding overall sound levels increasing from 122 dB to 148 dB. An important feature to note, in addition to the effect of increased current on overall levels, is that the spectral slopes at frequencies below the maxima levels become more steep while slopes at frequencies greater than the maxima levels become less steep with increase of current. This non-linear effect on spectral shapes must be taken into account if the spectral shape is set during a preliminary spacecraft test at lower levels, e.g. at -10 dB or -5 dB. The asymptotic value of about 111 dB which is reached at frequencies between 1 kHz and 10 kHz, when the drive current is reduced below 9 IdB, is due to the residual noise of air flowing through the noise generator at 30 p.s.i.g.

The sound pressure levels in each 1/3 octave band and the overall level are plotted against the current level in figure 5. These curves are valuable for predicting sound level spectra at any selected drive current and for anticipating areas in which spectral control may be difficult. Distinct characteristics are recognisable in the set of frequency band levels up to 630 Hz which are directly controllable by the equaliser and in the set of frequency band levels above 630 Hz which are related to harmonic distortions. The modulator residual airflow noise also makes significant contributions to the levels for frequencies below 630 Hz and for the overall level when the current falls below 6 IdB. A general characteristic is that the slopes of the sound pressure level curves increase with increase of frequency and decrease with increase of current. Typical slopes range from 1 dB/IdB for the 25 Hz band to 2 dB/IdB for the 400 Hz band, while the overall level has a slope of approximately 2 dB/IdB at 10 IdB and 0.9 dB/IdB at 20 IdB. A current level increase of 6.5 IdB would be required in this case to raise the overall level by 10 dB from a 136 dB pretest low level to the target qualification level of 146 dB overall.

Variation of Sound Spectra Levels with Air Pressure (18.5 IdB)

The air pressure to the noise generator was set at a series of values between 30 p.s.i.g. and 5 p.s.i.g. while the drive current remained at the qualification level of 18.5 IdB. Typical spectral levels are shown in figure 6. The effect of decreasing the drive air pressure was to progressively decrease the overall sound pressure level from 145.8 to 138.4 dB and to steepen the slopes of the spectra levels on either side of the maxima which occurred at 400 and 500 Hz. The sound pressure levels in each frequency band are plotted against air pressure in figure 8. As the air pressure is reduced from 30 to 5 p.s.i.g., the sound pressure levels for the 1/3 octave frequency bands of 25, 500 and 10,000 Hz fall 9.5, 4.5 and 16 dB respectively. It will be noted that the overall sound pressure falls only 1.9 dB as the air pressure is reduced to 15 p.s.i.g. and therefore a significant saving can be made in compressed air flow requirements in cases where a trade off is possible between higher drive current and lower air pressure. In some cases it may be advantageous to run the generators at lower pressure when spectra with steeper slopes on either side of the maxima are required or because more linear response characteristics are needed for more accurate performance predictions. To illustrate this a new set of sound level spectra were recorded for various drive currents with the supply air pressure set at 10 p.s.i.g.

Variations of Sound Spectra Levels with Drive Current (10 p.s.i.g.)

Sound level spectra with the generator's air pressure set at 10 p.s.i.g. were repeated for a series of drive currents. Typical spectra for a range of drive current levels from -5 IdB to 21 IdB are plotted in figure 7 and detailed plots of the 1/3 octave and overall levels are plotted against current level in figure 9. The most significant change in performance when comparing figure 9 (10 p.s.i.g.) with figure 5 (30

p.s.i.g.) is that, over the direct control frequency range of 25 to 630 Hz, the slopes of the sound pressure level curves are close to 1 dB/1dB for the 10 p.s.i.g. and therefore in this frequency range spectral shapes are much less sensitive to current level changes than those found at 30 p.s.i.g. In the case of sound pressure levels at frequencies of 800 Hz and higher, it will be seen that the slopes are greater, but are similar to those found at 30 p.s.i.g. for the higher frequency range. The airflow generated background noise effects are now lowered to approximately 99 dB for the highest frequencies and are only marginally detectable in the lower frequency range between 50 and 25 Hz. It will be noted that the overall levels are 143 dB at 20 lbf and 132 dB at 8 lbf for an air pressure of 10 p.s.i.g. (figure 9), but corresponding levels in the 30 p.s.i.g. case (figure 5) are 147.5 and 128.5 dB respectively.

When comparing overall sound pressure levels at 10 p.s.i.g. with those at 30 p.s.i.g. it will be noted that, for current levels above 12 lbf, the overall sound pressure levels for 30 p.s.i.g. are greater, whereas below 12 lbf those for the 10 p.s.i.g. case are greater. This explains the anomaly that with certain selected lower drive currents the overall level and some 1/3 octave levels will decrease as the drive pressure is increased.

ACOUSTIC PERFORMANCE TEST (AUTOMATIC CONTROL)

Automatic Control System

An analog random-noise vibration automatic control system that is no longer in production was added to the generator system, as shown in figure 2, with the object of reducing the pretest time involved in accurate manual testing and in compensating for spacecraft acoustic absorption.

A target spectrum is preselected on the control unit's equaliser and the automatic controller adjusts the drive current until the spectrum levels in the test chamber match the target spectrum levels. The technique for switching from a preset acoustic level to a test acoustic level differs from the vibration technique because of the non-linear effects in acoustic generation. The acoustic technique achieves a step increase of acoustic levels by decreasing the gain of the microphone amplifier signal by an amount exactly equal to the required increase. At the same time the gain of the controller's amplifier may be increased by an amount that would not allow acoustic spectral levels to overshoot. (The maximum allowable control gain increase may be assessed from the performance curves for the appropriate air supply pressure; e.g. figure 5 gives 6.5 lbf for an overall level increase from 136.6 to 146.6 dB).

Set-up Procedure

The generator's air supply was set to a pressure of 30 p.s.i.g. and the controller's equalisers in the frequency bands between 25 and 600 Hz were adjusted until the empty chamber's sound pressure levels spectrum met the qualification launch spectrum tolerance as shown in figure 10. This qualification level was met with the microphone amplifier attenuation set to 20 dB.

Variation of Sound Spectra Levels with Selected Levels

Various gains (microphone attenuation settings) were selected over the range of 0 dB to 23 dB and the acoustic spectra recorded after steady conditions had been reached on the analyser. A selection of achieved spectra are shown in figure 11. The overall and 1/3 octave band levels have been plotted against the selected gain in figure 12. It will be noted in the latter figure that the 1/3 octave levels for 80 to 500 Hz are parallel and increase accurately with a slope of 1 dB/dB. Therefore the automatic controller has an advantage over the manual control system in that pretest and test acoustic levels can be set up accurately with the same spectral shape and that non-linear and spacecraft absorption effects can be corrected.

COMPARISON OF AUTOMATIC CONTROL WITH MANUAL CONTROL FOR QUALIFICATION TEST WITH -10 dB PRETEST

Automatic Control Pretest (-10 dB) and Qualification Test

The compressed air supply to the generator was adjusted to 30 p.s.i.g. with the relative humidity in the chamber stabilising at 2 % with an ambient temperature of $22^{\circ}\text{C} \pm 2^{\circ}\text{C}$. The automatic control system with its equaliser target spectrum as previously set up was switched on with the pretest gain setting of 10 dB. The 1/3 octave real time analyser was selected with a 4 sec. exponential averaging time and a sampling rate of 2 per sec. The qualification test level was selected by switching the controller gain to 20 dB at a time of 20 sec. The generator was switched off at a time of 70 sec. The time histories of the overall and selected 1/3 octave sound pressure levels are given in figure 13 with the achieved qualification test spectrum and tolerances being shown in figure 15.

Manual Pretest (-10 dB) and Qualification Test

The manual control equaliser settings remained as set for all the previous manual tests.

The air pressure, the chamber ambient conditions and the analyser settings remained as in the above automatic control test. The power amplifier was adjusted to provide an overall level of 136.6 dB for 20 sec. before being readjusted to the setting which gave an overall level of 146.6 dB. The generator was then switched off at a time of 70 sec. The time histories of the overall level and selected 1/3 octave levels are plotted in figure 14 with the achieved qualification test spectrum and tolerances being shown in figure 16.

CONCLUSIONS

Details are contained of the non-linear acoustic performance of the I.A.R. Spacecraft Acoustic Chamber while it was being driven by a 30 kW electro-pneumatic generator and a 32 Hz horn using a manual control system to provide qualification and pretest acoustic spectra levels to simulate typical rocket launch noise. This type of performance data becomes increasingly important as tighter test tolerances require the development of more accurate test methods. The acoustic performance became more linear when the noise generator's air pressure was reduced from 30 p.s.i.g. to 10 p.s.i.g..

The second part of this paper reports on the performance of an analogue random noise vibration automatic control system which was adapted to cater for the non-linear characteristics of the noise generators. This automatic control system proved itself capable of matching the spectral accuracy of the manual control system during a typical qualification test and is likely to demonstrate considerable saving in time when testing spacecraft with large acoustic absorptions or when the pretests require the same spectral shape to be produced at lower levels.

REFERENCES

1. Westley, R.; Baranowski, M.; Westley, M.S.; Hurtubise, L.C. High Level Acoustic Noise Generating Capability at the N.A.E. Aeroacoustic Facility, Structures and Materials Laboratory, N.A.E./N.R.C.C. Proceedings of the 36th Annual Technical Meeting of the Institute of Environmental Sciences, New Orleans, Louisiana, April 23-27, 1990, p.p. 587-609.
2. Westley, R.; Brown, M.J.; Baranowski, M. High Level Frequency Noise Generation in the NAE Spacecraft Test Chamber. Proceedings of the 34th Annual Technical Meeting of the Institute of Environmental Sciences, King of Prussia, Pennsylvania, May 3-5, 1988, pp. 136-149.
3. Hieken, M.H.; Levo, R.W. A High Intensity Reverberant Acoustic Test Facility. Proceedings of the 34th Annual Technical Meeting of the Institute of Environmental Sciences, King of Prussia, Pennsylvania, May 3-5, 1988, pp. 131-135.

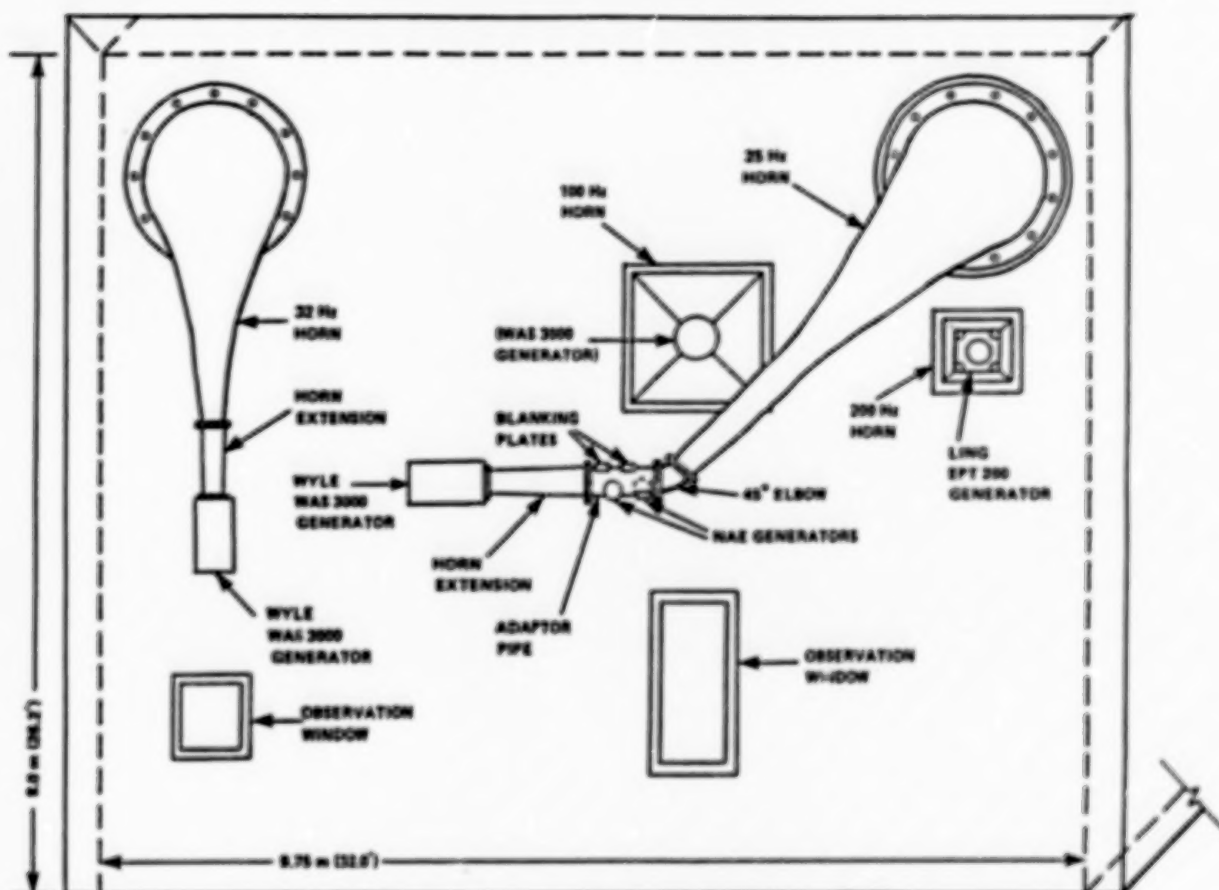


FIG. 1: SIDE VIEW OF NAE SPACECRAFT ACOUSTIC CHAMBER AND GENERATORS

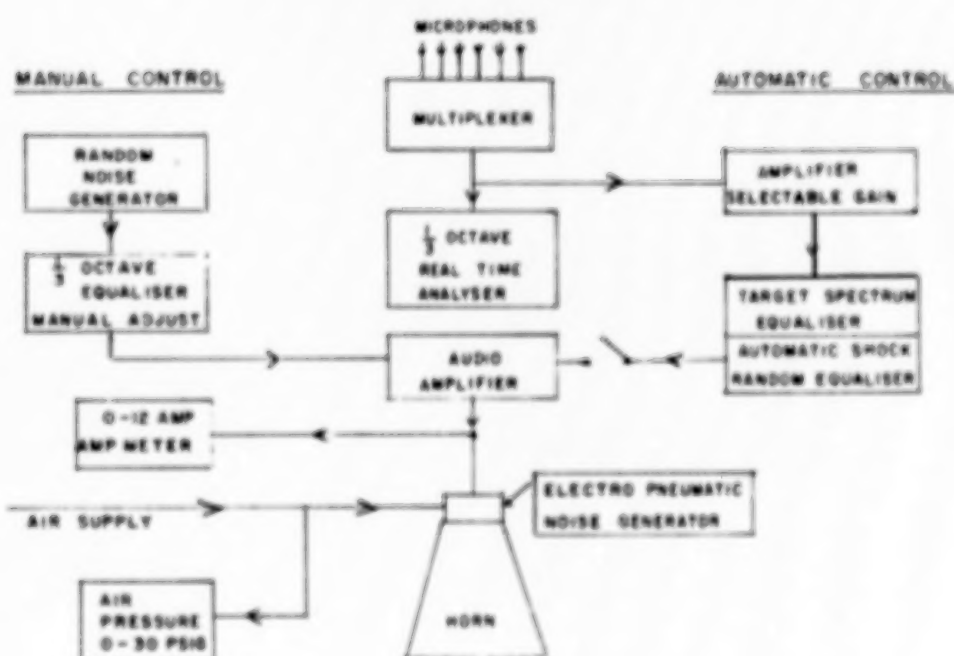


FIG. 2: NOISE GENERATOR CONTROL SYSTEM

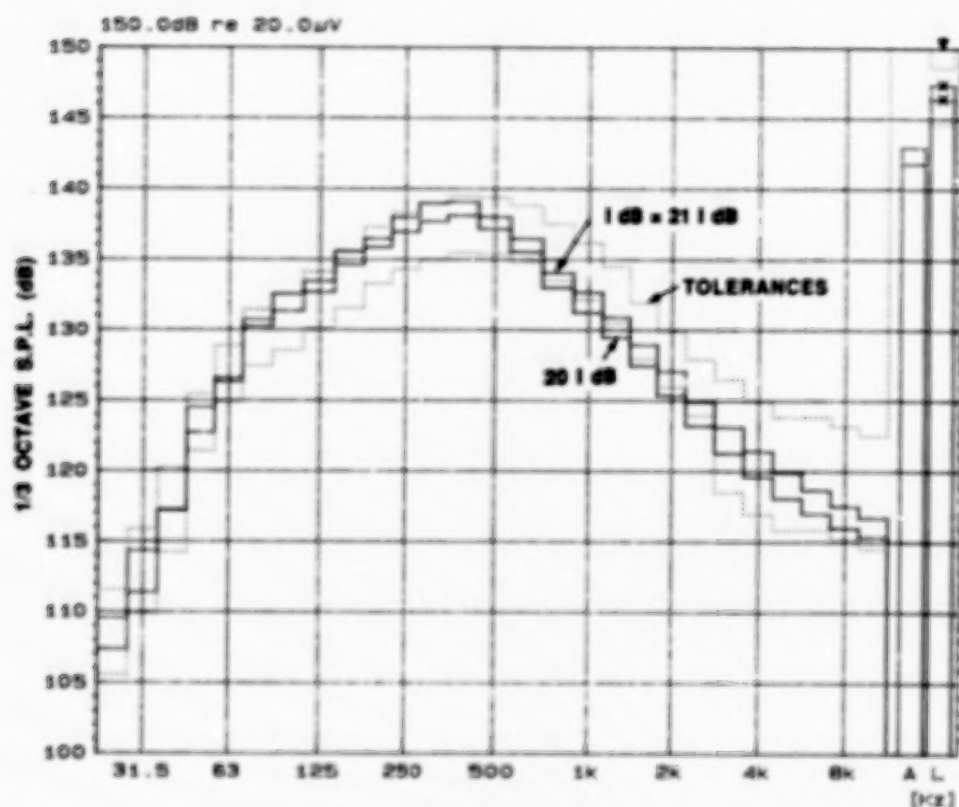


FIG. 3: QUAL. LAUNCH SPECTRA AND TOLERANCES (30 psig)

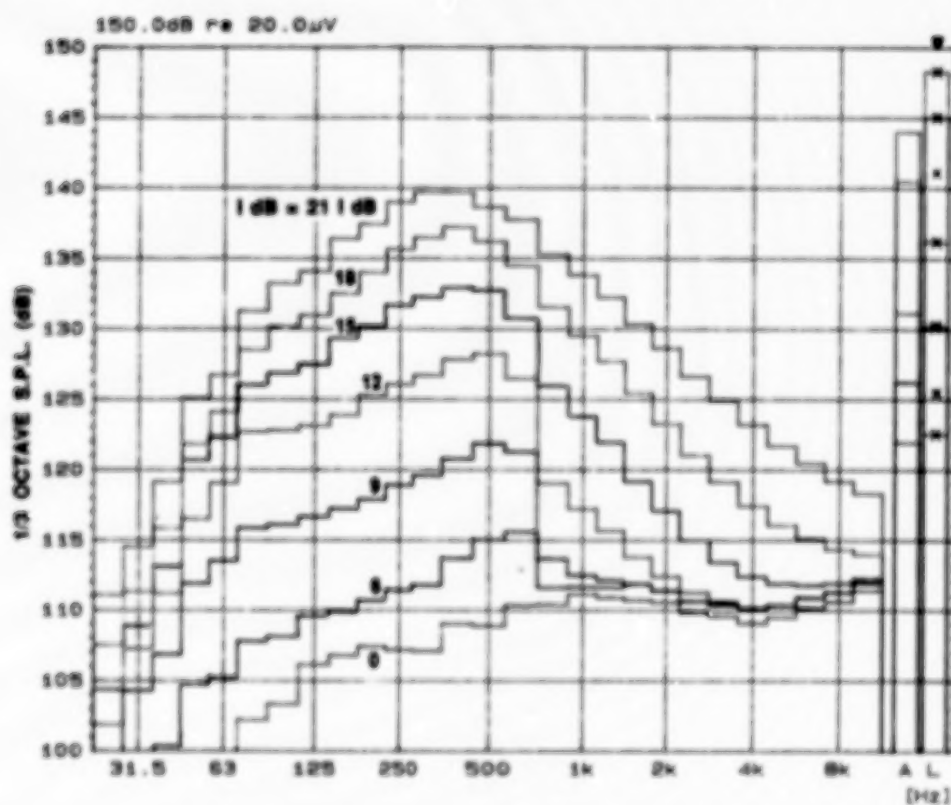


FIG. 4: VARIATION OF 1/3 OCTAVE S.P.L. SPECTRUM WITH DRIVE CURRENT (P = 30 psig)

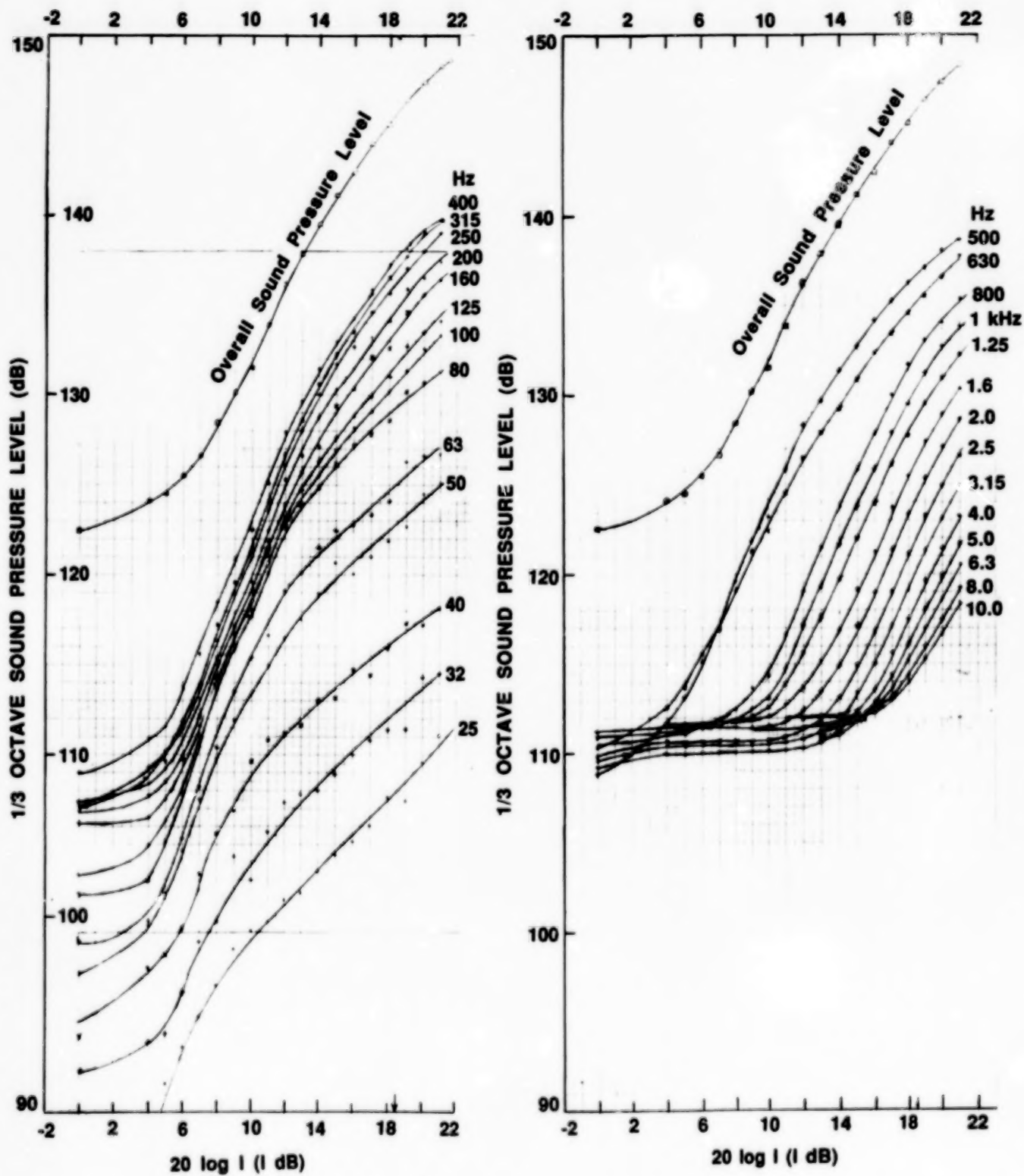


FIG. 5: 1/3 OCTAVE S.P.L. vs. DRIVE CURRENT
(P = 30 psig)

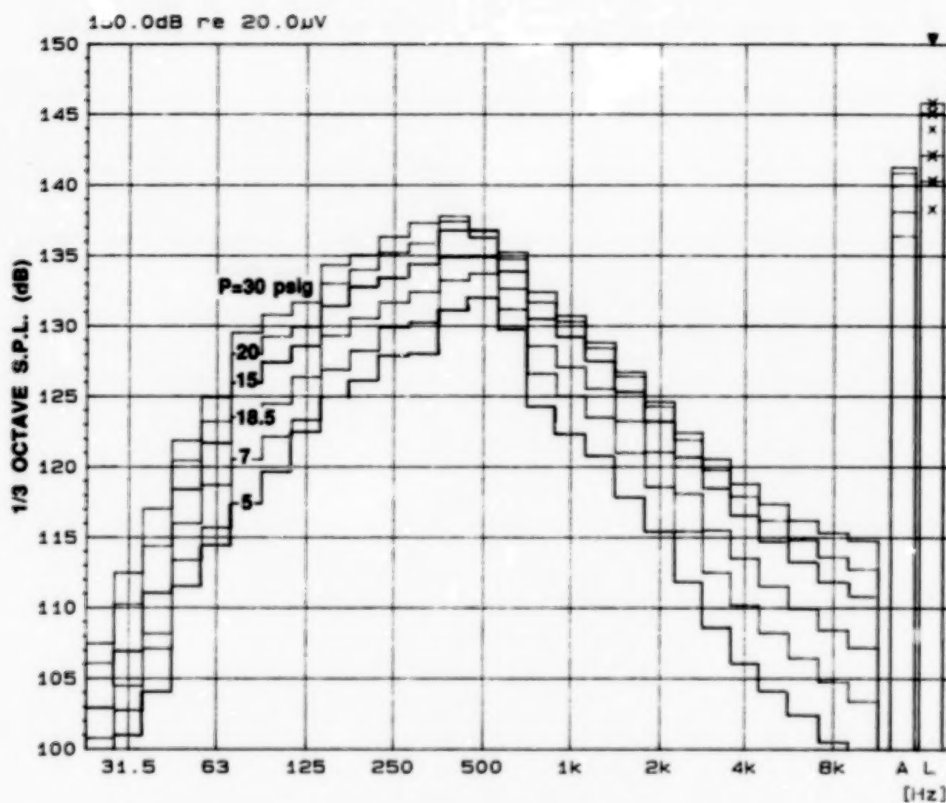


FIG. 6: VARIATION OF 1/3 OCTAVE S.P.L. WITH AIR PRESSURE (18.5 l dB)

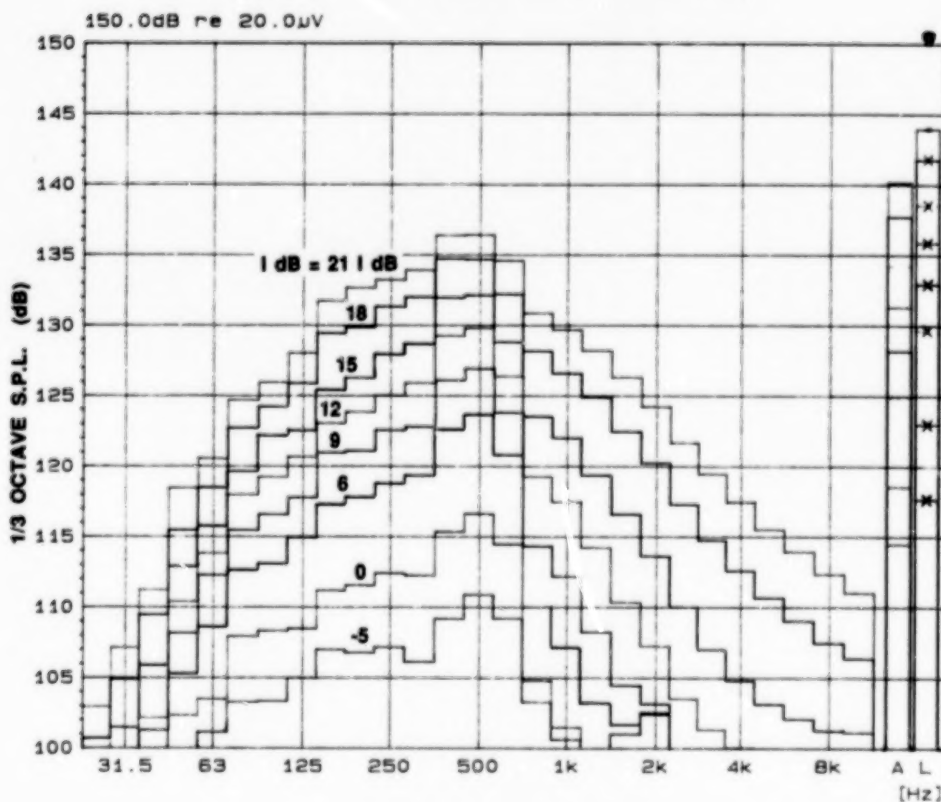


FIG. 7: VARIATION OF 1/3 OCTAVE S.P.L. WITH DRIVE CURRENT (P = 10 psig)

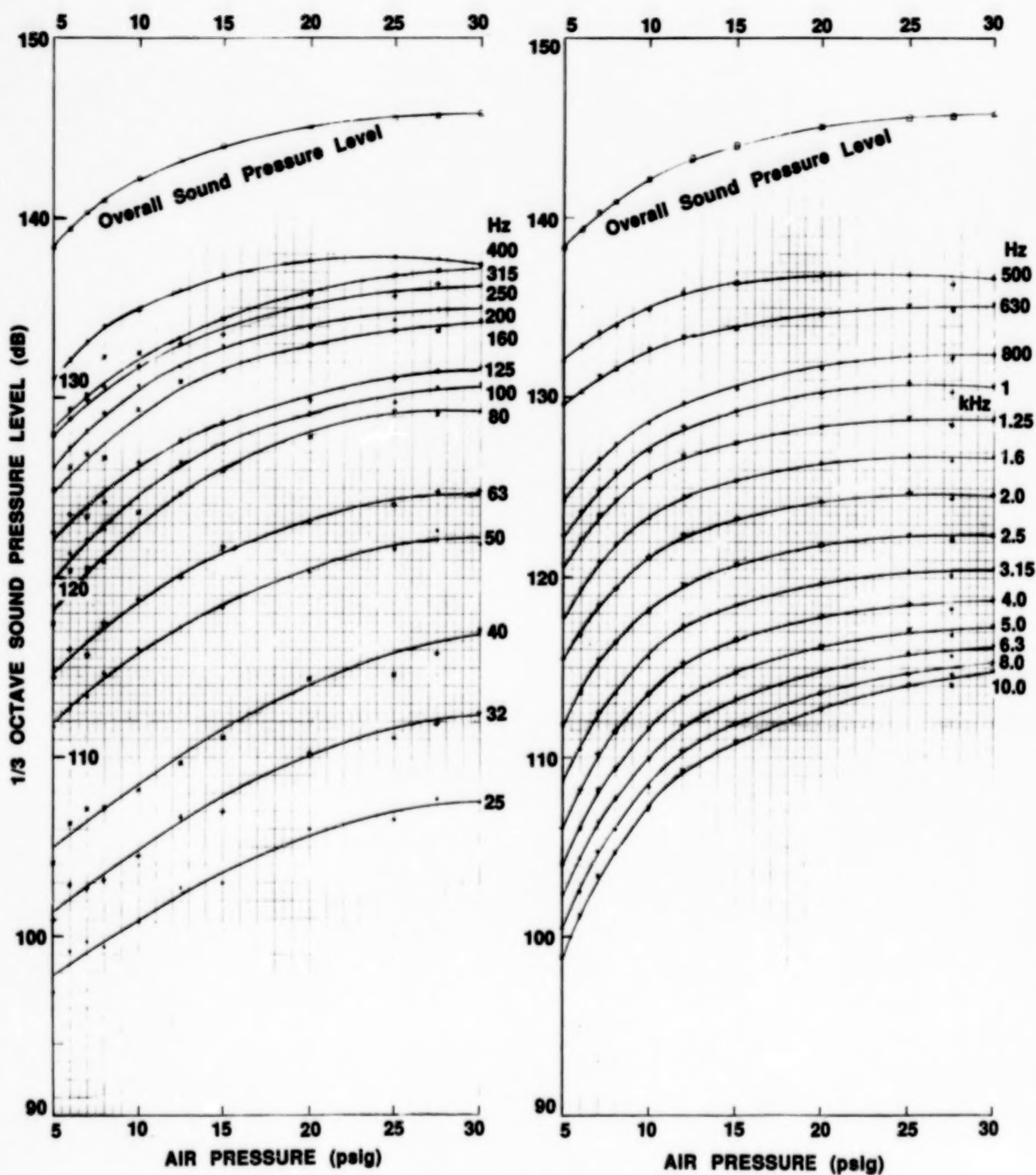


FIG. 8: 1/3 OCTAVE S.P.L. vs. AIR PRESSURE
(1 db = 18.5 dB)

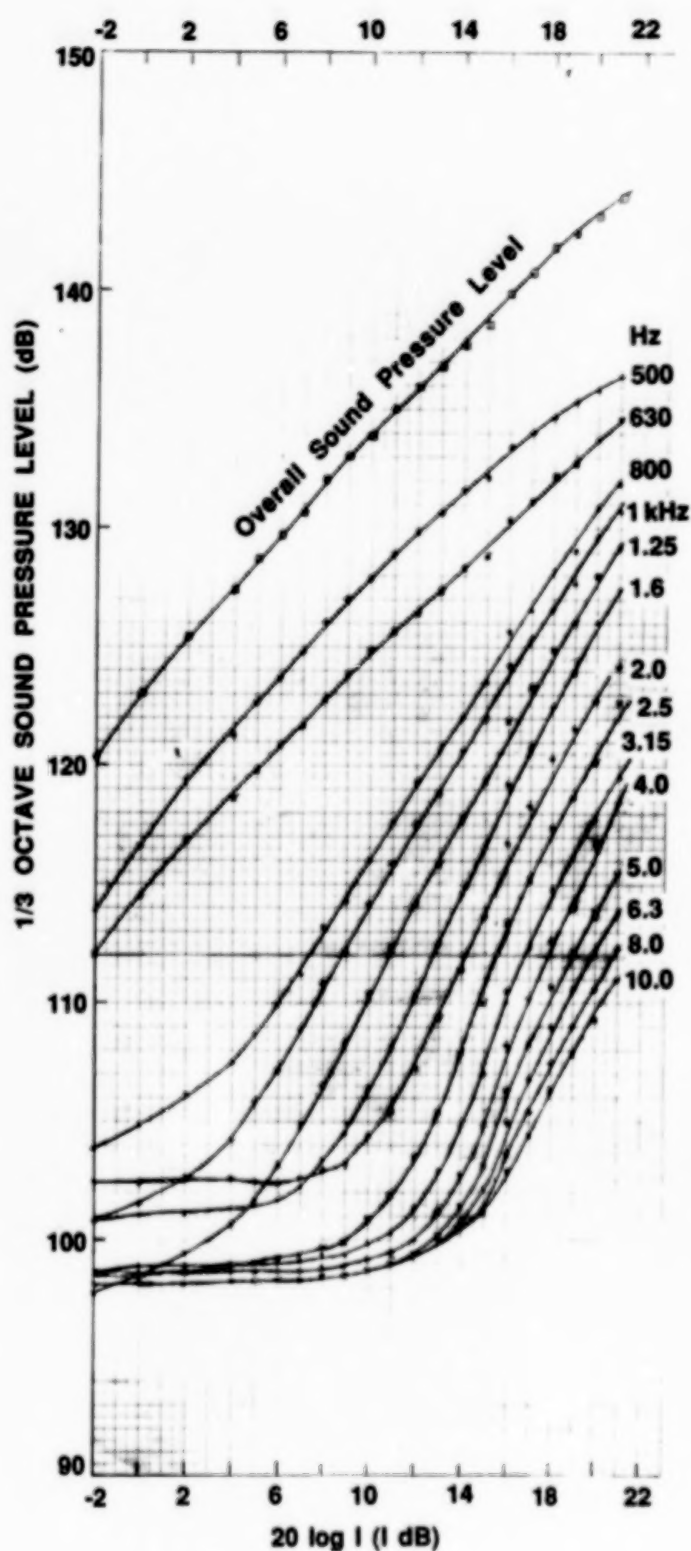
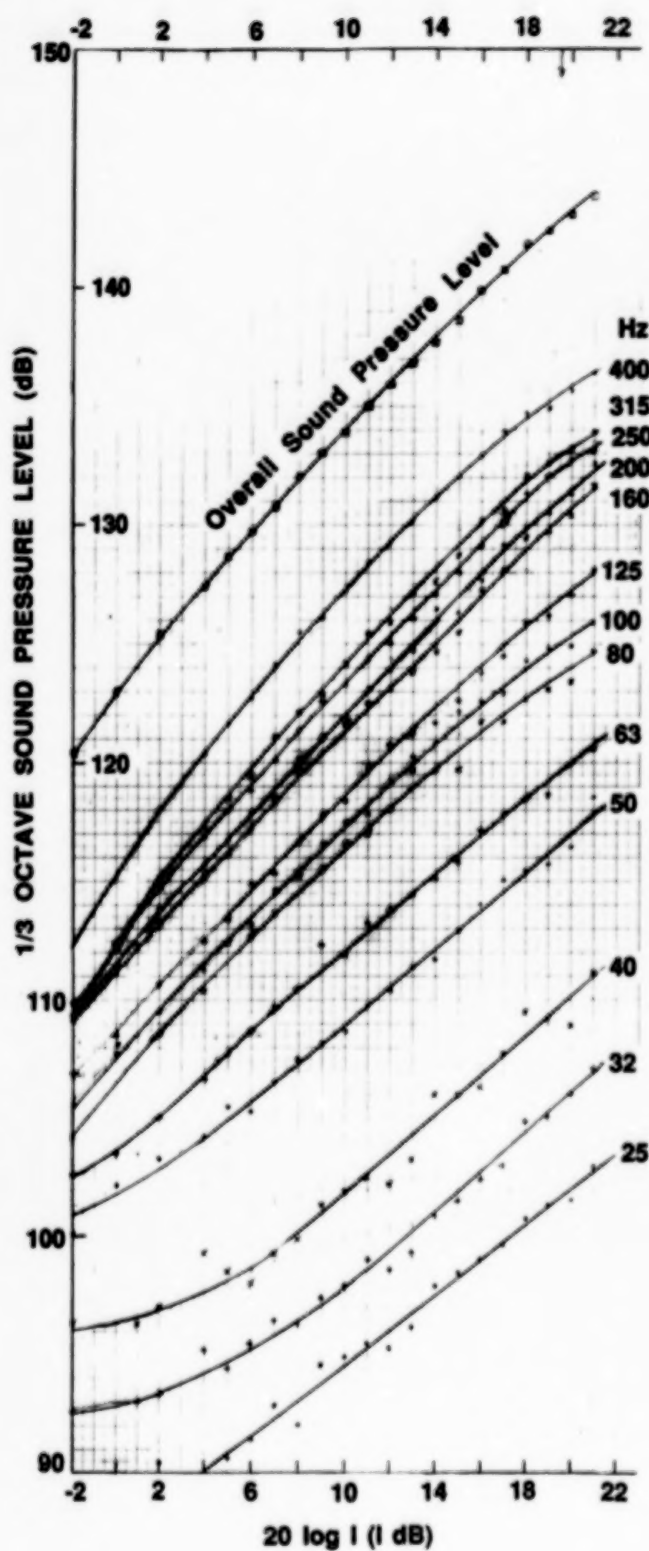


FIG. 9: 1/3 OCTAVE S.P.L. vs. DRIVE CURRENT
($P = 10$ psig)

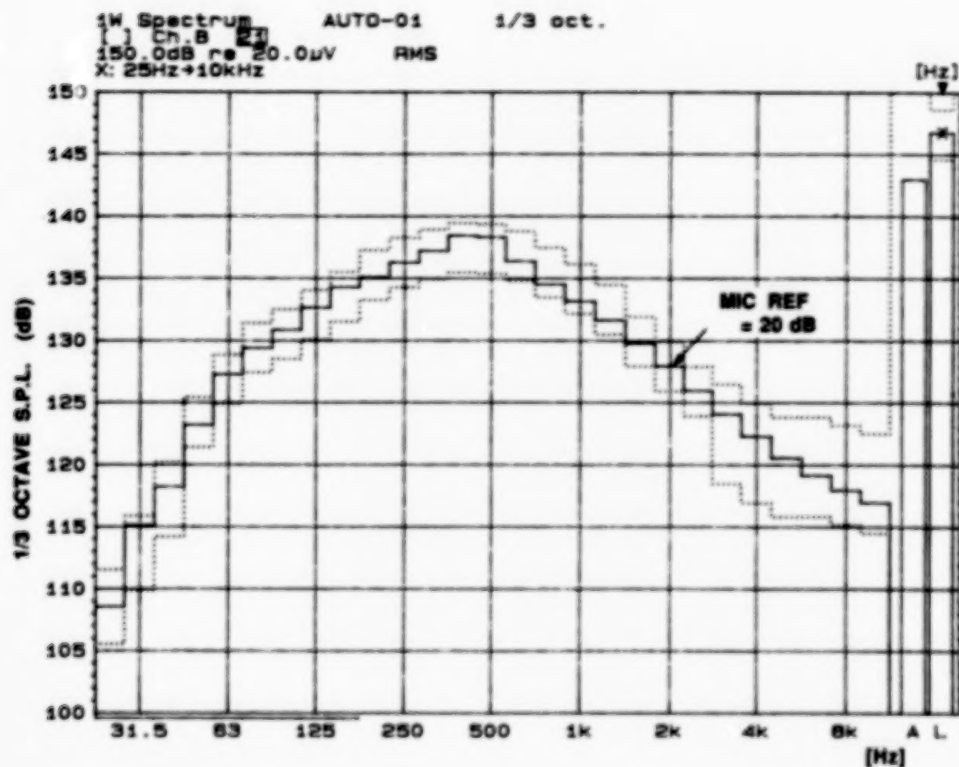


FIG. 10: QUALIFICATION SPECTRUM (AUTOMATIC CONTROL)
(P = 30 psig)

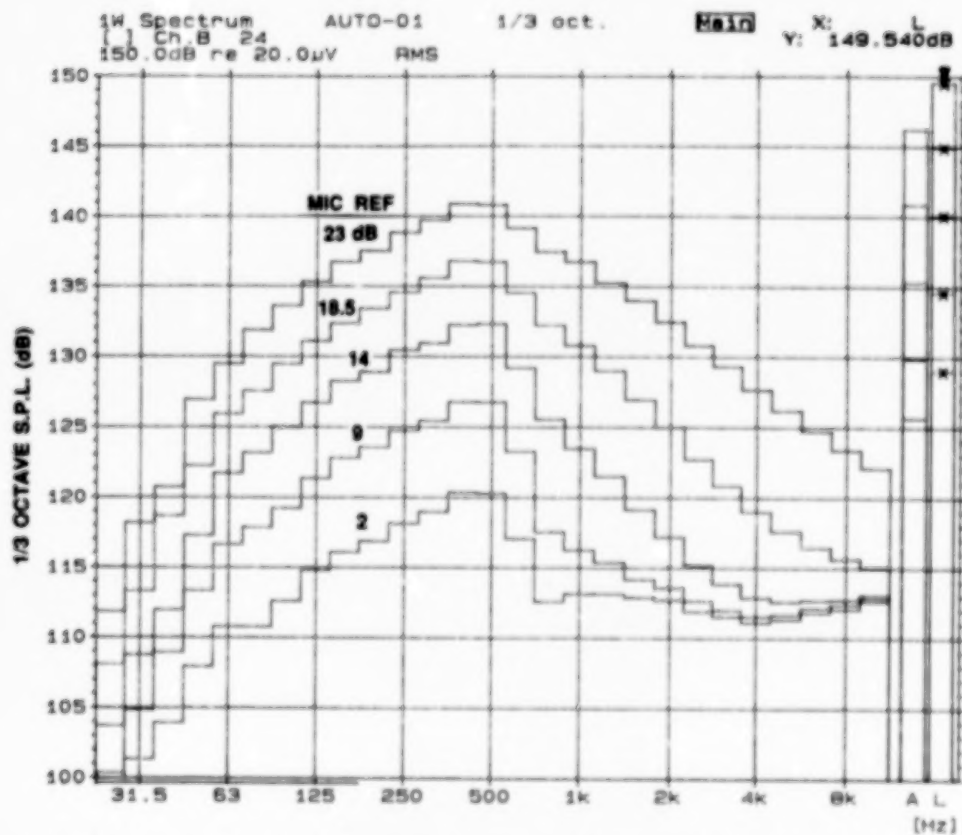


FIG. 11: PARALLEL SPECTRA (AUTOMATIC CONTROL)
(P = 30 psig)

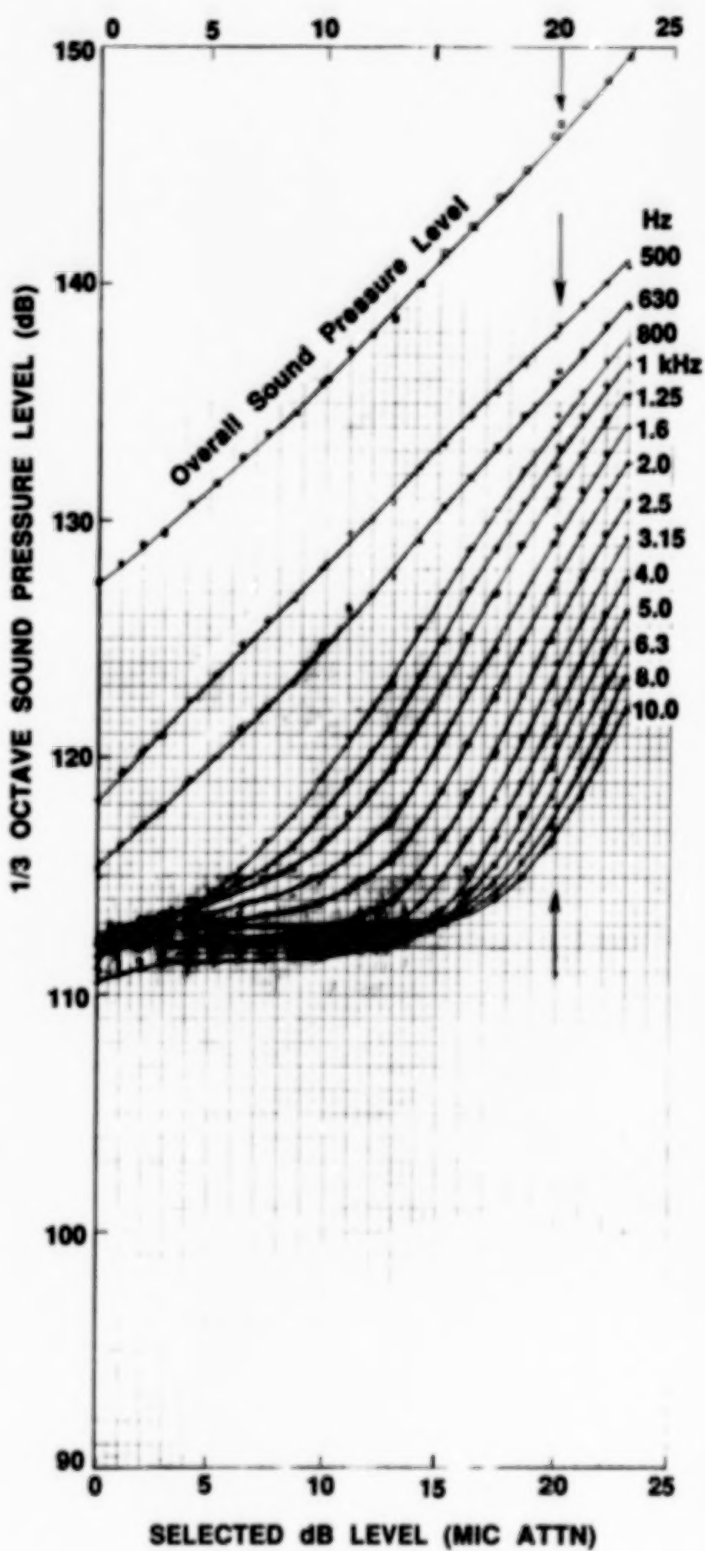
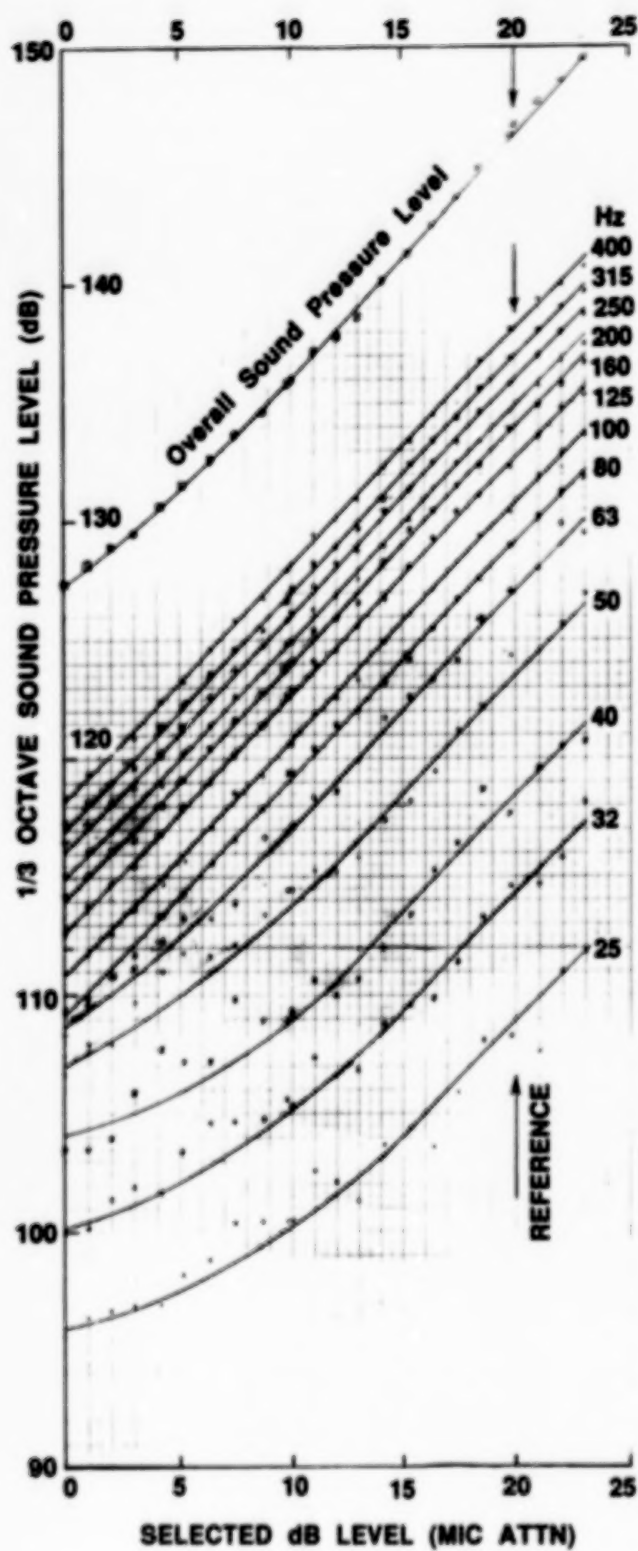


FIG. 12: 1/3 OCTAVE S.P.L. vs. SELECTED GAIN
(AUTOMATIC CONTROL) PARALLEL SPECTRA

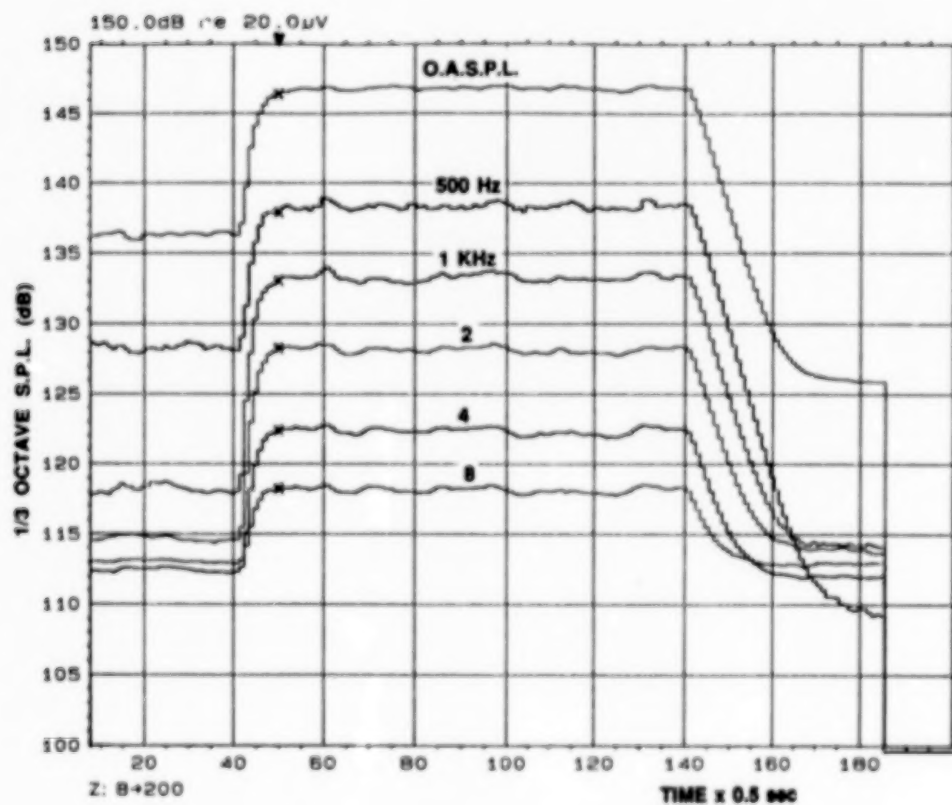
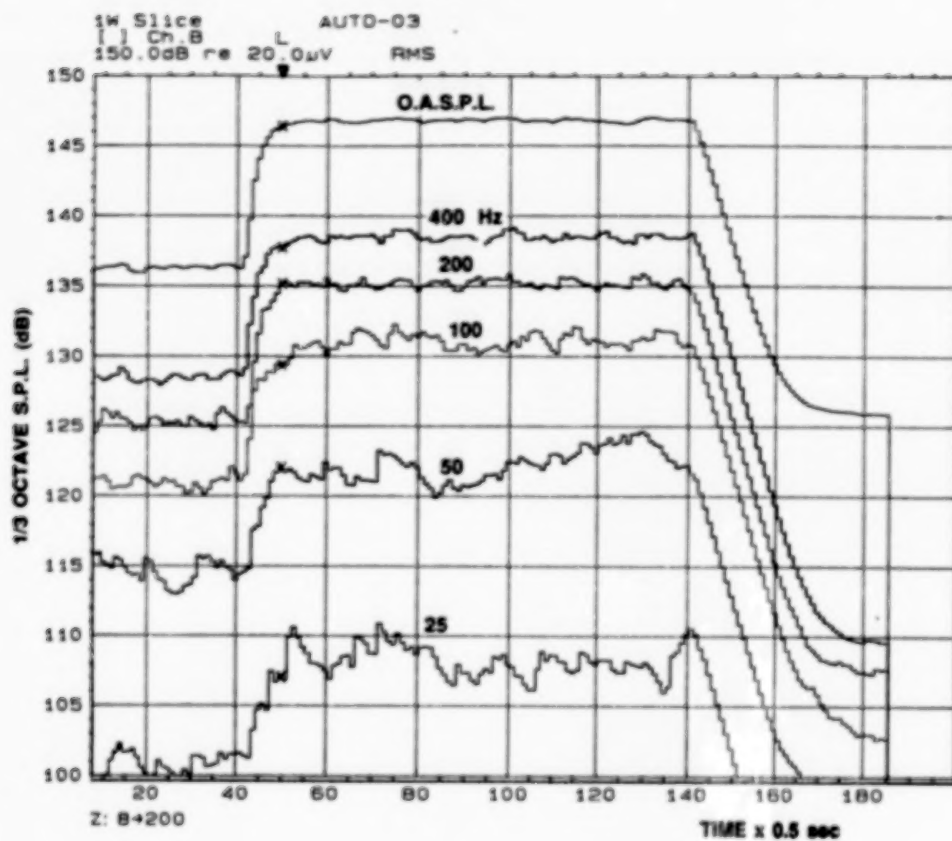


FIG. 13: QUALIFICATION TEST (AUTOMATIC CONTROL)
(P = 30 psig) (20 sec at 136.6 dB; 45 sec at 146.6 dB)

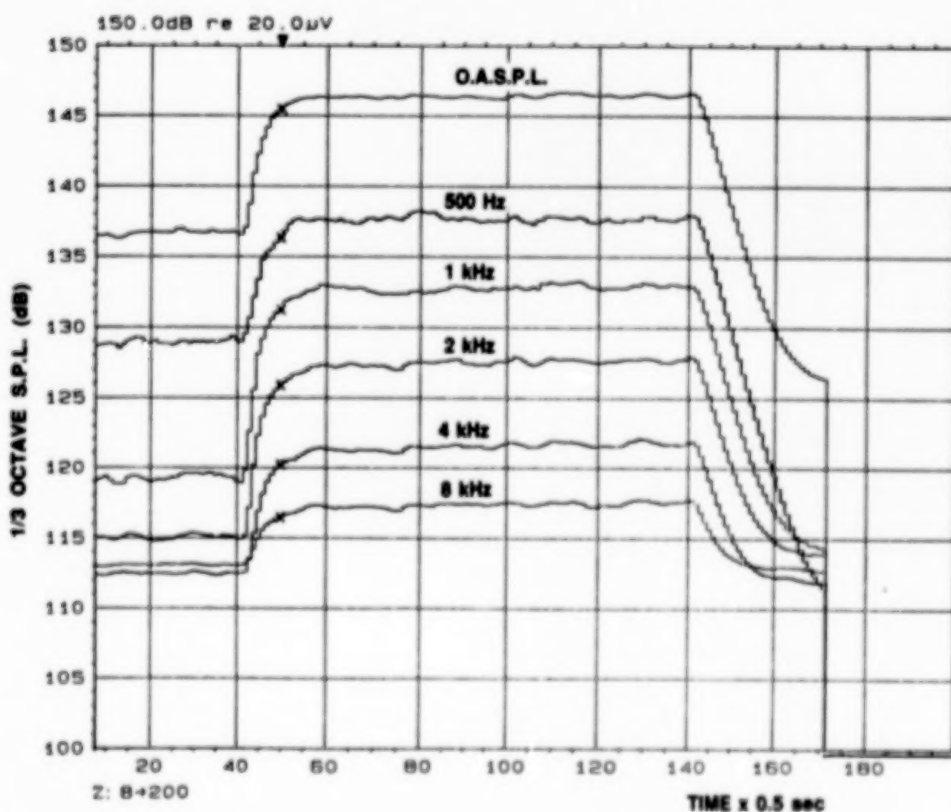
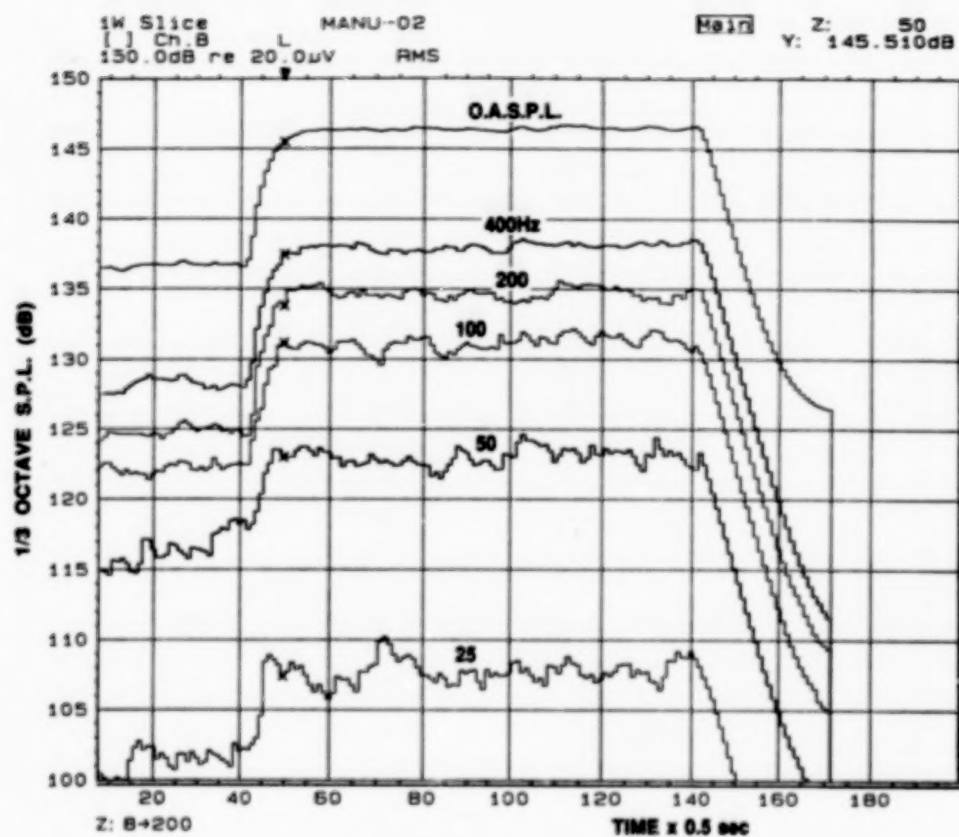
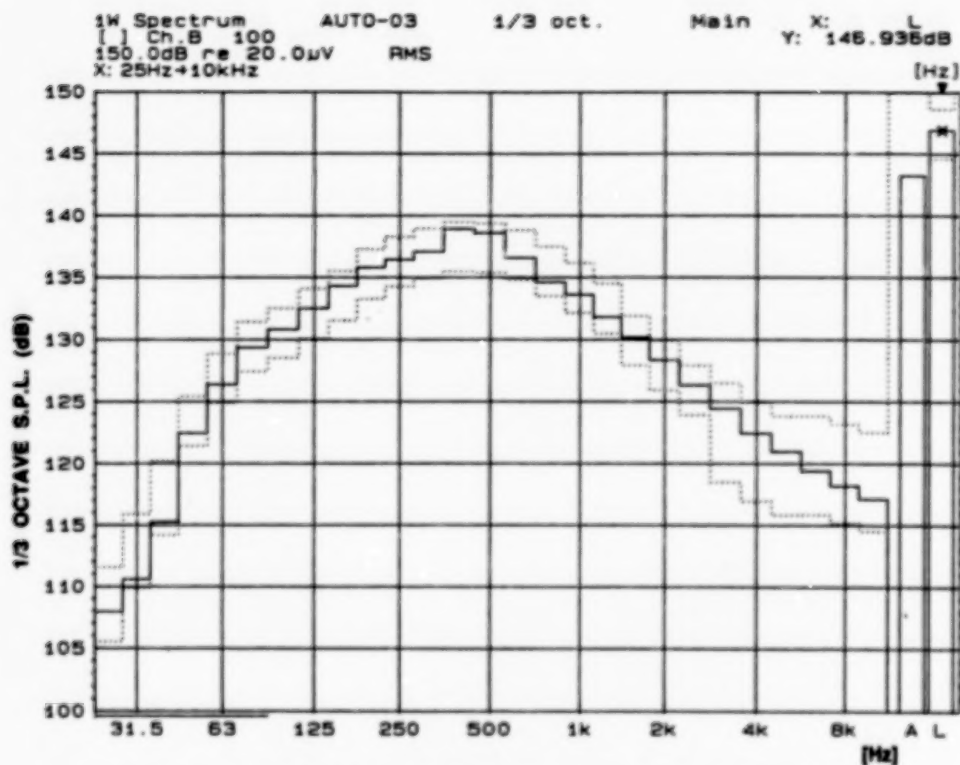
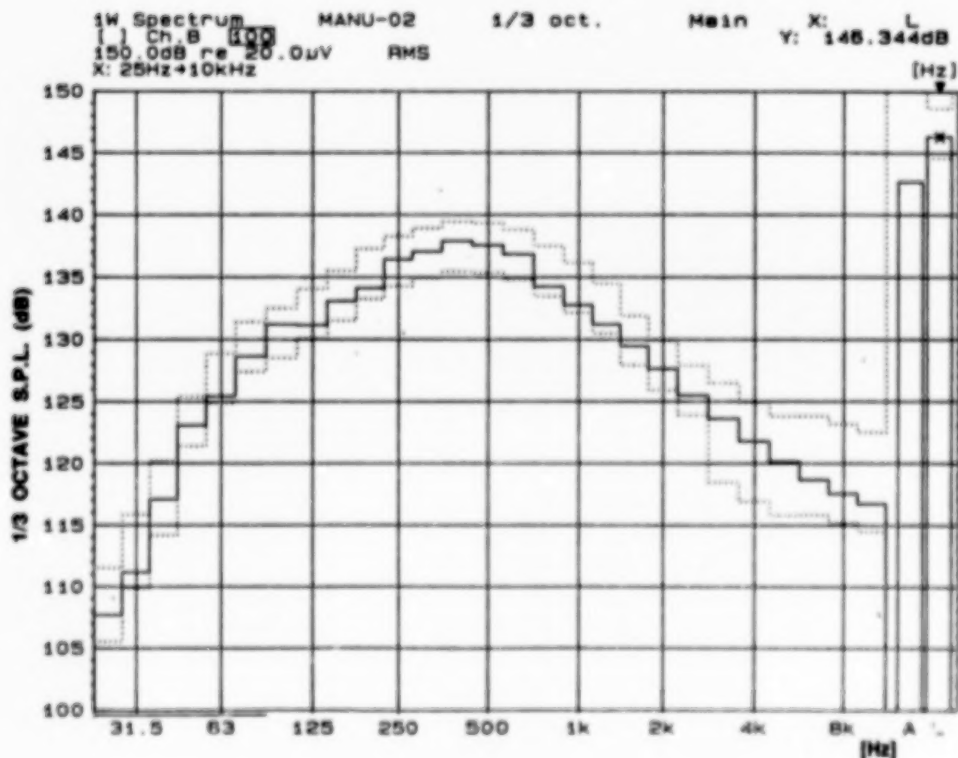


FIG. 14: QUALIFICATION TEST (MANUAL CONTROL)
(P = 30 psig) (20 sec at 136.6 dB; 45 sec at 146.6 dB)



**FIG. 15: QUALIFICATION TEST SPECTRUM
 (AUTOMATIC CONTROL) (P = 30 psig)**



**FIG. 16: QUALIFICATION TEST SPECTRUM
 (MANUAL CONTROL) (P = 30 psig)**

DETAILED MODAL TESTING OF A SOLID ROCKET MOTOR USING A PORTABLE TEST SYSTEM

Dr. Vladimir Glozman
California State Polytechnic University, Pomona

Ralph D. Brillhart
SDRC Engineering Services Division

ABSTRACT

Modern analytical techniques have expended the ability to evaluate solid rocket motors used in launch vehicles. As more detailed models of solid rocket motors were developed, testing methods were required to verify the models. Experimental modal analysis (more commonly known as modal testing) of space structures and launch vehicles has been a requirement for model validation for many years. However, previous testing of solid rocket motors has not typically involved dynamic modal testing of full scale motors for verification of solid propellant or system assembly properties. Innovative approaches to the testing of solid rocket motors were developed and modal testing of a full scale, two-segment Titan 34D Solid Rocket Motor (SRM) was performed to validate detailed computer modeling. Special modifications were made to convert an existing facility into a temporary modal test facility which would accommodate the test article. The assembly of conventional data acquisition equipment into a multiple channel count portable test system has made modal testing "in the field" feasible. Special purpose hydraulic exciters were configured to apply the dynamic driving forces required. All instrumentation and data collection equipment were installed at the test site for the duration of the test program and removed upon completion. Conversion of an existing test facility into a temporary modal test facility, and use of a multiple channel count portable test data acquisition system allowed all test objectives to be met and resulted in validation of the computer model in a minimum time.

INTRODUCTION

The Titan 34D design was reassessed following the 34D-9 launch failure in 1986. Two SRM make up the solid propellant portion of the Titan 34D launch vehicle. An individual motor comprises of 5 1/2 segments. Each segment is about 3.3 meters (130 inches) long, 3.05 meters (120 inches) in diameter, and weighs about 3.6×10^5 N (8×10^4 pounds). A cutaway view of a segment is shown in Figure 1.

The recovery program involved development of detailed finite element analysis models of the motor segments and the full motor assembly¹. These detailed models were then evaluated to assess the loads (both static and dynamic) which occur prior to and during launch. The effects of launch dynamics on the segment joints as well as the overall system were evaluated during this program. A finite element model representation of the SRM is shown in Figure 2.

Previous testing of SRM typically involved static evaluation of the loads and deflections which were used to correlate computer models. Beam representations of the SRM were used to evaluate dynamics for controls information. The latest recovery program also focussed attention on the participation of dynamics in the behavior of the SRM joints. In order to validate the model dynamic predictions, an extensive modal test was performed on a two-segment portion of SRM in a specially modified test facility. Testing was performed with segments containing live propellant so that the true propellant properties were included in the test. Two segments were used in the test so that the joint which is used to connect the segments was an integral part of the evaluation and verification of the model.

An existing facility, which permitted testing of live propellant articles, was modified to handle the large test article while accounting for the live propellant. This facility was used in order to keep the program cost under control while allowing the facility to be readied in as brief a time as possible.

Because the remote test facility did not include test hardware, a portable system was assembled to allow all parts of the system to be moved to the site, set up for the test and then removed at the completion of testing.

This paper describes the configuration of the test facility for this special testing program and details the portable test system which was used for conducting the test.

TEST FACILITY

The test article size and weight required that a test facility be identified which would accommodate the two-segment SRM specimen. In addition, the test was to be conducted below ground level for safety reasons. The test facility which was selected would satisfy this requirement, but its isolated location required that portable test equipment be used to perform the modal test. While the identified test site would accommodate the SRM test article, the existing site needed to be converted into a temporary modal testing facility.

The modal survey test facility consisted of two primary buildings. The main test building, where the modal testing was performed, contained a 6.1 meter (20 feet) deep by 5.3 meters (18 feet by 18 feet) square concrete lined test pit to accommodate the test article. A temporary instrumentation building was fabricated adjacent to the main

¹"Dynamic analysis and testing for the Titan 34D Recovery Program". SDRC Final Report to CSD, October, 1987.

building to serve as a storage and temperature conditioning facility for the SRM segments prior to their installation in the main test facility. This temporary building was also used to install some of the instrumentation to be used in the modal test prior to the assembly of the test article. Movement of the SRM segments between the buildings was accomplished using a crane. Each of the SRM segments was lowered into the test pit through a roof opening in the main test building. Final assembly of the segments then occurred in the main test facility where the test article was installed in the vertical orientation.

Since the main building was an existing one, special modifications to the building and the test pit had to be made in order to perform the modal test. The modal testing was to be performed with the two segments assembled and then suspended to simulate a free-free boundary condition. This free-free boundary condition was simulated by supporting the test article from the forward segment joint with an airbag suspension system. The two segment test article was supported from above to place the joints in tension as it is in flight. Since this suspension system had a very low stiffness associated with it, the rigid body modes of the test article on the suspension system were very low in frequency (below 2 Hz) which gave the appearance of a free boundary condition.

The suspension system was built over the top of the test pit. The overhead support assembly consisted of a tubular ring attached to the floor by four vertical strut assemblies. Twenty airbag isolators were mounted on top of the tubular ring for suspension of the test article as shown in Figure 3. A load plate was installed on top of the airbags. Steel rods and cables were attached to this load plate on one end and the test article on the other. A handling ring, installed on the upper joint of the test article, was used to attach the steel cables which ran from the test article to the suspension system. The parameters used for the generation of a finite element model to analyze the overhead support are listed in Table 1. The general layout of the test facility is shown in Figure 4.

In addition to the suspension system, a support stand had to be installed in the bottom of the pit to allow the test article to be stacked and assembled prior to the suspension system being attached and activated. This base support was comprised of a main supporting ring with eight equally spaced legs around the circumference. The base support was analyzed using a finite element model, and its main parameters are also summarized in Table 1. Final instrumentation was installed on the test article after the two segments were joined while resting on this base support stand. Once all of the test article assembly and instrumentation were completed, the airbag suspension system was inflated, lifting the test article off of the support stand.

Work platforms were also installed in the test facility which allowed access to different levels of the test article for installation of instrumentation and the attachment of hydraulic exciters. The dimensions of the specimen and the pit allowed access to install instrumentation around the joint between the two segments.

TEST FACILITY STRUCTURAL EVALUATION AND VERIFICATION

Proof load testing of the overhead support structure was performed to verify structural integrity of the main elements of the assembly. This included testing of the upper ring with steel cable sling assemblies as well as the main frame with the airbags under the designed loading conditions. The test setup for the proof loading was as shown in Figure 5. A specially designed bottom ring was secured to the bottom of the test pit and connected to the sling assemblies by twenty steel stranded cables. Separate turnbuckles on each cable were used to achieve equal cable tension prior to pressurization of the suspension system. Four pressure gauges were used to control the airsprings as the air pressure was increased to that required for the proof test (8.27×10^5 Pascal or 120 psi). Four LVDT's monitored airspring heights in the range from 0.05 to 0.15 meter (2 to 6 inches). The total maximum proof load was limited to 3.9×10^5 N (2.0×10^5 pounds) which is 25% higher than the suspended weight of the assembled test article.

During the proof test, the air pressure in the air springs was gradually increased and recorded every 3.45×10^4 Pascal (5 psi), together with the recording of airspring heights and the upper ring position. After the maximum load of 9.07×10^5 N (2.04×10^5 pounds) had been achieved, the air pressure was removed and the overhead support assembly and its mounting was thoroughly inspected. Since no sign of failure or plastic deformation was observed, the fixture had passed the proof load test and was approved for subsequent operations. At this time the positioning and stacking of the two-segment test article was performed in preparation for the execution of the modal testing program.

PORTABLE TEST SYSTEM

A portable large channel modal test system allowed the remote testing to be setup and performed in six days. The excitation systems and the data collection equipment used were both designed and assembled to be easily transported and installed at remote facilities. The next sections describe the equipment which was used.

Excitation Equipment

The size and heavy damping properties of solid rocket propellant dictated that large excitation forces be used for conducting the modal survey. Hydraulics exciters were chosen since the system size could be kept to a minimum which would allow it to be much more portable than electrodynamic exciters with equivalent force capability. The hydraulic exciters were powered using portable hydraulic pumps and actuated with high speed servo valve actuators. The high speed actuators allowed the frequency range of interest (2 to 128 Hz) to be met for the modal survey. Four hydraulic exciters were employed for the test. Two of the exciters were installed at the aft joint of the aft SRM segment. The other two exciters were installed at the handling ring of the forward segment. The exciter locations are shown in Figure 6.

Exciter locations were selected by using the finite element analysis model prior to the test. Predictions of the test article frequency response functions (FRF) were made and these were evaluated to determine whether all of the dynamic modes in the frequency

range of interest could be extracted with the exciters positioned at these locations. This type of evaluation allowed the fixturing which was required to attach the exciters to the test article to be fabricated ahead of time while giving high confidence for a successful test. The two shakers at the aft end of the test article were rigidly constrained to a backup structure. The shakers installed at the forward end of the test article were attached to reaction masses since there was no rigid structure which could be used to react against.

The hydraulic shakers are shown in Figure 7. Special consideration was given to the safety of using a hydraulic shaker attached to a solid propellant test article. Fittings were designed for attachment of the shakers to the test article which would serve as a mechanical fuse and limit the amount of force which could be applied to the SRM segments. With these fittings, if a preset force level limit was exceeded, the fitting would slip, thereby keeping any additional force from transmitting to the test article.

Both random and sinusoidal excitation signals were used to drive the test structure. The random signals were provided by independent sources so that burst random (or random transient) excitation [1] could be employed. Multi-Point Random (MPR) excitation [2] was used as the primary investigative excitation type for the modal survey. Confirmation of mode shapes and investigation of damping characteristics were performed using sinusoidal excitation with a closed loop Multi-Phased Stepped Sine (MPSS) [3] shaker control and mode measurement system.

Signal Measurement and Conditioning Equipment

A high channel count data acquisition system was required for the test program to obtain all of the necessary FRF for the modal survey. Due to the nature of modal tests and the requirements for the stationarity of the data [4], roving instrumentation was not used. As a result, all of the instrumentation was installed prior to the test so that all data could be collected quickly once the testing was underway. A total of 230 accelerometers were installed on the two SRM segments, on the propellant bore, on the propellant inhibitor, and on the outer casing. These transducers were installed at 132 locations which had been defined by pretest analysis efforts. Figure 8 shows the distribution of the measurement locations which were used in the test. An equal number of amplifier channels were provided so that there was a one-to-one correspondence between the accelerometers and the signal conditioning. Load cells were installed at each of the shaker excitation locations to measure the applied force. The resulting force and accelerometer measurements were used to compute the FRF for the test article.

All of the signal conditioning equipment was installed in a standard 19-inch instrumentation rack which was used to transport the equipment to the test site. The same rack contained a switch box to select the set of data which was acquired at any time during the test. Oscilloscopes, which were used to monitor the signals from all channels during the data acquisition process, were also rack mounted for portability.

Having all of the test equipment installed in racks prior to shipment to the test allowed the setup time to be kept to a minimum while the test hardware was tied up. All of the

accelerometers, as well as the other control equipment and the data acquisition system, were installed over a four day period.

Data Acquisition Equipment

The data acquisition system for this modal survey was built around a GenRad 2515 computer aided test system. This system is a 16 channel data collection and processing system. Using the four excitation signals from the load cells and twelve response measurements at a time, all of the measurements on the test article were made. The excitation signals were monitored continuously while groups of twelve responses were measured and the corresponding FRF were obtained. Multiple time ensembles were collected and averaged to compute the FRF. As each set of FRF was computed, the data was stored on the data collection system disk and transferred to the data analysis computer for processing. In order to collect all of the FRF data using random excitation, twenty data sets of twelve each were collected.

Sinusoidal data acquisition was performed in addition to the random excitation. The test data acquisition system has been modified with the addition of a 240 channel multiplexed data collection system for MPSS operation [5]. Using this hardware single frequency sine dwell mode shapes were measured and stored on the data acquisition system storage media. Multiple force levels were also used to determine the linearity of the dynamic response of the system. The mode shapes were transferred to the data analysis system where they were compared to the data obtained from the random survey; orthogonality checks were completed with respect to the analysis mass matrix.

Data Analysis Equipment

A Vax computer was used to process the modal data at the test site. By having the data analysis computer available, the test data was immediately transferred to the analysis system for review. Data processing was performed while further data acquisition proceeded. This arrangement of the test system permitted rapid evaluation of the modal results to determine whether further testing was needed and allowed quick identification of any instrumentation errors which could be fixed prior to further data collection.

Data transfer between the data collection system and the data analysis system was performed using direct transfer of the storage disk as well as a communications link between the two systems. All of the modal parameters were extracted on the data analysis system. Then the mode shape results were transferred back to the data acquisition system where animation of the mode shapes were performed.

Figure 9 shows the entire setup which was used during the modal test program.

CONCLUSION

Requirements for specialized tests often demand that remote facilities be used for testing. Even when test locations are convenient, extensive effort may be required to install all of the test equipment prior to the start of a test. Portable test equipment allows a test to be setup rapidly to reduce the impact on the overall program schedule. New sophisticated numerical algorithms have been developed and greatly improved the

collection of data during modal tests. The assembly of a complete portable modal testing capability has allowed modal testing to be performed in virtually any location with reduced setup time. This has kept overall test time and program costs to a minimum. Further improvements in the test hardware computational capability and portability have taken place since this test was conducted. Extremely sophisticated modal test laboratories can be quickly transported from one site to another keeping test time to a minimum.

REFERENCES

1. Olsen, N.: "Excitation Functions for Structural Frequency Response Measurements". Proceedings of the 2nd International Modal Analysis Conference, 1982, pp. 894-902.
2. Hunt, D.L.; Peterson, E.L.: "Multishaker Broadband Excitation for Experimental Modal Analysis". SAE Paper 831325, 1984.
3. Vold, H.; Williams, R.: "Multiphase-Step-Sine Method for Experimental Modal Analysis". IJMA, 1986.
4. Chen, J. C.; Hunt, D. L.: "Application of Multiple Input Random and Polyreference Analysis Techniques to the Galileo Spacecraft Modal Test". 25th Structures, Structural Dynamics, and Materials Conference, AIAA-84-1069, 1984.
5. Hunt, D. L.: "A Modern Approach for Modal Testing Using Multiple Input Sine Excitation". AIAA Dynamics Specialists Conference, AIAA-87-0964-CP, 1987.

Table 1. Support Structure Parameters.

<u>Structure</u>	<u>Base Support</u>	<u>Overhead Support</u>
Dimensions	3.1 m diameter by 1 m height	6.7 x 6.7 x 2.5 m
Material	A36 Steel Weldment	A36 Steel Weldment
Weight, kN	6.7	29.4
Design Load, kN	800	815
Maximum Vertical deflection, mm	0.3	1.7
Maximum calculated stress, MPa	74.4	64.5
Factor of safety on yield	3.34	3.85

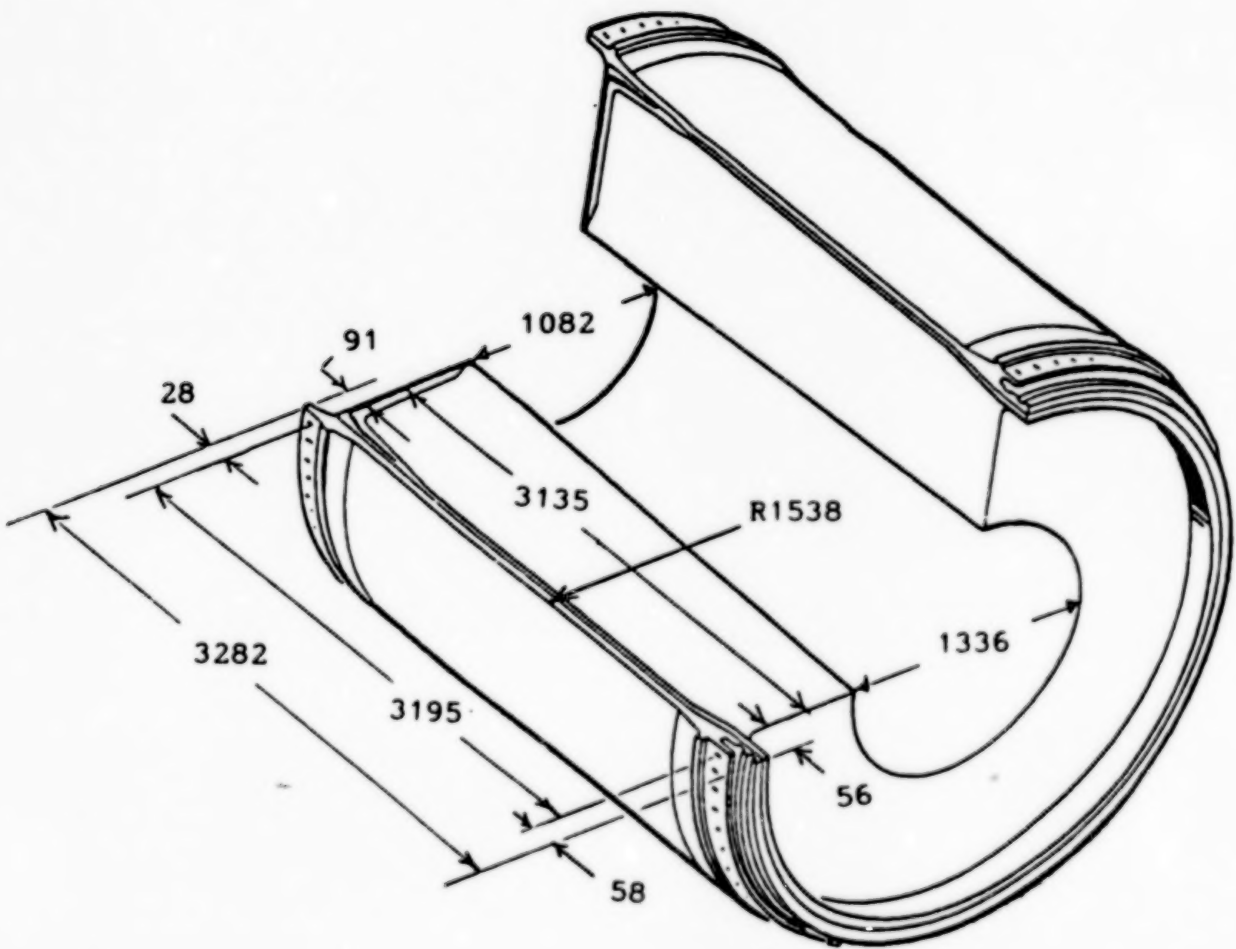


FIGURE 1. A cutaway view of the Titan 34D SRM segment showing the dimensions.

DISPLAY OPTIONS, HIDDEN_LINE
SELECT MENU

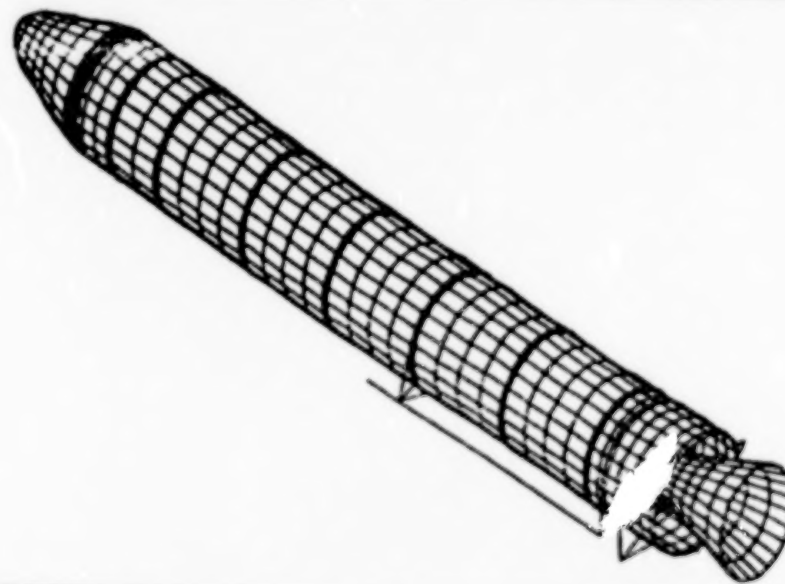
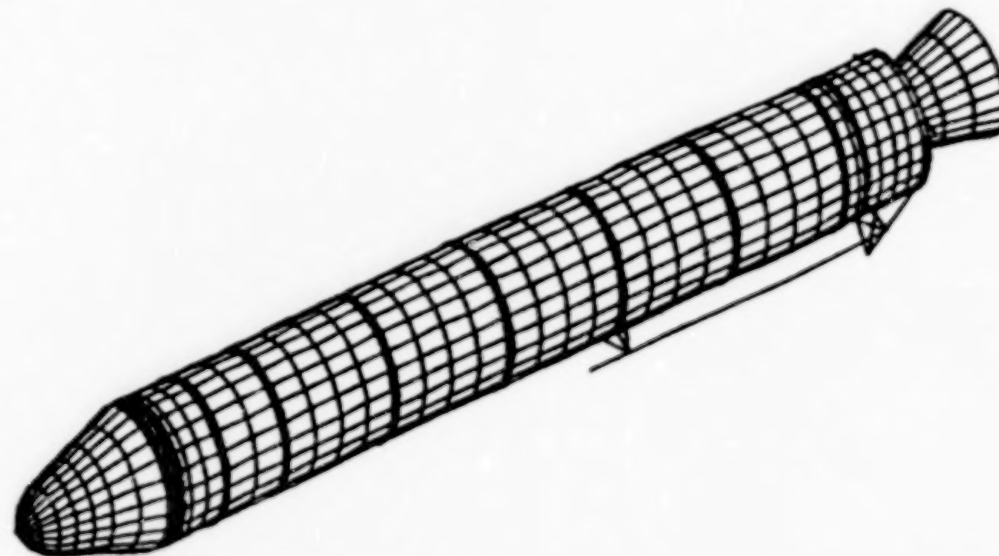


FIGURE 2. A finite element model of the Titan 34D SRM was developed in preparation for the modal test and for loads analysis.

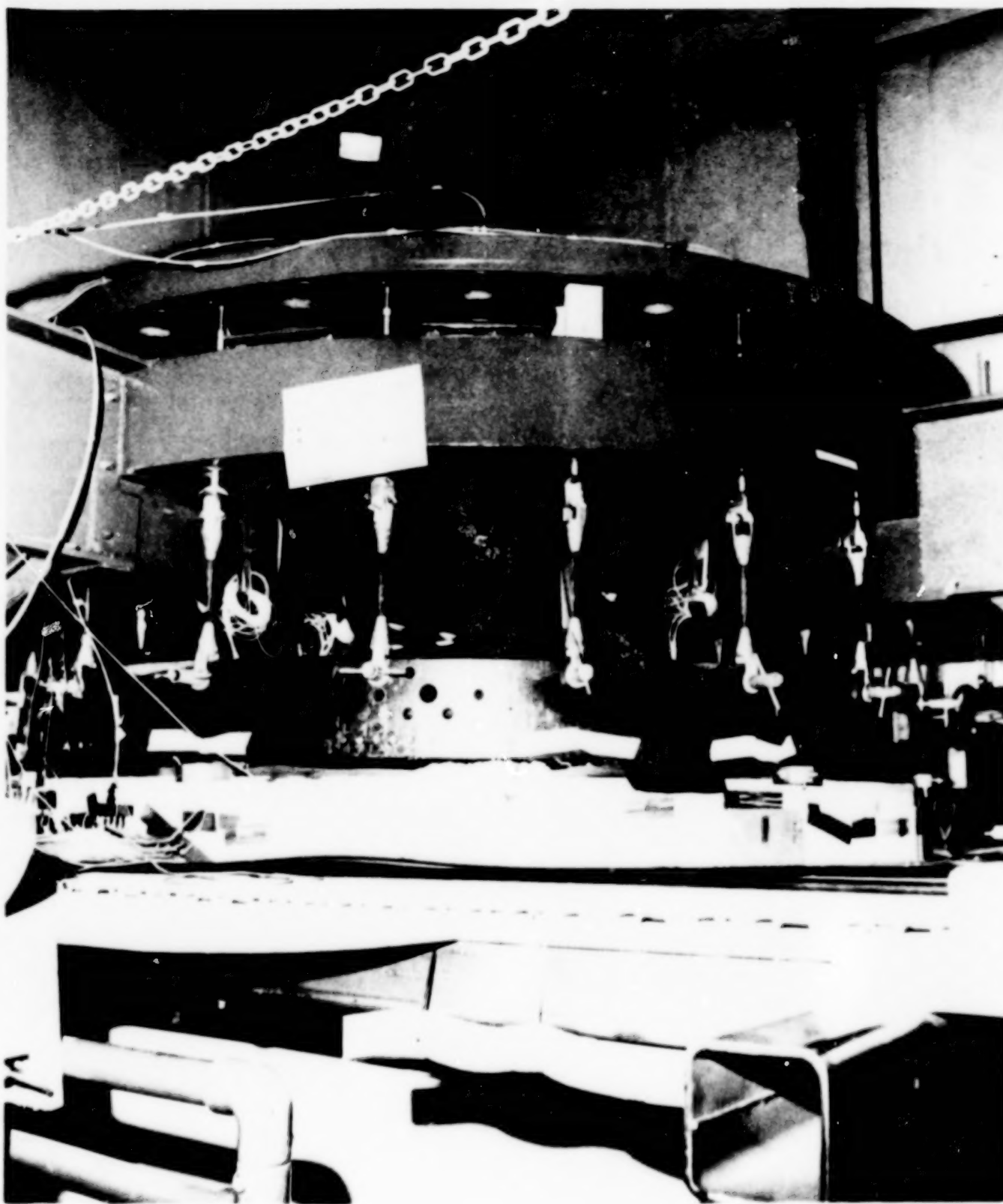


FIGURE 3. The test article suspension system used twenty airbag isolators to support the two segment assembly.

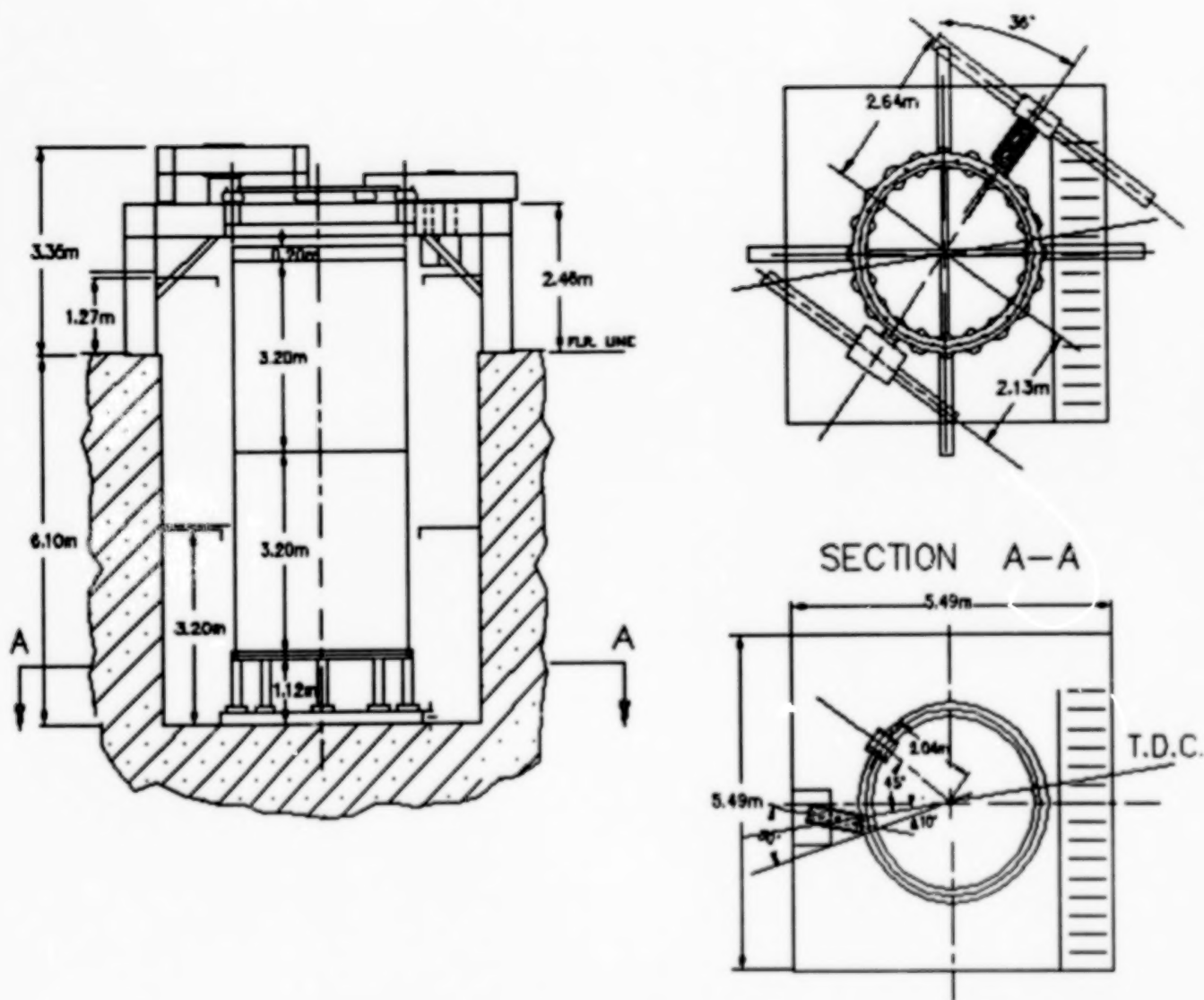


FIGURE 4. The test facility layout shows the orientation of the test article as installed.

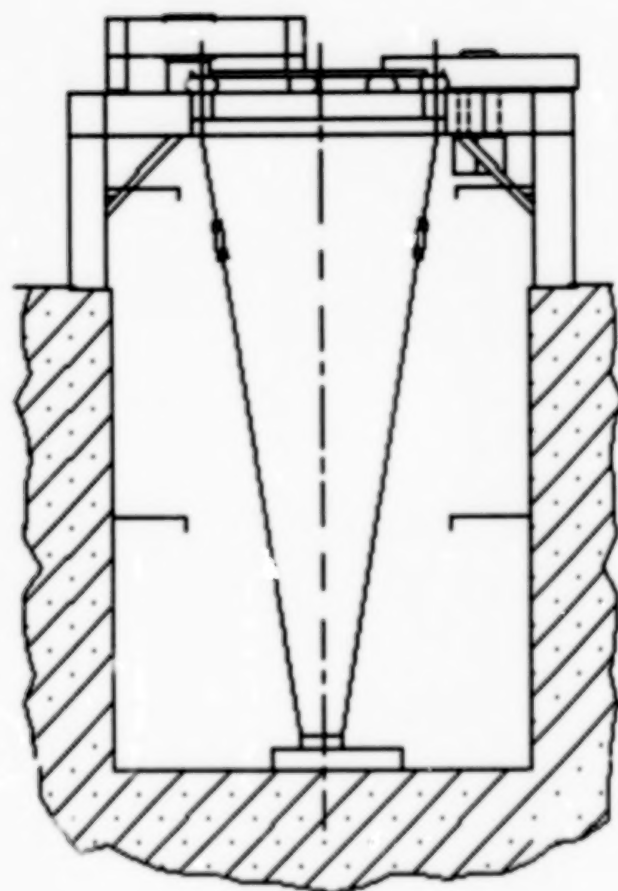


FIGURE 5. The configuration of the proof load test which was performed prior to installation of the test article to verify the suspension system.

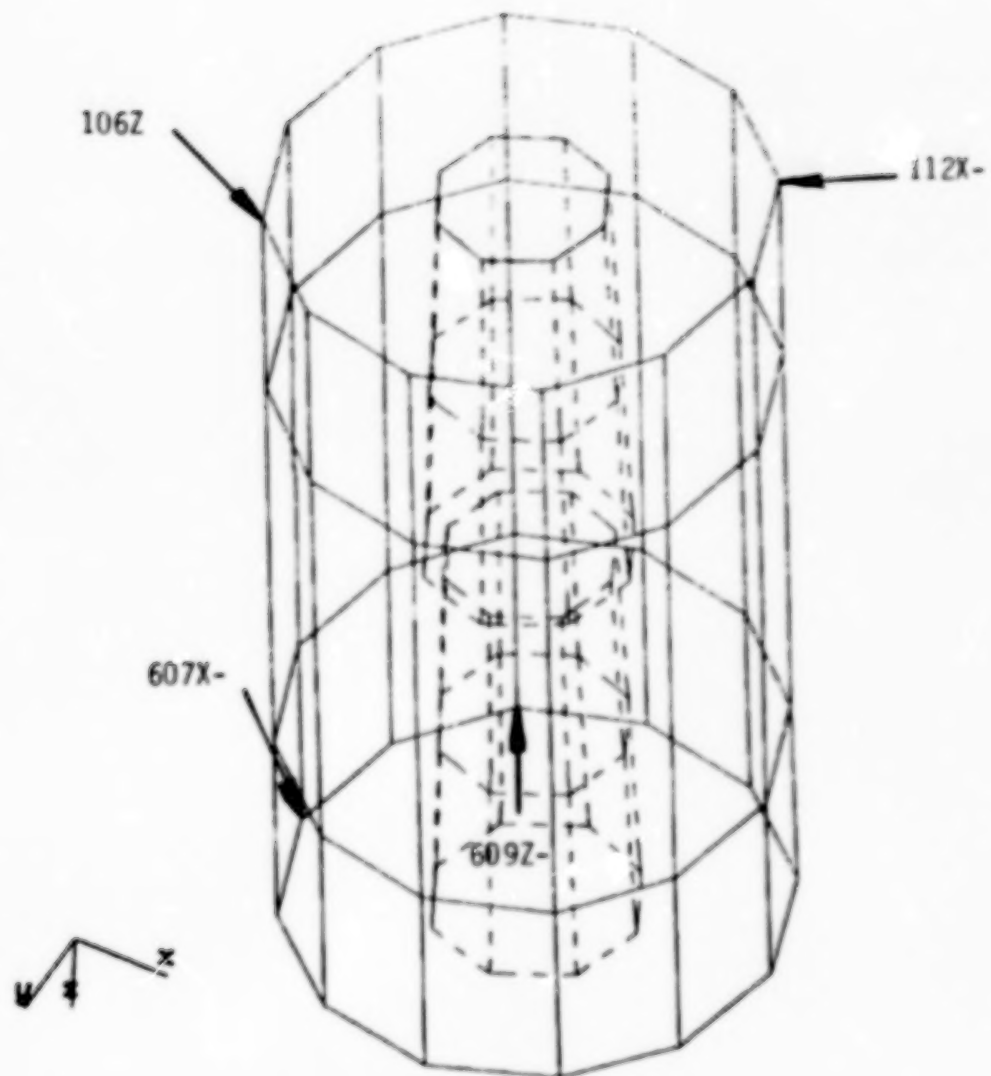
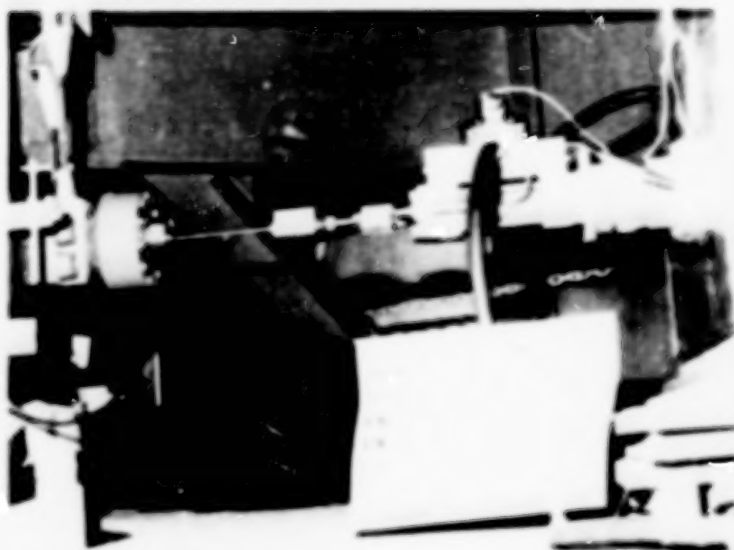


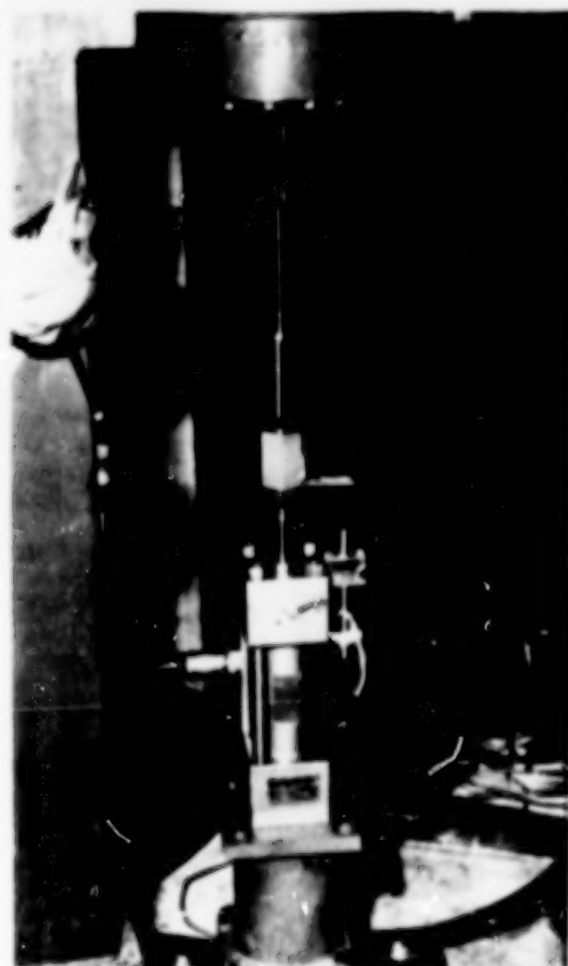
FIGURE 6. Four exciter locations were used to perform the modal survey: two at the top segment handiing ring and two at the bottom segment flange.



a)



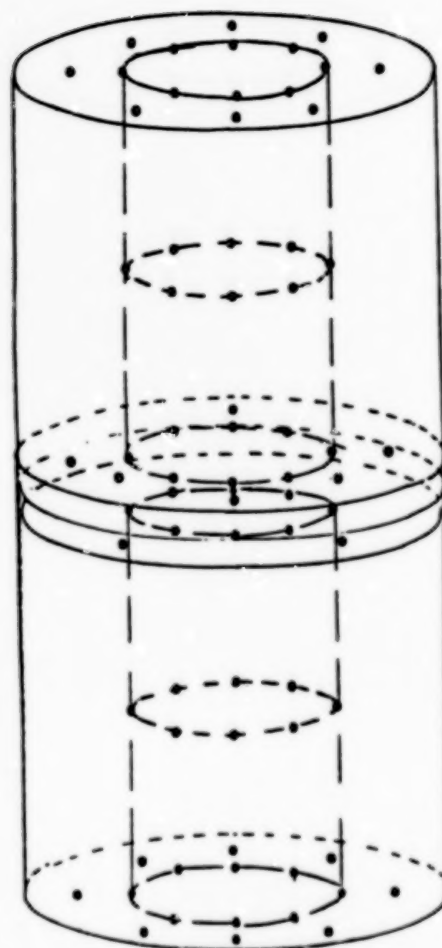
b)



d

FIGURE 7. The hydraulic exciters as installed:
 a) top segment radial exciter
 b) top segment skewed exciter
 c) bottom segment horizontal exciter
 d) bottom segment axial exciter

230 Accelerometers total were installed on the test article



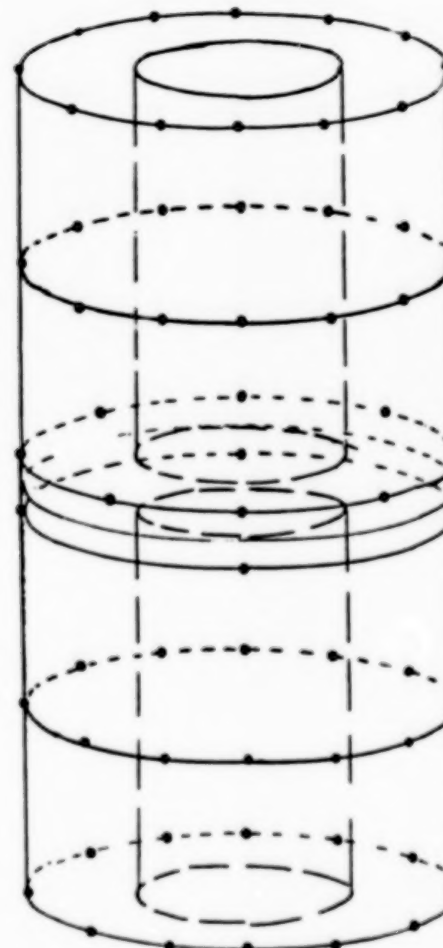
Top segment

**Radial = 24
Tangential = 12
Axial = 36**

Bottom segment

**Radial = 24
Tangential = 12
Axial = 36**

**144 accelerometers
installed on exposed
propellant**



Top segment

**Radial = 32
Tangential = 8
Axial = 7**

Bottom segment

**Radial = 24
Tangential = 8
Axial = 7**

**86 accelerometers installed
on segment casing**

FIGURE 8. Accelerometers were installed on the propellant bore, propellant faces, and on the casing of both segments.

INNOVATIONS IN DYNAMIC TEST RESTRAINT SYSTEMS

Christopher J. Fuld

McDonnell Douglas Space Systems Company

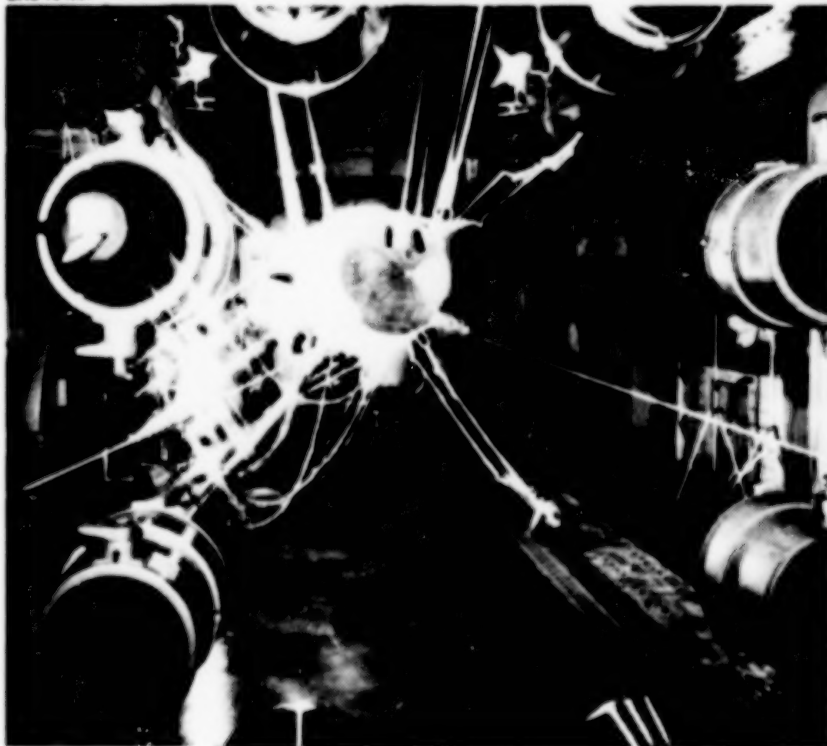
ABSTRACT

Recent launch system development programs have led to a new generation of large scale dynamic tests. The variety of test scenarios share one common requirement: restrain and capture massive high velocity flight hardware with no structural damage. The Space Systems Laboratory of McDonnell Douglas Space Systems Company in Huntington Beach Ca. has developed a remarkably simple and cost effective approach to such testing using ripstitch energy absorbers adapted from the sport of technical rockclimbing. The proven system reliability of the capture system concept has led to a wide variety of applications in test system design and in aerospace hardware design.

INTRODUCTION

Falling is a common occurrence in sport rock climbing. As a result, technical rock climbing safety systems have reached extremely high levels of reliability and simplicity. A climber's restraint system consists essentially of a rope and its anchors. The rope serves as a high strength energy dissipation system which effectively limits restraint forces. Specialized devices, ripstitch energy absorbers, further augment the force limiting capabilities of the system. The climber skillfully integrates the parameters of his situation with safety system elements to form a system which assures a "safe motion envelope" should a fall occur.

DAC 104367



SSC 113446

103216



Restraint System Design is Applicable to a Wide Variety of Test Applications

An analogous challenge exists in aerospace dynamic testing. Test articles must be exercised and captured within a safe motion envelope large enough to record pertinent dynamic response data. Structures must be restrained in a controlled force manner. The test engineer integrates high reliability restraint elements with a wide variety of system parameters to assure success. These parameters include the test article, the safe motion envelope, test data parameters and the restraint system itself.

THE TEST ARTICLE

Kinematic and Mass Properties

Restraint systems apply external forces to control and ultimately bring to rest the test article. The motions of the test article before during and after the application of the restraint forces are all equally important. The initial free motion of the test article involves some combination of translation, roll, pitch and yaw velocities and accelerations. The restraint system applies a set of forces which modify the motions of the test article. The magnitude and location of the restraining forces determine the resulting kinematic properties of the test article (Figure 1).

103185

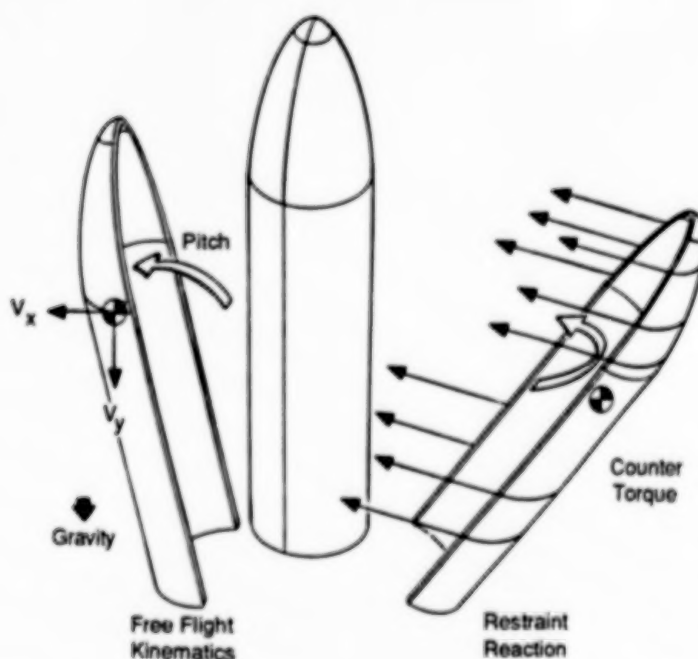


Figure 1. Dynamic Test Kinematics

The mass and kinematic properties of large test articles result in great restraint system design challenges. Large fairing structures have enormous moments of inertia and significant angular velocities. Angular velocities are reduced by applying restraint forces which generate a counter torque (and hence an angular acceleration) which suitably positions the body at rest. Computer modeling has proven quite helpful in simulating the dynamic response of the system.

Structural Strength

The test article structural strength must be considered from the standpoint of restraint system loading. Aerospace structures are designed for optimum strength to weight ratios, hence reverse

loading situations encountered in restraint situations tend to load structures in their weakest mode. While single point loading (as incurred with rebound restraint systems) can present real problems, the distributed nature and loading magnitudes of primary restraint systems have proven in our applications to be orders of magnitude less than the loadings incurred during the ordnance separation event.

SAFE MOTION ENVELOPE/ TEST DATA PARAMETERS

Dynamic motion tests are performed to gather pyroshock and flexible body motion data. While shock event is completed relatively soon after the separation event, motion data is usually significant for a period of time thereafter (depending on the natural frequency of the test article). As this freeflight time is typically on the order of .25-.5 seconds, the test article must translate for an appreciable distance, .45-1.5 meters (1.5-5 feet), to allow for high speed camera and strain gage data acquisition prior to restraint system engagement. The safe free motion and catch envelope is thus tailored to this data constraint and the external geometries of associated facilities and support structure. Restraint loading and free motion parameters are hence variables to be optimized.

RESTRAINT SYSTEM ELEMENTS

Restraint system design involves predicting system behavior and then designing for beyond envelope margin. The Space Systems Laboratory has extensively tested system elements to fully characterize element performance.

Rip-Stitch Energy Absorbers (Figure 2)

While rip-stitch energy absorbers (or rippers) are nothing new to climbers, the application of the device to test is somewhat novel. A length of webbing folded over and stitched appropriately, the shock loaded ripper tears the stitches at a constant mean force level, and in the process absorbs energy. Altering the thread material, thickness or stitch pattern alters the tear force. Modern industrial sewing machines are capable of mass-producing low cost assemblies with impressive tear out force repeatability ($\pm 5\%$) at a low unit cost (\$10 and up).

SSC 113445

103218

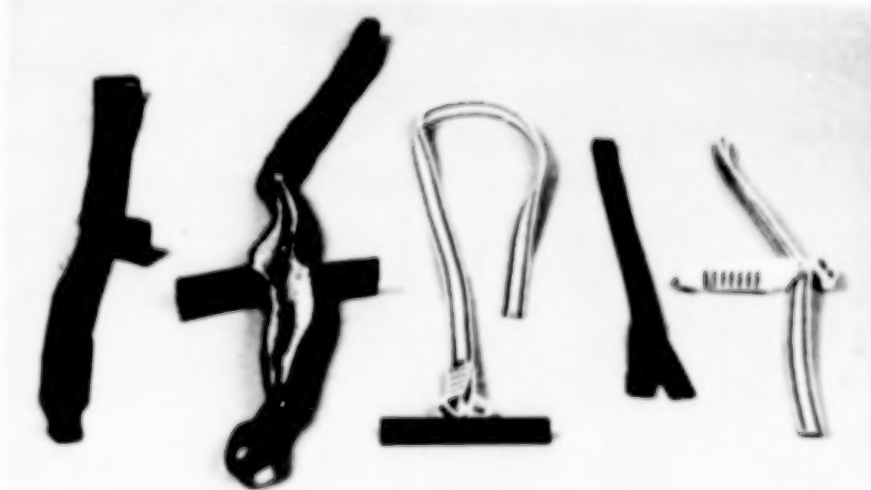


Figure 2. Ripstitch Energy Absorber Assemblies

How Rip-Stitch Energy Absorbers Work

Rippers absorb energy through the classic work equation:

$$E = \int_{x=0}^{x=S} F \cdot dx$$

where

- E = net energy dissipated by the ripper
- F = mean ripper tear force
- S = total ripper tear out distance

07/30/90

Ripper assemblies are sewn in a variety of force values, tear out distances and stitch patterns. Overall average rip force levels for readily available single assemblies range from approximately 445-4450 Newtons (100 lb_f to 1000 lb_f). Arrest force values can be increased by employing parallel ripper assemblies. Such arrangements amplify the force in a relationship dependant on the assemblies stitch pattern.

Rip-Stitch Energy Absorbers Stitch Pattern

Ripper stitch patterns vary between manufacturers. Typical stitching methods include bar tacks sewn normal to the webbing in long stripes, bar tacks sewn perpendicular to the webbing, and sinusoidal stitch patterns. Rip stitch energy absorber force profiles are unique to the type of stitch pattern (Figure 3).

103176.1M400

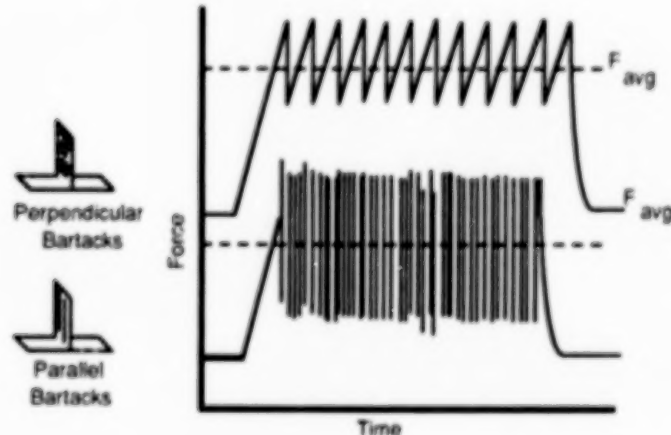


Figure 3. Ripstitch Energy Absorber Force Profiles

Most restraint applications are insensitive to energy absorber frequency response, hence stitch patterns are usually not a significant system design issue. One exception occurs in parallel ripper arrangements (to amplify restraint force). Ripper elements utilizing perpendicular bar tacks may demonstrate a 'phasing' effect which reduces the system restraint force (Figure 4).

Rip-Stitch Energy Absorber Testing

While high speed data acquisition has been successfully employed to measure ripper tear out force, a simple evaluative test has been devised by SSL to characterize vendor shipments and validate uniformity. The method employs a simple vertical drop test utilizing a known rigid weight

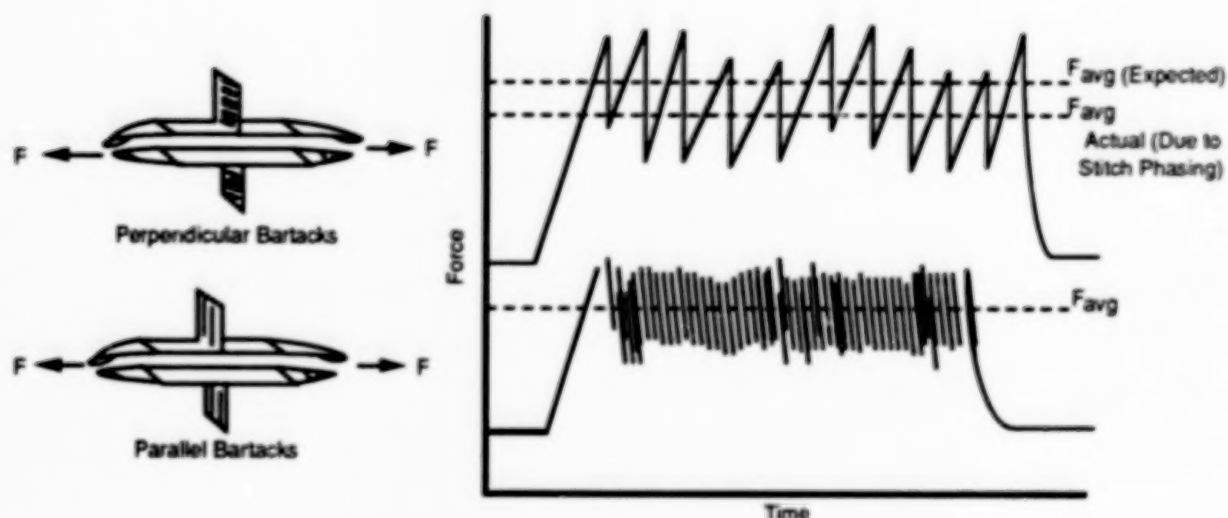


Figure 4. Parallel Ripstitch Energy Absorber Force Profiles

with measured freefall and tear out distances (Figure 5). The relationship of net ripper force for the measured setup distances can be shown to be:

$$F = \frac{(W \times D)}{S} + W$$

- F = average ripper force
 W = weight of rigid drop mass
 D = total mass free fall distance
 S = total ripper tearout distance

07/27/90

103174.30M

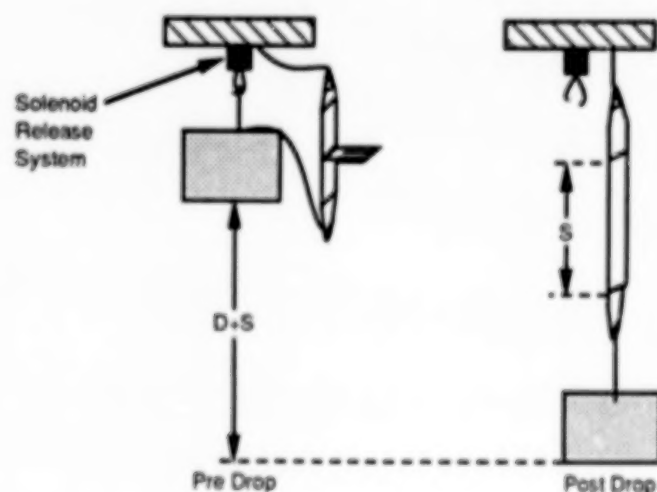


Figure 5. Energy Absorber Drop Test Approach

Restraint System Strength and Elasticity

Rippers, webbing and rope are typically fabricated from synthetic materials such as nylon or polyester fiber. Such software possesses impressive strength and an elastic behavior defined by the chemistry of the fiber and the weave of the assembly. Rip stitch energy absorbers limit element loading to levels determined by the test article, kinetic energy, safe catch envelope and the amount of residual stored energy in the system.

In normal situations, rip stitch energy absorbers limit the amount of stored spring energy in the system (due to inherent elasticity) to extremely low levels. The amount of stored energy resulting from elasticity is a function of the system spring constant and effective damping resulting from the assembly. Measurement of these parameters has been achieved through modeling tests involving the spring/damper system during transient oscillatory motion (Figure 6). System stored energy is an obvious consideration; large tests such as the Titan 86 Foot PLF Separation Test required extensive analysis.

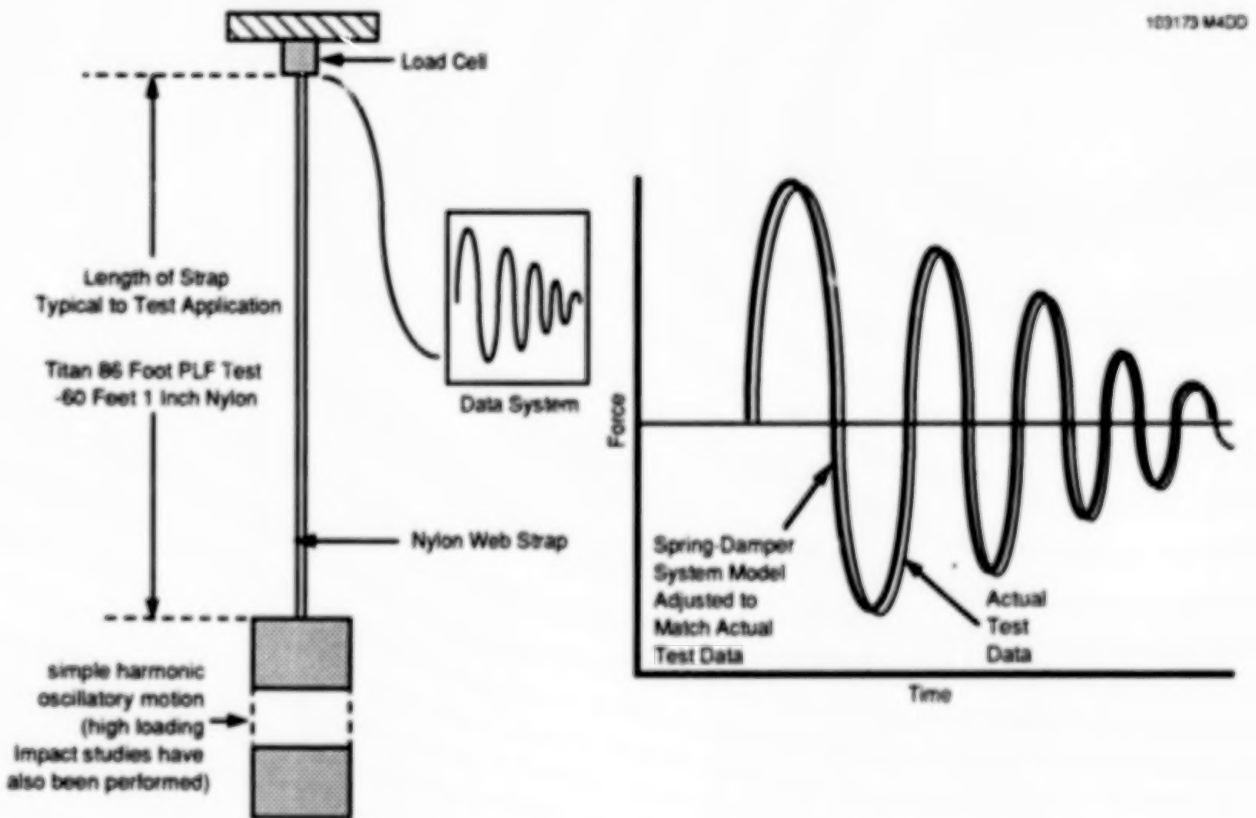


Figure 6. Experimental Technique To Measure Restraint System Element Kinematic Properties

Elasticity is not a completely undesirable element in restraint systems. Elasticity preserves an extra safety factor; should an off margin scenario occur, the fiber elements absorb an incredible amount of energy during impact stretching. The importance of rebound restraint systems increases in these situations.

Rebound Restraint

Dynamic restraint systems are always designed to accommodate an off-nominal event, indeed such possibilities justify testing. As such occurrences raise the likelihood of increased stored

energy, the limiting of rebound effects is essential. Rebound limiting is accomplished by applying a benign restraining force to the test article in a manner which is conducive to the overall test requirements.

Some tests have utilized gravity to limit rebound. The HEDI 1D018A Interstage separation test employed a unique overhead suspension system which utilized gravity to mitigate rebound effects (Figure 7). The Modified Titan PLF separation test utilized an overhead compound pendulum suspension technique to dampen rebound (Figure 8).

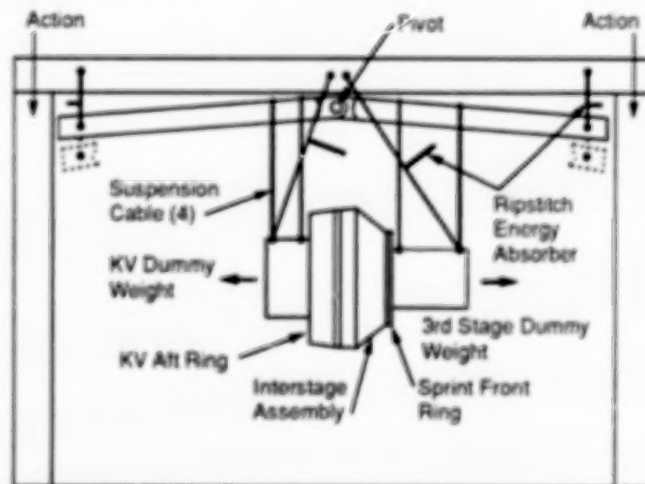


Figure 7. HEDI 1D018A Overhead Suspension System

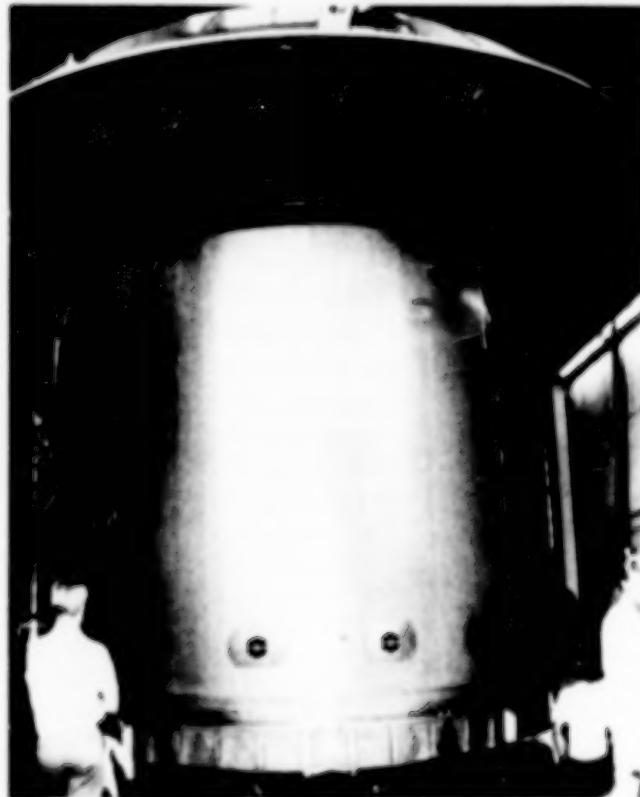


Figure 8. Titan Overhead Compound Pendulum Suspension

Active retracting clutch systems have been used with complete success by SSL. Nylon ropes are suitably attached to the test article and routed to pulleys and rope clutches (Figure 9). A tensioned bungee cord propels the systems during test to prevent excessive rope slack. The clutches engage during rebound and limit control resulting motion. Engagement shock is significantly reduced by integrating a ripper in the retractor line.

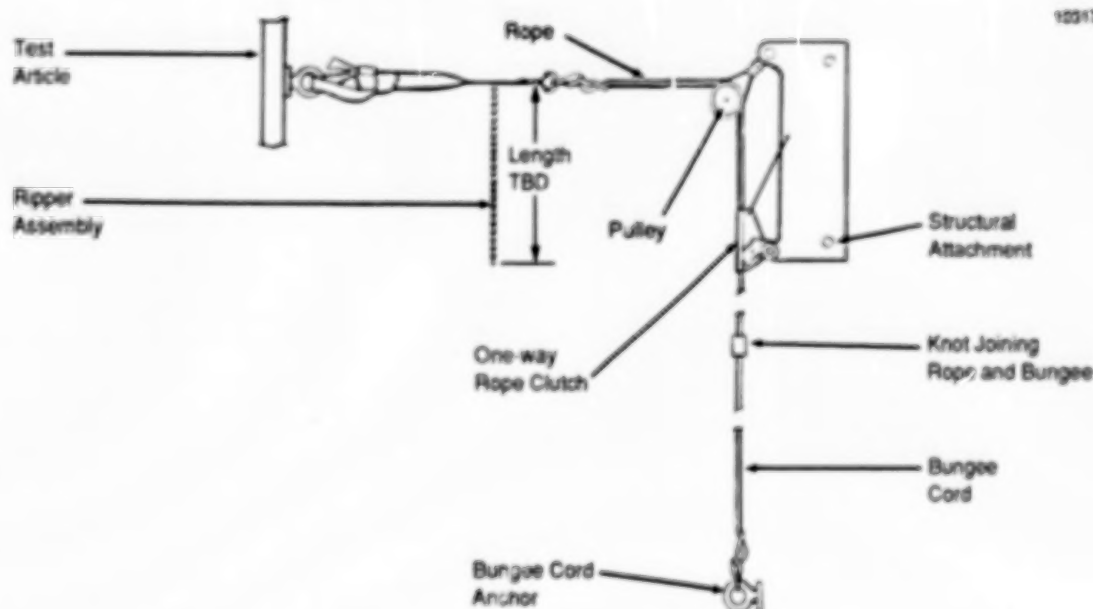


Figure 9. Active Rebound Restraint System

TEST APPLICATIONS

HEDI 1D018A Interstage Separation Test, 19 July 1988 (Figure 10)

Test Article Specifications

Length: Interstage: 0.58 m (1.95 ft)

Kill Vehicle (KV): 0.54 m

Diameter: 0.5 m (1.6 ft) nominal

Weight: Interstage - 407 kg (898 lb) KV - 367 kg (810 lb)

Separation System: Severance/thruster system

Predicted Separation Velocity: Interstage - 5.27 m/s (17.5 ft/s) KV - 5.67 m/s (18.9 ft/s)

Actual Separation Velocity: Interstage - 5.9 m/s (19.8 ft/s), KV - 6.57 m/s (21.9 ft/s)

Restraint System Specifications

Configuration: external harness/reaction frame, overhead pivotal suspension tube with integral rip stitch energy absorbers.

Rip stitch energy absorbers: Horizontal - Twelve, 1424-N (320 lbf) energy absorbers,

Vertical - Four, 1424-N energy absorbers incorporated in overhead pivot suspension

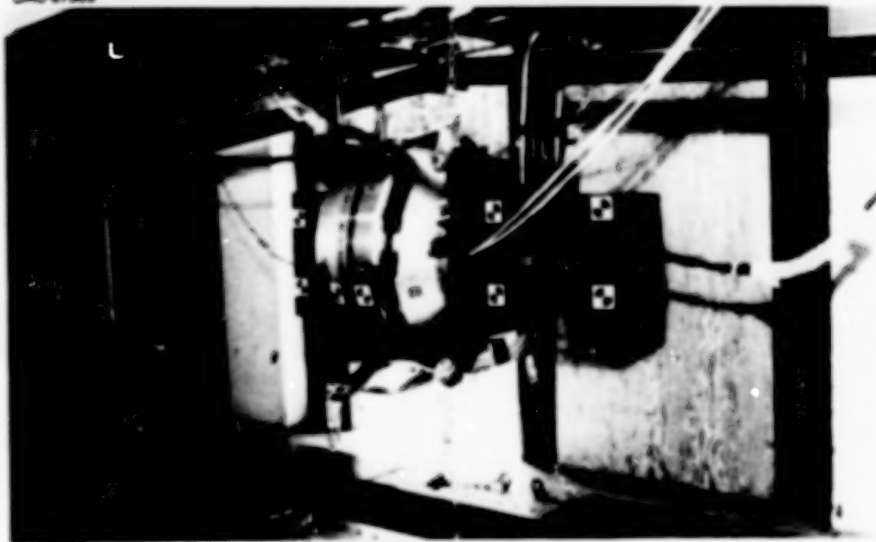
Rebound Restraint: pendulum suspension

Free Travel: Horizontal - 0.65 m (2.1 ft), Vertical - 0.08 m (0.25 ft)

Restraint Distance: Horizontal - 0.65 m (2.1 ft), Vertical - 0.15 m (0.5 ft)

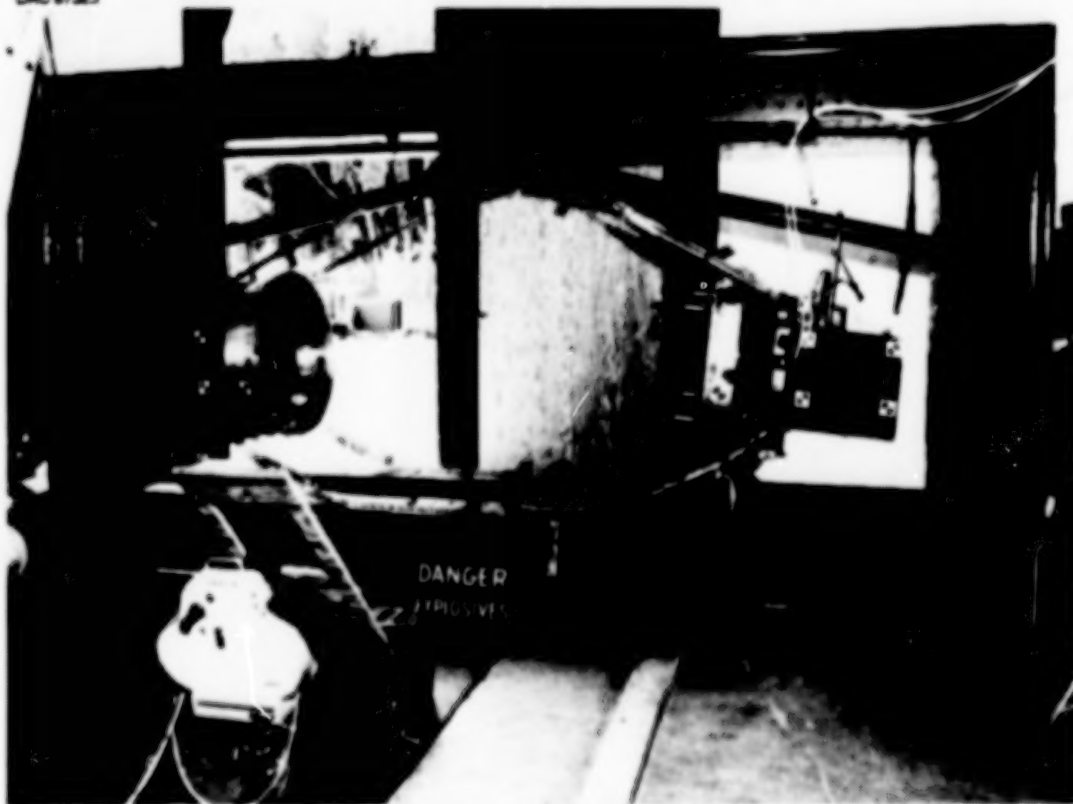
DAC 87305

103222.1



(a) Final Pre-test Configuration

DAC 87323



(b) Post-Test Configuration

Figure 10. HEDI ID018A Separation Test

Test Instrumentation Specifications

High-Speed Cameras: Two Hicam cameras, 1000 fps positioned perpendicular and tangentially to separation plane.

One Hicam, overall view 500 fps

Other: Twenty-eight accelerometers; Eight pressure transducers

Test Summary

The HEDI 1D018A test successfully demonstrated the separation system performance and acquired necessary pyroshock data. The test restraint system functioned flawlessly and was the laboratory's first implementation of rip-stitch energy absorbers.

Delta II Payload Fairing Separation Test, March through November 1988 (Figure 11)

Test Article Specifications

Length: 8.6 m (28 ft)

Diameter: 2.5/2.9 m (8 ft/9.5 ft)

Weight: 658 kg (1452 lb)

CG location: 3.6m (12 ft from aft end)

Moment of Inertia: 2283 kg m²(1587 slug ft²) (pitch axis)

Separation System: Ordnance separated bisector

Predicted Separation Velocity: 5.4 m/s (18 ft/s)

Actual Separation Velocity: 6.3 m/s (21 ft/s)

Predicted Pitch Rate: 0.034 rad/s (2 deg/s)

Actual Pitch Rate: 0.034 rad/s (2 deg/s)

Restraint System Specifications

Configuration: external capture net, 5 cm polyester webbing. Vertical restraint foam cushion
Rip stitch energy absorbers: twenty-two (11 per net side) attached to horizontal net members.

■ Eight 667 N (150 Lb_f) fwd CG

■ Fourteen 445 N (100 Lb_f) aft CG

Rebound Restraint: four active retracting clutch system six (3 per half) attached to PLF 4 m fwd of CG

Free flight: 0.9 m (3 ft) horizontal

Restraint Distance: 0.6 m (2 ft)

Test Instrumentation Specifications

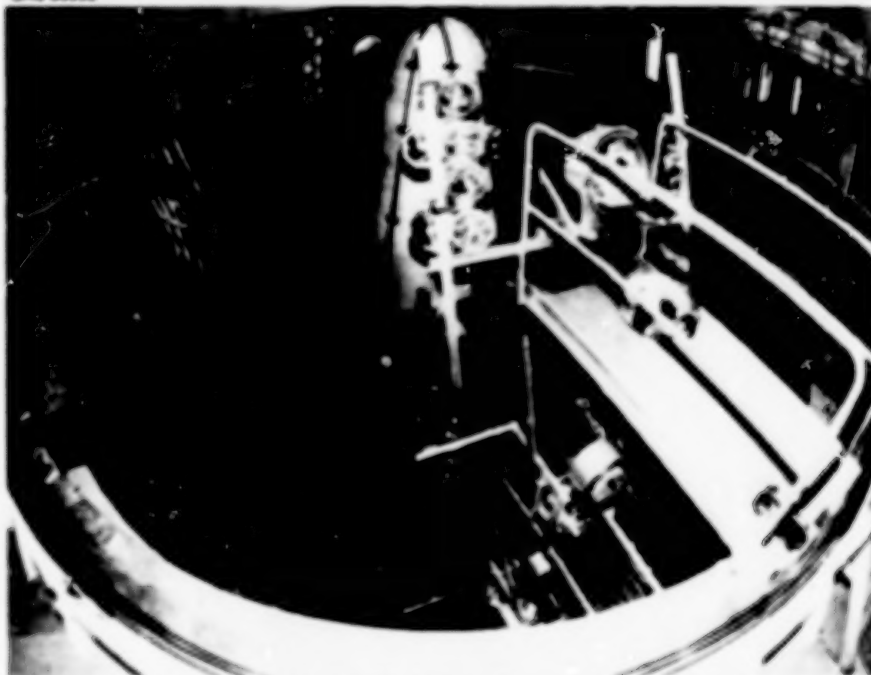
High speed cameras: Twelve 1000 fps Hicam cameras positioned along PLF separation plane

Accelerometers : Forty-four

Strain gages: Twelve

Test Summary

The Delta II PLF Separation shock test program consisted of four tests of the flight and force-margin separation systems. Testing included evaluation of an alternate separation system configuration and simulated separation at 0.7 g due to diminished gravitational effects. The test effort was successfully completed in November 1988 qualifying the Delta II PLF for flight. The separation test capture systems functioned flawlessly enabling four ordnance separations to be performed on the same PLF with no test induced damage.



(a) Delta II PLF Installed in 39-Foot Chamber Prior to Separation



(b) Delta II PLF Post-Test Configuration

Figure 11. Delta II PLF Separation Test

Modified Titan Fairing Separation Test, 5 October 1988 (Figure 12)

Test Article Specifications

Length: 5.25 m (17.5 ft)

Diameter: 5 m (16.7 ft)

Weight: 1208 kg (2664 lb)

Cg location: 2.52 m (8.4 ft) from aft end

Moment of inertia: 2100 kg m² (1459 slug ft²) (pitch axis)

Separation System: ordnance separated trisector

Predicted Separation Velocity: 5 m/s (16.6 ft/s)

Actual Separation Velocity: 5.8 m/s (19.4 ft/s) Avg.

Predicted Pitch Rate: 0.14 rad/s (8.3 deg/s) (Forward End Out)

Actual Pitch Rate: 0.04 rad/s (2.2 deg/s) Avg

Restraint System Specifications

Configuration: internal reaction radial restraint, overhead compound pendulum vertical restraint

Rip stitch energy absorbers:

Horizontal restraint system: total twenty-four attached to each trisector to central reaction frame.

■ Six 667 N (150 lb_f); tearout 0.8 m (2.6 ft) distributed forward of cg for anti-pitch effect

■ Eighteen 445 N (100 lb_f) tearout 0.8 m distributed aft of CG

Vertical restraint: total four per trisector 3337 N (750 lbf) tear out 0.2 m (0.67 ft).

Rebound Restraint: 12 active retracting clutch systems

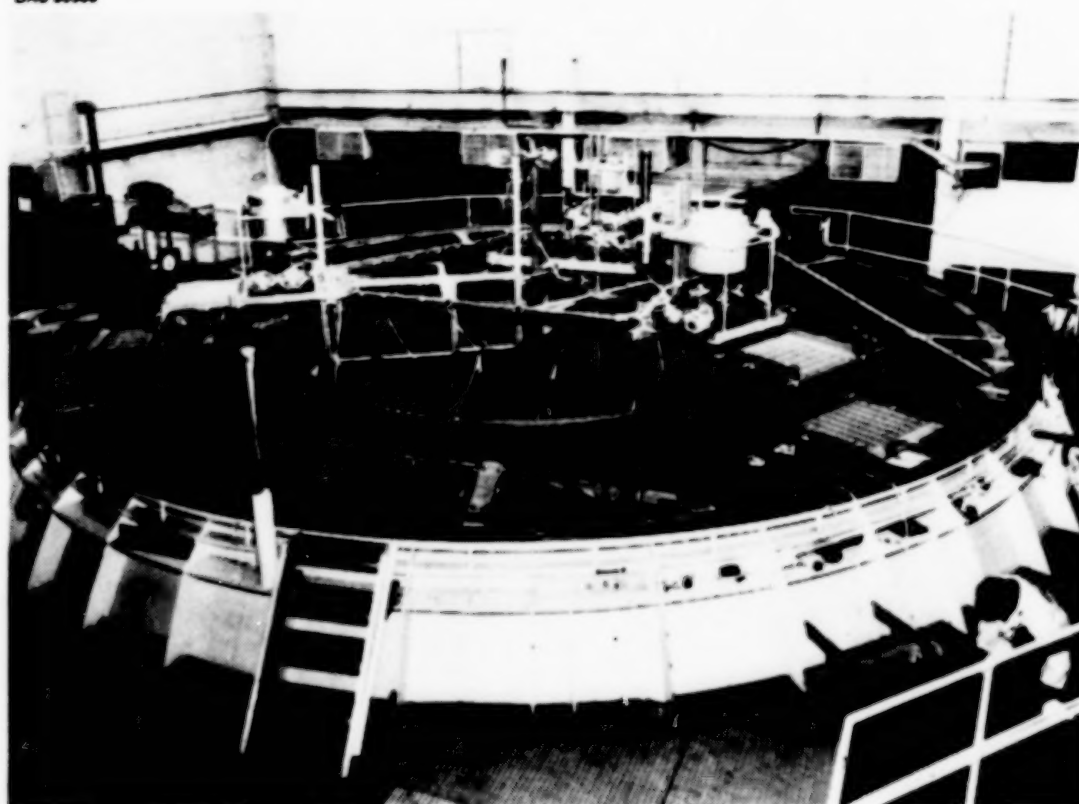
Test Instrumentation Specifications

High Speed Cameras: Sixteen 1000 fps Hicam cameras positioned along PLF separation planes, Two video cameras

Other: Twenty-seven accelerometers, Eighteen strain gages, Three pressure transducers

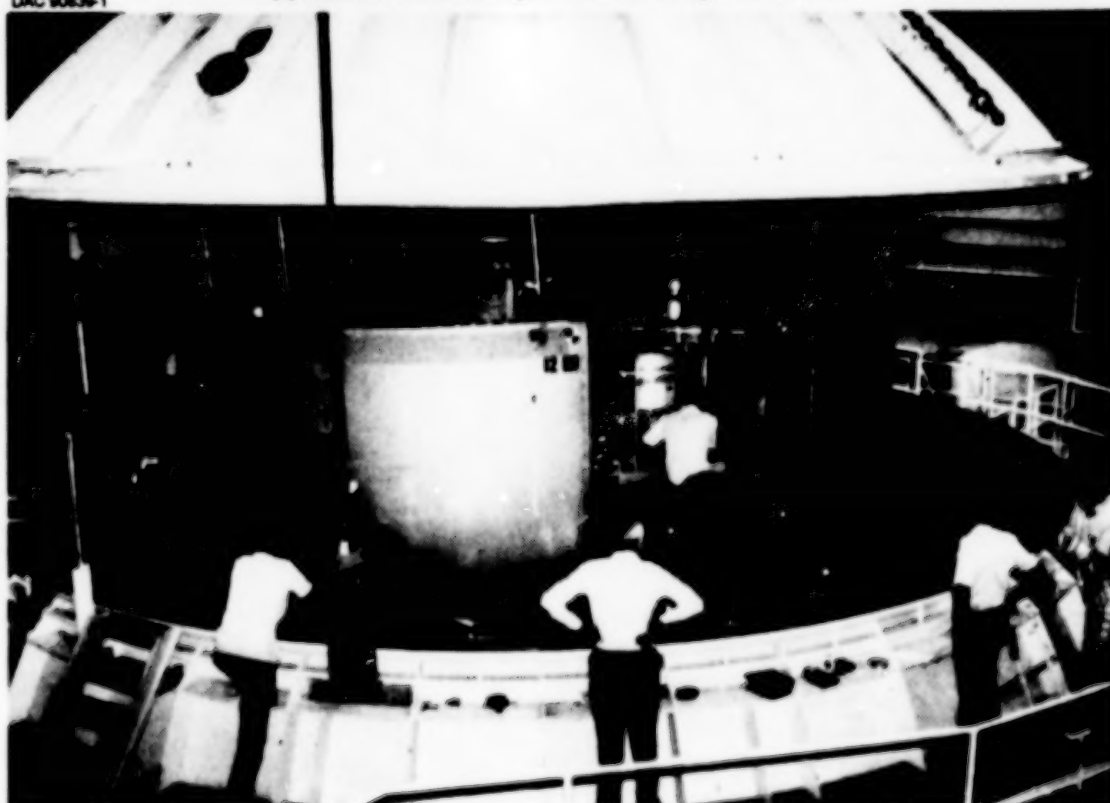
Test Summary

The modified Titan PLF separation test posed a tremendous challenge to SSL. The required safe free motion envelope was extremely small relative to the 39-foot Space Chamber's cryogenic shroud walls. In a major departure from traditional fairing restraint methods, the radial capture system was placed inside the fairing and directly attached to the structure with ripper straps. This significantly improved the efficiency of the restraint system over external net based approaches and increased restraint control of the fairing trisector trajectories. The fairing was vertically restrained with an overhead suspension system designed to reduce rebound effects. The test was a complete success despite significant variations from expected pitch rates. The energy margin designed into the radial capture system was expended and the resulting rebound was controlled by the rebound restraint system.



(a) Modified Titan PLF Separation Test Setup Prior to Test

DAC 90636-1



(b) Removal of PLF Following Successful Test

Figure 12. Modified Titan PLF Separation Test

Delta 10 Foot Payload Fairing Separation Test, 14 November 1989 (Figure 13)

Test Article Specifications

Length: 3.6 m (12 ft)

Diameter: 2.4 m/3m (8/10 ft)

Weight: 517 kg (1140 lb)

Cg location: 1.44 m (4.8 ft) from aft end

Moment of inertia: 192.8 kg m² (134 slug ft²) (pitch axis nominal)

Separation System: ordnance separated trisector

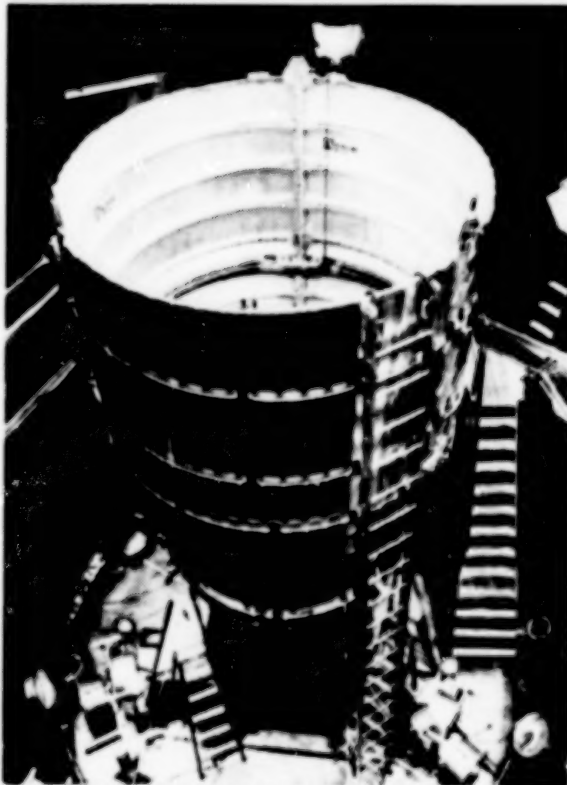
Predicted Separation Velocity: 4.5 m/s (15 ft/s)

Actual Separation Velocity: 4 m/s (13.3 ft/s)

Predicted Pitch Rate: 1.19 rad/s (70 deg/s) (Forward End Out)

Actual Pitch Rate: 1.6 rad/s (95.7 deg/s)

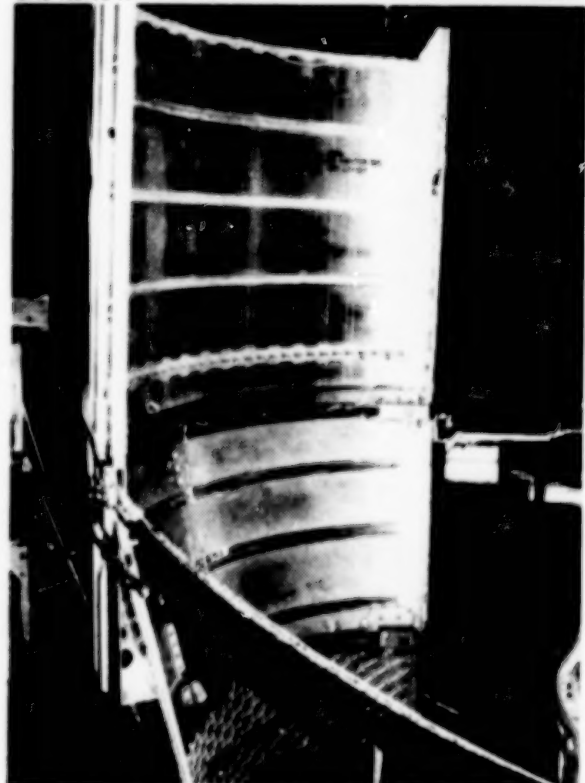
DAC 103638



(a) Delta 10-Foot PLF Test Set-Up Prior to Test

DAC 103778-11

103227



(b) Delta 10-Foot PLF Trisector Captured in Restraint System Following Separation

Figure 13. Delta 10-Foot PLF Separation Test

Restraint System Specifications

Configuration: Radial restraint: circumferential ripper band (structureless)

Vertical restraint: 2-point overhead suspension with integral ripstitch energy absorbers

Rip stitch energy absorbers:

- Radial restraint system- Five bands with three 245 N (55 lb_f) ripstitch energy absorbers installed in each band. Bands vertically positioned offset PLF pitch rate.

■ Vertical restraint system- Two 1602 N (360 lb_f) ripstitch energy absorbers attached to overhead support structure.

Rebound Restraint: Six (2 per trisector) active retracting clutch systems.

Free flight: 0.45 m (1.5 ft) horizontal

Restraint Distance: Radial 1.2 m (4 ft), Vertical 0.54 m (1.8 ft)

Test Instrumentation Specifications

High Speed Cameras: Six 400 fps Hicam cameras positioned along PLF separation plane viewing upward at LED self-lighting camera targets; Two video cameras

Other: Thirty-six accelerometers, Twelve strain gages, Six pressure transducers

Test Summary

The test successfully qualified the Delta 10-foot diameter PLF. The test approach significantly simplified both PLF dynamic restraint and photo data acquisition. The circumferential ripper band radial restraint system reduced support structure requirements; the vertical restraint system utilized existing handling points eliminating test article structural loading concerns. The test article was successfully captured despite variations from predicted pitch rates which depleted much of the energy margin designed into the restraint system. The photo data acquisition reduced test camera and lighting requirements as well as greatly simplifying photo data reduction. The test served as a proving ground for the test approach utilized for the Titan 86-Foot PLF Separation test.

HEDI 1CD02 Interstage Separation Test (Figure 14)

Test Article Specifications

Length: 4 m (13.6 ft)

Diameter: 0.5 m (1.6 ft) nominal

Weight: 661 kg (1458 lb)

Cg location: Sprint/interstage: 1.1 m (3.6 ft) from aft end, KV: 0.84 m (2.8 ft) from aft end

Separation System: Severance/Thruster System

Predicted Separation Velocity: 5.4 m/s (18 ft/s)

Actual Separation Velocity: 5.6 m/s (18.7 ft/s)

Restraint System Specifications

Configuration: horizontal restraint external reaction frame, vertical restraint pendulum suspension. Restraint system directly attached to test article with webbing harness.

Rip stitch energy absorbers:

Horizontal: four compound ripper assemblies per separating half. Each ripper assembly consisted of three rippers per assembly. Rip force 1691 N (380 lb_f) per energy absorber.

Vertical: four ripstitch energy absorbers per separating half. Rip force 1691 N (380 lb_f) per energy absorber.

Rebound Restraint: four active retracting clutch systems, pendulum suspension

Free travel – horizontal: 0.6 m (2 ft), vertical: 0.15 m (0.5 ft)

Arrest distance – horizontal: 0.4 m (1.3 ft), vertical: 0.19 m (0.63 ft)

Test Instrumentation Specifications

High speed cameras: Two Hicam cameras 1000 fps positioned perpendicular to test specimen.

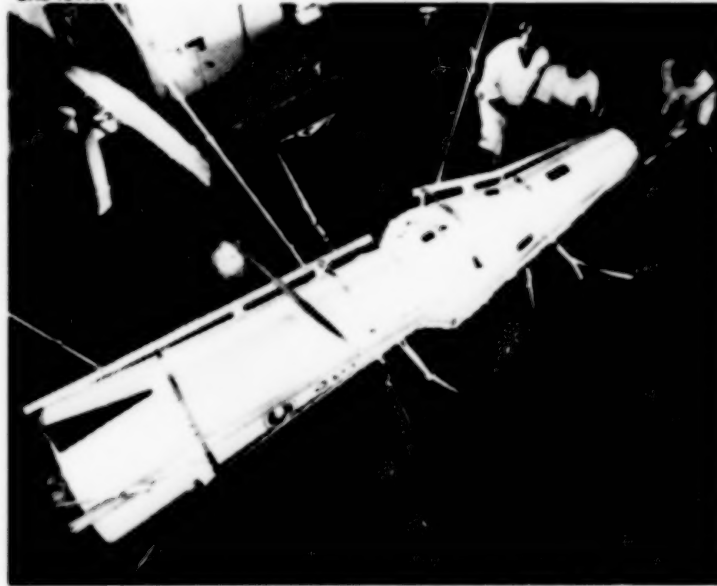
One Hicam camera 1000 fps aligned at nose viewing aft. Two 200 fps overall cameras

Accelerometers: Sixty-six

Pressure Transducers: Four

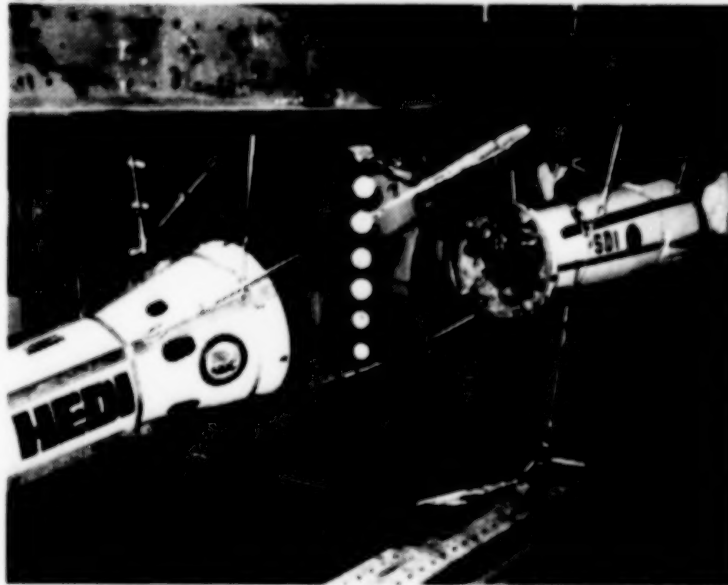
DAC 104417

103228



(a) HEDI ICD02 Separation Test Prior to Test

DAC104391



(b) HEDI Test Article Following Successful Separation

Figure 14. HEDI ICD02 Separation Test

Test Summary

The HEDI ICD02 test repeated the 1D018A test of July 1988 in an actual airframe to increase the fidelity of the separation pyroshock data. The test was performed one month after ATP, demonstrating the advancement of test design techniques. The test was a complete success and gathered useful data.

PAM-S Separation Tests, December 1989-January 1990 (Figure 15)

Test Article Specifications

Length: 2 m (6.7 ft)

Diameter: 1.14 m (3.8 ft)

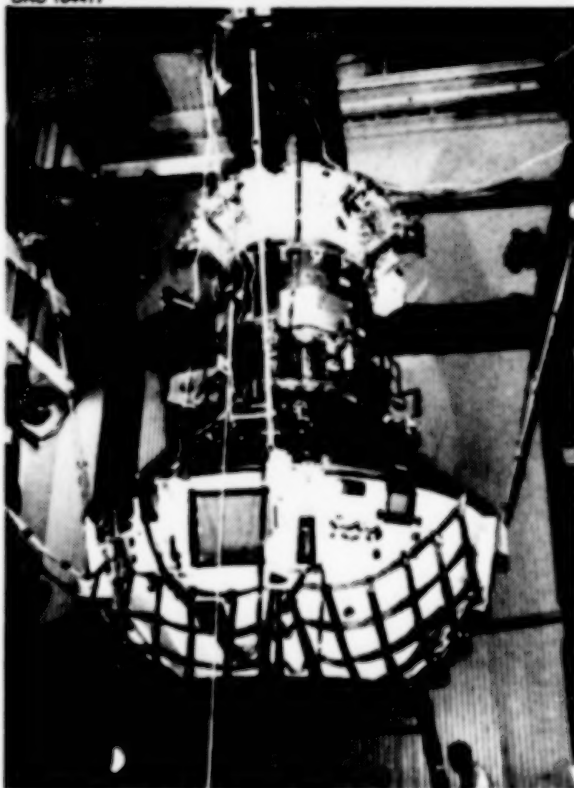
Weight: 1072 kg (2364 lbs)

■ Aft Adapter: 907 kg (2000 lb) offloaded with bungee cord and counter weights.

■ Motor Support: 79.38 kg (175 lb)

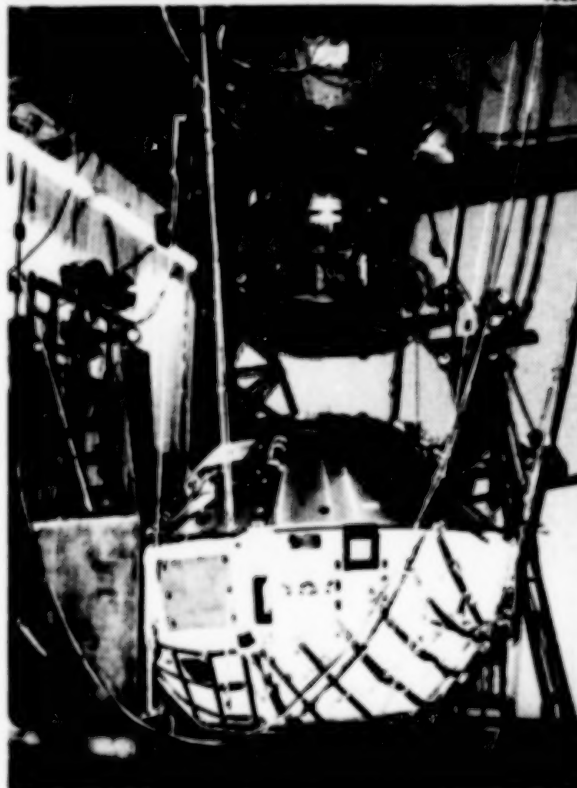
Separation System: Two Phase separation event (Aft adapter and Motor Support). Dual Clampband/Spring Thrusting System

DAC 104477



(a) PAM-S Separation Pre-test Configuration

103230.1



(b) Test Article Following Separation Test

Figure 15. PAM-S Separation Test

Restraint System Specifications

Configuration:

■ Aft Adapter Restraint: Four rip stitch energy absorbers directly attached to external frame. Zero G simulation utilizing counterweights and bungee cord

■ Motor Support: Four rip stitch energy absorbers directly attached to external frame.

Rip stitch energy absorbers: vertical restraint: Eight

Rebound Restraint: Four clutch systems installed on Aft Adapter counter balance system

Free travel:

■ Aft Adapter: 1.125 m (3.75 ft)

■ Motor Support: 0.15m (0.5 ft)

Arrest Distance:

- Aft Adapter: 0.08 m (0.25 ft)
- Motor Support: 0.1 m (0.35 ft)

Test Instrumentation Specifications

High Speed Cameras: Four Hicam cameras 1000 fps. Two overall video cameras
Accelerometers : Seventy-four

Test Summary

The PAM-S separation test qualified a specialized Payload Assist Module (PAM) design for the Ulysses solar mission. The successful effort consisted of five total separation tests; two separations of the Aft Adapter/IUS, two separation tests of the motor support assembly, and a full system test of the two stage system using the vehicle ordnance sequence system. The restraint system function included a zero-G simulated separation of the Aft Adapter/IUS.

Titan 86 Foot Payload Fairing Separation Tests, October/November 1990 NASA Sverdrup Plumbrook Station (Figure 16)

Test Article Specifications

Length: 25.8 m (86 ft)

Diameter: 5 m (16.7 ft)

Weight: 6124 kg (13500 Lb)

CG Location: 9.3 m (31 ft) from aft end (nominal)

Moment of Inertia: 43083 kg m² (29940 slug ft²) (pitch axis, nominal)

Separation System: ordnance separated trisector

Predicted Separation Velocity: 5.61 m/s (18.7 ft/s) (nominal)

Predicted Pitch Rate: 0.2 rad/s (12 deg/s) (forward end out, nominal)

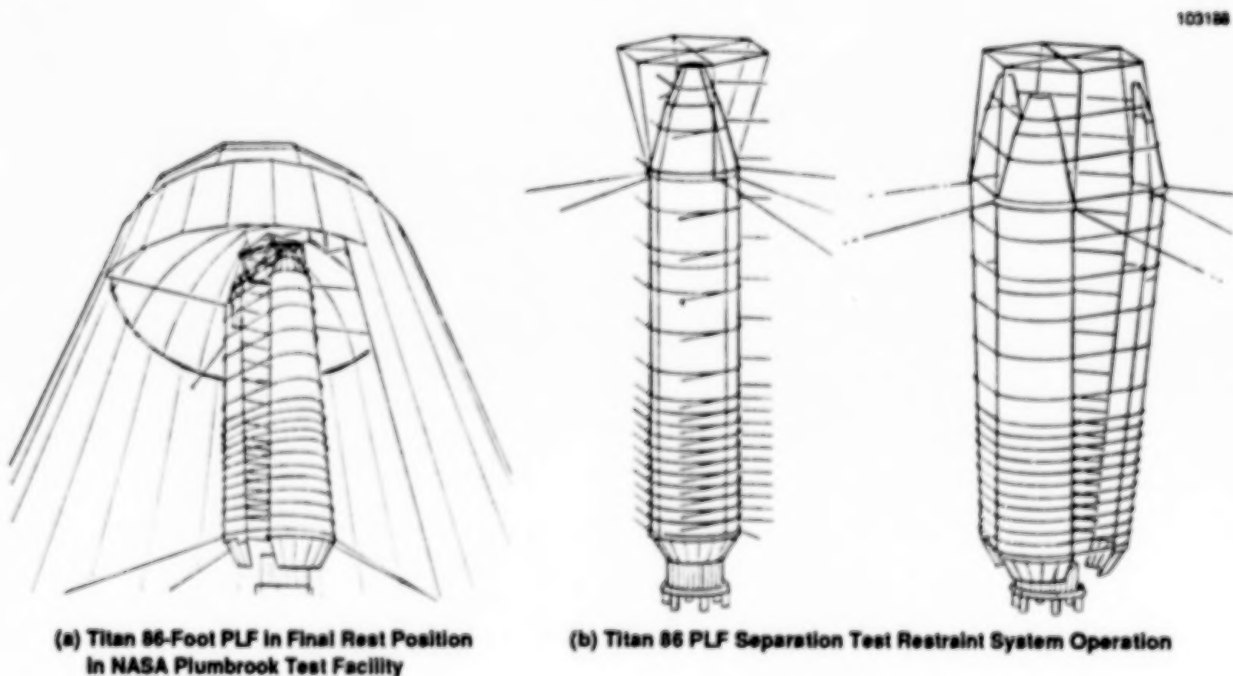


Figure 16. Titan 86-Foot PLF Separation Test

Restraint System Specifications

Configuration:

Radial restraint: circumferential ripper band (structureless)

Vertical restraint: 2-point overhead trisector suspension with integral ripstitch energy absorbers.

Trisectors suspended from spreader bar structure attached to chamber polar crane.

Rip stitch energy absorbers:

Radial restraint system- Twenty bands with three 1157 N (260 lb_f) ripstitch energy absorbers installed in each band at separation joints. Vertical position of bands determined to offset PLF pitch effects.

Vertical restraint system- Six energy absorber assemblies (two per trisector) attached to overhead support structure. Each assembly consists of Five 4227 N (950 lb_f) ripstitch energy absorbers.

Rebound Restraint: Twelve (4 per trisector) active retracting clutch system with integral 2448 N (550 lb_f) rip stitch energy absorbers.

Free flight: 1.5 m (5 ft) nominal horizontal

Restraint Distance: Radial 0.9 m (3 ft) nominal, Vertical 0.54 m (1.8 ft)

Test Instrumentation Specifications

High Speed Cameras: six 400 fps cameras positioned along PLF separation plane viewing upward and downward at LED self-lighting camera targets, three 400 fps cameras positioned along PLF trisector center lines; two 400 fps overall cameras; two video cameras.

Other: One-hundred-twenty-one accelerometers; three-hundred-sixty-one strain gages; twenty-four pressure transducers

Test Summary

The Titan 86 Foot PLF separation test will be the largest fairing separation test attempted to date and reflects significant advances in restraint system design. The test restraint system is essentially structureless, moreover an innovative high speed camera instrumentation approach has greatly reduced the camera quantity, lighting, and related support structure requirements for a test of this magnitude.

CONCLUSIONS

Large scale dynamic tests include a significant element of risk. The application of a deceptively simple and effective restraint system approach has significantly reduced this risk. The high reliability restraint technology has evolved from a systems oriented approach which utilizes industry proven components. The versatile technology has been successfully applied to a wide variety of test applications.

• **SESSION VI**

MATERIAL DEGRADATION IN ORBIT

ATOMIC OXYGEN EFFECTS ON BORON NITRIDE AND SILICON NITRIDE: A COMPARISON OF GROUND BASED AND SPACE FLIGHT DATA

J. B. Cross
Los Alamos National Laboratory

E. H. Lan and C. A. Smith
McDonnell Douglas Space Systems Company

W. J. Whatley
Sparta, Inc.

ABSTRACT

The effects of atomic oxygen on boron nitride (BN) and silicon nitride (Si_3N_4) have been evaluated in a low Earth orbit (LEO) flight experiment and in a ground based simulation facility at Los Alamos National Laboratory. In both the in-flight and ground based experiments, these materials were coated on thin ($\sim 250\text{\AA}$) silver films, and the electrical resistance of the silver was measured in situ to detect any penetration of atomic oxygen through the BN and Si_3N_4 materials. In the presence of atomic oxygen, silver oxidizes to form silver oxide, which has a much higher electrical resistance than pure silver. Permeation of atomic oxygen through BN, as indicated by an increase in the electrical resistance of the silver underneath, was observed in both the in-flight and ground based experiments. In contrast, no permeation of atomic oxygen through Si_3N_4 was observed in either the in-flight or ground based experiments. The ground based results show good qualitative correlation with the LEO flight results, indicating that ground based facilities such as the one at Los Alamos National Laboratory can reproduce space flight data from LEO.

INTRODUCTION

The low Earth orbit (LEO) environment, consisting primarily of atomic oxygen, reacts with and degrades many commonly used spacecraft materials.^{1,2} For spacecraft traveling at 8 km/sec, atomic oxygen strikes forward facing surfaces with a collision energy of about 5 eV. The effects of the LEO environment, especially atomic oxygen, on materials need to be understood in order to predict long term material behavior. Materials such as boron nitride (BN) and silicon nitride (Si_3N_4) are of interest to the space materials community because they are candidate optical coatings for spacecraft mirrors. For use on long duration missions, these materials must withstand the environment without undergoing significant changes in optical properties.

Due to the scarcity and high cost of space flight experiments, ground based simulation facilities provide an alternate means of evaluating space effects on materials. In order to validate ground based testing, however, correlation of ground based data with space flight data is necessary. In this paper, space flight and ground based results for BN and Si₃N₄ are presented. These materials were flown in a Space Materials Experiment (SME) funded by the Strategic Defense Initiative Organization (SDIO) through the U.S. Army Materials Technology Laboratory (AMTL) and integrated by Sparta, Inc.³ The SME was a LEO experiment flown as a part of the Delta Star mission, launched March 24, 1989. A variety of materials, including BN and Si₃N₄, were flown on an active panel which was instrumented so that telemetry to a ground station for evaluation was possible. Experiments on BN and Si₃N₄ were also conducted at the Los Alamos National Laboratory (LANL) simulation facility. The LANL facility is capable of exposing materials to hyperthermal atomic oxygen (1-5 eV) at real-time and accelerated fluxes ($1-10^3$ X that of LEO).⁴

TECHNIQUE TO EVALUATE THIN FILMS

The technique used to evaluate the BN and Si₃N₄ films in both the Delta Star space flight and LANL ground based experiments consists of using silver oxidation as a sensor for atomic oxygen penetration through the films.⁵ A schematic of the sensors used is shown in Figure 1. The sensor has two strips of silver ($\sim 250\text{\AA}$) deposited on top of an alumina or sapphire substrate. Coatings of known thickness are deposited over the silver films, and the electrical resistance of the silver is measured in situ during exposure to detect atomic oxygen penetration through the coating. Silver oxidizes in the presence of atomic oxygen to form silver oxide, and the electrical resistance of the oxide is much higher than that of pure silver. The electrical resistance data for silver can be converted to electrical conductance (inverse of electrical resistance) to evaluate the layers of silver remaining since electrical conductance is proportional to the thickness of a conductor.

EXPERIMENTAL CONDITIONS

For the Delta Star SME, the spacecraft was flown in LEO at an altitude of 500km and inclination of -48° with an estimated flux of 1.8×10^{13} atoms/cm²-sec. During the orbiting of the spacecraft, sample temperatures varied between 10°C and 40°C . At the LANL facility, samples were exposed to atomic oxygen at kinetic energies of 1.0 eV and 2.2 eV. The estimated O-atom flux for the 1.0 eV exposures was 4.5×10^{16} atoms/cm²-sec, using an Ar/O₂ gas mixture for the beam. The estimated O-atom flux for the 2.2 eV exposures was 1.9×10^{16} atoms/cm²-sec, also using an Ar/O₂ gas mixture. In both the space flight and ground based experiments, electrical resistance of the silver was measured in situ during exposure to the atomic oxygen environment.

Auger electron spectroscopy (AES) and scanning electron microscopy (SEM) were performed at Photometrics Microanalytical Laboratories (Huntington Beach, California). Transmission electron microscopy (TEM) was performed at the University of California at Irvine.

SAMPLE PREPARATION

For the samples exposed at LANL, the sample substrates were made of sapphire, with surface roughness of $<0.05\text{ }\mu\text{m}$. Silver ($\sim 250\text{Å}$) and either BN (750Å) or Si_3N_4 (700Å) were then deposited on the sensors. The Si_3N_4 thin films were sputter-deposited at the McDonnell Douglas Space Systems Company (MDSSC-HB) Microelectronics Center using an ion beam system. These films were reactively sputtered using a Si target in N_2 gas to a total thickness of about 700Å . The BN thin films were sputter-deposited at Naval Weapons Center (China Lake, California) using rf diode reactive sputtering. These films were sputtered using a BN target in Ar/N_2 gas to a total thickness of about 750Å .

For the samples flown on the Delta Star SME, the sample substrates were made of alumina, with surface roughness on the order of $2\text{--}3\text{ }\mu\text{m}$. The Si_3N_4 samples were coated by Battelle Northwest Laboratories and provided through the Air Force Weapons Laboratory. Si_3N_4 of $0.35\text{ }\mu\text{m}$ and $0.70\text{ }\mu\text{m}$ thicknesses was coated on the flight samples. The BN samples were coated by Spire Corporation and provided through the Army Materials Technology Laboratory. The thickness of the BN coated on flight samples was $1.0\text{ }\mu\text{m}$.

RESULTS

To evaluate the data from the oxygen sensors, the silver films were assumed to be of uniform thickness across the surface, and the electrical resistance of the silver was converted to electrical conductance to evaluate the rate of decrease in silver film thickness as a function of atomic oxygen fluence. In both the space flight results from the Delta Star mission and the ground based results from LANL, no permeation of atomic oxygen through Si_3N_4 was observed. The data from the Delta Star flight experiment is presented in Figure 2, which shows the conductance of silver underneath the Si_3N_4 films plotted as a function of atomic oxygen fluence. Data for both the $0.35\text{ }\mu\text{m}$ and $0.70\text{ }\mu\text{m}$ Si_3N_4 indicated no silver oxidation. Similar results were obtained from LANL. Data taken at LANL for Si_3N_4 (700Å) during exposure to an atomic oxygen beam at 1.0 eV energy (Figure 3) and at 2.2 eV energy (Figure 4) also indicated no silver oxidation or permeation of atomic oxygen through Si_3N_4 .

Auger analysis of a sample with 700Å Si_3N_4 coated over Ag ($\sim 250\text{Å}$) on a Si wafer substrate showed that after atomic oxygen exposure at LANL (2.2 eV , 210°C , total fluence of $4.7 \times 10^{20}\text{ atoms/cm}^2$), the oxygen concentration at the surface increased from 23 atomic % to 42 atomic %, while the nitrogen concentration at the surface decreased from 24 atomic % to 12 atomic %. Auger depth profile of the exposed sample indicated that oxygen was present only within 50Å of the surface. Optical microscopy up to 100X magnification and SEM up to 10,000X magnification of Si_3N_4 coated oxygen sensors did not reveal microcracking of the Si_3N_4 films after exposure at LANL. TEM was used to study Si_3N_4 films which had been deposited on sodium chloride (NaCl) crystals before and after atomic oxygen exposure at LANL. This technique permitted easy removal of the film for TEM; the NaCl was dissolved in water and the Si_3N_4 films were then collected on copper grids. The films showed

some microcracking which appeared to be primarily in areas where there were irregularities on the NaCl surface. Electron diffraction was also done on the Si₃N₄ films, and it indicated that the film was amorphous before and after atomic oxygen exposure.

Permeation of atomic oxygen through BN was observed in both the space flight results from the Delta Star mission and the ground based results from LANL. The data from both the flight experiment and LANL clearly indicated that there was transport of atomic oxygen through BN. Data from the Delta Star flight experiment for a sensor with two strips of Ag ($\approx 250\text{\AA}$) coated with $1.0\text{ }\mu\text{m}$ BN are presented in Figure 5. Data from the LANL simulation facility taken with a 1.0 eV atomic oxygen beam (Figure 6) and with a 2.2 eV atomic oxygen beam (Figure 7) for sensors coated with 750\AA BN are presented in Figures 6 and 7. In both sets of results, the conductance data indicated a steadily decreasing silver thickness (oxidation of silver to silver oxide) underneath the BN films with increasing atomic oxygen fluence.

For samples exposed at LANL, Auger depth profiles of a sample with 750\AA BN coated over Ag ($\approx 250\text{\AA}$) on a Si wafer substrate showed that there was oxygen and carbon, in addition to boron and nitrogen, through the entire thickness of samples both before and after atomic oxygen exposure (2.2 eV, 45°C, total fluence of 1.7×10^{20} atoms/cm²-sec). Because a pure BN standard was not available, absolute atomic compositions of the elements present were not calculated using Auger analysis since the sensitivity factors required were unknown. The carbon concentration in both the exposed and unexposed samples was estimated to vary between 5 and 15 atomic % through the thickness of the films. The oxygen concentration in both the exposed and unexposed samples was estimated to vary between 5 and 20 atomic % through the thickness of the films. A 25% decrease in the thickness of the BN film after exposure at LANL was detected in the Auger depth profile and confirmed using ellipsometry. Optical microscopy up to 100X magnification and SEM up to 10,000X magnification of BN coated sensors after exposure at LANL did not reveal microcracking in the film.

Data on BN from the Delta Star SME, however, did not indicate erosion of this material from exposure to the LEO environment. A BN ($0.1\text{ }\mu\text{m}$) coated quartz crystal microbalance (QCM) was included in the SME, and results showed a slight mass gain of $0.75\text{ }\mu\text{g/cm}^2$ after 150 days of mission elapsed time. It is unclear at this time whether the mass gain was due to contamination of the surface or due to oxygen incorporation into the BN.

DISCUSSION

The experimental data from the LANL ground based facility shows good agreement with space flight data from the LEO Delta Star mission in that the same trends were observed for Si₃N₄ and BN. Both space flight and ground based data for Si₃N₄ showed that this material did not allow oxygen transport through it. The stability of Si₃N₄ to atomic oxygen may be attributed to the conversion of Si₃N₄ to SiO₂ during exposure. The conversion of Si₃N₄ to SiO₂ has been observed in both thermal atomic oxygen⁶ and hyperthermal atomic oxygen systems.⁷

The space flight and ground based data for BN, however, showed that there was oxygen transport through this material. In both the space flight and ground based experiments, oxidation of silver underneath BN was observed. Direct correlation of the rate of oxygen transport through the BN (rate of oxidation of the silver) from the space flight and ground based data was not attempted because of the differences in the preparation techniques and thickness of the BN films as well as the differences in the substrate surface roughness on the sensors. Even though the LANL results showed a thickness loss in the BN, the remaining thickness of this material during atomic oxygen exposure was sufficient to completely cover the silver surface. There was oxidation of silver underneath, and therefore, oxygen transport through the remaining BN overlayer.

The loss of BN material under ground based exposure conditions needs to be studied further. The ground based exposures were performed under atomic oxygen fluxes which were $>10^3$ greater than the orbital conditions. Atomic oxygen surface catalyzed recombination may have heated the surface to drive off volatile oxide intermediates⁸ into the gas phase thereby producing surface recession. Under the relatively low fluxes at the Delta Star altitude, surface catalyzed recombination would have been greatly reduced. Results from the Delta Star SME showing oxidation of silver underneath BN but no mass loss in BN with LEO environment exposure confirmed that there was oxygen transport through this material, even under low atomic oxygen flux conditions. Since the characteristics of the BN (purity, density) probably play an important role in the behavior of these films in an atomic oxygen environment, a quantitative comparison of the silver reaction rates between the ground based and space flight data was not attempted.

In summary, the ground based experimental results from LANL show good qualitative agreement with space flight results from the Delta Star mission. The ability to reproduce LEO space flight results in a ground based simulation facility using the same technique (oxygen sensors) indicates that ground based facilities are able to simulate the LEO atomic oxygen environment. In the future, additional experiments to quantitatively correlate ground based data and space flight data using identical samples and techniques are needed.

ACKNOWLEDGEMENTS

The authors wish to thank SDIO and AMTL for the use of the data from the Delta Star Space Materials Experiment. We also thank Steven Koontz and Lubert Leger of NASA/JSC for many helpful discussions and their support of the LANL facility, and Linda Johnson and Terry Donovan of Naval Weapons Center for many helpful discussions and their work on the BN samples. The invaluable technical assistance of Frank Archuleta (LANL) is gratefully acknowledged.

References

1. Visentine, J.T., Leger, L.J., Kuminecz, J.F., and Spiker, I.K., "STS-8 Atomic Oxygen Effects Experiment," AIAA paper 85-0415, Proceedings from the AIAA 23rd Aerospace Sciences Meeting, January 1985.
2. Slomp, W.S., Santos-Mason, B., Sykes, G.F., and Witte, W.G., "Effects of STS-8 Atomic Oxygen Exposure on Composites, Polymeric Films, and Coatings," AIAA paper 85-0421, Proceedings from the AIAA 23rd Aerospace Sciences Meeting, January 1985.
3. Rosenwasser, S., "Delta Star Space Materials Experiment Data Analysis," 7th US/UK SDI Key Technologies SCORE Group Meeting, June 1990.
4. Cross, J.B. and Blais, N.C., "High Energy/Intensity Atomic Oxygen Beam Source for Low Earth Orbit Material Degradation Studies," Proceedings from the 16th International Symposium on Rarefied Gas Dynamics, July 1988.
5. Cross, J.B., Lan, E.H., Smith, C.A., and Arrowood, R.M., "Evaluation of Atomic Oxygen Interaction with Thin-Film Aluminum Oxide," Proceedings from the 3rd International Conference on Surface Modification Technologies, August 1989.
6. Gulino, D.A., Egger, R.A., and Banholzer, W.F., "Oxidation-Resistant Reflective Surfaces for Solar Dynamic Power Generation in Near Earth Orbit," J. Vac. Sci. Technol. A, vol. 5, no. 4, Jul/Aug.1989, pp. 2737 - 2741.
7. Gregory, J.C., Edgell, M.J., Cross, J.B., and Koontz, S.L., "The Growth of Oxide Films on Metals under the Influence of Hyperthermal Atomic Oxygen," 119th TMS Annual Meeting and Exhibit, February 1990.
8. Kirk-Othmer Encyclopedia of Chemical Technology, 3rd ed., vol. 4, 1978, pp. 68-70.

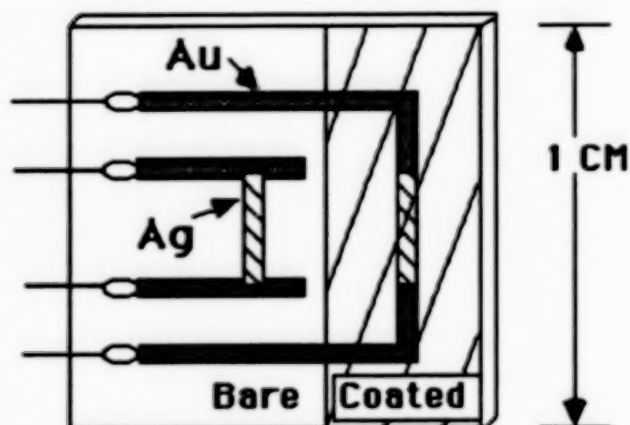


Figure 1: A schematic of the atomic oxygen sensor. The thickness of the silver is $\approx 250\text{\AA}$, and substrates are made of sapphire or alumina.

Conductance of Ag vs. Atomic Oxygen Fluence
Si₃N₄ Coated Sensor
Flown on Delta Star Flight Experiment

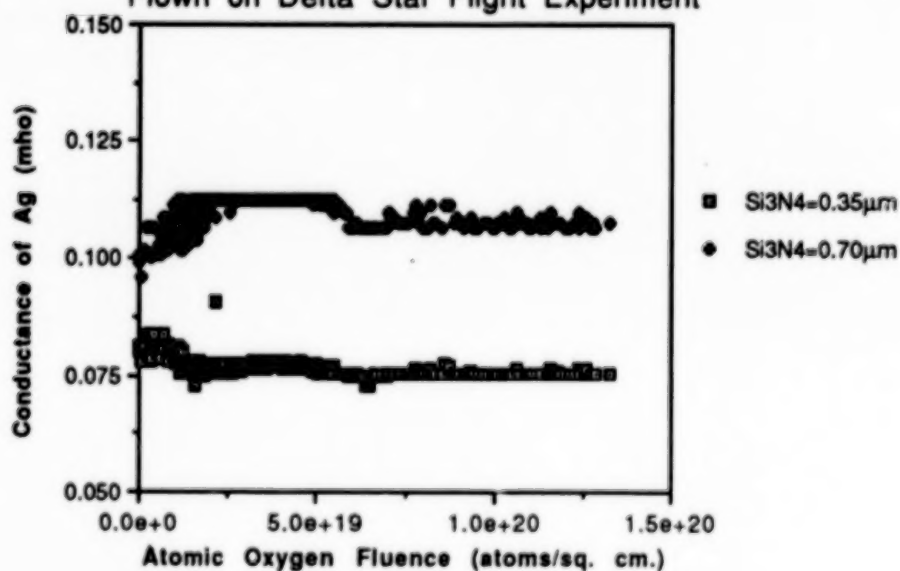


Figure 2: Plot of conductance of silver underneath films of Si₃N₄ as a function of atomic oxygen fluence for a sensor flown on the Delta Star Space Materials Experiment. The data indicates no silver oxidation; there was no atomic oxygen transport through the Si₃N₄ films.

Conductance of Ag vs. Atomic Oxygen Fluence

Si₃N₄ (700Å) Coated Sensor

Exposed at LANL Atomic Oxygen Facility

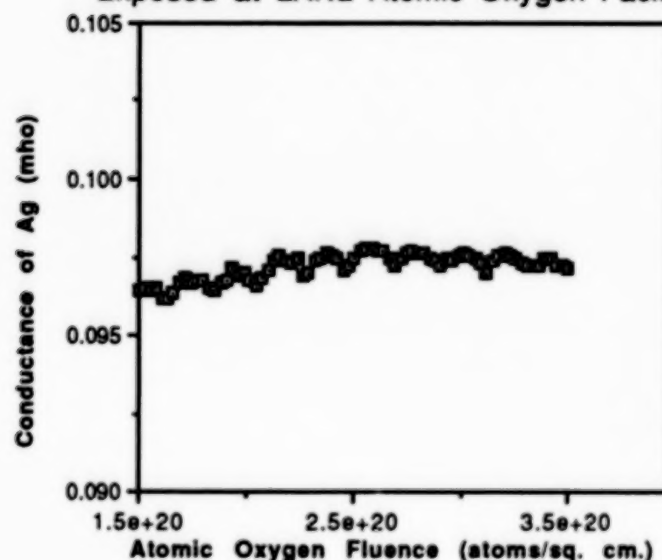


Figure 3: Plot of conductance of silver underneath a 700Å film of Si₃N₄ as a function of atomic oxygen fluence. The sensor was exposed at Los Alamos National Laboratory to an atomic oxygen beam of 1.0 eV energy and at a sample temperature of about 45°C. The data indicates no atomic oxygen transport through the Si₃N₄, as was observed in the Space Materials Experiment.

Conductance of Ag vs. Atomic Oxygen Fluence

Si₃N₄ (700Å) Coated Sensor

Exposed at LANL Atomic Oxygen Facility

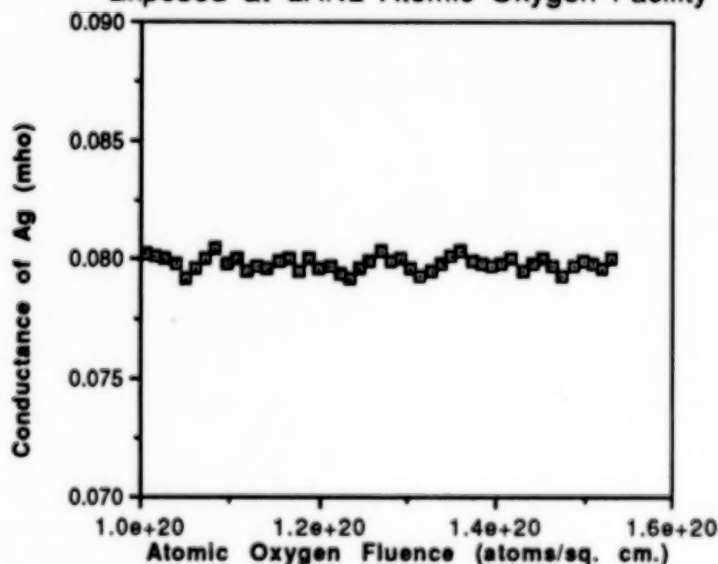


Figure 4: Plot of conductance of silver underneath a 700Å film of Si₃N₄ as a function of atomic oxygen fluence. The sensor was exposed at Los Alamos National Laboratory to an atomic oxygen beam of 2.2 eV energy and at a sample temperature of about 60°C. The data indicates no atomic oxygen transport through the Si₃N₄, as was observed in the Space Materials Experiment.

Conductance of Ag vs. Atomic Oxygen Fluence
BN (1.0 μ m) Coated Sensor
Flown on Delta Star Flight Experiment

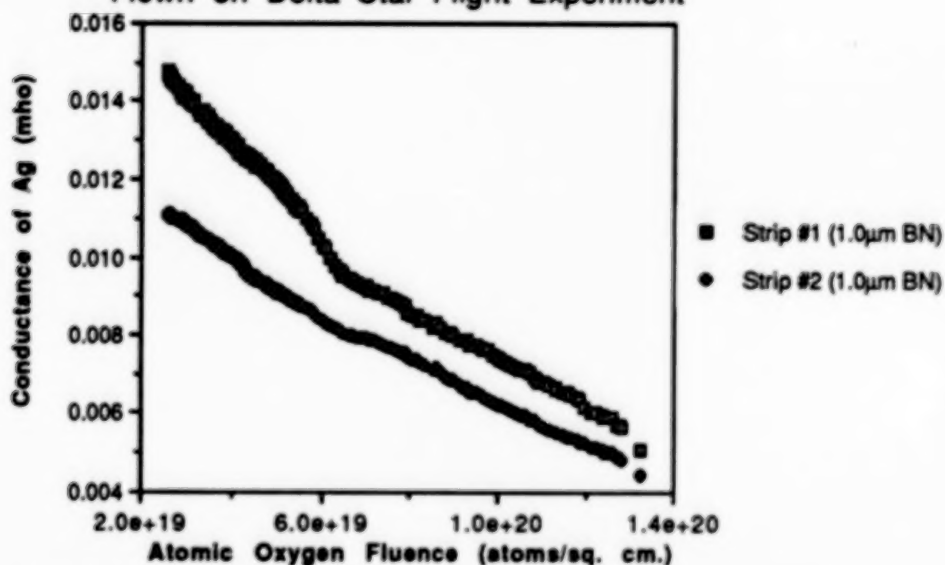


Figure 5: Plot of conductance of silver underneath 1.0 μ m films of BN as a function of atomic oxygen fluence for a sensor flown on the Delta Star Space Materials Experiment. The data shows steadily decreasing conductance (layers of remaining silver) as the silver is oxidized to silver oxide, indicating atomic oxygen transport through the BN.

Conductance of Ag vs. Atomic Oxygen Fluence
BN (750Å) Coated Sensor
Exposed at LANL Atomic Oxygen Facility

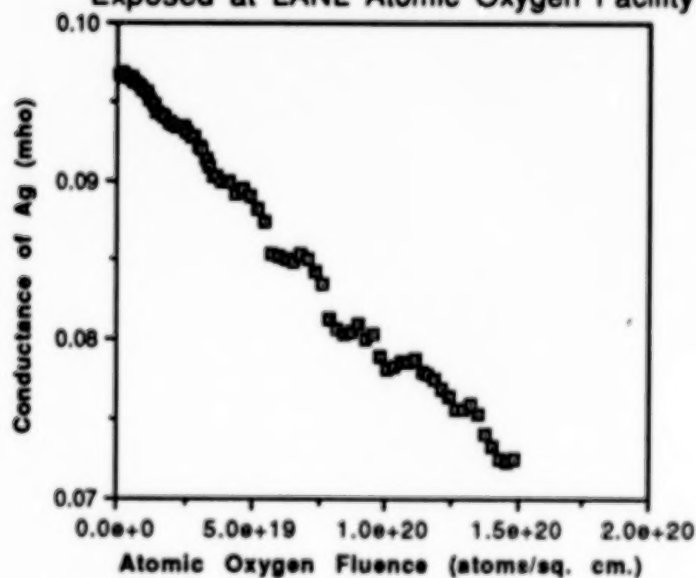


Figure 6: Plot of conductance of silver underneath a 750Å film of BN as a function of atomic oxygen fluence. The sensor was exposed at Los Alamos National Laboratory to an atomic oxygen beam of 1.0 eV energy and at a sample temperature of about 70°C. Atomic oxygen transport through the BN was observed, as was also observed in the Space Materials Experiment.

Conductance of Ag vs. Atomic Oxygen Fluence
BN (750Å) Coated Sensor
Exposed at LANL Atomic Oxygen Facility

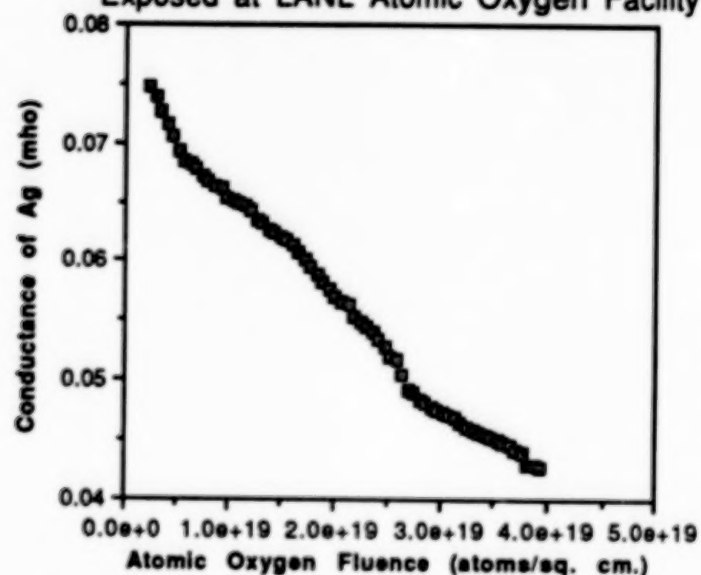


Figure 7: Plot of conductance of silver underneath a 750Å film of BN as a function of atomic oxygen fluence. The sensor was exposed at Los Alamos National Laboratory to an atomic oxygen beam of 2.2 eV energy and at a sample temperature of about 40°C. Atomic oxygen transport through the BN was observed, as was also observed in the Space Materials Experiment.

ADVANCES IN ATOMIC OXYGEN SIMULATION

Joseph F. Froechtenigt and Lyle E. Bareiss
Martin Marietta Astronautics Group
Denver, Colorado

ABSTRACT

Atomic oxygen (AO) present in the atmosphere at orbital altitudes of 200 to 700 km has been demonstrated to degrade various exposed materials on Shuttle flights. The relative velocity of the AO with the spacecraft, together with the AO density, combine to yield an environment consisting of a 5 electron volt (eV) beam energy with a flux of 10^{14} to 10^{15} oxygen atoms/cm²/s. An AO ion beam apparatus that produces flux levels and energy similar to that encountered by spacecraft in low-Earth orbit has been in existence at Martin Marietta Astronautics Group since 1987. Test data has been obtained from the interaction of the AO ion beam with materials used in space applications (carbon, silver, kapton) and with several special coatings of interest deposited on various substrates. The ultimate design goal of the AO beam simulation device is to produce neutral AO at sufficient flux levels to replicate on-orbit conditions. A newly acquired mass spectrometer with energy discrimination has allowed 5 eV neutral oxygen atoms to be separated and detected from the background of thermal oxygen atoms of ≈ 0.2 eV. Neutralization of the AO ion beam at 5 eV has been demonstrated in the Martin Marietta atomic oxygen facility. Research is in progress to increase the flux of the neutral beam to perform testing in a realistic exposure time. Neutral AO testing will be performed and the results compared to those obtained on materials exposed to the actual space environment.

INTRODUCTION

Much has been written in recent years about the phenomena related to spacecraft interactions with the ambient molecular environment at orbital altitudes (Ref 1). The subject phenomena include the effects of neutral AO on spacecraft materials and the emitted radiation (or "Shuttle Glow") observed on or near spacecraft surfaces in low-Earth orbit. These phenomena can result in extremely deleterious effects on spacecraft systems exposed to the environment through degradation of thermo-optical and physical properties of exposed materials and through the induced background radiation detectable by on-board optical sensors.

To address these obvious concerns by spacecraft and instrument designers, Martin Marietta developed the Oxidation/Materials Erosion and Glow Analysis (OMEGA) facility to simulate the high-velocity (8-km/s) AO "wind" experienced by low-Earth orbiting spacecraft (Fig. 1). The initial challenge in the development of OMEGA was to produce a clean AO beam at 5 eV (equivalent to 8 km/s) at sufficient uniform flux levels to simulate on-orbit conditions. This was achieved over 3 years ago for AO ions (i.e., O⁺), however, concern arose within the technical community that a purely neutral beam was required to eliminate questions about ion vs neutral surface chemistry effects. It is interesting to note that essentially all other AO simulation systems in the industry today have at least one such major deficiency which limits their credibility (e.g., low beam energies, impure beams, flux rates that are too high or too low, etc). Recent research on OMEGA has, therefore, concentrated on: 1) O⁺ ion surface chemistry, and 2) developing a neutral AO beam. We now have promising evidence that a neutral beam has been achieved.

ION GUN FACILITY

The ion gun facility at Martin Marietta is an ion beam device that utilizes electrostatic lenses and magnetic fields to control the kinetic energy and beam purity of the selected ion species (Ref 2). A schematic diagram of the ion beam optics is shown in Figure 2. The ion beam apparatus is divided into four subsystems: an ion source, an acceleration and focusing lens subsystem, a mass analyzer, and a decelerator lens subsystem. A neutralizer subsystem is being investigated to convert the beam of ions exiting from the decelerator into a beam of neutral atoms.

The ion source consists of an electron emitting filament, an anode to accelerate the electrons, and a magnet surrounding the ion source to increase the path length of the electrons for more efficient dissociation of the molecular oxygen (O_2) and subsequent ionization of the AO. A beam energy power supply is provided at the anode which allows the energy of the AO ions to be controlled to 5 eV above ground. Along with the AO ions, a mixture of various ions formed from the residual gases in the ion source chamber are extracted by the booster plate of the accelerating lens with an energy of approximately 6,000 eV. This beam of various ions immediately passes through a modified Einzel lens which decreases the energy of the ions to 3,000 eV and, thus, acts as a focusing lens. The energy of 3,000 eV is needed to transport the ions from the exit of the focusing lens, through the mass analyzer, to the entrance of the decelerator lens (a distance of ≈ 1 meter). As the beam passes through the mass analyzer, the magnetic field of the analyzer is adjusted so as to pass only the AO ions. This beam of AO ions is then transported through the decelerator where the beam energy is lowered from 3,000 eV to 5 eV at the exit lens of the decelerator.

ATOMIC OXYGEN TESTS

Test Configuration

For the AO ion beam testing, the sample holder is situated approximately 0.32 cm (0.25 in.) in front of the exit lens of the decelerator. The sample holder is an aluminum block which has anodized surfaces to electrically insulate the test specimen from the holder. The AO ion beam at 5 eV impinges upon the test specimen through a well-defined aperture of 1.27 cm^2 (0.50 in.^2), and this current is continuously monitored to allow the AO ion fluence to be calculated.

Test Materials

The samples tested consisted of ten thermal control type coatings deposited on various substrates, an optical transmission filter, and a mirror sample. The shapes and dimensions of the substrates plus coatings were either 2.54 cm (1 in.) square or 2.54 cm (1 in.) diameter and 0.15 cm (0.06 in.) thick. The type of coating and substrate materials for the samples tested is shown in Table I.

Procedure for AO Ion Tests

Prior to testing, the solar absorptivity (α) and total normal emissivity (ϵ) were measured for each sample, and then a weight measurement was taken. The sample was then photographed and placed in the sample holder. With the test configuration in place, the system was evacuated to 6×10^{-7} torr. Oxygen gas flow was initiated, and the AO ion beam was selected and focused on the sample. The pressure during exposure increased to 2×10^{-6} torr. The current was monitored continuously with an electrometer and the data recorded. After exposure to the AO ion beam, the system was brought to ambient conditions and the sample removed. The same test procedure was followed for all samples. The posttest procedure consisted of photographs, weight measurements, solar absorptivity, and emissivity measurements. In addition, the filter sample had pre and posttest transmission measurements performed.

RESULTS AND DISCUSSION

The total fluence of AO ions was calculated using the time-averaged current during exposure and the 1.27 cm^2 (0.50 in.^2) aperture area. The reaction efficiency, R , for each sample was calculated from the mass change measurements and the time-averaged current using the expression:

$$R = \frac{\Delta m q}{\rho I \Delta t} \text{ cm}^3 / \text{O}^+ \quad (1)$$

where Δm is the mass change, q is the electronic charge, ρ is the coating density, I is the average current, and Δt is the total exposure time.

The test results are given in Table I. The reaction efficiencies for the thermal coatings all appear to be somewhat high compared to similar test data (Ref 1 and 4). The apparent discrepancies may be attributed to differences in the surface chemistry experienced for ions and neutrals or possibly test sample preconditioning issues which are still under investigation. Most of the carbon compound coatings exhibit a low tolerance to the AO environment for mass loss with the exception of the SiC (C-C) sample. It was found out later that the ZrSiO_4 (Mo)-BN sample had been exposed to other environmental testing prior to this test and this may have influenced its results. The transmission filter and the silicon-coated mirror both performed excellent after the AO ion exposure. With regards to the thermo-optical absorptivity and emissivity measurements, the CaO/ZrO_2 (Mo) and the ZrSiO_4 (Mo)-BN samples both had substantial changes. Both of these samples were white coatings and were visibly discolored after exposure. Auger electron spectroscopy measurements indicated that the discoloration may have been caused by some carbon deposition during exposure.

With the persistent concern over the uncertainties induced between ion and neutral AO surface chemistry coupled with the apparent variations in materials reaction efficiencies with ion and neutral beams discussed herein, basic research into optimum beam neutralization techniques has continued at Martin Marietta.

After investigating numerous approaches, the proposed method of neutralizing the AO ion beam is by a grazing incidence technique. The neutralization subsystem is shown in Figure 3. Figure 4 shows the neutralization subsystem in place in the target chamber. As the AO ions exit the last lens of its decelerator with an energy of 5 eV, the effect of space charge in the beam results in the beam expanding radially as it transverses the copper charge exchange cell longitudinally. As the positive AO ions approach the cylindrical surface of the cell at low grazing angles of incidence, free electrons available at the surface attach themselves to the AO ions resulting in partial neutralization of the AO ion beam. This technique is being investigated using nickel as the charge exchange material (Ref 3). Any positive AO ions that are not neutralized are removed from the longitudinal direction by using deflection plates as shown in Figure 3. The neutral AO beam is detected and the flux measured by a VG mass spectrometer which incorporates a cylindrical mirror analyzer (CMA) so that not only is the mass of the species determined but also its energy. This technique enables the oxygen atoms at 5 eV to be distinguished from the natural background of thermal oxygen atoms at 0.2 eV.

Although the results of the current beam neutralization research are quite preliminary at this writing, the data are indicating up to a 50% neutralization efficiency of the 5 eV O^+ beam. Further testing is currently underway to confirm these results, however, such a major breakthrough would provide the technical community with the only ground test facility capable of simulating all of the key AO environmental parameters simultaneously.

REFERENCES

1. Bareiss, L. E., R. M. Payton, and H. A. Papazian, "Shuttle/Spacelab Contamination Environments and Effects Handbook," MCR-85-583, December 1986.
2. Froechtenigt, J. F and E. B. Ress, "Ion Cleaning of Silicone-Based Contaminants," Proc. of 24th IECEE, August 1989, pp. 393-398.
3. Johnson, C. L. et al., "The Vanderbilt University Neutral O-Beam Facility," Report Written Under Contract A71052-A2.
4. Visentine, J. T. et al., "STS-8 Atomic Oxygen Effects Experiment," AIAA Paper 85-0415, 1985.

TABLE I. - ATOMIC OXYGEN TEST DATA FOR VARIOUS MATERIALS

Sample (Substrate)	Fluence O ⁺ /cm ²	Reaction Efficiency cm ³ /O ⁺	Thermal Properties			
			Before α	ϵ	After α	ϵ
C-C	1.3E18	3.4E-23	—	—	—	—
TiB ₂ (Mo)	4.3E17	8.3E-22	—	—	—	—
B ₄ C (C-C)	3.5E17	1.65E-21	.96	.89	.97	.90
TiB ₂ (C-C)	7.3E17	5.4E-22	.89	.78	.90	.82
C-C	1.7E18	4.0E-23	.86	.66	—	—
Al ₂ O ₃ (Mo)	1.6E15	— — —	.37	.80	.51	.82
B ₄ C/SiC (C-C)	7.9E17	1.9E-22	.71	.71	—	—
SiC (C-C)	1.1E18	2.3E-24	.79	.82	.82	.82
CaO/ZrO ₂ (Mo)	2.8E15	— — —	.56	.80	.59	.78
Al ₂ O ₃ /BN/Cu/BN (SiO ₂)	1.7E15	— — —				
ZrSiO ₄ (Mo)-BN	6.7E14	1.3E-20	.45	.90	.44	.89
Al ₂ O ₃ /Ag (Si)	7.8E16	— — —				

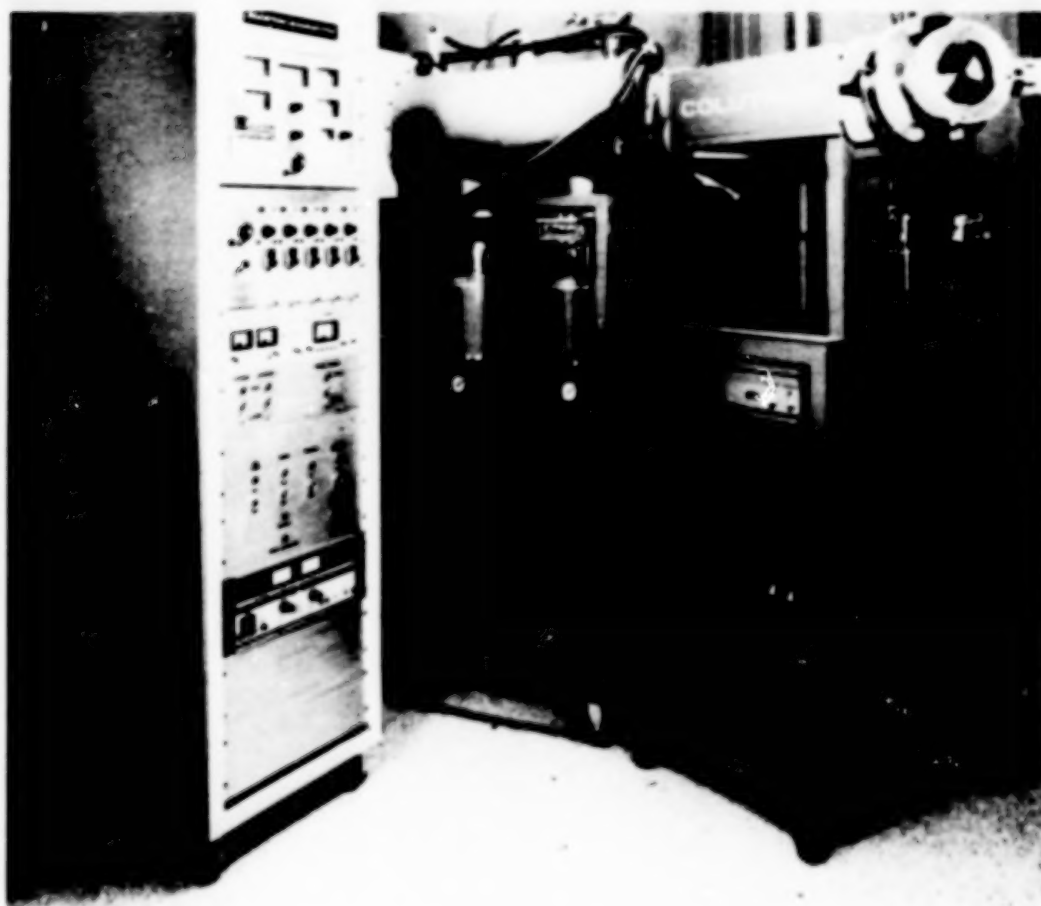


FIGURE 1. - OMEGA TEST FACILITY

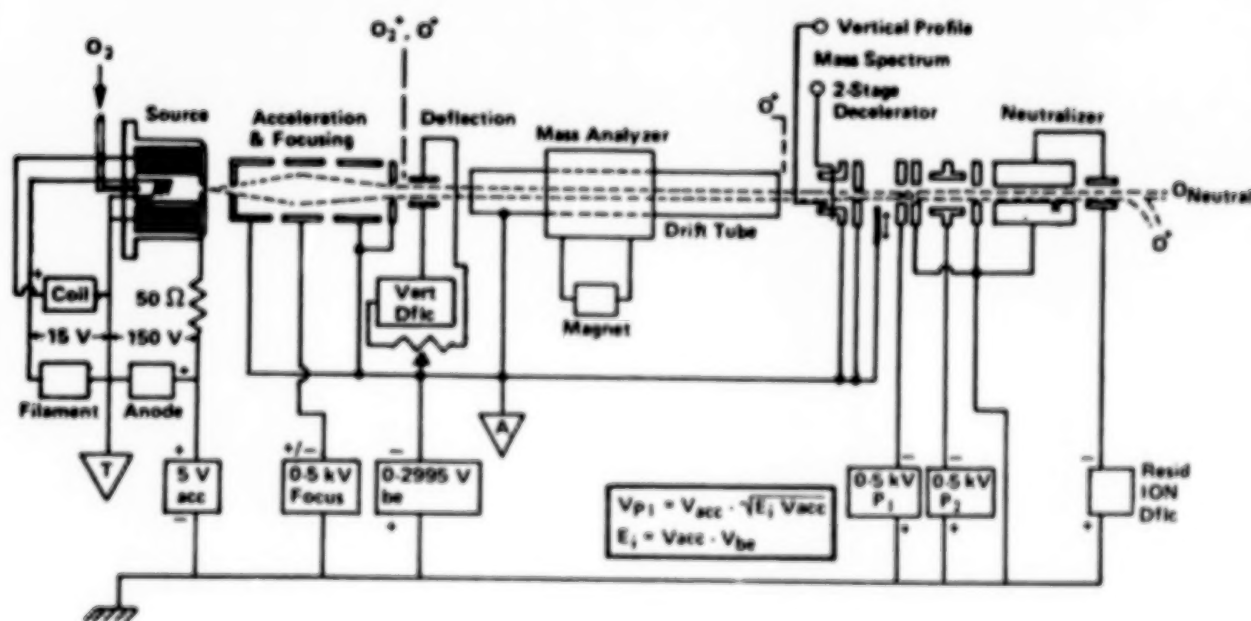


FIGURE 2. - MAJOR ELEMENTS OF ATOMIC OXYGEN BEAM APPARATUS

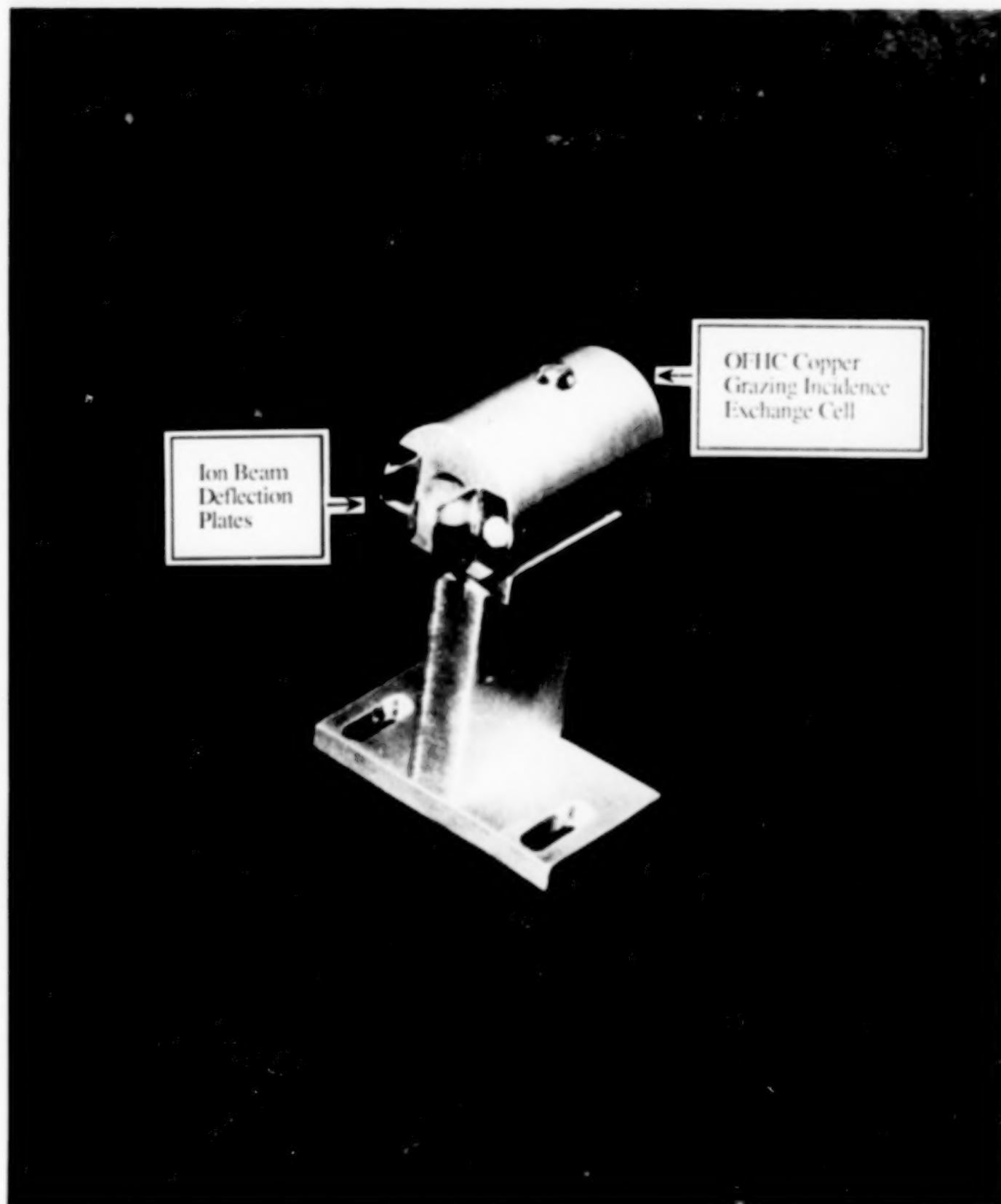


FIGURE 3. - NEUTRALIZATION SUBSYSTEM

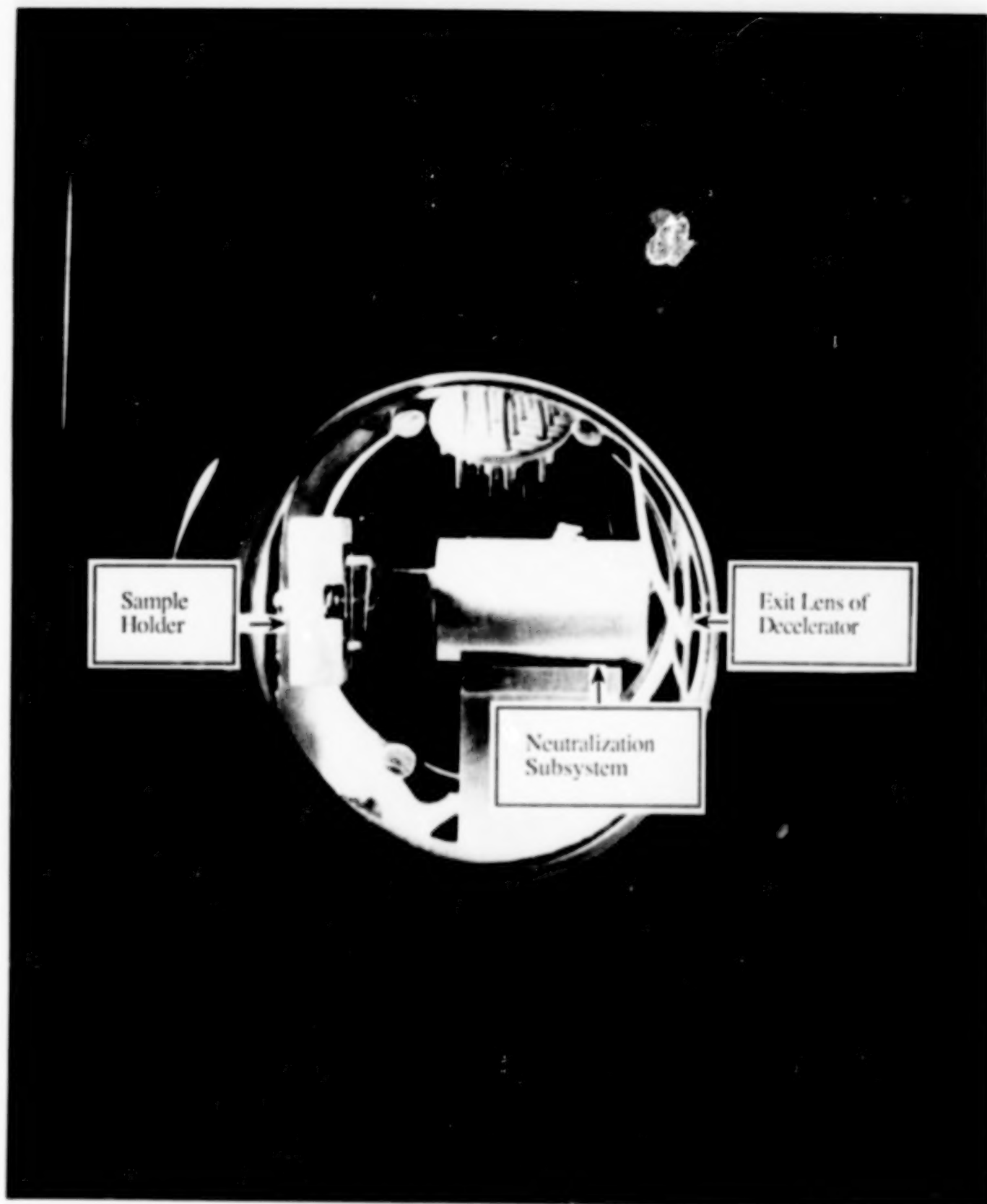


FIGURE 4. - NEUTRALIZATION SUBSYSTEM IN TARGET CHAMBER

SPACE ENVIRONMENTAL EFFECTS ON SPACECRAFT THERMAL CONTROL COATINGS

L.G. Bartosik and H.W. Babel
McDonnell Douglas Space Systems Company

ABSTRACT

A large portion of the space based applications in the near future are for low Earth orbit including the Space Station Freedom. The lifetime requirement for materials on the Space Station Freedom is 30 years. Materials must be selected which will withstand the deleterious effects of low Earth orbit. Environmental effects in the low Earth orbit include atomic oxygen, ultraviolet radiation, ionizing radiation, and hypervelocity impact. These effects can adversely affect the surface properties of materials. This is particularly critical in the case of thermal control materials where the efficiency of the thermal control is dependent on the stability of the surface properties.

The current baseline thermal control coating for the Space Station Freedom radiators is silver Teflon. The surface property requirements for the coating are a solar absorptance of 0.2 and an infrared emittance of 0.8. These optical properties yield the most desirable radiator efficiency. The effects of atomic oxygen and ultraviolet radiation on the baseline coating and several other candidate thermal control materials were studied.

The thermal control radiator materials in this study included silver- and aluminum-backed Teflon, sulfuric acid anodized aluminum, sputter-deposited silicon dioxide on aluminum, and silver- and aluminum-backed polychlorotrifluoroethylene (PCTFE). The samples were exposed to an atomic oxygen fluence of approximately 10^{20} atoms/cm². The atomic oxygen fluence for long-life spacecraft in low Earth orbit such as Space Station Freedom is approximated as 10^{22} to 10^{23} atoms/cm². Therefore, this simulation yields a fluence that is two to three orders of magnitude less than the thirty-year life. Several of the samples were exposed to an ultraviolet radiation environment of 600 hours at two solar constants in the near ultraviolet radiation region of the spectrum. The radiators will be positioned edge-on to the sun and are expected to be exposed to approximately 10,000 equivalent sun hours. Therefore, this simulation models 1/10 of the expected exposure. However, it has been shown that the majority of change in optical properties occurs in the first 400 equivalent sun hours of exposure.

The simulation of several of the low Earth orbit environment constituents provided a valuable data base to aid in the selection of the radiator thermal control material to meet the life requirements of the Space Station Freedom. This study illustrates the effects of the environment on thermal control coatings and the importance of this factor in the selection process for long life spacecraft materials.

SPACE SIMULATION TEST FOR THERMAL CONTROL MATERIALS¹

W.R. Hardgrove
TRW Space and Defense Sector

ABSTRACT

Tests were run in TRW's Combined Environment Facility to examine the degradation of thermal control materials in a simulated space environment. Thermal control materials selected for the test were those presently being used on spacecraft or predicted to be used within the next few years. The geosynchronous orbit environment was selected as the most interesting. One of the goals was to match degradation of those materials with available flight data. Another aim was to determine if degradation can adequately be determined with accelerated or short term ground tests.

INTRODUCTION

These tests were run in TRW's optical test chamber which is one of three chambers in the Combined Environment Facility (See schematic in Figure 1). This chamber exposes samples to a combined environment of low energy protons, low energy electrons, high energy electrons, near ultraviolet, and far ultraviolet. Thus, synergistic effects of the space environment can be studied. The chamber design permits in situ measurement of solar absorptance so that its degradation can be measured without removal from vacuum.

The nature of thermal control material degradation, being a thin layer or first surface phenomenon, requires a simulation of space radiation environment different from the depth penetration model standards. A radiation survivability analysis has converted the particle population to low energy particles which penetrate thin surface layers. Monte Carlo techniques adapted the low energy particle levels to the potential test materials. Results of the analysis were adjusted to match the capabilities of the facility.

Testing consisted of a battery of three tests. Three different samples of each material were included in the tests for repeatability. The third set of samples was run at a different acceleration rate in an attempt to compare the effects of test acceleration between tests as well as to actual flight data.

1. This work was done under TRW IRAD, "Advanced Thermal Management of Spacecraft," Project No. 88330122, 89330122.

SYMBOLS AND ABBREVIATIONS

Symbols:

A	entrance area to the Faraday cup, .312 cm ²
α_s	solar absorptance
b	adjustment factor for relative lengths from the source to the sample plane and Faraday cup, .80
I	Faraday cup current
K	charge per proton or electron
n	efficiency of the Faraday cup screen
ϕ	flux desired ~ p+/cm ² sec or e-/cm ² sec

Subscripts:

e	denotes electrons
p	denotes protons

Abbreviations:

CEF	Combined Environment Facility
EUVSH	Equivalent Ultraviolet Sun Hours
FUV	Far Ultraviolet
HEE	High Energy Electrons
LEE	Low Energy Electrons
LEP	Low Energy Protons
NUV	Near Ultraviolet

SELECTION OF MATERIALS

Although many different materials have been run in TRW's combined environment facility, the thrust of this testing was to examine thermal control materials presently used on spacecraft or potentially to be used in near term, i.e., within the next five years. The presently used materials included the usual white paints, i.e., Z93, ZOT, and S13GLO as well as second surface mirrors. Thermal analysis engineers were polled for other near-term candidates.

Based upon these inputs, seventeen different thermal control materials were selected for study as listed in Table 1. Since the sample plane of the CEF is capable of handling 26 samples and three samples of each material were desired for repeatability, these prospective samples were broken down into two sets as shown in Table 1. The SSM's, which are normally used as contamination monitors during tests of this kind, were used with both sets.

ENVIRONMENTAL PARAMETERS

Since many spacecraft are being designed for geosynchronous orbit, this environment was selected as most interesting. TRW's radiation survivability department was tasked to determine the environment which best matches the CEF capabilities with the radiation environment of geosynchronous orbit. Based upon requirements of present TRW spacecraft and various environmental studies, they were able to determine a fluence profile for a spacecraft in geosynchronous orbit.

With this data and computer techniques which use Monte Carlo methods to establish penetration levels in different materials, analysts modeled the penetration depth of the various types of particles into the materials of interest. Details of the models are discussed in footnote 2. For the analysis, particle levels which were available in the test facility were matched with the same penetration levels as those in the geosynchronous environment.

In this study it was postulated that surface property damage is a function of ionization rather than displacement. With this assumption, a greater number of penetrations through the materials causes a worse degradation of the thermal control surface. Based upon the analysis, the corresponding fluxes which penetrated each thermal surface completely were determined. These fluxes are presented for the first set of samples in Table 2.

Since this test was a multiple sample test, i.e., a test to evaluate more than one type of sample simultaneously, it was necessary to establish a flux to be used on the complement of the samples. Because complete penetration was determined to cause the most damage due to ionization, the maximum fluences on each sample would cause the most damage. Therefore the maximum fluence for each type of radiation would cause the most severe damage for the total. These selected worse or dominating cases are outlined for each particle type in Table 2.

PRE TEST MEASUREMENTS/CALIBRATION

Prior to the test the NUV source was calibrated using a water-cooled, TRW designed, resistor sensor device. This device was attached to the chamber front which places its test plane at the same location as the sample plane. Flux at various settings on the lamp were determined by measuring the resistance change at small openings representing each sample location. This data was read into a computer which with software automatically compares the change between the NUV source and a known source at each location. The same procedure was performed after test shutdown to determine overall NUV fluences during the test sequence.

Normal emittance measurements were made ex situ before and after the test sequence. These values were found by using a Gier-Dunkle Instruments Model DB100 Infrared Reflectometer. Details of the operation of this instrument are described in reference 1.

Ex situ spectral directional reflectance measurements of the samples were made prior to the test using a Beckman DK2A ratio recording spectrophotometer with an integrating sphere attachment of the Edwards type. Details of how these instruments function are discussed in references 2 and 3. These solar absorptance measurements were also made ex situ after completion of the test and removal of the samples from the chamber.

IN SITU MEASUREMENT/CALIBRATION

After the chamber was at vacuum (approximately 1×10^{-6} torr), the solar absorptance of the samples was measured in situ with the Beckman DK2A and repeated periodically during the test sequence to establish the solar absorptance degradation of the sample with time. Next the preliminary calibration of the LEP and LEE was performed. Both sources were calibrated with a Faraday cup which is mounted on an adjustable wand in the chamber. For the pre test calibration the proton source was turned on and adjusted to maintain the required 30 KeV voltage. Then the source was adjusted to maintain the necessary current to give an average flux as desired at the sample plane. Current was measured by a picoammeter and was determined through the characteristics of the Faraday cup in the chamber in relation to the flux by the following equation

$$I_p = \frac{\phi_p A n K_p}{b}$$

A standard nine point calibration was used to describe the average flux over the sample plane. This calibration covers the corners and midpoints. Fluxes at other sample locations were determined by averaging the flux between any two calibration points based upon relative distances to that location.

Calibration of the electron source utilized the same Faraday cup and techniques as described under the proton source calibration. For the pre test calibration, the electron gun was set at the desired voltage of 7 KeV. After the required current was derived from the equation for the desired flux, the electron source was adjusted to project this current on the Faraday cup in front of the center sample in the sample plane. Since the source is angled into the chamber, there is a fall off from left to right over the sample plane. A kill switch on the proton source allows the electron source to be calibrated with the proton source activated.

For the test runs the NUV was set at the maximum current run level at which the pre test calibration was performed. The FUV was set to maximize the energy level at the sample plane. The FUV beam was reflected off a mirror in its path thereby allowing adjustments to direct the beam into its own Faraday cup. Flux at the sample plane was based upon past calibration matches with this current using both an open and an SiO_2 filter condition.

The HEE has a scattering plate in line with the chamber. Current at the plate has been previously calibrated as discussed in reference 4. A current accumulator was used with this previous data to determine when various fluence levels were met.

TEST CONDUCT

Since the proton and low energy flux can be monitored in situ, they were checked periodically utilizing the standard nine point calibration method and adjusted, if necessary, to maintain the required flux levels. For test runs 1 and 2, i.e., sample sets 1 and 2, the samples were exposed for an equivalent of 10 years in geosynchronous orbit. During the tests, in situ spectral reflectance measurements were made at equivalent proton and electron fluence levels to

represent 1, 3, 5, and 10 years of orbital flight. The third test run was a decelerated test which represented 1-1/2 years in orbit. In this test measurements were made at fluences which were equivalent to 3, 6, 12, and 18 months in orbit.

DISCUSSION

The purpose of these tests was to determine if short term ground tests could closely approximate long term, i.e., 5 years or more, degradation of thermal control surfaces. Therefore tests 1 and 2 were accelerated at a high rate to gain the maximum results in the shortest time. For this test series, the maximum acceleration rate was governed by the LEE source. This source was able to provide enough flux to simulate a year of fluence in 72 hours, or an acceleration rate of approximately 120:1. Since both the proton and high energy electrons could provide higher acceleration rates, they were backed down to match the acceleration of the LEE.

Acceleration capability of the solar simulating source was much less than that of the particle sources. The maximum intensity of the NUV varies between 2.0 and 3.0 equivalent suns. The FUV source has no real acceleration capability, i.e., each exposure hour is equivalent to approximately 1 hour in real time. Therefore both the NUV and FUV were run at their maximum levels.

One of the ground test uncertainties in simulating long term degradation is that the acceleration affects the change in properties. Therefore, the third test served as an acceleration effect evaluation by approximating real time exposure rates. This test used the same material types as used in test 1 except that Z93 white paint from set 2 was also included. The final acceleration rate was 2 π times the proton and electron levels. This level was chosen to match the NUV acceleration rate of 2 EUVSH and the effects of a rotating spacecraft, i.e., 1/ π suns.

TEST RESULTS

FLUENCES

During the test sequences, current readings at the nine calibration locations were periodically recorded. The readings from the FUV Faraday cup were also recorded at each monitoring time. These data and times were entered along with the pre- and post- test NUV calibrations into a computer program. The program accumulates data during the test sequence and prints out the accumulated fluences of these four sources at any desired time period. Since the high energy electron source uses an accumulator it is integrated in real time and stopped when it reaches the required fluence level. The measured accumulated fluences and the desired levels are compared in Table 3.

PROPERTY DEGRADATION

At any point of interest, when the accumulated flux of the sources was near that desired for that time, the sources were shut down and spectral reflectance

measurements made. In situ spectral measurements were performed by moving each sample from the sample plane into a quartz tube on one side of the vacuum chamber. This test tube fits into the side of an Edward's sphere so that measurements can be made with the attached DK2A. Since the tube introduces some error, these measurements are relative to the initial in situ measurements; i.e., delta changes.

Spectral reflectance data was entered into an HP9000 computer with the aid of an HP9874A. A standard TRW computer program was used to integrate the spectral data over the Thekaekara/NASA solar irradiance curve to determine the solar absorptance, α_s , for each specimen. An HP9872S plotter graphed reflectance curves for each sample.

Spectral reflectance data was used with another TRW-developed program to determine end-of-life properties. This program assumes that solar absorptance degradation is an exponential function. Through a series of curve fitting and cross-referencing at various wavelengths, the program derives an optimum exponential curve fit of the existing data and calculates the maximum solar degradation. Average degradations of the samples are presented in Table 4. Also included in the table are the calculated end-of-life values.

ACCELERATED/DECELERATED TEST COMPARISON

For this parametric evaluation, samples with high degradations were chosen since low degrading samples would match well by definition. Therefore, the most significant changes would appear in the highly degrading samples or, in these tests, ZOT, S13GLO white paint and silvered Teflon. Solar absorptance data from these tests are plotted in Figures 2 through 4 for the three materials. Included with the silvered Teflon data of Figure 4 are results from a previous low rate of acceleration test as discussed in Reference 4.

Data from the two tests for the S13GLO match reasonably well although the lower acceleration environment initially causes a higher degradation in the sample. However, the curve seems to cross over around one year and the high acceleration rate test appears to predict more degradation than the test nearer real time. This condition holds true for both the ZOT and the silvered Teflon as shown in Figures 3 and 4. The ZOT samples actually exhibit a significant deviation between the two tests for the first year to a year and a half. However, the data also appears to cross over at approximately 20 months so that the highly accelerated test data becomes more conservative, i.e., higher degradation.

The silvered Teflon follows the same pattern initially. However, between the 6 month and 9 month measurement there was a significant change in solar absorptance. Originally this was thought to be a measurement problem. But an examination of the samples showed a definite darkening of the sample which would probably cause the deviation in absorptance. At present, the reason for this abrupt change cannot be explained. Interestingly, the 0 to 6 month data seems to project a curve which may line up with the curve for the data from the highly accelerated test.

For comparison purposes, data from a low acceleration test run in 1977 per Reference 4 is included for this sample. Acceleration rates for the test 1977 in were 3 π :1. This data shows reasonable agreement with the high acceleration test as run in 1987/1988.

FLIGHT/TEST COMPARISON

Crux of the simulated space test is how its results correlate with actual flight data. Therefore a comparison was made between flight data from three sources and the accelerated simulation test. Data from References 5 and 6 were used as two of the sources for the flight data. The other information includes the most recent property degradation data acquired from TDRSS which is one of TRW's long term satellites.

For this comparison the same three materials were used for the same reason as before, i.e., higher degradation exhibits maximum deviation. Test data for the S13GLO illustrated in Figure 5 shows good agreement with the TDRSS data although it is slightly more conservative. The curve shapes for the test and flight data seem to be the same. Conversely, the ZOT data, as both shown in Figure 6 seems to differ drastically between flight and test. ZOT data from the flight shows very little degradation. For the silvered Teflon as depicted in Figure 7 the test appears to be more conservative than the flight data. There is a good match between the 2 mil samples from the flight and the test sample which, however, was 5 mil.

CONCLUSIONS

Overall the test environment causes a solar absorptance degradation conservatively higher than flight. Nevertheless, the test can be useful in determining if a material will exhibit high degradation in space. Therefore, samples of new materials can be evaluated by short term acceleration simulations. However, for accurate data on a candidate material a limited acceleration is in order.

One interesting note from the tests is that the S13GLO data shows the match between flight and test data. Also, the S13GLO test and flight proton dosages matched best. Since there is conjecture that protons are the most damaging environmental component for materials of this type, perhaps a better proton match for other materials would exhibit correspondingly better correlation.

In conclusion, these tests indicated that an accelerated combined environment simulation may be used to evaluate thermal control materials which exhibit a high degradation in space or are stable. Further, the tests are generally conservative so that this data can be used for "worst case" analyses. Possibly, with a better environmental match and minimum allowable acceleration times, accurate end-of-life properties extrapolations can be obtained.

REFERENCES

1. K.E. Nelson and E.E. Luedke, and J.T. Bevans, "A Device for the Rapid Measurement of Total Emittance," J. Spacecraft Rockets 3:758-760 (1966).
2. L. Cahn and B.D. Henderson, "Performance of the Beckman DK Spectrophotometer," J.O.S.A. 48:380-387.
3. D.K. Edwards, et al, "Integrating Sphere for Imperfectly Diffuse Samples," J.O.S.A. 51:1279-1288 (1961).
4. "Properties of Metallized Flexible Materials in the Space Environment Final Report," TRW 26177-6048-RU-00/SAMSO TR78-31, Contract F04701-74-C-0562 Seq. No. A002, January 1978.
5. D.F. Hall and A.A. Foote, "Long-Term Performance of Thermal Control Coatings at Geosynchronous Altitude," AIAA-86-1356, AIAA/ASME 4th Thermophysics and Heat Transfer Conference, Boston, MA, June 1986.
6. C.C. Anderson and M.M. Hattar, "Calorimetric Measurements of Thermal Control Surfaces at Geosynchronous Orbit," Journal of Thermophysics and Heat Transfer, Volume 2, April 1988, pp. 145-151.

Set 1

Sample Type	Thickness	
	Cm	(In)
1) Second Surface Quartz Mirror	.015-.020	(.006-.008)
2) Silvered Teflon	.019	(.0085)
3) ZOT White Paint	.013-.020	(.005-.008)
4) S13G White Paint (with new binder)	.013-.020	(.005-.008)
5) Astroquartz	.023	(.009)
6) Aluminized Kapton, Sputtered ITO Overcoat	.003	(.001)
7) Leafing Aluminum Paint	.003-.005	(.001-.002)
8) Fibrous Reinforced Composite Insulation (FRCI)	.508	(.200)

Set 2

Sample Type	Thickness	
	Cm	(In)
1) Second Surface Quartz Mirror	.015-.020	(.006-.008)
2) Black Kapton	.005	(.002)
3) Z-93 White Paint	.013-.020	(.005-.008)
4) Chem Filmed Aluminum	- - - - -	- - - - -
5) FRCI-II	.508	(.200)
6) Beta Cloth	.020	(.008)
7) White Chem-Glazed Paint	.013-.020	(.005-.008)
8) Expanded Teflon on Kapton	.013/.005/.003	(.005/.002/.001)
9) VDA on Coated Aluminum	1000A	

Table 1 Spacecraft Thermal Control Materials

Sample	30 KeV Proton $\phi(p/cm^2)$	7 KeV Electron $\phi(e/cm^2)$	800 KeV Electron $\phi(e/cm^2)$
1) Second Surface Quartz Mirror	3.57×10^{16}	6.02×10^{16}	1.88×10^{16}
2) Silvered Teflon	3.35×10^{16}	6.74×10^{16}	3.58×10^{16}
3) ZOT White Paint	2.92×10^{16}	9.03×10^{16}	1.73×10^{16}
4) S13G White Paint	4.02×10^{16}	4.98×10^{16}	1.85×10^{16}
5) Astroquartz	3.55×10^{16}	7.07×10^{16}	1.93×10^{16}
6) Aluminized Kapton-Sputtered ITO Overcoat	1.42×10^{16}	1.08×10^{17}	4.10×10^{16}
7) Leafing Aluminum Paint	3.09×10^{16}	8.40×10^{16}	1.71×10^{16}
8) FRCI	3.86×10^{16}	5.64×10^{16}	1.88×10^{16}

Table 2 Recommended Test Particle Fluences for Simulation of 10 Years on Geosynchronous Environment

Source	Goal	Actuals	
		Set 1	Set 2
30 keV Protons	4.02×10^{16} p/cm ²	6.64×10^{16} p/cm ^{2**}	7.31×10^{16} p/cm ^{2**}
7 keV Electrons	1.08×10^{17} e/cm ²	1.11×10^{17} p/cm ^{2**}	7.49×10^{16} e/cm ^{2**}
800 keV Electrons	4.10×10^{16} e/cm ²	- - - - -	4.10×10^{16} e/cm ^{2**}
NUV	27884 EUVSH*	2290 EUVSH	1900 EUVSH
FUV	27884 EUVSH*	1073 EUVSH	1651 EUVSH

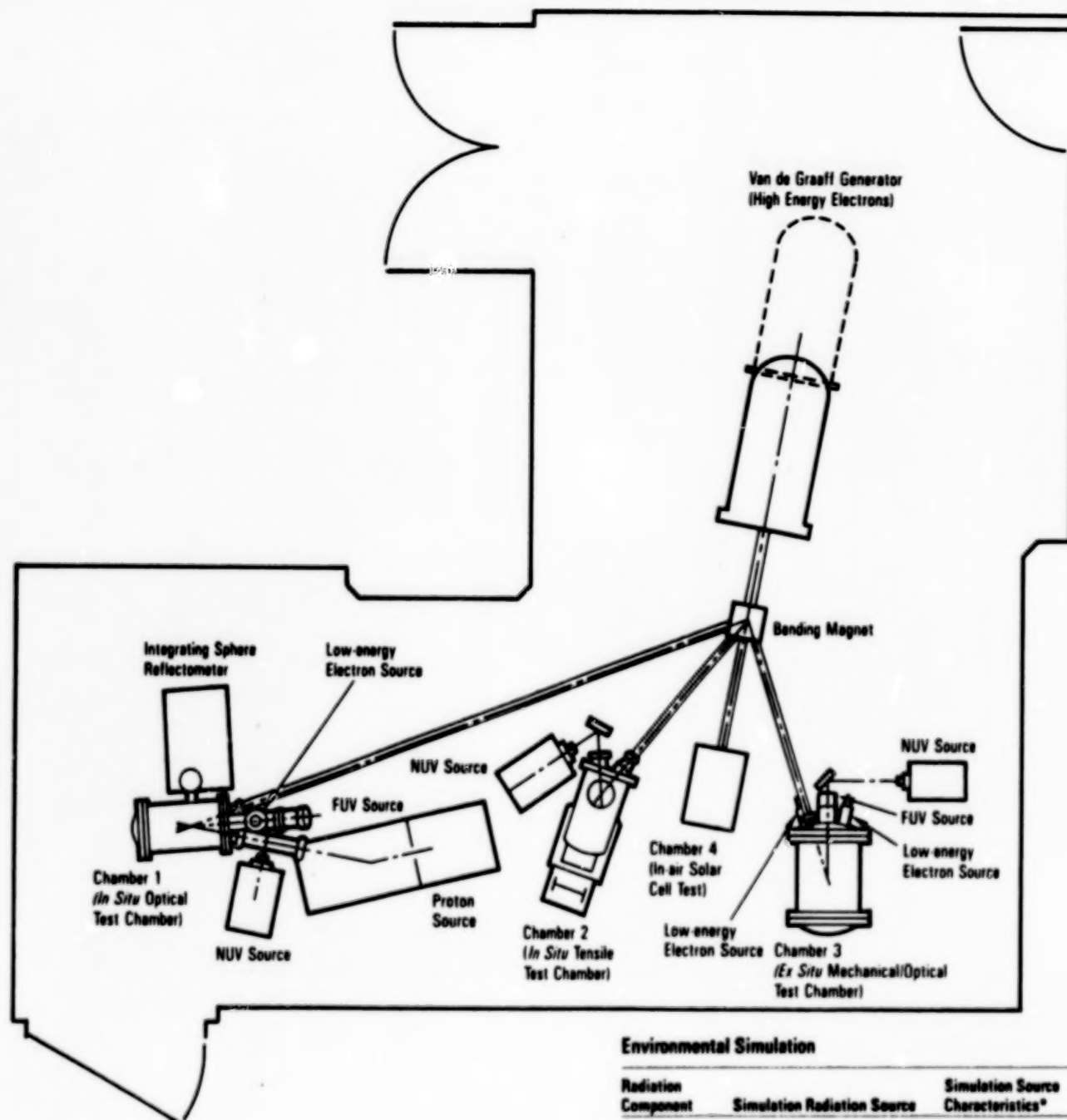
* NUV and FUV requirements are for a spinning or earth-oriented spacecraft (orbit time/π) These sources are run at maximum levels during the accelerated test. NUV values are averages over the sample plane while FUV values are maximums.

** Protons and electron fluences are average values over the sample plane.

Table 3 10-year Equivalent Test Fluences

	Solar Absorptance After Time in Orbit (Years)					• (extrapo- lated)	Hemispherical Emittance After Time in Orbit	
	0	1	3	5	10		0	10
Set 1								
1) Silvered Teflon	0.09	0.13	0.19	0.22	0.25	0.27	0.78	0.78
2) ZOT White Paint	0.15	0.40	0.55	0.62	0.65	0.65	0.85	0.85
3) S13G/LO White Paint (with new binder)	0.26	0.56	0.62	0.68	0.71	0.71	0.86	0.81
4) Astroquartz	0.32	0.38	0.44	0.47	0.50	0.51	0.83	0.83
5) Aluminized Kapton, Sputtered ITO Overcoat	0.38	0.38	0.39	0.39	0.40	0.40	0.12	0.12
6) Leafing Aluminum Paint	0.30	0.32	0.34	0.34	0.35	0.36	0.31	0.29
7) FRCI	0.22	0.31	0.31	0.31	0.37	0.37	0.84	0.84
Set 2								
1) Black Kapton	0.93	0.92	0.92	0.92	0.91	0.89	0.77	0.77
2) Z93 White Paint	0.19	0.28	0.38	0.45	0.52	0.52	0.87	0.85
3) Chem Filmed Aluminum	0.41	0.37	0.37	0.38	0.41	0.41	0.06	0.06
4) FRCI-II	0.23	0.27	0.25	0.27	0.32	0.47	0.84	0.84
5) Beta Cloth	0.30	0.47	0.50	0.54	0.59	0.59	0.86	0.86
6) White Chem Glaze Paint	0.29	0.68	0.71	0.74	0.77	0.77	0.85	0.83
7) Expanded Teflon on Kapton	0.18	0.37	0.46	0.60	0.62	0.65	0.68	0.68
8) VDA on Coated Aluminum	0.10	0.12	0.13	0.14	0.14	0.14	0.02	0.06

Table 4 Average Thermal Control Material Degradation in Simulated Geosynchronous Orbit



Environmental Simulation

Radiation Component	Simulation Radiation Source	Simulation Source Characteristics*
Far Ultraviolet	Electrodeless Krypton Gas Lamp	0.10 to 0.18 μm Up to 5X Sun Intensity
Near Ultraviolet	3-kW Short-arc Xenon Lamp	0.18 to 0.40 μm Up to 3X Sun Intensity
Radiation Belt Electrons	Van de Graaff Accelerator	70 keV to 1.1 MeV 10^7 to 10^{12} e/cm ² sec
Plasma Sheet Electrons	Electron Flood Gun	0.5 to 10 keV Up to 10^{11} e/cm ² sec
Radiation Belt Protons	Ionization Equivalent Electrons from Van de Graaff Accelerator	70 keV to 1.1 MeV 10^7 to 10^{12} e/cm ² sec
Solar Flare Protons	Ionization Equivalent Electrons from Van de Graaff Accelerator	70 keV to 1.1 MeV 10^7 to 10^{12} e/cm ² sec
Plasma Sheet Protons	Hydrogen-ion Plasma Generator	Up to 30 keV Up to 10^{12} p/cm ² sec
Vacuum	GN ₂ Aspiration, Cryosorption, and 400 1/sec Ion Pumping	10^{-6} to 10^{-8} torr

*Radiation zone at the target plane is ≈ 15 cm (6 in) diameter.

Figure 1. CEF Schematic

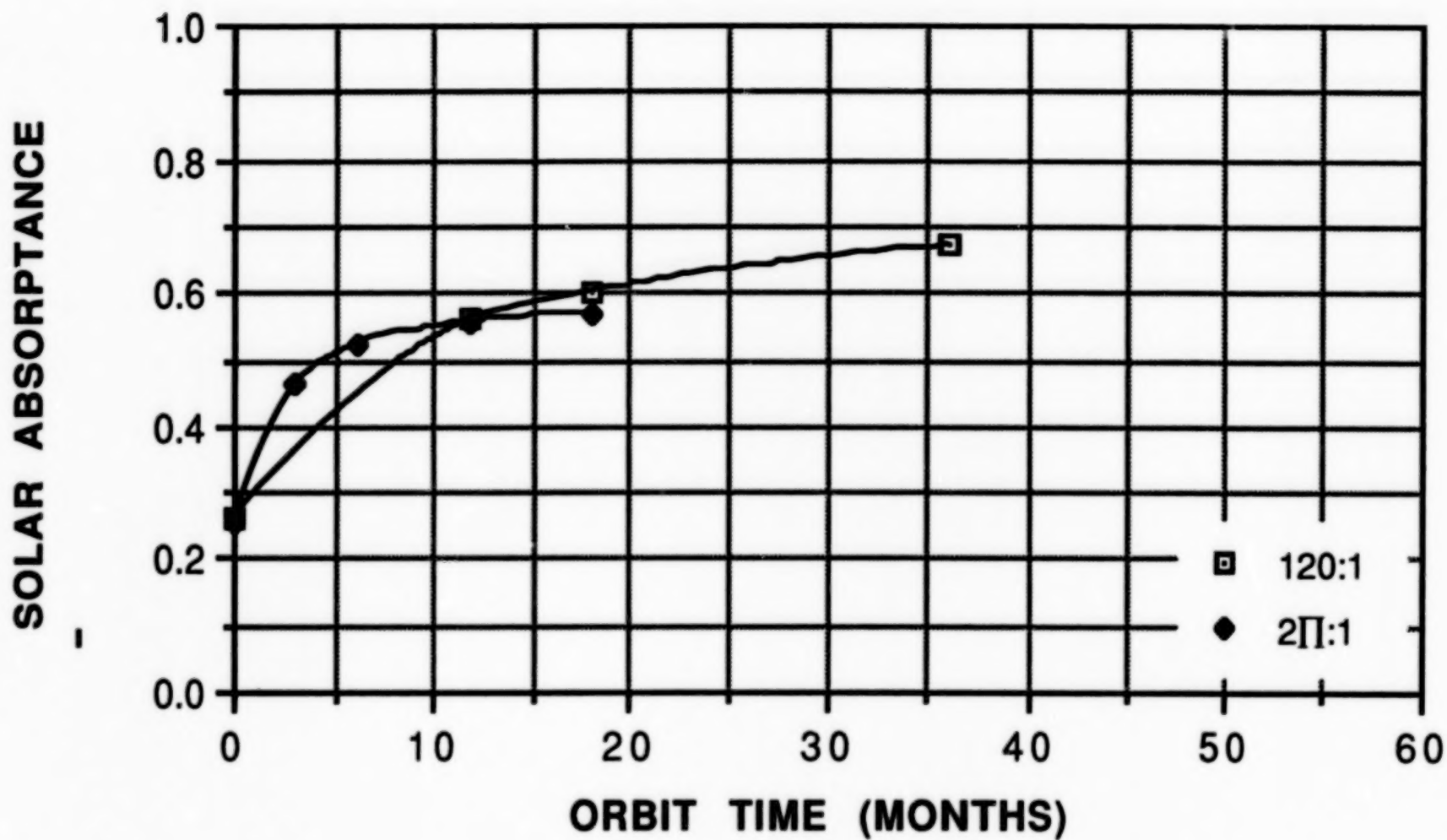


Figure 2. Comparison of Solar Absorptance Degradation of S13G-LO Paint for High and Low Accelerated Simulated Environmental Tests

SOLAR ABSORPTANCE

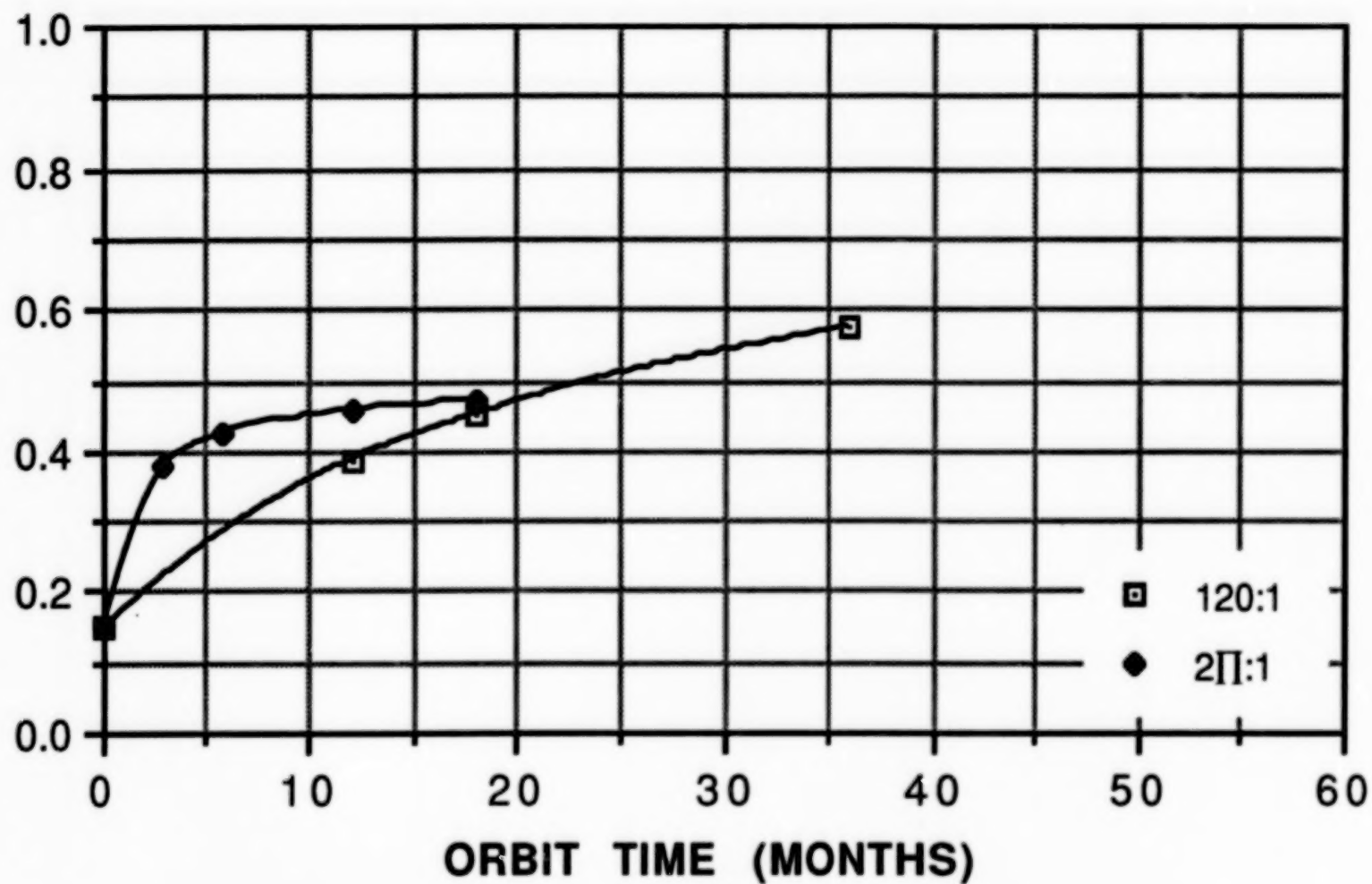


Figure 3. Comparison of Solar Absorptance Degradation of ZOT Paint for High and Low Accelerated Simulated Environmental Tests

SOLAR ABSORPTANCE

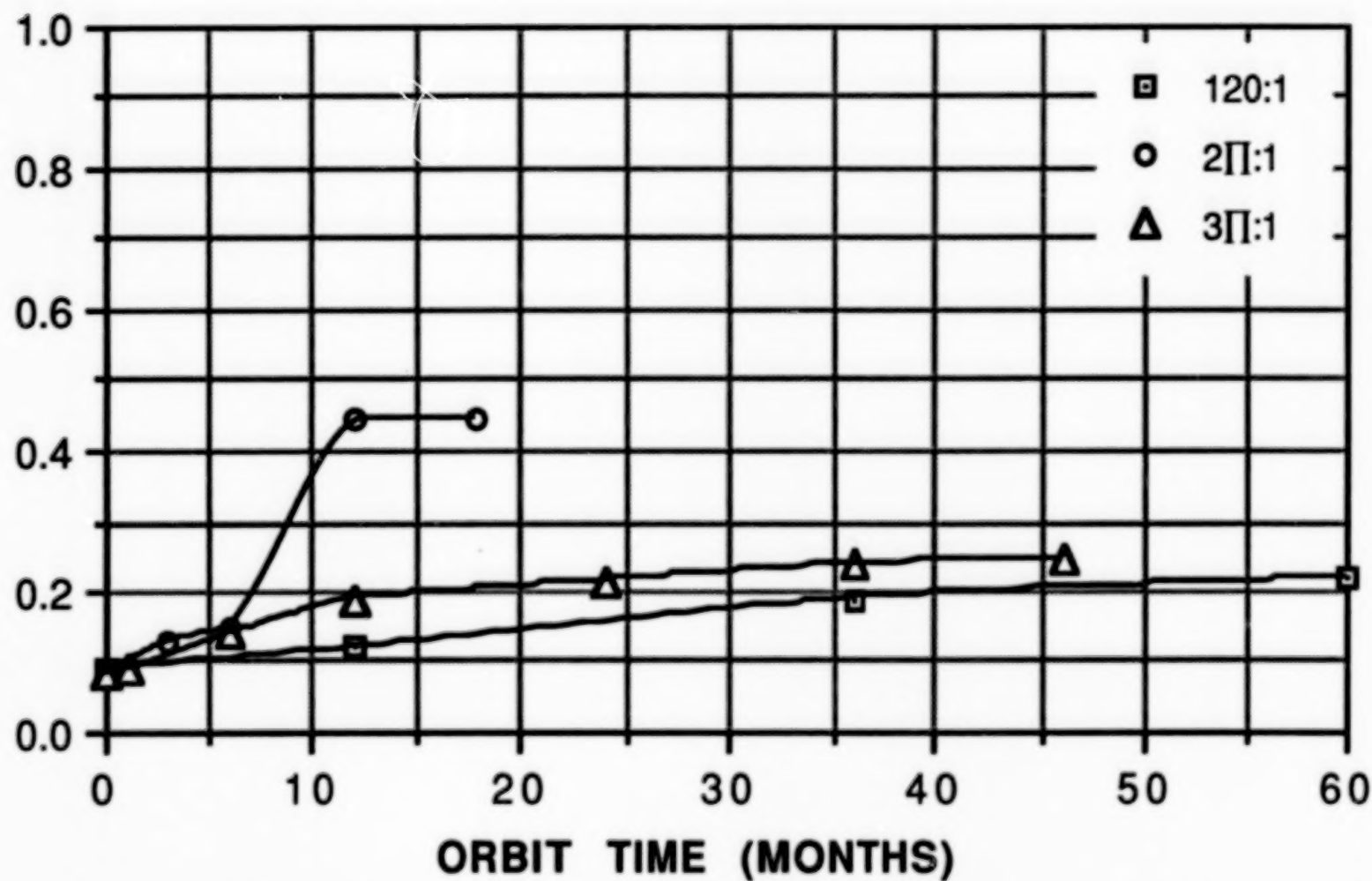


Figure 4. Comparison of Solar Absorptance Degradation of Silvered Teflon for High and Low Accelerated Simulated Environmental Tests

SOLAR ABSORPTANCE

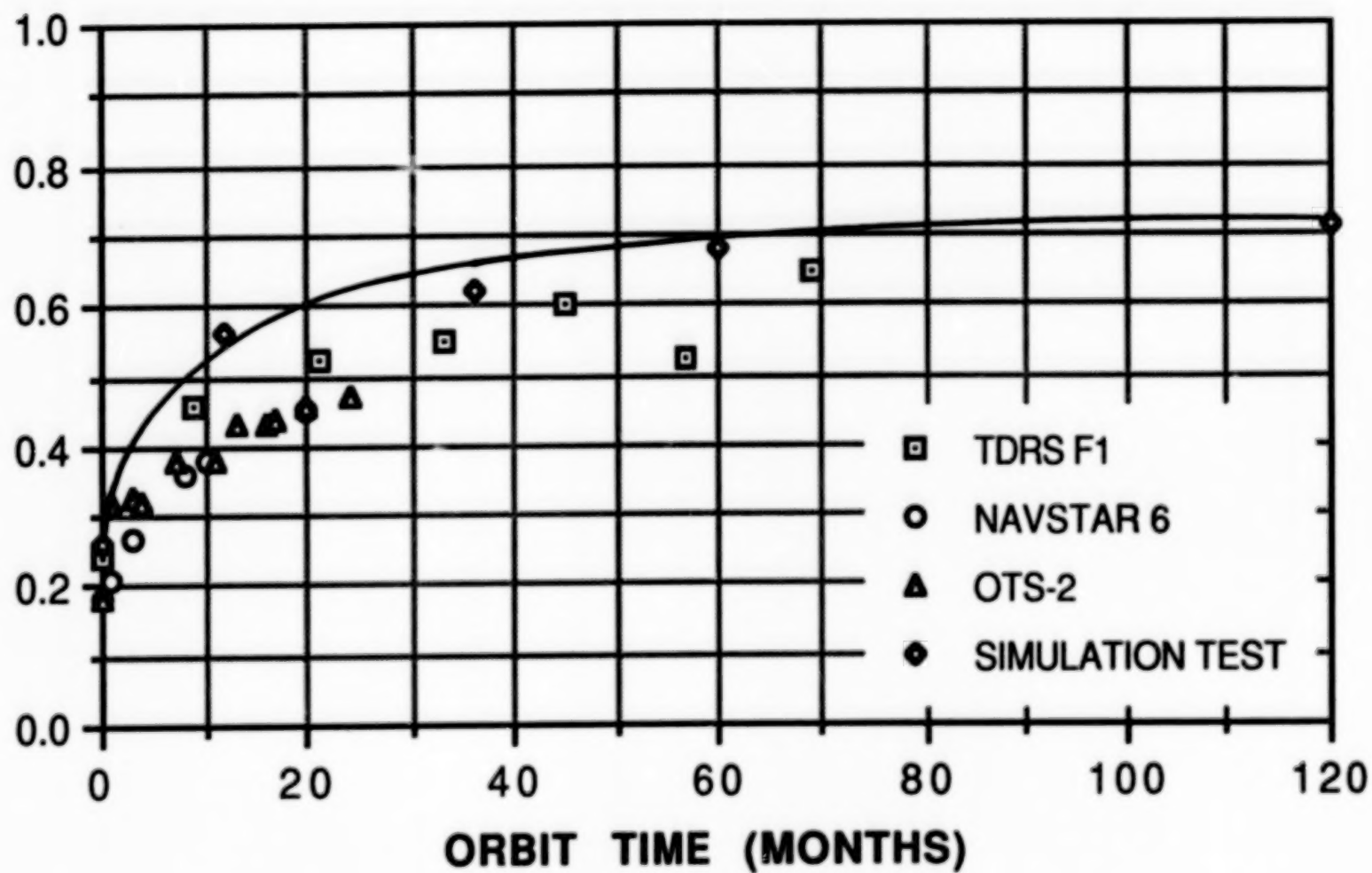


Figure 5. Comparison of Solar Absorptance Degradation for S13G-LO Paint for Simulation Test vs. Flight Data

SOLAR ABSORPTANCE

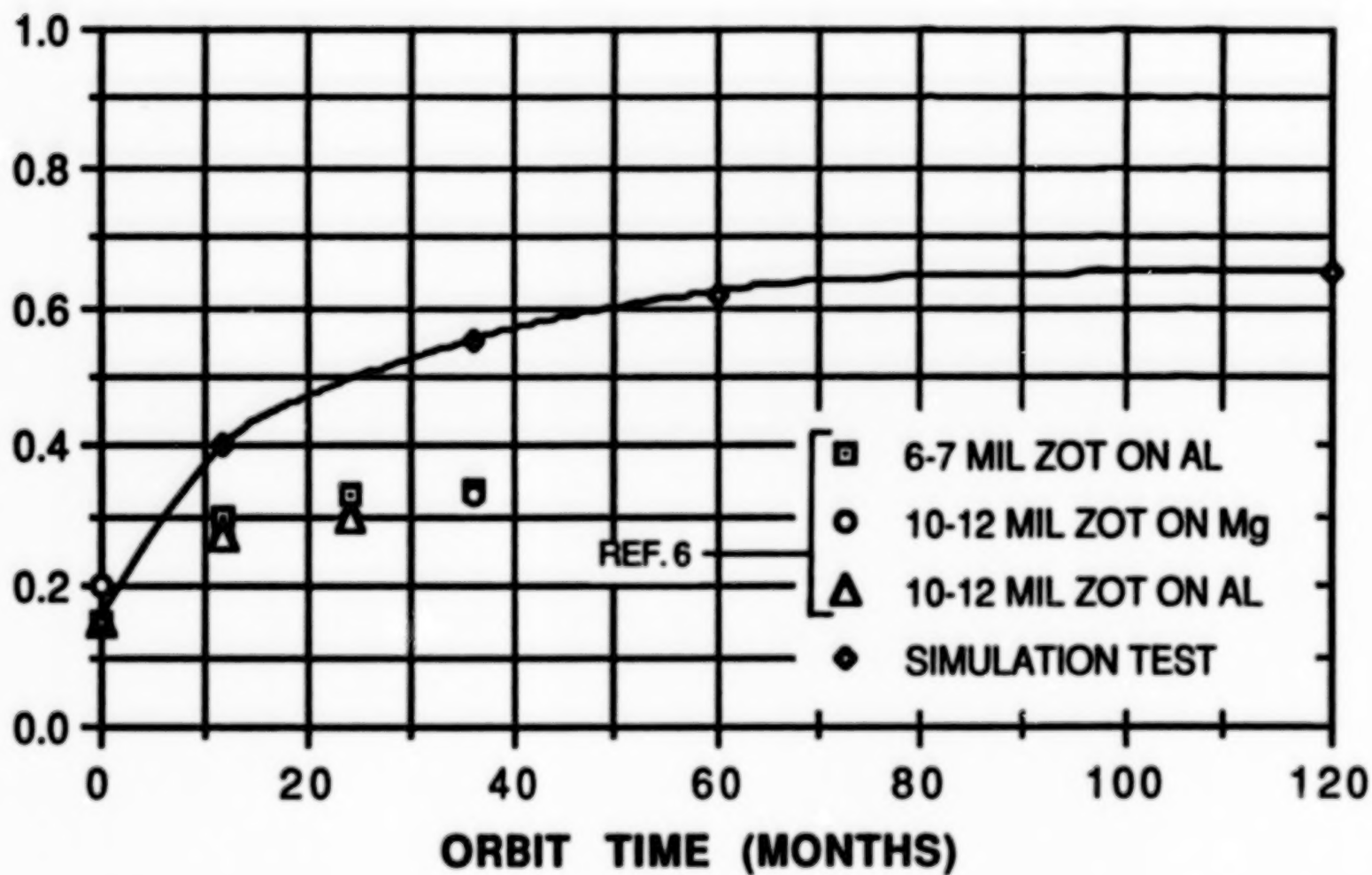


Figure 6. Comparison of Solar Absorptance Degradation for ZOT Paint for Simulation Test vs. Flight Data

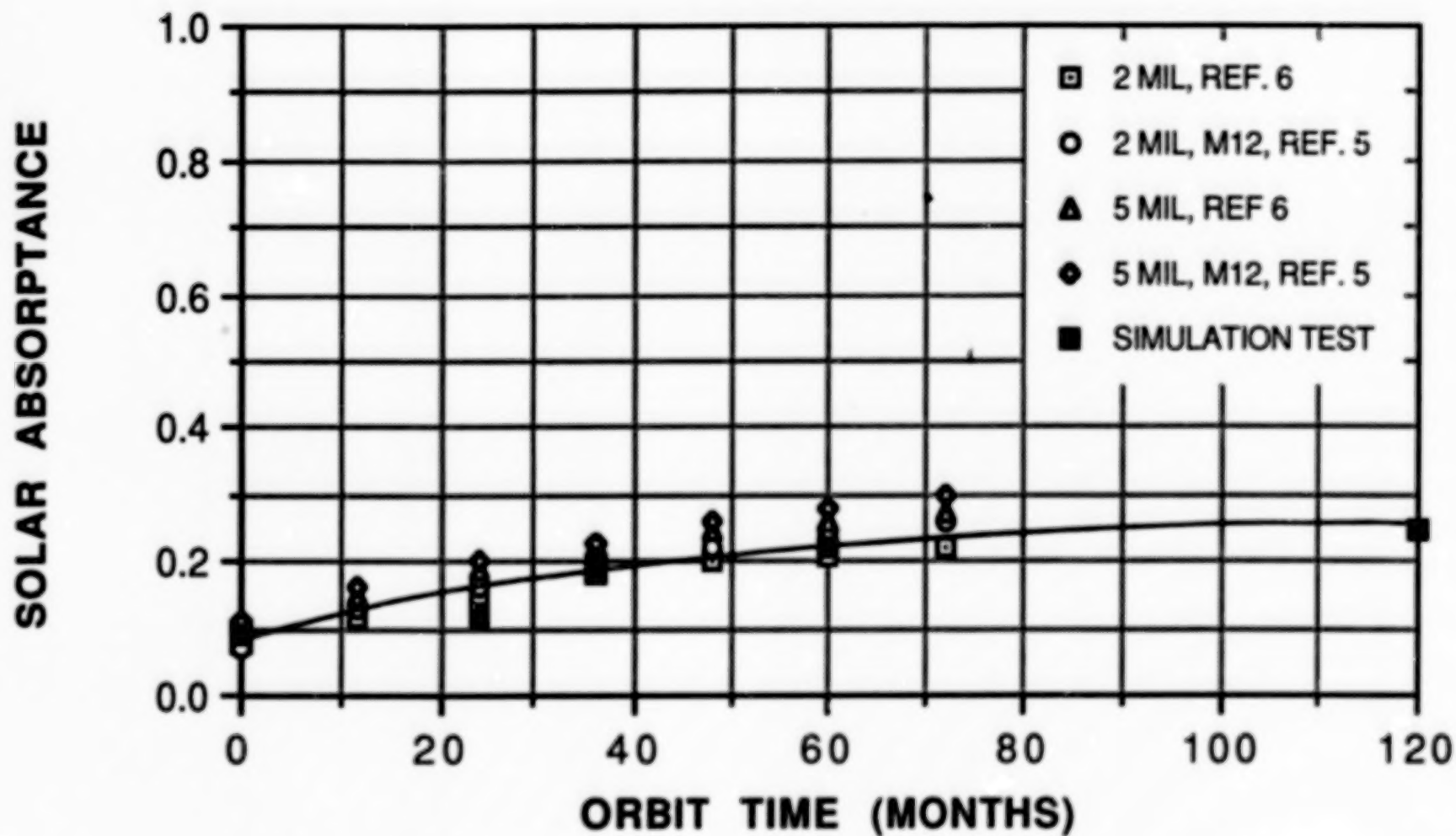


Figure 7. Comparison of Solar Absorptance Degradation for Silvered Teflon for Simulation Test vs. Flight Data

SESSION VII

FACILITIES

SPACE SIMULATION FACILITIES PROVIDING A STABLE THERMAL VACUUM FACILITY

Martin L. Tellalian
Chicago Bridge & Iron Company
Oak Brook, Illinois

ABSTRACT

CBI has recently constructed the Intermediate Thermal Vacuum Facility for Grumman Aerospace Corporation at Bethpage, N.Y. Built as a corporate facility, the installation will first be used on the Boost Surveillance and Tracking System (BSTS) program. It will also be used to develop and test other sensor systems. Completed in March 1989, the facility is composed of a 79.3 cubic meter (2800 ft³) stainless steel chamber, a liquid nitrogen cooled shroud and a pumping system to enable evacuation from one atmosphere to 2.7×10^{-5} Pascals (2×10^{-7} torr) in 24 hours or less. The horizontal chamber has a horseshoe shaped cross section and is supported on pneumatic isolators for vibration isolation. The chamber structure was required to have a minimum natural frequency of 50 Hz or higher. Through the use of consultants and in-house expertise, CBI designed the foundation configuration, pneumatic isolation system, and stiffened shell to meet the stability and stiffness requirements. The design process included measurement of the ambient ground vibrations, analysis of various foundation test article support configurations, design and analysis of the chamber shell and modal testing of the chamber shell. A detailed 3-dimensional finite element analysis was made in the design stage to predict the lowest three natural frequencies and mode shapes and to identify local vibrating components. The modal testing of the chamber shell was made on site with the isolated chamber in place including all piping and attachments. This paper describes the design process used by CBI and compares the results of the finite element analysis to the results of the field modal testing and analysis for the 3 lowest natural frequencies and mode shapes. It also presents concepts for stiffening large steel structures and methods to improve test article stability in large space simulation facilities.

INTRODUCTION

Space simulation facilities often require extremely stable test article support systems. It is increasingly common for owners to specify the stiffness of the chamber and/or maximum allowable displacements of the test article support system. Chamber stiffness is typically specified as a minimum dynamic natural frequency. CBI recently completed Grumman's BSTS thermal vacuum facility which had both a specified minimum chamber natural frequency and a maximum test article support displacement. To meet these stability requirements,

CBI developed and coordinated the entire design, analysis, procurement, installation, and testing of the facility.

Ambient ground vibrations were measured and applied to finite element models of 5 potential chamber and test article support configurations. The different configurations contained various pneumatic isolation systems for the support of the chamber and/or test platform. A three dimensional model of the selected configuration was analyzed to produce the most economical design of the entire support system, including the seismic mass foundation, while meeting stability requirements. In addition, the chamber shell was designed to have a minimum natural frequency of 50 Hertz.

The preliminary chamber design was based on classical solutions of geometric sections and panels. A detailed finite element model of the chamber was analyzed to determine the significant structural frequencies. The analysis predicted a minimum natural frequency of 53 Hertz. The analysis also identified local vibrating elements which were subsequently restrained with additional reinforcement. Once installed, the lowest three chamber natural frequencies were field measured through modal analysis. The measure results compared well with the finite element results. In addition, the measured test article displacements were within the minimum specified.

FACILITY DESCRIPTION

VACUUM CHAMBER

As shown in Figure 1, the chamber has a horseshoe shaped cross section in a vertical plane with a flat bottom. The shell is 6.9M (22'-6) long. The inside radius of the upper cylindrical section is 1.9M (6'-2). The vertical height from the floor to the top of the cylinder is 3.9M (11'-8). The width of the flat floor is 2.7M (9'-0). One end of the chamber is fixed and contains ports for three 889mm (35") cryopumps and a 1.1M x 1.8M (3'-6" x 6'-0") personnel door. The other end of the chamber is a full opening door. All interior surfaces are A240 Type 304L stainless steel with a #4 finish. The test article can be supported from ten hard points. The hard points are in five pairs which straddle the chamber centerline and are spaced 1.2m (4' - 0) apart. The chamber is designed per ASME Section VIII Division 1 where applicable. The chamber is supported on six pneumatic isolators. The six isolators are connected in three pairs to form a 3 point system. Each pair has a height sensor servo valve to control the isolator height. The isolators are supported on a 136,000 kg (300,000 lb) concrete seismic mass which is 4.6m (15') wide, 7.6M (25') long, and 1.8M (6') deep with cut outs on both sides for the isolators. The chamber foundation is independent from all other foundations to minimize the transmission of equipment vibrations to the chamber foundation.

PUMPING SYSTEM

The chamber can be evacuated from atmospheric pressure to 2.7×10^{-5} Pa (2×10^{-7} torr) in less than 24 hours. CBI installed two Leybold Heraeus WAU-2000/S400F blower/roughing trains and two nominal 35" diameter High Vacuum Equipment Corporation cryopumps with vibration isolated cold heads. The system also includes a Balzer 500 l/s turbomolecular pump for helium removal during high vacuum and leak checking. The cryopumps were installed nearly flush with the rear head plate to minimize conductance losses.

THERMAL SYSTEM

The facility contains a 100% optically dense aluminum shroud which is composed of six sections. The shroud provides a 3353 mm (11'-0") diameter x 6096mm (20'-0") long test envelope. The LN₂/GN₂ shroud can be maintained at a -190°C +5°C (-310°F +10°F) temperature with a uniformly distributed heat load of 5 kW. In addition, the shroud can maintain any temperature between -171°C to 116°C (-275°F to +240°F) within +3°C (+5°F). The design pressure of the shroud is 1034 kPa (150 psig) with design temperatures of -195°C and 149°C (-320°F and +300°F).

SYSTEM PSD VIBRATION ANALYSIS

SUPPORT SYSTEM REQUIREMENTS

During the proposal stage of the facility, CBI offered to assist Grumman in the design of the test article support system. CBI proposed that the entire system be studied from the soil to the test article platform. The goal of the study was to economically design a system which would limit the relative displacement of the test article platform to one micron or less. To accomplish this goal, CBI proposed and received acceptance for a Power Spectral Density, PSD, seismic study. The support system design included the design of the test article platform isolation and attachment details as well as the chamber support system. CBI provided a site survey specification which was used by Grumman to acquire a PSD seismic survey of the site. CBI hired the Ralph M. Parsons Company, Pasadena, California to assist CBI in the selection of a suitable support system configuration through a PSD study. The analysis was based on the PSD for the site, the chamber details, and the basic characteristics of the test platform.

PSD METHOD OF ANALYSIS

Initially, five sets of two dimensional analyses were conducted to determine which support configurations of the vessel and internal platform satisfied the relative motion requirements. Isolation system frequencies in the range of 0.5 Hz to 2.5Hz were considered in the two dimensional analysis. The five configurations examined are shown in Figures 7 through 11. These two dimensional analyses demonstrated that any of the five combinations of vacuum chamber

and/or internal platform isolation systems would satisfy the one micron relative motion limitation.

RELATIVE MOTIONS ON THE INTERNAL PLATFORM

Case	Vertical Displacement (micron)	Angular Rotation (nano-radians)
A	.216	135
B	.180	150
C	.204	147
D	.312	173
E	.048	47

The most simple and economical configuration studied consisted of a pneumatically isolated chamber with the test platform rigidly attached to the chamber. In addition to the economy of keeping isolators outside of the chamber, this configuration facilitates future modifications if additional stability were required. Thus, this configuration was chosen for further study.

A three dimensional finite element model was then developed which included the vacuum chamber, the external chamber isolation system, and the internal platform. The three dimensional model assumed that the chamber was isolated from the ground using six pneumatic isolators with a nominal isolation frequency of 1.0 Hz. The internal platform was assumed to be connected directly to the chamber structure without using an isolation system. The models of the chamber and platform were analyzed separately to ensure that their stiffnesses were accurately represented. This chamber mode gave a first model frequency of 60 Hz which compared well with the preliminary results. At the time of the analysis, the platform had not been designed but it's approximate mass and stiffness were known. The possible platforms first three modal frequencies were 42, 61, and 102 Hz which was consistent with Grumman's estimated first mode frequency for the platform. When the chamber and platform were confined and supported on the 1 Hz isolation system, the first two modal frequencies were 37 Hz and 44.6 Hz. The analysis identified 33 modal frequencies of the chamber platform system below 150 Hz. These 33 modes were used to determine the overall modal response.

The stiffnesses of each of the mechanical connections to the chamber penetrations were included in the three dimensional finite element model. The mechanical connections consist of flex hose and pipe bellows. The ground motion vibrations were applied to the chamber through the connections to the vessel penetrations as well as through the six external chamber isolators. The stiffness of the nozzle connections are shown in the table below. N-S is the north-south direction which is along the horizontal longitudinal axis of the chamber. E-W is the east-west direction.

NOZZLE STIFFNESS

NOZZLE #	QUANTITY No.	N-S STIFFNESS Kg/mm	E-W STIFFNESS Kg/mm	VERT STIFFNESS Kg/mm
1	2	1.34	1.79	1.34
2	1	5.84	5.57	5.57
6	2	1.07	1.07	1.07
7	5	2.68	2.68	2.68
9	1	2.55	2.55	3.39
10	1	7.04	5.18	5.18
11	1	2.55	2.55	3.39
14	1	0.89	0.89	0.89

The input PSD spectra was 5.0×10^{-10} g^2/Hz over the frequency range of .1 Hz to 10 Hz and 5.0×10^{-9} g^2/Hz over the frequency range of 10 Hz to 300 Hz. The PSD spectra were applied in both the vertical and horizontal directions simultaneously.

The PSD analysis was performed on the Stardyne computer program by the Boeing Computer Service in Seattle, Washington. The system model contained 267 nodes, 291 beam elements, 34 triangular plate elements, and 175 quadrilateral plate elements.

PSD ANALYSES RESULTS

The two dimensional model of the selected configuration produced a minimum displacement of .05 microns while the three dimensional analysis maximum displacement was .94 microns. The three dimensional analysis included the stiffness and vibration input of the major chamber attachments which may account for the increase in the relative displacements for the 3-D model.

PSD SUMMARY

The results of the PSD study indicated that the use of external isolators would meet the stability requirements. The high natural frequencies of the chamber and platform system increases the performance of the isolation system. The primary method of vibration attenuation of the isolation system is to have the natural frequency of the isolation system as low as possible and to have the natural frequency of the isolated structure as high as possible. Generally, structural frequencies should exceed the isolation frequency by a factor for 10 to 15. In this case, this ratio was approximately 37 which results in a very large attenuation of the ground vibrations.

FOUNDATIONS AND ISOLATION SYSTEM DESIGN

A large concrete seismic mass was used to support the chamber isolation system. The 160,000 kg (300,000 lb) seismic mass is roughly 5 times the weight of the entire chamber. The design is based on the concept that the foundation should be rigid and

independent of surrounding foundations. A rigid foundation will tend to force the ground motions introduced into the base of each isolator to be in phase. The independent foundation will help prevent equipment vibrations from direct transmission to the chamber foundation. The concrete foundation and surrounding sandy soil provide excellent damping to improve the vibration attenuation.

The isolation system was procured and installed by CBI based on the results of the PSD study. The isolators are 635 mm (25") in diameter and 1194 mm (47") high. Each isolator has a 9072 kg (20,000 pound) capacity and lifts the chamber approximately 6 mm when activated. The isolators were connected in three pairs to form a three point support system. The height sensor servo valves are capable of maintaining each of the three isolator pairs within .13mm of each other to provide an active vibration isolation system. The isolators operate with nitrogen gas between 552 and 690 kPa (80 and 100 psig).

SHELL STRUCTURE DESIGN PROCEDURE

The chamber shape was selected by CBI to provide the flexibility required for the support configuration, proper frequency response, transportability, and economy. In the preliminary stage, equivalent cylinders and flat panels were analyzed with classical solutions to determine the theoretical natural frequencies. A similarly stiffened cylinder was analyzed by a CBI Technical Services program entitled "General Shell of Revolution Stress Analysis - Dynamic Version". This is a multi-segment numerical integration procedure developed by A. Kalnins and presented in the Journal of Applied Mechanics, September 1964. A 6.9M long cylinder with simply supported ends and identical circumferential stiffening was chosen which had a minimum natural frequency of 60 Hertz. The flat portions of the chamber, namely the lower shell and heads, were compared to the classical solutions for flat plates as presented by Blevins in his text entitled "Natural Frequencies and Mode Shapes". These design elements were then combined to provide the preliminary design. The design was checked per ASME Section VIII, Division 1. Procurement and fabrication of the chamber shell was initiated based on this design.

CHAMBER FREQUENCY ANALYSIS

METHOD OF ANALYSIS

The preliminary design was then modeled to determine the lowest dynamic frequencies and mode shapes. This analysis was done entirely in-house by CBI analysts using programs either developed by CBI or commercially available. The approach was to use the finite element method, FEM, to analyze the chamber. The lowest natural frequencies and mode shapes were calculated using a CBI Technical Services computer program, entitled "Automatic Dynamic Incremental Nonlinear Analysis (ADINA)." The ADINA program is a general purpose computer code for the linear and nonlinear, static and dynamic, displacement and stress analysis of solids, structures and fluid-structure

systems. The ADINA program is licensed from ADINA R&D, Inc. of Watertown, Massachusetts and is verified for use on CBI's IBM 4381 computer through the solution of over 75 linear and over 70 nonlinear verification problems.

GEOMETRY & MODELING

The chamber is geometrically symmetric about a vertical plane which runs along the length and passes through the center of the chamber. The structure is also symmetric about a vertical plane through the cross section at the mid length except for the ends of the chamber. The chamber has a full cross section stiffened closure door at one end and a stiffened fixed head at the other end. The stiffening patterns on the door and head are completely different. In addition, the fixed head contains large openings for the cryopumps and a personnel access door. To enable the use of two planes for symmetry, two chamber configurations were analyzed with 1/4 models. The two models represent chambers with identical ends, either two full doors or two fixed heads. Although two models had to be analyzed, the final results were finite element models with good detail and limited size due to two planes of symmetry.

The element types used to model the chamber were sixteen-noded shell elements, four-noded shell elements, four-noded isoparametric beam elements and two-noded beam elements. All stiffening was discretely modelled. Rigid links, constraint equations or contiguous modelling methods were used to connect the stiffening to the pressure boundary. The "vessel-door" model contained about 1350 nodes, 460 elements, and 5800 degrees of freedom. The "vessel-head" model contained about 1430 nodes, 710 elements, and 6500 degrees of freedom. Figures 2 and 3 show finite element plots of the "vessel-door" and "vessel-head" models, respectively.

Constraint equations were used in the "vessel-door" model to connect the chamber door to the vessel shell. Only displacement compatibility was enforced across the door to shell interface. This permitted independent rotation of the door and shell interface. This accurately represented the pressure seated closure. In the "vessel-head" model, the same modelling approach was used to connect the personnel access door to the fixed head.

The high vacuum valves and cryopumps were assumed rigid. The vessel contains penetrations for three cryopumps. Cryopumps are installed on the two outer ports only. The center port is blanked off and is for future use. The chamber was modeled with the third cryopump in place. Their mass was connected to the fixed head using rigid links. Items such as closure door hinges and mounting brackets, small penetrations and viewports, and access holes cut through the webs of stiffeners were assumed insignificant and were not modelled. The mass of the internal shroud was assigned to the model nodes nearest the shroud support points.

The chamber isolation supports were included in the model. Each

isolator was modelled using a set of four beams. The beams were oriented vertically. They were fixed at the bottom and pinned at the top where they connect to the chamber bottom. The assumed stiffness values used for each isolator were 1500#/in vertical and 750#/in lateral.

MATERIAL PROPERTIES

Linear elastic material behavior was modelled. The important material properties are modulus of elasticity, Poisson's ratio, and weight density. The vacuum chamber is made of two materials. The pressure boundary material in contact with the vacuum is A240 TP 304L stainless steel. The stiffening and non-pressure parts are A36 carbon steel.

LOADING AND BOUNDARY CONDITIONS

Only inertial loading was considered. The mass of the chamber shell, door, head, personnel access door, and stiffening was included by discretely modelling these components. The mass of the high vacuum valves, cryopumps and internal shroud was included through the use of concentrated nodal mass input.

Each model was run using four different sets of boundary conditions along the planes of geometric symmetry. These were: symmetry-symmetry, symmetry-antisymmetry, antisymmetry-symmetry, and antisymmetry-antisymmetry.

CHAMBER FEM RESULTS

The first mode has a frequency of 53 Hertz and is shown in Figure 4. The mode shape is essentially an ovaling of the central portion of the chamber shell about the vertical & horizontal center lines. The mode shape is symmetric about the vertical planes of symmetry along the length for the chamber and at the mid-length of the chamber. It is shown using the mesh from the vessel door model.

The second mode has a frequency of 63 Hertz and is shown in Figure 5. The mode shape is essentially an ovaling of the central portion of the chamber shell about a set of axes inclined approximately 45°. The mode shape is anti-symmetric about the vertical plane of symmetry which runs along the length of the vessel and is symmetric about the vertical plane of symmetry at the mid-length of the chamber. It is shown using the mesh from the vessel door model.

Three modes are closely spaced in the frequency range of 68 to 72 Hertz. The only mode of these three which does not include movement of the center cryopump has a frequency of 72 Hertz and is shown in Figure 6. Its mode shape is movement of the cylindrical portion of the shell between the end and middle circumferential stiffeners. This mode shape is symmetrical about the vertical plane of symmetry which runs the length of the chamber and is anti-symmetric about the vertical plane of symmetry at the chamber mid-length across its

width.

The FEM results were consistent with the theoretical dynamic results of the preliminary design. As stated earlier, an equivalent cylinder was analyzed and found to have an $n=2$ mode frequency of approximately 60 Hz. The $n=2$ mode is an ovaling of the cross section which will take place at any angle around a cylinder. By using an irregular cross section like a horseshoe, two $n=2$ modes are developed which occur at consistent orientations. Both the FEM analysis and the modal analysis identified two $n=2$ modes with frequencies of approximately 50 Hz and 63 Hz. The test platform supports are located near the node lines for the lower $n=2$ mode and all support points move in phase which minimizes the effect of the lowest chamber mode on the test article stability.

The initial configuration of the chamber was slightly modified due to the results of the FEM analysis. The FEM analysis identified local stiffener modes whose natural frequencies were below fifty Hertz. The modes were local lateral displacement of the stiffener flanges. These modes were eliminated by adding gusset plates to prevent lateral movement of the stiffeners. In addition, the middle circumferential stiffener initially was composed of the 305 mm x 19 mm (12" x 3/4") bar only. The lowest shell mode with this stiffener was 51.5 Hertz. The addition of the 250mm x 31.7 mm (10" x 1 1/4") flange to this stiffener raised the first shell mode frequency to 53.5 Hertz. The chamber was built with this flange added to the middle circumferential stiffener.

MODAL ANALYSIS

FIELD VERIFICATION

The chamber, foundation, and isolation system were furnished and installed by CBI based on the results of the design and analysis. Once the chamber was completed including all attachments and systems, the chambers three lowest structural natural frequencies were determined by experimental modal analysis. Experimental modal analysis is the process of combining field measured dynamic response data to determine the dynamic behavior of a structure. It was used in this case to verify the FEM results. The modal analysis was performed at the direction of CBI by Wiss, Janney, Elstner Associates, Inc. of Northbrook, Illinois.

MODAL DATA ACQUISITION

Due to the longitudinal symmetry of the chamber, a grid pattern of 50 points was laid out on half of the chamber. Ten additional data acquisition points were established on the chamber door and fixed end. Dynamic frequency response function (FRF) data was obtained at all 60 points on the chamber with piezoelectric accelerometers. A hand-held impulse force hammer was used to strike the middle circumferential stiffener. The FRF data is basically a ratio of the output response to force input. Piezoelectric accelerometers, type

4335, manufactured by Bruel & Kjaer (B&K) were used for measuring acceleration response vibration amplitudes. The electrical signal from each accelerometer was routed to a B&K type 2635 charge amplifier. This amplifier was used to electrically condition the signal from the high impedance accelerometer. The hand-held impulse force hammer, type 086B05, manufactured by PCB Piezotronics, Inc., was used to apply a transient, dynamic force to the vacuum chamber. This impulse hammer produces an electrical signal proportional to the force output. It was routed to a PCB Piezotronics type 480D06 battery power unit for electrical conditioning.

The conditioned accelerometer and impulse force signals were analyzed and recorded on a Scientific Atlantic Model SD3802, four channel spectrum analyzer. One channel received impulse force time history data from the modal hammer and two other channels received acceleration response data from two perpendicular accelerometers. Computer analyses were subsequently performed at the WJE laboratories using Star Modal Software (SMS) which is a product of Structural Measurement Systems Inc. This software uses frequency response function data to identify the modal properties for a structure. The modal parameter outputs of this software are frequency, damping, and mode shape characteristics. All frequency data are given in units for Hertz (Hz). Damping values are given in units of percentage relative to critical damping.

MODAL ANALYSIS RESULTS

The sum of the FRF amplitudes for the 50 shell positions are shown in the Figure 12. This preliminary summation identified three significant resonant frequency ranges of approximately 46-50 Hz, 63-66Hz, and 71-74 Hz. The peak at 60 Hz was determined to be electrical leakage noise. The Star Modal Software uses these selected frequency ranges and a curve fit process to identify the modal parameters. An analytical expression for a FRF is matched to the measurement data and modal parameters identified. A global curve fitting process developed by Structural Measurement Systems was used to determine their frequency and damping of the structure with the following results.

Mode Number	Frequency Hertz	Damping % Critical
1	48.0	.60
2	64.3	.44
3	72.3	.56

The mode shapes identified by the modal analysis confirmed or agreed with the results for the finite element analysis. The modal analysis confirmed the ovaling of the shell between the ends for modes 1 and 2. The modal data was insufficient to determine the third mode shape but agreed with the FEM results in that the only significant distortions were located in the cylindrical portion of the shell between the stiffeners.

The central stiffeners on the front door were found to have a resonant frequency of 54 Hz. The door plate frequency between the stiffeners was 120 Hz. Similarly, the lowest frequencies of the fixed end of the chamber were 120 and 136 Hz.

COMPARISON OF FEM ANALYSIS AND EXPERIMENTAL MODAL ANALYSIS

The table shown below compares the results of the FEM analysis and the Modal Analysis. Although the modal analysis is dependent on the curve fitting procedure used and the frequency ranges selected, the accuracy is within 2%.

MODE	FEM Hz	MODAL Hz
1	53	48.0
2	63	64.3
3	72	72.3

The frequency results for the first mode are within 10% of each other. The second and third mode values are within 2% and .5% of each other, respectively. In addition to the inherent approximations of the FEM, the following items may account for some of the discrepancy in the results.

Although there are a number of areas where the model differs from the actual structure, the greatest difference is the attachment of the full door to the chamber. The FEM analysis assumed that the door was seated against the chamber with a force sufficient to prevent displacement of the door relative to the vessel end. When under full vacuum, the door is seated against the chamber with a force in excess of 115,000 Kg. The modal analysis was conducted with the chamber at atmospheric pressure. C-clamps were used to hold the door against the chamber. Although firmly held in place, the clamping force was not sufficient to compress the o-ring seal sufficiently to cause metal to metal contact between the door and chamber. Thus, the door to shell contact was through the elastomeric o-ring. The mode shape identified by modal analysis did not indicate excessive displacement of the chamber at the door. However, the modal analysis mode shapes were not sufficiently detailed to identify anything more than the general mode shape. It should be noted that an equivalently stiffened cylinder with one open end has an ovalling first mode frequency of approximately 30 Hz.

The mass of the FEM model did not completely correspond to that of the chamber configuration when field tested. The locations of some attachment were not known when the chamber was analyzed and thus were not included. The chamber contains 14 nominal 300 mm diameter view ports. Ten of these are located 90° from the top of the chamber with five viewports on each side. These 50 Kg viewports are located at the location of maximum radial displacement for the first mode and at a node line for the second mode. The chamber also contains a platform at the top of the chamber which is at a location of maximum radial displacement for the first mode. The mass of the thermal

shroud was distributed over the entire chamber in the FEM analysis. The shroud was not in place during the modal analysis.

The FEM model discretely models the chamber stiffening but does contain some variations. The actual stiffening is stitch welded to the chamber but continuously attached in the model. These variations are minor and most likely not significant. It should be noted however that the third mode shape does not include stiffener displacement and was accurately predicted by the FEM analysis.

CONCLUSIONS

Through the use of design and analysis procedures, CBI successfully provided a thermal vacuum facility which exceeded the customer's stability requirements. The following points should be considered for future installations.

The specific ambient ground vibrations and soil conditions of a proposed facility must be determined and analyzed to accurately predict the facility stability. A Power Spectral Density analysis can be used to select and design the most economical support configuration. So important is the PSD analysis that CBI has developed the in-house capability to perform the PSD analysis since the completion of the Grumman facility.

Vibrations transmitted to the test article foundation must be limited. In this facility the test article was supported indirectly by the seismic mass. The seismic mass was independent of all other foundations. In addition, all the vibrating components associated with the system were supported on vibration isolated equipment skids even though supported on independent foundations.

Vibration inputs to the facility through penetrations and attachments can significantly increase the accelerations and resulting displacement of the test platform. Flexible hose and bellows were used on all attachments. Their stiffness was known and included in the analysis of the facility.

Detailed finite element models can successfully predict the mode shapes and corresponding frequencies of the chamber. Models must represent the final configuration as closely as possible. Basic geometric shapes can be used to identify general behavior of the facility. Naturally, the accuracy will be dependent on how closely the facility corresponds to the configurations studied.

Experimental modal analysis can be used to accurately determine the dynamic characteristics of a completed facility. Natural frequencies can be determined with a relatively small number of data points. Mode shapes are more difficult to determine and thus require closely spaced data points.

Knowledge of the vessel behavior can be used to limit both the test platform support vibrations and the vibration inputs through chamber

attachments. Supports and attachments should be placed at low frequency node lines. An irregular cross section or irregular stiffness is required to orient the modes and establish a consistent phase angle. Minimizing the effect of low frequency modes can be extremely beneficial for very large chambers which require tremendous stiffening to provide similarly high natural frequencies.

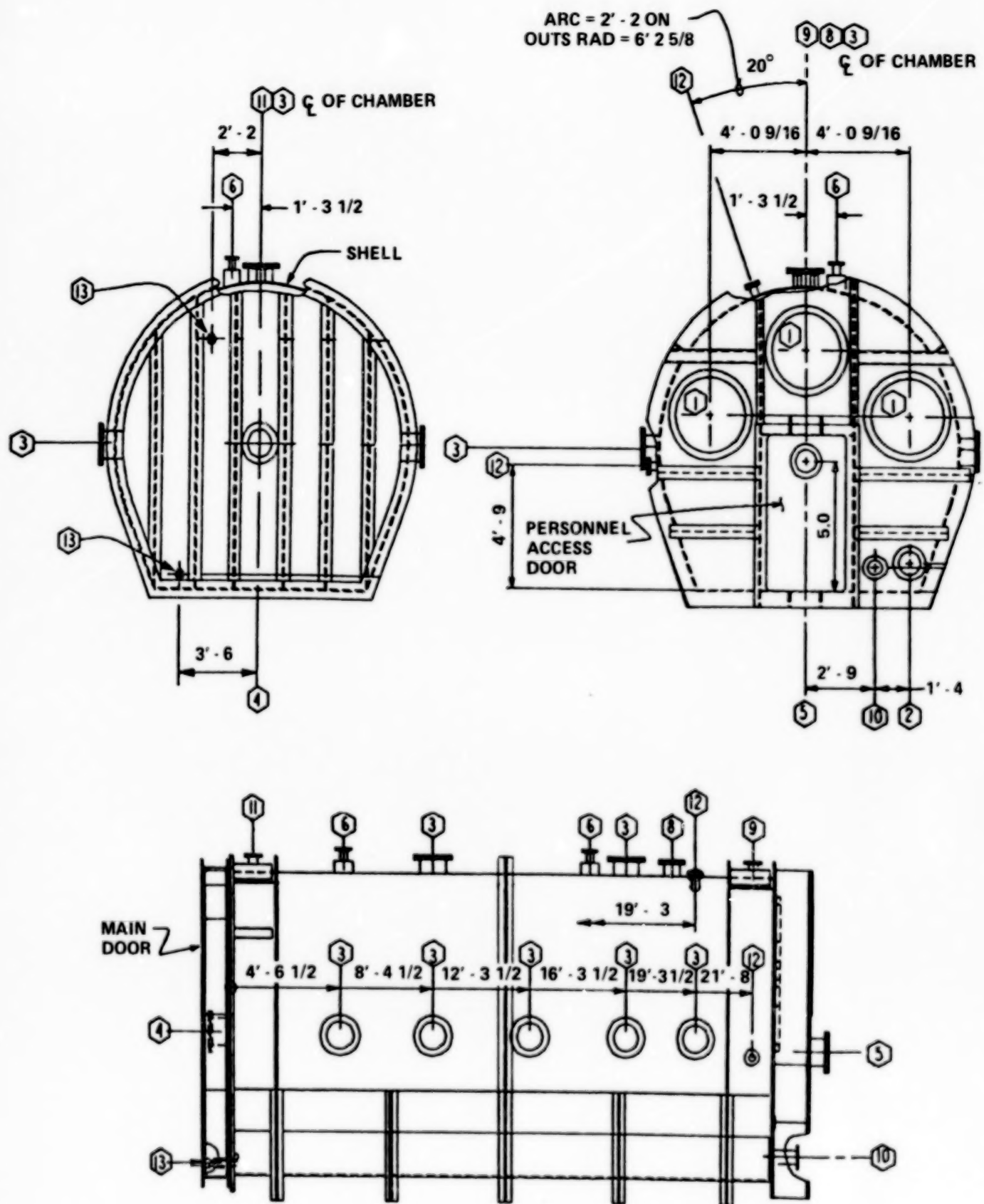


Figure 1. Chamber Configuration

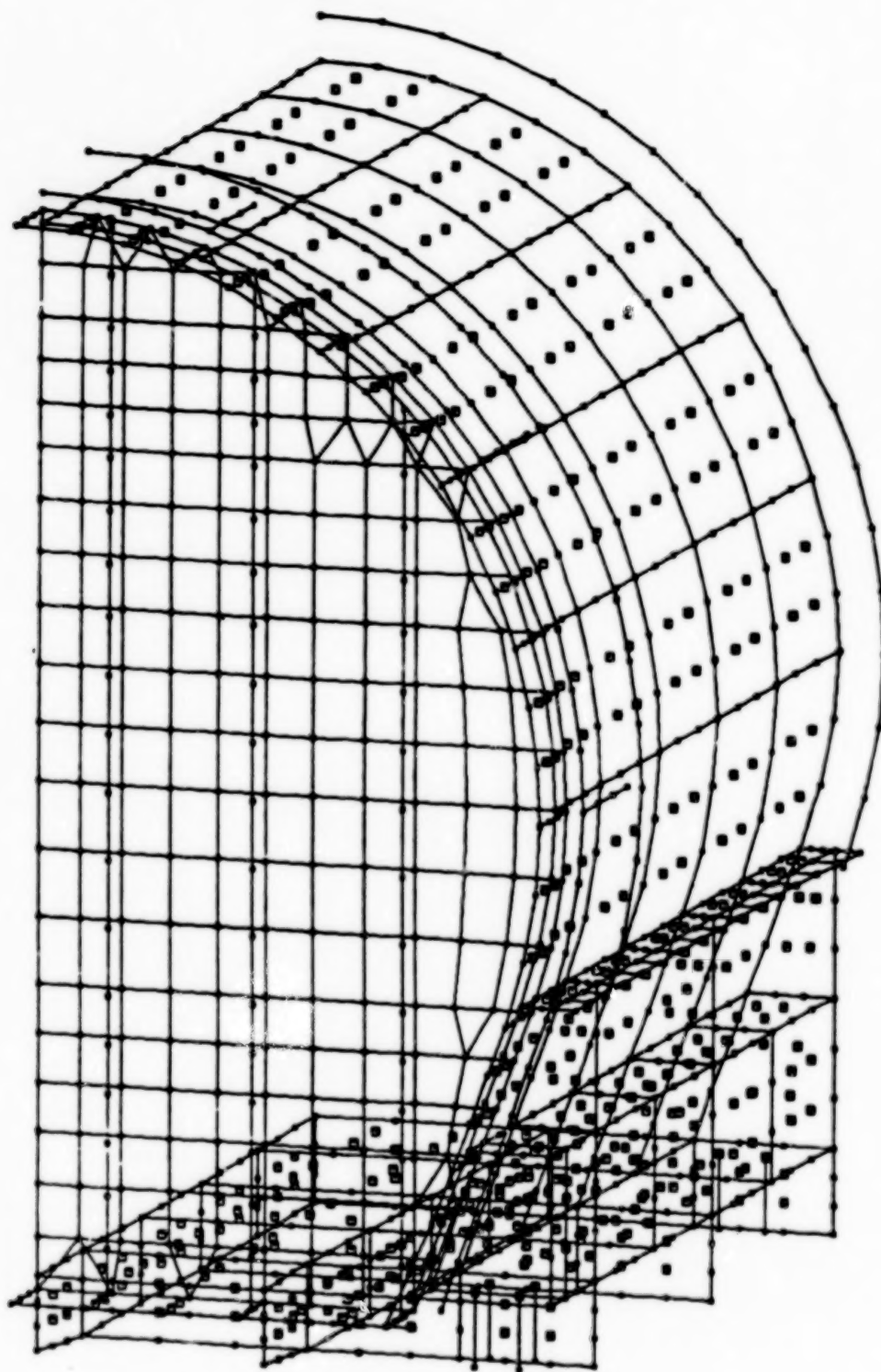


Figure 2. Vacuum Chamber Shell with Door – Quarter Model

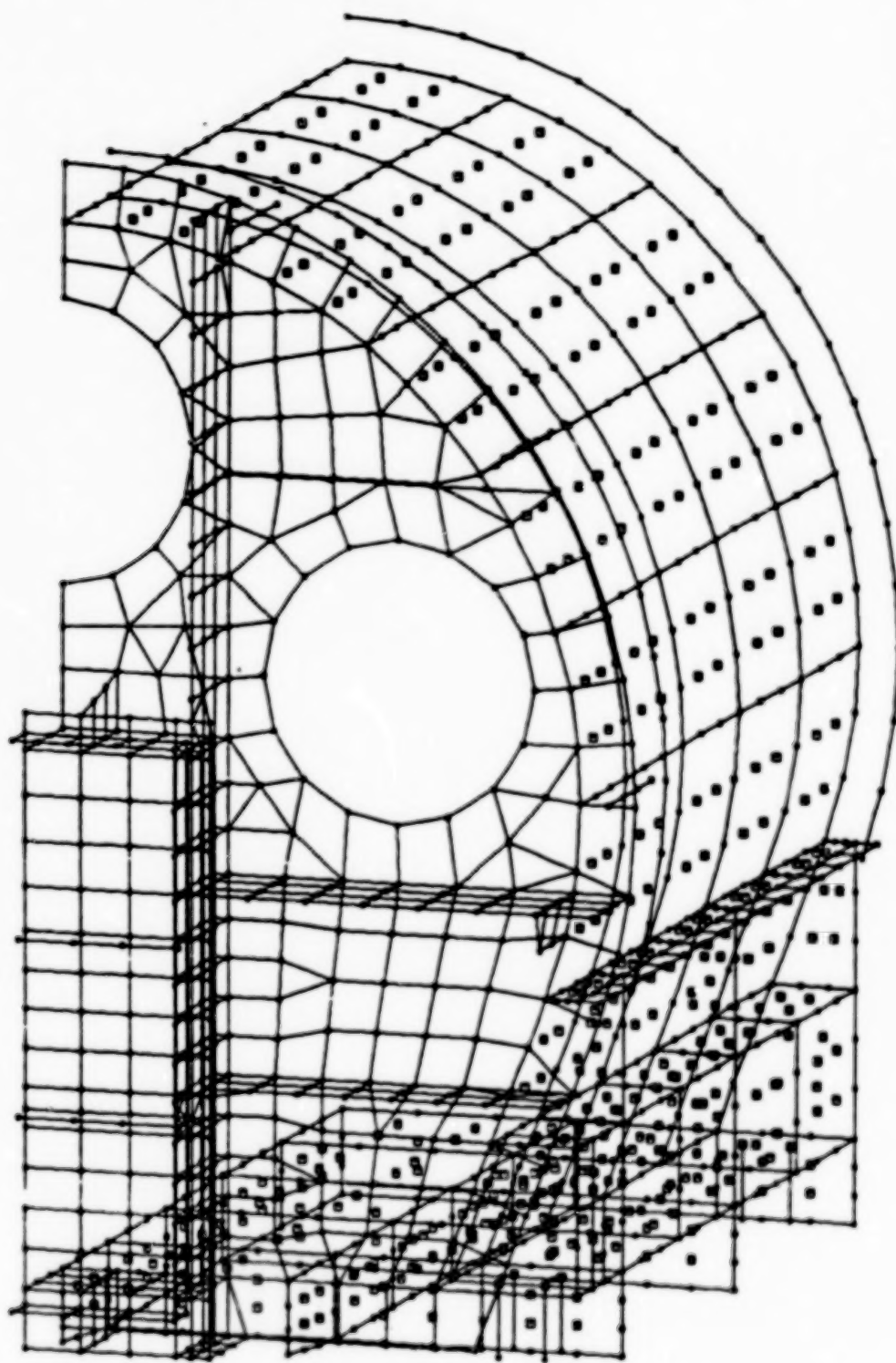


Figure 3. Vacuum Chamber Shell with Fixed Head – Quarter Model



Figure 4. First Mode Frequency of the 1/4 Model — 53 Hz



Figure 5. Second Mode Frequency of the 1/4 Model - 63 Hz



Figure 6. Third Mode Frequency of the 1/4 Model – 72 Hz

CASE A

- VACUUM CHAMBER SUPPORTED ON CONCRETE FOUNDATION
- INTERNAL OPTICAL BENCH ISOLATION SYSTEM FREQUENCY = 1.0 Hz

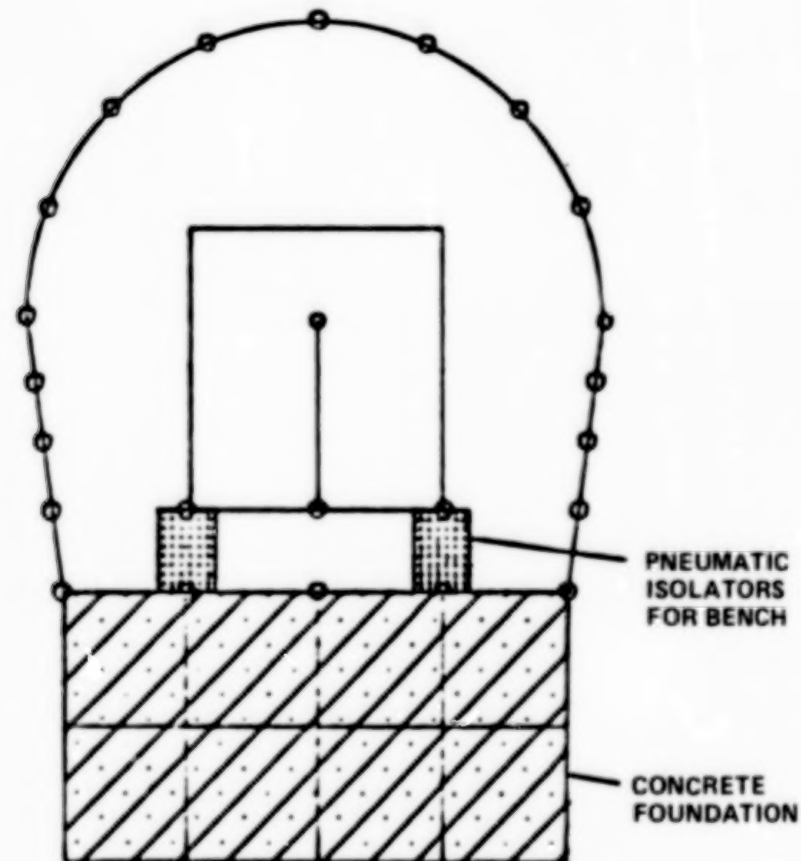


Figure 7. PSD 2-D Case A

CASE B

- VACUUM CHAMBER SUPPORTED ON 2.0 Hz ISOLATION SYSTEM
- INTERNAL OPTICAL BENCH ISOLATION SYSTEM FREQUENCY = 0.5 Hz

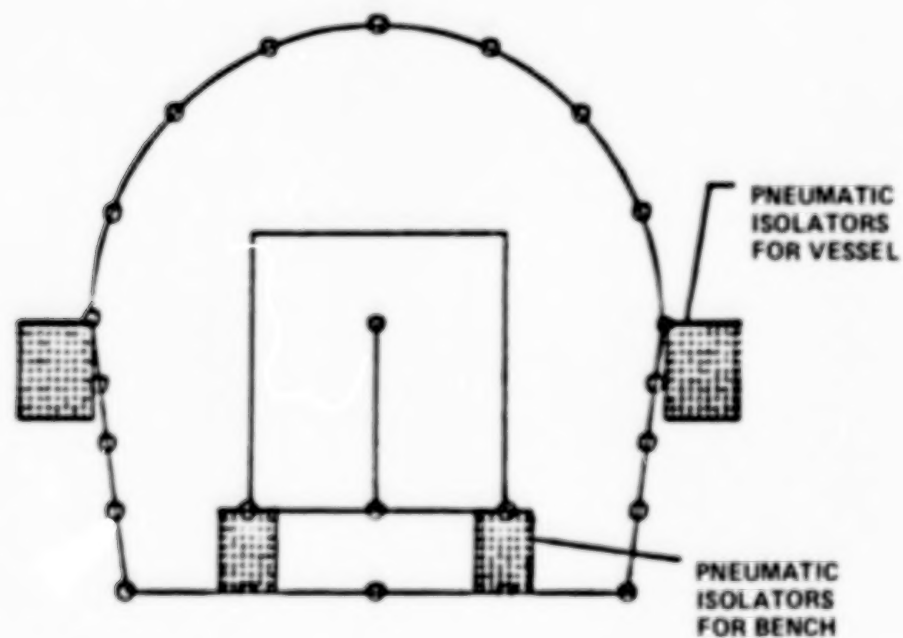


Figure 8. PSD 2-D Case B

CASE C

- VACUUM CHAMBER SUPPORTED ON CONCRETE FOUNDATION
- INTERNAL OPTICAL BENCH SYSTEM ISOLATION FREQUENCY = 0.5 Hz

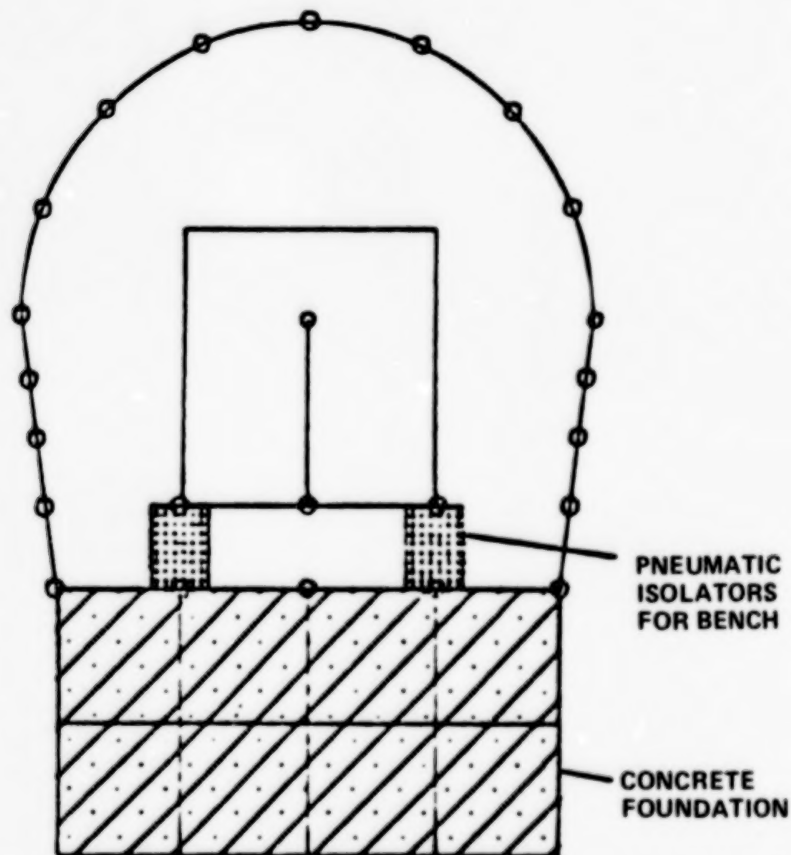


Figure 9. PSD 2-D Case C

310

- CASE D
- VACUUM CHAMBER SUPPORTED ON 1.0 Hz ISOLATION SYSTEM
 - INTERNAL OPTICAL BENCH ISOLATION SYSTEM FREQUENCY = 2.5 Hz

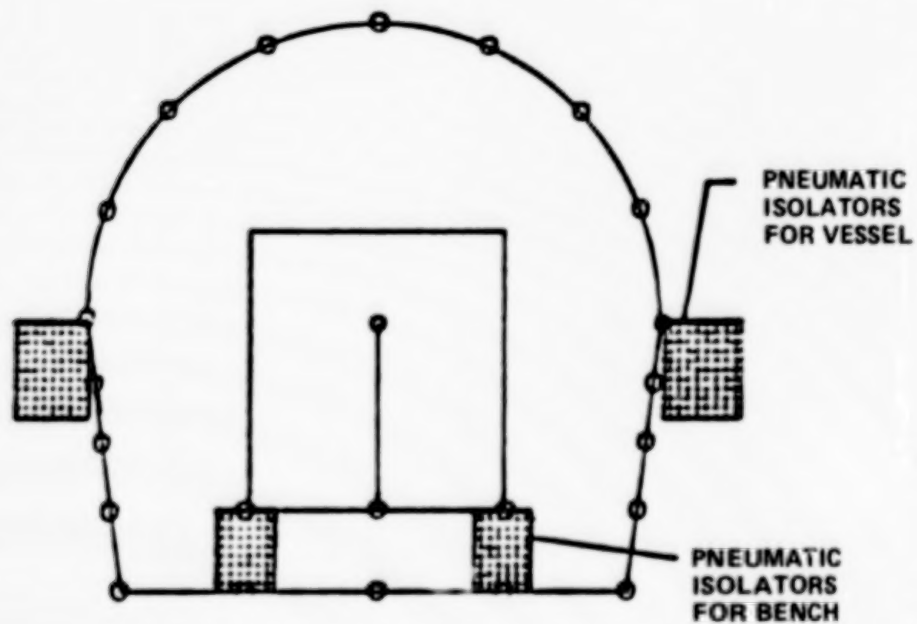


Figure 10. PSD 2-D Case D

CASE E

- VACUUM CHAMBER SUPPORTED ON 1.0 Hz ISOLATION SYSTEM
- INTERNAL OPTICAL BENCH ISOLATION SYSTEM FREQUENCY = 2.5 Hz

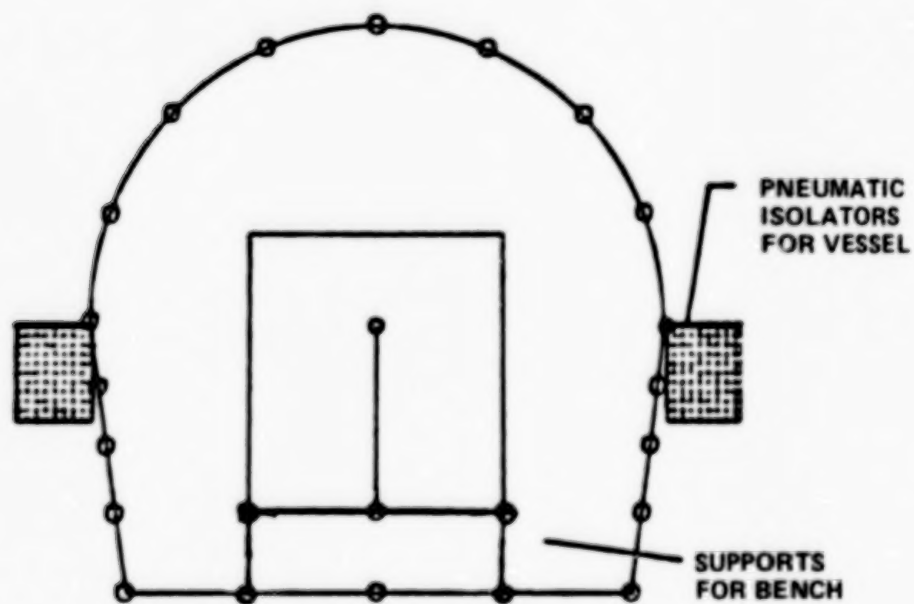


Figure 11. PSD 2-D Case E

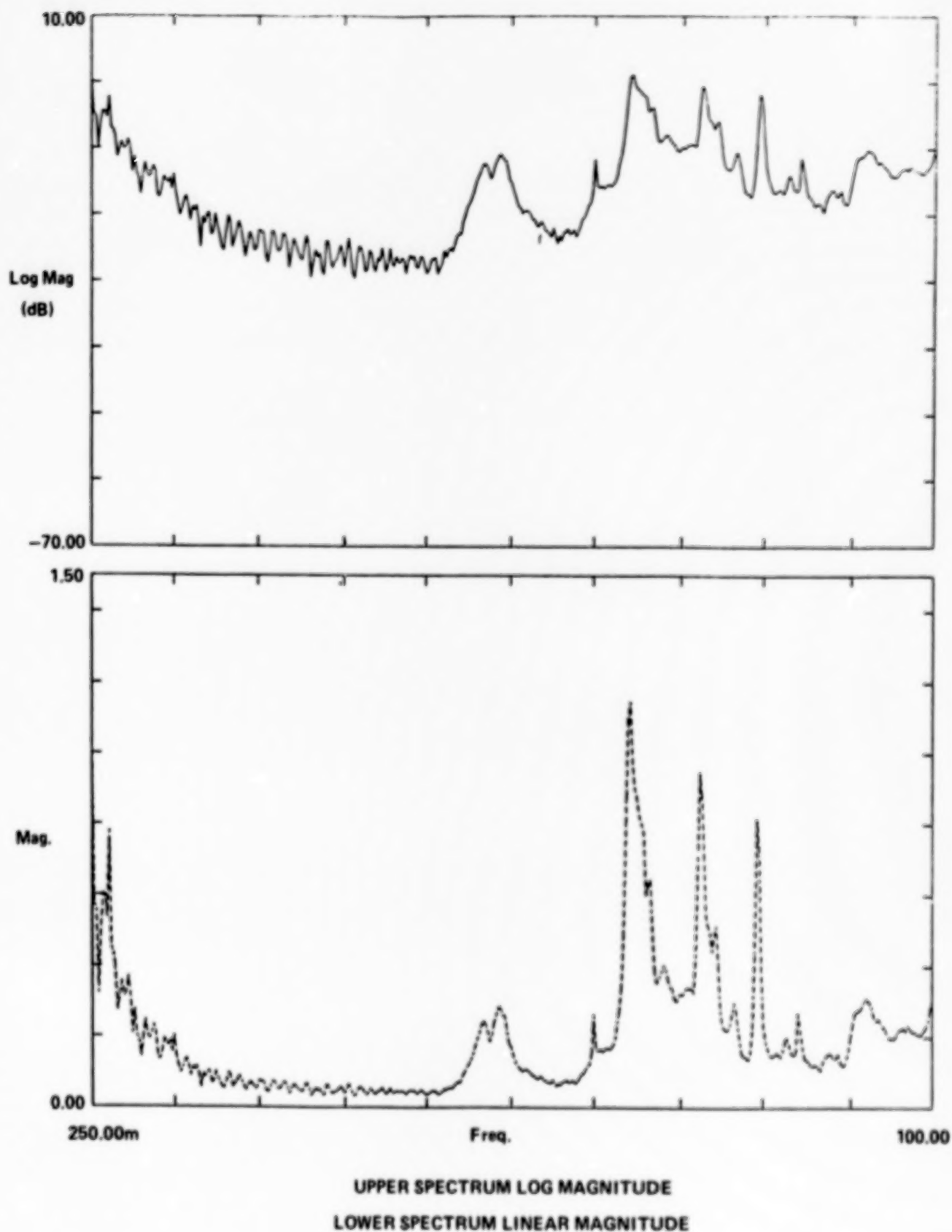


Figure 12. Model Peaks FRF Spectra, Shell and Base

THE SPACE SIMULATION FACILITIES AT IAL SPACE

M. HENRIST, A. CUCCHIARO, I. DOMKEN and J.P. MACAU

Centre de Recherches IAL SPACE - Université de Liège
ANGLEUR - LIEGE (Belgium)

ABSTRACT

The thermal vacuum facilities of IAL SPACE have been tailored for testing of the ESA payloads. They have been progressively upgraded for cryogenic payloads including 4K (liquid helium temperature) experiments.

A detailed review of the three vacuum chambers, ranging from 1.5 meter to 5 meter diameter, is presented including the corresponding capabilities in the vacuum, thermal and optical fields.

The various aspects of cleanliness, product assurance and quality control are also presented.

INTRODUCTION

IAL SPACE is a research center of the University of Liege, Belgium, which has been devoted since 1962 to space research, in close cooperation with the European Space Agency (ESA) from the beginning. After a series of sounding rocket payload development, IAL SPACE has been involved mainly in the thermal vacuum testing of optical payloads for satellites. Some major steps of this activity are listed hereafter :

- ultraviolet telescope (S2/68 experiment) aboard the TD1 satellite, launched in 1962 by a THOR DELTA vehicle;
- infrared radiometer of the weather forecast METEOSAT satellite;
- Hubble Space Telescope : detectors of the European experiment, called Faint Object Camera (FOC);
- imaging camera of the GIOTTO probe, launched at the encounter of the Halley comet;
- complete payload of the HIPPARCOS astrometry satellite;
- infrared telescope of the Infrared Space Observatory (ISO) satellite, to be launched from 1992 by an ARIANE vehicle.

The latter payload is quite ambitious. It is composed of a 600 mm diameter telescope, placed into a cryostat with 2200 liter of liquid helium in order to keep the experiment at around 4K during 18 months. All necessary tests have to be carried out in this temperature range.

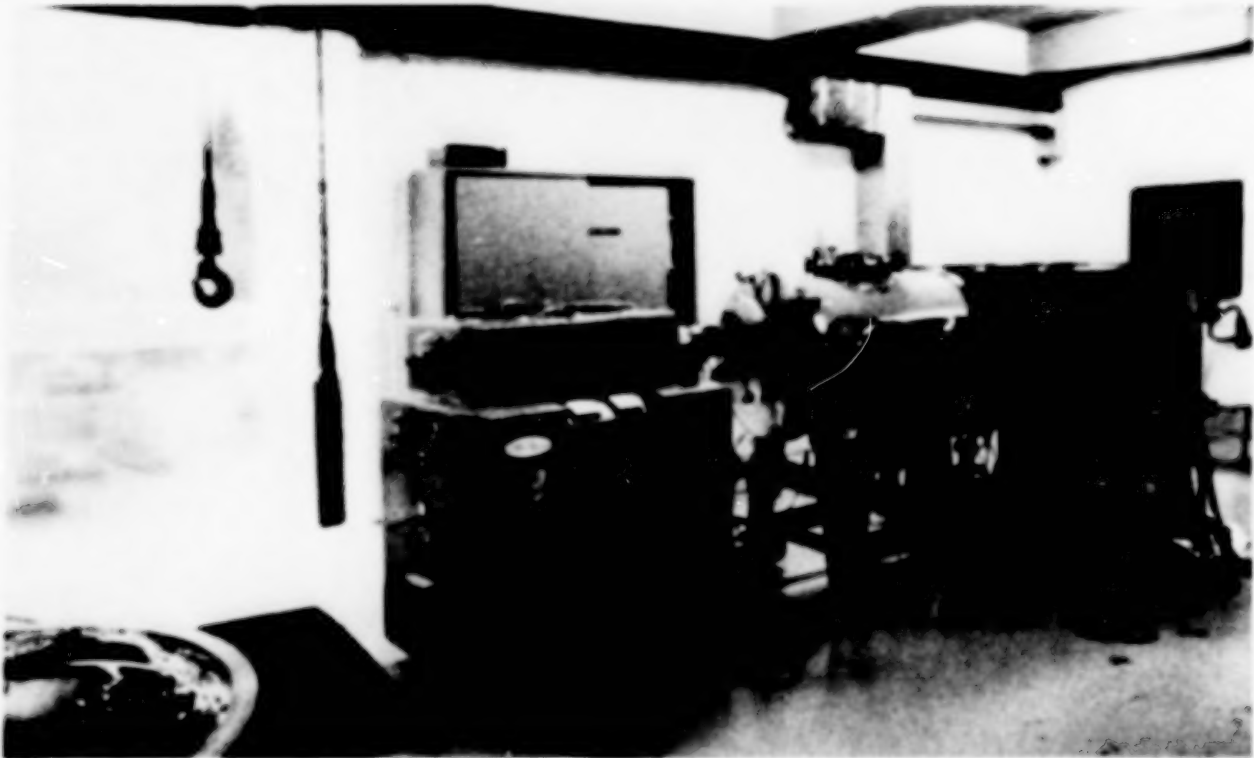


Figure 1 : view of FOCAL 1.5 From left to right : monochromator, imaging telescope, vacuum chamber.

The pumping system is composed of a mechanical roughing pump, a turbomolecular pump and, when necessary, a cryopump. The ultimate vacuum is better than 10^{-5} mbar in the whole temperature range.

2) FOCAL 2

This chamber is made of stainless steel with an horizontal axis; the diameter is 2 meter and the length is 5 meter without lids. It is equipped with an optical bench (1.3 X 4.7 meter), the feet of which are resting on an external seismic block. The optical bench does not touch either the chamber or the ground of the clean room. The resulting stability is quite good (vibration level in the 10^{-6} g range), so that interferometric measurements can be carried out under vacuum.

For thermal regulation, FOCAL 2 had been completely lined with thermal shrouds for the TD and METEOSAT test campaigns. In order to get more flexibility to install viewports, feedthroughs, ..., the shrouds have been removed and replaced by a railway system, which allows dedicated shroud assemblies to be attached and moved along. The modification enhances the available space, and greatly improves the flexibility of the facility. In particular, the modified chamber can accommodate experimental setups coming from the large chamber FOCAL 5 (see next paragraph) and vice-versa,

provided the overall dimensions are compatible. This was purposely designed in the case of the ISO project, in order to have a backup test facility in case of planning problems.

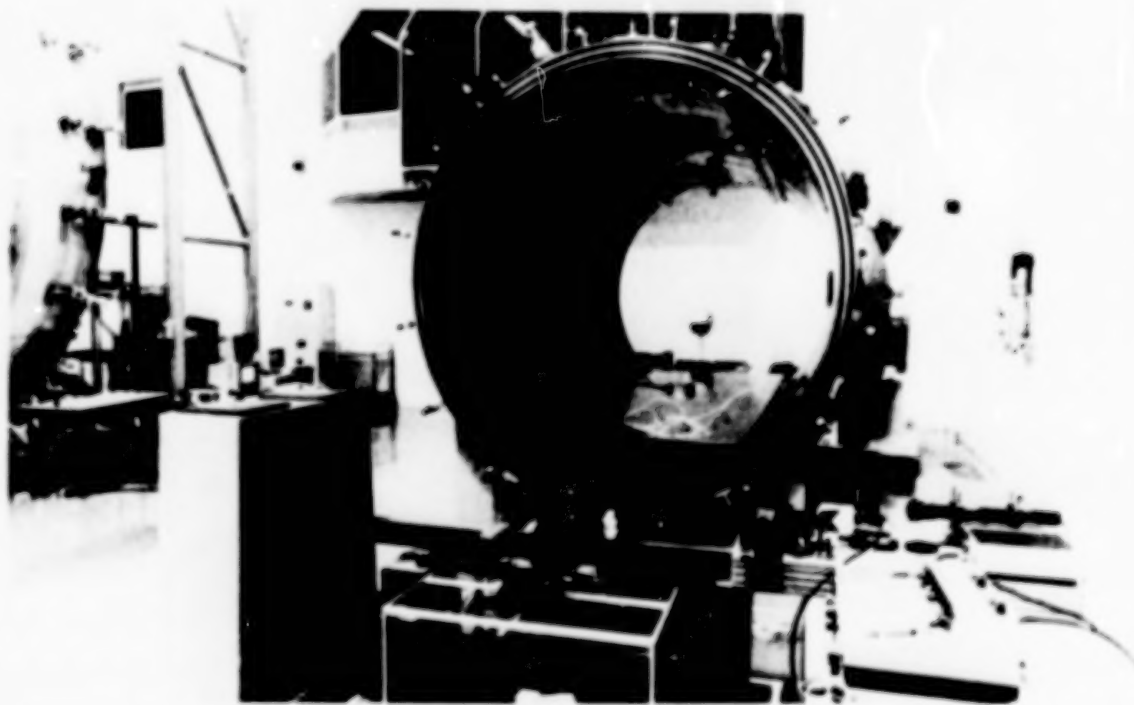


Figure 2 : view of FOCAL 2 (lids removed). The optical bench (below) and the railway system (top) are clearly visible.

The thermal connections of FOCAL 2 are fixed on interchangeable flanges of a standard type. They are able to feed the shroud assemblies in the range -190°C to $+80^{\circ}\text{C}$, by using nitrogen which is prepared in a thermal group with an automated valve assembly.

The pumping system is able to reach a vacuum of 10^{-5} to 10^{-6} mbar, depending on the outgassing of the test setup. It is composed of a mechanical roughing group, a turbomolecular pump and two cryopumps with large vacuum valves. This configuration authorizes long vacuum sequences on experiments with significant outgassing rates, by using the cryopumps in alternance, while enabling fast returns to the atmospheric pressure since the cryopumps can be isolated from the chamber.

3) FOCAL 5

This chamber is one of the largest in Europe. It has a diameter of 5 meter and a length of 6 meter without the lids, with an horizontal axis. It is equipped with a large optical table

(1.8 X 6 meter) which is mechanically insulated from the chamber and rests on a separate 350 ton seismic block. The resulting

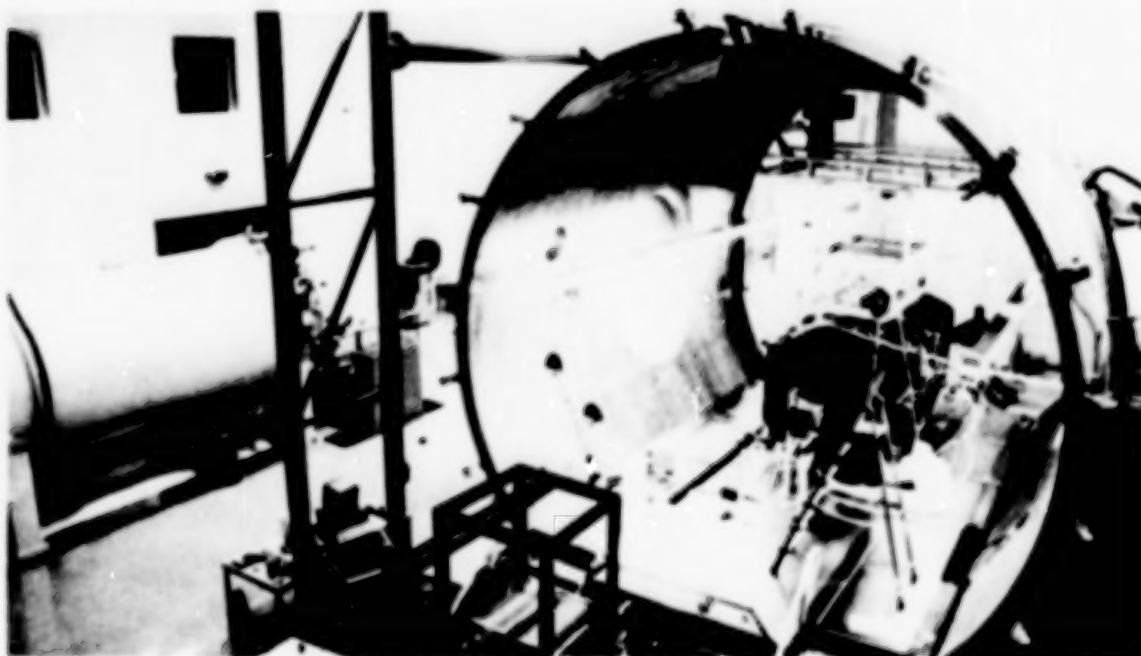


Figure 3 : view of FOCAL 5 (lids removed) with a part of the ISO shroud assembly attached on the trolley.

vibration level is between 2 and $4 \cdot 10^{-6}$ g, with a first resonant frequency around 16 Hz, giving access to the interferometric measurements on tall payloads. The seismic block has the shape of a cross, the arms of which can support the external optical equipment needed for the optical measurements (interferometers, theodolites,...).

The pumping system is able to achieve a vacuum of 10^{-6} mbar within 3 hours, depending on the setup. It is composed of a mechanical roughing group, one turbomolecular pump and a large duplex cryopump fed by a helium liquefier.

A number of flanges, the diameters of which vary between 350 and 2000 mm, are distributed over the chamber with a comprehensive set of electrical and fluid feedthroughs, and of optical windows.

The payloads can be handled throughout the length of the chamber by means of a monorail crane of 1000 kg capacity, one section of the rail being permanently attached inside the chamber and the other section being fixed to a movable trolley outside the chamber. In case of need, an extra length of rail enables an unloading at any end of the chamber.

The thermal shroud system has been designed in an original way,

in order to accommodate various payload shapes while keeping the fluid rates to a minimum. To achieve that, no permanent shrouds are installed. Instead, a trolley is rolling on two bars under the "ceiling" of the chamber. The trolley can be equipped with dedicated thermal shrouds which can surround the test payload without touching neither the optical bench nor the payload (in order to avoid vibration caused by the fluid circulation). All fluid feedthroughs are located in the bottom of the chamber, so that the piping is also decoupled from the optical bench.

Presently, FOCAL 5 has 10 independent thermal loops, each one being able to control the temperature of a shroud between -190C and +60C by means of a mixture of hot and cold nitrogen. For each, loop, the process control software can achieve either a stable temperature (to 0.1C in the whole range) or temperature changes with preset speeds. Additionally, two loops can deliver liquid nitrogen without temperature regulation, for simple cold space simulations.

In order to fulfill the ISO test requirements, three cold helium loops have been installed, which are able to cool the shrouds and the experiment either with a gaseous or a liquid phase helium, supplied by the liquefier system. The results indicate that a effective temperature of less than 5K has been obtained in the whole test setup, the total weight of which exceeds 500 kg.

The data handling and command system is based on a data logger, several HEWLETT-PACKARD 9000 workstations and a home-made process control software based on MONITROL. It can handle up to 500 thermal channels, record them and give realtime displays as well as historical graphs, temperature and gradients automatic control,...

4) CLEAN ROOM

All the above facilities are located in a controlled environment area of 650 square meter and 10 meter high, with two airlocks in series (each one being 10 meter high and 80 square meter area). The temperature and humidity are regulated, and the cleanliness class is 10000 (Fed.Std. 209). An external room (100 square meter) can receive the customer's payload checkout equipment. The air cleanliness is obtained by a bank of filters, installed under the clean room; filtered air is injected from the ceiling of the room through a distribution of diffusers and taken back at the ground level, along the walls.

Around FOCAL 5, a class 100 enclosure of 500 cubic meter has been built inside the clean room with a laminar flux bench which

blows HEPA-filtered air throughout the vacuum chamber (horizontal air flux). The class 100 assembly also comprises a double airlock for personnel (GORETEX garments are extensively used) and a preparation/cleaning/storage area, also of class 100, which serves as an equipment airlock.



Figure 4 : general view of the clean room. From left to right : class 100 enclosure, FOCAL 5 chamber, FOCAL 2 chamber.

In the course of a test, all equipments (apart from the main air circulation in class 10000) are connected to a no-break power supply, in order not to loose data or stop the activities in case of mains breakdown. An emergency fuel generator can take the relay of external mains within 30 seconds.

5) CONTAMINATION CONTROL

5.1. Dust particles.

In the frame of the ISO activities, very stringent cleanliness requirements were asked and lead to a careful monitoring of dust particles. Indeed, the optical surfaces are gold coated and no cleaning process has been considered; moreover, several tests have

been scheduled on the same optical components at various levels of integration (bare mirror, mounted mirror, assembled optical combination, whole telescope with experiments). This testing philosophy leads to a maximum required contamination level of 15 ppm per test (fallout obscuration factor, expressed in parts per million). In order to achieve this requirement, the air dust contents is regularly measured by means of a HIAC/ROYCO dust counter, in order to ensure that the class 100 airborne level is kept at all times. In addition, a number of particle fallout samples (PFO) are distributed all over the working area and measured every day by a PFO photometer (URAMEC, Netherlands, under ESA license).

The theoretical PFO rate is 1.5 ppm/day for a class 100 zone, but this equivalence refers only to a normal distribution of dust. When a large amount of equipment is handled by several people, the above correspondance is lost and our actual results are around 3 ppm/day. Even to achieve this result, a stringent discipline is mandatory in the clean room and during the test :

- frequent vacuum cleaning of most equipment;
- limited use of wipers, which all produce fibers during the cleaning of machined surfaces;
- use of GORETEX garments with a strict clothing procedure (other garments produce small fibers and are not leak tight enough);
- frequent inspection of the hardware with ultraviolet light in order to actually see the dust particles;
- during the vacuum sequence of the test, a very slow pumpdown is mandatory, in order to avoid turbulences inside the chamber which could move the remaining dust particles;
- at the end of the test, the return to ambient pressure is allowed through an HEPA filter, at a speed similar to that of the pumpdown for the same reason.

A number of further actions are constantly taken for still improving the cleanliness levels towards the limit.

5.2. Molecular contamination.

Since the tests at IAL SPACE are mostly vacuum optical tests, a number of equipment items have to be designed in order not to outgas when in vacuum. In the case of ISO, the situation is still more complicated, because the test specimen is cooled to cryogenic temperatures and it can trap any released contaminants. The requirement is down to $2 \cdot 10^{-8}$ g/cm² for a complete test sequence, as measured by witness samples which follow the temperature cycle of the telescope.

Nevertheless, the requirement has been fulfilled, mainly by means of the following precautions :

- preliminary chemical cleaning of the cleanroom plastic walls, in order to remove the volatile plasticizers;
- severe selection of all the vacuum-used materials;
- no paint except black CHEMGLAZE Z306 without primer;
- no lubrication except FOMBLIN Z25 grease and oil;
- in-depth analysis of the cool down and warm-up sequences, in order to ensure that the test specimen is never the coldest point in the setup;
- use of a cold trap which catches most of the released contaminants;
- repressurization of the chamber only with clean gaseous nitrogen (taken from the main nitrogen tank and filtered).

6) PRODUCT ASSURANCE AND QUALITY CONTROL

Since IAL SPACE is a coordinated facility of ESA, all testing activities are managed under a product assurance organisation which is compliant with the ESA system (PSS : Procedures, Standards and Specifications). The administrative position of IAL SPACE within of expertise (chemical analysis,...), whereas its autonomy can cope with the management and planning aspects of space programs.

7) CONCLUSION

The IAL SPACE facilities represent a major tool for thermal vacuum testing of satellite payloads. They are able to cope with simultaneous requirements regarding temperature, optical stability, experiment volume, vacuum and cleanliness. The necessary ground support equipment is essentially designed and manufactured, either in-house, or in a series of neighbouring companies with a high expertise.

The experimental test setup is presented elsewhere in this conference. The purpose of the present paper is to give a review of the main test facilities at IAL SPACE.

Three vacuum simulation chambers are currently operated at IAL SPACE, with a regular upgrading to high performances. Their uniqueness is due to the integrated optical benches with a very low vibration level (in the 10^{-6} g range), giving access to interferometric measurements under vacuum. Thanks to a Memorandum of Understanding with ESA, all the facilities are continuously kept to the state-of-the-art by a highly experienced team.

All the chambers bear the name of FOCAL (acronym of "Facility for Optical Calibration"), with a figure corresponding to their diameter. Depending on the required volume and specifications, a given test can be run with the optimum cost and duration by choosing the appropriate chamber. A strong effort has been made on the modularity and flexibility of the chamber systems, together with the standardization of components.

FOCAL 1.5

This small chamber (1.5 meter diameter; 0.7 meter height; horizontal axis) has been extensively used for HST-related activities. It is made of stainless steel in 3 parts : a baseplate, a main cylinder and a lid, giving a very high transportability. The chamber is connected to a vacuum monochromator (range : 120 to 650 nm) by means of an imaging telescope assembly. Hence it is possible to project the monochromatic images of a test pattern inside the chamber, or to supply a flat field illumination.

Inside the chamber, specimens up to 100 kg can be remotely aligned by means of 3 crossed-axis translators and 1 rotator. The whole test setup in the chamber can rest directly on one of the existing seismic blocks, by means of columns which pass through the baseplate via bellows without touching anything else.

The temperature regulation can be ensured between -40C and + 60C, both at the specimen level by means of fluid feedthroughs, and around the specimen by a set of removable shrouds which cover the inner skin of the chamber. Within the temperature range, stable values or programmed cycles can be controlled by a process software, together with the data recording and retrieval. Recently the temperature range has been extended by a liquid nitrogen connection and internal heaters, in order to allow fast (15 minutes) cyclings to be applied on specimens between -120C and +200C.

CONTAMINATION CONTROL PROGRAM FOR THE COSMIC BACKGROUND EXPLORER:

AN OVERVIEW

Richard D. Barney

NASA/Goddard Space Flight Center

1. ABSTRACT

Each of the three state-of-the-art instruments flown aboard NASA's Cosmic Background Explorer (COBE) (2) were designed, fabricated, and integrated using unique contamination control procedures to ensure accurate characterization of the diffuse radiation in the universe. The most stringent surface level cleanliness specifications ever attempted by NASA were required by the Diffuse Infrared Background Experiment (DIRBE) which is located inside a liquid helium cooled dewar along with the Far Infrared Absolute Spectrophotometer (FIRAS). The DIRBE instrument required complex stray radiation suppression that defined a cold primary optical baffle system surface cleanliness level of 100A.** The cleanliness levels of the cryogenic FIRAS instrument and the Differential Microwave Radiometers (DMR) which were positioned symmetrically around the dewar were less stringent ranging from level 300A to 500A. To achieve these instrument cleanliness levels, the entire flight spacecraft was maintained at level 500A throughout each phase of development. This paper describes the COBE contamination control program and the difficulties experienced in maintaining the cleanliness quality of personnel and flight hardware throughout instrument assembly, spacecraft integration, flight environmental qualification, and launch site operations.

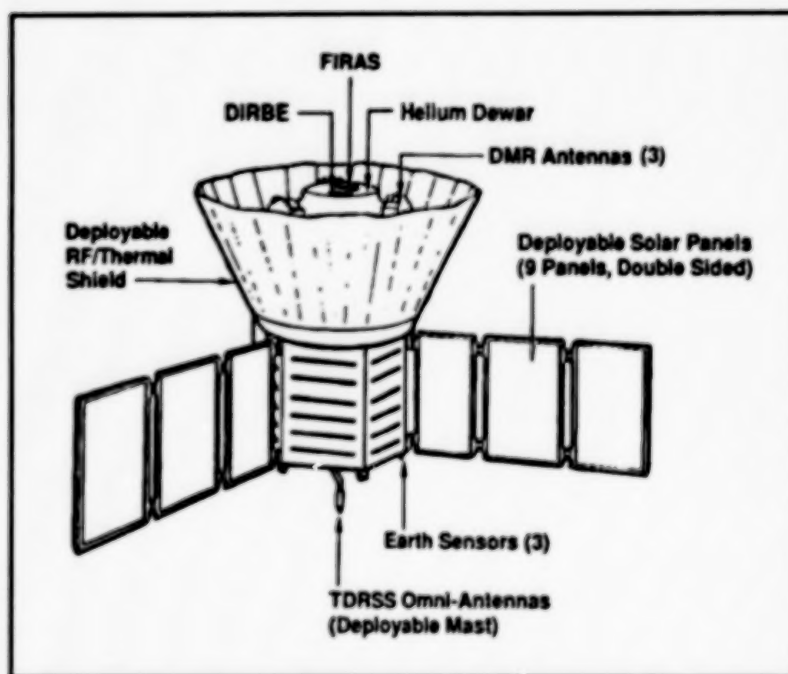


Figure 1. Cosmic Background Explorer

2. INTRODUCTION

The COBE spacecraft was launched on a Delta Rocket into a 559 nautical mile polar orbit on November 17, 1989 to study the dynamics of the origin of the universe. Figure 1 shows a schematic drawing of the spacecraft's deployed on-orbit configuration and relative locations of the DIRBE, FIRAS, and DMR instruments inside the Radio Frequency (RF)/thermal shield. The deployable mechanisms aboard the spacecraft include the omni-antenna, three solar array wings, RF/thermal shield with attached DMR contamination covers, and the dewar aperture cover that protected the FIRAS and DIRBE instruments from particulate and molecular contamination during the first 72 hours of orbital operations.

** Surface Cleanliness Levels and Air Quality Class results are stated according to Federal and Military Standards (References #1 & 3)

Both the FIRAS and DIRBE instruments operate at temperatures below 2 Kelvin inside the dewar. This required innovative contamination control measures to prevent condensation of outgassing materials on critical cold optical components. FIRAS is a modified Michelson interferometer that operates in the wavelength range from 0.1 to 10 mm to determine the spectrum of the cosmic background radiation.(2) It utilizes a polished aluminum input skyhorn to direct cosmic radiation into the optical system. Particulate or molecular contamination in excess of level 300A would decrease off-axis rejection performance of the skyhorn and possibly destroy tiny elements inside the bolometer detectors at the base of the skyhorn.

The DIRBE is located above FIRAS inside the liquid helium dewar and is currently measuring the diffuse galactic radiation in the wavelength range from 1 to 300 microns. The first optical element in this off-axis Gregorian system is a super polished, gold-coated aluminum parabolic mirror that was cleaned and maintained at level 100A to minimize radiation scattering.(5) DIRBE was assembled in a Class 100 vertical flow clean room, and completely sealed with the exception of a 70 micron pore filter positioned in the optical baseplate under the primary mirror. This filter allowed pressure equalization between the two instruments inside the COBE dewar during vacuum pump down procedures.

The final instrument flown aboard COBE was the DMR which has three individual receiver heads positioned symmetrically around the periphery of the dewar to determine whether the cosmic background radiation is equally bright in all directions. The DMR antennas operate at wavelengths of 3.3, 5.7, and 9.6 millimeters respectively to map the entire sky.(2) The internal surfaces of the corrugated horns were protected from particulate contamination at all times to preserve the cleanliness of the horn throats and the switching mechanism that is used to calibrate each receiver on orbit. A particle of 180 microns in length would cause blockage in the horns and interrupt signal throughput.

3. CONTAMINATION CONTROL SPECIFICATIONS

During early design phases, cleanliness specifications for the COBE instruments described above were established to protect critical components such as the DIRBE optics and detectors from unknown contamination. They were based on theoretical instrument performance degradation studies performed early in the project's design phases and contamination data obtained from previous successful satellites such as the Infrared Astronomical Satellite (IRAS). However, this data did not describe the effects of molecular depositions and particulate debris on the performance of the unique COBE instruments. There was also limited data defining the contamination transport mechanisms in a space environment that could coat critical cold optics with molecular layers of contamination from high energy atomic oxygen bombardment or particulate contamination from micrometeoroid collisions with the spacecraft. Based the lack of scientific data, the COBE design team defined cleanliness specifications as stringent as possible based on the availability of state-of-the-art cleaning procedures, cleaning facilities, clean room garments, and clean room operating procedures.

COBE flight hardware was cleaned and certified to the design phase specified cleanliness levels at the component level prior to spacecraft integration. Once flight integration started, it became extremely difficult to maintain these cleanliness levels due to fabrication and integration operations that took place after the instrument components were originally cleaned. Additional contamination control analytical data was obtained using flight-like breadboard instruments and experimental techniques such as white light scattering photography, detector Non-Volatile Residue (NVR) analysis, and Bidirectional Reflectance Distribution Function (BRDF) measurements which describe the scattered radiance produced by particulate or molecular contamination on optical surfaces. These analyses showed that the strict cleanliness levels defined during the design phase of the COBE project were only required on critical optical surfaces such as the DIRBE primary mirror and forebaffle, FIRAS sky horn, and DMR corrugated antennas. As a result of this data, new flight hardware was designed to protect critical areas such as the DIRBE input aperture and DMR antennas, and contamination control specifications for less-critical instrument surfaces were relaxed to more achievable levels as shown in Figure 2.

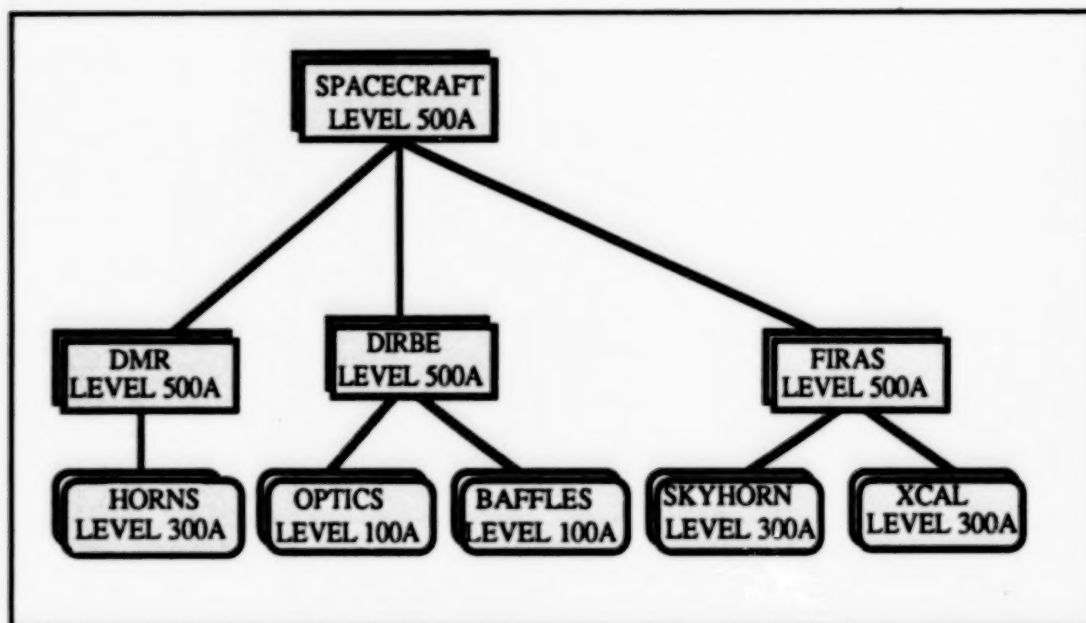


Figure 2. COBE Amended Contamination Control Specifications

4. CONTAMINATION CONTROL FLIGHT HARDWARE

Due to the stringent COBE contamination control specifications, sensitive surfaces of the FIRAS, DIRBE and DMR instruments were protected by deployable contamination control covers during launch and the early orbital outgassing period. A dewar aperture dome was the primary protection device that covered the FIRAS and DIRBE instruments inside the dewar. This dome was installed prior to pumpdown operations and remained attached to the dewar until the spacecraft had orbited the earth for 72 hours. The primary contamination concern during this time period was the possibility of water condensing on the primary optical surfaces of the cold instruments. Outgassing characteristics of the COBE were determined utilizing data obtained from the thermal vacuum qualification test that essentially baked out the entire spacecraft for 3 days then exposed it to both hot and cold orbital simulations. Since the thermal vacuum chamber contributed to the dissipation of water and other volatiles, it was necessary to compare the actual thermal test data to a statistical spacecraft outgassing model based on theoretical flux data. Outgassing data from multi-layered thermal blankets was used to evaluate the outgassing characteristics of the COBE thermal shield and top deck blankets. Once the outgassing model was established, other factors such as the dewar temperature profile, spacecraft orientation on orbit (90 degrees off velocity vector), and redistribution probabilities were factored in to arrive at the 72 hour safe outgassing period.

A secondary DIRBE contamination cover was attached to the inside surface of the dewar aperture cover to protect the primary mirror from contamination generated inside the dewar during spacecraft vibration testing, launch site transportation and launch. An optical scatterometer was mounted to the viewed aluminum surface of the oval DIRBE cover to measure the amount of radiation scattering produced by particles on the gold coated primary mirror. This scatterometer was activated throughout ground testing and just before deployment of the dewar aperture cover to measure the contamination generated during launch. Figure 3 shows the position of the scatterometer and contamination cover inside the dewar aperture cover.

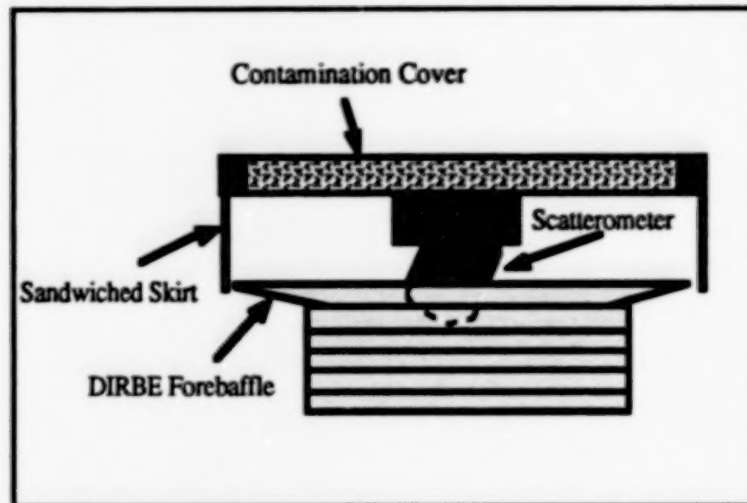


Figure 3. DIRBE Contamination Control Cover Skirt

Additional contamination control covers were also designed to protect the DMR antennas from particulate debris until the covers were deployed with the thermal shield approximately one hour into orbit. Although the Delta Rocket fairing halves were cleaned and verified to Level 500A for the first time in the history of Delta projects, debris generated during launch could dislodge and migrate into the corrugated horns effecting the switching mechanism that allows on-orbit calibration. Therefore, light weight covers were fabricated to protect the horns. Silicon foam was sealed with aluminized kapton and hinged from the stowed thermal shield panels. The covers rested 0.3 inches above each set of DMR horns on a honey comb support plate that contacted each radiometer in the center section through a smooth delrin rail. When the thermal shield deployed, the delrin guide slid across a kapton track that was attached to the center of each radiometer. This provided a relatively particle free interaction between the delrin and kapton. Figure 4 shows the DMR contamination covers in the stowed position. The covers were successfully deployed with the thermal shield and each DMR is functioning as planned.

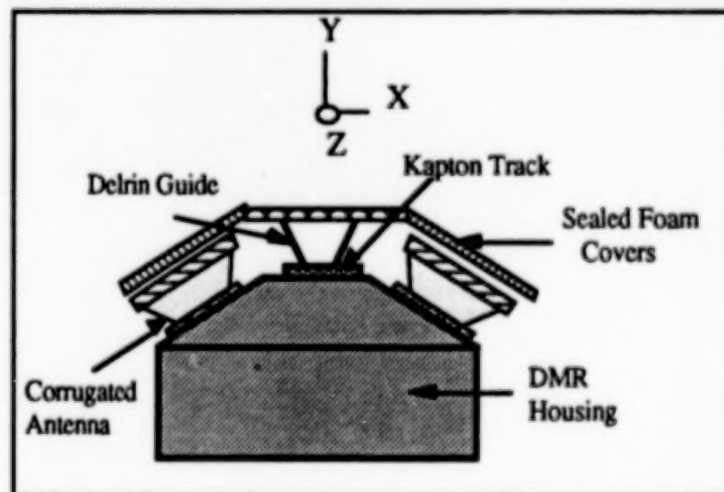


Figure 4. DMR Contamination Control Covers

5. CLEANING and INSPECTION TECHNIQUES

All COBE surface cleanliness levels were maintained throughout fabrication, integration, environmental qualification, and launch operations. These cleanliness levels were achieved through initial component level cleaning in the COBE Precision Cleaning Facility (CPCF) along with routine cleaning of the entire spacecraft. The CPCF is a Class 10,000 vertical laminar flow clean tent equipped with an exhaust bench for chemical cleaning, ultrasonic cleaning station, and contamination inspection stations. During spacecraft integration, a Quadrex Precision Cleaning Unit was installed in the CPCF. It uses a high pressure Freon spray to remove surface contaminants from compatible materials. The CPCF was continuously supported by two contamination control technicians who cleaned and inspected each piece of COBE flight hardware prior to integration to the spacecraft.

Standard cleaning procedures included a combination of thermal bakeouts, solvent rinsing, vacuuming, gaseous nitrogen blasting, vibration testing, and ultrasonic techniques. Each of the COBE flight components were required to undergo a thermal bakeout to reduce potential contamination due to outgassing. The thermal vacuum chambers were equipped with a cold finger and Quartz Crystal Microbalance (QCM) to measure outgassing rates and amounts.

The COBE Contamination Control Group and Quality Assurance (QA) personnel utilized three different inspection techniques to verify the levels of cleanliness of COBE flight hardware. First, the component was visually inspected using a minimum 100 foot-candle intensity White Light and a Long Wave Blacklight (365 nm) to determine the presence of molecular and particulate contamination. Second, a tape lift sample was taken and analyzed to provide a statistical estimate of the total number and size distribution of particles per square foot that was present on the sampled item. If the item failed this tape test, it was recleaned according to the steps identified in the cleaning procedure. Third, if molecular contamination levels needed to be verified, a solvent wash was taken and analyzed using infrared and mass spectrometry techniques. By utilizing these contamination inspection techniques, we were assured of launching a COBE spacecraft that met the functional contamination performance requirements.

6. FLIGHT QUALIFICATION CYCLE

The COBE flight environmental qualification cycle was designed to ensure survivability and functional performance of each spacecraft subsystem during launch and orbital operations. Flight hardware was environmentally qualified at the component level as well as the fully integrated spacecraft level. The qualification sequence included thermal vacuum cycling, three axis vibrations, acoustic bombardment, microphonics, electromagnetic capability (EMC), and radio frequency interference (RFI) tests. Special precautions were taken during each test to minimize contamination of the instruments and spacecraft.

During each test, the spacecraft was located in a <Class 10,000 clean room environment and all testing hardware was cleaned per COBE cleaning procedures. For example, the spacecraft was double bagged in a clean antistatic Nylon film during transportation to the vibration, acoustic, thermal vacuum, and RFI chambers. Once inside the thermal vacuum and RFI chambers (both are Class 10,000), the outer bag was removed and the environment was stabilized prior to removal of the inner bag and exposure of the spacecraft. The vibration and acoustic chambers were not clean rooms and the bags remained on the spacecraft throughout testing. The bags were purged with Class 100 air conditioned atmospheric air to maintain thermal specifications on the instrument electronics. The 18X8 feet diameter bags used during the environmental qualification cycle were fabricated and cleaned at GSFC using a bagging fixture designed and built by the COBE Contamination Control Team.

6.1 Component Level Qualification Testing

The critical FIRAS, DIRBE, and DMR components were individually flight qualified prior to integration to the instrument and spacecraft module. Throughout this testing, maintaining the cleanliness level of the DIRBE primary mirror was the major contamination control goal. The DIRBE baffle system as first assembled, was painted with Chemglaze Z-306 black paint filled with microballons to decrease optical scattering. However, these microballons flaked and collected on the primary mirror during both ambient and cryogenic vibrations. To alleviate this problem, the baffle system was stripped of paint and black anodized. After completion of additional ambient and cold temperature vibration tests, tape lift samples from the center of the primary mirror were analyzed using an energy dispersive spectrometer and scanning electron microscope. The tapes showed no evidence of anodized aluminum flakes on the post vibration tape samples. The corresponding cleanliness levels met the Level 100A COBE specification.

Although the anodize surface was adequate for the DIRBE baffle system, FIRAS experienced flaking of its anodize outer shell portion of the skyhorn during contamination certification. Long (400 microns) strips of anodize material were lifted off the skyhorn by the tape samples used to test flight components for particulate contamination. An anodized test sample was chosen that exhibited similar tape test results and vibrated to the same levels as the anodized DIRBE forebaffle described above.

Upon completion of the vibration testing, the test sample was visually inspected and several tape samples were taken from the clean bag that surrounded the sample. Final materials analysis showed the anodize material was not shedding from the test piece due to vibration. The long strips of anodize material seen on the previous tape tests were definitely not found in the post vibration particle analysis. Therefore, it appears that the only way to cause the anodize material to shed is to physically remove it with tape. The FIRAS skyhorn was qualified and flown with the original anodized outer surface.

6.2 Thermal Vacuum Testing

To simulate thermal environmental conditions imposed on COBE during launch and mission operations, the spacecraft was thermally cycled in a Space Environmental Simulator (SES) at GSFC. During the thermal vacuum portion of the simulation test, spacecraft temperatures averaged 5-10 C above and below the predicted flight temperature extremes. Figure 5 profiles the thermal vacuum chamber average temperature throughout the duration of the test.

The primary contamination control objective for the thermal simulation test was to determine the possibility of the spacecraft self-contaminating its instruments either during launch or on-orbit. Secondary objectives were: 1) bakeout the entire spacecraft during the first three days of hot soak conditions 2) measure the amount of condensed contamination throughout each phase of the test, and 3) determine the chemical makeup of the residue collected on cold surfaces in the chamber. All of this data was combined with a statistical on-orbit outgassing model of the COBE spacecraft to determine an optimum outgassing period prior to dewar aperture cover deployment.

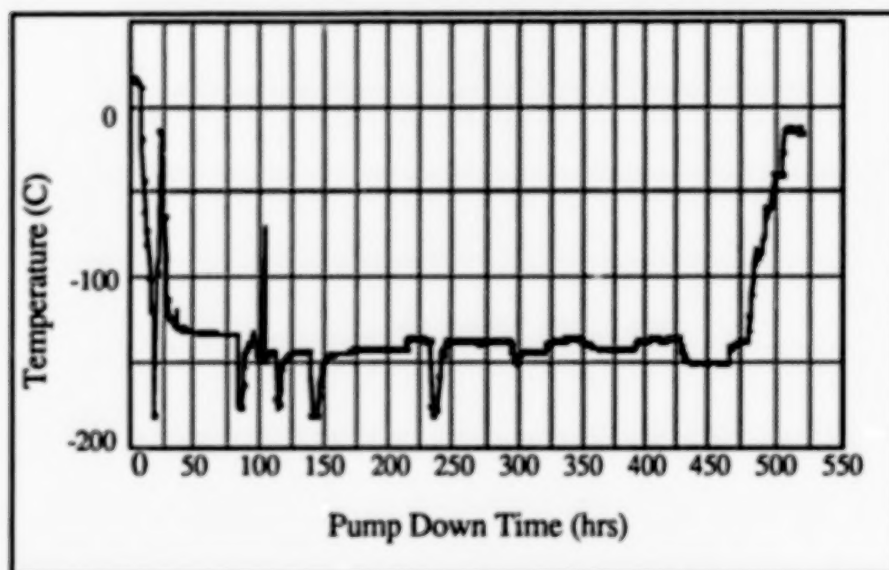


Figure 5. COBE Thermal Vacuum Cycle Temperature Profile

6.2.1 Contamination Monitoring Techniques

Three quartz crystal microbalances (QCM) were spaced symmetrically around the spacecraft and initially cooled with liquid nitrogen to provide a real-time means of measuring the quantity of outgassing contaminants throughout testing. A QCM displays the difference between beat frequencies of two 10Mhz crystals in Hertz which can be analytically converted to a quantitative amount of outgassing from the spacecraft. The QCMs were placed symmetrically around the spacecraft and two feet from the flight hardware.

Along with the QCMs, a residual gas analyzer (RGA) was used to measure the ratio of mass-to-electric charge of gas molecules in the thermal vacuum chamber. The gasses and vapors isolated for the COBE test included water, oxygen, nitrogen, and helium. RGA scans were recorded each eight hour shift, and the data was reduced to profile outgassing rates as a function of chamber pumping time.

In addition to outgassing rates, the quantity and chemical background of condensed material was determined using a cold finger, scavenger plate, and six polished aluminum mirrors. The mirrors were mounted to the DMR support ring to collect condensed residue from the most contamination sensitive portions of the spacecraft. The cold finger and scavenger plate were attached to the chamber and actively cooled with liquid nitrogen so outgassing molecules from the spacecraft would stick to the cold surfaces. The 4 foot diameter aluminum scavenger plate was flooded with nitrogen throughout the duration of the test, whereas, the cold finger was actively cooled for the last eight hours of the test. Upon completion of the thermal cycling test, the mirrors, cold finger, and scavenger plate were rinsed with a solvent, and the residue was analyzed using Infrared and Mass Spectrometry techniques.

6.2.2 Thermal Vacuum Test Results

QCM

Once the QCMs stabilized, temperature and frequency data was recorded hourly to establish trend profiles. The frequency data was further reduced by calculating the difference between two subsequent frequency readings to obtain a delta (Δ) frequency value. A representative graph of the QCM temperature versus Δ frequency profiles is shown in Figure 6. The erratic amplitude spikes occurring throughout the scan are the result of the instability in the QCM temperature controller which occasionally varied by more than 5 C and caused delta readings to vary up to 100 Hz/Hr.

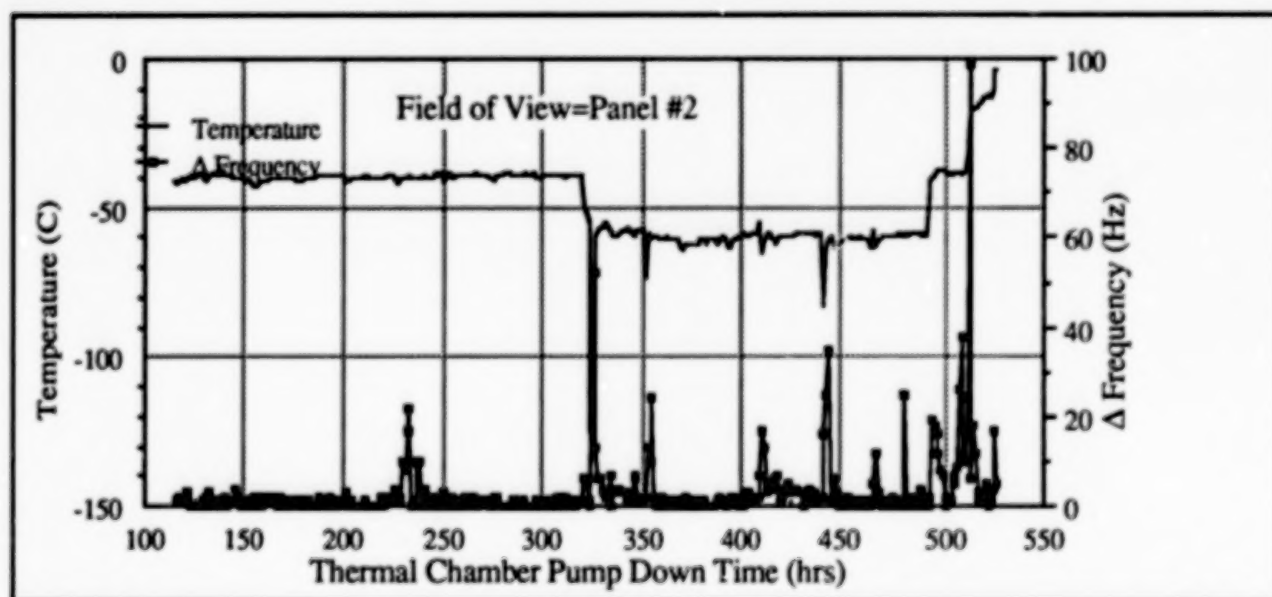


Figure 6. QCM #1 Delta Frequency Profile

Despite lowering the QCM temperature to -60 C, the final Δ frequency results successfully met the specifications outlined in the COBE Contamination Control Plan Phase II which calls for the QCM Δ frequency to be < 200 Hz/Hr, for five consecutive hours.

RGA

The RGA trend data was compiled for water, nitrogen, helium, and oxygen. A representative RGA trend profile for water is shown in Figure 7. The initial spikes on the graph at the end of the first day are the result of a helium leak in the dewar pump lines. The diffusion pumps were turned off, and the chamber was brought back to ambient conditions before the leak was isolated and controlled.

Once the chamber was pumped back down to 10^{-7} TORR, the outgassing rates of helium, oxygen, and nitrogen decreased to the 10^{-9} scale. Water dissipated at a slower rate, stabilizing after 50 hours of hot soak conditions. The temperatures of the spacecraft during this first hot bakeout phase averaged 10 C higher than mission temperature predicts. Thus, outgassing rates should be slower on orbit than seen in the thermal vacuum tests.

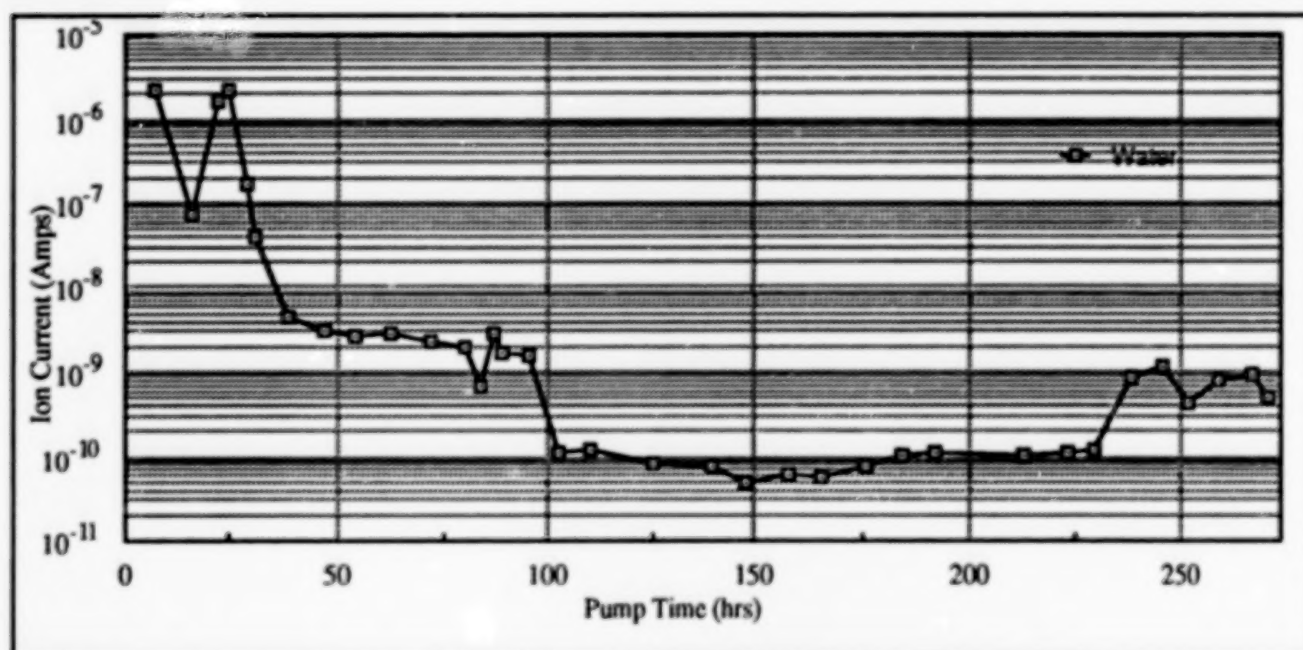


Figure 7. RGA Trend Profile for Mass#=18 (Water)

Cold Finger

The cold finger was activated during the last eight hours of the thermal vacuum test, and the residue was rinsed into a petri dish for analysis which showed 1.3 mg of contaminants. This unusually low level of contamination included Caprolactam, Tributyl Tin Chloride, Triallyl Cyanurate, Benzoic Acid, DC 704, and Phthalate Esters. With the exception of DC 704 diffusion pump oil and Phthalate Esters, the other materials that condensed on the cold finger are frequently used in the insulation of electrical harnesses. The most abundant condensed material was Caprolactam which is the anti-static agent in the Richmond Corporation Anti Static (RCAS) 2400 Nylon bagging material. COBE eliminated this contamination source by changing the bagging material that was used after thermal vacuum testing to a mylar type material known as Llumaloy-HSC (Martin Processing). The components that were extracted from the cold finger rinse are acceptable according to the flight levels specified in the COBE Contamination Control Plan Phase II.

Scavenger Plate

Residue from the scavenger plate showed essentially the same chemical characteristics as the contamination rinsed from the cold finger. The amount of residue was 3.3 mg, however it was rinsed from a surface area of 12.5 square feet which is 10 times the area of a cold finger. This residue contained normal chamber and spacecraft materials.

Witness Mirrors

The witness mirrors were strategically placed on the DMR support ring to collect contamination that would condense on the most critical external surfaces of the dewar and DMR instruments. The post test chemical analysis of the witness mirrors showed no detectable organic residue.

6.3 VIBRATION/ACOUSTIC TESTING

The COBE flight spacecraft was also subjected to acoustic testing along with a 3-axis sinusoidal vibration sweep. It was double bagged and purged throughout the duration of the tests because the vibration and acoustic cells were not clean rooms. Primary contamination control objectives were to measure the generated debris and spacecraft self-contamination, analyze the effectiveness of the DMR contamination control covers, and assess the possibility of debris created during the launch reaching sensitive areas around the DMR heads and cryogenic dewar.

Prior to vibration and acoustic testing, machined witness plates containing mylar disks coated with transfer adhesive were mounted to the DMR honeycomb support ring in the same locations as the witness mirrors used during the thermal vacuum tests. The witness plates were designed to gather the contamination generated between the external surfaces of the DMR blanket material and the painted dewar. Upon completion of the tests, the mylar disks were removed and analyzed.

6.3.1 Vibration Test Results

The level of contamination measured on each witness plate met the level 500 COBE mission specification. These results are shown in Table 1 below. The debris seen on the mylar plates was a combination of metal particles and small polyester fibers generated by clean room garments. The fibers are removed during the routine spacecraft cleaning shifts and will not contaminate the spacecraft during launch or in orbit.

There were also many tape lift samples taken at various locations on the spacecraft after it returned to the clean room. A majority of the tape lifts were from the upper deck regions close to the DMR instruments. Aluminum and black anodized particles of various sizes were found on the top portion of MLI attached to the bottom deck. Additional tape samples showed migration of the debris from inside the cowling to the solar arrays and other portions of the bottom deck. The particles were generated by a scraping interaction between the backside of the cowling and the spacecraft frame during testing. A layer of isolating Nylon material was added between the spacecraft and the painted flight cowling panels to provide a smooth surface that would not shed during launch.

<u>Witness Plate #</u>	<u>Location</u>	<u>Results</u>
1	Left side of the 90 GHz DMR head	Level 500
2	Right side of the 53 GHz DMR head	Level 300
3	Left side of the 31 GHz DMR head	Level 300
4	Right side of the 90 GHz DMR head	Level 500
5	Right side of the 31 GHz DMR head	Level 500
6	Left side of the 53 GHz DMR head	Level 300

* All measured contamination levels on the witness plates meet the functional performance specifications outlined in the COBE System Performance Specifications for a Delta Launch.

TABLE 1. Post-Vibration Contamination Witness Plates Results

7. TRANSPORTATION TO LAUNCH SITE

A unique COBE transporter trailer was built to control the temperature, pressure, humidity, and cleanliness of the environment that surrounds the spacecraft while protecting it from induced vibrations and stresses. The filtration system used in the transporter enabled the pressure to stabilize at equilibrium inside the clean container during both takeoff and landing of the C-5 transport plane that carried the spacecraft from Andrews AFB in Maryland to Vandenberg AFB in California. This transporter is shown schematically in Figure 8.

Prior to mounting the spacecraft to the transporter, large Llumaloy-HSC bags were fabricated and fitted with 70 micron pore filters mounted symmetrically around the center and top of the bags. These bags were fabricated at GSFC because the estimates from various contractors around the U.S. were extremely high and they could not meet the required delivery schedule. The final acceptance testing of the bags consisted of particle counts, rinse samples (to test for non-volatile residue) and tape lift samples. The particle counts and tape lift samples inside the bag were all <level 500, and the rinse sample residue was < 1mg/sq. ft. which is the COBE molecular contamination specification.

Once the bags were completed, they were sealed around the spacecraft and it was mounted vertically to the transporter using an engineering model of the 6019 Delta adapter ring. A breathable air purge line equipped with a desiccant and 2 micron particulate filter was inserted into the inner bag to provide positive pressure between the inner bags and the air inside the outer hard shell which was insulated and isolated from the skid base. A thick outer bag equipped with three HEPA filters was then placed around the double bagged spacecraft and supported by a cage to add further weather protection. The outer bag was a two piece design with zippers to provide sudden decompression relief. The HEPA filters protected the spacecraft from the incoming air supplied by the HVAC system which consisted of dual air conditioners and heaters and was powered by a diesel generator. The design supply air flow rate was 800 cubic feet/minute (cfm) with a fresh air flow rate of 100 cfm which provided two air changes per minute inside the outer hard box. The HEPA filter system and the outer bag ensured a < Class 1000 environment around the spacecraft throughout transportation.

Contamination measurements were taken once the spacecraft was unbagged at VAFB to verify surface cleanliness levels. During the application of tape samples and solvent wiping, technicians noticed moisture on the bottom deck multi-layered-insulation (MLI) under the vent lines from the helium dewar. Although the humidity was controlled by the transporter, the venting of helium caused moisture to condense onto the vent tube next to the spacecraft which increased the humidity inside the inner bags. A thin layer of contamination was also noticed on the top deck thermal shield standoffs, MLI, and aluminum panels. Extensive analysis showed that the contamination was Caprolactam which is the monomer that the RCAS 2400 clean bags were made from. Caprolactam becomes a contaminant at room temperature when an acceptor substrate such as silicon based paint or potting material is present and the relative humidity is around 50% or more.

The presence of caprolactam was realized early in the integration phase of the spacecraft and the solution called for a complete thermal bakeout prior to TV/TB testing because the rate of volatilization is diffusion controlled and recondensation can occur on cold surfaces such as the thermal shield. An effort was made to remove the Caprolactam from the spacecraft through thermal vacuum testing, but apparently, some still remained absorbed to the polyurethanes (paint, potting, conformal coating and staking material). The moisture (condensation) attracted the Caprolactam from the vapor phase, since it is hygroscopic. All of these facts were verified using IR and mass spectral analysis in the laboratories. The Caprolactam was removed with absolute (200proof) ethyl alcohol and the spacecraft showed no further signs of contamination due to the transporter environment.

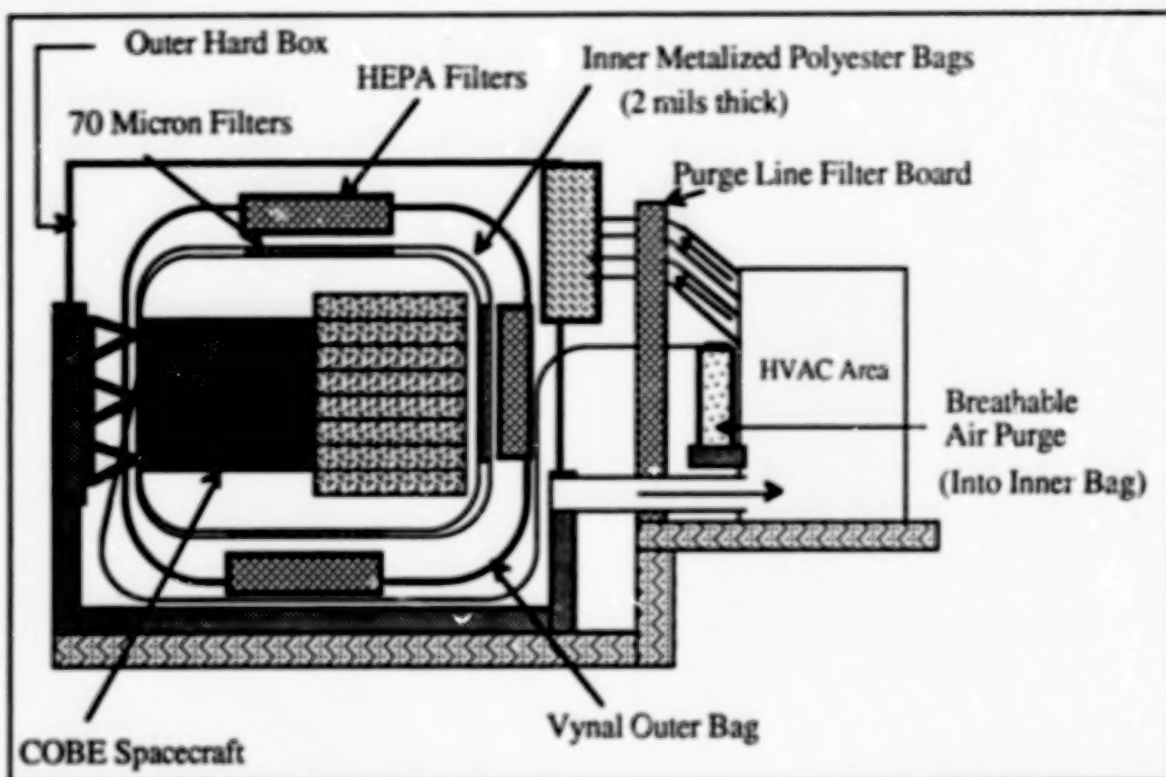


Figure 8. COBE Launch Site Transporter Clean Environmentally Controlled System

8. DELTA FAIRING CLEANING PROCEDURE

The Delta rocket fairing halves were submitted to the same contamination levels and inspection techniques as the external surfaces of spacecraft because the spacecraft was not adequately protected from contamination generated during fairing installation and launch.

The COBE/Delta fairing "super cleaning" task began with an initial inspection of the building 1610 white room (VAFB) (Class 10,000 at best) and both fairing halves by representatives from McDonnell Douglas, Kennedy Space Center, and GSFC. During this inspection, all parties noticed loose sections of silicon sealant that was used to seal gaps between machined aluminum flanges and the fairing skin in the upper nose cone. By sealing these areas, the debris between the flanges and fairing skin is trapped which eliminates the possibility of metal particles redistributing on the spacecraft during launch. This section was the most critical portion of the fairing because it was directly above the COBE dewar and DMR instruments during launch. Therefore, materials experts from McDonnell Douglas were summoned to VAFB to inspect the silicon adhesion. The material was physically stripped from the fairing, and new silicon was applied with emphasis on proper surface cleaning and preparation.

Once the new silicon had cured for seven days, it adhered strongly to the aluminum fairing skin and the super cleaning procedures continued. These procedures which were developed by the COBE project combined high pressure freon spraying with tedious vacuuming and wiping techniques to achieve the final cleanliness level of 500A. This level was ultimately reached despite inefficient equipment and facilities and the fairings were double bagged for transportation and storage on the gantry.

The final cleanliness levels of the fairings were verified by visual inspection under both UV and white light. Thirteen tape lift samples were taken to document the effectiveness of the newly developed super cleaning techniques. These levels were comparable to the external cleanliness level of 500A on the COBE spacecraft.

9. LAUNCH SITE OPERATIONS

Once the spacecraft arrived at the launch site, it was positioned in a horizontal laminar flow clean tent that ranged between Class 100 and 1000 depending upon the amount of activity and number of personnel working in the area. Cleaning stations and a garment changing area was built adjacent to the large opening of the tent and a curtain that covered 60% of the opening was added to increase the airflow velocity to 300 feet/second in the change room and 150 feet/second in the clean tent. This tent proved to be a stable environment that maintained the cleanliness of the spacecraft throughout final launch integration prior to transporting to the gantry.

The gantry was a Class 100,000 facility located on the shores of the Pacific ocean. We were extremely concerned about maintaining the cleanliness levels on the spacecraft during Delta rocket mating and fairing installation. Several unique measures were incorporated into the standard procedures to maintain the cleanliness of the spacecraft in such a dirty environment. First, the gantry was cleaned a several times by the McDonnell Douglas technicians, however, the resulting air class levels were still unsatisfactory for our spacecraft. Further cleaning by our technicians lowered the contamination levels from around Class 300,000 to 10,000 as shown in Figure 9. Second, the spacecraft was double bagged and purged with Grade C gaseous nitrogen during transportation to the gantry, then the purge was changed to conditioned air provided by a portable A/C unit that was positioned on level five of the gantry until the fairings were installed. Third, the clean bags and purging hoses remained on the spacecraft until just before the fairings were installed to protect the spacecraft as long as possible. Finally, a "shower" cap was installed on the spacecraft to protect the exposed DMR instruments and cryogenic dewar until just before the second half of the fairing was installed.

Once the spacecraft was securely inside the fairing, a HEPA filtered A/C hose was connected which was certified to Class 100 and provided positive air flow (100 cfm) through each stage of the Delta rocket. The air flow inside the fairing was routinely sampled for 20 minute time periods to measure the air quality around the exposed spacecraft. A sample of the data is shown in Figure 10. Although the gantry environment was dirty, the air quality data showed a clean environment inside the fairings and gave us confidence that the strict cleanliness specifications outlined earlier were met.

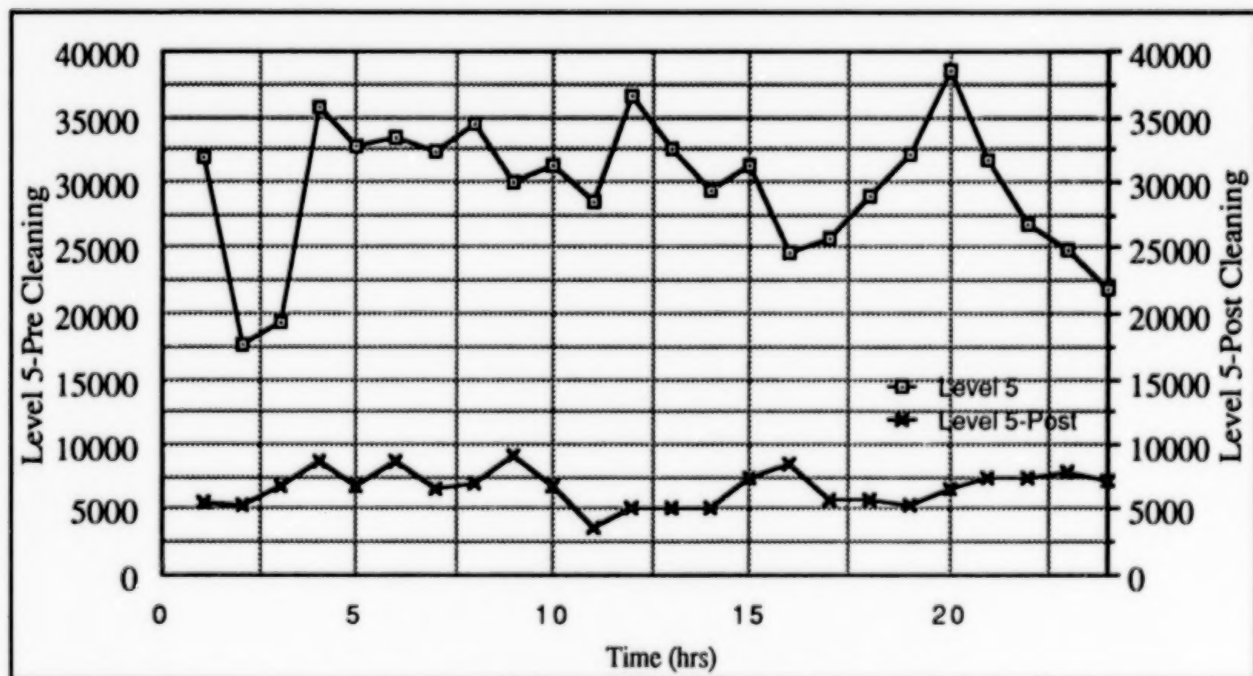


Figure 9. Delta Gantry-Level 5 Cleanliness Certification Particle Counts

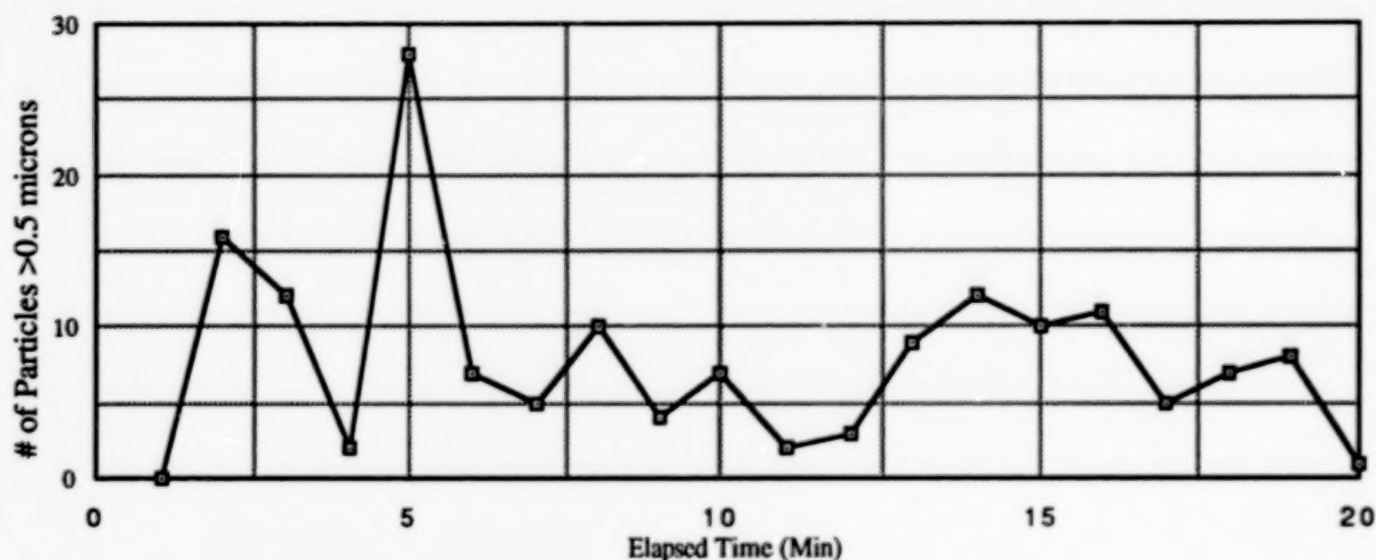


Figure 10. Delta Fairing Cleanliness Certification Particle Certification

10. FINAL CONTAMINATION RESULTS

The final contamination levels of all flight hardware were verified at different times throughout spacecraft integration, launch site operations, and Delta fairing installation. These verifications consisted of visual inspections, tape test readings, and solvent wipe analysis. All contamination verification occurred at the last possible time that we had access to the flight hardware. For example the FIRAS and DIRBE flight contamination verification was completed during integration into the cryogenic dewar, whereas, the DMR instrument and thermal shield readings were taken on the gantry-fifteen minutes prior to fairing installation. A representative sample of the tape lift data taken just prior to launch is shown in Table 2. All measured contamination levels from the flight instruments and spacecraft met or were below the required levels as stated in the COBE Contamination Control Plan.

11. CONCLUSION

The stringent cleanliness specifications required by the FIRAS, DIRBE, and DMR instruments were initially met and maintained by implementing strict clean room operational procedures, routine cleaning and inspections of flight hardware, and unique environmental control systems that protected the spacecraft from contamination during transportation and launch operations. Flight instrumentation was initially cleaned and certified to specified levels at the component level prior to instrument integration. These cleanliness levels were amended during integration because new flight hardware was designed to protect contamination sensitive instrument components, and additional analytical data was obtained that justified relaxing the specifications to more achievable levels.

These levels were maintained throughout environmental qualification, transportation to the launch site, and launch operations by protecting contamination sensitive hardware, performing routine cleaning of the spacecraft, and controlling daily operations of support personnel in the clean rooms (which proved to be most effective means of maintaining a clean spacecraft). The spacecraft was located in a Class 10,000 clean room environment which consisted of either a clean room, purged double bagged assembly, HEPA filtered transporter or purged Delta fairings. The GSFC Contamination Control Team was consistently developing new cleaning, inspection, and contamination monitoring techniques that are now being used by other clean satellites such as EUVE and ROSAT. Private companies such as McDonnell Douglas have also benefited from the COBE contamination control program by incorporating our clean room operation and hardware cleaning and

<u>Location</u>	<u>Result</u>
Panel 2-Black Painted Surface of Transponder Electronics Box	Level 300
Panel 2-MLI Surface of the Battery Wall	Level 300
Panel 2-Bottom Deck MLI Surface next to the Batteries	Level 300
Cowling Panel #1-Bare Aluminum Surface	Level 500
Cowling Panel #1-2-Bare Aluminum Surface	Level 300
Panel 1-Bottom Deck MLI	Level 200
Panel 1-Black Painted Surface of the PSE Electronics Box	Level 500
Panel 1-Black Painted Surface of the SCU Electronics Box	Level 300
Panel 3-Black Painted Surface of DMR IPDU Electronics Box	Level 300
Panel 3-Black Painted Surface of FIRAS IPDU Electronics Box	Level 300
Panel 3-Bottom Deck MLI	Level 500
Payload Attach Fitting Surface on the Delta Second Stage	Level 300
Shunt Panel Surface	Level 500
Sun Sensor MLI Surface	Level 300
DMR 90 GHz CC Covers	Level 300
DMR 31 GHz CC Covers	Level 300
DMR 53 GHz CC Covers	Level 300
Omni Antenna Aluminum Surface	Level 500
Kapton MLI Surface of the Thermal RF Shield	Level 500
Silver Teflon Surface of the Thermal RF Shield	Level 300
Solar Array Aluminum Surface S/N 05	Level 500
Dewar Sun Shade Painted Surface	Level 500
Solar Array Aluminum Surface S/N 08	Level 300
Earth Scanner MLI Surface	Level 300
Delta Fairing Iso Grid Surface	Level 750
Delta Fairing MLI Surface	Level 500

TABLE 2. Final Flight Tape Lift Sample Results

inspection techniques such as the fairing cleaning procedures into their launch preparation documents for future contamination sensitive spacecraft. The COBE contamination control program briefly outlined in this paper can be applied to future "clean" spacecraft projects to obtain stringent cleanliness levels that until now have been unachievable.

Early observations from COBE show the instruments are operating nominally and optical scattering principally caused by particulate and molecular contamination is an order of magnitude smaller than originally budgeted with the spacecraft's contamination specifications. Although we do not have an active means of measuring on-orbit contamination, scientific data suggests that the FIRAS, DIRBE, and DMR instruments have not suffered any performance degradation due to presence of particulate or molecular contamination.

12. RECOMMENDATIONS

1. Contamination sensitive projects should develop a detailed cause and effect contamination analysis during the design study phase, and establish the Contamination Control Team early in the hardware phase to reduce inefficiencies and logistical problems.
2. The Contamination Control Team must design, build and operate efficient flight hardware cleaning and inspection facilities. A little creativity can go along way in designing cost efficient facilities.
3. A materials study and early orbital outgassing model of the spacecraft should be developed during the design phase to determine realistic contamination control specifications.
4. Real-time contamination monitoring devices should be mounted next to sensitive hardware to measure on-orbit outgassing rates. COBE was baselined with flight QCMs that were supposed to operate at 4 Kelvin, however, the technology was not developed and the instrumentation was removed.
5. The Contamination Control Team must isolate super clean operations from the standard clean room environment with the use of clean tents, separate change areas, and GSE cleaning stations.
6. Contamination sensitive hardware must be protected at all times throughout each phase of spacecraft development and launch---Do not rely on the cleanliness of the surrounding environment.
7. Learn from COBE!! We have generated a wealth of contamination control data that should be utilized by future projects to prevent them from making similar mistakes.

13. REFERENCES

1. Fed. Std. No. 209B: Federal Standard for Clean Room and Work Station Requirements, Controlled Environment. 24 April 1973.
2. J. C. Mather, "The Cosmic Background Explorer (COBE)", Opt. Eng. 21(4), 769-774 (1982).
3. Mil-STD-1246A: Military Standard Product Cleanliness Levels and Contamination Control Program. 18 August 1967.
4. R.D. Barney and T.J. Magner, "Far IR Absolute Spectrophotometer (FIRAS) Wire Grid Characterization Techniques", SPIE Proceedings, Cryogenic Optical Systems and Instruments III, Vol 973, 139-146 (1988).
5. T.J. Magner, "Diffuse Infrared Background Experiment (DIRBE) Optics Module Breadboard Alignment Methods and Results", Opt. Eng. 26(3), 264-269 (1987)

SESSION VIII
NEW APPROACHES

A UNIQUE APPROACH TO SPACE THERMAL SIMULATION

**D.Q. Durant, MS 31-2
McDonnell Douglas Space Systems Company**

ABSTRACT

The Space Systems Laboratory of McDonnell Douglas Space Systems Company, Huntington Beach, developed several innovative techniques to perform the DELTA Star System thermal vacuum test. Test design constraints included an accelerated test schedule and an ambitious test plan focusing on cyclic absorbed orbital flux simulation. Test design and fabrication was completed in only 4 months, producing a 21-zone computer-modeled reflectorless lamp array system. Array zone control was based on discrete absorbed flux measurements, provided by adiabatic coupons conceived to eliminate the need for conventional radiometers. Test requirements, methodology, and test thermal model-flight data correlation are presented.

THERMAL/VACUUM VS. THERMAL
ATMOSPHERIC TESTING OF
SPACE FLIGHT ELECTRONIC ASSEMBLIES

By: Mark Gibbel

The Gibbel Corporation

ABSTRACT:

For space flight hardware the thermal vacuum environmental test is the best test of a system's flight worthiness. Substituting an atmospheric pressure thermal test for a thermal/vacuum test can effectively reduce piece part temperatures by 20°C or more, even for low power density designs. Similar reductions in test effectiveness can also result from improper assembly level T/V test boundary conditions. The net result of these changes may reduce the effective test temperatures to the point where there is zero or negative margin over the flight thermal environment.

INTRODUCTION

Assembly level thermal testing on hardware intended for space flight is the most perceptive test for uncovering design deficiencies and workmanship flaws. It can also be effective as a reliability demonstration indicator¹. However, there are many opportunities to compromise the effectiveness of the test starting in the design definition phase of the program. Some compromises can be so bad that the pertinent temperatures during the test are less than what they would be under flight allowable conditions. Compromises which relate to performing thermal testing in an atmospheric pressure environment (T/A) in lieu of thermal testing in a vacuum environment (T/V) for electronic systems intended for space flight will be addressed.

This work focuses on introducing the tools necessary to support a technical

risk evaluation of performing a T/A test in lieu of T/V test. Results of several analyses and tests for the effect of performing a T/A test in lieu of a T/V, are also presented.

BACKGROUND

In 1985 a client began the process of reevaluating their technical rational and methodology for choosing between performing thermal testing in a vacuum environment (T/V testing) or in a ambient pressure environment (T/A testing). Their pre 1985 assembly level thermal test rational was to always perform T/V testing unless two conditions were met. These conditions were that the hardware was not sensitive to "pure vacuum" effects AND the watt density of the assembly was low (0.04 watts/cm² or less). By mid 1987, it was demonstrated that the old rational was suspect. New rational and methodology were developed to quantify the temperature effects (level/gradients). Research performed on failure physics of space flight electronic assemblies from 1985 to the present has been used in-conjunction with the temperature effect data to evaluate the new approach recommended in 1987.

A survey of industry on assembly level "thermal" testing on space flight electronic hardware, was performed in 1990². One of the questions on the survey was, what are your criteria for subjecting a box to a vacuum environment? The survey found a wide difference of opinion as to when and why the substitution of a T/A test for a T/V test was appropriate. One organization's decision criteria is based on thermal analyses and failure physics factors. Another organization uses a checklist of conditions to be met via analyses before the substitution is allowed. At the other end of the spectrum it was found that only boxes that were known to be sensitive to "pure vacuum" effects (corona, multipactoring etc.) are vacuum tested. Furthermore, this company believed that "digital and

low voltage analog boxes" do not need to be T/V tested at the assembly level. Moreover, the survey found many misconceptions and invalid rule-of-thumbs in use.

The background information necessary to perform an evaluation of the technical risk arising from performing a T/A test in lieu of a T/V test includes:

- (1) An overview of the effects of performing T/A testing in lieu of T/V testing
- (2) The goals of assembly level thermal testing
- (3) A summary of reliability theory, failure physics for electronics assemblies and reliability demonstration theory
- (4) Definition of the appropriate thermal analysis methodology, assumptions and boundary conditions
- (5) Definition of the proper implementation of the T/V test based on the results of the piece part thermal analysis.

A synopsis of these topics along with analyses and test results are presented.

Vacuum Effects - An Overview

There are two different physical phenomena/effects that result from substituting a atmospheric pressure environment for a vacuum environment. They are "pure vacuum" phenomenon and temperature level/gradient effects.

The "pure vacuum" phenomenon include corona and multipactoring. Corona is of concern in the pressure region from about 0.1 to 0.001 torr. Multipactoring can occur starting from the middle of the corona region all the way to near hard-vacuum conditions. These phenomena are most often associated with RF or high voltage circuits and devices.

The addition of an ambient pressure gas alters key temperature levels and gradients. For a conductively coupled (baseplate to S/C) design the prime thermal path is from the parts to the baseplate via the boards and housing. The addition of a gas into the "simulated" flight environment results in two significant thermal alterations. First, the dominate thermal path from key elements of the assembly (piece parts, solder joints, etc.) are altered because the gas adds a parallel path from these elements to the chamber ambient via the total housing skin. Secondly, artificial parallel paths from the key elements to the flight heat sinking surface are added. These short out any of the high flight thermal resistance paths. The net result of these alterations is the reduction in temperature of key elements at both test temperature extremes. This test temperature reduction is referred to as the ΔT effect.

ANALYSES & TEST RESULTS

Table 1, presents a summary of analyses and test results supported by the author over the last 5 years to evaluate the ΔT effects of performing T/A testing in lieu of T/V testing. Performing T/A testing in lieu of T/V testing reduces the temperature rise from the thermal control surface to key elements (boards, solder joints, parts, etc.) internal to the assembly. Observe that this effect reduces the operating temperatures of the key elements over the whole temperature range i.e. hot testing becomes less severe while cold testing becomes more severe. Reductions in the temperature rises can be on the order of 15°C to 20°C or more. In many cases T/A test reduces temperatures rises by a factor of 2 to 4.

Table 1 also presents power density and hardware type (analog, digital, RF, power supply, etc.) data. Note that neither of these are appropriate "yardsticks" for gauging the sensitivity of a particular design to the effects of

performing T/A testing in lieu of T/V testing. Reference 3 discusses the implications of the packaging design (housing type, board attachment method piece part mounting method, etc.) as they relate to the box level thermal design. It illustrates the synergistic nature of the thermal design parameters on the vacuum flight conditions. This would also be true for a T/A test environment but the additional convection effects must be considered. Therefore, a piece part thermal analysis which includes all parts is required to make a quantitative risk assessment by analyzing both conditions.

OBJECTIVES of ASSEMBLY LEVEL THERMAL TESTING

The objectives of an assembly level qualification "thermal environmental test" should be:

(1) Design Verification.

Both electrical and mechanical design verification over the expected flight temperature range with margin should be demonstrated. The objective of design verification goal is to verify that the design is not marginal. This is achieved typically by requiring in specification operation in the qualification environment. Moreover, the hardware must still perform in specification after exposure to the non-operating qualification temperature range.

Mil Handbook 1540 qualification test requirements are intended to "verify" the design and workmanship. Moreover, it is intended to be an indication of mission reliability from launch thru "on orbit" spacecraft system checkout. For earth orbiters this process usually requires less than 45 days.

(2) A workmanship screen.

Space flight electronic assemblies (black boxes) are becoming more and more complex. For example, complex circa 1970 boxes typically contained on the order of 500 semiconductors. A vintage 1980 box (a Command Data assembly) contained approximately 10,000 semiconductors, 150,000 to 200,000 hand made solder joints and upwards of one hundred million junctions. This trend to more and more complex designs can be expected to continue. As a result workmanship flaws will be impossible to avoid. Mil Handbook 1540 acceptance test requirements are primarily intended to be a workmanship screen.

(3) Reliability demonstration.

In an era where customers from congress on down are demanding more cost effective programs, it becomes increasingly important to incorporate a reliability demonstration goal into the environmental test program. In the commercial instrument world where companies are very concerned about warranty costs, prototype testing would be performed to reveal the weakest link. This weak link would be eliminated and testing would continue until the next weakest link was revealed, and so on until the desired level of reliability was demonstrated. The Mil 781 AGREE testing, used in the aircraft industry predominantly as low cycle fatigue life test, is performed on not-to-be-flown hardware. For one-of-a-kind or first-of-a-design protoflight spacecraft, the test to failure approach of the MIL 781 AGREE fatigue testing violates the protoflight concept. Thus a different approach is necessary for this class of spacecraft.

FAILURE PHYSICS

Reference 1 presents a detailed derivation of the tools required to evaluate the temperature effects of performing T/A testing in lieu of T/V testing. In particular, it presents current reliability theory and derives reliability demonstration models for failure mechanisms found in today's space flight electronic assemblies. A synopsis of these topics will be presented herein to maintain continuity.

Current Reliability Theory

Old reliability theory⁴ (the Bathtub Curve, derived from vacuum tube theory) held that once thru infant mortality, additional testing would not reduce the hazard rate for flight. Current reliability theory (the Roller-Coaster Curve^{5,6}) indicates that the longer an environmental test program is, the lower the in flight hazard rate will be, up to wearout. In Figure 1, both theories are illustrated. Individual bumps in the Roller-Coaster Curve can be thought of as being caused by failure mechanisms of a given activation energy. Their order of occurrence is from highest activation energy mechanisms first to lowest last. This weak link elimination continues until wearout.

Semiconductor Failure Mechanisms

Semiconductors are produced by a series of complex chemical, diffusion and metallurgical processes. The failure mechanisms of these processes are related to imperfections in the manufacturing processes and are most often accelerated by increasing the temperature and/or electrical stress levels (voltage and/or current). The equation which best describes the failure mechanisms for piece parts is a chemical reaction rate equation where, temperature and activation energy are the key parameters. This equation is called the Arrhenius Rate Equation. Figure 2, illustrates the relationship

between reaction rates, temperature level and activation energy. For common piece part failure mechanisms, activation energies range from⁷ 0.3 eV to 1.5 eV with 1.0 eV the most frequent⁸. For an activation energy of 0.6 eV, a 10°C increase in temperature (25°C to 35°C) increases the failure rate by a factor of 2.1. For an activation energy of 1.4 eV the reaction rate increases by a factor of 5.7.

Table 2, presents reductions in relative reaction rates associated with various d T effects and activation energy levels. The assumed shearplate (thermal control surface) hot test temperature level is 65°C. The numbers are an indication of the reduction in demonstrated reliability that would result from performing a T/A test in lieu of a T/V test, given the d T effects values shown.

Semiconductors can also have non Arrhenius reaction rate failures. These are most often packaging related and due to low cycle fatigue. However, for most mature device technologies Arrhenius reaction rate type of failures tend to dominate.

Piece Part burn-in tests are designed to screen for Arrhenius types of failure mechanisms. Reference H data for DoD satellite programs found that 30 to 40 percent of the problem/failures reported during assembly level thermal testing (of all types) were due to piece part failures. From this data it is obvious, that burn-in testing does not eliminate all "weak" piece parts. The manufacturing process builds-in workmanship problems AND Arrhenius failures¹.

Thermal Fatigue Failure Mechanisms

Thermal fatigue (as a result of thermal cycling) is another failure mechanism which occurs in electronic assemblies. This mechanism is also used to precipitate out many workmanship flaws

(solder joints, PCB shorts/opens, fastener torquing, etc.). Thermal cycling is an accrued damage failure mechanism because failure only surfaces/occurs after exposure to a number of strain cycles. In Figure 3 the log-log relationship between strain and cycles is illustrated. Current solder joint theory indicates that the stiffness of the solder joint/lead system, hot/cold extreme temperatures and the rate of temperature transition affect the rate of strain in solder joints. Moreover, these factors act synergistically^{9,10}. For compliant PCB/solder-joint/lead systems, temperatures below room temperature may not strain the joints, assuming that the cold test temperatures are above the glass transition temperature for all materials involved. For stiffer joints, 0°C is currently thought to be the lower limit of the strain range¹⁰.

Workmanship screens operate on the assumption that a screening strength of S is required to precipitate the required number of latent failures. A specific screening strength is expressed as N cycles of magnitude y , in a given environment (T/V or T/A). For a given temperature range the screening strength varies linearly with N ; for example, 8 T/V cycles over the range of -24°C to +45°C (shearplate). Performing a T/A test in lieu of a T/V test reduces the upper temperature level obtained. Therefore, to achieve the same test effectiveness would require performing X times N cycles. Table 3, presents these "X" factors for various dT effects and upper test temperature levels assuming compliant "joints". Note that for a 45°C shearplate upper test temperature level and a 10°C dT effect, more than twice as many cycles would be required to achieve the same test effectiveness. A 20°C dT effect would require more than four times as many cycles. Thus, a reduction in the hot solder joint temperature can significantly reduce the test effectiveness.

PROPER TEST SETUP

Choosing the proper test setup is fundamental to performing a thermal test which truly delivers the desired level of demonstrated reliability and/or screening strength. Most often, the assembly level environmental tests are performed by a different group than the one that designed it. Moreover, the thermal implications of the design are not transmitted in a sufficient manner. As a result, comprises often go unrecognized until spacecraft level T/V testing. A brief discussion of the typical T/A environment and the proper T/V test setup for a space flight design which is to be conductively coupled to the S/C thermal control surface, is presented.

T/A Environment

To maintain a stable environment within an environmental chamber, small temperature differences air-to-box-skin are required. Thus, chamber manufacturers employ large mass flow rates. This in turn translates into high air velocities inside the chambers. Unit's under test are usually placed on a stand inside the chamber. As a result, the "skin" temperature is nearly uniform and about the same temperature as the inlet air. Inside the unit significantly large free convection and gaseous conduction paths exist. Because these paths are added in parallel to the "natural" (conduction and radiation) T/V test environment paths, they short out any "naturally" high thermal resistance paths. High power parts are by necessity almost always well conductively coupled to the housing and therefore they are seldom affected significantly by substituting a T/A environment. However, piece parts that have high thermal resistance case-to-board and board-to-shearplate can be significantly effected. Therefore, the piece part thermal analysis must be performed on all piece parts in both environments.

T/V Environment

For a unit which was designed to be conductively coupled to the external environment, the unit should be coupled to an isothermal heat sink in the same manner as in flight i.e. same size and number of fasteners, and torqued the same as in flight. If the box level thermal analysis indicated significant gradients in the S/C mounting surface then an isothermal heat sink would not be an adequate representation of the mounting configuration. If the test was performed anyway the result would be lower temperatures and smaller gradients than in reality. Recent test experiences has shown that the effect of not properly simulating the mounting configuration can result in substantially reductions in key temperatures. Where the flight surface can not be presented as isothermal, a prototype of the flight interface (for example a honeycomb panel) should be used such that the baseplate of the unit would have gradients and temperature rises similar to flight conditions. In either case the unit should be blanketed to force all the heat to be conducted to the baseplate of the unit and then conducted across the interface and ultimately into the isothermal heat sink.

Furthermore, the other external surfaces should be blanketing so that all heat is transferred by conduction to the thermal control surface. Not blanketing can significantly compromise the test just as substituting at TA environment for a T/V environment can. For designs which are to be tested in a vacuum environment without a blanket, the external radiant environments must be specified and specifically designed for. The extra costs of specifying and designing for a radiant environment are considerable.

Other Findings

Flight telemetry sensors are almost always located near these well conductively coupled parts which are the least likely parts to be effected. Thus

using the flight sensors "inside" the unit to evaluate the effect of performing a test in one environment/mounting configuration vs. another is a poor measure of the effect in general.

An environmental test program can be tailored to compensate for the hot level compromise created by performing T/A testing in lieu of T/V testing. This can be done by increasing the number of cycles performed, raising the hot test level or some combination of these. However, this would require extensive thermal mapping testing in a vacuum environment on the first unit or extensive thermal analyses to quantify the temperature effects. Moreover, compromises in temperature gradients can not be compensated for by any practical means.

One clients current rational is to always perform T/V testing. However, if it can be that a unit is not sensitive to pure vacuum effects and the ΔT effect for all piece parts is less than 5°C a T/A test may be allowed.

CONCLUSIONS

A T/V test is clearly a more effective test since it is a flight like environment. The material presented in this paper allows the increase in risk associated with performing a T/A test in lieu of a T/V test to be quantified. The temperature level effects of performing T/A testing in lieu of T/V testing reduces the hot temperature margin, screening strength and test demonstrated reliability. Hot temperature margins can be compromised to the point where there is zero or negative margin between environmental test levels and the flight allowable level (e.g. a test with a planned 10°C margin and a T/A effect 15°C to 20°C would result in negative test margin). Screening strengths can be reduced by a factors of 2 to 4 or more. Test demonstrated reliability can be reduced by factors of 2 to 15 or more.

Decision criteria based on power density or hardware type is suspect. Piece part thermal analyses for both T/A and T/V environments is required. These analyses must include all parts/joints, etc. before a quantitative risk assessment can be made.

Using the Roller-Coaster reliability concept of Figure 1, T/V testing should eliminate more weak links than T/A testing. Therefore, hardware which was T/V tested should have a lower hazard rate in flight than T/A tested hardware.

REFERENCES:

- (1) Mark Gibbel & J. F. Clawson, "Electronic Assembly Thermal Testing- Dwell/Duration/Cycling", Proceedings of the 12th Aerospace Testing Seminar March 1990.
- (2) Mark Gibbel, et all, "Survey of Assembly Level Thermal Test Methods: thermal Cycling vs. Thermal Dwell Testing in Industry", 1990, publication pending.
- (3) Mark Gibbel, "PACKAGING: Evaluating the Choices from the Thermal Prospective", Proceedings of IEEE Computer & Reliability Societies Mini Course on Improving the Process in Hardware/Software Systems, El Segundo California, May 1990.
- (4) K. L. Wong, "Unified Field (failure) Theory - Demise of the Bathtub Curve," Proceedings of the Annual Reliability and Maintainability Symposium, 1981.
- (5) K. L. Wong & D. L. Lindstrom, "Off the Bathtub Onto the Rollercoaster Curve," Proceedings of the Annual Reliability and Maintainability Symposium, 1988.
- (6) K. L. Wong, "The Bathtub Curve Does Not Hold Water Anymore," Quality and Reliability Engineering

International, Volume 4, Pages 279-282 (1988).

- (7) E.A. Amerasekera & D. S. Campbell, "Failure Mechanics in Semiconductor Devices", 1985.
- (8) A. Moeller, "Microelectronics and Reliability on the Term 'Activation Energy' in Accelerated Lifetime Tests of Plastic Encapsulated Semiconductor Components", Pages 651 to 664.
- (9) Donald Stone, Simo-Pekka, Che-Yu Li, "The Effects of Service and Material Variables on the Fatigue Behavior of Solder Joints During the Thermal Cycling", 1985.
- (10) W. Engelmaier, "Surface Mount Attachment Reliability: Issues, Design, Testing, Prediction", JPL December 1989.

For comments or questions please contact Mark Gibbel at:

The Gibbel Corporation
1536 Palos Verdes Drive west
Palos Verdes Estates, California 90274

Telephone No. (213) 378-7268
Pager No. (800) 759-7243
(PIN 8673726 # then your No.)

Fax. No. (818) 249-5714

Fn:C:\word\papers\tvta.042

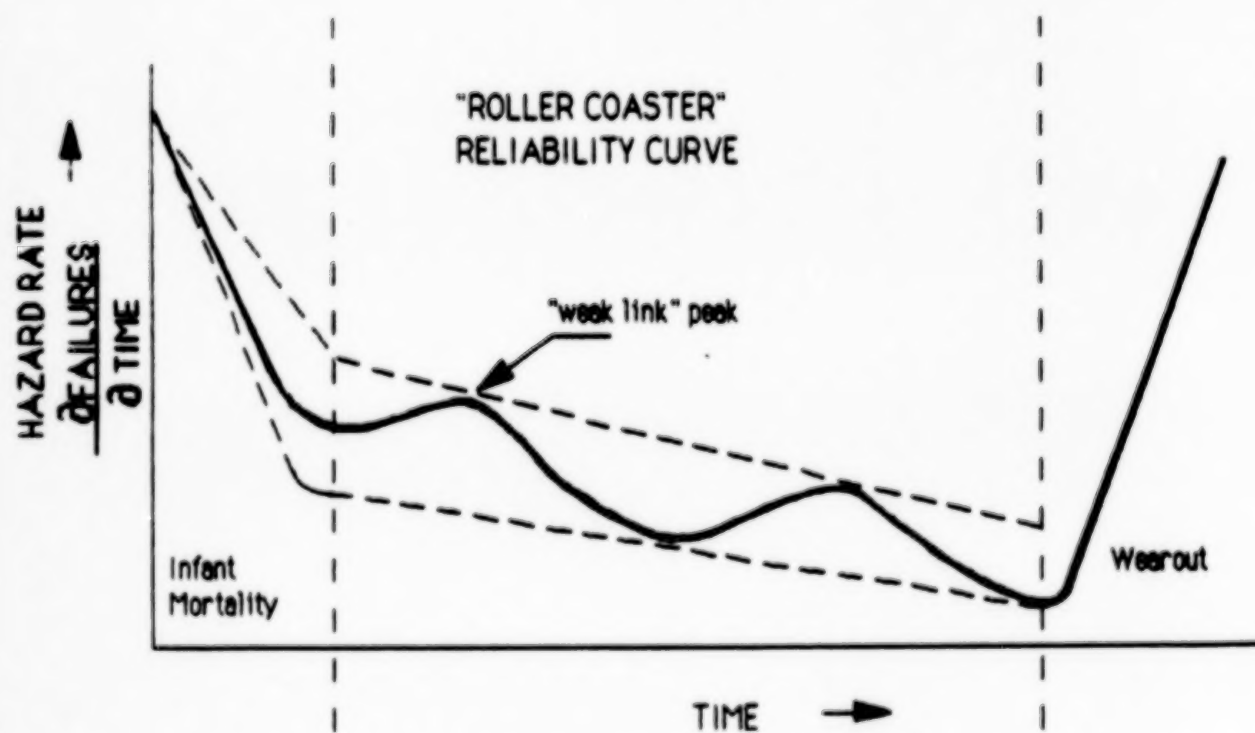
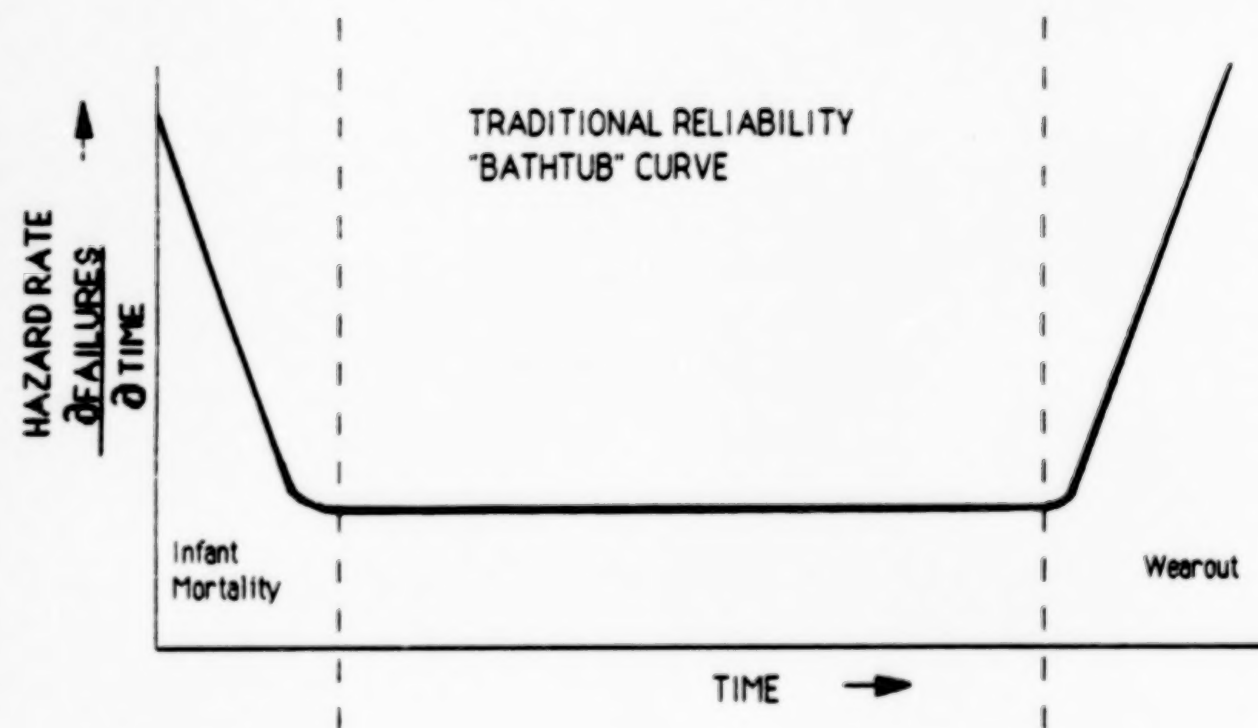


Figure 1. "Roller Coaster" vs. "Bathtub" reliability curves.

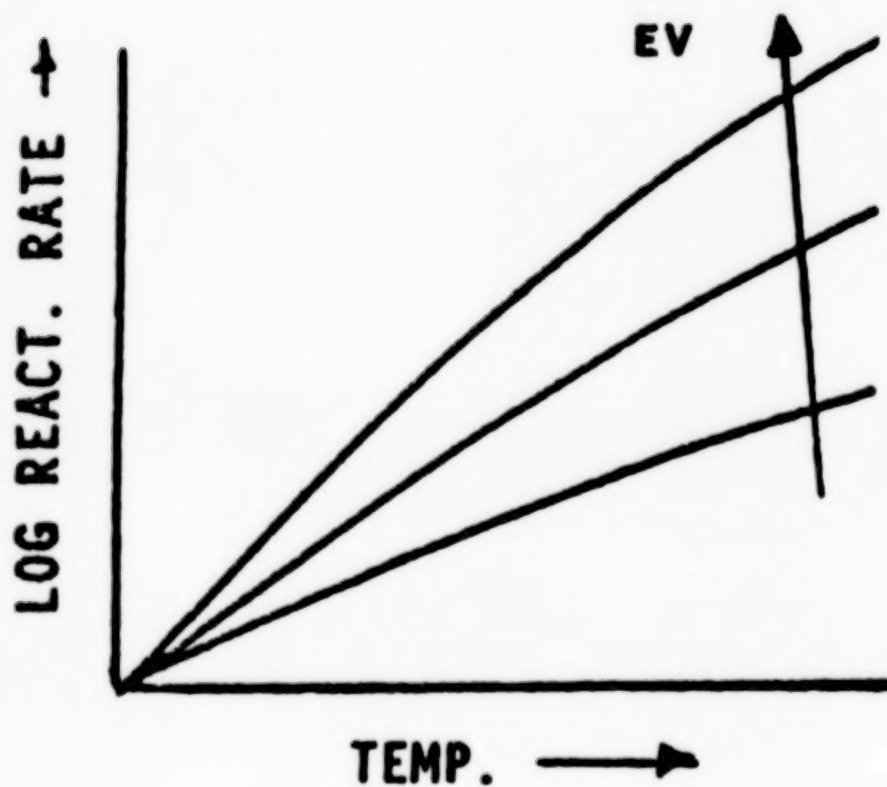


Figure 2. Arrhenious reaction rates vs. temperature and activation energy.

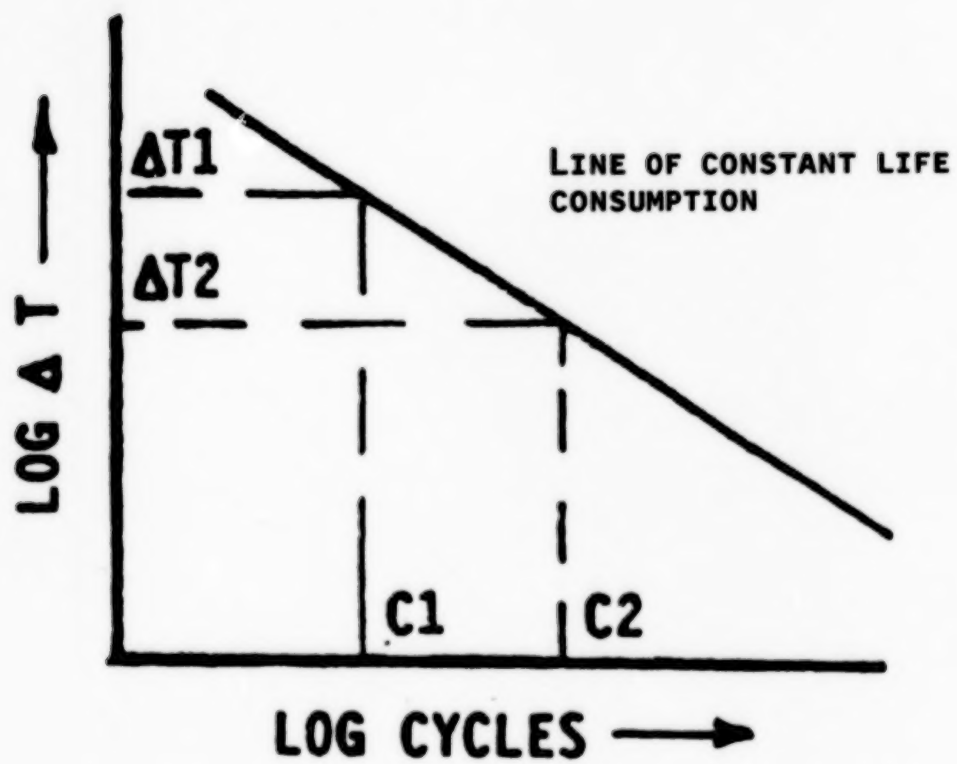


Figure 3. Strain vs. cycles of life for solder joints (strain caused by thermal cycling).

TABLE 1. SUMMARY OF ANALYSES & TEST RESULTS FOR THE d T effect
ASSOCIATED WITH PERFORMING T/A TESTING IN LIEU OF T/V TESTING

ASSEMBLY	TYPE	POWER DENSITY W/CM*CM	d T effect		Deg C
			Analysis	Test	
Radar Transmitter	R. F.	0.04	16		(1)
Radar Transmitter	Power Supply	0.04	9		
Radio Reciever	R. F.	0.10	< 9		
Power Distribution	Analog	0.01	< 5		
Data Formater	Digital/analog	0.15	10		10 (2)
Range Dispersion	Digital/analog	0.19	10		
Command Data Bay 3	Digital/analog	0.02	21		
Command Data Bay 4	Ditigal	0.01	16		18
Science Instrument	Digital/analog	0.03	22		20
Output Network	R. F.	0.01	3		

Notes:

- (1) Unit not blanketed during initial T/V test. Estimates for the effect of this indicated that the load on the heat exchanger was approximatly twice that dissipated by the unit.
- (2) Test performed for the d T effect part case-to-housing. Full d T effect shown is a combination of test and analysis.

TABLE 2. ARRHENIOUS REACTION RATE REDUCTION
FACTORS FOR VARIOUS ΔT effects &
ACTIVATION ENERGIES

ΔT effect	Activation Energy (eV) (*)		
Deg. (C)	.6	1.0	1.4
20	3.1	6.5	14.7
10	1.8	2.6	4.0
5	1.3	1.6	2.0

* Assuming a 65 C shearplate.

TABLE 3. SCREENING STRENGTH REDUCTION FACTORS
("X" FACTORS) FOR VARIOUS d T effects
& SHEARPLATE TEMPERATURES

SHEARPLATE TEMPERATURE Deg c	d T effect Degrees C (*)		
	5	10	20
45	1.5	2.2	4.1
55	1.4	1.8	3.0
65	1.3	1.6	2.5
75	1.2	1.5	2.2

* For compliant solder joints and cold test temperatures above the glass transition temperature for all materials involved.

PROPOSAL FOR A CONCEPTUALLY NEW COMPACT COLLECTING OPTICS FOR POWERFUL LIGHT SOURCES

G. Saenger

European Space Research and Technology Centre (ESTEC)

SUMMARY

Testing of a S/C under simulated outer space conditions is the best guarantee for a successful mission, and for almost all of the parameters a good match (to within a few %) may be reached in relevant test facilities (e.g. I.R. background, earthshine and albedo radiation, residual atmosphere, intensity stability, - distribution and spectrum of the solar radiation).

The collimation angle of the sun (32 arc min.) is, however, a drastic exception, here only ± 1.5 to $\pm 2^\circ$ are achieved which means a relative deviation by nearly one order of magnitude.

The main reason for this is the presently used collecting optics having unnecessary large diameters. Here a lens - mirror combination is proposed which allows to reduce the diameter by nearly a factor of two and to achieve with the present Xenon arc lamps a collimation angle of $\pm 0.8^\circ$.

SCOPE

The best guarantee for a successful mission of a S/C project is a careful testing on the ground, and since the S/C's became even more sophisticated requiring more stringent specifications, one must assume that this remains also valid for the future.

The most important tests are the thermal balance tests; however, because of the costly simulation of the solar radiation they are also the most expensive ones.

Present solar simulators show an intensity stability better than 1% and a uniformity of the intensity distribution in the test volume within ± 3 to $\pm 5\%$; hence they match in this aspect to a high degree the real solar radiation. The spectral intensity distribution is simulated actually by the Xenon spectrum, sometimes the high Xenon peaks in the range from 0.8 to 1.0 μ are filtered to achieve a better match with the solar spectrum. Certainly there are numerous peaks left which do not agree with the solar spectrum but because most materials do not show a great selectivity within these spectral ranges, also this less good simulation of the solar spectrum satisfies most customers so far (Fig. 1).

As for the collimation angle, there was for thermal balance testing neither a serious demand nor is there a technical possibility to match the sun's collimation angle (32 arc min.) to a similar degree as the previous parameters. The solar simulators today have collimation angles of ± 1.5 to $\pm 2^\circ$ in the test volume, hence there is a deviation with the real one by a factor of 6 to 8.

For the near future, however, one has to expect a demand for a better simulation of the collimation angle, since on the light weight structures already short shadowing and half shadowing effects will influence considerably temperature, temperature gradient and temperature profile as function of time and hence cause thermal stress and/or degradation on these structures, which are a vital and substantial part of the future S/C generation.

BOUNDARY CONDITIONS

The Light Source

Of course, when using a powerful light source of high plasma temperature, there is no problem anticipated to achieve also a small collimation angle. Considerable effort was spent in the past to develop powerful lamps, and the outcome is the high power Xenon arc lamp with watercooled electrodes allowing an arc power of 25 to 35 kW dependent on the lifetime requirements. This lamp reached technical maturity, is commercially available, and for the near future no other powerful light source is expected to replace this type of lamp.

The radiation intensity distribution of a Xenon arc is typically shown in Fig. 2 and the polar radiation characteristics in Fig. 3 (here a Durotest lamp) [Ref. 1].

Because Xenon and solar spectrum show a fair agreement (Fig. 1), also the plasma temperature of the arc must be approximately the same as at the sun's surface. Therefore, a considerably better match of the collimation angle should be achievable in case the collecting optics is properly adapted; even when considering the light losses due to absorption and/or surface reflections of $\sim 12\%$ on each optical element, an improvement by nearly a factor of three is feasible in case the most intense part of the arc is used. The mean arc temperature as function of radius is shown in Fig. 4.

The Projection System

The principle of the projection system is illustrated in Fig. 5. The condensor - or collecting mirror - (C) directs the more or less spherically emitted light of the light source towards the projection lens (F) and the projection lens focusses the condensor plane into the reference plane (P). Optimum performance is obviously achieved in case the condensor is designed such that also the light source is focussed onto the projection lens since then there is no loss of light due to spill over and the lens may have minimum diameter. Naturally one may add in the same way another optical element (e.g. field lens) with the consequence that not the condensor plane but the light source (via an image) is focussed in the reference plane, of course also with the corresponding intensity distribution (Ref. 2, 3, 4).

In order to achieve a high intensity, one should keep the radius (R) of the reference plane (P) as small as possible which requires a small exit angle (α'); this exit angle, however, cannot be made smaller than the entrance angle (α) because then part of the collector would not be covered, hence severe light losses would be the consequence.

On the other hand is the collimation angle (ξ) given by the ratio of the projection lens diameter to the distance of the reference plane (D). Thus for a small collimation at a high intensity level (\triangle small beam diameter) one should keep both exit (= entrance) angle and the image of the light source as small as possible. The first demand means a small diameter of the collecting optics, the second a small but intense light source (and, as mentioned before, the best one can use is the high power Xenon arc lamp).

When using such a Xenon lamp one could capture and lead the emitted light to the field lens plane e.g. by means of optical fibres, clustered around the Xenon bulb; the spheric light emitting surface ($4\pi \cdot R^2$ bulb) is then converted into a circular plane ($\pi \cdot R^2$ plane) with the same exit angle of the light, in other words the smallest achievable diameter of the collecting optics is twice the diameter of the light source:

$$R_{\text{plane}} = 2 \cdot R_{\text{bulb}}$$

The Xenon lamps have a bulb diameter of $13 \div 14$ cm, therefore it seems likely to reduce the diameter of the collecting optics from presently 56 - 60 cm to 30 cm, which means an improvement by nearly a factor of two.

Since in addition the polar radiation as well as the intensity across the arc is highly non-uniform, a further improvement is feasible when only the most intensive parts are used; of course this will be on account of the overall efficiency.

Review of Presently Used Optics

The parabolic reflector

The well-known and by far mostly used parabolic (or shaped close to a parabola) mirror is mechanically the simplest solution; from the optical point of view it is, however, a bad one. It is actually an optical element where the focal length varies.

Close to the optical axis is the focal length short and increases steadily for larger mouth angles (see Fig. 6). Consequently the rays of small entrance angle (close to the optical axis) produce a large image in the field lens plane and vice versa produce the light rays of large entrance angle (\triangle at large mouth angles) small images; thus, in order to capture a high percentage of the emitted light with a parabolic mirror, both a large entrance angle and a large image of the light source in the field lens plane results. In addition the percentage of captured light for large radii is relatively low (\triangle per cm radius), see figs. 6, 7.

Of course, one could use a small spherical secondary mirror so that the light leaving the upper part of the bulb (to the anode) will be reflected back through the arc, hence a considerably smaller mouth angle (\triangle smaller collector diameter) would result. The efficiency of such a mirror is, however, rather low; according to Kirchhoff's law a good emitter is also a good absorber. We measured at ESTEC on our HBF3 space chamber when operating the solar simulator with a secondary mirror, a contribution of only $15 \div 20\%$.

The Koehler Collector

The less applied Koehler integrator (Ref. 5) is mechanically more complicated, from the optical point of view, however, a better solution; actually two lens + deflecting mirror arrays (2×7) are clustered around the light source (Fig. 8). Since the distance to the light source centre is for all lenses the same, all the individual arc images are of the same dimensions. When looking from the field lens plane into the collector along the optical axis, one will see a shining area composed by 2×7 circular areas arranged in a circle around the Xenon lamp (Fig. 9).

It is a pity that from the total cross-sectional area only the outer part is used, making the entrance angle unnecessary large. Of course one could place the upper deflecting mirrors closer to the centre, but there is no way to reduce the overall diameter since the lower deflecting mirrors will have to be kept in their position. (When using instead of a 2×7 lens array one of 2×6 it seems feasible to achieve a hexagon arrangement which would have a higher package density for clustering of lamp units.

Naturally various constructions are possible to fill up the gap in the cross-sectional area using additional deflecting mirrors; however, all these solutions will be highly complex and costly and do not allow standardisation of a lamp module.

COMPACT COLLECTING OPTICS

General Considerations

As outlined in the foregoing paragraph the requirements for achieving a small collimation angle boil down to:

1. To capture the light leaving the light source as soon as possible, that means to align it parallel and avoid further expansion of the light beams.
2. To use optical elements of identical focal length.
3. To convert the spherical light emitting area into a circular or hexagonal plane of preferably the same area.

The Koehler integrator meets only the first two requirements; on account of the third one instead it was designed relatively simple; the lenses are identical, they have both the same focal length and the same diameter, hence also the lens plane may be superimposed and projected into the reference plane because the optical orientation is ruled out, and since the intensity distribution across the lens plane is considerably more uniform than across the arc image one may achieve a fair intensity distribution without integrator or mixer.

The fact that the arc images are of the same dimensions (requirement 2) allows to make effective use of the most intense part of the arc (above the cathode tip, Fig. 2). In Fig. 10 the emitted light is shown as function of the arc diameter used, and obviously it is unfortunate to go for more than ~ 6 mm arc diameter, since here already $\sim 66\%$ of the emitted light is captured and for larger radii the gain of light is substantially reduced.

Three Lens Array

In order to reduce the overall diameter of the collecting optics one has to disregard the advantages of the simplicity of the Koehler integrator, since only with a third lens array one may make use of the inner parts of the circular plane. The beams of the equatorial lens array (Fig. 11) may be deflected by the inner circle of deflecting mirrors, whilst the beams of the upper (anode) and lower (cathode) lens array will be deflected by mirrors positioned at the same radius, one in the gap of the other, naturally at different height. The diameter of such a collector unit would be ≈ 33 cm and hence only 60% of the parabolic reflector. The amount of captured light is 80%, which is approximately the same as for the parabolic reflector (Ref. 4). The light losses, however, are higher due to spill over and surface reflections on the lenses. A detailed breakdown of the light losses is given in Table 1, see also Fig. 11 a, b and Fig. 9.

The gaps between the deflecting mirrors of the inner circle may be used for the supporting structure for lenses and mirrors, thus they are not only a disadvantage. Compared with the Koehler integrator this design has considerably more elements and is more complicated. However, the lenses have a smaller opening requiring less refractivity and may therefore be provided with normal spherical surfaces which is substantially cheaper than for parabolic ones.

Considering the arc utilisation, the light losses, the diameter of the collecting optics and the optimum arc image, it should be possible to achieve at 1 S.C. level with a 25 kW lamp a collimation angle of $\pm 1^\circ$.

Four Lens Array

The three lens array leaves mainly two fields open for improvement:

1. the inner part of the light emitting area is not used (smaller than bulb diameter)
2. the spill over losses are relatively high.

Naturally, when more optical elements are used to convert the spherically light emitting surface into a circular plane, also a higher package density is possible. However, when using more optical elements, also the spill over losses will increase, besides the fact that the arrangement will also become more complicated and more costly. A four lens array seems to be sufficient to achieve the desired improvements mentioned without complicating the whole arrangement too much. The main difference compared with the three lens array is that on the top (to the anode) two deflecting mirrors are required (Fig. 12 a, b and Fig. 9).

The breakdown of the light losses and the resulting overall efficiency is given in table 2. For 1 S.C. level this should allow a collimation angle of $\pm 0.8^\circ$, (only the lower intense part of the arc is used) with sufficient margin (Fig. 13).

CONCLUDING REMARKS

In general one may say that the high power Xenon arc lamps allow to achieve a smaller collimation angle in case a properly adapted collecting optics is used. The widely used parabolic reflector is for this purpose not applicable.

Certainly the proposed collecting optics is very expensive due to the high number of optical elements and beyond that it will be a total loss in case of a lamp failure (explosion). On the other hand one should keep in mind that most lamp explosions occur after shutdown (during cooldown of the quartz bulb) and may therefore be avoided in case the Xenon gas is frozen out after operation in a small stainless steel bottle which is cooled down to LN2 temperature and then valved off; thus in case of a thermal crack there is no longer a gas pressure in the quartz bulb (Ref. 1).

Another critical issue is the cooling of the quartz bulb, and the question may come up to mind whether the closely clustered lens arrays are not a serious impedance for the cooling. Considering, however, the fact that most critical for cooling is the upper part of the bulb (above the equator) where turbulent flow dominates, the contrary is to be expected: the lens arrays force the cooling gas to keep in close touch with the quartz bulb and to guarantee a steady and uniform cooling flow also above the equator.

Obviously there is a real possibility to reduce the risk of lamp failure (explosion) drastically and to avoid major damage during operation. Irrespective, such a collecting optics will be a costly investment and will contribute to the besides expensive space simulation facilities. Compared, however, with a single major S/C project the costs are often within the contingency; reliability and accuracy would be considerably improved.

OTHER APPLICATIONS

The proposed collecting optics may of course be used for any other light source. Compared with the parabolic reflector it is much more complicated; however, the high number of optical elements allow besides the compactness:

1. a better directivity of the beam
2. a better uniformity of the intensity in the reference plane
3. to illuminate an area of special shape by individual adjustment of the deflecting mirrors.

In the car industry there is in recent years a demand for more compact collecting optics; here the high production number would reduce the production costs per unit substantially.

REFERENCES

1. W.E. Thouret, FIES, J. Leyden, H.S. Strauss, G. Shaffer, H. Kee "20 to 30 kW Xenon Compact Arc Lamps for Searchlights and Solar Simulators", Journal of IES, Oct. 1972
2. Eddy, R.P., "Design and Construction of the 15-Foot Beam Solar Simulator SS 15 B", Technical Report 32-1274, Jet Propulsion Laboratory, Pasadena, Calif., Oct. 1, 1968.
3. Harrell, J.W. and Argoud, M.J., "The 25-Foot Space Simulator at the Jet Propulsion Laboratory, Pasadena, Calif., Oct. 15, 1969.
4. Dr. Frey, IABG, Ottobrunn, FRG, private communication
5. P. Dejong, "Les simulateurs Spatiaux", Revue Générale de l'Electricité, October 1966, t. 75, no. 10

TABLE I: III LENS ARRAY, EFFICIENCY OF COLLECTOR**(48% of emitted light, 24.9% of arc power)**

	ANGLE °	INTENSITY RANGE %	LOSSES ON LENSES		LOSSES ON MIRRORS		EFFICIENCY PER LENS ARRAY %
			REFLECTION %	OVER- SPILL %	REFLECTION %	OVER- SPILL %	
Lens array I	50- 75	8 - 30	10	3.3	15	25	12.2
Lens array II	75-105	30 - 61	10	3.3	15	5	21.8
Lens array III	105-135	61 - 88	10	3.3	15	30	14

TABLE II: IV LENS ARRAY, EFFICIENCY OF COLLECTOR**(59% of emitted light, 30.6% of arc power)**

	ANGLE °	INTENSITY RANGE %	LOSSES ON LENSES		LOSSES ON MIRRORS		EFFICIENCY PER LENS ARRAY %
			REFLECTION %	OVER- SPILL %	REFLECTION %	OVER- SPILL %	
Lens array I	45- 70	5 -22.5	10	3.8	2 x 15	20	10.15
Lens array II	70- 95	22.5-48.5	10	3.3	15	5	20.3
Lens array III	95-120	48.5-75	10	3.3	15	10	17.6
Lens array IV	120-145	75 -93.5	10	3.8	15	20	10.9

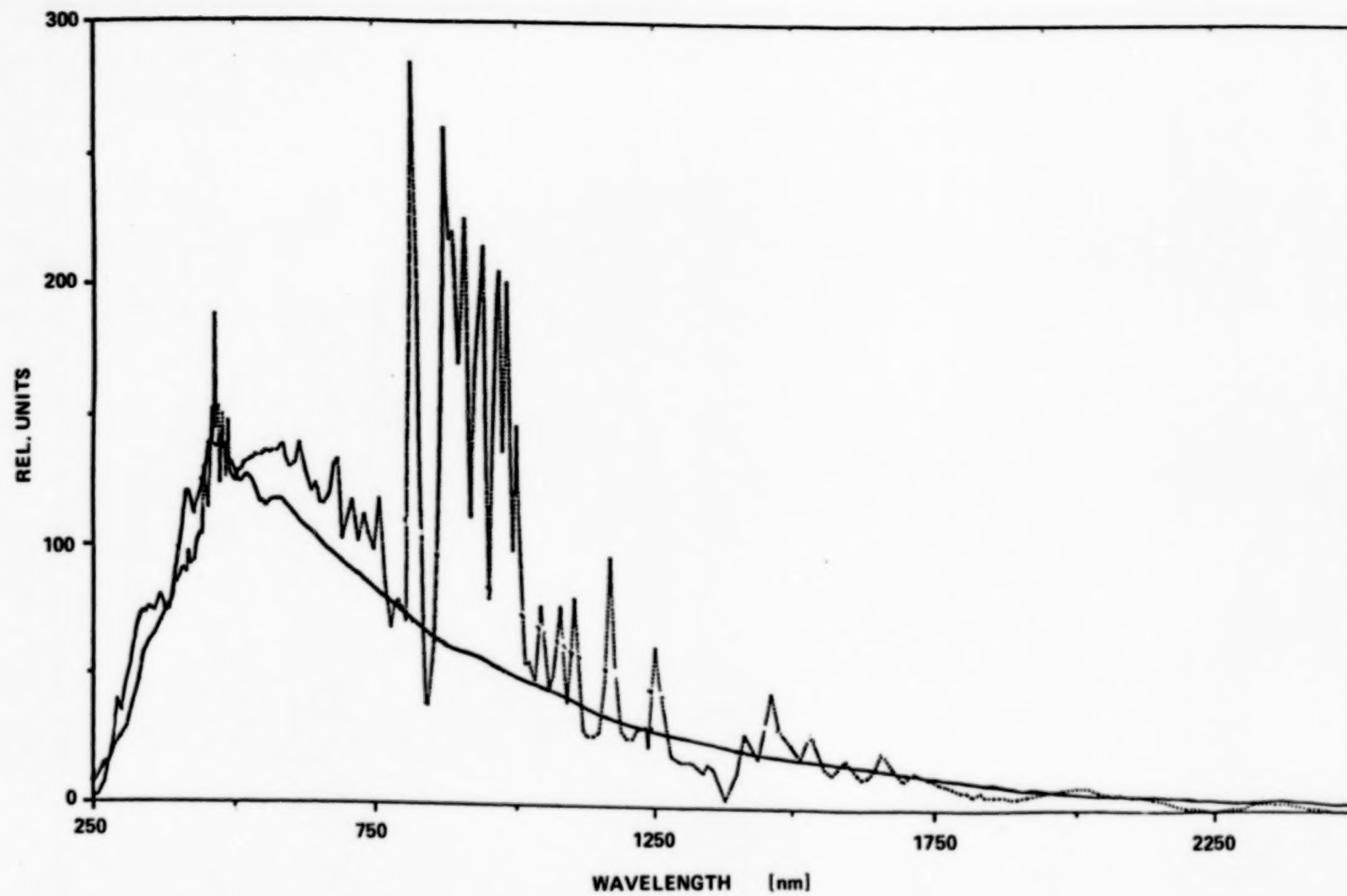


Figure 1. The Continuum of the Xenon spectrum Is in Fair Agreement with the Sun Spectrum

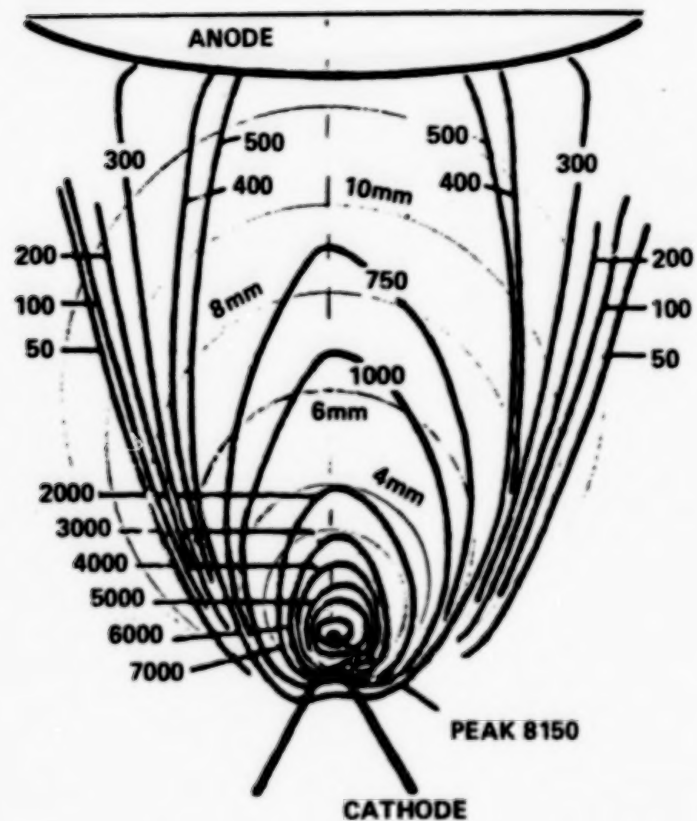


Figure 2. Luminance Distribution of a High Power Xenon Arc

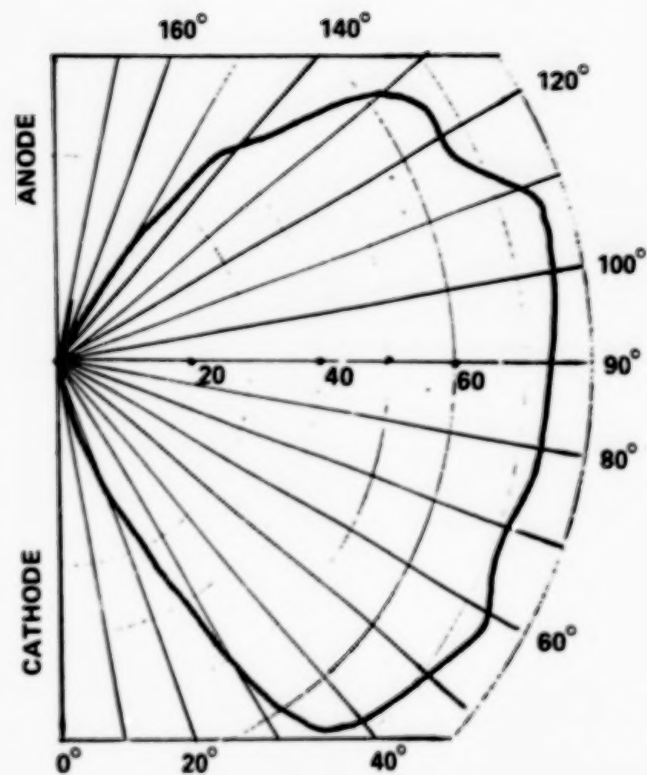


Figure 3. Polar Radiation Distribution of a High Power Xenon Arc Lamp

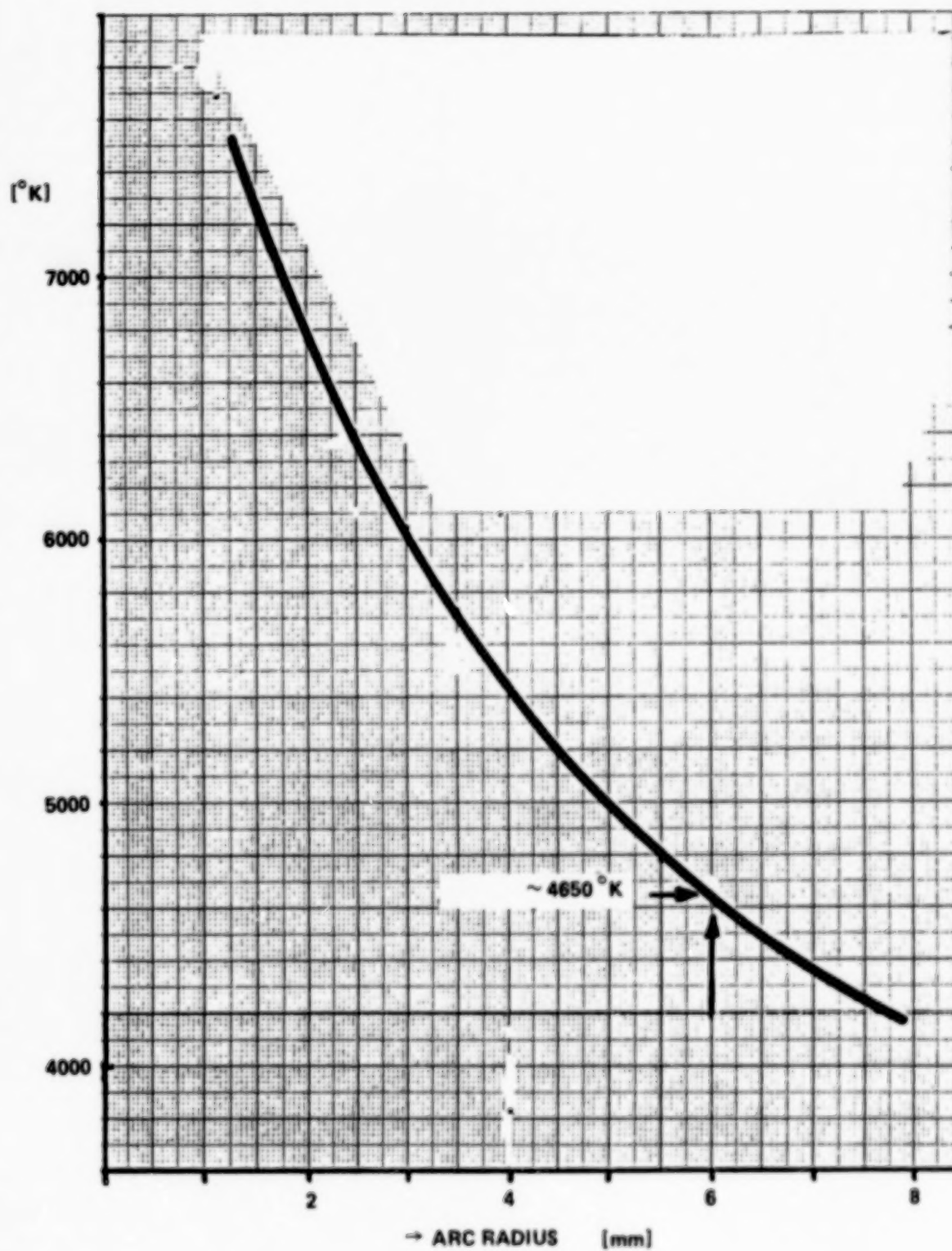


Figure 4. Mean Arc Temperature As Function Radius; 52% of the Arc Power Is Emitted as Light (~ Blackbody Radiation)

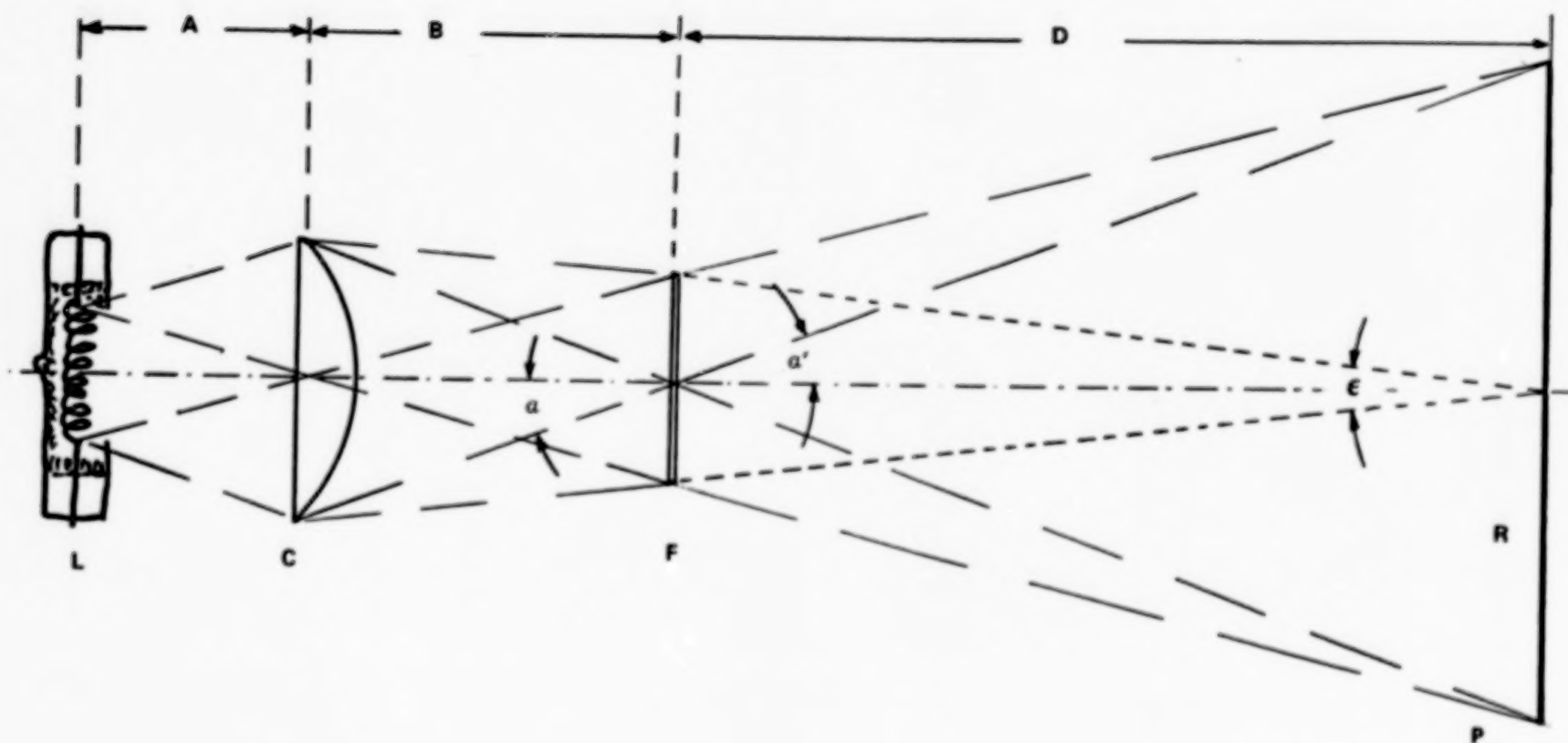


Figure 5. Projection System, Schematic
 ϵ = Collimation Angle
 α = Entrance Angle; α' = Exit Angle
 L = Light Source; C = Collector; F = Projection Lens

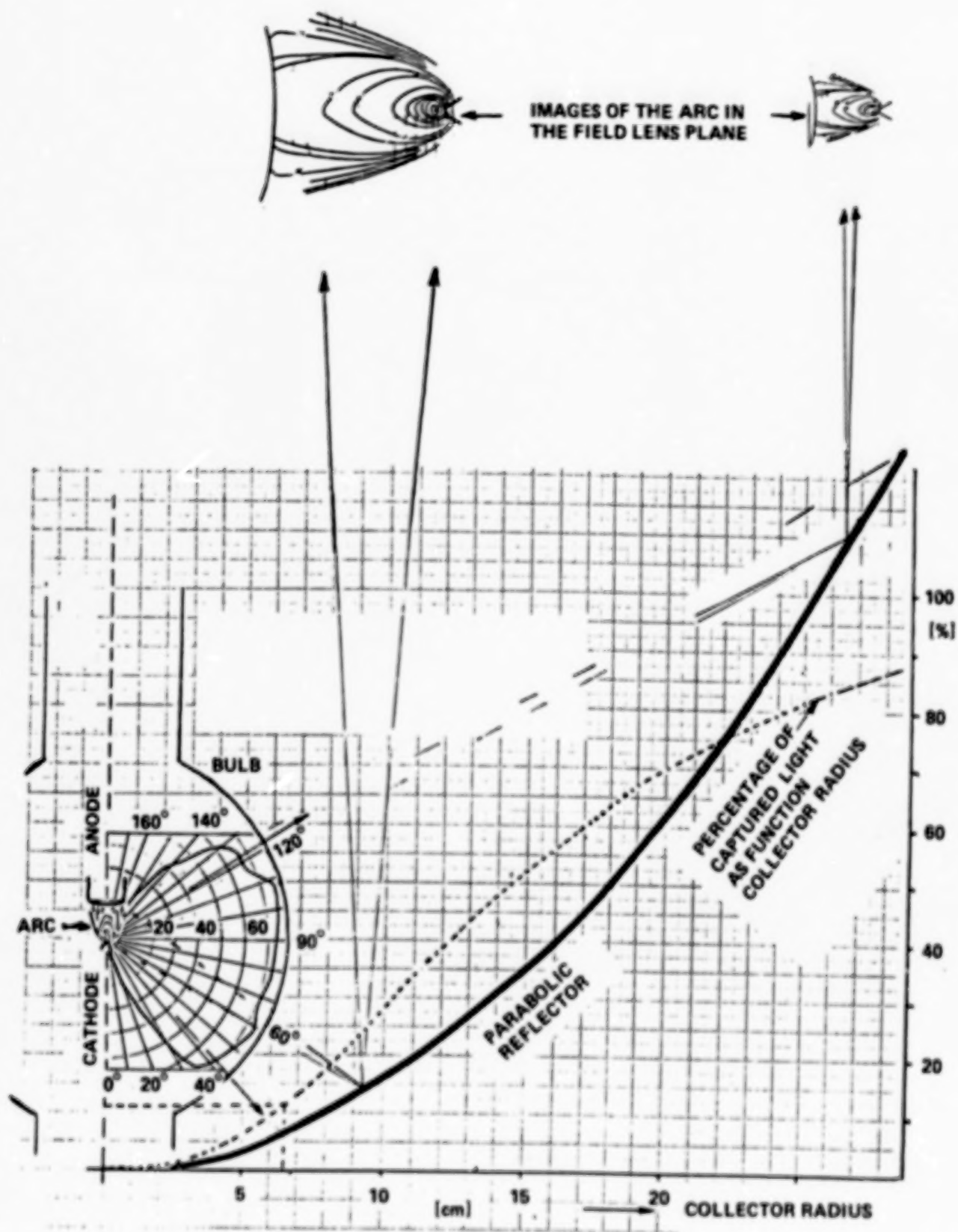


Figure 6. Parabolic Reflector, Schematic

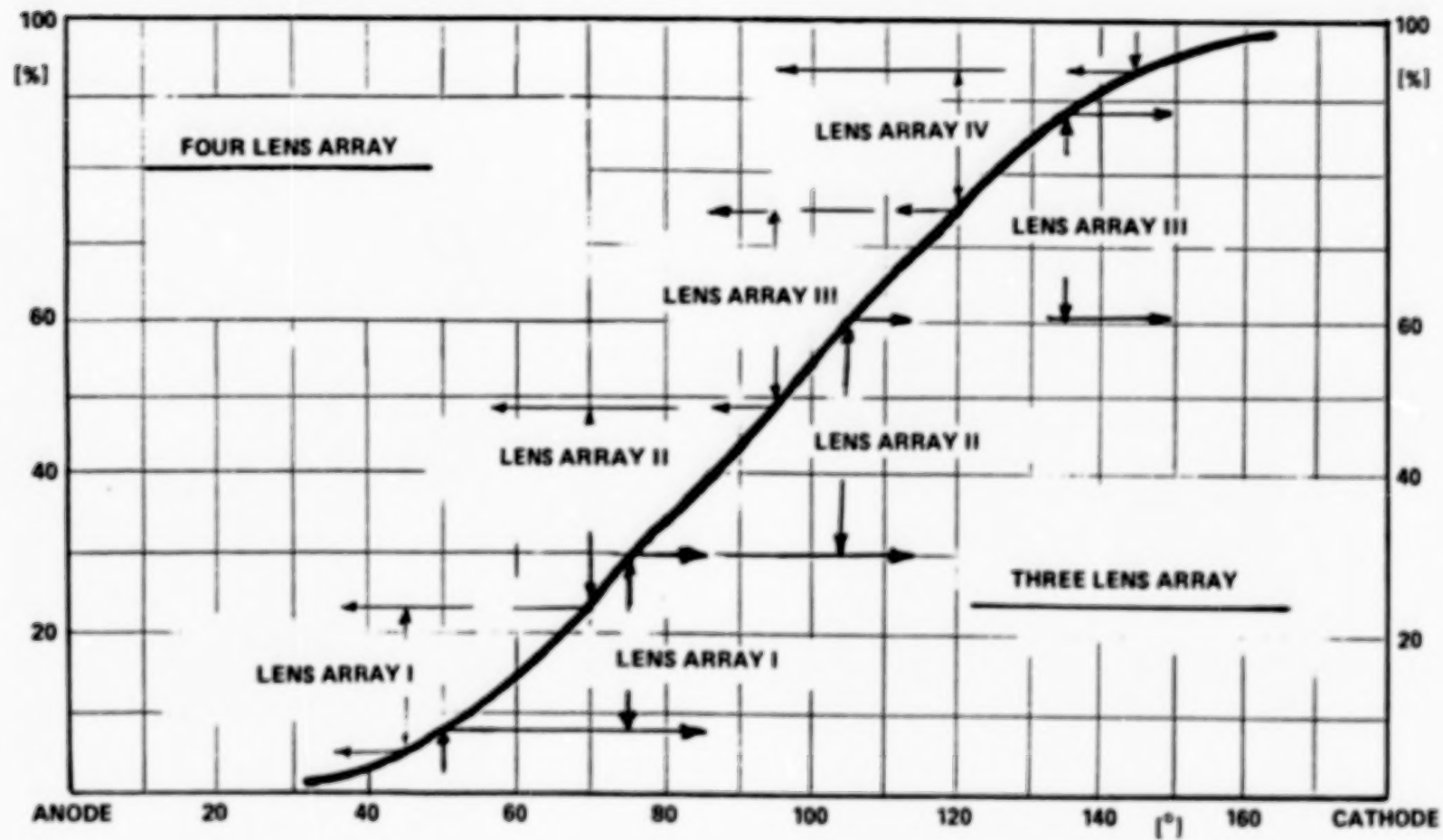


Figure 7. Percentage of Light Intensity Captured by the Collector as Function of Incident Angle

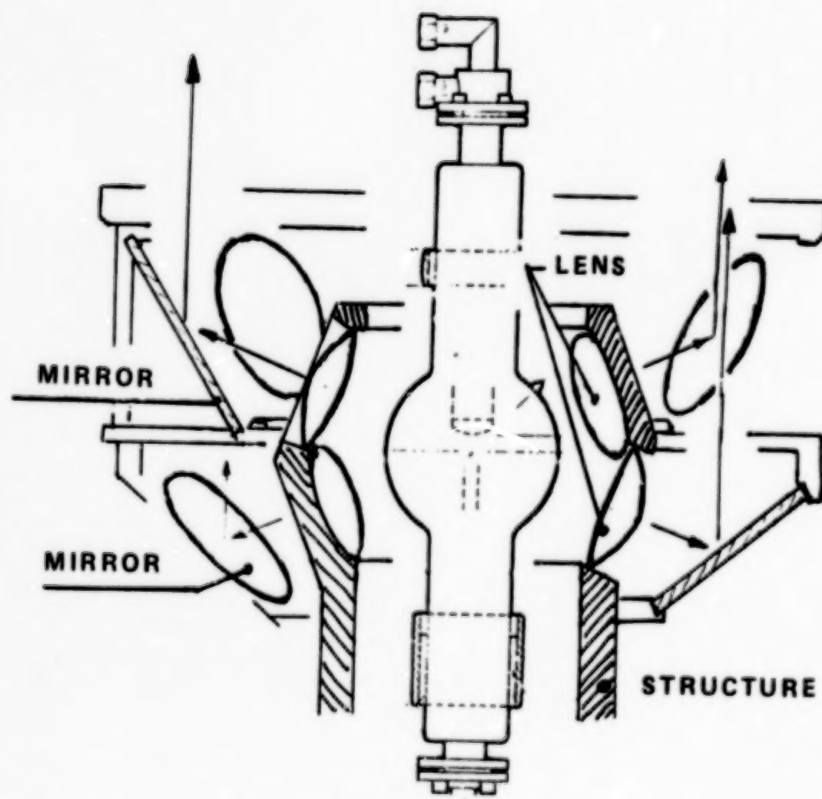


Figure 8. The Koehler Collector of BBT; 2 x 7 Lens-Mirror Combination

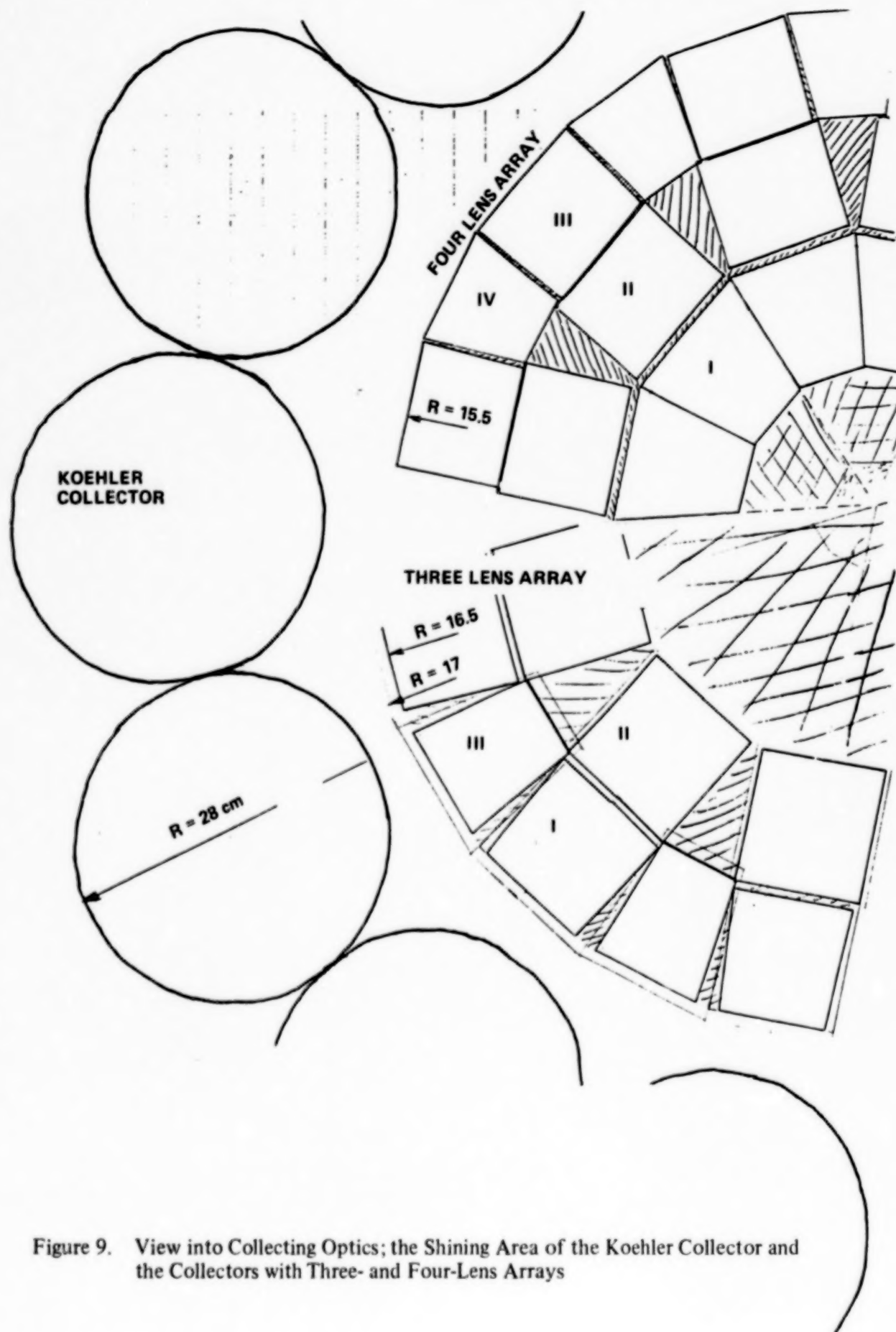


Figure 9. View into Collecting Optics; the Shining Area of the Koehler Collector and the Collectors with Three- and Four-Lens Arrays

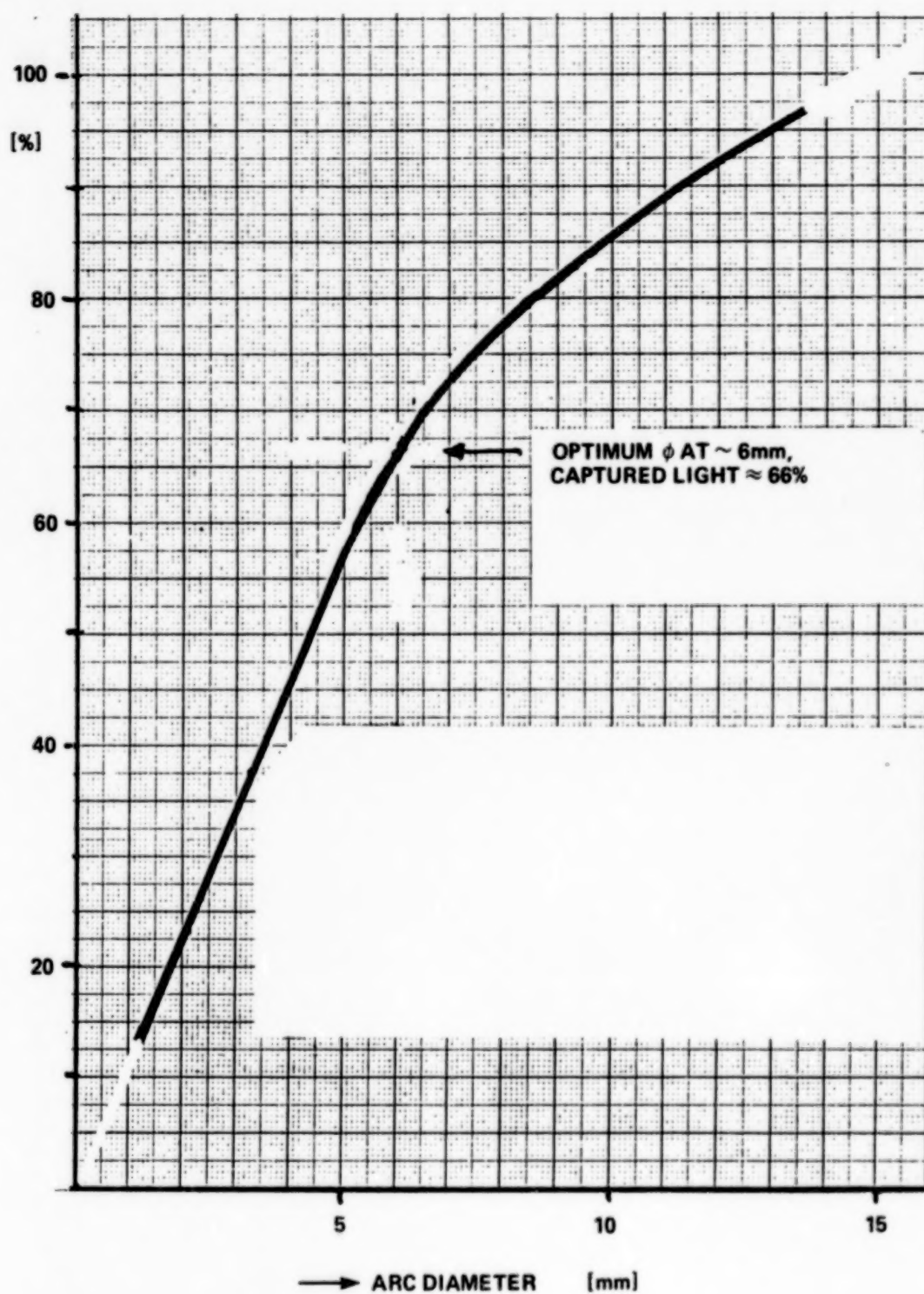


Figure 10. Light Output of a Xenon Lamp a Function of Arc Diameter Used

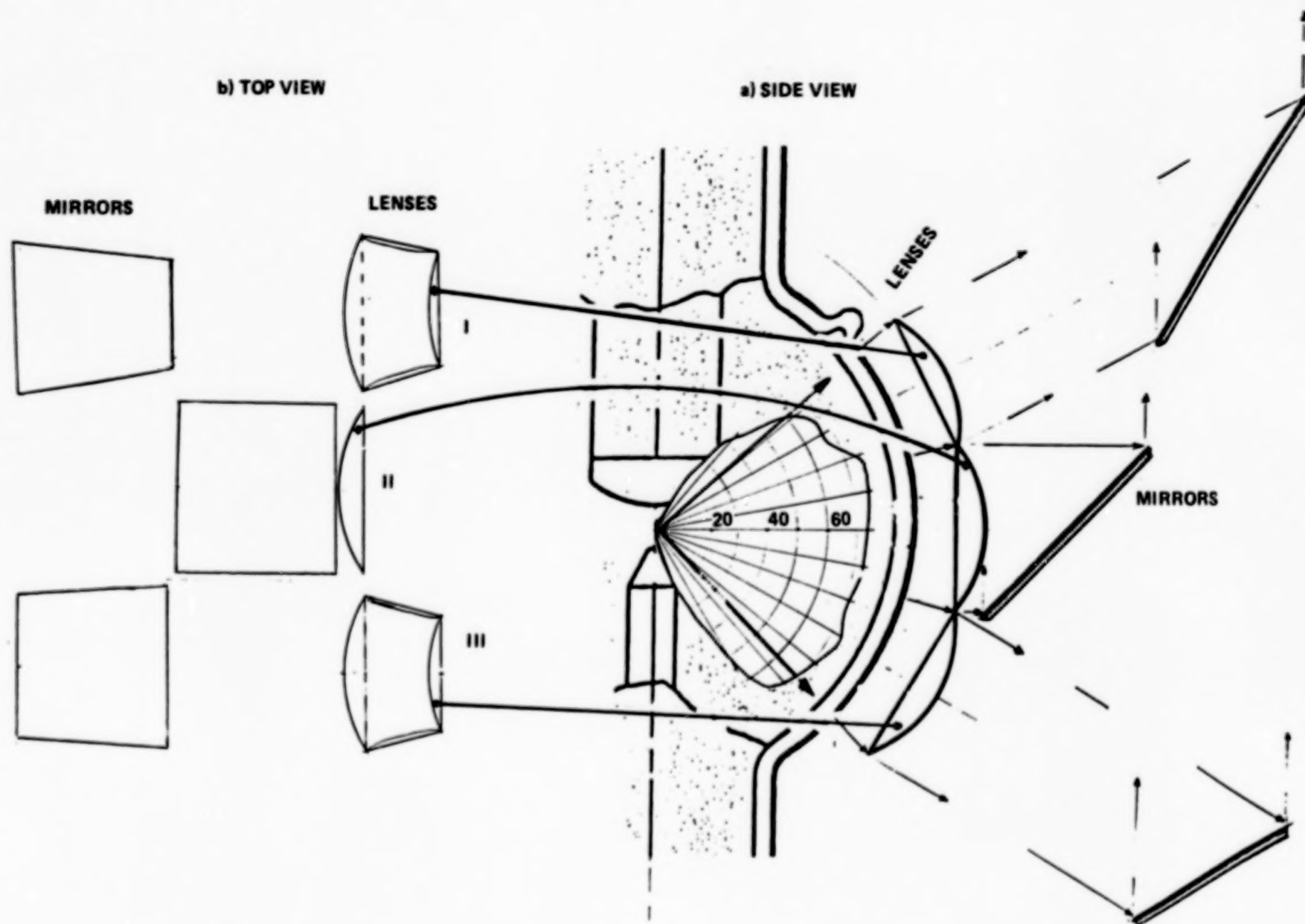
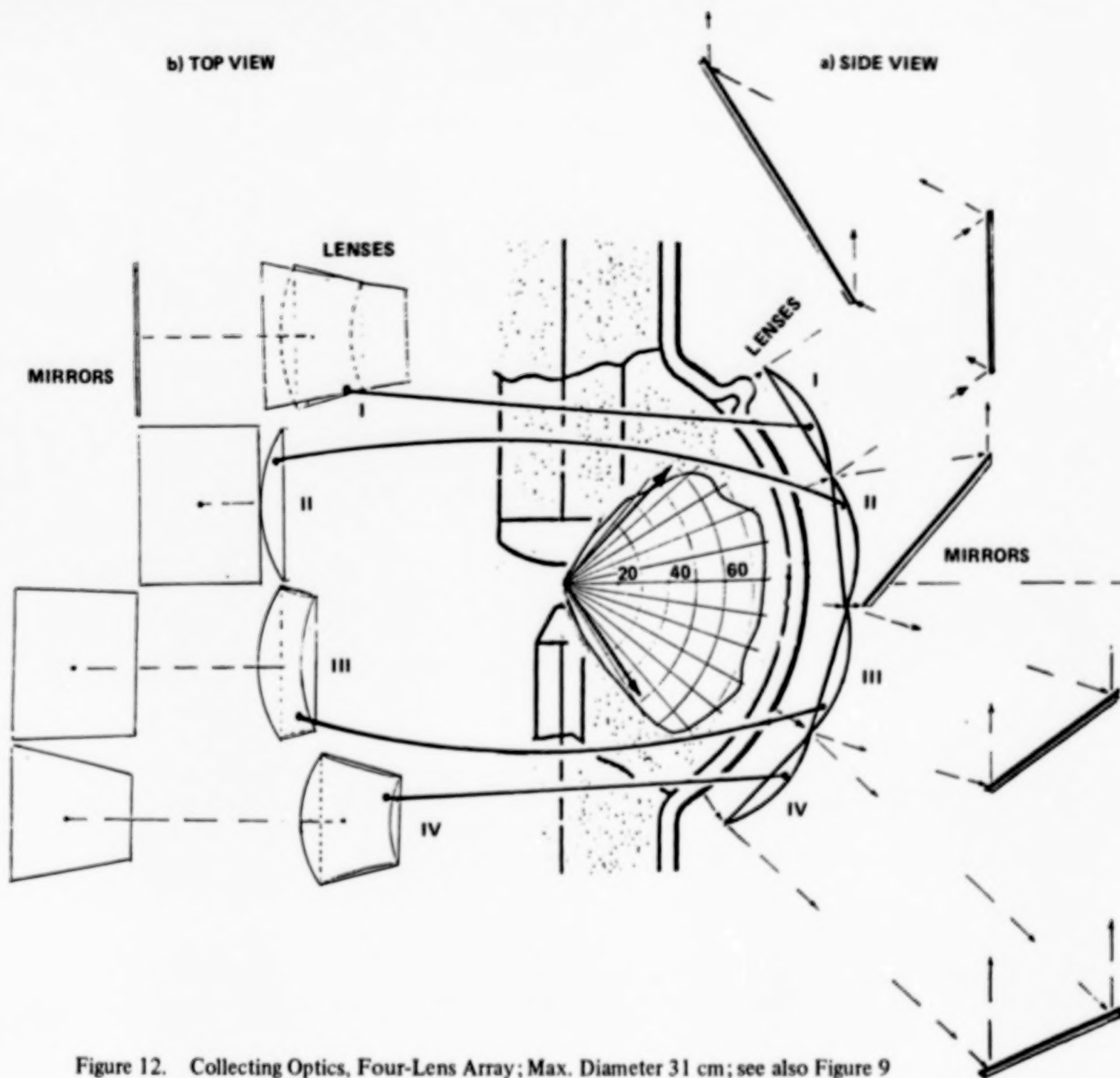


Figure 11. Collecting Optics; Three-Lens Array; Max. Diameter 33 cm; see also Figure 9



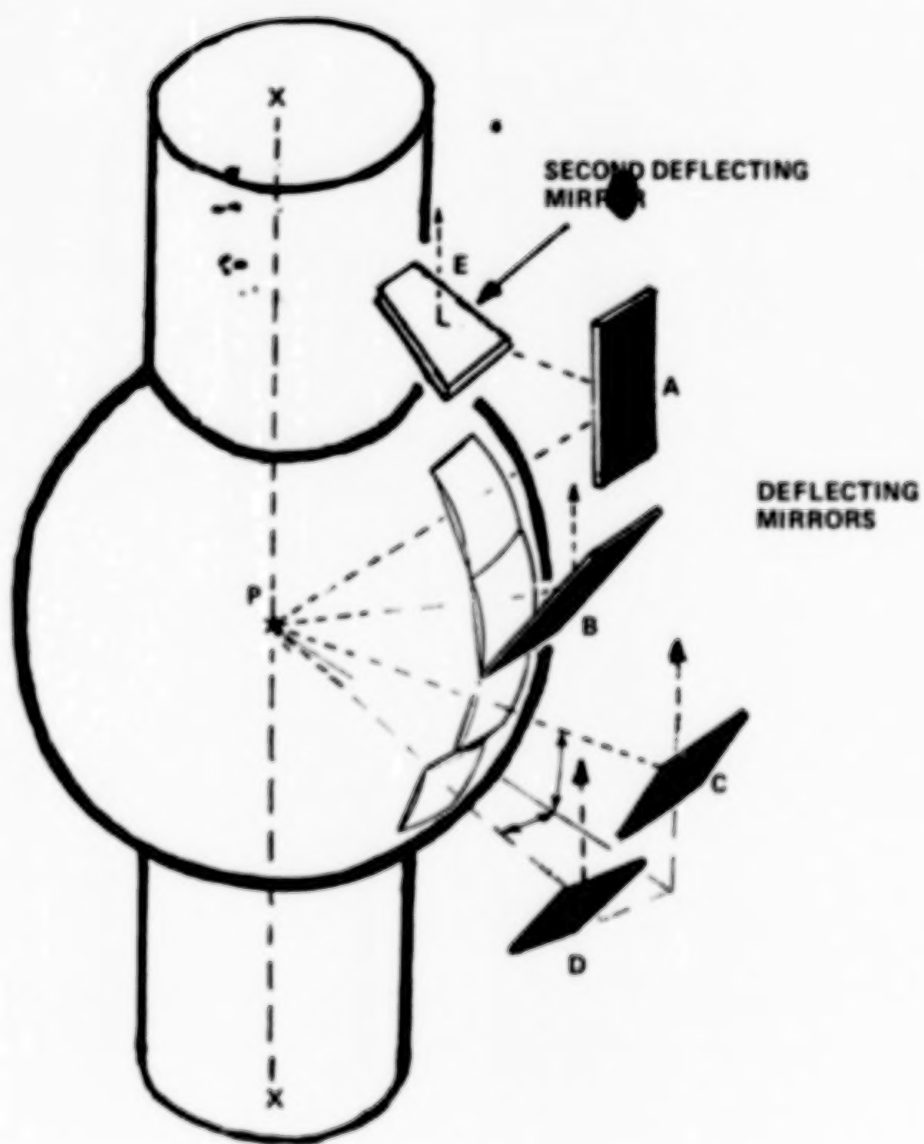


Figure 13. General View of Four-Lens Array Collector

SESSION IX
UNIQUE TESTS AND REQUIREMENTS

AEOLIAN REMOVAL OF DUST TYPES FROM PHOTOVOLTAIC SURFACES ON MARS

James R. Gaier and Marla E. Perez-Davis
NASA Lewis Research Center
Cleveland, Ohio 44135

Mark Marabito
Cleveland State University
Cleveland, Ohio 44115

ABSTRACT

Dust elevated in local or global dust storms on the Martian surface could settle on photovoltaic (PV) surfaces and seriously hamper their performance. Using a recently developed technique to apply a uniform dust layer, PV surface materials were subjected to simulated Martian winds in an attempt to determine whether natural aeolian processes on Mars would sweep off the settled dust. Three different types of dust were used; an optical polishing powder, basaltic "trap rock", and iron (III) oxide crystals. The effects of wind velocity, angle of attack, height above the Martian surface, and surface coating material were investigated. It was found that arrays mounted with an angle of attack approaching 45° show the most efficient clearing. Although the angular dependence is not sharp, horizontally mounted arrays required significantly higher wind velocities to clear off the dust. From this test it appears that the arrays may be erected quite near the ground, but previous studies have suggested that saltation effects can be expected to cause such arrays to be covered by soil if they are set up less than about a meter from the ground. Particle size effects appear to dominate over surface chemistry in these experiments, but additional tests are required to confirm this. Providing that the surface chemistry of Martian dusts is not drastically different from simulated dust and that gravity differences have only minor effects, the materials used for protective coatings for photovoltaic arrays may be optimized for other considerations such as transparency, and chemical or abrasion resistance. The static threshold velocity is low enough that there are regions on Mars which experience winds strong enough to clear off a photovoltaic array if it is properly oriented. Turbulence fences proved to be an ineffective strategy to keep dust cleared from the photovoltaic surfaces.

INTRODUCTION

In the past few years there has been a growing consensus that the United States will, perhaps in the next 30 years, send a manned spacecraft to land on the surface of Mars. Because of the length of the journey, astronauts will probably stay on the surface for an extended period of time, perhaps several weeks. During their stay there will be power requirements which will exceed those of present spacecraft (ref. 1), and an important component of that power will no doubt be supplied by photovoltaic arrays.

Photovoltaic arrays will be subjected to an environment unlike those in which they have heretofore been used. The atmosphere of Mars consists of CO₂ (95.3 percent), N₂ (2.7 percent), Ar (1.6 percent), O₂ (0.13 percent), CO

(0.07 percent), H_2O (0.03 percent), and ppm or less of O_3 , Ne, Kr, and Xe (ref. 2). Natural environmental conditions on Mars such as high velocity winds, dust, ultraviolet radiation, rapid temperature changes, soil composition, and atmospheric condensates (H_2O and CO_2) may pose a threat to photovoltaic arrays. Results of the soil analysis experiments on board the Viking landers suggest the presence of highly oxidizing species in the soil (ref. 3). Although 99.9 percent of the wind measurements from the Viking landers showed velocities of 20 m/s or less (ref. 4), dust storms were observed to move at higher velocities (up to 32 m/s) (ref. 5), and aeolian features (sand dunes, etc.) suggest that on occasion there are very high winds (>100 m/s) (ref. 6), albeit at low pressure (5 to 8 torr). The surface temperatures range from 135 to 300 K (ref. 7), and daily temperature swings ranging from 20 to 50 K are not uncommon (ref. 8).

One of the possible threats comes from local and/or global dust storms which engulf the planet nearly annually. Infrared spectra from the Mariner 9 spacecraft suggested that the dust is a mixture of many minerals (granite, basalt, basaltic glass, obsidian, quartz, andesite or montmorillonite), and that the average particle size in the atmosphere is about 2 μm (ref. 9). A significant amount of dust may be deposited on the array surface during a dust storm (ref. 10) which could occlude the light and significantly degrade the performance of the array. It is not known at this point how serious a problem dust accumulation might be or whether the tenuous but high velocity winds would blow the dust off of the array. Perhaps the photovoltaic array can be designed so as to maximize the ability of the array to be self-clearing.

The purpose of this study is to determine whether dust will be removed from photovoltaic arrays by natural aeolian processes, and how the composition of the dust, the shape and the orientation of the array can affect this process.

The authors would like to thank R. Leach of Arizona State University and the support staff at NASA Ames Research Center for their thought-provoking discussions and essential assistance with the MARSWIT facility. We would like to acknowledge the contributions of S.K. Rutledge of NASA Lewis Research Center, J. Mihelcic of Cleveland State University, and M. Kussmaul of Sverdrup Technology, Inc. for their assistance in preparing the optical coatings. J. Tillman and R. Greeley provided us with helpful discussions and expertise on the Martian environment.

METHODS AND MATERIALS

There are a variety of variables which could effect dust removal from a photovoltaic surface on Mars. In these tests we evaluated the effects of photovoltaic cell surface, angle of attack, wind velocity, height from the planetary surface, and turbulence. In addition, we used three different dust types to determine the effects of particle size and composition.

Glass coverslips 2.54 cm^2 , and 0.13 mm thick were used for the sample substrates. These were left bare or ion beam sputter deposited with a coating of SiO_2 , polytetrafluoroethane (PTFE), 50 percent mixture of SiO_2 and PTFE,

indium tin oxide (ITO), or diamond-like carbon (DLC). Table I summarizes the coatings. These coatings were chosen because they are candidate materials for protective coatings for photovoltaic arrays. The substrates were thin, both to minimize turbulence and for low mass, to improve the accuracy of weight determinations of the dusted substrates.

The samples were mounted in specially designed sample holders by means of foil tabs which stretched across two corners, and held down by a foil tab attached to a removable pin (see fig. 1). Samples were held at a tilt angle of 0°, 22.5°, 45°, 67.5°, or 90° from horizontal. The sample holders could also be held horizontally for dust deposition and optical transmittance measurements.

Initially, the sample holders were tilted so that the samples were held horizontally, and then subjected to a dusting which simulates dust accumulation in the aftermath of a dust storm. The method of dusting and the resulting dust distribution are discussed in detail elsewhere (ref. 11).

The composition of the Martian dust is not well understood. The elemental composition was determined by the Viking landers (ref. 12), and based on optical properties developed from terrestrial minerals, analogs have been proposed (ref. 9). The Viking biology experiments, however, dramatically showed that the chemistry of the dust is unique to Mars. Three different types of dust were chosen for preliminary experiments to determine how large a role the chemical composition might play in dust clearing from power surfaces.

The first dust used in these experiments was 1800 grit optical grinding powder from American Optical Company. It is principally an aluminum oxide powder which is not greatly affected by moisture in the air. This powder showed the least tendency of the three to agglomerate, and so gave us the cleanest distribution of particles on the surfaces.

The second dust was a basalt known as trap rock which is thought to be similar in properties to the Martian dust. This material, while our best approximation of Martian dust, did show some agglomeration. The fact that the dust is a grey-green color also indicates differences from the orange Martian dust.

The third dust was iron (III) oxide. Higher oxides of iron have been invoked to explain the Viking biology experiments, and are thought to be present in Martian dust. The particle size of this material was an order of magnitude smaller than that of the other two materials.

The elemental composition and particle size of the three dusts used in this experiment are compared to that of the Martian dust in table II. However, it should be noted that the purpose of this experiment was not to try to accurately simulate the Martian soil, but to try to determine how sensitive dust clearing is to composition. Also, although the values for dust clearing wind velocities on Mars may differ from those in these simulation experiments, the order of magnitude and the trends in angle and height from the surface are expected to be similar.

Because of size limitations imposed by the dusting apparatus, no more than four sample holders could be dusted at once. The amount of dust which accumulated on the samples was difficult to control, being critically dependent upon the amount of dust in the chamber, the height to which the dust is elevated, the pressure, and the time allowed for larger particles to settle out. Thirteen dusting runs were required for this study, and the resulting samples had ratios of transmittance of the dusted samples (T_d) to transmittance of the pristine samples (T_0) which were as low as 0.18 and others as high as 0.89. The spatial uniformity of each dusting operation was much better. The T_d/T_0 for each sample is shown in figure 2.

The winds on Mars were simulated using the Martian Surface Wind Tunnel (MARSWIT) at NASA Ames Research Center. The MARSWIT is a low pressure (down to a few hundred Pa) wind tunnel 14 m in length with a 1 by 1.1 by 1.1 m test section located 5 m from the tunnel entrance. This flow-through wind tunnel is located within a 4000 m³ vacuum chamber. The windtunnel injected either CO₂ (for the aluminum oxide samples) or air (for the basalt and iron oxide samples) to create the windflow. Its characteristics are described in detail elsewhere (ref. 13). The samples were placed in the MARSWIT and tested under the wind conditions listed in table III.

The samples were weighed before dusting, after dusting, and after MARSWIT exposure. However, the weight of the dust added to the optical surfaces was below the sensitivity of the balance used (0.1 mg).

Optical transmittance measurements were made by sliding the transmittance measurement device (TMD) over the sample. In the TMD a white light source is suspended above the sample, and the sensing head of a Coherent Model 212 Power Meter is beneath the sample. Specular transmittance measurements were made before and after the samples were dusted (T_0 and T_d , respectively), and after the dusted samples were subjected to winds in the MARSWIT (T_f).

The amount of dust which was cleared from the samples was evaluated using a dust clearing parameter, which was defined as the ratio of the transmittance change on wind exposure of the dusted samples ($T_f - T_d$) to that of the transmittance change upon dusting ($T_0 - T_d$). This function is a transmittance recovery fraction and is constrained to vary from zero to one. There is, unfortunately, a dependence of the value of T_d used in different sample dustings on this parameter.

The final transmittance (T_f) is a function of wind velocity, angle to the wind, surface chemistry, particle size, and time. It may also be a function of the amount of dust initially deposited assuming that the degradation of T_f from T_0 arises solely from particles remaining on the surface. Typically, the particles are sufficiently small that surface adhesion is stronger than the forces that can be exerted by the dynamic pressure of the wind. The number of particles at the surface interface will increase as the total number of particles dusted on the sample increases (i.e., as T_d decreases) up until a monolayer is built up. Beyond that there is only particle-particle cohesion. Thus, T_f will be a function of T_d until the monolayer is established, and beyond that it will not. If T_f is a function of T_d then, for dusting runs of low T_d , the dust clearing parameter would take a higher value for the same

dust clearance effectiveness. For dusting runs of high T_d , the dust clearing parameter should be independent of T_d .

Two different heights from the floor of the wind tunnel were used for dust clearing tests using the aluminum oxide dust. Samples were placed at about 2.5 cm, which should be within the floor's boundary layer, and at about 50 cm, which should be well above it.

A turbulence fence was constructed to increase the wind turbulence at the sample. It was thought that the turbulent flow might be effective at clearing the dust at wind speeds lower than those in the free stream. It was constructed with a vertical array of eight 3.2 mm diameter horizontal rods spaced every 9.5 mm.

RESULTS AND DISCUSSION

The two most important variables to dust clearing efficiency were found to be the angle of attack and the velocity of the wind. Accordingly, they will be discussed first, and turbulence and coating material will be discussed as small perturbations on the effects.

Higher wind velocities are expected to clear photovoltaic surfaces more effectively. It might also be suspected that there will be a threshold value for the wind velocity below which there will be no clearing, and above which, given sufficient time there will be significant, perhaps even total clearing. The static threshold velocity is that velocity at which dust particles leave the surface without impact from upwind particles. There are several factors which will affect the static threshold velocity including particle size, particle shape, and surface chemistry. In these experiments the particle size was chosen to match that which it is believed to become suspended during a global dust storm, but which would settle out under calmer conditions. Particles less than about 1 μm in size will stay suspended for very long periods of time, and those larger than about 50 μm will never be transported far from the site where they first become airborne. The particles used in this experiment mimic the Martian dust size and shape (ref. 11), the surface chemistry of the particles, however, is likely to be quite different from that found on Mars.

Soils on Mars are thought to be basaltic, and rich in iron oxides (ref. 9). Further, the Viking results infer the possibility of peroxide and superoxides which may be generated by the ultra-violet radiation that constantly bombards the surface (ref. 5). Accurate duplication of the exotic Martian surface chemistry is difficult at the present time due to the limited understanding of Martian soil composition. In addition, the presence of much more water vapor in the Earth environment would change the surface chemistry even if we did know how to simulate Martian soil. The optical polishing powder has been shown to dust the samples evenly with little particle aggregation (ref. 11). Thus, this material is a reasonable starting point for these studies, and that trends in angle, height, turbulence, etc. should still be valid. In addition, results of experiments to determine the threshold dust clearing values for the basalt and iron oxide, which have different surface chemistries, were compared to evaluate its effect.

Figure 3 shows the dust clearing as a function of angle for various velocities of simulated Martian wind using the aluminum oxide dust. The amount that some of the data points lie below zero give some indication of the experimental error. There is a clear indication from figure 3 that the optimum value was near 45° . Samples with an attack angle of zero showed virtually no dust clearing at velocities below about 100 m/s, while those at 45° cleared to about 92 percent of their original transmittance value at wind velocities as low as 35 m/s. Samples held at angles of 22.5° and 67.5° cleared slightly less efficiently than those at 45° . Samples held at 90° showed still less clearing, but more than those held at 0° . This trend was found with velocities varying from 30 to 85 m/s. In the test with a higher velocity (124 m/s) all of the samples were cleared comparably. In the test with a lower velocity (10 m/s) none of the samples cleared appreciably. Note that the time exposed to the wind was not the same in all cases (see table I), but the angular dependence of dust clearing is not expected to be time dependent.

In one series of samples in the 85 m/s wind test, vertical (90°) sample holders were angled at 0° , 30° , 60° , and 90° from the wind around a vertical axis. This should be an equivalent configuration to having samples on 0° , 30° , 60° , and 90° tilts, provided gravity does not play a significant role. The angular dependence was indeed consistent with the other experiments (see fig. 3).

The threshold clearing velocity predicted by Iverson and White is considerably below the measured values (ref. 14). Using the 0° data we find a threshold velocity of somewhat less than 85 m/s, about an order of magnitude higher than predicted. The experimental conditions, however, were not the same as the theoretical assumptions. Iverson and White assumed a layer of spherical particles laying on a bed of similar particles. In the experiment, there was less than a monolayer of non-spherical particles on various substrates. Intuitively, however, one might expect the threshold velocity to be smaller in the experiment because of the smooth substrate.

Given the angular dependence of the dust clearing, one might suspect that the mechanism of detachment would involve the rolling or sliding of dust particles. For the most part, however, this did not appear to be the case. Photomicrographs of the dust layer remaining on dusted glass surfaces subjected to 35 m/s winds at different attack angles showed no directionality to the dust removal. Only on the samples with an attack angle of 22.5° could it be discerned from the photographs the direction of the wind arrival. This was further confirmed by the photograph of a half-round sample subjected to the same conditions. Only as the attack angle became very low was there appreciable streaking. Thus, turbulence at the surface must act to aerodynamically lift the particles out in a direction which is approximately normal to the surface. This view is supported by classical models of Bagnold (ref. 15) in which aerodynamic lift plays a key role in particle motion from a surface at the threshold velocity.

Given the cautions above, the static threshold velocity to remove dust particles from the surface was determined. The data taken at 45° is of most interest, because that will give us the minimum static threshold value. In figure 4 it can be seen that the minimum threshold value for the optical

polishing grit was between 30 and 35 m/s. Although this is higher than the average daily maximum wind speed at the Viking landing sites of about 9 m/s (ref. 16), it is not uncommon on some parts of the Martian surface (ref. 5).

The importance of turbulence in the clearing of dust from surfaces was studied from two different sources: boundary-layer turbulence, and artificially induced turbulence. Turbulence will result in a lower mean velocity (and so a lower mean dynamic pressure to move the particles) but it may result in higher local velocities.

Identical samples were run at about 3 cm and about 50 cm from the floor of the MARSWIT. Figure 5 shows the approximate height of the boundary layer (where the velocity becomes the free-stream velocity) at several different velocities and the height of the samples. It can be seen that the lower samples were within the boundary layer, and the upper ones were not. As can be noted from figure 6, however, there was no appreciable differences between these two heights. In one experiment, in a 55 m/s wind, a sample holder was placed on end so as to fix the samples nearer to the floor. The holder was placed at a 45° angle to maximize the dust clearing. Figure 7 shows that in this extreme case there may have been small boundary layer effects observed, with the lower samples showing slightly less clearing.

Turbulence was also induced by placing a "fence" of cylindrical rods in front of the samples at a wind speed near the threshold. The hope was that the turbulence fence would lower the threshold wind speed, but the fence was found to actually hinder the clearing slightly (see fig. 8).

A wide variety of photovoltaic cell coatings was tested to determine which coatings would be most effective in shedding the dust. Because of the probable differences in surface chemistry between the test material and actual Martian soils this is risky, but perhaps some general surface principles can be determined. Even though there was a wide variety of materials both conducting and insulating, hard and soft, and high and low coefficients of friction, there were only slight differences among the ability of the coatings to shed the dust. For each angle of attack (0°, 22.5°, 45°, 67.5°, and 90°) and for wind velocities of 55, 85, and 124 m/s, each coating was ranked on the basis of dust clearing parameter from highest (1) to lowest (3 or 6, depending on the number of samples). The average ranking over all of the angles at a given wind speed for each of the coatings is shown in table IV. The last column in table IV shows the average ranking for each coating over all of the angles and all of the wind speeds. Although the error is probably large, there may be some validity to the rankings. Glass and SiO₂ have nearly equal scores, as do PTFE and PTFE/SiO₂. ITO was the easiest to clear, and DLC the hardest. Surface adhesion tests are planned to test the validity of the ranking.

The dust clearing using basalt instead of aluminum oxide produced similar results, as illustrated in figure 9. The threshold velocity at 45° appears to be between 30 and 40 m/s, within the same range as the aluminum oxide. From this test it appears that surface chemistry (within limits) does not play a large role in determining the dust clearing threshold velocity. Given the uncertainties in knowledge of Martian dust, this is fortunate.

However, when iron oxide dust was used the threshold velocity was much higher, between 85 and 95 m/s, as shown in figure 10. The surface chemistry of iron oxide differs considerably from either of the other two materials, and that could certainly affect the results. However, a more important effect may well be the particle size. The mean particle size of the iron oxide is an order of magnitude smaller than that of the other two materials, and so one would expect the threshold velocity to be between two and three times higher based on particle size effects alone (ref. 17). Further studies are required to separate particle size from surface chemistry effects in any definitive way.

The angular dependences of the threshold velocity for the basalt and the iron oxide raise some interesting questions. In the case of basalt in 30 m/s winds it can be seen in figure 9 that there is more efficient clearing at 22.5° than at 45°. Streaks which indicate the wind direction are also visible in the 22.5° case. It appears that at low angles the particles begin to roll off the surface. The threshold velocity for this is evidently somewhat lower than for the aerodynamic lift removal that is dominant at higher angles. It appears then, that the aerodynamic removal is more efficient, but requires a somewhat higher velocity.

Figure 10 reveals that iron oxide was most efficiently removed at 22.5° at wind velocities even as high as 95 m/s. This could have two possible explanations. The first is that this velocity is not high enough for the aerodynamic lift mechanism to begin to dominate, or in other words, the aerodynamic threshold velocity still had not been reached. The second explanation is that particle size effects cause the rolling dust clearing to dominate at all velocities, that is, that even at much higher velocities the 22.5° samples would have cleared more efficiently.

CONCLUSIONS

Even in this first preliminary study principles have been found which can help to guide the design of photovoltaic arrays bound for the Martian surface. Most importantly, if an array is to be self-cleaning it should be tilted at an angle approaching 45°. Although there is wide latitude with this requirement, it seems most important that the arrays are not erected horizontally. Although the angular dependence is not sharp, horizontally mounted arrays required significantly higher wind velocities to clear off the dust. From the perspective of dust clearing it appears that the arrays may be erected quite near the ground, but saltation can be expected to cover the arrays if they are set up less than about a meter from the ground (ref. 18). Providing that the surface chemistry of Martian dusts is comparable to the simulated test dusts, the materials used for protective coating may be optimized for other considerations such as transparency, and chemical or abrasion resistance. Given the same assumption, there are regions on Mars which experience winds strong enough to clear off a photovoltaic array which is properly oriented, though there are other regions where some other clearing technique will have to be employed. Turbulence fences proved to be an ineffective strategy to keep dust cleared from the photovoltaic surfaces.

There seem to be two dust removal mechanisms at work. At low angles (22.5° and less) the dust particles are rolled off of the surface, and at high angles (45° and higher) the particles are aerodynamically lifted from the surface. The threshold value for the rolling mechanism appears to be lower, but the aerodynamic lift mechanism appears to be more effective.

REFERENCES

1. Giudici, R.J.: Electrical Power Systems for Mars. The Case for Mars: Proceedings of a Conference, American Astronautical Society, 1983, pp. 873-887.
2. Owen, T.K.; Biemann, K.; Rushneck, D.R.; Biller, J.E.; Howarth, D.W.; and Lefleur, A.L.: The Composition of the Atmosphere at the Surface of Mars. *J. Geophys. Res.*, vol. 82, Sept. 30, 1977, pp. 4635-4639.
3. Klein, H.P.: Viking Biological Experiments on Mars. *Icarus*, vol. 34, no. 3, 1978, pp. 666-674.
4. Kaplan, D.: Environment of Mars. NASA TM-100470, 1988.
5. Peterfreund, A.R.; and Kieffer, H.H.: Thermal Infrared Properties of the Martian Atmosphere. III - Local Dust Clouds. *J. Geophys. Res.*, vol. 84, June 10, 1979, pp. 2853-2863.
6. Pollack, J.B.; Colburn, D.S.; Flasar, F.M.; Hahn, R.; Carlston, C.E.; and Pidek, D.: Properties and Effects of Dust Particles Suspended in the Martian Atmosphere. *J. Geophys. Res.*, vol. 84, June 10, 1979, pp. 2929-2945.
7. Kieffer, H.H.; Martin, T.Z.; Peterfreund, A.R.; Jakosky, B.M.; Miner, E.D.; and Palluconi, F.D.: Thermal and Albedo Mapping of Mars During the Viking Primary Mission. *J. Geophys. Res.*, vol. 82, Sept. 30, 1977, pp. 4249-4291.
8. Tillman, J.E.: Martian Meteorology and Dust Storms from Viking Observations. The Case for Mars, II: Proceedings of the Conference, American Astronautical Society, 1985, pp. 333-342.
9. Toon, O.B.; Pollack, J.B.; and Sagan, C.: Physical Properties of the Particles Composing the Martian Dust Storm of 1971-1972. *Icarus*, vol. 30, Apr. 1977, pp. 663-696.
10. Arvidson, R.E.; Guinness, E.A.; Moore, H.J.; Tillman, J.; and Wall, S.D.: Three Mars Years, Viking Lander 1 Imaging Observations. *Science*, vol. 222, Nov. 4, 1983, pp. 463-468.
11. Perez-Davis, M.E.; Gaier, J.R.; Kress, R.; and Grimalda, J.: Simulation of Martian Dust Accumulation on Surfaces. Sixteenth AIAA-NASA/ASTM/IEA Space Simulation Conference, NASA CP- , 1989. (Paper of this compilation.)

12. Toulmin III, P.; Baird, A.K.; Clark, B.C., Keil, K.; Rose, Jr. H.J.; Christian, R.P.; Evans, P.H.; and Kelliher, W.C.: Geochemical and Mineralogical Interpretation of the Viking Inorganic Chemical Results - for Martian Surface Materials. *J. Geophys. Res.*, vol. 82, Sept. 30, 1977, pp. 4625-4634.
13. Greeley, R.; White, B.R.; Pollack, J.B.; Iversen, J.D.; and Leach, R.N.: Dust Storms on Mars: Considerations and Simulations. NASA TM-78423, 1977.
14. Iversen, J.D.; and White, B.R.: Saltation Threshold on Earth, Mars, and Venus. *Sedimentology*, vol. 29, no. 1, 1982, pp. 111-119.
15. Bagnold, R.A.: The Flow of Cohesionless Grains in Fluids. *Philos. Trans. R. Soc., Ser. A*, vol. 249, 1956, pp. 239-297.
16. Pollack, J.B.; Leovy, C.B.; Mintz, Y.H.; and Van Camp, W.: Winds on Mars During the Viking Season - Predictions Based on a General Circulation Model with Topography. *Geophys. Res. Lett.*, vol. 3, Aug. 1976, pp. 479-482.
17. Iversen, J.D.; Greeley, R.; and Pollack, J.B.: Windblown Dust on Earth, Mars, and Venus. *J. Atmos. Sci.*, vol. 33, Dec. 1976, pp. 2425-2429.
18. Greeley, R.; and Iversen, J.D.: Wind as a Geological Process: On Earth, Mars, Venus, and Titan. Cambridge University Press, 1985.

TABLE I. - PHOTOVOLTAIC ARRAY COATINGS TESTED

Coating	Thickness	Deposition	Substrate
None	-----	-----	Glass
SiO ₂	650Å	Ion beam	Glass
PTFE	≈1000Å	Ion beam	Glass
50 percent/ SiO ₂	≈1000Å	Ion beam	Glass
ITO	≈1000Å	Ion beam	Glass
DLC	≈1000Å	Ion beam	Glass

TABLE II. - COMPOSITION OF DUSTS

	Percent by weight			
	Viking	Opt Grt	Basalt	Fe ₂ O ₃
SiO ₂	44.7	6.6	46.6	0
Fe ₂ O ₃	18.1	0.6	13.0	100
MgO	8.3	0.0	6.1	0
Al ₂ O ₃	5.7	89.0	16.6	0
CaO	5.6	0.0	11.1	0
TiO ₂	0.9	3.0	2.0	0
Cr ₂ O ₃	0.0	0.6	0.0	0
Na ₂ O	?	0.0	2.3	0
K ₂ O	0.0	0.0	1.1	0
MnO	0.0	0.0	0.3	0
CO ₂	?	0.0	0.1	0
P ₂ O ₅	0.0	0.0	0.1	0
Size, μ m		7 to 25	5 to 20	0.5 to 2.5

TABLE III. - WIND CONDITIONS WITHIN THE MARSWIT

Velocity, m/s	Stat Pres, Pa	Dyn Pres, Pa	Temp, K	Time, sec	Dust
10	1000	1.2	290	600	Al ₂ O ₃
23	1000	6.3	290	600	Al ₂ O ₃
30	1000	10.7	290	600	Al ₂ O ₃
30	1000	10.9	285	300	Fe ₂ O ₃
31	1000	11.4	290	900	Al ₂ O ₃
31	850	9.9	285	600	Basalt
35	1000	14.5	290	300	Al ₂ O ₃
42	950	20	285	600	Basalt
50	1000	30	285	90	Fe ₂ O ₃
55	1000	36	290	120	Al ₂ O ₃
60	1000	43	285	600	Fe ₂ O ₃
85	1000	86	290	30	Al ₂ O ₃
85	900	78	285	600	Fe ₂ O ₃
95	1200	131	285	600	Fe ₂ O ₃
124	1000	182	290	45	Al ₂ O ₃

TABLE IV. - RELATIVE EASE OF DUST CLEARANCE FROM
PHOTOVOLTAIC COATINGS

Coating	55 m/s	85 m/s	124 m/s	Overall
ITO	1.0	1.6	2.5	1.9
PTFE/SiO ₂	1.0	1.8	3.0	2.2
PTFE	2.0	2.3	2.3	2.3
SiO ₂	3.0	1.9	3.6	2.8
Glass	2.0	2.4	3.8	2.9
DLC	3.0	2.1	4.3	3.2

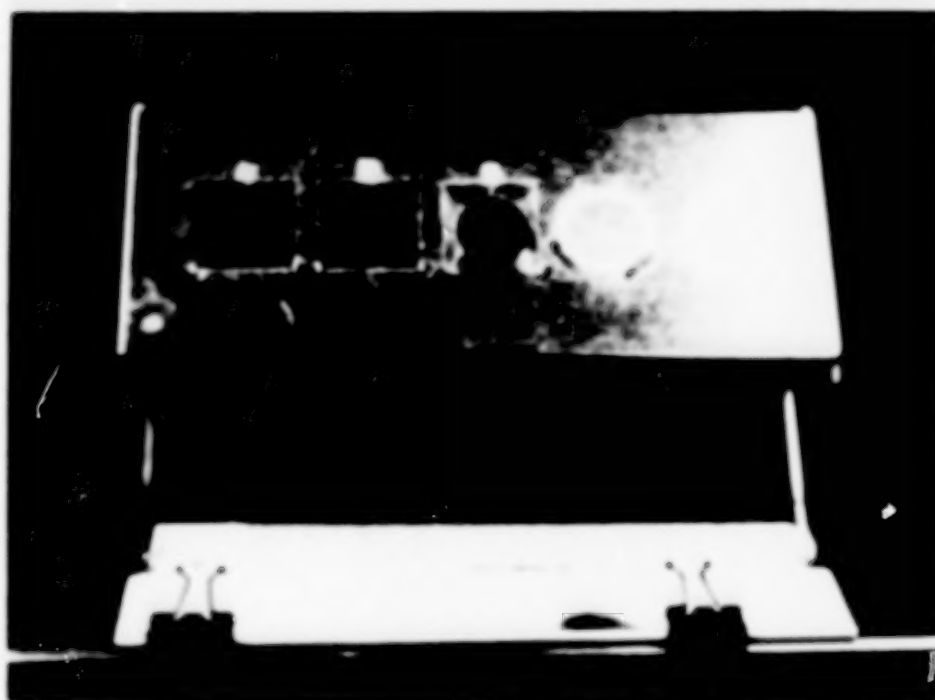


Figure 1. Sample Holder Designed to Test Aeolian Dust Removal from Photovoltaic Surfaces

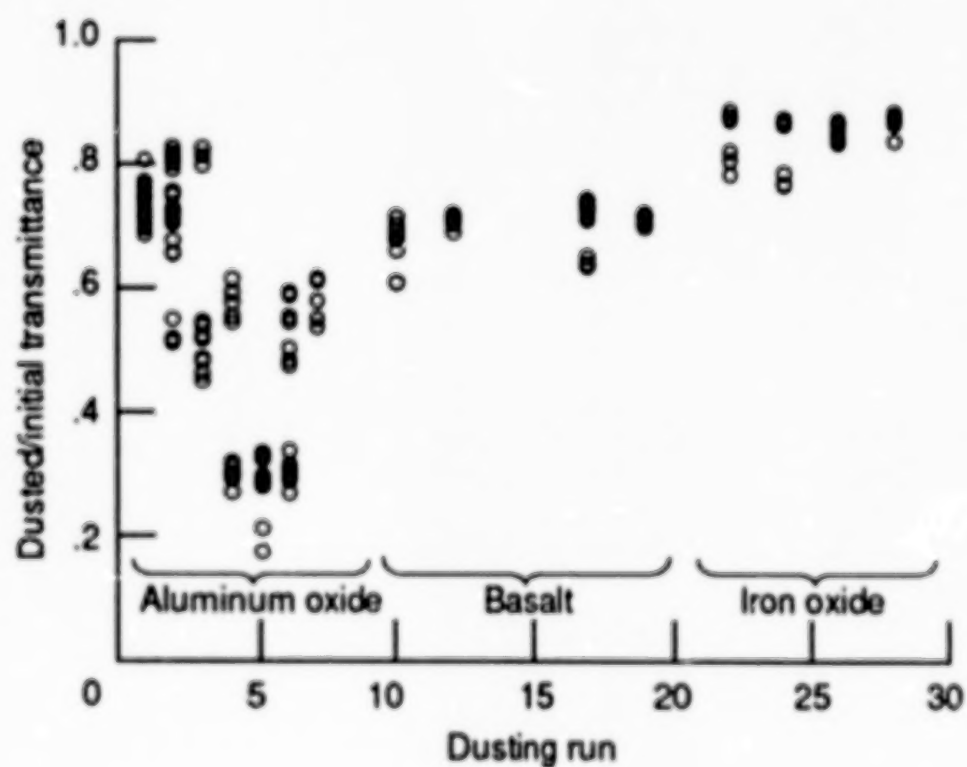


Figure 2. Uniformity of Dust Deposition

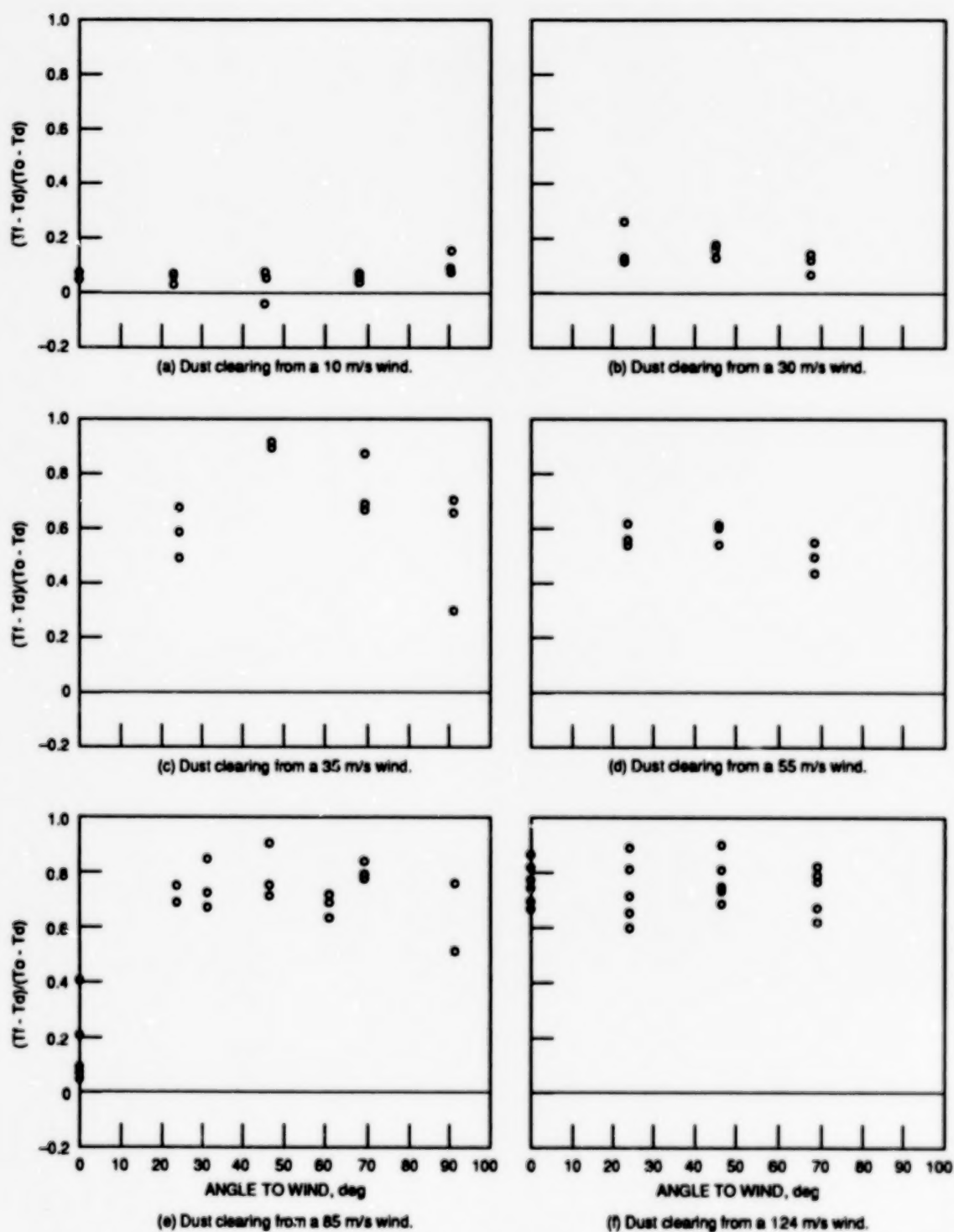


Figure 3. Dust Clearing as a Function of Angle for Several Different Martian Wind Speeds

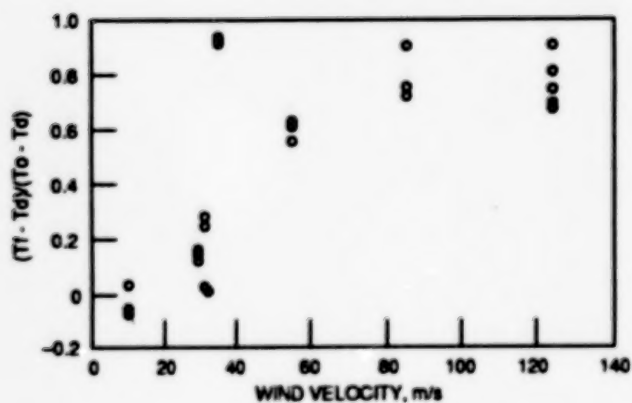


Figure 4. Dust Clearing from a Smooth 45° Angle Surface

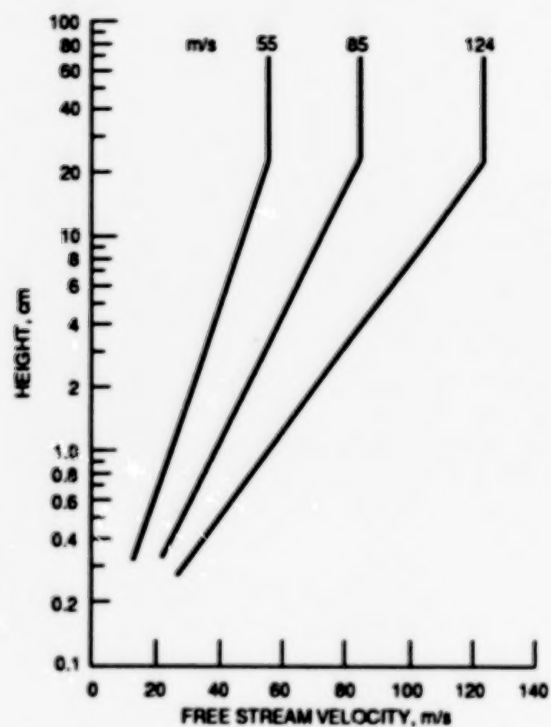


Figure 5. Nominal Boundary Layer Profiles

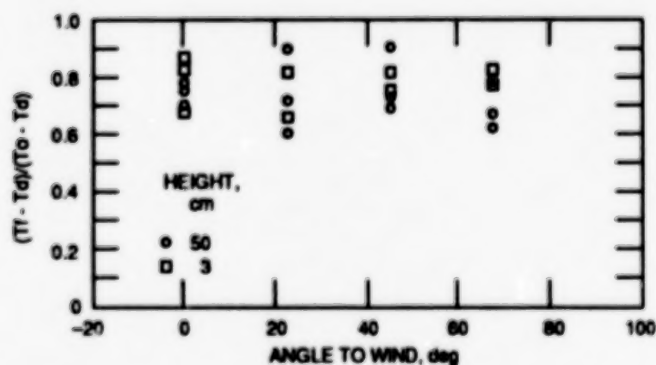


Figure 6. Dust Clearing at Different Heights from Wind Tunnel Floor

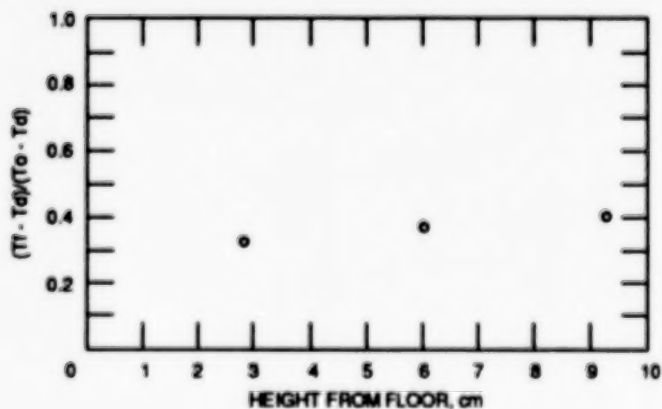


Figure 7. Dust Clearing in Boundary Layer at 55 m/s

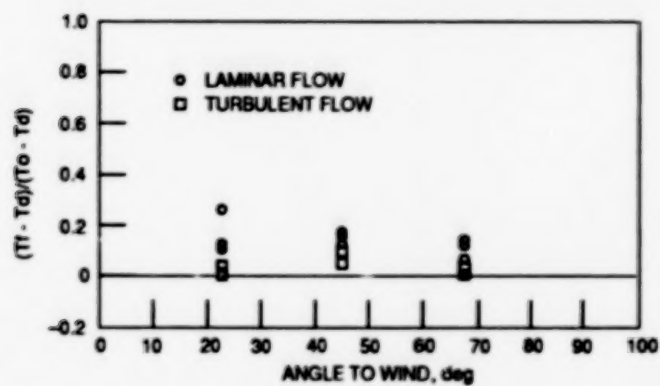


Figure 8. Dust Clearing from a 30 m/s Wind

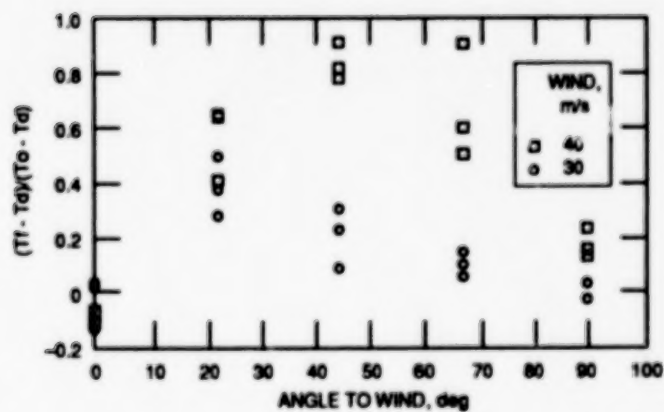


Figure 9. Trap Rock Dust Clearing

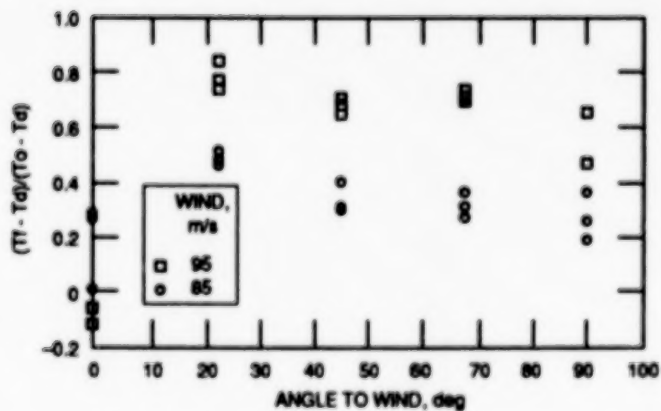


Figure 10. Iron Oxide Dust Clearing

EXPERIMENTAL DETERMINATION OF SATELLITE BOLTED JOINTS THERMAL RESISTANCE

Marcia Barbosa Henriques Mantelli and José Edson Basto
Brazilian Institute for Space Research

ABSTRACT

The main objective of this work is to determine experimentally the thermal resistance of the bolted joints of the first Brazilian satellite (SCD1). These joints, used to connect the satellite structural panels, are reproduced in an experimental apparatus, keeping, as much as possible, the actual dimensions and materials. A controlled amount of heat is forced to pass through the joint and the difference of temperature between the panels is measured. The tests are conducted in a vacuum chamber with liquid nitrogen cooled walls, that simulates the space environment. Experimental procedures are used to avoid much heat losses, which are carefully calculated. Important observations about the behaviour of the joint thermal resistance with the variation of the mean temperature are made. All the experimental work is developed in the Brazilian Institute for Space Research Thermal Control Laboratory.

INTRODUCTION

The determination of bolted joint thermal resistance is very important for satellite temperature distribution calculations. In the first Data Collection Brazilian Satellite (SCD1), where only thermal control passive methods are used, the bolted joints between structural panels are of primary importance in the satellite thermal design. The heat conducted by the satellite panels and/or their electronic boxes depends on the joints' thermal resistance values, so they are projected taking into account thermal and structural considerations.

The theoretical calculation of the thermal resistance is very difficult, because it depends on a series of factors like:

- shape and physical properties of junction materials,
- type and material of bolts,
- materials and number of washers,
- joint aperture strength,
- thermal contact resistance between: washers, bolts and washers, bolts and panels, washers and panels, etc.

The numerical determination of this thermal resistance, using nodal modelling technic, is also hard to do because all the physical properties must be well known before making the calculations (frequently these data, or the measurement equipment, are not available).

An always useful procedure, that is adopted in this work, is to obtain this resistance by experimental simulation of the bolted joints. The satellite junctions are reproduced and tested in a vacuum chamber with liquid nitrogen cooled walls, in the Satellite Thermal Control Laboratory of the Brazilian Institute for Space

Research (INPE). Some series of tests were performed at INPE, but only the last one, with the best results, is described here.

SATELLITE BOLTED JOINTS

There are several types of junctions in the SCD1 satellite, but only the joints placed between the external vertical and the central horizontal structural panels are studied. In the central panel many dissipating equipment are installed. They are connected to the external vertical panels by two types of junctions: one with blind threaded insert (where the nut is fixed) and the other with a floating nut insert. Their positions in the satellite and the studied junctions schematic views are shown in the figure 1. Some electronic boxes are fixed to the horizontal panel by junctions very similar to these ones, so that the resistance obtained in this work can be used in the thermal control design of the satellite electronic equipment.

The described joints fasten two 2024 aluminum (ANSI standard) panel closing sheets (thickness: 2 and 1 mm, see figure 1), to the honeycomb panel inserts. For the panels' thermal insulation, two 1.6 mm thick epoxy+fiberglass intercalated by a 0.4 mm thick stainless steel washers, are used between the insert and the aluminum sheet. An epoxy+fiberglass washer is in contact with the insert, and a stainless steel one, with the closing sheets. The epoxy+fiberglass and stainless steel washers are present between the bolt head and the aluminum sheet either. The washers' materials were chosen to satisfy the thermal (epoxy+fiberglass) and structural (stainless steel) requirements. The washers have external diameter of 10 mm; their internal diameters are 5 mm for the fixed nut insert joints, and 4.5 mm for the floating ones. As they do not have standard sizes, they were fabricated specially for the SCD1. The bolts used are made of titanium and have two different sizes, according to the insert type: #10 (see ASA standard) for fixed, and #8 for the floating nut insert.

EXPERIMENTAL SIMULATION

The objective of the experimental work is to measure the thermal resistance of the two types of bolted joints described in the previous section. So, the experimental apparatus were designed to reproduce, in the laboratory, the same thermal conditions found in the satellite. To enable data statistical treatment, ten similar joints are mounted for each junction and tested simultaneously. The mean resistance values and the associated standard errors (the range of values) are calculated. To study the joints behaviour with the variation of the temperature, five levels of temperature are adopted. All the tests are made in steady state conditions. It is supplied a controlled amount of heat to each apparatus, the temperatures are left to stabilize and heat flow and temperature measurements are done. The ratio between closing aluminum sheets and insert temperature difference (see figure 1), and the heat flux through the bolts and washers determines the thermal resistance of the joint.

The tests are made in the experimental facilities of the Brazilian Institute for Space Research Thermal Control Laboratory. It is used an inside volume 1 meter X 1 meter vacuum chamber with liquid nitrogen (LN_2) cooled walls. This chamber operates in high vacuum (10^{-7} Torr), with wall temperatures of -190 Centigrades. An acquisition and control data system is used to control the temperatures in levels previously established, and to store the temperature and voltage data. A PC

microcomputer program controls the experiment, through a GPIB interface and the data is recorded in its hard disk.

APPARATUS DESCRIPTION

The joints' experimental thermal simulation is made by two types of apparatus, corresponding to the two different junctions described in the previous section.

In the apparatus design, to reproduce the thermal and physical characteristics of the actual bolted joints, it was first necessary to analyse the heat flow lines across the junction components. Supposing the heat coming from the vertical panel to the horizontal panel (see figure 1), there is first a concentration of heat flow lines in the bolt direction. Then, the heat flows through two main paths: across the bolt and across the washers. The heat arrives to the insert, passes through the silicone glues that fastens the insert to the honeycomb panel, and finally reaches the horizontal panel. The value of the effective honeycomb panel thermal conductivity is very low if compared with the conductivity of the insert material, and, as all the external insert surfaces are in contact with the epoxy glue, it is considered that the heat flux rate is the same in all directions. Note that, as the floating nut insert joints have more surfaces in contact (see figure 1), it is expected a thermal resistance value bigger than the fixed nut insert one. To force the heat to flow through the washers and bolts, each apparatus has a heat source and a heat sink, with their temperatures measured by copper/constantan thermocouples. figure 2 shows a schematic view and thermocouples' localizations of the experimental apparatus for the fixed nut insert joint, while figure 3, shows them for the floating one.

The washers and their arrangements are equivalent to the actual satellite joints. As the titanium bolts were not available for testing, they are substituted by high alloy steel ones.

The closing aluminum sheets, working as heat sources, are replaced by plan heaters, made of two circular 80mm diameter 2024 aluminum sheets, 1 and 1.5 mm thick. Between the aluminum plates there is a Nickel-Chrome resistive wire (resistivity of 30 Ohms/meter), rolled in a plan spiral, electrically insulated by two 25 microns thick Polyester films. The total resistance achieved in each heater is between 15.5 and 19.0 Ohms. The heater aluminum sheets were chosen so that the total thickness value is almost the same of the joints' closing sheets. The heater size and shape was designed to simulate the effect of the radial heat flow lines in the direction of the bolt, near the joint.

Only the inserts are considered in the simulation of the honeycomb panels, as the stainless steel's conductivity is higher than those of the epoxy glue and of the honeycomb panel. They work as heat sinks (coolers), and have some of their dimensions different for the two types of the analysed junctions. They are made of the actual joints' material (stainless steel) and have a 60 mm thin circular black painted base (2mm thick) to favor the heat transfer to chamber environment. Without this base, it would not be possible to generate a well measurable heat quantity, because this dissipation would make the apparatus very hot, the difference of temperature between the heater and the cooler very small, and the measurements' uncertainties too large.

The total cooler height is 9.5 mm for the fixed nut insert and the diameter of its main body is 14.2 mm. In the center of the main body there is a screw thread hole for a #10 screw. A thermocouple is installed in the heater to measure its temperature, in a region where the heat flux has not reached the bolt and/or washers. The insert

thermocouple is installed in a point considered as the mean heat flux path (see figure 2).

The floating nut insert is simulated by a 9.4 mm diameter cylinder with a #8 screw thread hole and a 15.4 mm diameter (1 mm thick) larger basis that interacts with the insert main body when the joint is fastened (see figure 3). The main body have a 17.4 mm diameter and a 9.4 mm height cylinder. Closing the main body, soldered in the top of the cylinder, there is a thin plate with a central hole slightly larger than the screw main body diameter. The heater thermocouple is in the same position as in the fixed nut insert apparatus. The cooler thermocouple is positioned near the insert base, in a region that is considered the mean heat flux path, since the heat conducted by the joint must pass through the contact between the nut and the insert body to reach the horizontal panel.

The ten similar apparatus constructed for the two types of bolted joints, are mounted in a Celeron table (heat insulating material), according to the figure 4. They are positioned in the table to avoid the interaction among the specimens in a way that all the apparatus coolers can see the chamber environment with the same view factor, i.e. around 1. The electrical wires of five apparatus heaters are connected in series and the four resulting rows are connected in parallel. In these lateral junctions two other big wires that connect the specimens' electrical wires to the vacuum chamber wall feed through are soldered, to feed all the specimens with only one power generator.

MOUNTING PROCEDURES TO AVOID HEAT LOSSES

Some past experiments showed that the heat losses must be well controlled to warrant small experimental results' uncertainties.

To avoid the heat loss to chamber walls, and direct radiant heat exchange between the heater and the cooler, multilayer thermal insulators (MLI) in heaters' both faces are installed. The external (lower) MLI has ten layers and the internal one, that has a central hole to fit the washers and bolt, eight.

As the thermocouples and electrical wires work as fins and dissipate part of the heat by radiation, they are wrapped up with aluminized mylar to lower the surface emissivity. Their original surfaces emissivities were big, causing too much heat losses.

All the external cooler faces are black painted to force the heat to pass through the joint, excepting the internal face that is polished, to insulate the cooler and the heater from the radiation exchange.

RESULTS

To study the joint temperature variation behaviour, five levels of heater and cooler mean temperatures are used in the experimental tests. Some data resulting from tests with detected problems like: breaking of thermocouples wires, bad positioning of the copper-constantan soldered junctions, bad electrical contact between the extension wires and thermocouples or feed through, etc, were not used.

The thermal joint resistance is calculated by the following equation:

$$R = \frac{\Delta T}{Q}, \quad (1)$$

where:

R : thermal joint resistance, °C/W,
 ΔT : temperature difference between heater and cooler, °C,
 Q : net heat flux in the joint, W.

The net heat flux is calculated through the equation:

$$Q = Q_P - Q_L \quad (2)$$

Where:

Q_P = heater dissipated power, W,
 Q_L = summation of all heat losses, W.

The heater dissipation power is determined by each heater electrical resistance and the electrical current that flows through it. The electrical resistance is directly measured (before the tests' beginning), and the current is obtained from the electrical power generator output. The following equation is used:

$$Q_P = (V/R_{eq})^2 R_e \quad (3)$$

Where:

V = electrical power generator output, V
 R_{eq} = equivalent electric resistance (summation of resistances connected in series), Ohms,
 R_e = heater electric resistance, Ohms.

All the heat losses must be carefully calculated to determine the net heat flux through the joint, as it will be discussed in the next section.

For the five temperature levels tested, the system was left for near one hour in the steady state condition. During this period, more than one hundred data were obtained at equal time intervals for each thermocouple, to verify the temperatures, presumably with small variations around a mean value. This procedure reduces the experimental errors in the results. To verify if there is electrical resistance dependence with the temperature variation, the resistances were measured in the experimental temperature levels, before the apparatus mounting. It was not verified any important variation, so that the electric resistance values obtained for each apparatus, are used in the data treatment.

Table 1 relates the following averages values for the equal apparatus: heater and cooler temperatures, heater power, summation of all heat losses and the thermal resistances, for the two types of bolted joints studied, in the five temperature levels.

HEAT LOSSES CALCULATIONS

Analysing the experimental apparatus, it is verified that there are four principal ways of heat losses: through the thermocouples wires, through the electrical wires, direct heat exchange between heater and cooler and through the MLI in the heater outer face. Each one of these heat losses is considered separately.

Thermocouples' Heat Losses

The thermocouples used in this experiment are made of copper and constantan wires. Each one of them is considered as a radiant fin so that the following well-known fin conduction and radiation equation are used to estimate the heat losses (see reference 1).

$$Q_w = (T_h - T_m) \tanh(mL) \sqrt{(h P K A)} \quad (4)$$

where:

$$m = \frac{\sqrt{(h P)}}{K A} \quad (5)$$

and:

$$h = \frac{\epsilon \sigma (T_h^4 - T_m^4)}{T_h - T_m} \quad (6)$$

Where:

Q_w = heat loss by the wire, W,
 T_h = heater temperature, $^{\circ}\text{C}$,
 P = wire perimeter, m,
 K = wire thermal conductivity, $\text{W/m}^{\circ}\text{C}$,
 A = wire transversal section area, m^2 ,
 L = wire length, m,
 ϵ = surface emissivity,
 σ = Stefan-Boltzmann constant, $\text{W/m}^2 \text{K}^4$.

Under the Celeron table, there is an aluminum platen where the experimental mounting is supported. T_m ($^{\circ}\text{C}$) is the environment mean temperature, or the mean value between the wall chamber and the table or the platen temperature, depending on whether they are under or over the Celeron table.

Electrical Wires' Heat Losses

The wires can be divided in two groups, according to their lengths: the short ones, which connect the heaters, and the long ones, which connect the peripheral wires to the chamber walls (see figure 4).

Studying the first group, it was verified that, in spite of connecting two heaters of different temperatures, they work as heaters' fins, exchanging heat with the chamber and the Celeron table. The fins length is the distance between the heater and the point of minimum wire temperature; as this point is always near the wire middle they will not be calculated.

In the second group, the wires work as fins of the nearest heater. It is expected that a larger amount of heat is lost by these wires, since they are connected to the chamber walls that are cooled with LN. In both cases the heat losses depends on the heater temperature. The same thermocouples' losses equations are used in these calculations.

Heater External MLI Heat Losses

The heater external MLI is in physical contact with the Celeron table near its external perimeter (see Figures 2 and 3). In the losses' calculation two mechanisms are considered: conduction from the heater to the Celeron table, and radiation to the platen.

In the radiant losses' calculation, the effective emissivity values obtained in experimental works developed in this laboratory for MLI constructed with brazilian components are used (see reference 2). The radiant area is the same of the Celeron hole made to fit the mounted apparatus. The following Stefan-Boltzmann equation is used in these calculations:

$$Q_{MLIr} = \frac{\epsilon A_r \sigma (T_h^4 - T_p^4)}{1/\epsilon_{eff} + 1/\epsilon_p - 1} \quad (7)$$

where:

Q_{MLIr} = radiative MLI heat losses, W,
 A_r = Celeron hole area, m^2 ,
 T_p = platen temperature, $^{\circ}C$,
 ϵ_{eff} = effective emissivity,
 ϵ_p = platen emissivity.

Note that the expression in the denominator is the MLI and platen equivalent emissivity.

The Fourier law is used to determine the conductive heat losses:

$$Q_{MLIc} = \frac{K_{eff} A_c}{t} (T_h - T_s) \quad (8)$$

where:

Q_{MLIc} = conductive MLI heat losses, W,
 K_{eff} = effective thermal conductivity, $W/m^{\circ}C$,
 A_c = MLI and Celeron contact area, m^2 ,
 T_s = MLI surface temperature, $^{\circ}C$,
 t = MLI thickness, m.

The effective thermal conductivity is calculated based on the effective emissivity value, on the MLI surface, platen and heater measured temperatures.

Direct Heat Exchange Between Heater and Cooler or Environment

The heat losses' calculation between heater and cooler and/or heater and environment, is made through the Stefan-Boltzmann equation. The view factor is determined by a finite difference program developed at INPE for satellite thermal designs. The apparatus were divided into 32 nodes. To simulate the heater internal MLI, the emissivity of the heater nodes was considered equal to the effective emissivity of the superinsulator. The following expression is used:

$$Q_{\text{rad}} = \epsilon_{\text{eff}} A_{\text{dr}} F_{\text{hc}} \sigma (T_{\text{h}}^4 - T_{\text{c}}^4) + \epsilon_{\text{eff}} A_{\text{dr}} F_{\text{hch}} \sigma (T_{\text{h}}^4 - T_{\text{ch}}^4) \quad (9)$$

where:

Q_{rad} = heater losses by radiation, W,

A_{dr} = direct radiation area, m^2 ,

F_{hc} = heat-cooler view factor,

F_{hch} = heat-chamber view factor,

T_{ch} = chamber walls temperature, $^{\circ}\text{C}$,

T_{c} = cooler temperature, $^{\circ}\text{C}$

Heat Losses' Values

Table 1 presents the mean heat losses values, for the similar apparatus, for the five temperature levels tested.

EXPERIMENTAL ERRORS ANALYSIS

The calculation of the experimental standard errors is done based in reference 3. There are two types of data: the measured ones, that include the temperatures, voltages and electrical resistances, and the data obtained through mathematical models, like the thermal resistance and losses.

Some procedures are adopted to minimize the first type experimental errors. The heater, cooler, Celeron table and chamber temperatures are taken several times (about 100 measurements) so as to allow the calculation of mean value and the associated standard deviation. As there are small temperature variations with time in some measurements (the steady state conditions are not perfectly achieved, but in levels considered satisfactory), a linear regression to calculate the standard deviation values is used. The voltage values are taken two times together with the first and last temperature measurements. To improve results, a high precision voltmeter is used. The same procedure is used to the electrical resistance measurements.

In the second case, where the results are obtained indirectly, it is necessary to make some error propagation studies. It is considered that the experimental errors have a Gaussian distribution around their mean. The associated uncertainty is considered as two times the standard deviation, that corresponds to the 95.4% probability level. Considering that the experimental measurements are independent, the following formulation, illustrated by a simple example, is used in this work: suppose that a certain quantity U is obtained indirectly through the independent measurement of three parameters with mean values u , v and w , and with the associated standard deviation: σ_u , σ_v and σ_w . The experimental error is given by:

$$\sigma_U^2 = \sigma_u^2 \left(\frac{\partial U}{\partial u} \right)^2 + \sigma_v^2 \left(\frac{\partial U}{\partial v} \right)^2 + \sigma_w^2 \left(\frac{\partial U}{\partial w} \right)^2 \quad (10)$$

The determination of the thermal resistance values, (see equation 1) is made by the ratio of the temperature difference between the heater and cooler and the net heat flow through the joint. The temperature difference uncertainty is obtained by the square root of the heater and cooler temperature uncertainties squared summation:

$$\Delta(\Delta T) = \sqrt{(\Delta T_h^2 + \Delta T_c^2)} \quad (11)$$

To the calculation of the net heat flow equation 2 to 9 are used. To the experimental uncertainties calculations, a formulation similar to equation 10 is applied. Some measurements like surface emissivities, component materials' thermal conductivity, some temperatures, etc, useful in the heat losses calculation are not available, being estimated (like their uncertainties), by literature data or some complementary calculation.

Table 1 presents the mean uncertainties values, for the similar apparatus, for the five temperature levels tested.

STANDARD ERRORS' DETERMINATION

Ten similar apparatus for the two types of bolted joints studied (a total of twenty) are tested in each temperature level, to allow statistical data treatment, and as a consequence, the thermal resistance standard error calculation, given by the equation (see reference 4):

$$\text{standard error} = \frac{\sqrt{\text{standard deviation}}}{\text{similar apparatus number}} \quad (12)$$

Note that this value is different from the experimental uncertainties. The first refers to the experimental measurements errors and the second to the actual variation found among several similar actual bolted joints. The standard deviation is obtained from the thermal resistance values calculated for each apparatus. The associated standard error, together with the resistance mean values must be used in the satellite thermal designs.

It was applied the Chauvenet Criterion (see reference 3) in the determination of possible bad results, so that the sample 11 thermal resistances results must be rejected to the mean and standard errors calculation.

In table 1, the standard errors' values are compared with the uncertainties' averages for all the temperature levels.

GENERAL REMARKS

The thermal resistance as a function of the heater and cooler mean temperatures, for the two types of joints studied is presented in figure 5. The resistance values for the floating nut insert are always greater than those for the fixed one. This effect is expected because there are more surfaces in contact in the floating nut insert, as can be seen in the Figures 2 and 3. In the floating insert, the heat coming from the washers or bolt, must pass through the contact between the nut base (in disk format) and the insert body, to reach the honeycomb panel. In the fixed insert the heat path is simpler, since the insert and nut form the same body.

Another important observed effect is the variation of the thermal resistance with the temperature. It is more evident at low temperature levels: as the mean temperature increases, the resistance tends to a constant value. This can be explained studying the thermal properties' behaviour of the joints' components with the temperature variation. The epoxy+fiberglass washers coefficient of thermal expansion is around 59 m/m/k; for the aluminum, this property is around 22 m/m/k, and for the stainless steel this value is near 18 m/m/k. So, there are different contractions among the several joints component materials, with the mean temperature decrease, causing a relief in the contact pressure; the thermal contact resistance is highly dependent on the pressure (see reference 5). Another explanation is the thermal conductivity variation with the temperature; it is small for the metals (7% variation in 200 Centigrades for aluminum) and big for the epoxy+fiberglass material (100% variation in 50 Centigrades).

In figure 6 the thermal resistance results are presented, with the associated experimental mean errors (vertical bars) and the standard errors (dashed lines). In both inserts, it is verified that the experimental and the standard errors are equivalent for the same temperature levels. The experimental errors are always lower than the standard errors, excepting the thermal resistance of the lowest mean temperature level. This means that the experience was planned correctly; if the experimental errors were bigger than the actual joint resistance variation, it would not be possible to determine, with confidence, the mean value and its variation, to be used in satellite thermal design. In the lowest temperature level resistance, the experimental uncertainty is bigger than the standard error, so that the resistance mean and its expected variation can not be well established.

An interesting point to note is the difference of the experimental errors for the several calculated parameters. As is shown in table 1, the heat losses' calculation presents the highest experimental uncertainty level, sometimes reaching 50% of the total heat losses calculated. This happens due to the coarse estimation of some physical and thermal properties. But, as the losses are small, this uncertainty has a small propagation in the joint thermal resistance uncertainty (its value is around 0.5 to 3 %).

It must be noted that the joints thermal behaviour could be better understood if more thermocouples were installed in the experimental apparatus; this was impossible due to the heat losses' increasing, and the consequent experimental uncertainty increasing.

CONCLUSION

The main objective of this work, that is to measure experimentally the thermal resistance of the first brazilian satellite bolted joints, was achieved. The resultant data have been used in the satellite designs and the satellite thermal model tests have confirmed the joints thermal resistance accuracy. The experiment planning, the apparatus design, the number of similar bolted mountings, the procedures to avoid heat losses, are good enough to give the expected results, so that equivalent experimental works are recommended for future bolted joints' thermal resistance researches.

In spite of the fact that the experiment is specific for these junctions, its results can be extended to other types of bolted joints, by some theoretical study.

The effect of the thermal resistance variation with the temperature suggests that these joints can be used as a satellite active temperature controller. It is necessary to make more measurements in the curves' elbow regions (see figure 6) to study this effect with more precision.

Some numerical analysis of the thermal resistance of bolted joints is always important to do in these studies. An apparatus nodal division was made in past experiments for use in a satellite thermal analysis program developed at INPE, but up to date numerical data is not available. The numerical studies are simpler and cheaper, and must be used if they produce good results; the main difficulty is that all the necessary physical properties and thermal contact resistances must be well known before the numerical calculation. The main advantage of the experimental work is that all the interactions between the components of the joints are reproduced, not requiring theoretical studies, neither physical properties' measurements (if the heat losses are kept low).

FUTURE WORK

These bolted joints thermal resistance studies are complex and has just begun. Some suggested future work is planned to be done. First, it is suggested to make more measurements, using this same experimental mounting, in low temperature levels (elbow curves regions) to study the joints' thermal behaviour. A numerical analysis of the experimental apparatus, would be interesting, and it is suggested here. Another suggestion is the study of the influence of the bolted joints' individual components, as washers, bolts, etc, in the joints' thermal resistance. This can be done with this same apparatus, just varying, for instance, the number or material of washers and comparing the experimental results.

REFERENCES

1. Arpaci, V.S.: Conduction Heat Transfer. Addison-Wesley Publishing Company, 1966, pp 144-149.
2. Mantelli, M.B.H.: Multilayer Thermal Insulation Tests. Proceedings of the First World Conference on Experimental Heat Transfer, Fluid Mechanics, and Thermodynamics, sept. 4-9, 1988, Dubrovnik, Yugoslavia.
3. Moffat, R.J.: Describing the Uncertainties in Experimental Results. Experimental Thermal and Heat Science. Vol.1, 1988, pp 3-17.
4. Cox, D.R.: Planning of Experiments. John Wiley & Sons Inc., New York, 1958.
5. Mantelli, M.B.H., Pilchowski, H.U.: Thermal Contact Resistance - A Comparison of Methods. Edited by A.E. Bergles, Rensselaer Polytechnic Institute, Troy, New York.

TABLE 1. RESULTS

											UNCERTAINTIES						
INSERT NUT TYPE	MEAN TEMPER. (°C)	TEMPERAT. (°C)		POWER DISSIP (W)	HEAT LOSSES (W)	THERMAL RESIST (°C/W)	HEAT LOSSES (WATTS)				TEMPERAT. (°C)		HEATER POWER (WATTS)	HEAT LOSSES (WATTS)	TH. RESIST. (°C/W)	STD ERR.	
		HEATER	COOLER				T.C.	ELECTR.	MLI	RADIAT.	HEATER	COOLER					
FLOAT.	0.685	35.125	-33.754	1.46290	0.0768	49.710	0.00607	0.01783	0.01540	0.03751	0.190	0.523	0.00608	0.02802	1.105	1.370	
FIXED	6.216	26.495	-14.062	1.42177	1.3507	30.111	0.00556	0.01652	0.01434	0.03507	0.198	0.427	0.00590	0.02133	0.620	1.012	
FLOAT.	-16.276	10.444	-42.996	0.99867	0.0490	56.402	0.00375	0.01200	0.00767	0.02617	0.264	0.289	0.00501	0.01855	1.216	1.575	
FIXED	-10.995	4.698	-26.681	0.96884	0.0454	34.075	0.00347	0.01061	0.00696	0.02439	0.306	0.261	0.00486	0.01375	0.717	0.996	
FLOAT.	-25.044	-1.705	-48.383	0.61250	0.0423	81.901	0.00348	0.01033	0.00672	0.02182	0.213	0.187	0.00471	0.01660	2.515	2.314	
FIXED	-22.877	-9.272	-36.482	0.59528	0.0364	49.165	0.00307	0.00839	0.00558	0.01931	0.205	0.227	0.00457	0.01194	1.455	2.347	
FLOAT.	-47.301	-29.168	-65.433	0.34592	0.0262	113.477	0.00199	0.00697	0.00288	0.01440	0.202	0.209	0.00295	0.01223	4.515	3.159	
FIXED	-42.762	-32.526	-52.997	0.33620	0.0243	65.912	0.00185	0.00604	0.00265	0.01371	0.231	0.207	0.00286	0.00829	2.131	2.204	
FLOAT.	-74.589	-61.907	-87.272	0.08371	0.0140	364.682	0.00109	0.00388	0.00117	0.00791	0.327	0.275	0.00145	0.01040	54.569	10.031	
FIXED	-72.249	-65.076	-79.422	0.08136	0.0128	210.475	0.00099	0.00324	0.00106	0.00750	0.230	0.505	0.00140	0.00577	20.307	9.017	

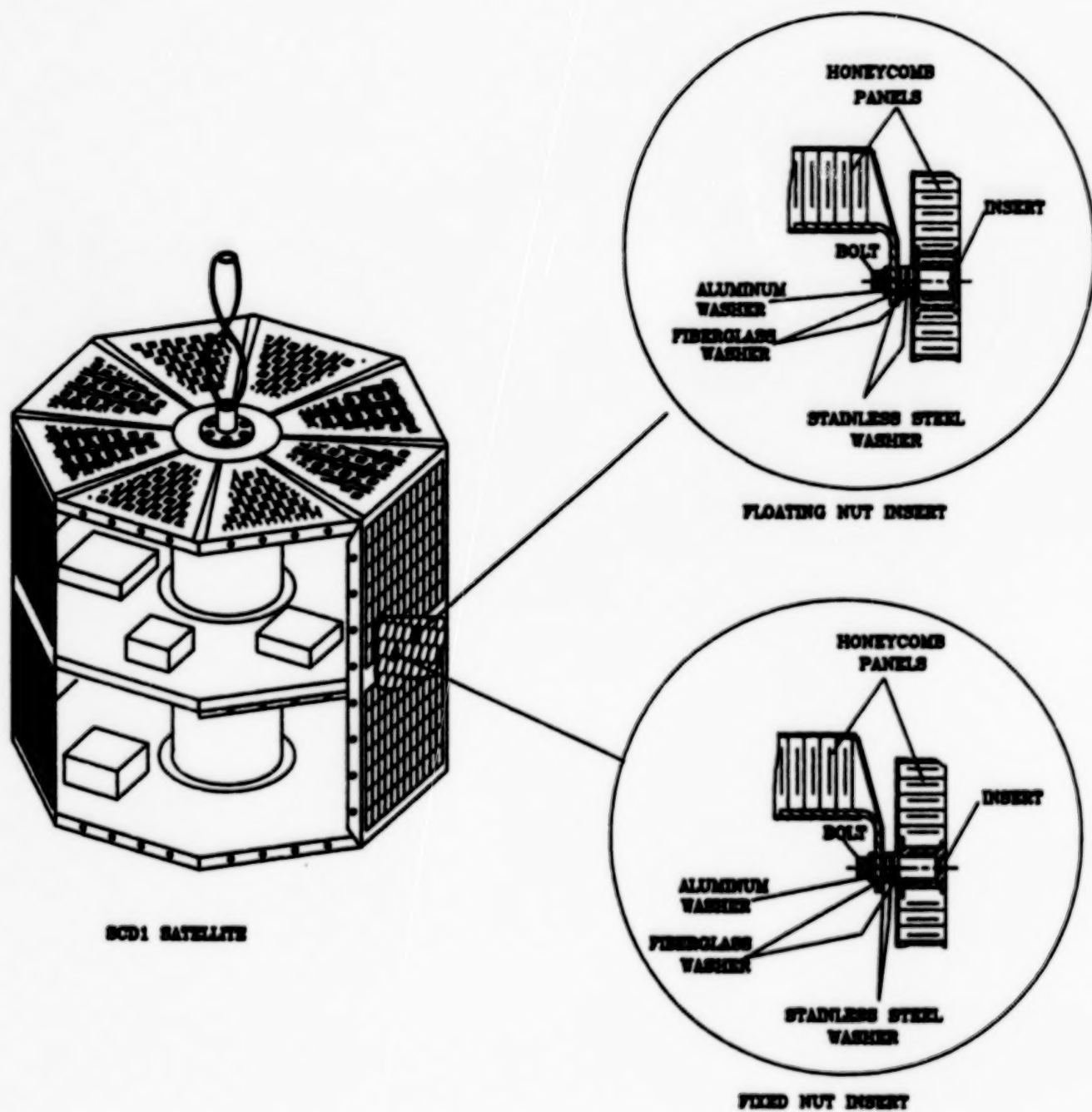


Figure 1. SCD1 schematic view, with the localization of the studied bolted joints.

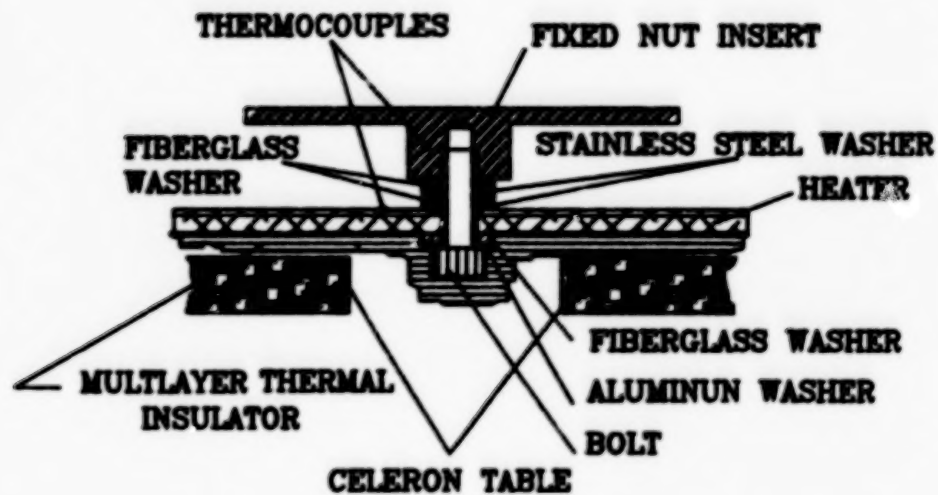


Figure 2. Fixed nut insert joint experimental apparatus

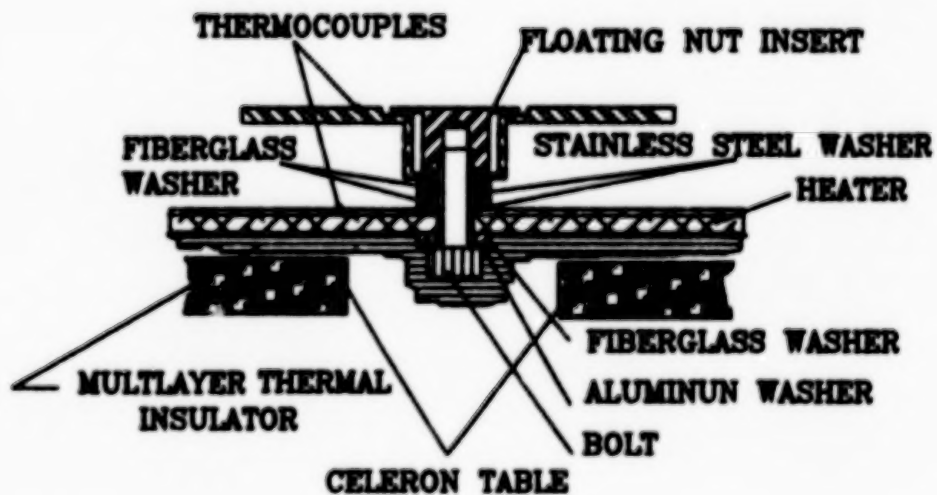


Figure 3. Floating nut insert joint experimental apparatus.

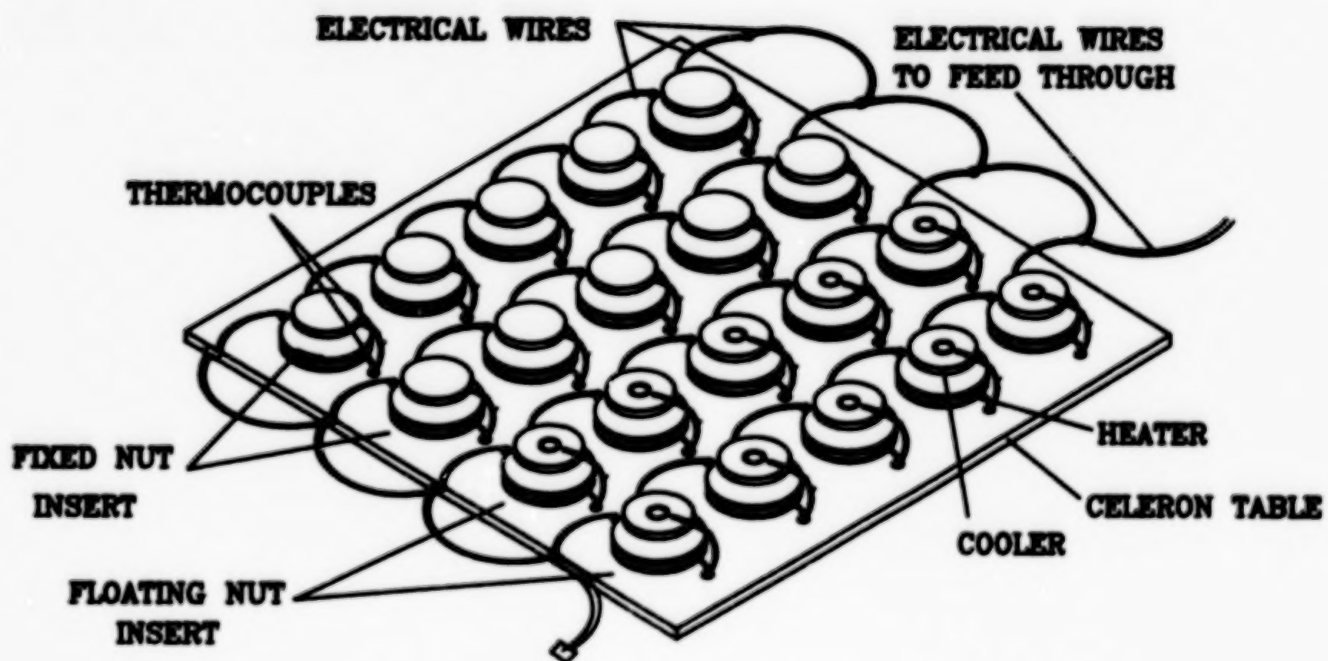


Figure 4. Final experimental mounting in Celeron table.

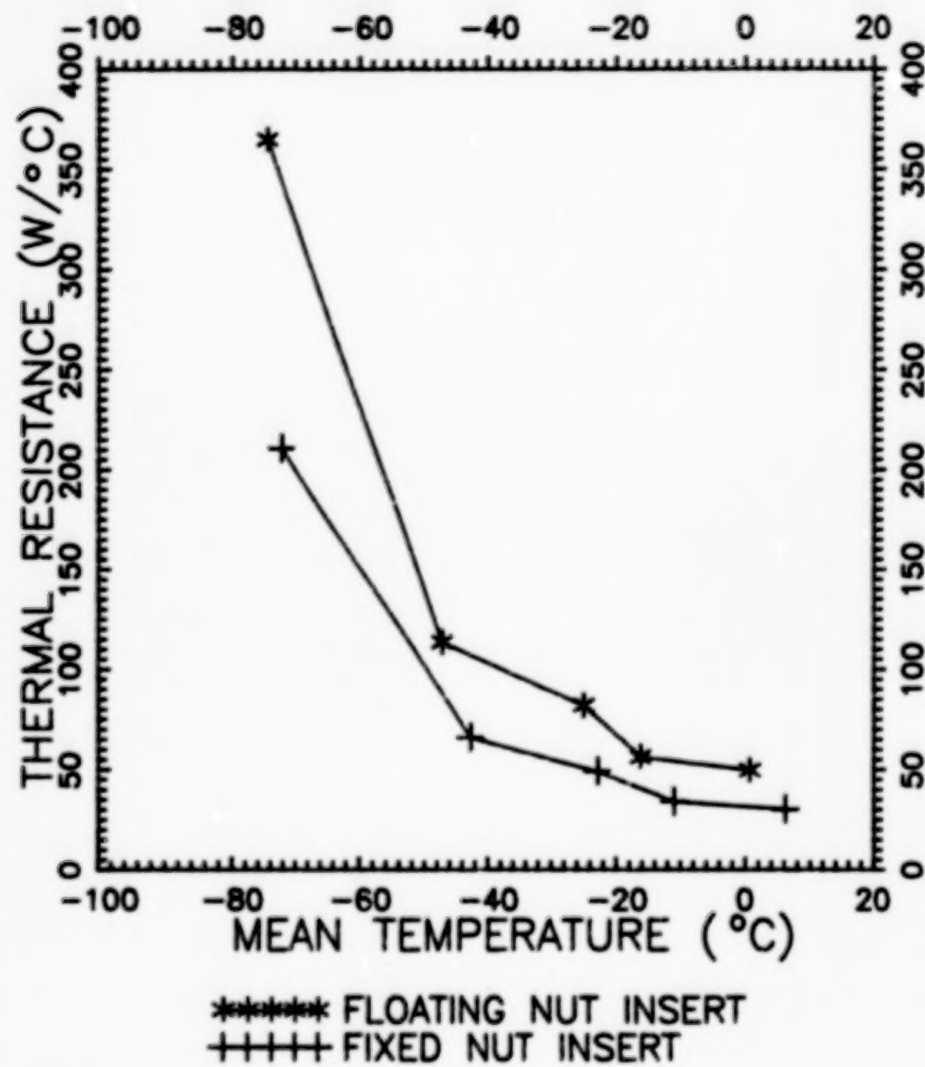


Figure 5. Thermal resistance as a mean temperature function for the two studied joints.

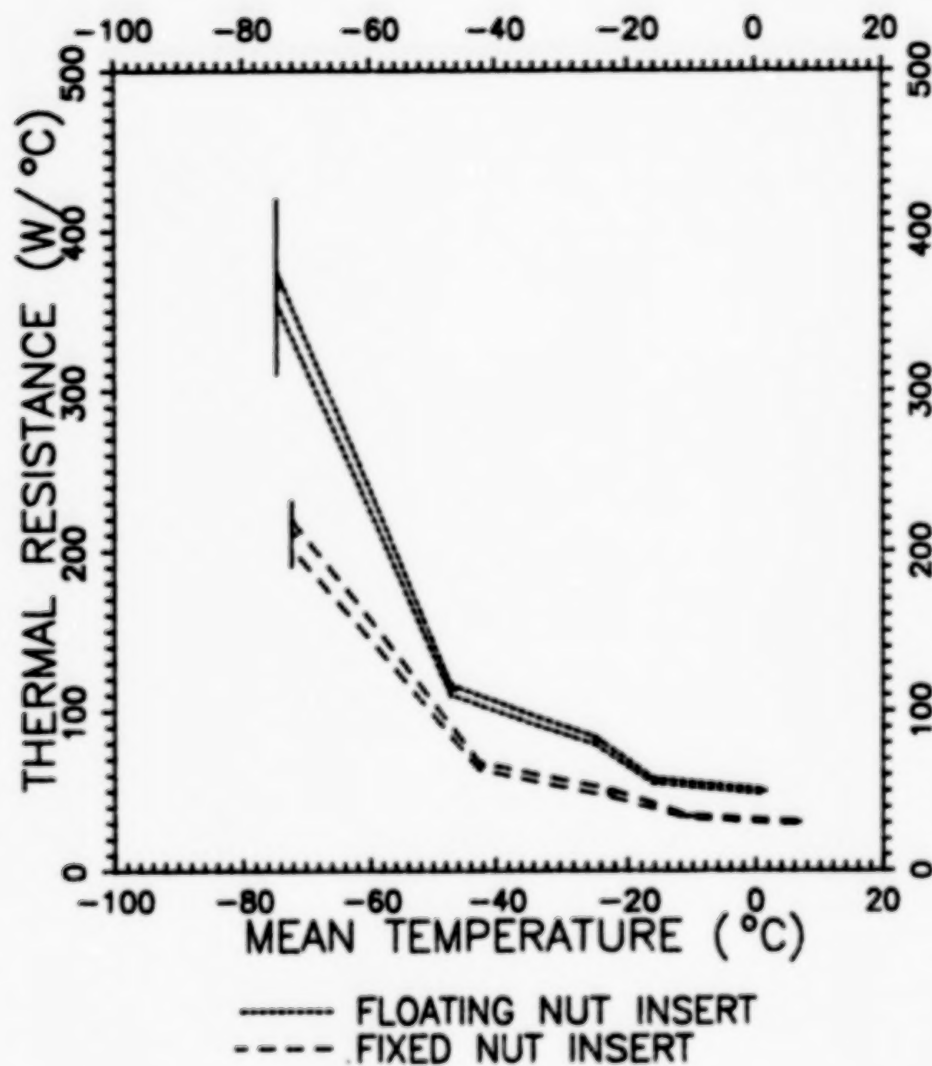


Figure 6. Thermal resistance as a mean temperature function with its associated experimental and standard errors.

MAGNETIC CLEANLINESS VERIFICATION APPROACH ON TETHERED SATELLITE

Piero MESSIDORO, Massimo BRAGHIN, Maurizio GRANDE

AERITALIA SAIPA
Space Systems Group
Torino - Italy

ABSTRACT

Magnetic cleanliness testing has been successfully performed on the Tethered Satellite as the last step of an articulated verification campaign aimed at demonstrating the capability of the satellite to support its TEMAG (TEthered MAGnetometer) experiment. Tests at unit level and analytical predictions/correlations using a dedicated mathematical model (GANEW programme) are also part of the verification activities. Details of the tests are presented, and the results of the verification are described together with recommendations for later programmes.

INTRODUCTION

Nowadays the complexity of earth magnetosphere and ionosphere research by satellites is increasing; in this sense new and more advanced and innovative research methods are necessary. An opportunity for improvement in the knowledge of the Earth Magnetic Field at Low Earth Orbit altitude is provided by the Tethered Satellite System (TSS).

It is a joint project between the Italian Space Agency (ASI) and the United States National Aeronautics and Space Administration (NASA). Its goal is to test the feasibility of deploying, controlling and retrieving a Tethered Satellite from the Space Shuttle, as well as to demonstrate the system's usefulness for scientific research.

The TSS consists of an instrumented satellite, a thin, flexible tether up to 100 km long, a deployer attached to an enhanced Spacelab pallet in the Shuttle cargo bay, and scientific experiments on the satellite as well as in the cargo bay.

The Aeritalia Space Systems Group is the Italian prime contractor for TSS, responsible for the satellite. Martin Marietta - Denver Aerospace (MMA) is the American prime contractor responsible for the deployer and furnishing the tether. NASA is providing the pallet and an experiment carrier for the cargo bay. Both NASA and ASI will provide the science payloads being developed by selected experimenters.

The tether and satellite will be deployed from the Space Shuttle while it remains in orbit at an altitude between 230 and 300 km. In the first TSS mission, scheduled for the second half of 1991, the satellite and an electrically conductive tether 20 km long will be deployed above the Shuttle (spaceward) to study the electrodynamic magnetic fields and plasma properties.

The first TSS Mission is shown in Fig. 1.

In particular, this mission will test the feasibility of generating electricity with the tether as it cuts through the Earth's magnetic field. This could demonstrate a new source of auxiliary power for future spacecraft and space stations.

During the second TSS mission, anticipated to follow about two years after, the satellite will be deployed on a 100 km tether below the Shuttle (Earthward). In this configuration it will be possible to lower the satellite as far down as 130 km above Earth to reach a region of the atmosphere that previously could only be studied for brief periods by sounding rockets.

The TEthered MAGnetometer (TEMAG) payload is the experiment dedicated to the magnetic exploration of the TSS-S flight mission environment, on a well-known satellite magnetic status base; in this sense a Magnetic Cleanliness programme, to acquire knowledge of the magnetic properties of the satellite seen as a multipole, was necessary. In particular, a Magnetic Cleanliness verification campaign, comprising unique analysis and test steps has been performed at both unit and system levels.

The paper presents the Tethered Satellite characteristics and related magnetic cleanliness requirements, for the proposed combined verification approach and the test methods/facilities/results at equipment and system level. Suitable conclusions and recommendations for the next programmes are also included.

TETHERED SATELLITE

CONFIGURATION

The TSS-1 Satellite (TSS-S) is a retrievable vehicle, capable of carrying and supporting various scientific payloads simultaneously, up to 20 km away from the Orbiter.

The main characteristics of the TSS-1 satellite are:

- Current mass 518 kg and Diameter 1.6 m
- Spin-up/spin-down capability from 0 to ± 1.0 RPM (Present baseline is ± 0.7 RPM)
- Electrical connection between P/L and Tether, skin treated to allow current flow
- Telemetry Rate 16 kbps and Command Rate 2 kbps.

Fig. 2 shows the TSS satellite during integration activities at Acritalia. Details on Tethered Satellite characteristics and operations can be found in Ref's 1 and 2.

The capacity of the TSS-1 is provided by a carrier approach and a modular concept of the Satellite configuration which comprises: an auxiliary propulsion module, a service module and a payload module.

Propulsion Module

The propulsion module has one subsystem, the auxiliary propulsion subsystem (APS) which includes the GN2 tank, the in-line, in-plane, out of plane and yaw control thrusters, piping and valves to allow yaw attitude, yaw spin and Satellite translational position control.

All the APS parts except for the in-line thrusters are located on the equatorial floor. The APS is a cold gas (nitrogen) propulsion system so as not to contaminate the sensitive payload or the satellite external environment.

Service Module

The service module includes the following subsystems.

- **Structure and Mechanism Subsystem (SMS)** - The basic concept and the main components of the TSS satellite structure are shown in Figure 3.
The satellite has two fixed booms, for mounting the S-band antenna and science instrumentation respectively and two deployable/retrievable booms carrying science instrumentation.
Four access doors are provided for battery installation at KSC in the Orbiter bay in the vertical position. The tether attachment is the mechanism provided to allow mechanical and electrical tether connection to the satellite.
- **Electrical Power and Distribution Subsystem (EPDS)** - The internal power source of the TSS-S is a battery system, consisting of four silver-zinc (Ag-Zn) batteries, arranged in series/parallel.
A power command distribution assembly (PCDA) basically performs the distribution of the power to the subsystems and the conditioning of some commands dedicated to the activation of relays and valves.
The payload power distribution assembly (PPDA) is a distribution unit dedicated to the payload and is in the payload module.
- **Harness Subsystem (HRNS)** - The HRNS provides electrical interconnections for the distribution of the electrical power and signals between all satellite units, units to EGSE skin connector, and units to umbilical connectors.
- **On-Board Data Handling Subsystem (OBDH)** - The OBDH S/S consists of the following units: Central Terminal Unit (2 microprocessors - 1 dedicated to AMCS processing), Memory Bank Unit, Remote Terminal Unit Service, Remote Terminal Unit Payload (mounted within payload module), Decoder and OBDH Busses.
The OBDH is immediately powered as soon as the PCDA receives power from the batteries or from the TSS-Deployer.
Upon power-up, the OBDH will automatically perform a self check providing the results in the TLM page and then the software programs to support the mission will resume. In addition, the OBDH will be ready to execute/distribute commands coming from the umbilical hardline sent through Radio Frequency (RF) link.

- **Attitude Measurement and Control Subsystem (AMCS)** - The AMCS determines the TSS-S attitude and provides telemetry on Satellite vector yaw, pitch and roll measurements. The AMCS controls the yaw attitude and the TSS-S spin rate. The AMCS processor is part of the OBDH subsystem. The AMCS includes the TSS-S gyroscope package, sun sensor package and earth sensor package.
- **Telemetry and Telecommand Subsystem (TT&C)** - The TT&C provides the S-band link between the satellite and orbiter when the TSS-S is in the detached mode.
TT&C functions include telecommand/data reception, telemetry data transmission, and subsystem housekeeping. It consists of the S-band antenna, S-band transponder and RF cable.
- **Thermal Control Subsystem (TCS)** - In order to guarantee a suitable thermal environment for the satellite, the TCS makes use of the following components/materials: paints on external skin, Multi-layer Insulation blankets on equipment, fillers, heaters and thermostats for heater control.
- **Engineering Instrumentation Subsystem (EIS)** - In order to verify that the satellite thermal environment remains within the allowed limits during the mission phases, the EIS provides monitoring by means of redundant thermal switches and sensors.

Figure 4 shows a TSS-S synthetic block diagram showing the interfaces with Deployer, Orbiter and Payloads.

Payload Module

The payload module provides accommodation for the four scientific payloads. Experiments/sensors are located inside the payload module, on the external Satellite skin, on an external dedicated fixed boom and on the Deployable Retrievable Booms. The payloads on the Satellite for TSS-1 are:

- Magnetic field experiment for the TSS missions (TEMAG) by University of Rome
- Research on Electrodynamic Tether Effects (RETE) by Institute Fisica Spazio Interplanetario, CNR
- Research on Orbital Plasma - Electrodynamics (ROPE) by Space Science Laboratories, MSFC
- Satellite Core Equipment (SCORE) by Aeritalia

In particular the TEMAG Experiment consists of the two magnetometers and their electronic package. Each FluxGate Magnetometer (FGM) unit contains three monoaxial fluxgate sensors in a mutually orthogonal array measuring the vector magnetic field in the frequency band from DC to 8 Hz. One unit (FGM/O) will be mounted at the tip of the Satellite fixed boom and the other (FGM/I) on the same boom close to the Satellite (see Fig. 2).

VERIFICATION AND TEST PROGRAMME

On the basis of the programme's industrial architecture, the overall design and performance requirements relevant to the TSS-Satellite are contained within a set of dedicated specifications and Interface Requirement/Control documents.

The levels through which verification of the above Tethered requirements has been performed incrementally are: system, satellite, payload, subsystem, unit. The verification methods established for the TSS are: Similarity, Analysis, Demonstration, Validation of Records/Design, Test.

The test effectiveness is for qualification of acceptance; development tests are not considered valid for formal verification close-out.

The definition of the applicable verification methods for each satellite requirement originated a coherent model philosophy as summarised in Fig. 5.

The correspondent system Integration and Test Programme foresees: a Structural Model on which a complete structural qualification test campaign (i.e. Physical Properties, Model Survey, Acoustic, Alignment and Leak tests) has been carried out at IABG's laboratories in Munich; an Engineering Model on which a functional test campaign (i.e. Magnetic Cleanliness Measurements, Service Module Test, Payload Module Test and Satellite Integrated Test) has been performed in Aeritalia; a Flight Model, subjected to functional and environmental acceptance tests (i.e. Functional, EMC, Physical Properties, Alignment, Thermal Vacuum/Balance, Acoustic, Leak and Magnetic Cleanliness Test) at the IABG facilities.

Ref. 3 contains details of the TSS Satellite Integration and Verification philosophy.

MAGNETIC CLEANLINESS VERIFICATION

Requirements and Verification Approach

Magnetic cleanliness requirements have been specified on TSS-S with the objective to know and possibly limit the magnetic contamination of the TEMAG experiment measurements due to the satellite magnetic field.

In fact, the satellite background has to be subtracted from the experiment measurements, performed at LEO altitude, in order to get reliable data of TEMAG magnetic exploration. The level of "cleanliness" for the satellite magnetic environment has been specified as a design goal in terms of 20nt at FGM/O location, associated with an acceptable degree of magnetic stability (± 1 nt).

The verification of the satellite compatibility to the above requirements and the associated evaluation of its magnetic emission and susceptibility was performed using a combined analysis/test verification approach as shown in Fig. 6.

In particular the approach used develops test activities at both unit and satellite levels associated with iterative analysis campaigns worked out by means of a suitable software programme.

The system analytical model has been developed by using test results of the majority of the satellite units and has been used to predict the system test results. Final validation of the system model, including the contribution of the parts not tested at unit level (for example the structure), has been performed correlating the system test results.

In addition, the chosen incremental verification approach allowed a better control of the TSS-S Flight Unit magnetic cleanliness because the verification campaign at unit level provided early evidence of difficulties in meeting the system cleanliness requirement and suggested useful recommendations for system design and test.

Model and Analysis

The tool used to perform the magnetic cleanliness analysis is an ESA programme called GANEW (see Ref. 4). It is based on a multiple dipolar modelling of the test object; this method is derived from the postulate that a given magnetic field configuration around a test object can be represented adequately by a finite set of discrete dipoles within the test object at a distance where the multipolar field components can be neglected. Unfortunately, the problem is in general conditioned in the sense that a unique solution identical with the real source involved does not necessarily exist; nevertheless, in some particular cases the approximation to have a dipole model can provide useful information about the real source.

A very effective optimisation procedure of the Gauss-Newton type is used in the programme to determine the dipole positions and moments of the model which reconstitute the magnetic field measurements.

The GANEW programme is associated with a suitable test procedure in the sense that, on the basis of unit test data results, it is able to calculate the magnetic field contribution individually of each unit, and totally of the complete satellite at specified points - for instance FGM/O location for TSS-1.

An important parameter in dipole modelling is the distance between the test object and the measurement probe which has a direct influence on the magnetic field momentum value. In this sense the GANEW programme is used to perform iterative analysis to optimise the test set-up and provide good estimation of the measurement errors.

This shall be possible, before starting with a test, comparing a set of field data generated by a well known magnet (position and moment) in the test object measurement position w.r.t. the probe data results of the coil facility used. After the set-up optimisation process, the results of the measurement performed on the test object rotating around a 360 degree coil turntable plane, elaborating the drift effects by computer, provided already formatted input data for the GANEW programme (see typical data for TSS in Fig. 7)

The programme operates with the above input of rotational measurement to calculate a best fit dipole as unit dipole model in unit coordinates which contributes to the S/L modelling by vectorial superposition of the unit models in S/L coordinates, finally to produce the Synthetic Satellite Model (see TSS example in Fig. 8).

Once a representative and minimum dipole model in the Form of the number of dipoles, their position coordinates and their moment vectors have been found, the S/L model can be used to calculate the magnetostatic field configuration around the test object at virtually any point but no closer to the test object than the nearest measurement point. This is possible by means of the direct mathematical summation of the moments.

By using the established analytical model, it is therefore possible to predict the relevant individual field at FGM/O location provided by one single unit, and the integrated field originated unit by unit (see Fig. 9 for TSS FU Perm phase) for each system test phases of a unit magnetic characterisation. Typical representation of the GANEW programme elaboration using the synthetic Satellite Model for TSS is sketched in Fig. 10 (plane representation) and in Fig. 11 (tridimensional representation). At the end of the system test activities, the analytical model is validated by comparing analysis results with respect to the test results; the final picture of the model represents the satellite configuration to be used for in-flight data evaluation.

Test at Unit Level

Dedicated Magnetic Cleanliness tests have been performed on TSS-S FU units as part of the overall verification campaign, with the objective to provide inputs for the satellite model definition for the following interested conditions: 50 GAUSS Deperm state, 5 GAUSS Perm state and Stray field contribution in the power-on state.

As part of the cleanliness control programme, rules for the design of magnetically clean hardware were established and advice given to TSS-S experimenters and all unit subcontractors. The unit level test campaign has been carried out in AERITALIA Space Systems Group's Integration area in Turin using a mobile coil facility, provided by Technical University of Braunschweig, in which about 41 boxes were automatically mapped through the following test phases (see Ref. 5 for details):

- Initial state
- Initial Deperm 50 GAUSS
- Perm 5 GAUSS
- Final Deperm

Measurements were performed on each box axis on a rotating non-magnetic platform, at the centre of the mobile coil facility, in which a compensating earth magnetic field down to about 0.1 nt is provided by using 2 vertical and 2 horizontal compensation coils.

To Perm/Deperm the unit placed at the centre of the facility as shown in Fig. 12, another 2 lateral Perm/Deperm coils were used, and for measurement a 3-axial-probe was positioned to originate an orthogonal axes reference system on one side of the test object. The probe x-axis pointed towards the centre of the turntable and the z-axis in the direction of the turntable rotation axis (see Fig. 13).

Measurements were taken with the test object turned over 360 degrees by a manual angular resolver of the turntable, and automatically taken in steps of 10 degrees for a total of 36 measurements for each test phase at the end of magnetic field application (Fig. 7 shows the results).

To evaluate stray field contribution due to electric current, the box was powered and measurement taken after performance of the Deperm field, with the unit in OFF and in ON condition.

Quite an important parameter for testing is, of course, the distance between probes and test object; the distance must be chosen reasonably in such a way that a field is mapped approximately on a sphere around the test object, and optimised by means of a calibration magnet before starting the tests.

For correct test results, evaluation was also necessary to specify and provide box Center of Gravity (CoG) geometry w.r.t. the Unit Coordinates System (unit reference hole); the box reference hole geometry relative to Satellite Coordinate System (SCS) and the CoG geometry relative to the centre of the turntable (UCS), as input data for the GANEW programme.

It was important to know the position of each single unit within the Satellite reference system because it was necessary to allocate the magnetic dipole moment representative of the unit, to these positions, to define finally the model of the S/L's global moment. The early verification at unit level was also useful to point out, before the system test, some criticalities, especially for DRBD/A FU experiments.

In fact, interest focussed on the cleanliness investigations of these last items of the model detected that a simple Deperm at Boom stowed, as foreseen during unit level characterisation, was not efficacious, but it was mandatory to effect a dedicated local degaussing to extinguish some hot spots present on accessible Boom parts in Deployed configuration only. In this way it was possible to reduce the otherwise compromised DRBD/A residual magnetic field to the required value.

This was a classic example of positive iteration that made it possible for the system test to evaluate the corrective solution to the problem; in fact an additional dedicated local degaussing of the DRBD/A Boom in deployed configuration was required at the final stage to guarantee the minimum value of residual field to reduce the S/L magnetic emission at FGM/O location.

Therefore, despite incomplete cleanliness (i.e. because of size limitation it was not possible to test structure, APM and Harness) during S/L integration, the results shown in Fig. 8 and in Fig. 9 have been of extreme importance for the overall cleanliness verification. The TSS-S magnetic cleanliness programme performed at unit level can be considered fully accomplished at this point.

Test at System Level

On completion of the overall TSS-S FU cleanliness verification campaign, the magnetic cleanliness test at system level was carried out at the IABG MSFA II coil facility in Munich-Ottobrunn. The test has been developed with the objectives to simulate the S/L in orbit as much as possible to obtain reliable characterisation of the TSS-S FU magnetic behaviour in space flight condition.

A testing of Satellite magnetic emission and susceptibility was mandatory with a complete marking of this influence on the space magnetic environment to be explored by the TEMAG experiment; this is to realise a defined requirements verification on a test method base in terms of: compatibility to the TEMAG environment, and validation of the system analytical model by correlation with the system test results.

The main test objectives pursued during system test were:

- S/L characterisation of emissivity as received
- S/L Deperm measurement and Stray field contribution in the power-on state
- S/L characterisation of susceptibility as Perm state
- S/L characterisation for Induced Fields and Eddy Current effects

The system test was performed within IABG's special Magnetic test facility (Fig. 14) with the satellite installed on a rotating "column" of non-magnetic adaptors positioned at the centre of the coil system, with the S/L x axis aligned with the Probes facility x axis, (measurement position).

During the test, a value of 20NT at FGM/O location was continuously monitored by 4 probes in the vicinity of two FGMO/I and together with a set of strip-chart analog recorders.

Four 3-axial fluxgate magnetometers were used for rotational measurement: complete 360 degrees around S/L z axis for 36 intervals of 10 degrees each one (partial mapping), and ± 20 degrees around S/L z axis for 10 intervals of 5 degrees each one (partial mapping), except the last one which equals the starting measurement (-20 degrees), w.r.t. the S/L measurement position.

The 4 MFSA probes were placed near the FGMO/I magnetometers, 2 vertically (5 cm up and 10 cm down from FGM/I) and 2 horizontally as near as possible to the FGM/O x plane, see Fig. 15.

The test objective has been reached through the following test conditions:

- **Initial State** - The complete 360 degree mapping in 10 degree steps of the S/L as received gives the most important status result of the magnetic behaviour of the TSS-S because, being moved to the ground field environment after the test, it could be permed up as it will be during launch.
- **Deperm state** - The residual magnetic state of the satellite is tested after demagnetisation provided by the facility's Perm/Deperm coils to get evidence of the stray magnetic field, to be kept to the minimum possible. It should be noted that the same values could not be achieved in the different Deperm states because of physical disorientation imparted to the magnetic parts. Magnetic effects could be increased, however, without risking stability.
- **Perm state** - The Perm shows the susceptibility of the Satellite to external fields, like earth field (0.5 Oe), structures, cranes, trucks, and launchers, which may show fields up to 1.5 Oe. Only S/L x axis was detected particularly susceptible to Perm Field. See Run 12 Fig. 17.
- **Stray** - This is the only test which shows the Satellite in power-on condition. Each S/L unit will be switched on, one after the other in the most powerful mode while TEMAG is watching. This is the only test to look for current loops throughout the Satellite as well as possible grounding problems and interference by currents in the structure. The stray field test has been performed actuating equipment critical from a magnetic emission point of view as DRBD/A boom motor and APS valves. The contribution by test estimated at FGM/O location for stray field effects is about 1.7 nt as calculated with linear interpolation of data. Linear interpolation is the worst case in an approximation law representative of the S/L magnetic field distribution in relation to the distance. In reality the S/L field distribution is represented by a hyperbole law on a ratio 1 of 3, and hence the obtained results by modelling are better than with linear interpolation.
- **Temag Calibration and Induced Fields** - Because the satellite contains soft and hard magnetic material, the ambient field (which should be measured) will be deflected if the satellite is moved into the field. Therefore the Magnetometers measurement will show a combination of ambient field and azimuth dependent inductions. This characterisation was also performed during system tests.

- **Eddy Currents** - Any conductive rotating or moving in an ambient field will cause eddy current and these will produce a magnetic field. So any conductive skin shield should be made as thin as possible and be of high resistance.

All conducting structural loops should be avoided. For this purpose, the test at system level has been conducted suspending the S/L with nylon ropes and with two facility magnetometers in differential mode set-up, to detect eddy current originated by S/L effect during a rotating magnetic fields application.

- **Final Deperm** - Final 50 Gauss Deperm field is mostly performed to get a Satellite as clean as possible ready for launch.

Because the TSS-S FU will be moved, transported or stored in the earth field or in possible stronger field environments, this test would not be representative if a dedicated magnetic cleanliness control campaign is not conducted to ensure the required environment of no more than 1.5 Gauss of magnetic field.

On the basis of the above test objectives and conditions the following sequence was executed during the S/L magnetic cleanliness test (see Ref. 6 for details):

- * facility calibration (well-known magnet used)
- * S/L as received measurement (partial mapping/mapping - RUN's 3 and 2)
- * DRBD/A deployment
- * S/L sniff test and DRBD/A local degaussing
- * DRBD/A retrieval
- * Initial S/L measurement (partial mapping/mapping - RUN 7)
- * First deperm
- * First deperm measurement (partial mapping/mapping - RUN's 6 and 7)
- * TEMAG calibration
- * Induced field
- * Perm S/L on each single X,Y,Z axes at four different levels of Perm field - 1,2,3,5 Gauss - executing at the end of each field application a sniffing of the fixed Boom and a partial mapping. Mapping measurement was only performed for the last 5 Gauss Perm field applications at S/L Z axis (RUN's from 8 to 21).
- * Second deperm 50 Gauss
- * Measurement (partial mapping/mapping - RUN's 23 and 22)
- * Stray field (measurement on S/L fixed position - RUN's 24)
- * Final deperm
- * Measurement (partial mapping/mapping - RUN's 26 and 27)
- * Eddy current

Sniff tests are included in most test phases to guarantee that the level of residual magnetic field is not disturbed by local sources of magnetism (hot spot) that often were the most frequent causes of an increase in the S/L magnetic contribution at FGM/O location. For example the field has been significantly reduced (see RUN's 4 and 7 of Fig. 17) by local degaussing of some hot spot presence on the ROPE experiment, positioned below the S/L FGM/O unit.

It is pointed out that to detect the hot spot a dedicated sniff test is needed, otherwise the usual rotational measurement is not able to locate these local sources.

To get the best value resolution of the 20 nT verification, a range measurement has been adopted about each 5 degree around ± 20 degree w.r.t. the Satellite measurement position. These data have been approximated to worst case requirement evaluation by means of a linear interpolation of the two probes data closed to FGM/O.

The local degaussing activity on DRBD/A boom, for hot spot extinguishing at boom deployed, decreased the value of magnetic field from 32.5 nT to 27.1 nT (RUN's 3 and 6 of Fig. 17)

From data observation of partial mapping measurement and mapping measurement of the same test phase, it is possible to have an idea of how real the modelling elaboration is w.r.t. to the linear interpolation of the facility probe data results. GANEW modelling elaboration and the facility test evaluation have revealed differences of about 2.5 nT (see RUN's 4/7/29 of Fig. 17. This 10% of difference between model and test results gives positive answer to the validation of GANEW mathematical model.

With regard to the testing environment, the design goal of 20 nT has been acceptably approximated (25.9 nT, see Fig. 18) with a good degree of S/L magnetic field stability, only 1 Gauss of difference between the 1st and 3th deperm, which is fundamental for the offset value to be subtracted from TEMAG reading performed in flight condition.

The complete Magnetic Cleanliness campaign on TSS-S FU could be considered successfully performed at this level. To preserve the Satellite Magnetic status until the launch date, only a detailed activity with interest of magnetic cleanliness control is required, i.e. not to expose the TSS-S FU to a field exceeding 1.5 Gauss.

CONCLUSIONS

The Tethered Satellite Magnetic Cleanliness Verification Campaign has been successfully carried out through a series of test activities at unit and satellite levels involving unique test set-ups and facilities. Those activities have been combined with analytical evaluation using a specific programme which originated a magnetic model able to support TEMAG flight measurements.

The Experience gained on Tethered Satellite supports possible improvements for future projects; the major recommendations are:

- the verification campaign should be helped by a more stringent magnetic cleanliness control in terms of design verification and magnetic cleanliness follow-on during manufacturing and integration
- a complete test campaign at unit level, including all the satellite parts as much as possible, is fundamental for early critical point discovery and fixing
- increasing sniff test executions during test at unit level will improve the knowledge of S/L hardware magnetic properties that is of extreme importance for implementation of the Magnetic Cleanliness control campaign
- an increasing of perm magnetic field on satellite level to values up to 10 Gauss should offer a suitable margin for the susceptibility verification not only for the flight environment but also for the ground environment
- final system test could not be recommended if the Satellite is not ready for launching after testing, but has to be moved, transported or stored to earth field or a stronger field environment. In this case the final deperm should be postponed.

REFERENCES

- 1] J. Sisson - *Tethered Satellite System, Workshop Proceedings, Applications of Tethers in Tethers in Space Conference, Venice, 15-17 October, 1985*
- 2] F. Bevilacqua, M. Pasta, F. Lucchetti, B. Musetti - *Tether Space Systems: current and future applications, AIDAA Symposium, Pisa, 1989*
- 3] M. Braghin, G. Pipino, P. Messidoro - *TSS-S Assembly Integration and Verification Plan, TS-PL-AI-005, issue 8 1989 (Aeritalia document)*
- 4] K. Mehlem - *Magnetostatic cleanliness analysis by the multiple dipole modelling method, ESA-SP-136 Proceedings of EMC Seminar, Estec, May 78*
- 5] S. Sferlazza - *TSS-S Magnetic Cleanliness Unit Test Procedure, TS-PR-AI-086 (Aeritalia document) July 1988*
- 6] M. Grande, M. Braghin, P. Messidoro - *TSS-S FU Magnetic Cleanliness Test Specification, TS-SP-AI-427, issue 2 1990 (Aeritalia Document)*



Fig. 1 - Tethered First Mission

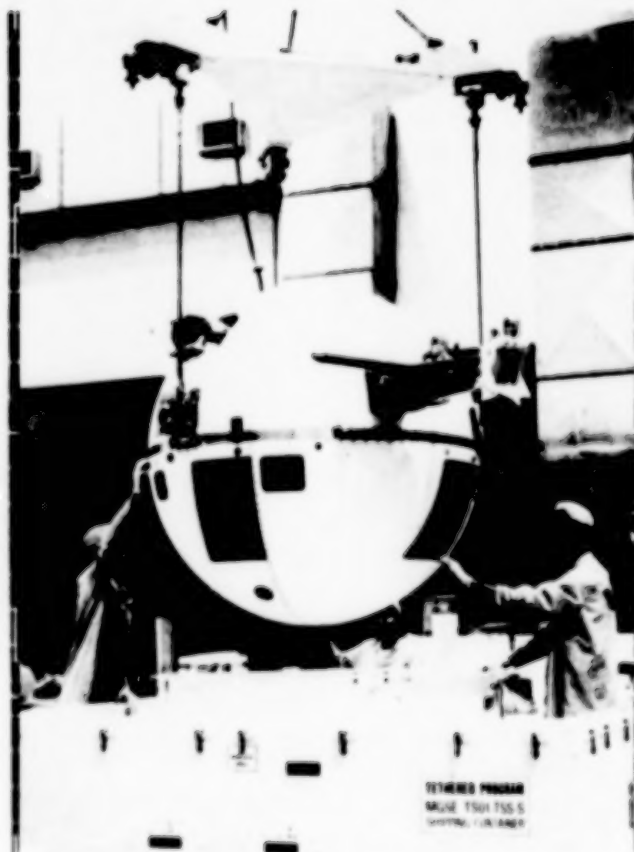


Fig. 2 - TSS Satellite

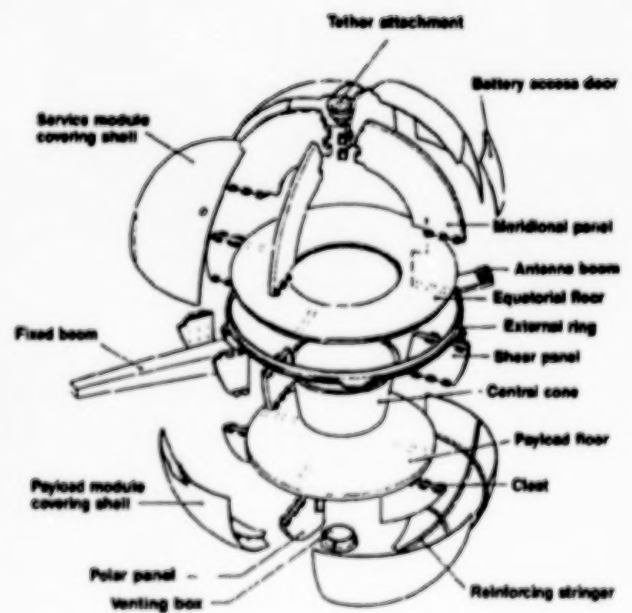


Fig. 3 - TSS-S Structural Exploded View

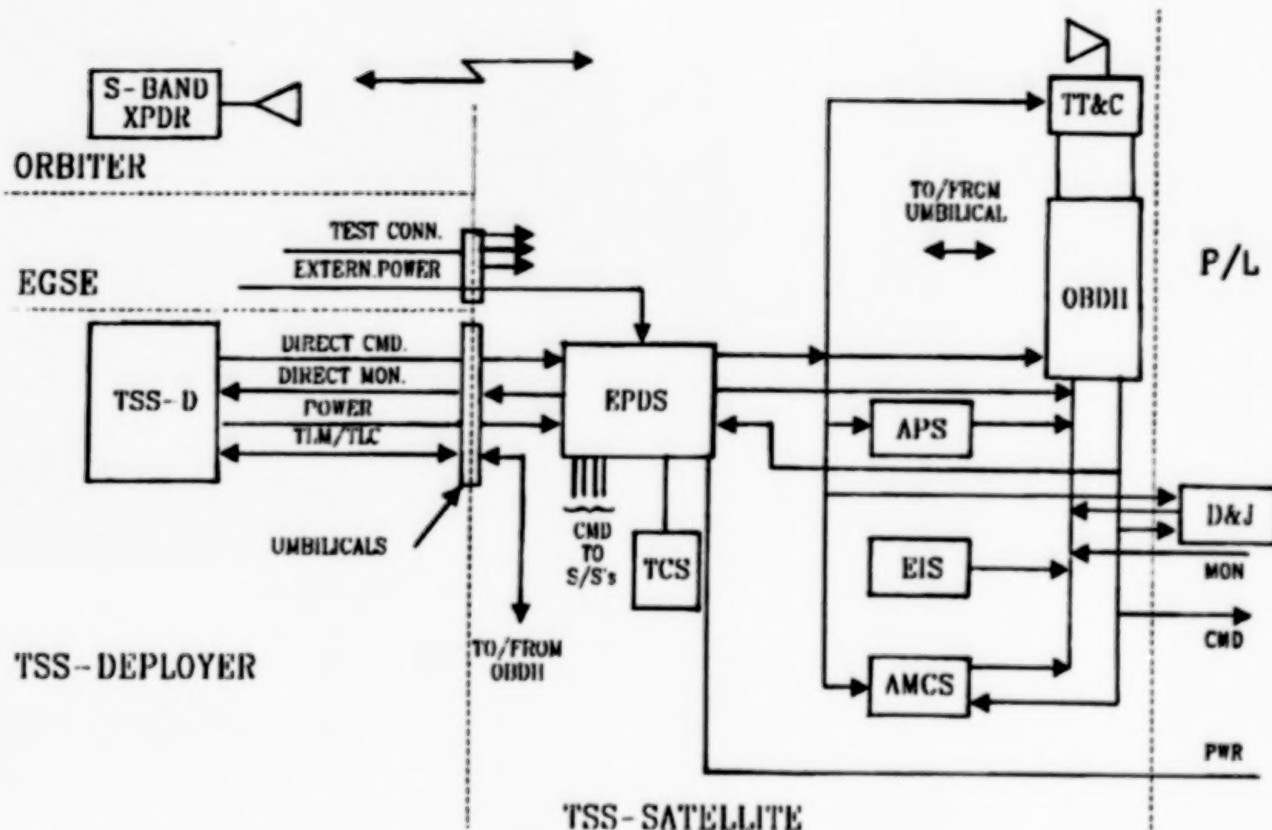


Fig. 4 - TSS-S Functional Block Diagram

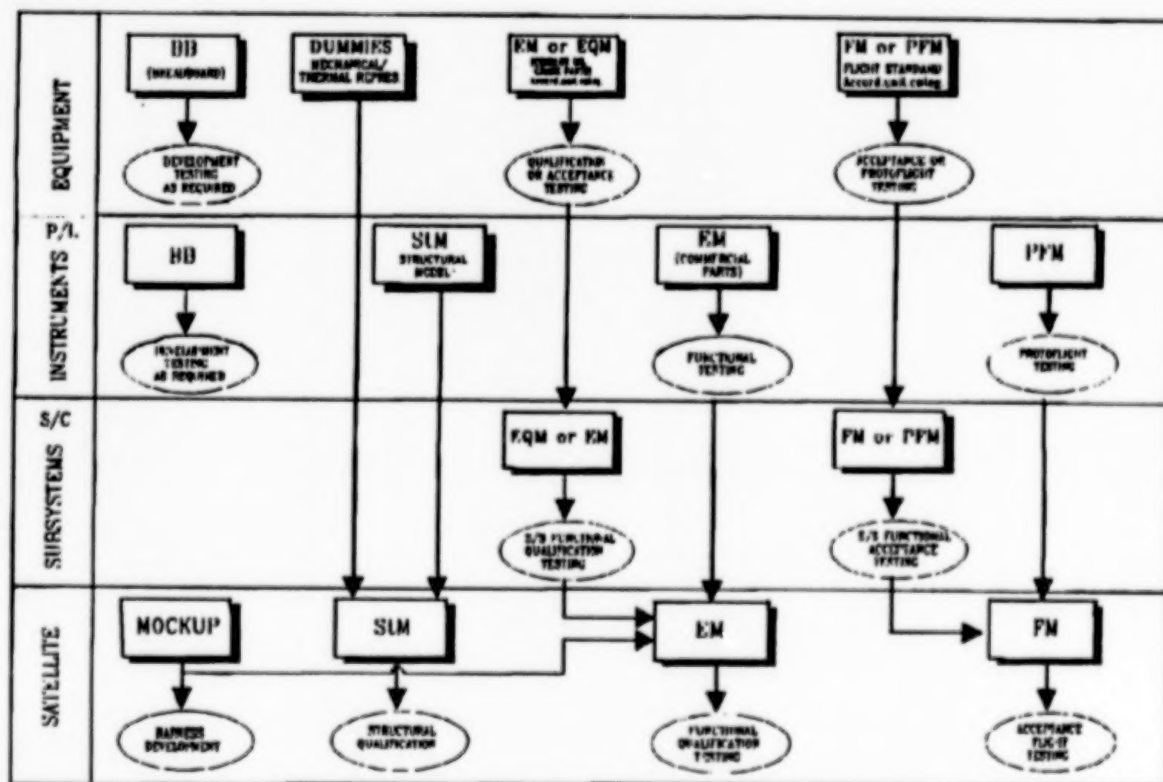


Fig. 5 - TSS-S Model Philosophy

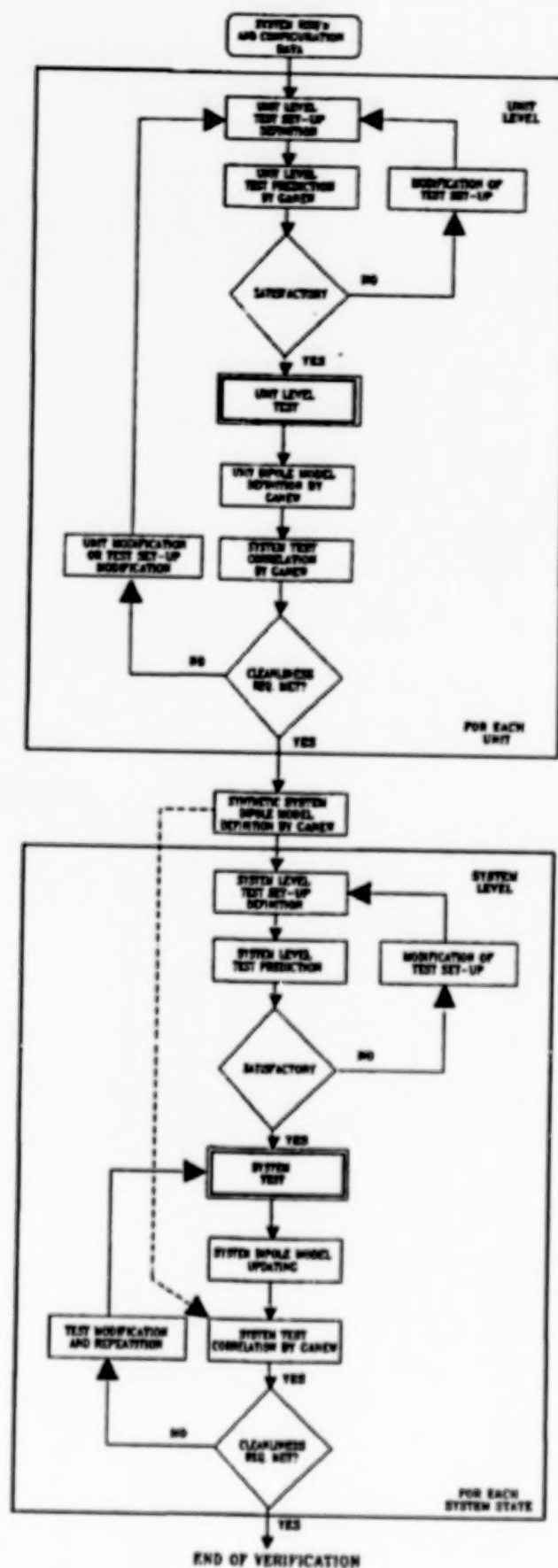


Fig. 6 Magnetic Cleanliness Verification Flow

AER-TURIN 03/11/89 14:54:48

FUDEC

Test No.: 5 PERM

Rotation increment: 10 deg. data triplets

PHI(deg.) BX(nT) BY(nT) BZ(nT)

ORIGINAL

0	10.0	-6.3	-1.1
10	16.0	-11.7	-4.0
20	14.2	-10.5	-1.4
30	0.9	-6.9	0.0
40	-3.7	-4.0	-1.8
50	-6.9	-3.4	-3.4
60	-4.3	-2.0	-5.6
70	-17.7	3.5	-13.6
80	-12.8	4.9	-22.4
90	-12.5	5.3	-22.4
100	0.5	1.5	-7.0
110	-1.5	1.8	-3.1
120	4.0	-1.8	-5.0
130	4.7	-2.9	-4.0
140	0.5	-2.4	-2.9
150	-2.6	-3.4	-7.0
160	1.4	-7.3	-12.8
170	-1.5	-4.0	-13.6
180	0.9	-2.1	-9.0
190	6.0	-1.4	-5.2
200	2.6	0.2	-7.3
210	5.0	-2.4	-11.1
220	6.1	-2.3	-9.2
230	-3.7	1.1	-11.6
240	9.2	1.1	-5.3
250	-4.0	3.4	-9.2
260	8.9	1.2	-6.7
270	-0.2	3.2	-10.4
280	13.3	1.7	-6.1
290	6.0	3.1	-7.6
300	20.0	-1.4	-6.6
310	15.3	-0.2	-2.9
320	23.8	-3.7	-4.9
330	15.9	-3.8	-3.5
340	21.1	-8.4	-3.4
350	15.9	-8.4	-1.4
360	14.5	-10.5	-3.2
DUT-DIM. (CM):	24.90	22.60	11.20
DUT-MASS (GR):	2627.0		
DUTRH-S/C (CM):	-16.60	19.40	-44.40
DUT-ROT. S/C :	0.65	-0.65	-0.38
	-0.27	0.27	-0.92
	0.71	0.71	0.00
DUT-CG (CM):	0.00	0.00	5.50
DUT-RH (CM):	-6.90	-10.30	0.00
DUT-LIMIT(CM):	-12.6 12.3; -11.1 11.5;	0.0	11.2
DUT-ROTATION :	1.00	0.00	0.00
	0.00	1.00	0.00
	0.00	0.00	1.00
SENS-CT (CM):	35.00	0.00	0.00
X-SENS. (CM):	0.00	0.00	3.00
Y-SENS. (CM):	0.00	0.00	6.70
Z-SENS. (CM):	0.00	0.00	10.50
OFFSET (NT):	2.98	-5.42	-41.43
RES-FIELD(NT):	-28.76	16.56	38.22
O/NO DUT (NT):	1834.72	46.84	-524.14
O-CHECK (NT):	1843.11	46.69	-530.55

Fig. 7 - Rotational Inputs for GANEW

MAGNETOSTATIC CLEANLINESS CONTROL CHART

Date: 130190

MSC41(FD)

Project : TSS-1

Model : FU

Magnetic Status: Final Deperm

Legend:

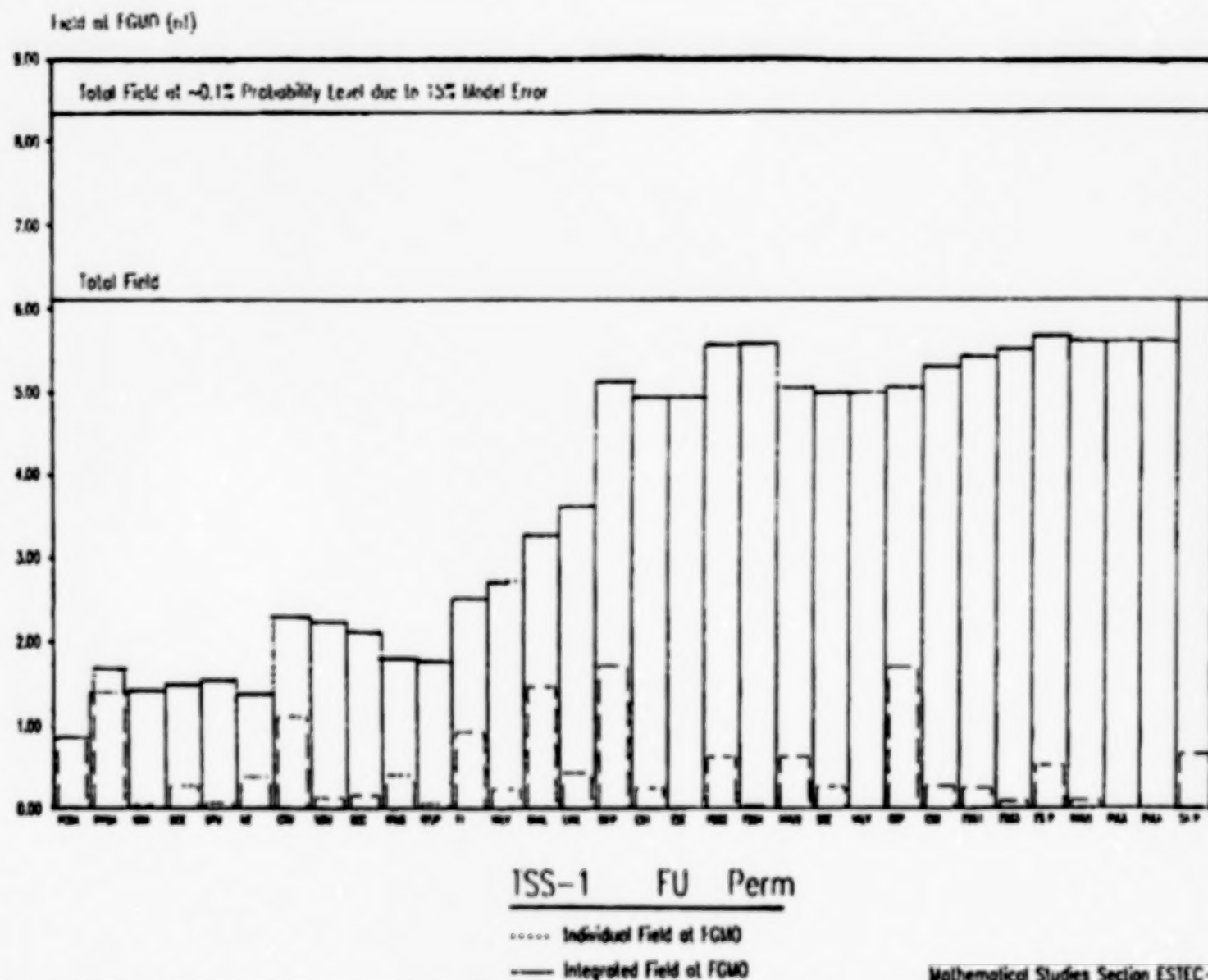
rms = Field Measurement Reconstitution Error (nT)
 M = Global Dipole Moment (Gcm3)
 FGMI = Field at FGMI Location (-126.70 1.90 22.50 cm) (nT)
 FGMO = Field at FGMO Location (-177.80 1.90 20.00 cm) (nT)
 mod = Module of Vector (nT)
 1 = x-Component of Vector (S/C Coordinates)
 2 = y-Component of Vector (S/C Coordinates)
 3 = z-Component of Vector (S/C Coordinates)

(Spacecraft fields are vector sums of unit fields)

Unit						Spacecraft			
	Unit	Run	rms	M	FGMI	FGMO	FGMI	FGMO	
1	FUPCDA FINAL DEPERM 7	5.	61.5	1.89	0.82	1.89	0.82	mod 1 2 3	
			9.5	-1.65	-0.54	-1.65	-0.54		
			-38.8	0.44	0.35	0.44	0.35		
			46.8	-0.82	-0.51	-0.82	-0.51		
2	FUPPDA FINAL DEPERM 5	4.	72.1	4.29	1.80	2.65	1.32	mod 1 2 3	
			65.8	4.10	1.76	2.46	1.22		
			-5.3	-1.25	-0.37	-0.81	-0.02		
			28.8	0.24	0.02	-0.58	-0.49		
3	FUWRA FINAL DEPERM 7	3.	7.7	0.13	0.06	2.67	1.31	mod 1 2 3	
			1.6	0.03	0.02	2.49	1.23		
			2.2	-0.04	-0.02	-0.85	-0.04		
			-7.2	0.11	0.06	-0.46	-0.44		
4	FUDCE FINAL DEPERM12	3.	12.8	0.75	0.31	2.40	1.21	mod 1 2 3	
			-9.4	-0.17	-0.15	2.32	1.08		
			-8.2	0.72	0.27	-0.14	0.23		
			2.8	-0.13	-0.05	-0.60	-0.49		

Fig. 8 - Elaboration of Synthetic Satellite Model

Fig. 9 - TSS-S Perm Phase Magnetic Field Contribution



probe number	35	/ 3	cm
probe distance	0.10		0=open
probe selection	3941.02		0T
RMS of residues	4.41		X
Number of dipoles	3		
Global dipoles	[9 4 47]	48	Gcm
Mag location	[-30 -81 177]	197	cm
Field at MAG	[-425 -825 877]	1276	pT

• • •	field measurements
—	field model
•	modulus of residues
•	residues
x y z	components of test coordinates

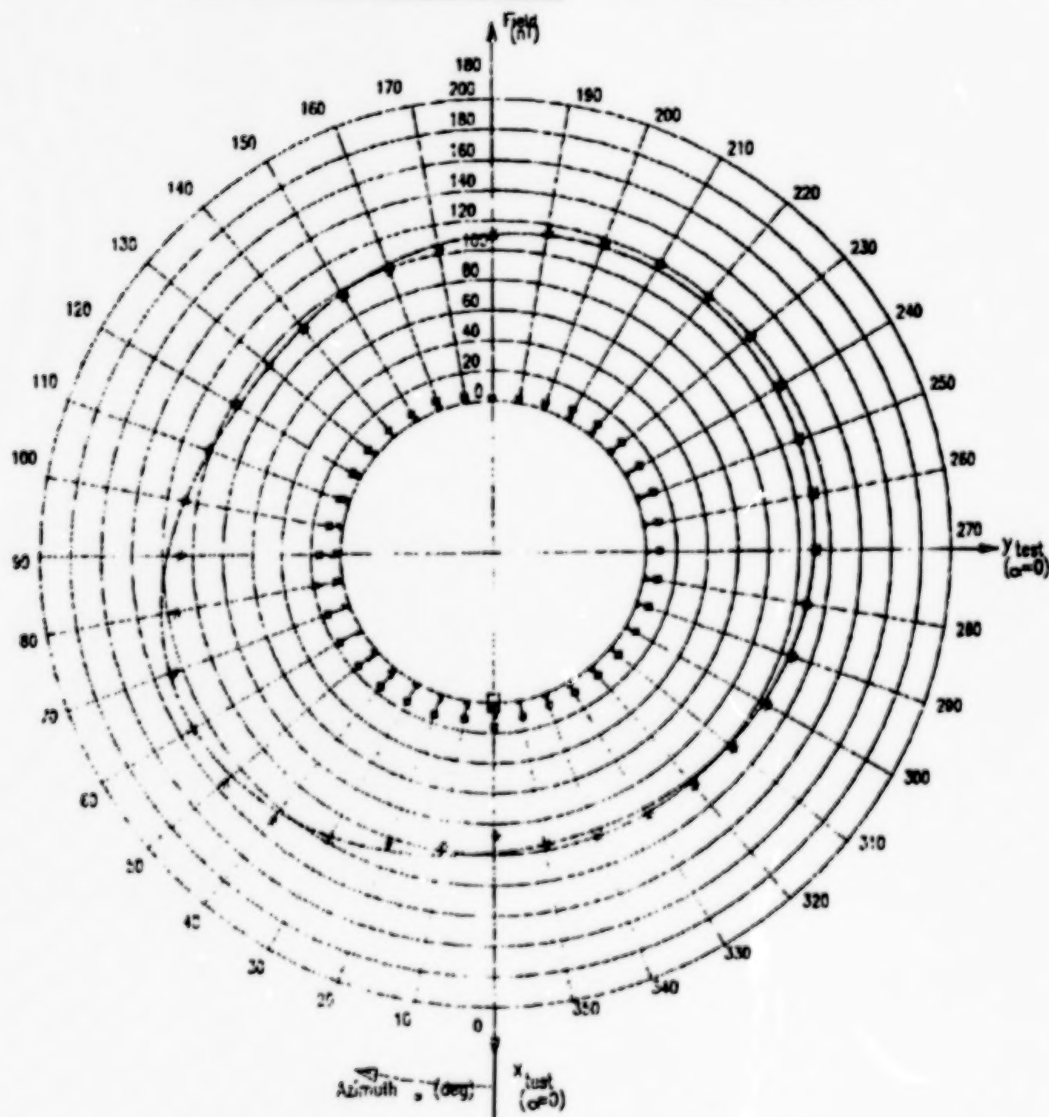
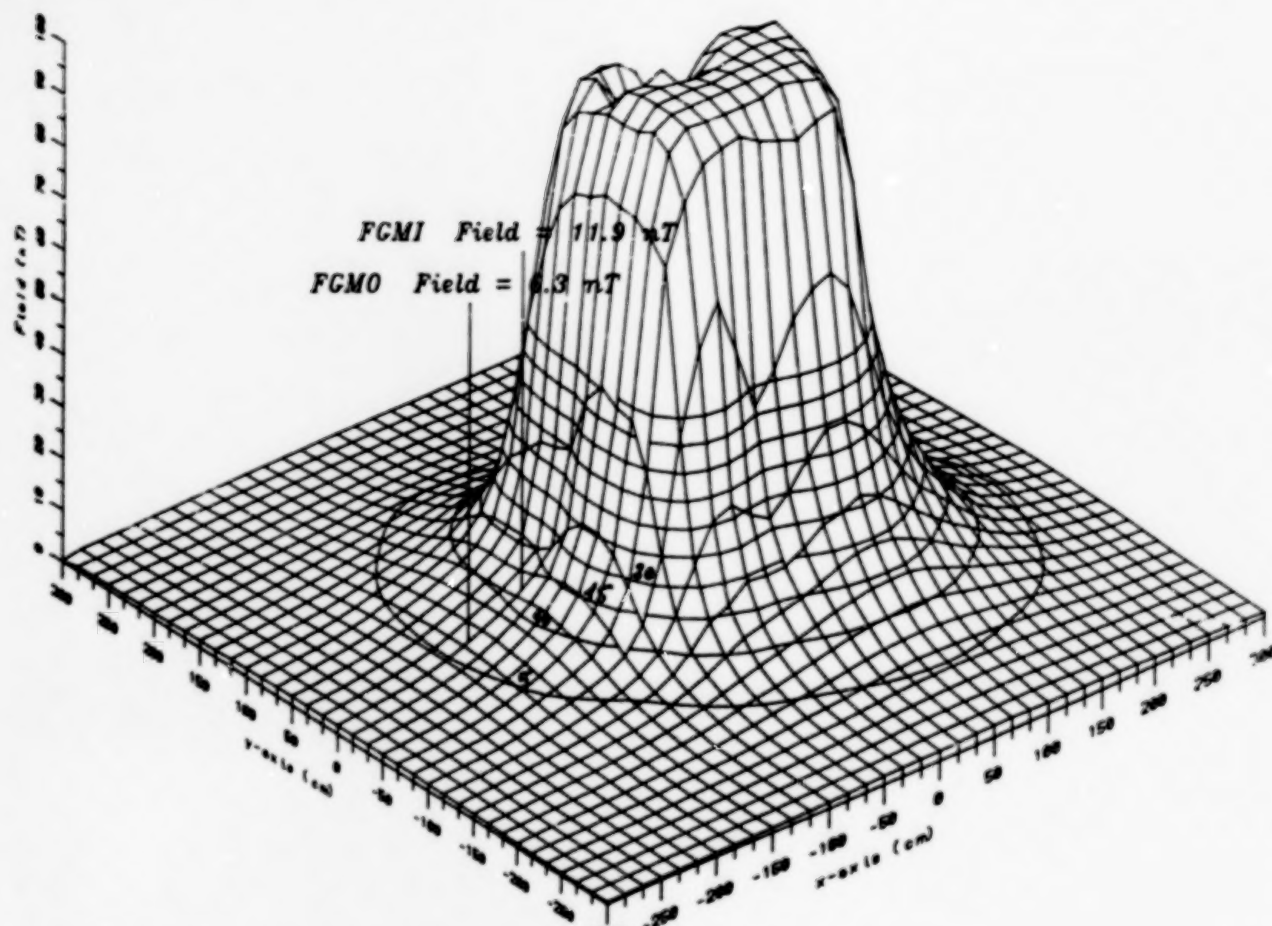


Fig. 10 - GANEW Synthetic Satellite Model Output (Plane)



TSS-1 Final Deperm in plane of FGM0

Fig. 11 - GANEW Synthetic Satellite Model Output (Tridimensional)

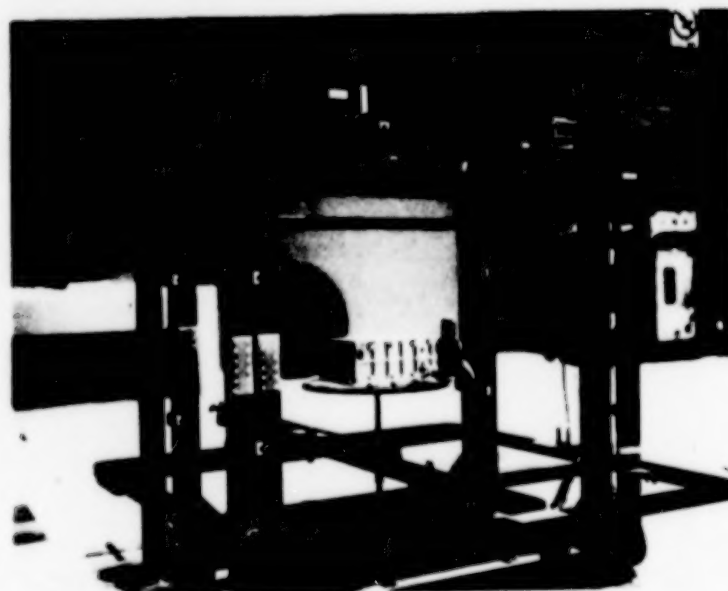


Fig. 12 - Typical TSS Unit Test

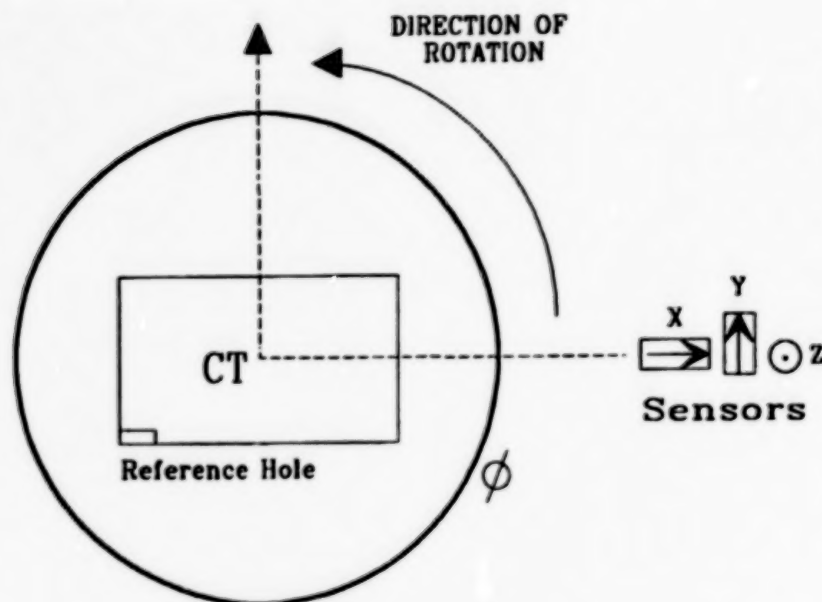


Fig. 13 - Test Set-up Sketch

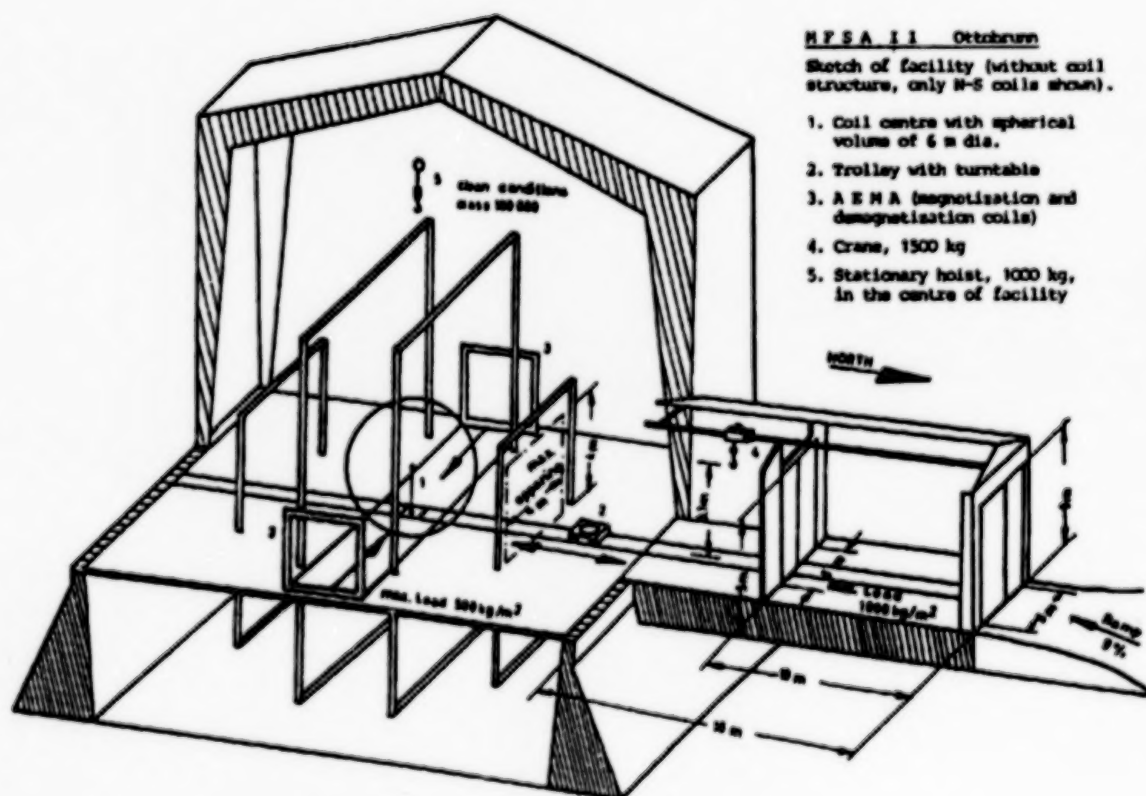


Fig. 14 - IABG MSFA II Magnetic Test Facility

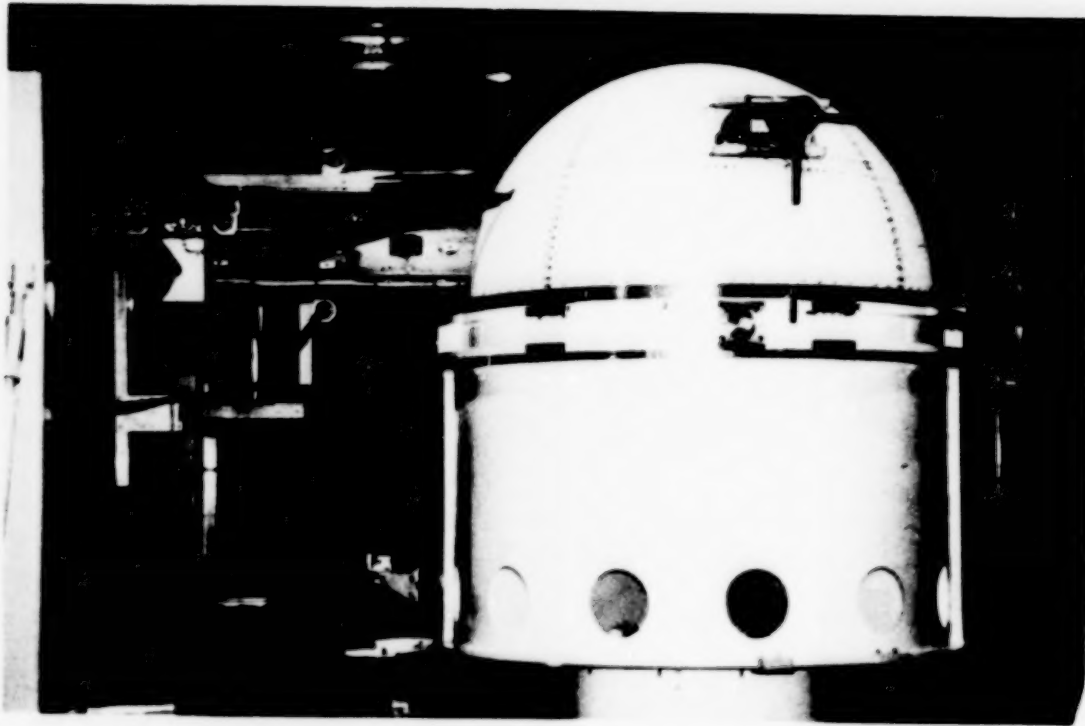


Fig. 15 - TSS-S FU Magnetic Cleanliness Test Set-up

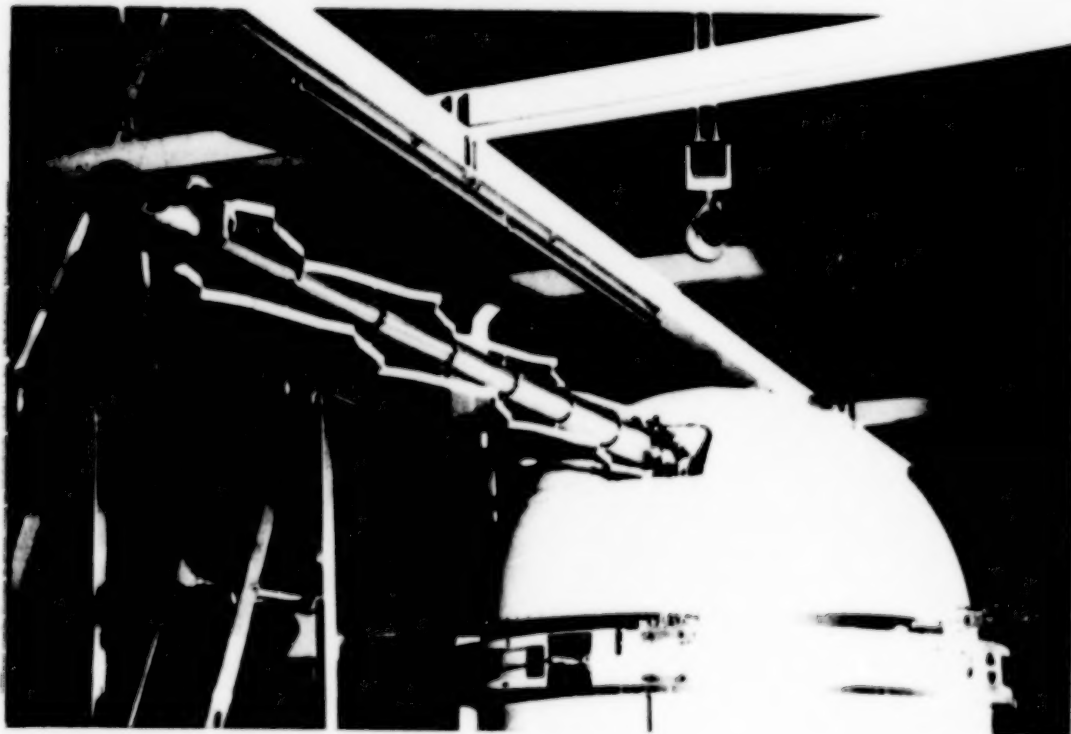


Fig. 16 - TSS-S FU Test Configuration During DRBD/A Boom Sniff Test

Coordinate system = IADG Test Coordinates

To obtain Spacecraft coordinates change sign of Bx and By

Only Probes 1 and 4 used (probes adjacent to FGMO)

Rot = Rotational Measurements 360 deg, step=10 deg

Scan = Rotational Scan plus minus 30 deg, step=5 deg

li = Linear Interpolation between Field Measurements of Probes 1 and 4

Model = Optimal Multiple Dipole Model

IADG	TSS Magnetic State	Mode	Data Source	Field at FGMO location (nT)			
				Bx	By	Bz	B
Run 2	As Received 1 before local depers	Rot	Model 2	-25.8	12.3	5.2	29.1
			Data li	-29.4	12.7	4.2	32.3
Run 3	As Received 1	Scan	Data li	-29.6	12.8	4.1	32.5
Run 4	As Received 2 after local depers	Rot	Model 4	-25.8	12.3	4.8	28.9
		Rot	Data li	-29.6	11.2	1.6	31.7
Run 6	Depers 1	Scan	Data li	-24.7	9.9	5.3	27.1
Run 7	Depers 1 after Rope exp. cleaned	Rot	Model 7	-22.1	10.0	5.2	24.8
		Rot	Data li	-24.7	9.9	5.3	27.1
Run 8	Perm X 1 Gauss	Scan	Data li	-27.1	9.7	4.9	29.2
Run 9	Perm X 2 Gauss	Scan	Data li	-27.7	10.2	5.1	29.9
Run 11	Perm X 3 Gauss	Scan	Data li	-28.8	9.7	4.7	30.8
Run 12	Perm X 5 Gauss	Scan	Data li	-32.6	9.2	4.1	34.1
	Perm X Susc. 5G		Calcul.	-7.9	-0.7	-1.2	8.0
Run 13	Perm Y 1 Gauss	Scan	Data li	-29.5	11.3	4.0	31.9
Run 14	Perm Y 2 Gauss	Scan	Data li	-29.1	11.5	4.6	31.6
Run 15	Perm Y 3 Gauss	Scan	Data li	-27.6	12.2	4.2	30.5
Run 16	Perm Y 5 Gauss	Scan	Data li	-25.6	14.9	4.5	29.9
	Perm Y Susc. 5G		Calcul.	-0.9	5.0	-0.8	5.1
Run 17	Perm Z 1 Gauss	Scan	Data li	-25.7	13.2	4.6	29.3
Run 18	Perm Z 2 Gauss	Scan	Data li	-24.9	12.6	6.0	28.5
Run 19	Perm Z 3 Gauss	Scan	Data li	-24.9	12.2	6.7	28.5
Run 20	Perm Z 5 Gauss	Scan	Data li	-25.9	11.3	8.8	29.6
	Perm Z Susc. 5G		Calcul.	-1.2	1.4	3.5	4.0
Run 21	Perm Z 5 Gauss	Rot	Model 21	-23.7	11.2	7.2	27.2
		Rot	Data li	-25.6	11.3	8.9	29.3
Run 22	Depers 2	Rot	Model 22	-22.2	9.2	5.7	24.7
		Rot	Data li	-25.1	12.2	8.0	29.0
Run 23	Depers 2	Scan	Data li	-25.0	12.1	8.3	29.0
Run 24	Stray alone	Scan	Data li	-0.7	-1.5	0.0	1.7
	Depers 2 + Stray		Calcul.	-25.7	10.6	8.3	29.0
Run 26	Depers 3	Scan	Data li	-22.1	17.0	3.0	28.0
Run 27	Depers 3	Rot	Model 27	-20.9	13.2	4.8	23.2
		Rot	Data li	-22.2	16.7	2.8	27.9
Run 29	Depers 4 + Transponder + Gyros	Rot	Model 29	-22.0	12.8	4.8	25.2
		Rot	Data li	-23.3	16.6	3.8	28.8
Run 30	Depers 4	Scan	Data li	-23.2	16.4	3.5	28.7

Fig. 17 - TSS-S FU Magnetic Cleanliness Test Results

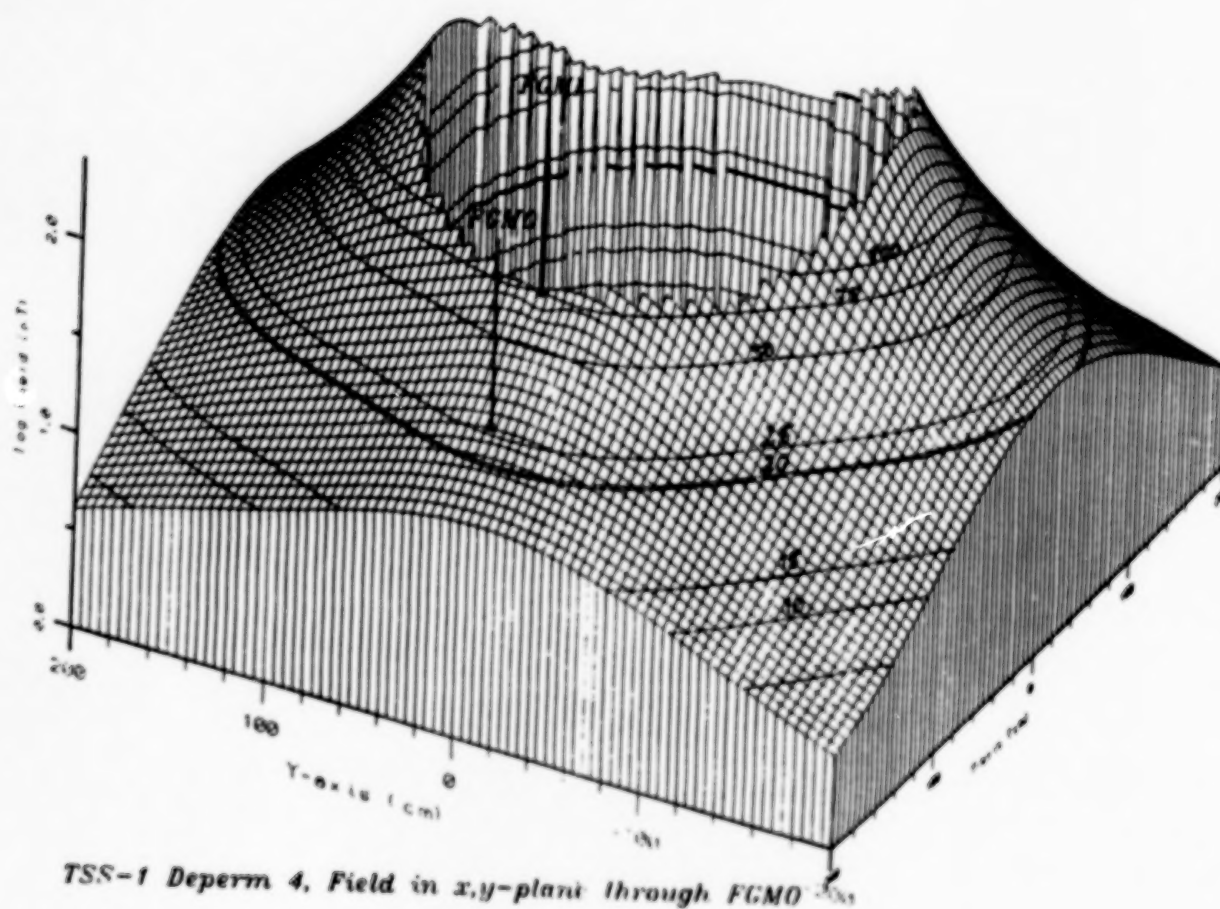


Fig. 18 - TSS-S FU Final Magnetic Field distribution

A Flight Experiment to Determine GPS Photochemical Contamination Accumulation Rates

A. C. Tribble and J. W. Haffner
Rockwell International

ABSTRACT

It has recently been suggested that photochemically deposited contamination, originating from volatiles outgassed by the spacecraft itself, may be responsible for the anomalous degradation in power seen on the GPS Block I vehicles. In an attempt to confirm, or deny, the photochemical deposition rates predicted, a study was undertaken to design a flight experiment to be incorporated on the GPS vehicles currently in production. The objective of this study was to develop an inexpensive, light-weight instrument package that would give information on the contamination levels within a few months of launch. Three types of apparatus were investigated, Quartz Crystal Microbalances (QCM's), modified solar cells, and calorimeters. A calorimeter was selected due primarily to its impact on the production schedule of the GPS vehicles. An analysis of the sensitivity of the final design will be compared to the predicted contamination accumulation rates in order to determine how long after launch it will take the experiment to show the effects of photochemical contamination.

SYMBOLS

- Q_L - heat loss due to thermal coupling
- $R(\lambda)$ - spectral reflectance
- S - incident heat flux (W/m^2)
- T - temperature (K)
- x - thickness of contaminants (m)
- α_s - solar absorptance of a clean material
- $\alpha_s(x)$ - solar absorptance of a contaminated material
- $\alpha(\lambda)$ - spectral absorptance (of an optical reflector)
- $\alpha_c(\lambda)$ - spectral absorptance of contaminant layer
- ϵ - emissivity
- $\Phi(\lambda)$ - solar flux
- σ - Boltzmann's constant
- λ - wavelength (m)

INTRODUCTION

An analysis of the molecular outgassing rates from the GPS vehicles, Figure 1, determined that there was a sufficient amount of matter being emitted by the spacecraft that if a small fraction of matter which impinged upon the solar panels were to stick this could account for the degradation in power production observed on the GPS Block I vehicles, Tribble and Haffner, [1]. It was proposed by Stewart et. al, [2], that a photochemical reaction initiated by the solar UV could be the mechanism responsible for fixing the contamination onto the solar panels as similar phenomena are known to occur in the laboratory, [3-5]. Subsequent to the investigation of the GPS Block I contamination similar calculations were performed for the GPS Block II vehicles currently being launched and it was found that there should be a noticeable degradation in power, attributed to photochemical contamination, on GPS Block II vehicles 13 - 21. GPS Block II vehicles 22 - 40 should be relatively immune to this contamination as EMI seals employed on these vehicles have effectively eliminated the outgassing paths from the vehicle to the solar panels. The objective of this study is to develop a design for a flight experiment, which could be included on one of the early GPS Block II vehicles, that could confirm, or deny, the accuracy of the predicted photochemical contamination accumulation rates.

The most obvious location for an experiment designed to measure the degradation of the solar panel output is on the solar panels themselves. Tribble and Haffner, [1], were able to predict the impact rate and accumulation rate of contaminants for various locations on the GPS Block II solar panels. Consequently, by placing a monitor in an area where high accumulation is expected and comparing it with a monitor in an area where little accumulation is expected any difference in readings should be attributable to contamination as the radiation environments for each monitor would be identical. A major concern in the development of a flight experiment is that any recommended design be able to be implemented on a production vehicle with a minimum of integration problems and/or scheduling delays. As was previously mentioned vehicles 22 - 40 have EMI closeouts which reduce the outgassing onto the arrays, consequently vehicles 13 - 21 are the best candidates for a contamination experiment, with GPS 15 currently offering the most lead time. A major constraint is that a workable design must be one that can be agreed upon, procured, and implemented into the acceptance test flow without delaying the processing of the vehicle. (As a check upon the effectiveness of the EMI seals on vehicles 22 - 40 the contamination experiment could also be flown on a later vehicle, but these launches are far enough into the future that time is not yet a significant factor.)

The sections that follow discuss some of the possible experimental methods that could be used to obtain data on the contamination levels and the problems involved in integrating these experiments into a production vehicle. It will be shown that a calorimeter, utilizing optical solar reflector's (OSR's) backed with thermistors, could be developed in time for inclusion on GPS 15. This experiment would have the advantage of requiring minimal qualification testing as it is essentially identical to one previously flown on GPS 5 and 6.

SPACECRAFT INTEGRATION REQUIREMENTS

GPS 15 is tentatively scheduled for launch in February of 1991. As the spacecraft systems are all intact maintaining this launch schedule implies that there can be no significant rewiring or telemetry changes. Since the most favorable location for the experiment is on the solar panels themselves the experiment must be light-weight and small enough that it not interfere with the stowing or deployment of the panels, or affect the balance of the vehicle. There is

also the problem of bringing the data from the solar panels to the body of the spacecraft.

All of the electronic leads to/from the solar panels are via slip rings on the solar array booms. Bypassing the slip rings and hardwiring an experiment directly into the body of the vehicle could conceivably cause interference with the deployment or normal operations of the panel. Also, during eclipse conditions the wiring could become so stiff that the torque supplied by the solar array drive would be unable to rotate the panels. Obviously, this is unacceptable, so the experiment is confined to the use of the slip rings.

GPS 15 currently has two spare slip rings per boom. The remainder of the slip rings are used for power or data transmission into the spacecraft. There are a number of thermistors located on the GPS solar panels which are used to record the temperature of the panels during orbital insertion or to verify the deployment of the panels. Data from the first 5 GPS Block II launches indicate that there is no problem with overheating of the panels during orbital insertion. Consequently, slip rings currently allocated to one thermistor (per boom) could be reallocated to a flight experiment leaving at most four available slip rings per boom.

REVIEW OF AVAILABLE EQUIPMENT

A review of the experimental equipment that is currently available on the market for use in determining contamination levels revealed three possible alternatives: Quartz Crystal Microbalance's (QCM's), modified solar cells, and calorimeters. Each of these alternatives is discussed individually in the subsections that follow, with particular attention being paid to the data that each experiment would yield and its ease of integration into the current spacecraft.

Quartz Crystal Microbalances

A QCM consists of 2 piezoelectric crystals which resonate at known frequencies. One crystal is exposed to the environment and as mass accumulates on its surface its resonant frequency is lowered in a predictable manner. By comparing the beat frequency between an exposed crystal and a shielded crystal one is able to determine the accumulated mass/unit area. The temperatures of the crystals, which are identical, may be controlled externally or allowed to float with the environment in order to eliminate, or measure, the effect of temperature on mass accumulation.

As QCM's are able to measure mass accumulation directly they have seen extensive use on spacecraft contamination monitoring programs, Wallace, [6,7], Hall, [8]. Unfortunately, QCM's require more supporting electronics than can be accommodated by the 4 available slip rings.* Consequently, QCM's were dropped from consideration as they did not meet the criteria for easy, quick integration into the spacecraft.

It should be noted that even though QCM's will directly measure the amount of mass collected, they yield no information about the transparency of the material. Since a very thin layer of a highly absorptive material may have the same effect on a solar cell as a thick layer of a more transparent material QCM's would not yield a complete analysis of the solar panel contamination.

Modified Solar Cells

As it was the degradation of power of the GPS Block I solar panels that was

*QCM Research, Laguna Beach, CA.

the first indication of a possible outgassing problem it would seem logical to devise an experiment that would measure the effects of contamination on solar cells directly. A typical solar cell is constructed by combining about 0.2 microns of an n-type silicon, (i.e., a type of silicon where there is an abundance of electrons in the conduction band, which can be obtained by doping silicon with phosphorous), with about 200 microns of a p-type silicon, (a type of silicon having a depletion of conduction electrons, which can be obtained by doping silicon with boron), Tada et. al, [9]. As a result of the different properties of the two silicons, electrons from the n layer will diffuse into the p layer and an electric field will be produced, typically within 1 - 5 microns of the junction. As photons enter the n layer they will undergo collisions with atomic electrons and, as a result, boost more electrons into the conduction band. Blue light of wavelength 0.35 microns is 99% absorbed within 0.2 microns of the surface, whereas red light of wavelength 0.94 microns travels 200 microns before being 99% absorbed. As the electrons are liberated within the silicon the electric field in the vicinity of the junction will accelerate electrons toward the front surface. By placing electrical contacts on the front and rear surface of the n-p cells the electrons can be drawn off as a current and used as a power source. (The voltage at which the current is supplied is related to the strength of the electric field at the n-p junction.)

Obviously solar cells, like everything else, will not be 100% efficient at converting the light to electrical power. When an electron undergoes a collision with a photon and receives enough energy to escape the pull of the atomic nucleus, the atom will be left with a net positive charge. As the liberated electron moves through the cell it will only be a matter of time before it passes too close to an atom which is missing an electron and is recaptured. The time that an electron is typically able to move through the cell is called the lifetime, τ (s), which is defined as the time before 1/e of the electrons are recaptured. During their lifetime the electrons are able to travel a distance called the diffusion length, L (m), where $L = \sqrt{D\tau}$, D (m^2/s) being the characteristic diffusion coefficient for the silicon material. Typically, diffusion lengths are on the order of 200 microns. Consequently, an n-p solar cell is much more efficient at converting blue light to electricity than red light, as the electrons produced by the red light must travel a distance on the order of the diffusion length, and are much more likely to recombine with an atom, before reaching the junction.

Similarly, it is seen that radiation, which decreases the diffusion length by creating atomic displacements, site defects, etc., would chiefly reduce the cells ability to convert red light to electricity by further limiting the fraction of 'red' electrons that are able to reach the junction, this is illustrated in Figure 2. Conversely, contamination mainly affects a cells ability to convert blue light to electricity, see Figure 3, by absorbing the blue light before it reaches the cell. Consequently, it would be straightforward to develop two groups of 'modified solar cells' to help determine the effects of contamination on the GPS solar panels. One group of such cells would be designed to be sensitive to blue light, by being thinner than usual so as to allow fewer red light photons to liberate electrons. The second group of cells would be designed to be sensitive to red light, by placing the p-type silicon towards the sun as opposed to the n-type, i.e. a p-n type solar cell. Since the majority of the conduction electrons produced by blue light originate within 0.2 microns of the surface the 'blue' electrons would then have a harder time reaching the junction, 200 microns away. By flying groups of the special cells on the GPS solar panels a reduction in power of the 'blue sensitive' cells would indicate a degradation due to contamination, while a loss of power from the 'red sensitive' cells would indicate radiation damage.

The advantage of this type of experiment is that the special cells could be used to supply extra power for the vehicle. Unfortunately, for the disadvantages outweigh the advantages. Due to the slow buildup of contaminants predicted on

the GPS solar panels it appears as though it would take more than one year for the 'blue sensitive' cells to show the effects of contamination once on-orbit, much longer than is desired. Also, more than one year would be required to manufacture and test the special cells.* In addition, the special cells would require significant rewiring and telemetry changes to the spacecraft which again implies that it would be impossible to implement on GPS 15. Consequently, this concept was not pursued further.

Calorimeters

A material that is in thermal equilibrium with its surroundings will absorb and re-radiate heat according to the relation

$$\alpha S = \epsilon \sigma T^4. \quad (1)$$

For materials carried into space, the incident heat flux will be supplied by the sun and the absorptance is given by

$$\alpha_s = \int \alpha_s(\lambda) \Phi(\lambda) d\lambda / \int \Phi(\lambda) d\lambda. \quad (2)$$

If a clean material becomes contaminated with a thin layer of contaminants its absorptance is changed according to the relation

$$\alpha_s(x) = \frac{\int [1 - R(\lambda) \exp^{-2\alpha_c(\lambda)x}] \Phi(\lambda) d\lambda}{\int \Phi(\lambda) d\lambda}. \quad (3)$$

$\alpha_c(\lambda)$ has been measured experimentally for typical spacecraft contaminants, Hall, [10], and references therein, therefore knowing $R(\lambda)$ will allow us to compute $\alpha_s(x)$.

The change in absorptivity is related to the measured temperature change by the relation

$$\Delta \alpha_s = \frac{4\epsilon \sigma T^3}{S} \Delta T + \frac{\sigma T^4}{S} \frac{\partial \epsilon}{\partial T} \Delta T. \quad (4)$$

For high emissivity materials, such as fused silica, the emissivity will be insensitive to both temperature changes and the presence of a thin contaminant layer. Consequently, the last term may be neglected. Therefore, we see that a change in temperature of a sample, can be related directly to the thickness of contaminants,

$$\Delta T = \frac{S}{4\epsilon \sigma T^3} [\alpha_s(x) - \alpha_s]. \quad (5)$$

Experimental apparatus based on this technique are referred to as calorimeters. A number of them have been flown as one method of determining contamination levels, Hall and Fote, [11], and Hall, [8]. Of particular interest however, is the calorimeter experiment flown on GPS vehicles 5 and 6, Pence and Grant, [12]. These instruments consisted of thermal control coatings over an aluminum substrate which was thermally isolated from the rest of the vehicle, see Figure 4. A thermistor on the underside of the aluminum substrate was used to infer the temperature of the thermal control coatings.

*Spectrolab, Sylmar, CA.

A simplistic design such as this, if properly calibrated, is capable of yielding information on the thickness of contaminants on the GPS solar panels. This design has the advantage of being previously space-qualified and flown, relatively quick and inexpensive to procure and assemble, and requires only 2 electrical leads per calorimeter. Consequently, this design was selected as the leading candidate.

RECOMMENDED DESIGN AND CALIBRATION TECHNIQUES

The calorimeters flown on GPS vehicles 5 and 6 are small, the inner sample itself measures 2.06" square and the outer holder measures 3.4" square, lightweight, 0.45 lbs each, and require only two electrical leads per calorimeter. It should be possible to include four of them, two per boom, on GPS 15. However, since time is a major constraint it would be quicker to install only one calorimeter per boom. In order to obtain the maximum amount of information in the smallest time the calorimeters could be placed on the solar array boom, one inboard and one outboard. This configuration would not offer redundancy in the case of failure of one of the calorimeters but would have the advantage of requiring no wiring changes. The redundant thermistors would simply be disconnected and the calorimeters would then be spliced into the existing wiring in a minimal amount of time. The resulting data should indicate changes in the temperatures, and thus the absorptances, of the inboard calorimeter within a few months. Since the outboard calorimeter would be subjected to an identical radiation environment, ignoring any shielding effects from the GPS vehicle itself, which are expected to be minimal, any differences in the absorptance of the inboard and outboard samples will be due entirely to contamination. GPS structures personnel have analyzed the effect of placing these calorimeters on the solar panel booms and have found it to be within tolerances. Consequently, once the authority to proceed has been given, the fabrication and testing of the calorimeter could be accomplished in parallel to the acceptance test flow for GPS 15. A brief discussion of the calibration of the calorimeters is warranted in order to understand the sensitivities of the experiment and the exact timescale that would be needed to obtain meaningful data on the contamination deposition rates.

As discussed by Brosmer et. al, [13], in all realistic applications there will be a heat leak, from the boundary to the thermally isolated substrate, affecting the thermal performance of the calorimeter. Consequently, the change in absorptance is more appropriately given by

$$\alpha_s = (\epsilon\sigma T^4 + \dot{Q}_L)/S \quad (6)$$

where \dot{Q}_L is the heat loss due to thermal coupling. The relative uncertainty of the absorptance is given by

$$\frac{\Delta\alpha_s}{\alpha_s} = \frac{(\Delta\epsilon/\epsilon) + (4\Delta T/T)}{1 + \dot{Q}_L/\epsilon\sigma T^4} + \frac{\Delta\dot{Q}_L/\dot{Q}_L}{1 + \epsilon\sigma T^4/\dot{Q}_L} + \frac{\Delta S}{S} \quad (7)$$

Thus, the uncertainty in α_s depends on the uncertainty associated with measurements of ϵ , T , S , and \dot{Q}_L .

As was previously mentioned, the change in emissivity of fused silica, due to a thin contaminant layer or temperature changes, is negligible. Brosmer et. al list the maximum uncertainty at 1.3%. The incident solar flux, S , can be measured to within 0.2%, Willson, [14], with daily fluctuations rarely exceeding 0.1%. The uncertainty in temperature is dependent upon the noise level associated with the slip rings and the calibration of the thermistor. This uncertainty is estimated at about 5.0% over a 170° C temperature range.* This can be greatly improved upon,

to about 1.0% or less, by confining the measurements of temperature to a smaller range. This will be the case with the calorimeters as variations in T during periods of solar illumination should be small. The final source of error is associated with the measurement of the heat loss term, \dot{Q}_L . The absolute value of \dot{Q}_L will have to be estimated during calibration tests, Brosmer et. al. [13], and is typically the largest source of error, being perhaps as large as 5.0%.

A few words are in order, concerning the values of α_s that we expect to measure on GPS 15. The inboard and outboard calorimeters are predicted to accumulate contaminant levels of 144 Å and 72 Å, respectively, at the end of 30 days. This would increase the value of α_s from 0.060, for a clean surface, to about 0.068, (0.064), for the inboard, (outboard), calorimeter. (A more realistic value for the beginning of life absorptance would probably be 0.080, which would result in end of life values of about 0.090 and 0.085, respectively, for the inboard and outboard calorimeters.) As this increase, (13.3% and 6.6%, respectively), is well within the accuracy we predict for our calorimeter, we would expect to see measureable changes in α_s within 30 days of arriving on orbit. This has been confirmed by the operation of the calorimeters on GPS 5 and 6.

SUMMARY AND CONCLUSIONS

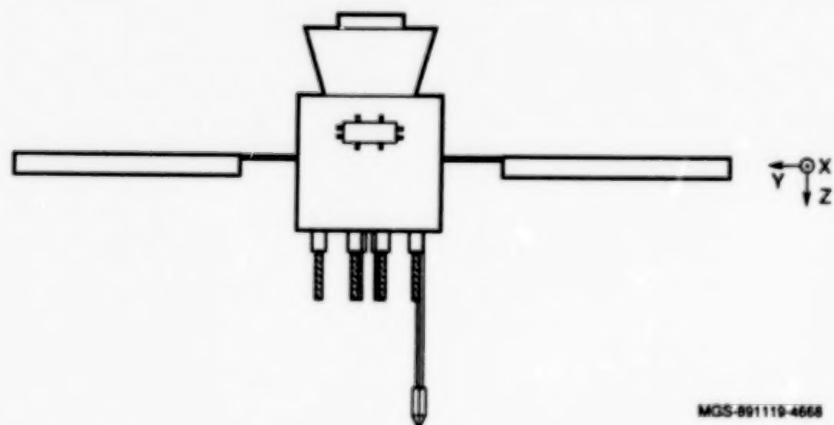
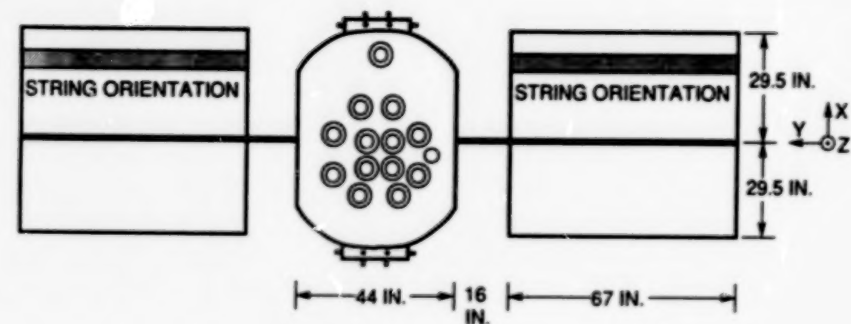
This report has examined a number of potential experiments that could be included on the GPS 15 vehicle in an attempt to directly measure the on-orbit accumulation of contaminants. It was determined that an experiment consisting of 2 calorimeters, based on the GPS Block I design, could yield the desired information and, at the same time, minimize the impact to the vehicles acceptance test flow schedule. The experiment should indicate the effects of the contamination within a few months of launch and would be an important in situ test of a topic that is currently the focus of intensive research efforts throughout the aerospace industry.

Unfortunately, as of 1 June 1990, authority to proceed with the installation of calorimeters on GPS vehicles 15 was still pending. Not enough time remains before the launch of GPS 15 to complete installation of a calorimeter on this vehicle. It may still be possible to proceed with a calorimeter experiment on a later GPS vehicle, however this decision has yet to be made.

*Herdt, B., Rockwell International, GPS Engineering, personal communication.

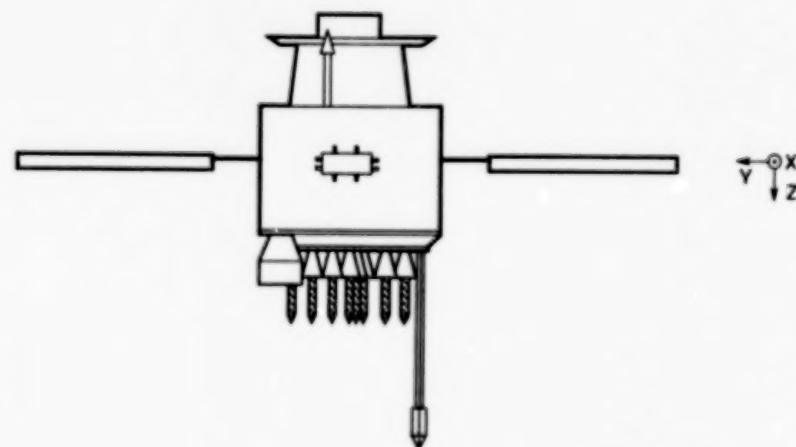
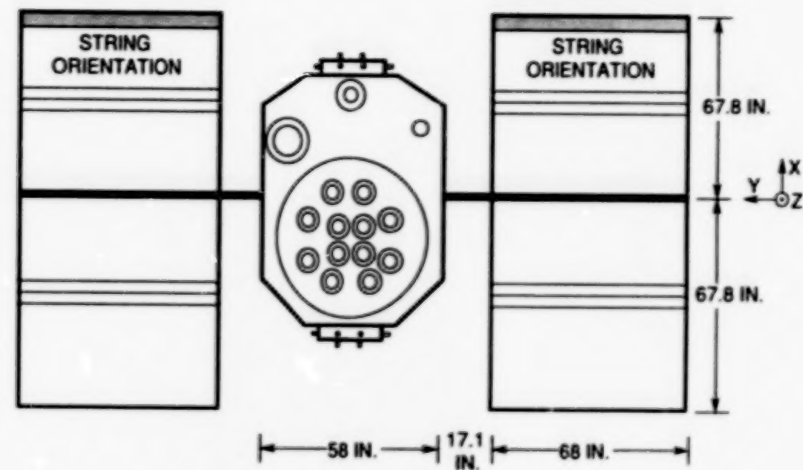
REFERENCES

1. Tribble, A. C., and Haffner, J. W., "Estimates of Photochemical Contamination on the Navstar GPS Satellites," J. Spacecraft Rockets, [in review].
2. Stewart, T. B., Arnold, G. S., Hall, D. F., Marvin, D. C., Hwang, W. C., Chandler, R. D., and Martin, H. D., "Photochemical Spacecraft Self-Contamination - Laboratory Results and Spacecraft Impacts," J. Spacecraft Rockets, Vol. 26, No. 5, p. 358, (1989).
3. Kruger, R., and Shapiro, H., "Experiments on the Effect of Ultraviolet on Contamination in Vacuum Systems," NASA TM-81999, (1980).
4. Hall, D. F., Stewart, T. B., and Hayes, R. R., "Photo-Enhanced Spacecraft Contamination Deposition," AIAA paper 85-0953, 20th Thermophysics Conf., Williamsburg, VA, 19-21 June 1985.
5. Stewart, T. B., Arnold, G. S., Hall, D. F., and Marten, H. D., "Absolute Rates of Vacuum Ultraviolet Photochemical Deposition of Organic Films," J. Phys. Chemistry, Vol. 93, p. 2393, (1989).
6. Wallace, D. A., "Use of the Quartz Crystal Microbalance for Outgassing and Optical Contamination Measurements," J. of Vac. Sci. and Tech., Vol. 9, No. 1, pp. 462-466, (Jan. - Feb. 1972).
7. Wallace, D. A., "Miniature Quartz Crystal Microbalance for Contamination Measurement," J. Spacecraft and Rockets, Vol. 17, No. 2, (Mar. - Apr. 1980).
8. Hall, D. F., "Spacecraft Contamination Flight Measurement Program," AIAA paper no. 87-1624, presented at the 22nd Thermophysics Conference, June 8-10, 1987, Honolulu, HI.
9. Tada, H. Y., Carter, J. R., Jr., Anspaugh, B. E., and R. G. Downing, Solar Cell Radiation Handbook, 3rd Edition, NASA JPL Publication 82-69.
10. Hall, D. F., "Current Flight Results From the P78-2 (SCATHA) Spacecraft Contamination and Coatings Degradation Experiment," ESA/CNES/CERT International Symposium, "Spacecraft Materials in Space Environment," Toulouse, France, (June 1982).
11. Hall, D. F., and A. A. Fote, " α_s/ϵ_h Measurements of Thermal Control Coatings on the P78-2 (SCATHA) Spacecraft," Heat Transfer and Thermal Control, A. L. Crosbie, (Ed.), Vol. 78 of Progress in Astronautics and Aeronautics, 1981.
12. Pence, W. R., and T. J. Grant, " α_s Measurements of Thermal Control Coatings on Navstar Global Positioning System Spacecraft," Spacecraft Radiative Transfer and Temperature Control, Thomas E. Horton, (Ed.), Vol. 83 of Progress in Astronautics and Aeronautics, 1982.
13. Brosmer, M. A., Fischer, W. D., and D. F. Hall, "Thermal Analysis of Flight Calorimeter Instrument Designs and Calibration Test Methods," AIAA paper no. 87-1622, 22nd Thermophysics Conf., 8-10 June 1987, Honolulu, HI.
14. Willson, R. C., "Solar Total Irradiance Variability Measurements by the SMM/ACRIM I Experiment," NASA CP 2310, pp. 1-16, 1984.



BLOCK I

MGS-891119-4668



BLOCK II

MGS-891120-4669

Figure 1. The GPS Block I and Block II Vehicles.

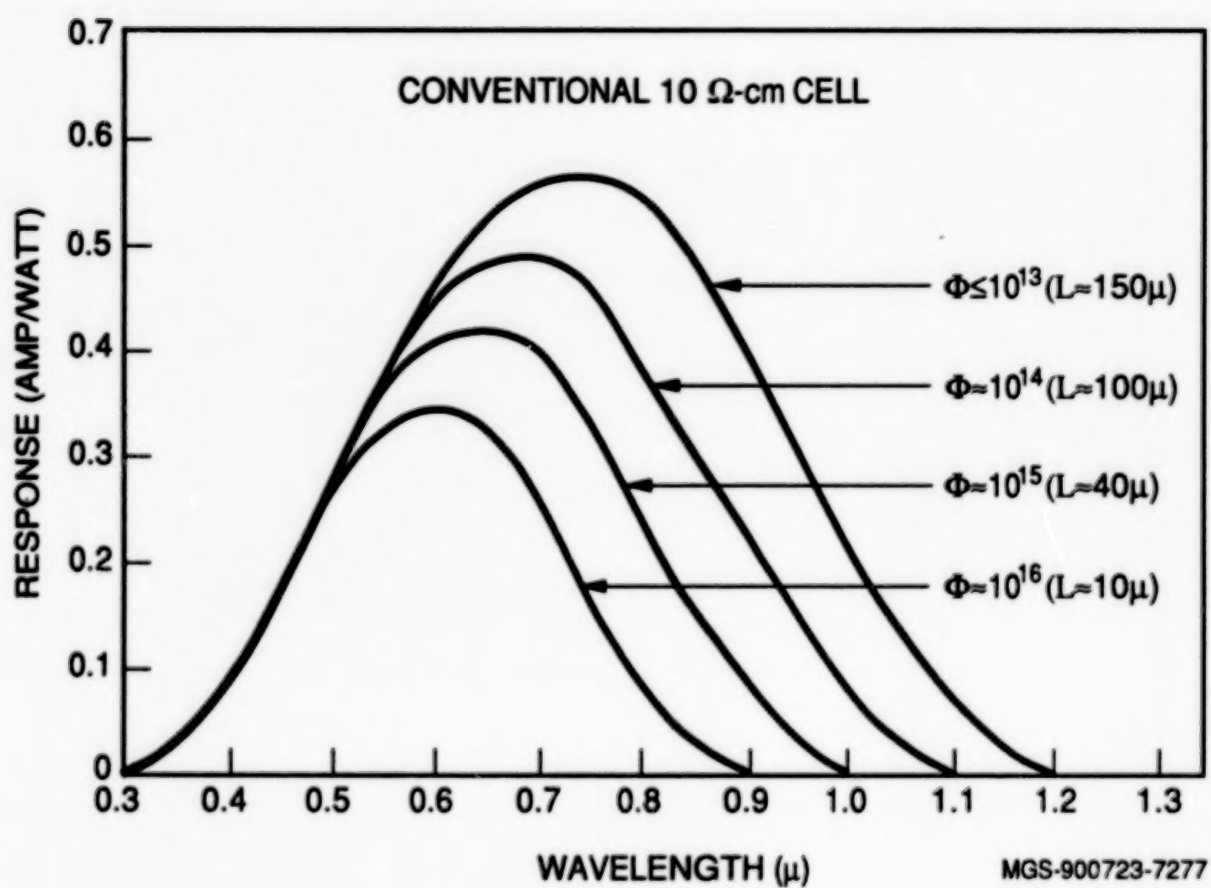


Figure 2. The Response of a Typical Solar Cell Subjected to Increased Radiation Fluences. (The units on Φ are equivalent 1 MeV electrons.)

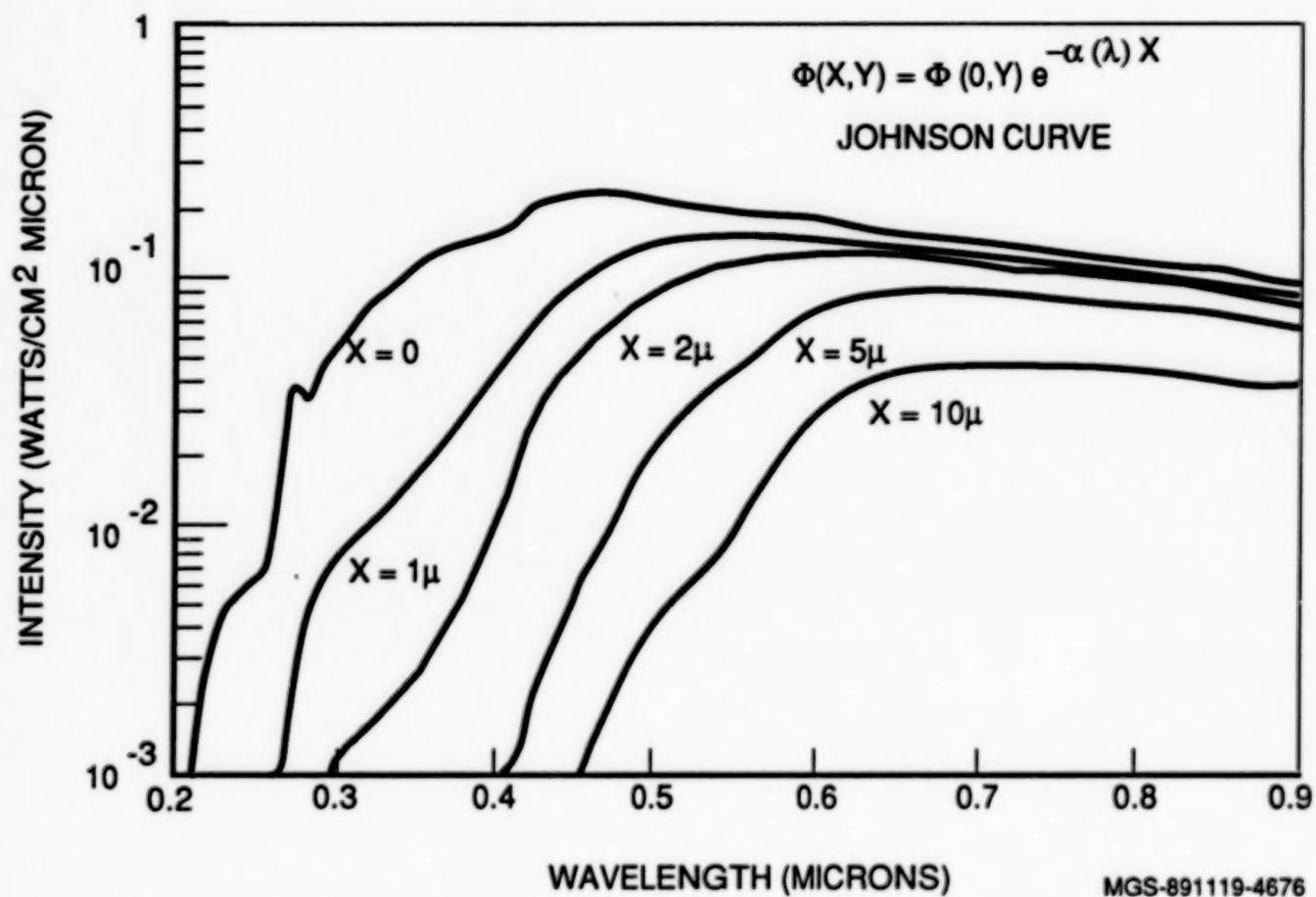
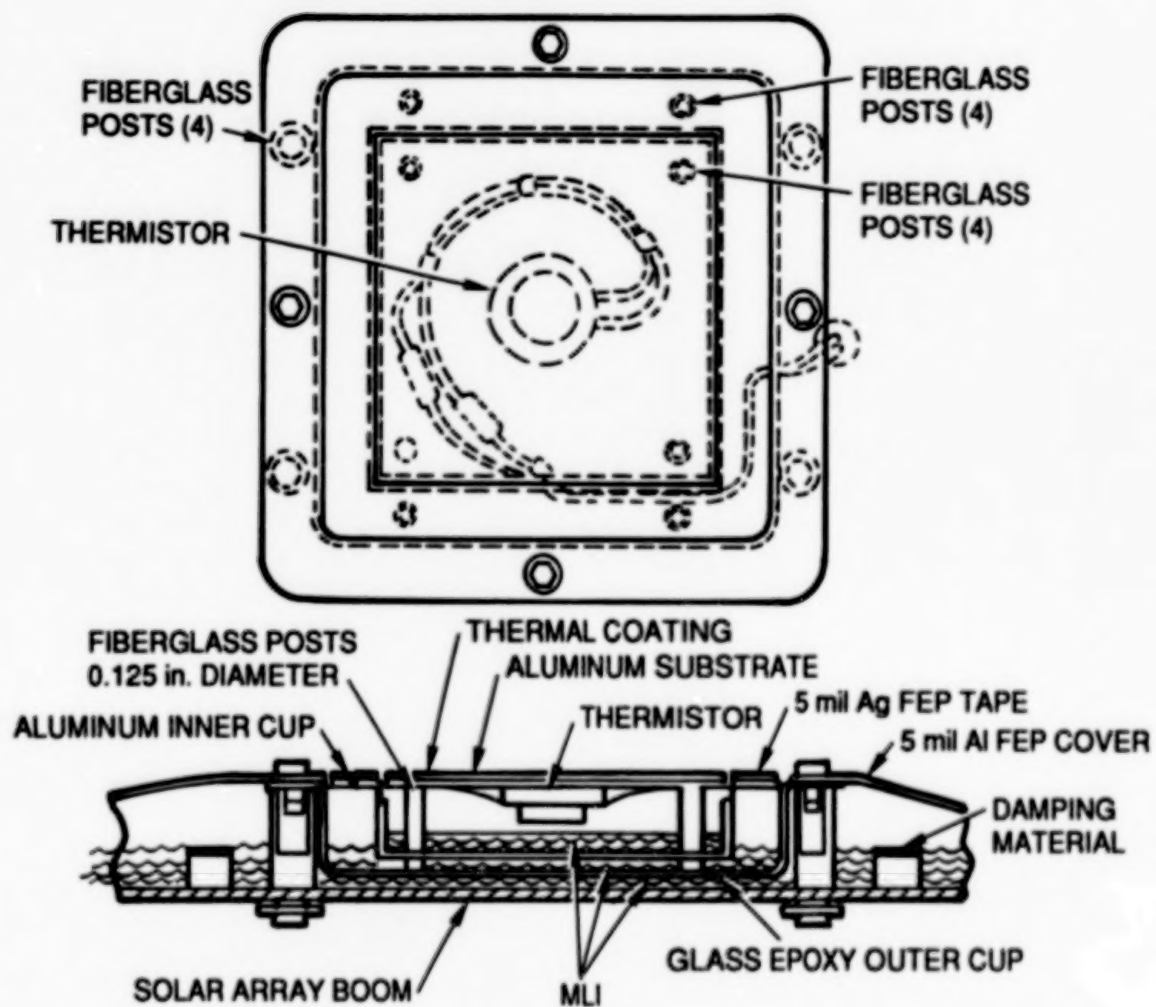


Figure 3. The Effect of Contamination Upon Light Transmission.



MGS-900725-7278

Figure 4. The Proposed Calorimeter Design.

SIMULATION OF MARTIAN DUST ACCUMULATION ON SURFACES

Marla E. Perez-Davis and James R. Gaier
National Aeronautics and Space Administration
Lewis Research Center
Cleveland, Ohio 44135

Robert Kress
University of Akron
Akron, Ohio 44311

Justus Grimalda
Massachusetts Institute of Technology
Boston, Massachusetts 02139

ABSTRACT

Future NASA space missions include the possibility of manned landings and exploration of Mars. Environmental and operational constraints unique to Mars must be considered when selecting and designing the power system to be used on the Mars surface.

This paper describes a technique which has been developed to simulate the deposition of dust on surfaces. Three kinds of dust materials were evaluated: aluminum oxide, basalt, and iron oxide. The apparatus was designed using the Stokes and Stokes-Cunningham law for particle fallout, with additional consideration given to particle size and shape.

Characterization of the resulting dust films on silicon dioxide, polytetrafluoroethylene, indium tin oxide, diamondlike carbon, and other surfaces are discussed based on optical transmittance measurements. The results of these experiments will guide future studies which will consider processes to remove the dust from surfaces under Martian environmental conditions.

INTRODUCTION

In the foreseeable future, a manned mission will land on the surface of Mars. Environmental and operational constraints unique to Mars need to be considered when selecting and designing the power system to be used on the Martian surface.

The natural environmental characteristics of Mars, such as dust, ultraviolet radiation, winds, temperature variations, atmospheric condensates and/or synergistic combinations of these, may pose a threat to the power systems established on the Martian surface. Most of the current information on the characteristics of the Martian atmosphere and soil composition was obtained from the Viking 1 and 2 missions in 1976. The Viking landers found that the Martian atmosphere is composed of CO₂ (95.5 percent), N₂ (2.7 percent), Ar (1.6 percent), O₂ (0.15 percent), and CO (0.07 percent) (ref. 1).

The Martian atmosphere contains suspended dust particles which result from many local and global dust storms that occur each year. The information obtained from the Mariner 9 and the Vikings missions suggest that the dust is a mixture of many

materials such as granite, basalt, basaltic glass, obsidian, quartz, andesite, or montmorillonite. Viking Landers' results also suggest the presence of highly oxidizing species (ref. 2).

Space power system components such as photovoltaic arrays, radiators, and solar concentrators are vulnerable to degradation in the Martian environment. Accumulation of dust particles may reduce the transmittance of photovoltaic arrays or reduce the thermal emittance of radiators thus permanently degrading their performance. Abrasion of power surfaces could also result from dust blown by the wind.

This paper describes a technique which has been developed to simulate the deposition of dust on surfaces on Mars. Characterization of the resulting dust films on various surfaces will also be discussed. The results of these experiments will guide future studies which will consider processes to remove the dust from surfaces under Martian conditions.

The authors would like to thank Bruce Banks, Chief of the Electro-Physics Branch at NASA Lewis Research Center for his constructive criticism and suggestions in the design and fabrication of the dust box and Kim De Groh for helping with the SEM pictures. Appreciation is also expressed to Robert Martineau from the Materials Division at NASA Lewis Research Center for providing the particle size analyses of all our dust material.

APPROACH

Materials

The observations made by the Viking lander imaging cameras on Mars were used to estimate dust particle size and composition. The fine-grained material in the atmosphere is considerably less than 100 μm in diameter. Three different dust composition materials were considered in this simulation. The first dust was 1800 grit optical grinding material from American Optical Company. The particle size ranged from 0.1 to 25 μm with a particle size distribution as shown in figure 1. The composition is principally aluminum oxide powder (89 percent), with significant amount of silicon dioxide (6.6 percent) and titanium dioxide (3 percent), and small amounts of iron (III) oxide (0.6 percent) and chromium (III) oxide (0.6 percent). The particles have a density of 3.67 g/cm^3 . The sample materials dusted included candidate materials for photovoltaic arrays and radiators. The photovoltaic arrays samples were 1 in. (2.54 cm) square, 5 mil (0.13 mm) thick coverslips left bare or coated with silicon dioxide (SiO_2), polytetrafluoroethane (PTFE), 50 percent SiO_2 - PTFE, indium tin oxide (ITO), or diamond-like carbon (DLC). The radiator samples used were 1 in. (2.54 cm) diameter discs of carbon-carbon composite, pyrolytic graphite, or arc-textured copper.

The second type of dust was a basalt (trap rock) with the following composition (percent by weight): SiO_2 (46.6), Al_2O_3 (16.6), Fe_2O_3 (13.0), CaO (11.1), MnO (0.3), MgO (6.1), Na_2O (2.3), K_2O (1.1), TiO_2 (2.0), CO_2 (0.1), and P_2O_5 (0.1). Glass coverslips were dusted with the trap rock of 3.0 g/cm^3 . The particle size distribution of this material is shown in figure 2.

Iron oxide (Fe_2O_3) particles (2.83 g/cm^3) were the third dust type deposited on glass coverslips. Figure 3 presents the particle size distribution of these particles.

METHOD

The forces of a particle falling through air are primarily those of weight in the direction of motion and the aerodynamic drag opposition. Figure 4 illustrates the forces acting on a spherical particle. The general solution of the equation in terms of the terminal velocity (V_t) is:

$$V_t = \frac{gd_p^2(\rho_p - \rho_g)}{18\mu} \quad (1)$$

where g is gravity, d_p is particle diameter, μ is viscosity of fluid, and ρ_p, ρ_g are density of the particle and fluid, respectively.

This expression is known as Stokes' law. This equation is quite accurate for spherical particles of diameters $<50 \mu\text{m}$; for particles $<5 \mu\text{m}$ in diameter, a multiplicative correction factor (ref. 3), K_c , is often applied given by:

$$K_c = 1 + \frac{2}{d_p} \left[1.257 + 0.40 \exp\left(-\frac{0.55 d_p}{\lambda}\right) \right] \quad (2)$$

here λ is the mean free path of the molecules in the gas phase defined by:

$$\lambda = \frac{\mu}{0.499 \rho u_m}$$

where u_m is the mean molecular speed, μ is the viscosity of the gas, and ρ is the gas density. Using the kinetic theory of gas u_m is defined by:

$$u_m = \left(\frac{8 RT}{\pi M} \right)^{1/2} \quad (3)$$

where M is the molar mass or molecular weight of the gas. This correction factor is used because the mean free path of the gas molecules in the atmosphere approaches the particle diameter for particles smaller than $5 \mu\text{m}$ in diameter. These small particles tend to slip past the gas molecules causing the terminal velocity to become greater than that predicted by Stokes' law. The relation used for these small particles is known as the Stokes-Cunningham law:

$$V_c = K_c V_t \quad (4)$$

The above equations were used to determine an approximate and reasonable height for the design and fabrication of a box to be used for the deposition of dust on sample surfaces. Figure 5 shows the terminal velocity of particles in atmospheric air at room temperature. A height of 0.7 m was selected, and the falling time for different particle sizes was calculated. Figure 6 shows the falling time for different particle sizes at the height of 0.7 m .

The dust particles were elevated by an air pulse blowing downward on the dust material. In order to reduce the aggregation of particles due to moisture, a moisture trap was inserted in the air line. The dust box was constructed of stainless steel (fig. 7) and consists of a square pyramidal recirculating chamber, a dusting chamber, a tray for samples, transparent windows, and the air lines. The purpose of the conical shape is to ensure the collection and distribution of the dust in a more uniform and efficient manner. In designing the recirculating chamber, careful

attention was given to the selection of the required angle to overcome the friction so the particles would slide and be collected at the bottom of the box. Theoretical and experimental calculations showed that the required angle should be $>40^\circ$ and $<90^\circ$, so based on these results the cone box angle selected was 64° . The transparent closed windows at opposite sides of the dust box were used to measure optical transmittance of the dust through the box.

Optical transmittance measurements were made using a transmittance measurement device (TMD). The TMD is made up of a white light source and a sensing head of a Coherent Model 212 Power Meter. Absolute transmittance measurements were converted into percent transmittance measurements. Measurements were made of the occlusion of light through the windows of the dust box at the beginning of each dusting simulation and of the samples before and after dusting.

The samples were mounted in specially designed sample holders (fig. 8), which tilt at different angles, 0° , 22.5° , 45° , 67.5° , or 90° from the floor. All the sample holders were held horizontally and subject to a dusting which simulates the aftermath of a dust storm.

The sample tray was inserted into the dusting chamber 30 sec after the dust was elevated to avoid collecting particles $>20\ \mu\text{m}$ (fig. 6).

RESULTS AND DISCUSSION

There are several factors which will effect the dusting process including particle size, particle shape, surface chemistry, amount of dust, and time. The particle sizes utilized in the dusting process were the ones which expected to become suspended during a global or local dust storm, but when normal weather conditions return, will settle out. It is important to note that Stokes-Cunningham fallout is probably not the dominant mechanism leading to dust storm clearing at Mars. Particles between 1 to $10\ \mu\text{m}$ suspended in the Martian atmosphere are more likely supported by turbulence with an eddy diffusion coefficient and do not experience the Stokes-Cunningham fallout (ref. 4). It is thought that these particles are mixed into the surface boundary layer where they impact the surface and fallout.

Examination of our experimental particles using the scanning electron microscope (SEM), showed a nonspherical shape (fig. 9). Evidence suggests that dust particles on Mars are also nonspherical (ref. 5), which makes our powder dust appropriate for the expected size and shape of the Martian dust. The chemistry of our dust, however, is not expected to be similar to Martian dust (ref. 4). The settling time of about 8 min for Al_2O_3 was selected in order to collect different particle sizes and also to reduce the transmittance of the samples. The settling time of 8 min for trap rock or iron oxide was not enough to get the same occlusion of light obtained for aluminum oxide dusted samples. Two settling runs were needed to obtain similar occlusion for samples dusted with trap rock and several runs were needed for the ones dusted with the iron oxide.

The samples were weighed before and after dusting, however, the weight of the dust added to the surface was below the sensitivity of the balance used ($\pm 0.1\ \text{mg}$). Examination of the dusted samples using SEM analysis showed a very evenly distributed dust layer and some particle aggregation (fig. 10).

The uniformity of the dust deposited on the samples as function of the number of sequential dust elevation and depositions (dusting runs) are shown in figures 11 and 12. The transmittance of the samples after being dusted (T_d) divided by the initial transmittance (T_0) was used to characterize uniformity of the samples. The uniformity of dust deposition by materials (photovoltaic candidate materials), is shown in figure 12. A variety of transmittance values were obtained for each sample batch. Several factors, such as amount of dusting material in the dust box (initially 150 g were deposited in the box), type of dust, time of inserting the samples, and duration of dust deposition in the box (which is directly related to particle size collected) could account for the differences in transmittance.

CONCLUSIONS

The technique developed to dust samples was successfully tested. The process was applied to candidate materials to be tested at MARSWIT for aeolian study. It was found that dust is uniformly distributed over the samples, however the transmittance values of the samples shows different values for different runs. This difference is probably related to the fact that the amount of dust (grams) changes slightly after each run. Additional material was added after each run to compensate for the lost dust. Increases in transmittance loss might be related to the increase in dust material and reduction could indicate loss of material inside the box when compared occlusion by the same type of dust material. Also, exposure times are critically related to the particle sizes collected and consequently the light occlusion obtained as is the case for iron oxide particles.

REFERENCES

1. Owen, T.C., Biemann, K., Rushneck, D.R., Biller, J.E., Howarth, D.W., and Lefleur, A.L., "The Composition of the Atmosphere at the Surface of Mars," Journal of Geophysical Research, Vol. 82, No. 28, Sept. 30, 1977, pp. 4635-4639.
2. Huguenin, R.L., Miller, K.J., and Harwood, W.S., "Frost-Weathering on Mars: Experimental Evidence for Peroxide Formation," Journal of Molecular Evolution, Vol. 14, Dec. 1979, pp. 103-132.
3. Wark, K., and Warner, C.F., Air Pollution: Its Origin and Control, 2nd Edition, Harper & Row, New York, 1981.
4. Toon, O.B., Pollack, J.B., and Sagan C., "Physical Properties of the Particles Composing the Martian Dust Storm of 1971-1972," Icarus, Vol. 30, No. 4, Apr. 1977, pp. 663-696.
5. Zurek, R.W., "Martian Great Dust Storms: An Update," Icarus Vol. 50, No. 2-3, May-June 1982, pp. 288-310.

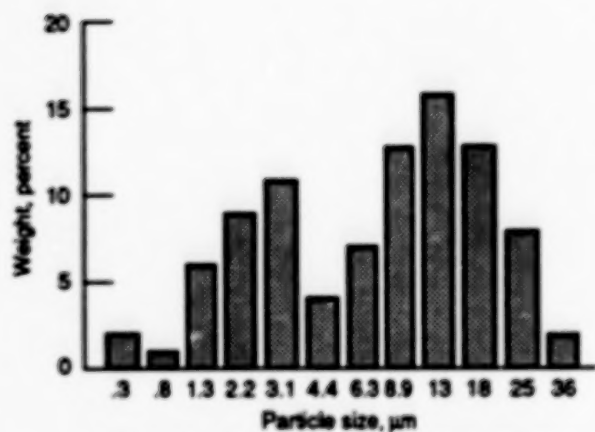


Figure 1.—Particle size distribution of aluminum oxide dust.

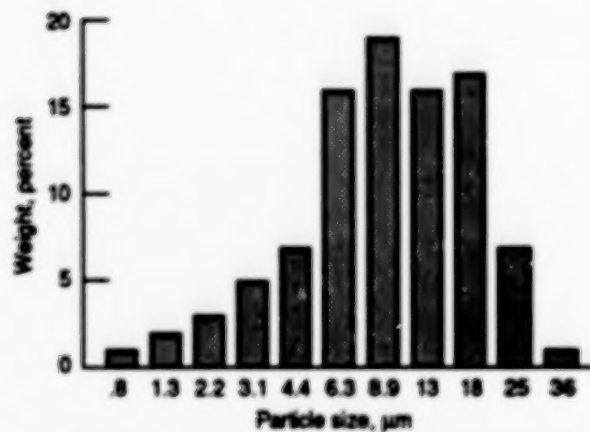


Figure 2.—Particle size distribution of basalt (trap rock).

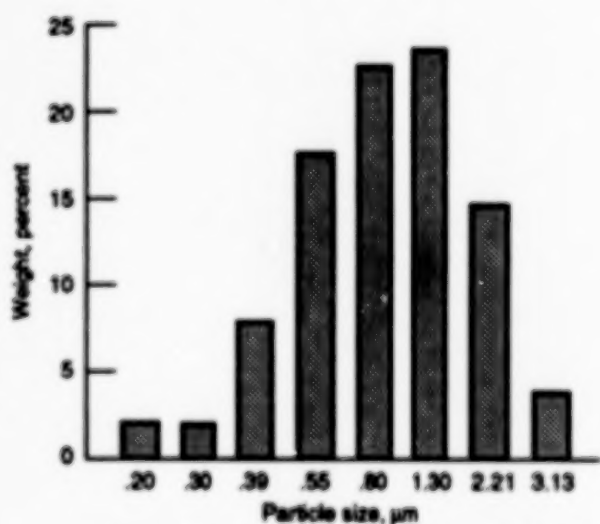


Figure 3.—Particle size distribution of iron oxide dust.

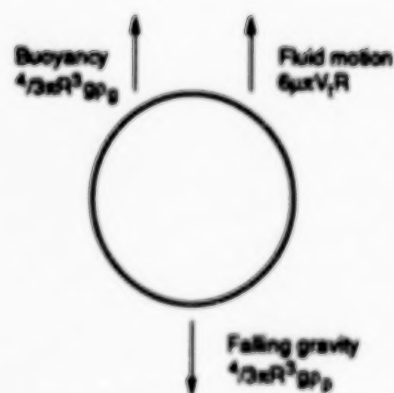


Figure 4.—Diagram of forces acting on a sphere.

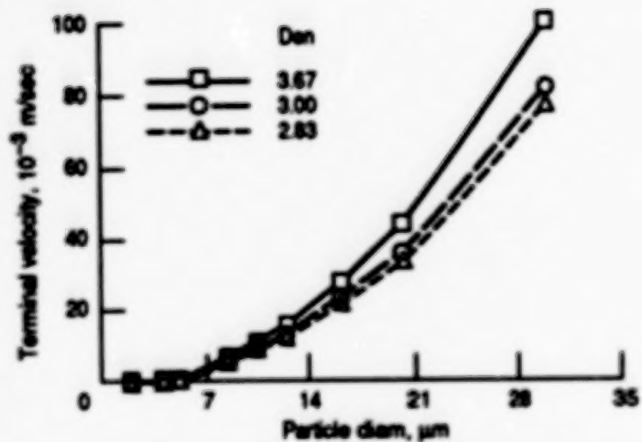


Figure 5.—Terminal velocity as a function of particle size.

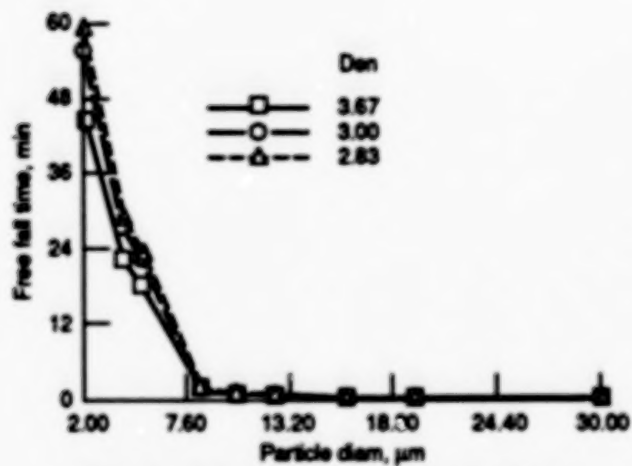


Figure 6.—Falling time versus particle size. Distance = 0.71 meters.

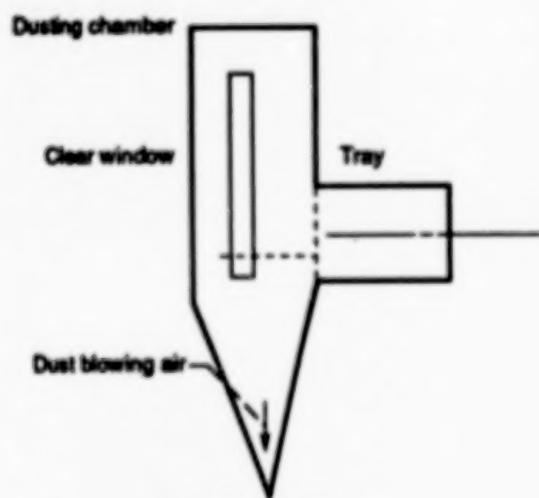


Figure 7.—Dust box.

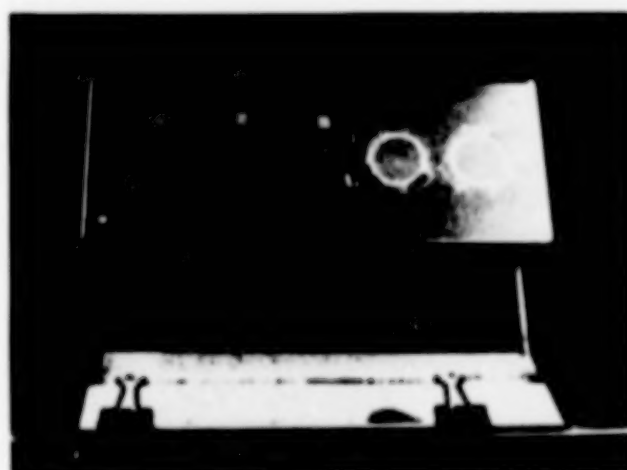


Figure 8.—Samples holder design.

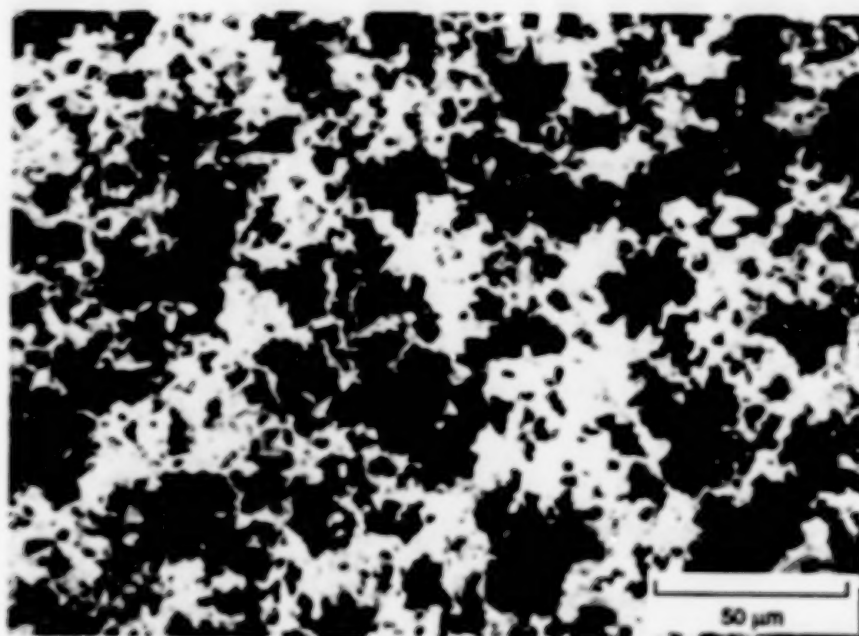


(a) Aluminum Oxide polishing grit.

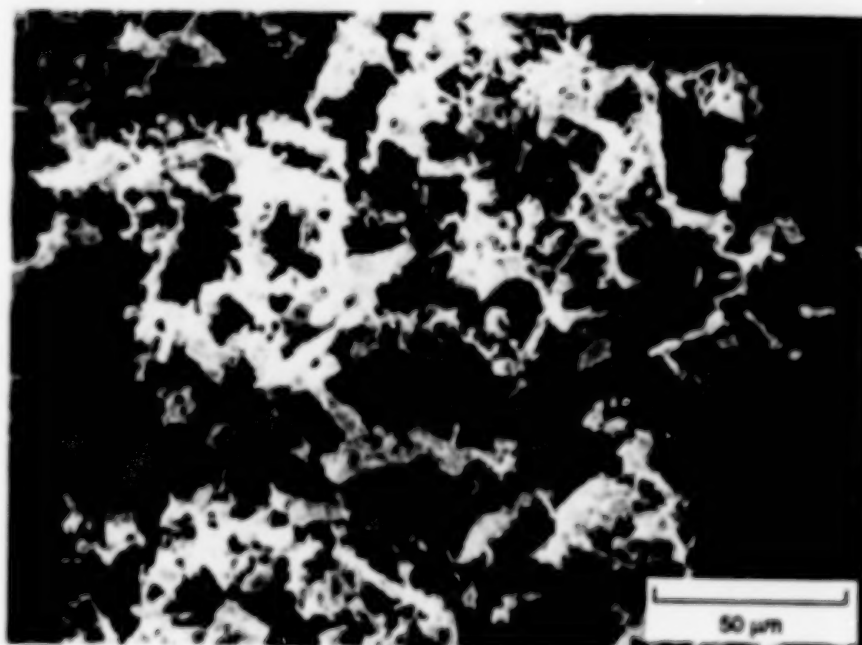


(b) Basalt.

Figure 9. Scanning Electron Microscopy (SEM) Showing Particle Shape



(a) Aluminum Oxide polishing grit.



(b) Basalt.

Figure 10. Scanning Electron Microscopy (SEM) of Dusted Samples

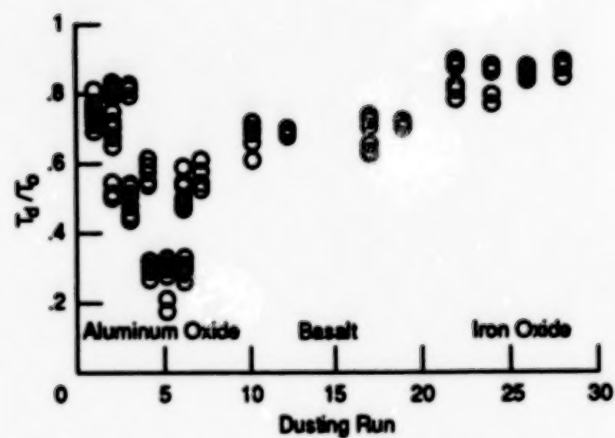


Figure 11. Uniformity of Dust Deposition

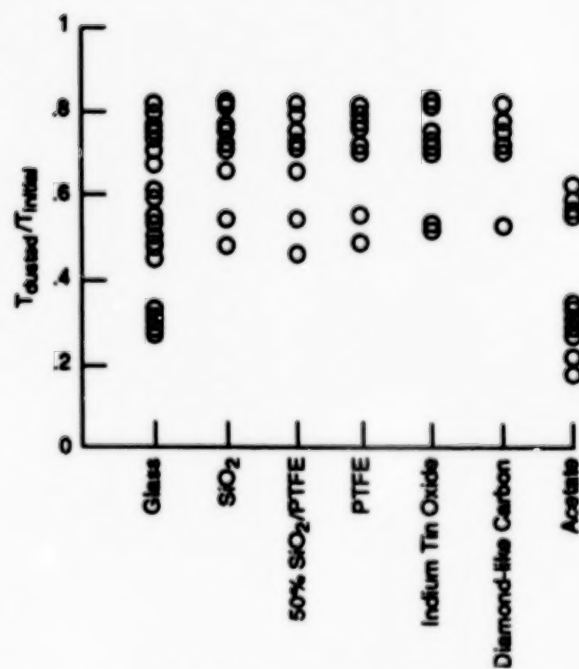


Figure 12. Uniformity of Dust Deposition by Material Using Aluminum Oxide Dust

TRANSFER ORBIT STAGE
MECHANISMS THERMAL VACUUM TEST
Scott T. O'Leary
Martin Marietta Astronautics Group

ABSTRACT:

Martin Marietta recently conducted a systems level mechanisms test on the Orbital Sciences Corporation's (OSC) Transfer Orbit Stage (TOS). The TOS is a unique partially reusable transfer vehicle which will boost a satellite into its operational orbit from the Space Shuttle's cargo bay. The mechanical cradle and tilt assemblies will return to earth with the Space Shuttle while the Solid Rocket Motor (SRM) and avionics packages are expended.

A mechanisms test was performed on the forward cradle and aft tilting assemblies of the TOS under thermal vacuum conditions. Actuating these assemblies under a 1 g environment and thermal vacuum conditions proved to be a complex task. Pneumatic test fixturing was used to lift the forward cradle, and tilt the solid rocket motor (SRM) and avionics package. Clinometers, linear voltage displacement transducers (LVDT), and load cells were used in the thermal vacuum chamber to measure the performance and characteristics of the TOS mechanism assembly.

Incorporation of the instrumentation and pneumatic system into the test setup was not routine since pneumatic actuation of flight hardware had not been previously performed in our facility. This paper presents the methods used and the problems experienced during the design, setup and test phases of the TOS mechanisms thermal vacuum test.

INTRODUCTION:

The TOS system uses mechanical actuators to open a forward cradle and tilt the aft assembly which holds a satellite and TOS SRM and avionics package (figure #1). Tests were conducted on the TOS system at ambient temperature and pressure conditions, and worst case cold at vacuum. The TOS Mechanisms test had five primary objectives:

- 1.) Measure the rotational resistance of the forward cradle hinge and the aft cradle trunnions due to:
 - a. manufacturing tolerances
 - b. worst case cold temperatures (-65°F)
 - c. locked aft trunnion pins
 - d. stiffness of ASE/orbiter wire harness
- 2.) Demonstration of complete latch operation of the forward cradle including the proper operation of system indicators. This also encompassed testing for the latch grab envelope for the system which demonstrated stow capabilities during a possible abort situation.
- 3.) Demonstrate overall system functionality, including MLI and structural interferences during system operation.
- 4.) Verification of system indicators and microswitch operation i.e., aft cradle tilt up, aft cradle full down, and forward cradle down indicators.

- 5.) Comparison of operation between ambient and worst case cold temperature conditions.

To accomplish these objectives a unique test setup was needed with a number of complex fixtures and special instrumentation.

TEST FIXTURING:

The test fixturing included:

- 1.) Two Pneumatic actuators in heated enclosures, mounted on an overhead structure and attached to the chamber lid hardpoints.
- 2.) Valve bank control assembly for the operation of the pneumatic actuators.
- 3.) Test support structure in which the vehicle was mounted horizontally (x-axis) by its forward and aft trunnions. This structure mounted to the chamber floor hardpoints, with allowances for thermal expansion and contraction.
- 4.) Heated enclosures for test instrumentation and test tools, such as the thrust vector control test tool (TVC), pneumatic actuators, trunnions, load cells, LVDTs, and clinometers.
- 5.) Aft trunnion locking fixtures were built to hold the aft trunnion bearings in place so the secondary rotation of the aft assembly could be proven and the resistance measured. These were secured to the trunnions and mounted to the vehicle support structure.
- 6.) A SRM Simulator was constructed. The actual SRM was too heavy to be used for this test.

PNEUMATIC CONTROL SYSTEM

The rotation (lifting) of the flight hardware was accomplished with pneumatic actuators which pulled cables that lifted the forward cradle and tilted the aft assembly.

The pneumatic actuators were operated manually by adjusting hand valves which were located on a system valve bank assembly (figure #2). This proved to be a simple and effective method of operating the actuators.

The pneumatic actuators were special ordered with Buna-N seals for compatibility. Functional tests were performed on the actuators to ensure their integrity.

A full system verification was performed with the actuators on the support assembly. During checkout, a frictional binding problem in the actuators was discovered. To reduce the side loading on the piston, a swiveled pulley was attached to the end of the actuator piston, allowing it to rotate freely (figure #3). The bolts which mounted the pneumatic actuator to the support structure were loose. To allow the actuator to float, thus reducing the torsion acting on the actuator. The tilt actuator was hung vertically and pinned at one end which allowed it to move freely (figure #4). This setup reduced the friction sufficiently to allow the hardware to be moved in a smooth manner.

The system was proofloaded to two times the expected operating loads. The pneumatic system applied the appropriate loads to pull the cable to mechanically proofload the pneumatic test fixture. Both actuators were pulled simultaneously. Load cells were used to verify the proper loads.

TEST INSTRUMENTATION:

Two hundred and thirty thermocouples were used to control kill and monitor temperatures on the unit, fixtures and chamber.

Four video cameras were used to monitor the actuation of the flight hardware. Three were installed in the chamber and enclosed in cases where they were maintained at ambient temperature and pressure. The first camera viewed the forward cradle latch microswitch to verify complete latch operation. The second was located at the aft cradle full up tilt microswitch to monitor its activation, the third viewed the hinge actuator during its deployment. The fourth camera was mounted to a viewport on the chamber lid, outside the chamber. It was used to view the entire operation. The valve bank operator used this monitor to control the lift and tilt operations.

Two load cells were used to obtain force vs angle data for post frictional analysis. To obtain the accuracy required for the frictional analysis, a special calibration was performed on the load cells. This special calibration gave a load cell accuracy of ± 2 lbs. One load cell was installed in line on the cable which lifted the forward cradle. The second was installed in line, on the cable which tilted the aft assembly.

Four clinometers were used to obtain force vs angle data, and rates of rotation in degrees/minute. Two were attached to the forward cradle and two to the aft assembly.

Two linear voltage displacement transducers (LVDT) were used to measure the initial unlatch displacement of the top side of the forward cradle with respect to the lower section of the forward cradle, and to verify the cradle returned to its original position after rotation. They were also used to place the upper forward cradle in the outer limits of the latch grab envelope, so the envelope could be verified. These were attached to the latch side of the forward cradle on the lower section. These too were heated and thermally isolated from the vehicle such that they could be maintained at their ambient calibration temperature.

All load cells, clinometers, and LVDT's were maintained at ambient temperature to ensure calibration integrity.

Redundancy was used for all critical test instrumentation except the load cells, physical restraints prevented their redundancy. A bound spring on one LVDT limited the plungers range. One of the aft assembly clinometers failed.

VEHICLE SETUP:

The TOS was mounted horizontally in its support structure in the thermal vacuum chamber (figure #5). The forward cradle flight hinge actuators and the aft cradle flight tilt actuators, two each, were disconnected so they could be operated without exceeding their zero g design limitations. The shuttle interface harness was configured in a flight like manner to simulate harness stiffness during rotation. Pneumatic actuator lifting interfaces were installed on the vehicle and the lift cables and instrumentation connected. MLI was not installed on the top section of the forward cradle for two reasons, first to help induce temperature gradients between the forward and aft sections of the forward cradle, secondly, eliminate MLI interference with the lift fixture.

MECHANISMS TESTS:

Deployment:

The test consisted of opening the forward cradle 60° . The full open position for the cradle is 102° , but due to chamber size limitations, 60° was the maximum it could be rotated. The full open microswitch activation for the forward cradle was verified through floor tests, using an overhead crane.

The aft assembly was tilted 42° to activate the deployment microswitch. When the activation of the microswitch was verified, the aft assembly was rotated to 45° to verify full tilt capability. This is done because the primary and secondary tilt actuators are offset, with the primary actuator capable of tilting 42° , the secondary 45° .

Stowing: Latch Grab Test

Stowing is accomplished by lowering the forward cradle onto the aft cradle, then latching the forward cradle, thus securing both the forward and aft sections. This test was conducted to ensure the forward cradle and aft assemblies would stow and latch properly under worst case conditions. The latching mechanism was designed with a two inch latching envelope. Since the latch actuators could exert enough force to damage the test actuators, precautions were taken during this test to prevent this occurrence.

The forward cradle was lowered within two inches of its stowed position. At this distance the latches were required to open to their maximum range to grab the cradle and pull it into a locked position. During latching operations, the test actuators supported the forward and aft assemblies.

The full up deployment, and stowing routines were repeated three times at ambient temperature and pressure and three times at worst case cold under vacuum conditions. The data received from these tests was used to extract forces due to gravity and rotation resistance.

THERMAL VACUUM TEST RESULTS:

The predicted loads for a given angle vs the approximate actual loads for the operation of the forward cradle are shown below:

	<u>Degrees Rotation</u>	<u>Predicted Loads</u>	<u>Actual Loads</u>	<u>Maximum Allowable Load</u>
Ambient	0°	1196 lbs	1220 lbs	1450 lbs
Cold (-65°F)	0°	"	"	"
Ambient	60°	960 lbs	480 lbs	"
Cold (-65°F)	60°	"	"	"

The predicted loads for a given angle vs the approximate actual loads for the operation of the aft cradle are shown below:

	<u>Degrees Rotation</u>	<u>Predicted Loads</u>	<u>Actual Loads</u>	<u>Maximum Allowable Load</u>
Ambient	0°	1678 lbs	1740 lbs	1750 lbs
Cold (-65°F)	0°	"	*1927 lbs (max)	"
Ambient	45°	1307 lbs	1376 lbs	"
Cold (-65°F)	45°	"	"	"

During lift and tilt operations, rates of 38.25 deg/min on the forward cradle and 15.75 degrees/min of the aft cradle were desired. Due to the time required to accelerate and decelerate, these rates were achieved only for a short period of time.

*During the first tilting operation of the aft cradle, the aft cradle would not move at the allowable loading of 1750 lbs. A decision was made to exceed the allowable load by a maximum of 200 lbs to see if the aft cradle would free itself from the lower section of the forward cradle. The aft cradle came free at 1927 lbs, loads through the remainder of the rotation returned to normal. The binding of the aft cradle was caused by preloading in the forward cradle pads, and the contraction of the forward cradle at cold conditions. The second actuation also exceeded the maximum load at 1815 lbs. The last actuation was within tolerance at 1725 lbs.

SUMMARY:

The mechanisms test successfully met its objectives by verifying the TOS's operational envelope, and qualifying the vehicle's mechanisms in a worst case cold environment. They revealed a problem in the design and preloading of the forward cradle pads. The two 10° pads were redesigned to prevent them from binding. The frictional analysis showed no major differences between the ambient temperature and cold temperature friction for the forward cradle and only a slightly higher loading for the tilting operation. These loads were acceptable and within the design range of the flight actuators.

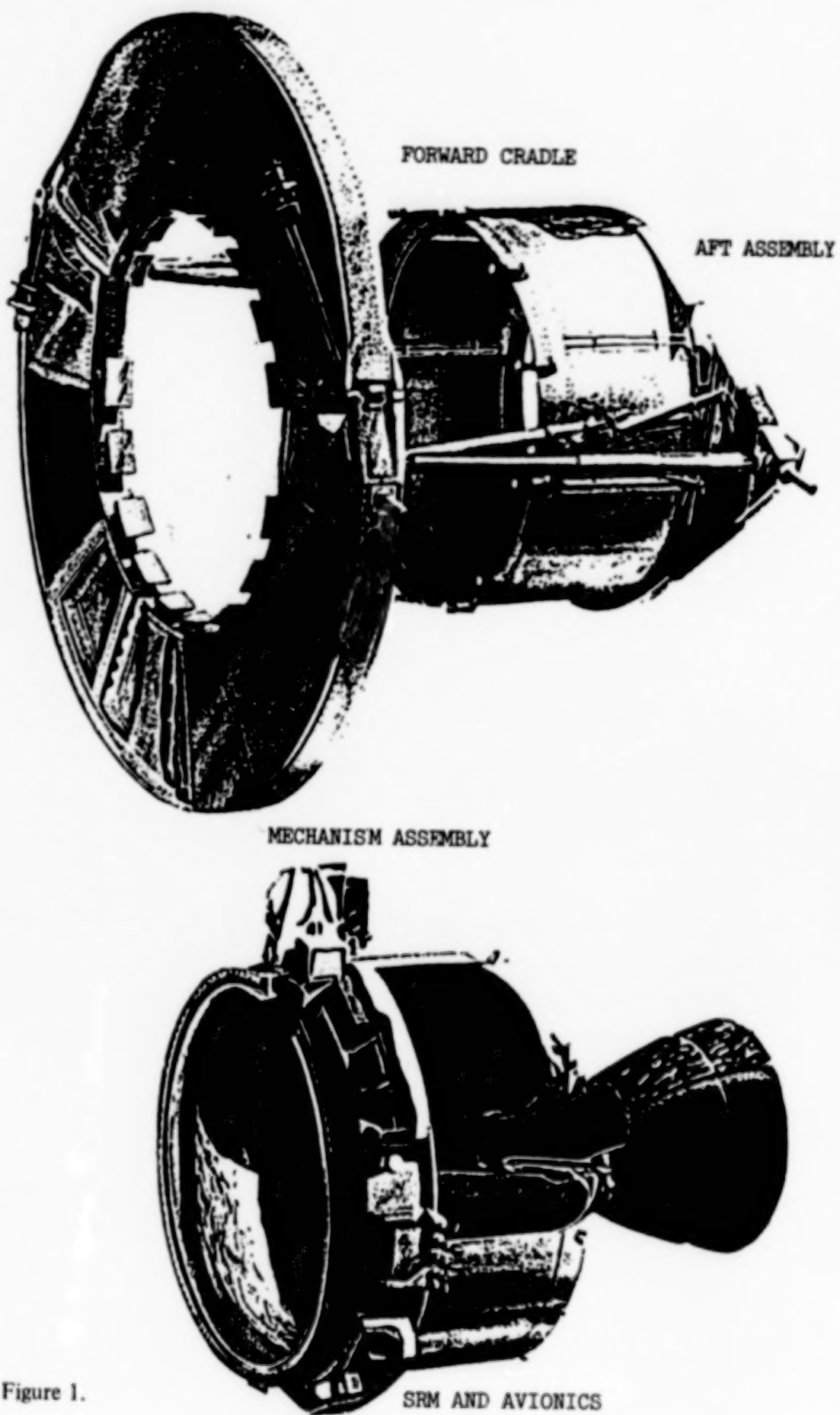
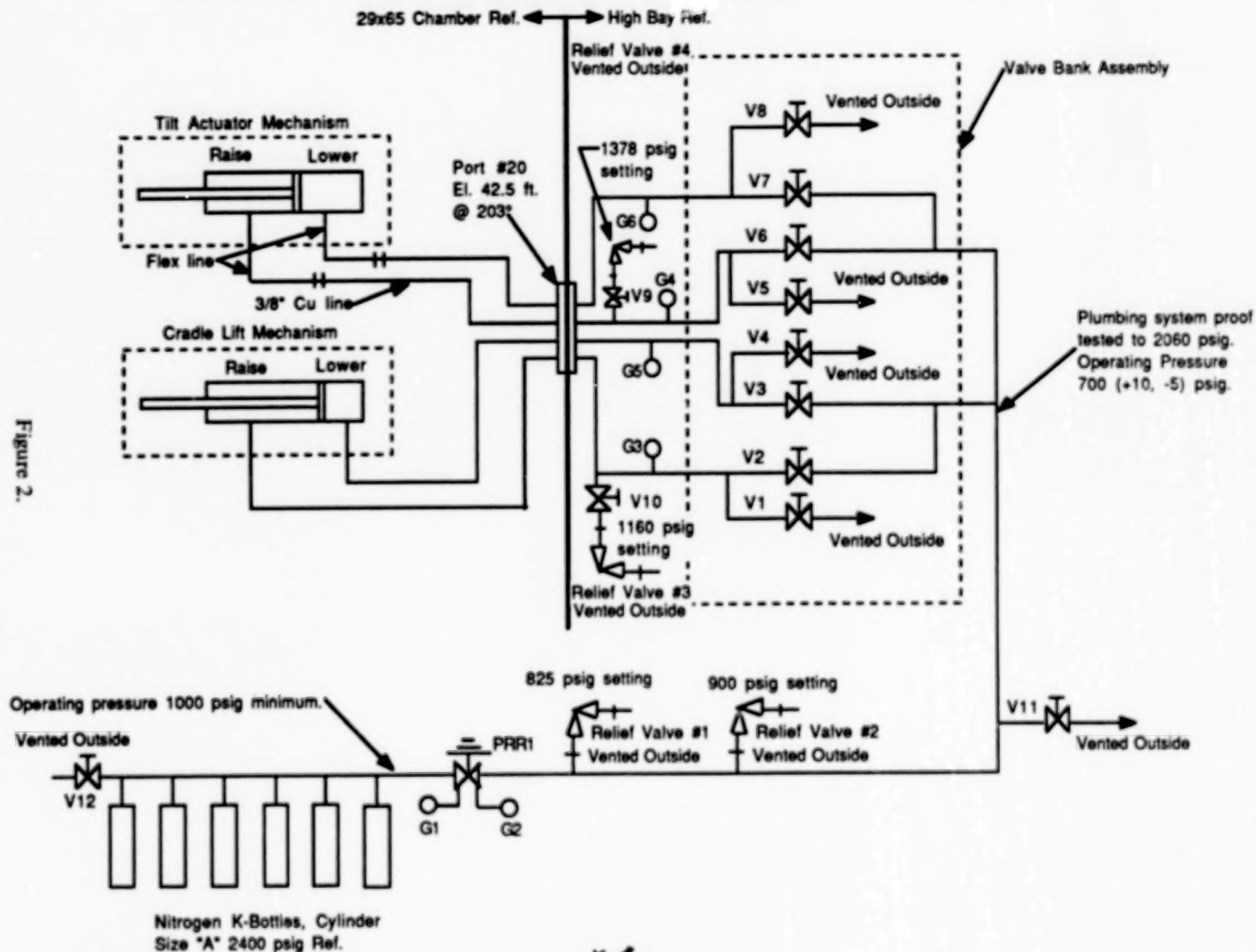


Figure 1.

LIFT AND TILT ASSEMBLY PLUMBING AND VALVING



463

Figure 2.

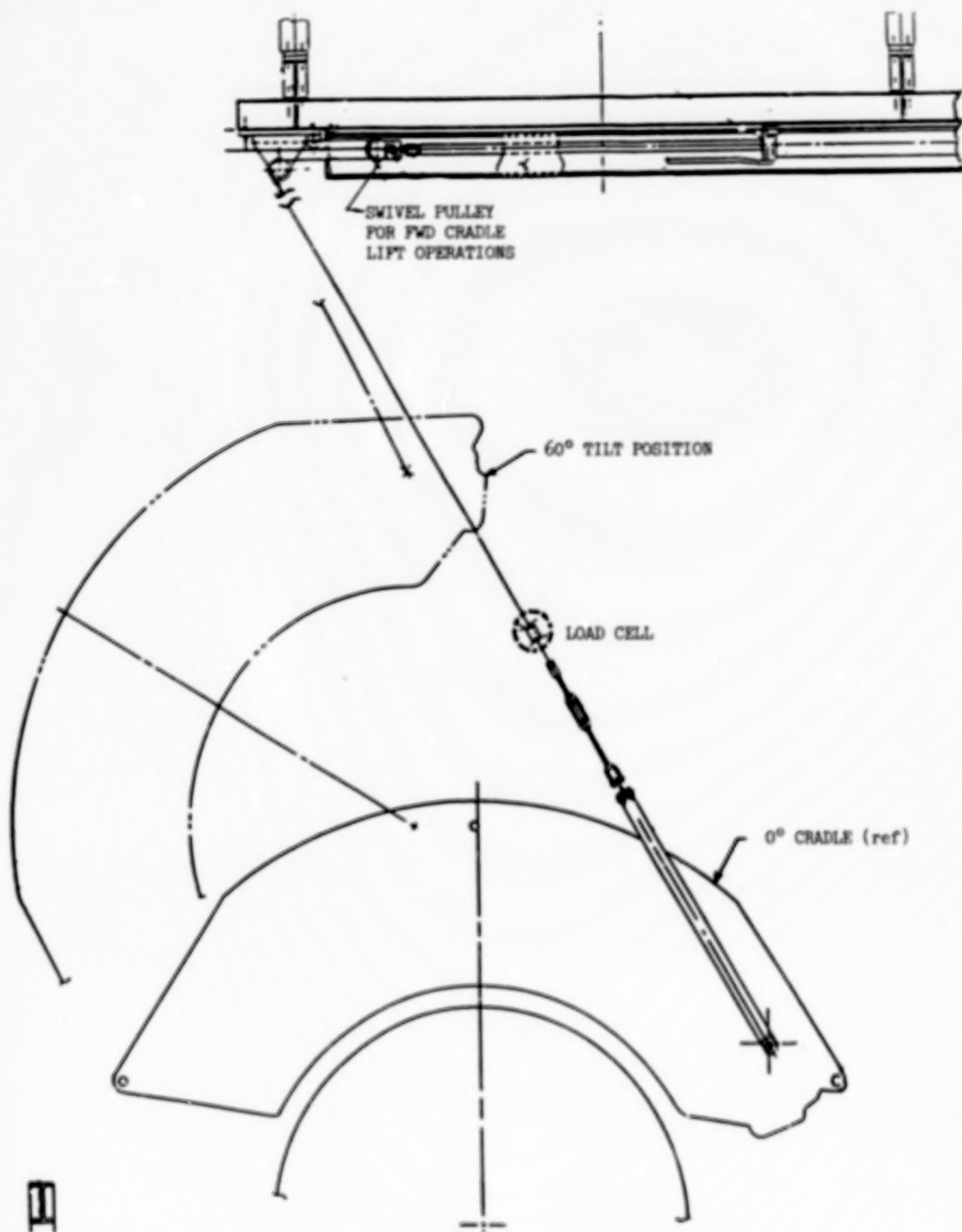


Figure 3. Forward Cradle Lift

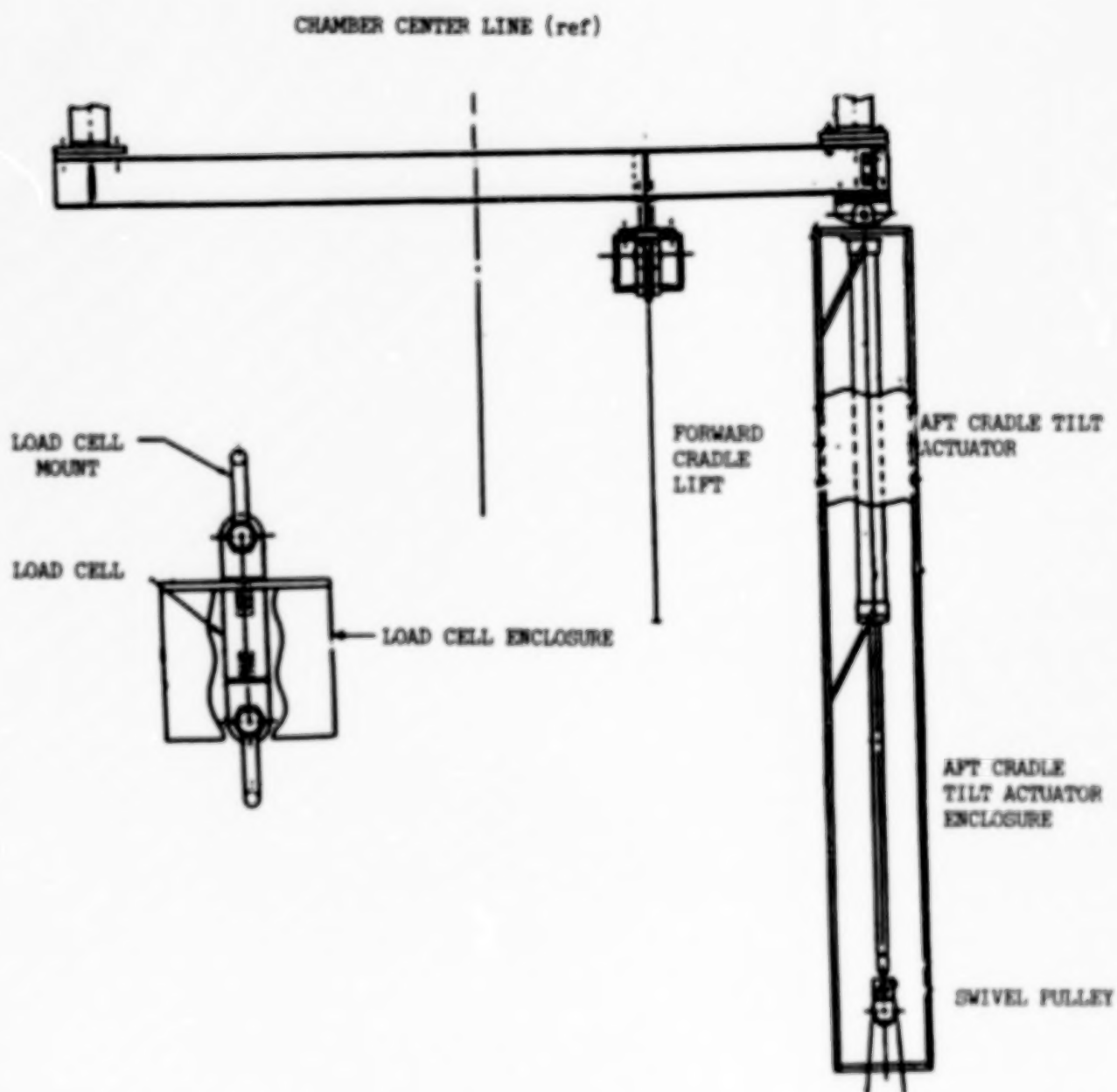


Figure 4. Aft Cradle Tilt Actuator

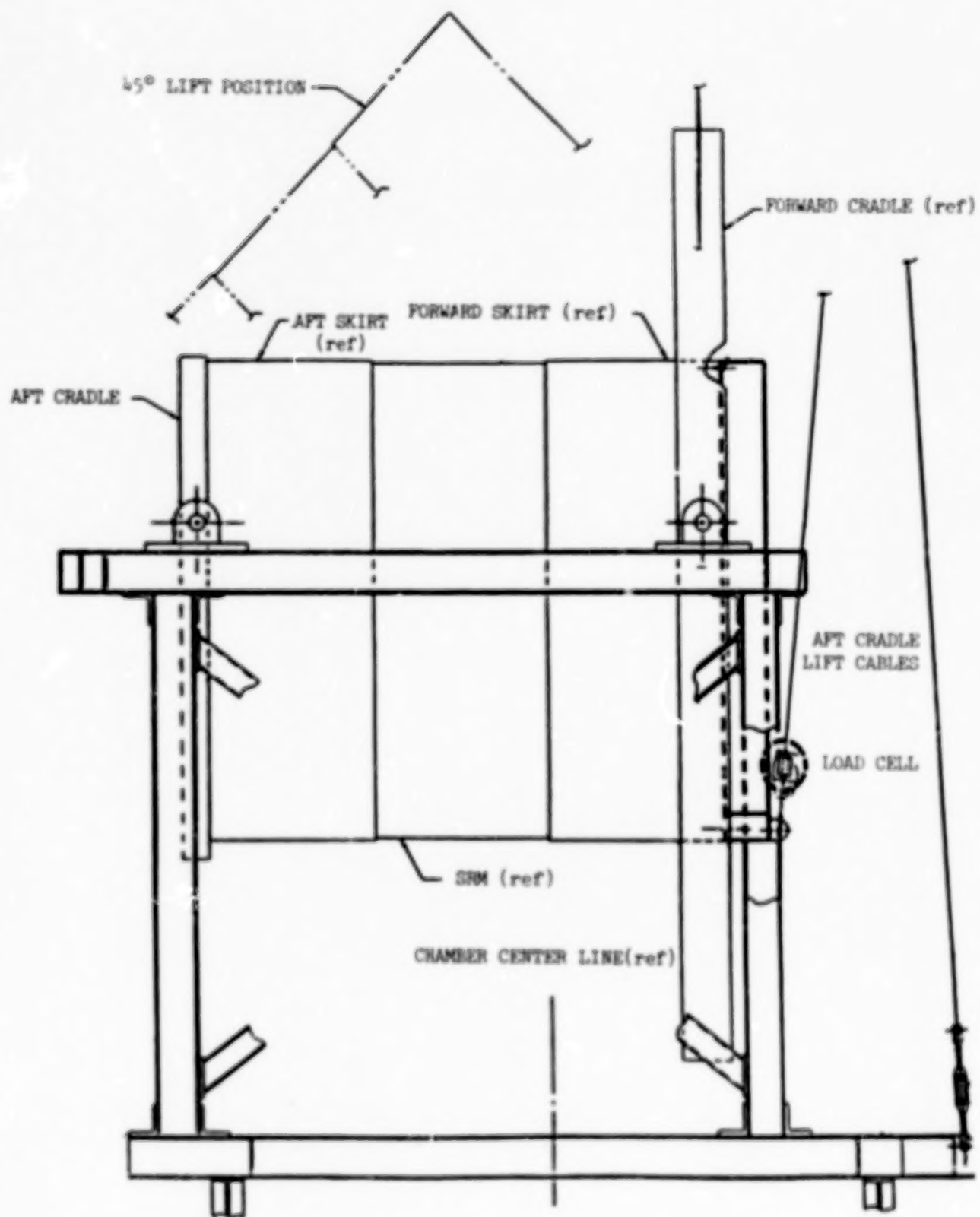


Figure 5. TOS in Chamber

SESSION X

PANEL DISCUSSION

Report Documentation Page

1. Report No. NASA CP-3096		2. Government Accession No.		3. Recipient's Catalog No.	
4. Title and Subtitle 16th Space Simulation Conference - Confirming Space Worthiness Into the Next Millennium				5. Report Date February 1991	
				6. Performing Organization Code 750	
7. Author(s) Joseph L. Stecher III, Editor				8. Performing Organization Report No. 90B00146	
				10. Work Unit No.	
9. Performing Organization Name and Address Goddard Space Flight Center Greenbelt, Maryland 20771				11. Contract or Grant No.	
				13. Type of Report and Period Covered Conference Publication	
12. Sponsoring Agency Name and Address National Aeronautics and Space Administration Washington, D.C. 20546-0001				14. Sponsoring Agency Code	
15. Supplementary Notes Joseph L. Stecher III: NASA/GSFC, Greenbelt, Maryland, 20771.					
16. Abstract The Institute of Environmental Sciences' Sixteenth Space Simulation Conference, "Confirming Spaceworthiness Into the Next Millennium" provided participants with a forum to acquire and exchange information on the state-of-the-art in space simulation, test technology, thermal simulation and protection, contamination, and techniques of test measurements. The papers presented at this conference and the resulting discussions carried out the conference theme of "confirming spaceworthiness into the next millennium."					
17. Key Words (Suggested by Author(s)) Space Simulation Thermal Simulation Contamination Control Dynamic Testing				18. Distribution Statement Unclassified - Unlimited Subject Category 18	
19. Security Classif. (of this report) Unclassified	20. Security Classif. (of this page) Unclassified	21. No. of pages 480	22. Price A21		

468